NASA
Technical
Paper
2640

1986

Parametric Study of Afterbody/Nozzle Drag on Twin Two-Dimensional Convergent-Divergent Nozzles at Mach Numbers From 0.60 to 1.20

Odis C. Pendergraft, Jr.,
James R. Burley II,
and E. Ann Bare

Langley Research Center
Hampton, Virginia

National Aeronautics
and Space Administration

Scientific and Technical
Information Branch

SUMMARY

An investigation has been conducted in the Langley 16-Foot Transonic Tunnel to determine the effects of external nozzle flap geometry on the external afterbody/nozzle drag of nonaxisymmetric (two-dimensional) convergent-divergent exhaust nozzles having parallel external sidewalls installed on a generic twin-engine, fighter-aircraft model. Tests were conducted over a Mach number range from 0.60 to 1.20 and over an angle-of-attack range from -5° to 9°. Nozzle pressure ratio (ratio of jet total pressure to free-stream static pressure) was varied from jet off (1.0) to approximately 10.0, depending on Mach number.

Results of this investigation indicate the best subsonic-transonic performance was obtained by using the two largest circular arc radii and terminal boattail angles between 7.8° and 20°. Flow separation on the nozzle flaps was usually caused by the sudden nozzle flap angle change of the straight line boattails having boattail circular arc radii of zero, and the steep boattail terminal angles of the smaller radius circular arc boattails. This separation caused a performance degradation by increasing nozzle boattail pressure drag.

INTRODUCTION

Recent studies (refs. 1 to 12) have shown that nonaxisymmetric nozzles have potential for substantial improvements in nozzle-installed performance and facilitate easier installation for thrust vectoring and reversing for improved maneuverability and short-field takeoff and landing. The nonaxisymmetric (two-dimensional) convergent-divergent (2-D C-D) nozzles have demonstrated internal performance levels equivalent to axisymmetric nozzles. However, these nozzles may be heavier and have greater cooling requirements than axisymmetric nozzles. Incorporation of thrust vectoring and reversing produces a larger weight penalty for the axisymmetric nozzle system than for the 2-D C-D nozzle system. The overall result is equal or less total nozzle weight for the 2-D C-D nozzles. Since thrust vectoring and reversing may be a requirement for the next generation fighters, 2-D C-D nozzles have the potential for improved overall performance if external nozzle boattail drag remains the same or can be reduced. The improved contouring created by blending the rectangular nozzles into rectangular fuselage shapes formed by the ramp-type, side-mounted, two-dimensional inlets should make this goal attainable.

To determine the external drag characteristics of this type afterbody/nozzle shape, an investigation has been conducted to obtain the effects of upper and lower external nozzle flap geometry on the afterbody and external nozzle pressure coefficient distributions. The flap geometry was formed by a parametric combination of circular arcs and straight lines with the nozzle sidewalls having parallel external surfaces. Afterbody forces and moments were also measured by using a six-component strain-gauge balance. Nozzle drag force was computed from an incremental force summation by using the nozzle surface pressures. Nozzle internal performance was not determined since all nozzles were identical internally except for two afterburning configurations which had larger throat areas but the same exit-to-throat area ratios.

Tests were conducted in the Langley 16-Foot Transonic Tunnel at Mach numbers from 0.60 to 1.20 and over an angle-of-attack range from -5° to 9°. Nozzle pressure ratio was varied from 1.0 (jet off) up to approximately 10.0, depending on Mach number.

SYMBOLS

Model forces and moments are referenced to the stability-axis system. Symbols in parentheses are the ones used in the computer-generated plots.

C_D	drag coefficient, $\frac{\text{Drag}}{q_\infty S}$
$C_{D,aft}$	afterbody drag coefficient (measured by afterbody balance)
$C_{D,fA}$	afterbody skin friction drag
$C_{D,fn}$	nozzle skin friction drag coefficient
$C_{D,n}$	$= C_{D,pn} + C_{D,fn}$
$C_{D,pn}$	nozzle pressure drag coefficient
$C_{D,t}$	$= C_{D,aft} + C_{D,n}$
C_p	pressure coefficient, $\frac{p - p_\infty}{q_\infty}$
$\bar{c}$	wing mean geometric chord, 17.47 in.
l (|)	length, in.
M (MACH)	Mach number
p	surface static pressure, psi
$p_{t,j}$	jet total pressure, psi
p_∞	free-stream static pressure, psi
q_∞	free-stream dynamic pressure, psi
R	radius, in.
S	wing reference area, 664.4 in^2
w	width, in.
x	distance downstream from FS 66.54
Y	spanwise distance from model centerline, in.

α (ALPHA) model angle of attack, deg

β boattail angle, deg

Subscripts:

A afterbody

c chord

e nozzle exit

f flap

i arc and straight-line tangent point

n (N) nozzle

o circular arc center

t throat or terminal

Abbreviations:

A/B afterburning

BL butt line

conf. configuration

FS fuselage station

NPR nozzle pressure ratio, $p_{t,j}/p_\infty$

2-D C-D two-dimensional convergent-divergent

APPARATUS AND METHODS

Wind Tunnel

The experimental investigation was conducted in the Langley 16-Foot Transonic Tunnel, a single-return, continuous-flow, atmospheric-pressure wind tunnel with a slotted, octagonal test section and continuous air exchange for cooling. The wind tunnel has a variable airspeed up to a Mach number of 1.30. Test section plenum suction is used for speeds of Mach number 1.10 and above. A complete description of this facility and its operating characteristics can be found in references 13 and 14.

Model and Support System

A sketch of the wingtip-supported, twin-engine model with a typical nozzle installed is shown in figure 1(a) along with details of the jet simulation system

and balance arrangement. The overall model arrangement represents a typical twin-engine fighter with tail surfaces removed and faired-over twin side inlets. Figure 1(b) is a half-span sketch showing the wing planform geometry. The wing was mounted 1.75 inches above the model centerline, had an aspect ratio of 2.40, a taper ratio of 0.43, and an NACA 64-series airfoil with thickness ratio of 0.067 near the root. The outboard area of the wing from BL 11.00 to the support booms at BL 20.00 increased from thickness ratio 0.077 to 0.10 for structural support and for compressed air and instrumentation passages.

The model fuselage is composed of five major parts located as follows:

Model part	Fuselage station, in.
Forebody	0.00 to 28.00
Wing-centerbody	28.00 to 44.75
Main balance block	44.75 to 48.25
Afterbody	48.25 to 66.04
Nozzle	66.54 to exit

The wing-centerbody together with the twin support booms formed the bifurcated-sting model support system. A complete description of this support system can be found in references 6 and 13. The forebody, the faired inlets, and the wing-centerbody form the nonmetric (not mounted on the force balance) portion of the twin-engine fighter model.

What normally would be the "metric" nozzle assembly was attached to the nonmetric centerbody by a six-component strain-gauge balance, carrying the balance block, and referred to as the "main balance" in section A-A of figure 1(a). However, for this investigation the air-line bellows assemblies were replaced with rigid air pipes, grounding the balance block, air pipes, and nozzles, and preventing the use of the main balance to measure nozzle thrust-minus-drag forces and moments. A second strain-gauge balance was mounted to the main balance block between the air pipes and used to measure forces and moments acting on the afterbody shell only. Clearance was provided between the metric and nonmetric portions of the model to prevent balance fouling. The clearance gap in the external shell was sealed with a Teflon polymer strip inserted into grooves machined in the nonmetric centerbody (FS 44.75), both forward and aft edges of the balance block, and the forward edge of the metric afterbody (FS 48.25). This prevented external flow from entering the model. The afterbody/nozzle clearance gap (FS 66.04) was sealed in the same manner as the centerbody/balance block, and balance block/afterbody junctions.

Photographs of the model installed in the test section of the Langley 16-Foot Transonic Tunnel are presented in figure 2. The twin-engine afterbody shown in figure 3 was designed to be representative of current fighters and also to house the propulsion simulation system, afterbody balance, and related instrumentation. The afterbody is constant in width so that all decrease in cross-sectional area (closure) is accounted for on the top and bottom surfaces. This closure was achieved with a circular arc radius of 22.95 inches starting at FS 57.19 and blending into a 5° boattail at FS 59.19. The boattail angle on the upper and lower surfaces remained constant from FS 59.19 to the end of the afterbody at FS 65.94. (See fig. 3(a).) Only the upper and lower surfaces were instrumented on the afterbody. (See fig. 3(b).)

Figure 4(a) presents a sketch and table giving geometry of the two-dimensional convergent-divergent (2-D C-D) nozzle models tested. All 21 configurations were designed to have the same internal nozzle expansion ratio. Configurations 1 and 16 represented afterburning (A/B) power nozzles, whereas all other nozzles are dry power configurations having identical internal nozzle geometry.

Twin-Engine Propulsion Simulation System

An external high-pressure air supply system provided the nozzles with a continuous flow of clean dry air at a controlled temperature of 70°F. Two remotely operated flow-regulating valves were used to balance the jet total pressure in the left- and right-hand nozzles. The airflow paths can be followed by using the sketch in figure 1(a). Compressed air flowed through the wingtip support booms, then through each side of the wing into the two solid pipes, which replaced the bellows assemblies, then to the tailpipes, into the circular-to-rectangular transition section, and finally through the nozzle configuration being tested. The air was used to simulate exhaust flow over a range of nozzle pressure ratios (NPR's) from about 1.0 (jet off) up to about 10.0, depending on Mach number.

Instrumentation

Forces and moments on the afterbody were measured by using a six-component strain-gauge balance rigidly mounted on the main balance block between the nozzle tailpipes. Static pressures were measured in the seal gaps at FS 48.25 and FS 66.04 and at several locations inside the afterbody to correct for tare forces created in these areas. Figure 4(b) shows the locations for the 23 static-pressure orifices on the top flap and the 11 orifices on the bottom flap of each nozzle. Each orifice, identified by a particular number, was located at the same ratio of nozzle length (x/ℓ_n), regardless of nozzle configuration. Jet exhaust conditions were measured in the instrumentation section (fig. 4(a)) upstream of each nozzle. Instrumentation consisted of a total-temperature probe and a total-pressure rake in each section. Each rake contained four total-pressure probes.

Data Reduction

All data from the model and wind-tunnel-facility instrumentation were recorded simultaneously on magnetic tape. For each data point, 50 frames of data were taken over a period of 5 seconds and the average value was used for computation.

The afterbody balance measured external aerodynamic and internal forces on the afterbody shell between FS 48.30 and FS 65.94. External forces on the afterbody were corrected for internal forces created by the difference between free-stream static pressure and the local pressures acting on the internal seal areas at either end of the afterbody and the external seal gaps at the same fuselage stations.

The external static-pressure orifice data on the right-hand nozzle were used to compute external force coefficients on the entire nozzle by a numerical summation of the local nozzle static-pressure coefficients multiplied by a projected area assigned to each of the orifices on the nozzle and all divided by the reference area. Flow on the model was assumed to be symmetrical right to left; therefore, each orifice was assigned both right- and left-side areas appropriate to the particular orifice.

Normal and axial projected areas were used to compute drag coefficient data used in this report.

Nozzle skin friction drag $C_{D,fn}$ and afterbody skin friction drag $C_{D,fA}$ were computed by using the method of Frankl and Voishel for compressible, turbulent flow on a flat plate, as described in reference 15. Tables I and II present nozzle $C_{D,fn}$ and total $C_{D,fA} + C_{D,fn}$ skin friction drag, respectively, for all the configurations at each Mach number.

Model angle of attack α was computed from an attitude indicator located inside one of the boom fairings and corrected for 0.1° flow angularity, which is the average angle measured in the 16-Foot Transonic Tunnel.

Test Conditions

This investigation was conducted in the Langley 16-Foot Transonic Tunnel at free-stream Mach numbers of 0.60, 0.70, 0.80, 0.85, 0.90, and 1.20. The nozzle pressure ratio was varied from 1.0 (jet off) to 10.0, depending on free-stream Mach number, with maximum NPR of 5.0 at $M = 0.60$ and maximum NPR of 10.0 at $M = 1.20$. The angle of attack was varied from -5° to 9° only at $M = 0.60$, 0.90, and 1.20. At all other Mach numbers, angle of attack was held constant at 0°.

Boundary-layer transition was fixed on the model in accordance with the criteria of reference 16 by means of 0.10-inch-wide strips of No. 120 silicon carbide grit sparsely distributed in a lacquer film, located 1 inch from the forebody nose and in a straight line along the wing leading edge from 0.05c at the root to 0.10c at the tip (where c is local chord). The average Reynolds number per foot varied from 2.1×10^6 to 4.2×10^6.

PRESENTATION OF RESULTS

Surface static-pressure coefficient data for this investigation are presented graphically in figures 5 to 46. Pressure coefficient distributions for the rows closest to the model centerline are presented in figures 5 to 25. Orifices of row 2 were located on the top surfaces, whereas orifices of row 7 (afterbody) and row 8 (nozzle) were located on the bottom surfaces. (See figs. 3(b) and 4(b) for row locations.) Data are presented at $M = 0.60$, 0.90, and 1.20 as pressure coefficient plotted against orifice longitudinal location divided by afterbody or nozzle length as appropriate. Afterbody length (18.24 inches), which includes a 0.1-inch metric gap and 0.5 inch of the instrumentation section, and nozzle length beginning at the nozzle connect station FS 66.54 (nozzle length variable with configuration) are indicated at the bottom of the figures for reference. Data are plotted at angles of attack from -5° to 9° as indicated by the various symbols but at only one nozzle pressure ratio - the one typical of operation at each Mach number.

Pressure coefficient distributions on each nozzle row, also plotted against orifice longitudinal location divided by nozzle length for each configuration at $M = 0.60$, 0.70, 0.80, 0.85, 0.90, and 1.20 are given in figures 26 to 46. For these data all plots are at $\alpha = 0°$, and the various symbols indicate the values of NPR from 1.0 (jet off) to 5.00 at $M = 0.60$ and up to 10.0 at $M = 1.20$.

The variation of total afterbody/nozzle drag coefficient and nozzle drag coefficient with nozzle pressure ratio and angle of attack is presented for

M = 0.60, 0.80, 0.90, and 1.20 in figures 47 to 67. Data were taken at $\alpha = 0°$ when NPR was varied; data were only taken at NPR = 1.0 (jet off) and the operating NPR for the particular Mach number when α was varied. Data were only taken for $\alpha = 0°$ at M = 0.80. Total afterbody/nozzle drag coefficient $C_{D,t}$ data are indicated by the circles, and the nozzle drag coefficient $C_{D,n}$ data are indicated by the squares. For figures 47 to 70, afterbody drag was derived from the afterbody balance measurements, and nozzle forces were obtained from the numerical summation process and computed skin friction drag as described in the section "Data Reduction."

Since the nozzle external shapes for the 21 configurations represent a parametric variation of three variables the data are compared in a similar manner in the remaining figures. The external nozzle shape parameters varied for this investigation include radius of curvature R, nozzle chord angle β_c, and nozzle terminal angle β_t. By careful selection of the combinations, it is possible to explore the following effects:

1. Varying terminal angle with constant radius of curvature

2. Varying nozzle length with constant terminal angle

3. Varying radius of curvature with constant chord angle and nozzle length

The following table shows how the data for the dry power configurations are arranged to achieve the appropriate comparison for each figure. See figure 4 for the exact dimensions of these parameters which have been rounded off to improve readability of the table. In figures 68 to 70 data are presented only for $\alpha = 0°$.

Figure	Constant	Value of constant	Configuration	Variable	Value of variable
68	R	0.0 in.	2, 3, 4, 5	β_t	10°, 12.5°, 15°, 20°
		3.8 in.	21, 20, 19		10.1°, 15.7°, 22.6°
		7.5 in.	17, 8, 7, 6		10.2°, 16.8°, 20°, 35°
		14.8 in.	11, 10, 9		10.5°, 15°, 25°
		23.5 in.	18, 12		12.5°, 20°
		43.9 in.	15, 14, 13		7.8°, 10°, 15°
69	β_t	10°	2, 17 (10.2°), 21 (10.1°), 14	l_n	7.5, 7.5, 7.5, 8.5 in.
		12.5°	3, 18		6.0, 6.9 in.
		15°	4, 10, 13		5.0, 5.8, 7.5 in.
		20°	5, 7, 12		3.6, 4.4, 6.0 in.
70	β_c, l_n	10°, 7.5 in.	2, 21, 17, 11, 13	R	0.0, 3.8, 7.5, 14.8, 43.9 in.
		12.5°, 6.0 in.	3, 12		0.0, 23.5 in.
		15°, 5.0 in.	4, 20, 8, 9		0.0, 3.8, 7.5, 14.8 in.
		20°, 3.6 in.	5, 19, 6		0.0, 3.8, 7.5 in.

DISCUSSION

Afterbody/Nozzle Pressure Distributions

Surface static-pressure coefficient distributions along the top and bottom surfaces from the rows nearest the model centerline are given in figures 5 to 25. Row 2 on the top surface of the afterbody and nozzle and row 7 on the bottom surface of the afterbody were 2.50 inches to the right of the model centerline, looking upstream, and row 8 on the bottom surface of the nozzle was 0.833 inch to the right of the model centerline. For these figures, the afterbody begins at FS 48.30 ($x_A/l_A = -1.0$) and ends at the nozzle connect station FS 66.54 ($x_A/l_A = 0$). Data are shown only for $M = 0.60$, 0.90, and 1.20 at the respective operating NPR's of 3.00, 5.00, and 8.00 for each of the 21 configurations.

The pressure coefficient distributions show an expansion at around x_A/l_A of -0.4 to -0.5 where the afterbody upper and lower surfaces are curved to obtain the 5° approach angle at the nozzle connect station. (See fig. 3(a) for details.) The pressure coefficients then recover to slightly below zero for both subsonic Mach numbers before decreasing again as the flow approaches the beginning of the nozzle, where closure rate again changes. There was some effect of angle of attack on the distributions near the beginning of the afterbody, especially for $M = 1.20$, but these effects diminished downstream of the curved afterbody surfaces and, at $M = 0.60$ and 0.90, nearly disappeared just ahead of the nozzles. This indicates that at least for subsonic conditions, the flow is well established and any effects exhibited on the nozzles should be a result of the nozzle shapes and not forebody or afterbody effects. For $M = 1.20$, there are substantial effects on the flow ahead of the nozzles and therefore some carry over onto the nozzles. These effects appear to be approximately the same for all configurations; therefore, flow effects of nozzle geometry changes should be independent of these upstream flow effects. Figures 6 through 9 show the data for the nozzles having $R = 0.0$, hence an abrupt change in boattail angle at the nozzle connect station (FS 66.54) occurs. The nozzle boattail angles, respectively, for each figure are 10°, 12.5°, 15°, and 20°, representing changes in boattail angle of 5°, 7.5°, 10°, and 15°. In spite of the sudden change in surface angle, none of the data show conclusive evidence of flow separation (i.e., a change to constant C_p level) on the nozzles with variation of angle of attack at the operating NPR. Further discussion of this phenomenon is included for the nozzle data where NPR is varied, additional Mach numbers are included, and all seven rows of nozzle pressure coefficient data are available for study (figs. 26 to 46).

The next group of figures (figs. 10, 11, and 12) include most of the nozzles with the steepest and shortest boattails, including configurations 6, 7, and 8 with $\beta_t = 35°$, 20°, and 16.8°, respectively. These nozzles should show the strongest evidence of separation on the boattails, especially configuration 6 where $\beta_t = 35°$. Separation is evident, by the flat C_p distributions, on the downstream part of the nozzle at all three Mach numbers for configuration 6 (fig. 10), but the other two configurations are not so consistent, with only the $M = 1.20$ data showing good evidence of flow separation. (See figs. 11(c) and 12(c).) The remainder of the configurations yield similar results with most nozzles showing pressure recovery at subsonic Mach numbers and mixed results for $M = 1.20$. The data shown in these figures demonstrate that angle-of-attack effects near the center of the upper and lower surfaces are minimal except at $M = 1.20$.

Nozzle Pressure Distributions

Surface static-pressure coefficient distributions for all seven orifice rows around the nozzles are given in figures 26 to 46. The rows were all to the right of the model centerline, looking upstream, and are arranged in a similar manner in the figure. Row 1 is on the top flap nearest the model centerline and row 4 is nearest the right-hand edge of the top surface. Similarly, row 8 is on the bottom flap nearest the centerline and row 5 is nearest the right-hand edge of the bottom surface. Row 7, which was included on the bottom surface of the afterbody was not installed on the nozzles, and hence, row 7 data do not appear in the figures. The locations of the rows can be found in figure 4(b). On these plots, all data are shown for $\alpha = 0°$ and symbols are used to indicate the NPR values. Therefore, these figures are used to determine the effects of varying Mach number, with data plotted for NPR = 1.0 (jet off) at M = 0.60, 0.70, 0.80, 0.85, 0.90, and 1.20. In addition, to determine the effects of varying NPR, jet-on data were taken at M = 0.60, 0.80, 0.90, and 1.20 for several NPR values ranging from 2.0 up to 10.0, depending on Mach number. The data points plotted at minus x_n/l_n values were located on the 1/2-inch-wide exposed surfaces of the instrumentation section (fig. 4) upstream of the nozzle connect station and are included in these plots to aid in fairing the nozzle boattail data. Where a corresponding nozzle orifice exists on the opposing row (i.e., top to bottom at same x_n/l_n or vice versa) but not on the row being studied, the data from the opposing row were used to aid in fairing the distributions.

In general, for most of the configurations, the flow moving outward around the outer edges of the upper and lower flaps causes a reduction in C_p as the flow approaches the nozzle exit; this can be seen by looking from the left side of the plot (near the model centerline) toward the right side of the plot (approaching the outer edge of the nozzle flap). This observation is especially true for the subsonic Mach numbers. Increasing Mach number causes NPR effects to become larger; this can be seen by comparing data for M = 0.60 with data for M = 0.90. For subsonic Mach numbers, the curve shapes are similar, but increasing NPR raises C_p more at M = 0.90 than at M = 0.60. (Compare for example fig. 26(a) with 26(e) or 29(a) with 29(e).) This increase is particularly noticeable near the nozzle exits ($x_N/l_N = 0.90$). Effects of nozzle pressure ratio at M = 1.20 are also very pronounced; indications of shock-induced separation are shown by the separation location moving upstream with increasing NPR. At M = 1.20, this separation occurs further upstream on the steep boattails than on the shallower ones. For example, compare the distributions at M = 1.20 for figures 31(f) ($\beta_t = 35°$), 34(f) ($\beta_t = 25°$), 38(f) ($\beta_t = 15°$), and 40(f) ($\beta_t = 7.8°$). At NPR = 10 for figure 31(f) over half the nozzle surface appears to be separated, whereas for figure 40(f), only a small area near the exit is separated.

Another general effect occurs on all the configurations at M = 0.80 and NPR = 8.0 and on most of the configurations at M = 0.90 and NPR = 8.0. For example, see figure 27(c), row 1, at $x_N/l_N = 0.3$. At first glance, this appears to be bad data, but closer study of all the nozzle configurations, test notes, and leak check sheets, shows that this is not true. Also, data taken immediately before and after this particular data point, at other NPR's and Mach numbers show no evidence of this phenomenon. A problem with hardware, such as improper surface shape around an orifice, leaking tubes, or plugged orifices or tubes, would be configuration dependent or show up during leak checks.

This same effect also occurs at M = 0.90 at NPR = 8.0 but is much less noticeable and is not evident for configuration 7 (fig. 32(e)) or configuration 16 (fig. 41(e)). The fact that this only occurs at NPR = 8.0 and M = 0.80 and 0.90 is significant, but if data were available it should also be evident at other conditions. For instance, since it occurs at both M = 0.80 and M = 0.90, it should also happen at M = 0.85. At M = 0.80 and 0.90, small changes in NPR around 8.0 not recorded for this investigation should reveal more about the characteristics and origins of this phenomenon. The most reasonable explanation of this pressure spike is that a convergence of vortex flow off the nozzle edge and flow separation produced by the expanding nozzle exhaust plume caused the very localized high pressure. For M = 0.80, the highest pressure is evident on configuration 11 (fig. 36(c)) and the smallest increase is evident on configuration 14 (fig. 39(c)). These configurations are not different enough to suspect one of the geometry parameters to correlate with this effect. Both were intermediate in length, and both had boattail angles of about 10°. Other configurations that have large pressure spikes are 3, 4, 5, 8, 9, 12, 13, and 17. (See part (c) of figs. 28, 29, 30, 33, 34, 36, 37, 38, and 42.) Other configurations having small pressure increases are 7 and 16. (See figs. 32(c) and 41(c).)

For effects of the individual parameters, look first at figures 27 to 30 which include the pressure coefficient data for the nozzles with R = 0.0. These data were discussed in the previous section in relation to flow separation. Since there is a sudden change in boattail angle at the nozzle connect station (FS 66.54 or $x_N/l_N = 0$ in the figures) flow separation would be expected, especially for the steepest boattails (i.e., β_t and $\beta_c = 20°$ for configuration 5, fig. 30). A closer look at the figures reveals no further evidence of separation than that shown for the afterbody/nozzle pressure coefficient distributions of the same configurations discussed in the last section, except at M = 1.20. At M = 1.20, flow separation occurs at all values of NPR except jet off for configurations 1 to 3 (figs. 27(f) and 28(f)) and also occurs at jet-off conditions for configurations 4 and 5 (figs. 29(f) and 30(f)). These results indicate that for flow produced with this forebody/afterbody, flow separation on the nozzles begins at nozzle boattail angles of less than 7.8° for M = 1.20 but is not evident for subsonic Mach numbers at nozzle boattail angles of 20° for the range of NPR investigated and angle of attack of 0°. Further study of this phenomenon can be obtained by using the configurations with steeper terminal boattail angles β_t with values of R greater than zero. The nozzles, therefore, have curved upper and lower surfaces with smooth transition from the afterbody closure angle of 5° to the nozzle terminal angle instead of a sudden change to the terminal angle at the nozzle connect station. See the sketch in figure 4(a) for a diagram of the nozzle showing the relationship between these variables. For R = 0.0, β_t is the same as β_c, but as R increases, the difference between β_t and β_c increases until the nozzle flap is a full circular arc without any flat part at the exit.

The next three configurations (6, 7, and 8) are for R = 7.5 inches and include the nozzle having the steepest β_c and β_t angles (configuration 6). This nozzle is also one of four having full circular arc nozzle flaps (the others are configurations 9, 12, and 13). The distributions for configuration 6 show evidence of a small area of separation near the centerline at the nozzle exit for M = 0.60 (fig. 31(a)), and increasingly larger separated regions with increasing Mach number. At M = 1.20, the region is very large and the effects of NPR are very pronounced (fig. 31(f)).

The remainder of the configurations all show similar trends with only one other configuration worth mentioning. Configuration 15 had the longest nozzle and the smallest boattail angles ($\beta_c = 7.5°$, $\beta_t = 7.8°$); therefore, it caused the least flow disturbance. This can be seen by observing it had the least negative C_p values overall and also not very high positive C_p values.

Afterbody/Nozzle Drag

The variation of total afterbody/nozzle drag coefficient and nozzle drag coefficient with nozzle pressure ratio and angle of attack is presented for $M = 0.60$, 0.80, 0.90, and 1.20 in figures 47 to 67. Angle of attack was varied at jet off and at operating NPR for only $M = 0.60$, 0.90, and 1.20; therefore, the drag coefficient data versus angle of attack is not shown in part (a) of the figures for $M = 0.80$. Total afterbody/nozzle drag coefficient $C_{D,t}$ data are indicated by the circles, and the nozzle drag coefficient $C_{D,n}$ data are indicated by the squares. The symbols without ticks represent the jet-off (NPR = 1.0) conditions and the symbols with ticks represent jet-on conditions at operating NPR for each Mach number. Note that in these plots, $C_{D,n}$ includes nozzle pressure drag $C_{D,pn}$ plus nozzle friction drag $C_{D,fn}$, and $C_{D,t}$ also includes pressure and skin friction drag on the afterbody measured by the balance. Therefore, $C_{D,t}$ includes total friction and pressure drag on the complete afterbody/nozzle assembly for each configuration.

General effects can be seen on any of the plots in figures 47 to 67. The effect of NPR is typical of rectangular or round nozzles, with the highest drag occurring at jet-off conditions, then a sudden drop in drag as NPR approaches 2.0, then an increase up to NPR = 3.0, and then decreasing drag until the maximum NPR. This effect is due to filling the base area at very low NPR's, the entrainment (viscous) effects at NPR's up to about 2.0, and the plume effects for NPR greater than about 3.0. For most configurations at $M = 0.60$ and 1.20, angle of attack shows minimum total drag near $\alpha = 0°$ with increasing drag for positive or negative angles of attack. Some asymmetry is apparent in the figures, which is probably due to the high wing location distorting the flow. Many of the configurations show a reverse of the angle-of-attack effects for nozzle drag only, especially at $M = 0.90$. See, for example, the $M = 0.90$ data on the right-hand side of figure 49(b). Several configurations which do not have reverse curvature have very flat curves for nozzle drag coefficient plotted against angle of attack; this indicates only slight effects for the α test range (-5° to 9°). Since these data are repeated again in subsequent figures, in bar chart form, where they can be readily compared, no attempt will be made to compare configurations in this section. As mentioned earlier, these figures are most useful for observing the effects of nozzle pressure ratio and angle of attack at the various Mach numbers on nozzle and total afterbody/nozzle drag coefficients for each configuration.

Drag Comparisons for Nozzle Parameters

Figures 68 to 70 give a summary of afterbody/nozzle drag coefficient data in bar chart form to facilitate comparison of the various configurations grouped by the nozzle parameters desired. As indicated by the sketch at the top of each figure, nozzle pressure drag coefficient $C_{D,pn}$ is indicated by an open bar, afterbody drag coefficient $C_{D,aft}$ by a hatched bar, nozzle skin friction drag coefficient by a

solid bar, and total afterbody/nozzle drag coefficient $C_{D,t}$ by the arrow on the left side of the bar. Note that negative nozzle pressure drag coefficients are plotted below the $C_D = 0$ line, and this locates $C_{D,t}$ below the top of the bar. Configuration number is indicated at the bottom of each bar and other nozzle parameters are shown above the bars and below the groups of bars which are for constant values indicated.

Constant circular arc radius.- Figure 68 includes the data grouped together by constant R with increasing R for the groups from left to right. Values of constant R are indicated under each group of bars and include R = 0.0, 3.750, 7.496, 14.769, 23.488, and 43.850 inches. At the top of each bar is a number indicating the boattail terminal angle for the configuration number shown below the bar. For the R = 0.0 configurations at the left of the figure, β_c is the same as β_t. Since R was the only truly independent variable, this is the only summary figure that includes all configurations - even the afterburning nozzle configurations (1 and 16).

Since the afterburning configurations incorporate less closure than the dry power configurations, they should be among the lowest drag configurations, but configuration 1 is higher than about 10 others at all Mach numbers, whereas configuration 16 only exceeds 2 or 3 at subsonic conditions and is the lowest at M = 1.20. This difference between the two configurations is not surprising since configuration 1 is designed to match configuration 8 with the nozzle opened up to the desired throat and exit areas. This creates a kink in the upper and lower nozzle flaps where the circular arc joins the straight section ($x_i = 1.509$, fig. 4(a)). Configuration 16 on the other hand was designed to let the straight section blend into the circular arc at a tangent point further upstream ($x_i = 1.101$). This produces a slightly steeper boattail terminal angle (13.5° compared with 13.3°) but eliminates the surface kink at $x_i = 1.509$ on configuration 1. This demonstrates a definite advantage for a sliding hinge point nozzle hardware design as compared with the type more commonly used on axisymmetric hardware where the hinge point is fixed in the axial direction.

Comparing the effects of varying boattail terminal angle for constant R values can be done with figures 68(a) for M = 0.60, 68(b) for M = 0.90, and 68(c) for M = 1.20. At M = 0.60, for R = 0.0, increasing boattail terminal angle causes an increase in drag. This is generally true for the other values of R except for the A/B nozzles previously discussed and configurations 7, 8, 12, and 19. These configurations all have lower drag than the trends in each group seem to indicate, and they, also, all have boattail terminal angles near 20°. This seems to be the boattail angle region where maximum pressure recovery occurs unless upstream disturbances cause the flow to separate and hence the drag to increase. Comparing all the dry power configurations at M = 0.60 indicates the order of the five with the lowest total drag $C_{D,t}$ is configurations 15, 12, 8, 14, and 11. For M = 0.90 this order is 15, 14, 12, 18, and 11; and for M = 1.20 it is 7, 15, 12, 14, and 11. Clearly over the test Mach number range, configuration 15 has the lowest overall drag $C_{D,t}$ with configuration 12 second. Since configuration 12 is much shorter than configuration 15, it may be the most practical for use since it would also be lighter.

The configurations having the highest $C_{D,t}$ are 20, 5, 6, 19, and 9 with the highest listed first. Configuration 20, the worst one, had only a terminal angle of 15.7° and R = 3.8 inches, apparently too sudden a change in surface curvature. Configuration 5 had a 20° terminal angle and R = 0.0, whereas configuration 6 had

R = 7.5 inches but β_t = 35°. Configuration 19 had R = 3.8 inches and β_t = 22.6°, whereas configuration 9 had β_t = 25°. All these configurations seem to have either too large a value of β_t or too small a value of R, and this causes flow separation or insufficient pressure recovery. These results indicate that a value of β_t of 20° or less and the largest values of R (23 to 44 inches) provide the nozzle configuration with the best external performance.

Constant boattail terminal angle.- Figure 69 includes the data grouped together by constant β_t with increasing β_t from left to right in each group. Values of constant β_t are indicated under each group of bars including β_t = 10.0°, 12.5°, 15.0°, and 20.0°. At the top of each bar is a number indicating nozzle length l_n. Note that for the first group (β_t = 10°) configurations 2, 17, and 21 all have nearly the same l_n instead of increasing values. Also note that the values of β_t for configurations 17 and 21 are not exactly 10.0° (10.2 for configuration 17, and 10.1 for configuration 21). Since l_n is inversely proportional to β_c, this can also be given above the bars as an aid in determining the relationship to β_t. For all three Mach numbers, it is apparent that increasing l_n causes a decrease in total drag with only one exception. At M = 1.20, configuration 7 (l_n = 4.4) has lower drag than configuration 12 (l_n = 6.0). The only explanation for this must lie in the fact that these nozzles have β_t = 20.0° and therefore have flow in that critical region between attached and separated flow. Note in figure 69 that the first bar in each group is for a nozzle configuration having R = 0.0, the shortest length. It is apparent from this figure as noted before for the previous figure that for β_t = 20°, the disturbance resulting from the sudden angle change has a detrimental effect on drag for all three Mach numbers. (See the bar for configuration 5 in figs. 69(a), (b), and (c).) Although other configurations with β_t = 20° show some pressure recovery and negative pressure drag at M = 0.60 and 0.90, configuration 5 shows positive drag, especially at M = 0.90. At M = 1.20, the pressure drag increase is very much higher than any other configuration and it has the highest drag. This indicates that nozzles designed as short as possible, but with attached flow, must not have upstream disturbances and should not exceed about 20° boattail terminal angle.

Constant boattail chord angle and length.- Figure 70 includes the data grouped together by constant β_c with increasing β_c for the groups from left to right. Values of constant β_c are 10°, 12.5°, 15°, and 20°. At the top of each bar is a number indicating the boattail radius of curvature R for the configuration number shown below the bar. As in figure 69, l_n can be indicated along with β_c in this figure since they are inversely proportional.

In figure 70, part (b) for M = 0.90 illustrates clearly how boattail chord angle β_c and boattail arc radius R interact with each other. Note on the left side of the figure for β_c = 10°, that configuration 2 has the highest pressure recovery on the nozzle but also the highest afterbody drag and configuration 13, which has a full circular arc nozzle surface, has the least pressure recovery but also the lowest afterbody drag. At the other end of the plot for β_c = 20°, all values of R demonstrate positive pressure drag, but again increasing values of R cause a reduction in afterbody drag. This result demonstrates that when comparing the performance parameters not only the nozzle drag but the effects on the afterbody ahead of the nozzles must be considered for subsonic Mach numbers. A look at the other Mach numbers for this figure (M = 0.60 and 1.20) reveals no other significant trends in the data as plotted in figure 70.

CONCLUSIONS

An investigation has been conducted in the Langley 16-Foot Transonic Tunnel to determine the effects of external nozzle flap geometry on the external afterbody/nozzle drag of nonaxisymmetric convergent-divergent exhaust nozzles having parallel external sidewalls installed on a generic twin-engine, fighter-aircraft model. Tests were conducted over a Mach number range from 0.60 to 1.20 and over an angle-of-attack range from -5° to 9°. Nozzle pressure ratio was varied from jet off (1.0) to approximately 10.0, depending on Mach number. The results of this investigation indicate the following conclusions:

1. For the generic twin-engine fighter model used in this investigation, the flow was well established, at least for subsonic conditions, and any effects exhibited on the nozzles should be a result of the nozzle shapes and not forebody or afterbody effects.

2. A comparison between the two afterburning nozzle configurations tested demonstrated a definite advantage for a sliding hinge point nozzle hardware design, as compared with the fixed hinge point design more commonly used on past designs.

3. The nozzle having the longest boattail and hence the shallowest boattail angle had the lowest drag. However, taking into account weight and balance penalties could make shorter length nozzles more practical. This would include nozzles having circular arc radii between 23 and 44 inches, for this model scale, and boattail terminal angles between 7.8° and 20°.

4. For nozzles designed as short as possible, but with attached flow, upstream disturbances must be minimized and boattail terminal angles should not exceed 20°.

5. When comparing nozzles to determine which produce minimum drag, the effects of the nozzle shape on the drag of the afterbody ahead of the nozzles must also be taken into account for subsonic Mach numbers.

NASA Langley Research Center
Hampton, VA 23665-5225
August 19, 1986

REFERENCES

1. Pendergraft, Odis C., Jr.: Comparison of Axisymmetric and Nonaxisymmetric Nozzles Installed on the F-15 Configuration. AIAA Paper 77-842, July 1977.

2. Berrier, Bobby L.; Palcza, J. Lawrence; and Richey, G. Keith: Nonaxisymmetric Nozzle Technology Program - An Overview. AIAA Paper 77-1225, Aug. 1977.

3. Stevens, H. L.: F-15/Nonaxisymmetric Nozzle System Integration Study Support Program. NASA CR-135252, 1978.

4. F-15 2-D Nozzle System Integration Study. Volume I - Technical Report. NASA CR-145295, 1978.

5. Capone, Francis J.: The Nonaxisymmetric Nozzle - It Is for Real. AIAA Paper 79-1810, Aug. 1979.

6. Yetter, Jeffrey A.; and Leavitt, Laurence D.: Effects of Sidewall Geometry on the Installed Performance of Nonaxisymmetric Convergent-Divergent Exhaust Nozzles. NASA TP-1771, 1980.

7. Stevens, H. L.; Thayer, E. B.; and Fullerton, J. F.: Development of the Multi-Function 2-D/C-D Nozzle. AIAA Paper 81-1491, July 1981.

8. Capone, Francis J.; Hunt, Brian L.; and Poth, Greg E.: Subsonic/Supersonic Non-vectored Aeropropulsive Characteristics of Nonaxisymmetric Nozzles Installed on an F-18 Model. AIAA Paper 81-1445, July 1981.

9. Nelson, B. D.; and Nicolai, L. M.: Application of Multi-Function Nozzles to Advanced Fighters. AIAA Paper 81-2618, Dec. 1981.

10. Re, Richard J.; and Leavitt, Laurence D.: Static Internal Performance Including Thrust Vectoring and Reversing of Two-Dimensional Convergent-Divergent Nozzles. NASA TP-2253, 1984.

11. Carson, George T., Jr.; Capone, Francis J.; and Mason, Mary L.: Aeropropulsive Characteristics of Nonaxisymmetric-Nozzle Thrust Reversers at Mach Numbers From 0 to 1.20. NASA TP-2306, 1984.

12. Leavitt, Laurence D.: Summary of Nonaxisymmetric Nozzle Internal Performance From the NASA Langley Static Test Facility. AIAA Paper 85-1347, July 1985.

13. Peddrew, Kathryn H., compiler: A User's Guide to the Langley 16-Foot Transonic Tunnel. NASA TM-83186, 1981.

14. Corson, Blake W., Jr.; Runckel, Jack F.; and Igoe, William B.: Calibration of the Langley 16-Foot Transonic Tunnel With Test Section Air Removal. NASA TR R-423, 1974.

15. Shapiro, Ascher H.: The Dynamics and Thermodynamics of Compressible Fluid Flow. Volume II. Ronald Press Co., c.1954.

16. Braslow, Albert L.; Hicks, Raymond H.; and Harris, Roy V., Jr.: Use of Grit-Type Boundary-Layer-Transition Trips on Wind-Tunnel Models. NASA TN D-3579, 1966.

TABLE I.- NOZZLE SKIN FRICTION DRAG COEFFICIENTS

Conf.	$C_{D,fn}$ for M of -					
	0.60	0.70	0.80	0.85	0.90	1.20
1	0.0026	0.0028	0.0029	0.0029	0.0031	0.0113
2	.0013	.0012	.0011	.0009	.0006	.0082
3	.0014	.0015	.0014	.0012	.0011	.0114
4	.0018	.0018	.0015	.0015	.0020	.0139
5	.0016	.0016	.0021	.0026	.0034	.0140
6	.0028	.0027	.0027	.0024	.0023	.0124
7	.0005	.0004	.0003	.0005	.0007	.0060
8	.0005	.0009	.0008	.0014	.0013	.0094
9	.0034	.0034	.0032	.0031	.0043	.0114
10	.0022	.0023	.0023	.0022	.0020	.0129
11	.0013	.0014	.0014	.0013	.0011	.0085
12	.0008	.0007	.0006	.0004	.0002	.0073
13	.0019	.0020	.0022	.0020	.0020	.0092
14	.0012	.0012	.0013	.0012	.0009	.0076
15	.0007	.0007	.0007	.0007	.0004	.0051
16	.0012	.0013	.0013	.0013	.0015	.0067
17	.0015	.0015	.0016	.0015	.0013	.0089
18	.0017	.0018	.0018	.0017	.0015	.0102
19	.0024	.0026	.0028	.0031	.0035	.0126
20	.0037	.0038	.0040	.0041	.0056	.0162
21	.0011	.0011	.0011	.0010	.0007	.0084

TABLE II.- TOTAL SKIN FRICTION DRAG COEFFICIENTS

Conf.	$C_{D,fA} + C_{D,fn}$ for M of -					
	0.60	0.70	0.80	0.85	0.90	1.20
1	0.0031	0.0033	0.0034	0.0033	0.0035	0.0117
2	.0020	.0019	.0017	.0015	.0013	.0088
3	.0020	.0021	.0019	.0018	.0016	.0119
4	.0023	.0023	.0020	.0019	.0025	.0144
5	.0020	.0020	.0025	.0030	.0038	.0143
6	.0032	.0031	.0030	.0028	.0026	.0128
7	.0010	.0008	.0008	.0010	.0012	.0064
8	.0010	.0014	.0013	.0019	.0018	.0099
9	.0039	.0039	.0037	.0036	.0048	.0118
10	.0028	.0029	.0028	.0027	.0025	.0134
11	.0020	.0021	.0021	.0020	.0017	.0091
12	.0013	.0013	.0012	.0009	.0007	.0078
13	.0027	.0027	.0028	.0027	.0027	.0098
14	.0020	.0020	.0020	.0019	.0017	.0083
15	.0017	.0016	.0016	.0016	.0012	.0059
16	.0018	.0018	.0018	.0017	.0020	.0071
17	.0022	.0022	.0022	.0021	.0019	.0095
18	.0024	.0024	.0025	.0023	.0022	.0108
19	.0028	.0030	.0032	.0034	.0039	.0129
20	.0042	.0043	.0045	.0046	.0061	.0166
21	.0018	.0018	.0018	.0016	.0014	.0091

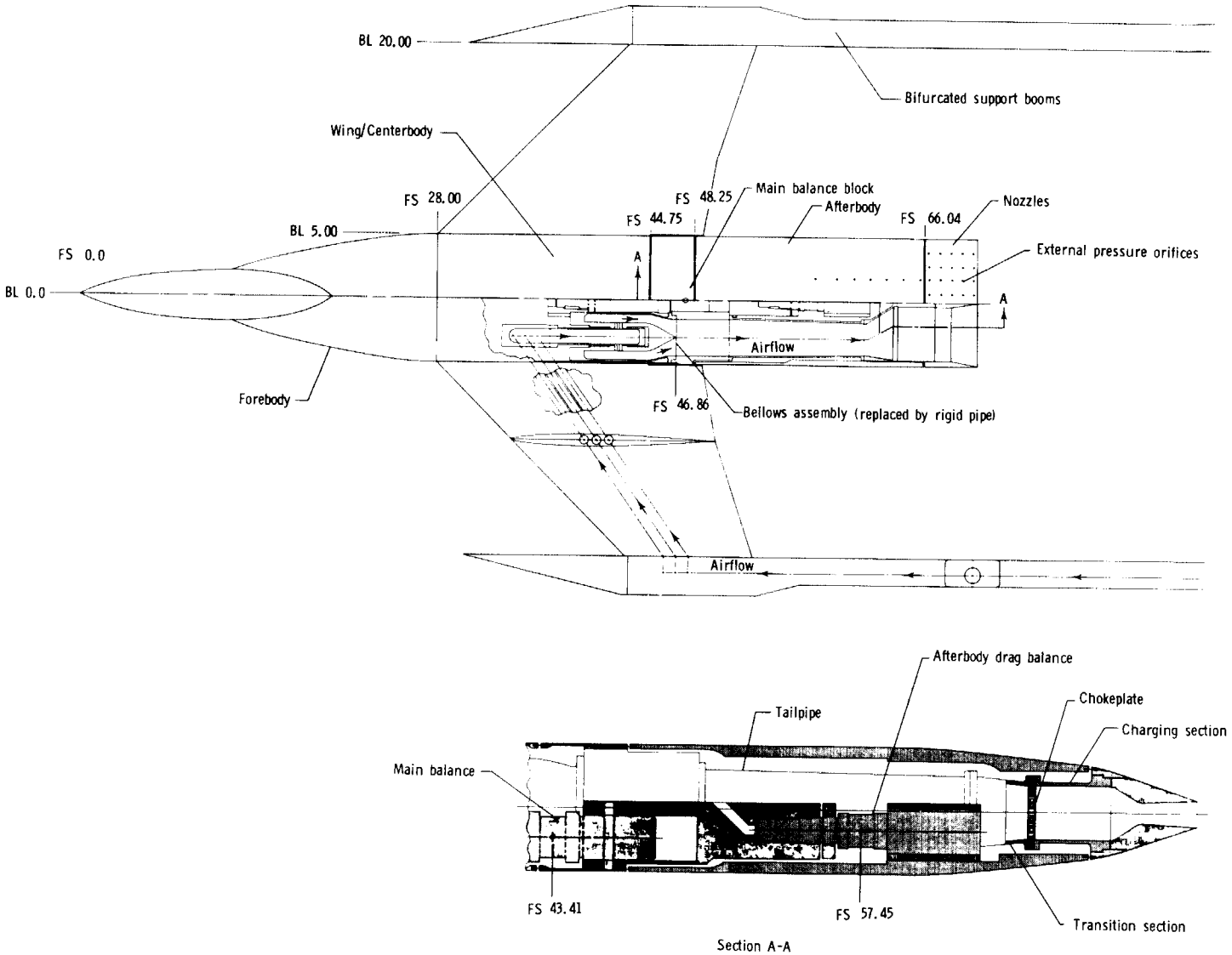

(a) Jet simulation system and balance arrangement.

Figure 1.- Sketch of air-powered, twin-engine, wingtip-supported model with two-dimensional convergent-divergent nozzles. Linear dimensions are in inches.

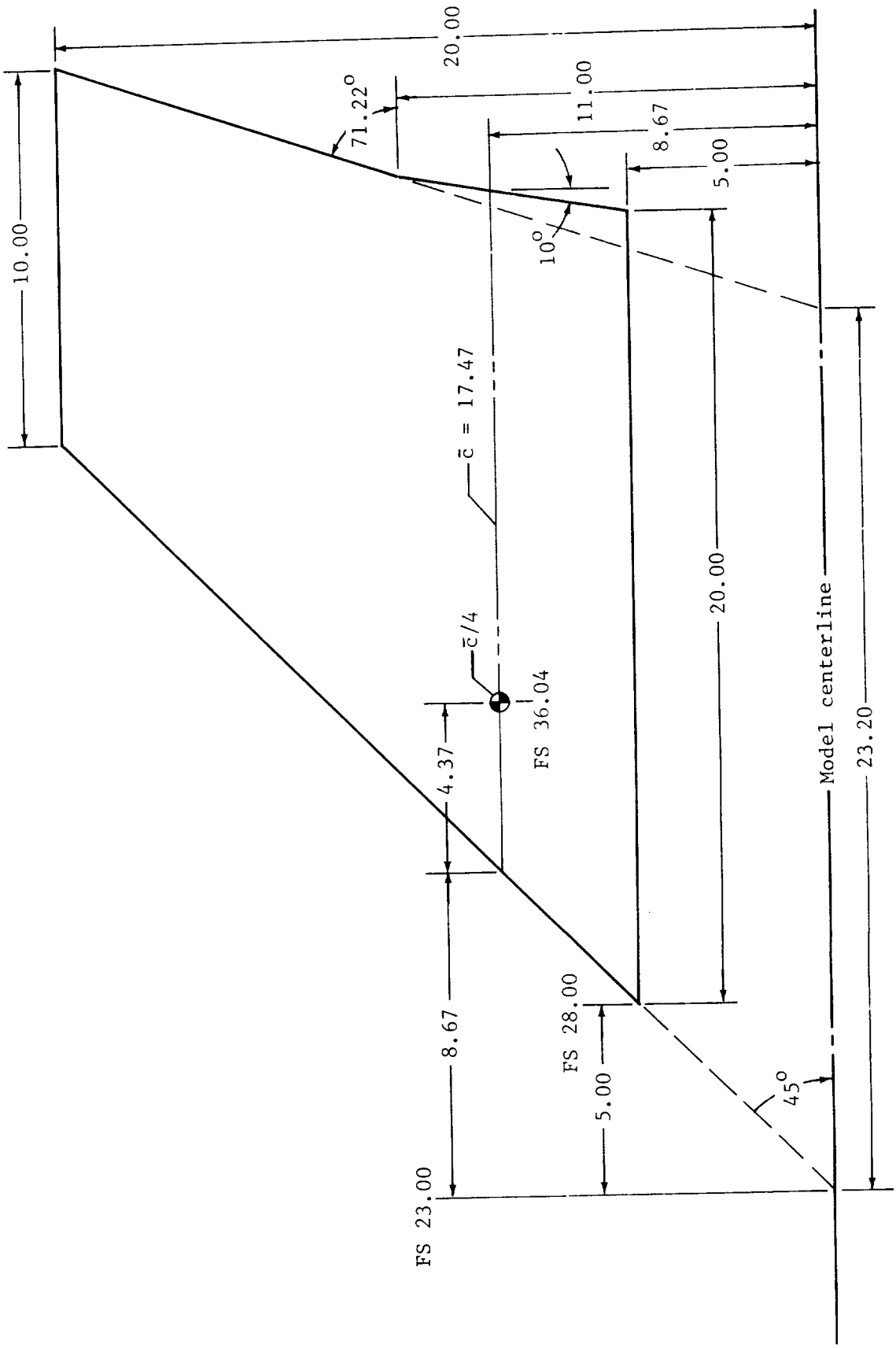

(b) Wing planform geometry.

Figure 1.- Concluded.

L-81-4089

Upstream view

L-81-4090

Downstream view

Figure 2.- Two-dimensional convergent-divergent nozzle installed on twin-engine wingtip-supported fighter model in test section of Langley 16-Foot Transonic Tunnel.

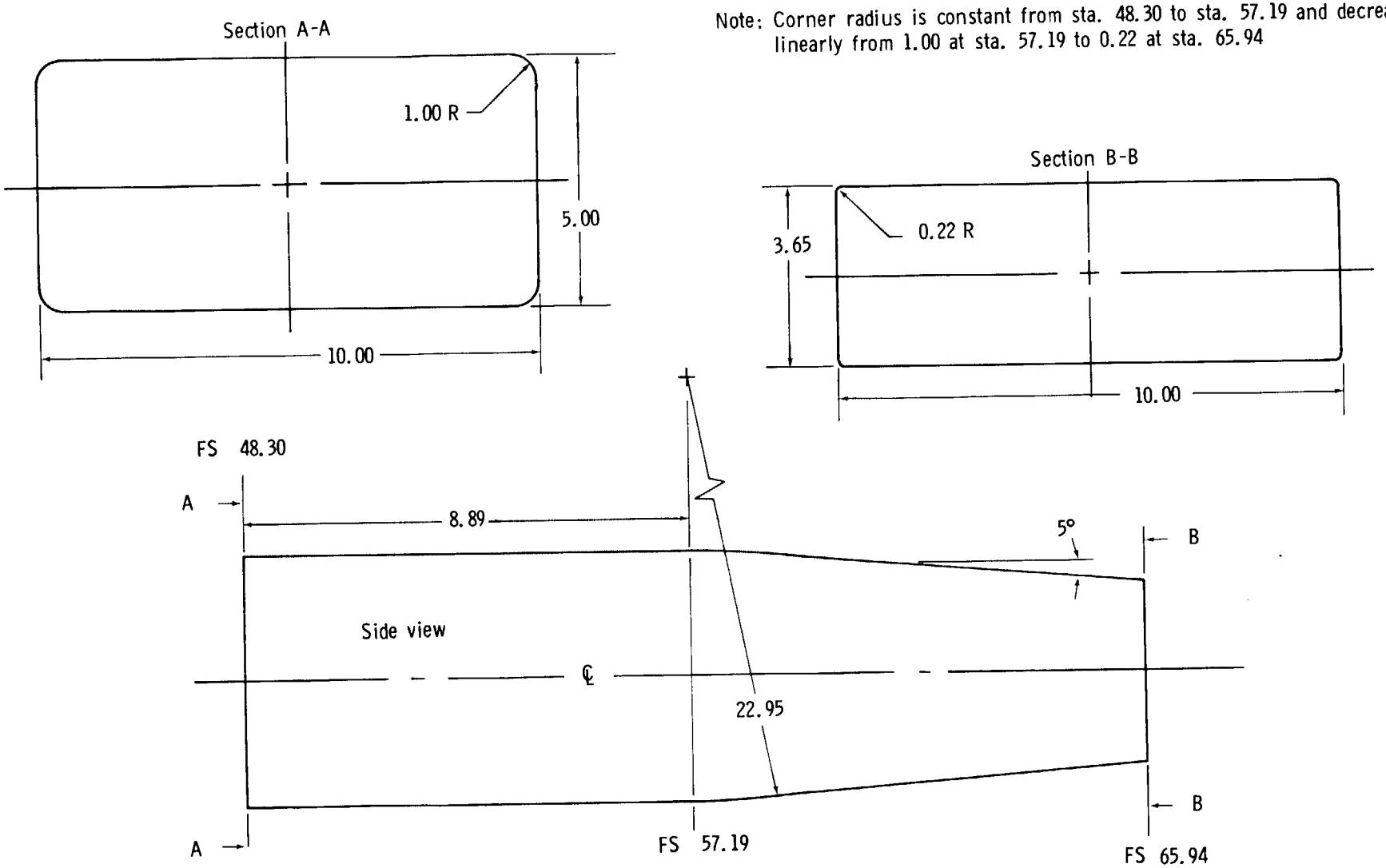

(a) Geometric details.

Figure 3.- Afterbody geometric description and static-pressure orifice locations. Linear dimensions are in inches.

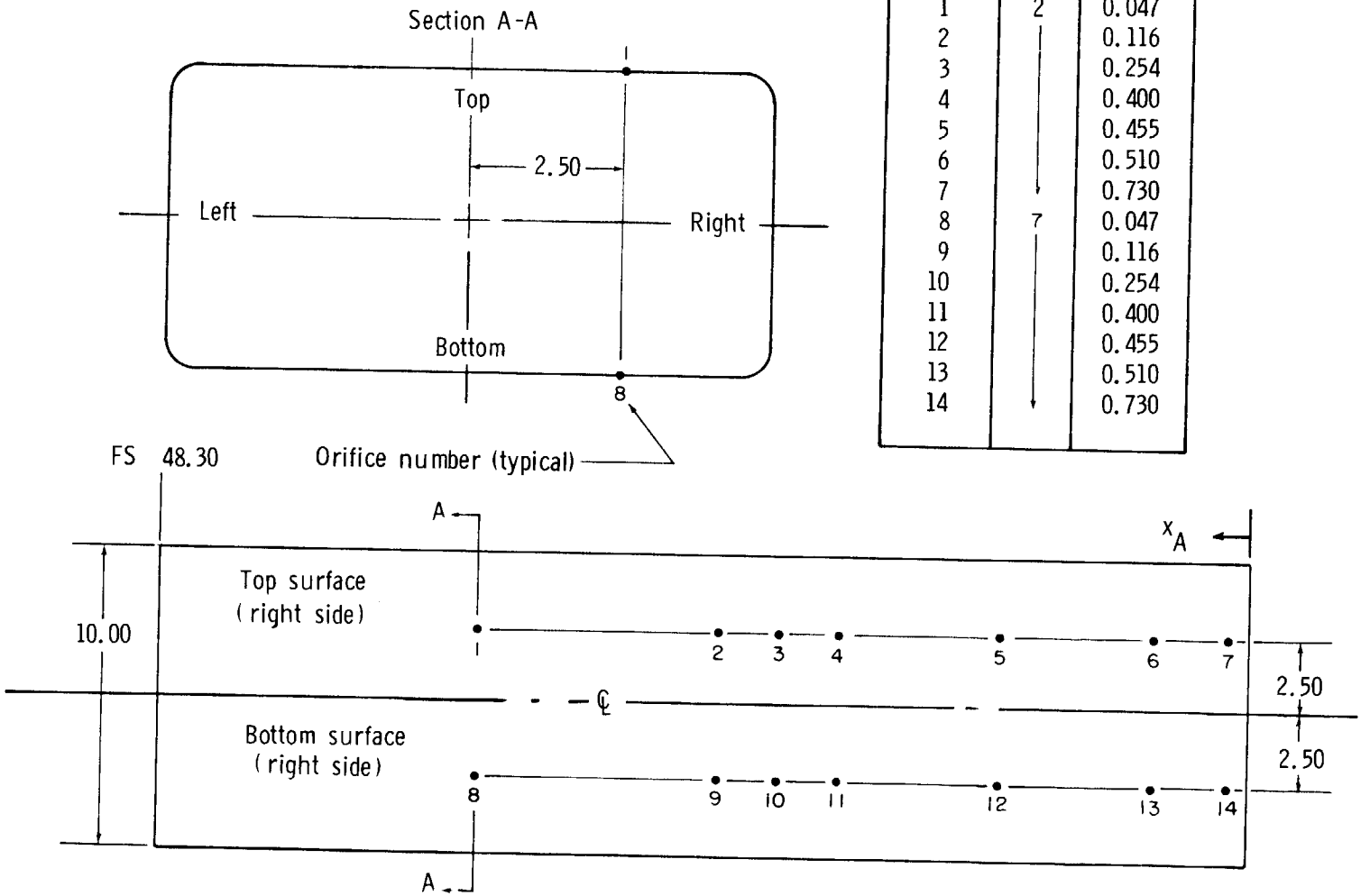

Orifice	Row	x_A/l_A
1	2	0.047
2		0.116
3		0.254
4		0.400
5		0.455
6		0.510
7		0.730
8	7	0.047
9		0.116
10		0.254
11		0.400
12		0.455
13		0.510
14		0.730

(b) Orifice locations.

Figure 3.- Concluded.

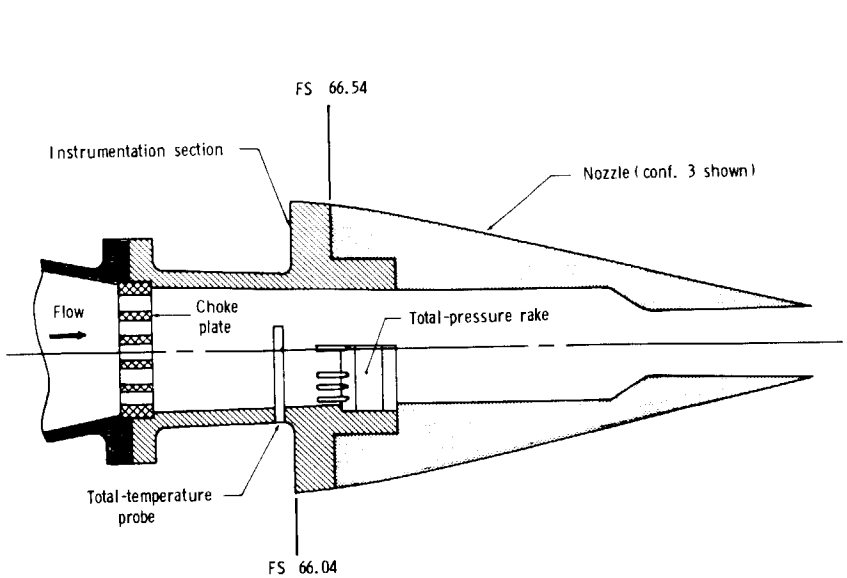

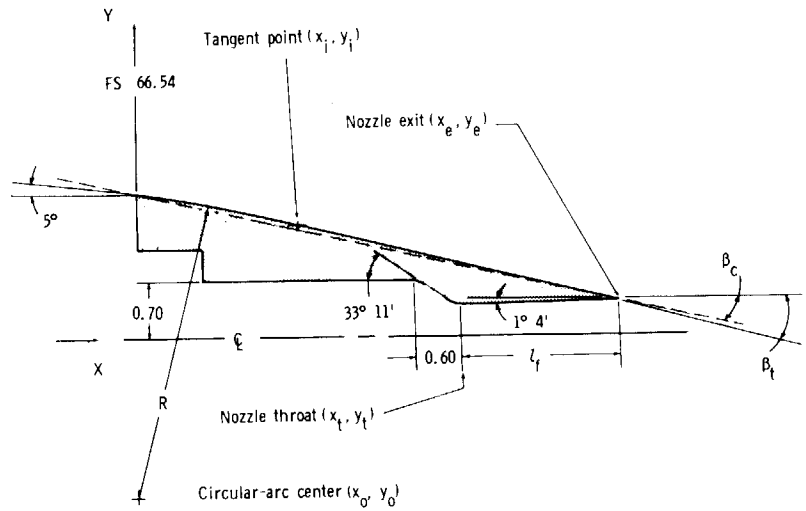

Conf.	R	x_o	y_o	x_i	y_i	x_t	y_t	x_e	y_e	l_f	β_c, deg	β_t, deg
1	7.496	-0.653	-5.698	1.509	1.480	2.071	0.595	5.009	0.650	2.938	12.601	13.336
+ 2	0.000	0.000	1.770	0.000	1.770	5.527	0.405	7.527	0.442	2.000	10.000	10.000
3	↓	↓	↓	↓	↓	3.986	↓	5.986	↓	↓	12.500	12.500
4						2.953		4.953			15.000	15.000
+ 5						1.646		3.646			20.000	20.000
6	7.496	-0.653	-5.698	3.646	0.442	1.646		3.646			20.000	35.000
7	↓	↓	↓	1.910	1.346	2.393		4.393			16.810	20.000
8				1.509	1.480	2.953		4.953			15.000	16.760
9	14.769	-1.287	-12.983	4.953	0.442	2.953		4.953			15.000	25.000
10	↓	↓	↓	2.534	1.322	3.819		5.819			12.850	15.000
11				1.407	1.578	5.527		7.527			10.000	10.514
12	23.488	-2.057	-21.629	5.986	0.442	3.986		5.986			12.500	20.000
+ 13	43.850	-3.822	-41.913	7.527	0.442	5.527		7.527			10.000	15.000
+ 14	↓	↓	↓	3.792	1.270	6.488		8.488			8.890	10.000
15				2.127	1.532	8.081		10.081			7.500	7.798
16	7.496	-0.653	-5.698	1.101	1.590	2.071	0.595	5.009	0.650	2.938	12.601	13.529
17	↓	↓	↓	0.679	1.679	5.527	0.405	7.527	0.442	2.000	10.000	10.234
18	23.488	-2.047	-21.629	3.037	1.302	4.914		6.914			10.864	12.500
19	3.750	-0.327	-1.966	1.114	1.496	1.646		3.646			20.000	22.594
20	↓	↓	↓	0.690	1.643	2.953		4.953			15.000	15.735
+ 21				0.331	1.726	5.527	↓	7.527	↓	↓	10.000	10.113

+ Configurations used in this comparison.

(a) Nozzle geometry.

Figure 4.- Sketches of nozzle assembly and geometric design parameters with static-pressure orifice locations on nozzle. Linear dimensions are in inches.

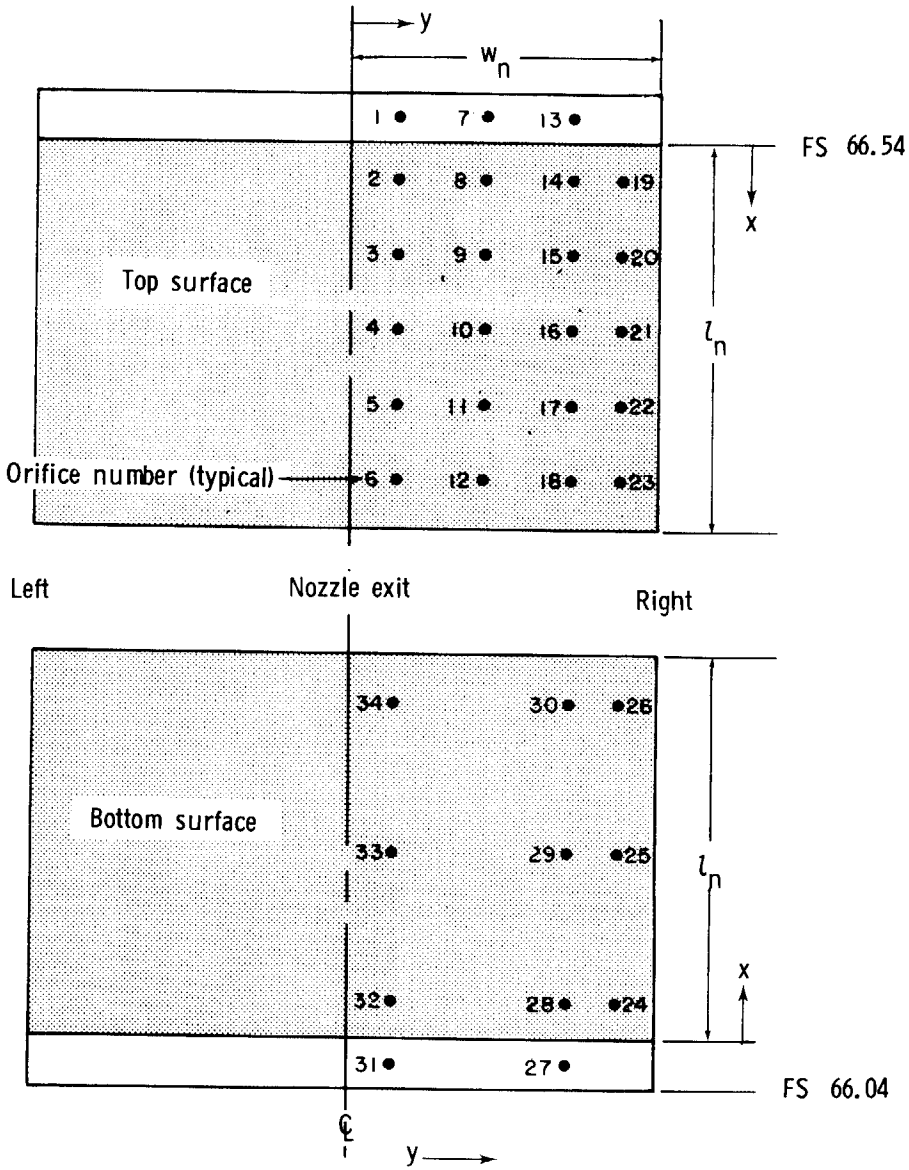

Orifice	Row	y/w_n	x/l_n
1	1	0.167	-0.0138
2			0.1
3			0.3
4			0.5
5			0.7
6			0.9
7	2	0.500	-0.0138
8			0.1
9			0.3
10			0.5
11			0.7
12			0.9
13	3	0.833	-0.0138
14			0.1
15			0.3
16			0.5
17			0.7
18			0.9
19	4	0.916	0.1
20			0.3
21			0.5
22			0.7
23			0.9
24	5		0.1
25			0.5
26			0.9
27	6	0.833	-0.0138
28			0.1
29			0.5
30			0.9
31	8	0.167	-0.0138
32			0.1
33			0.5
34			0.9

(b) Orifice locations.

Figure 4.- Concluded.

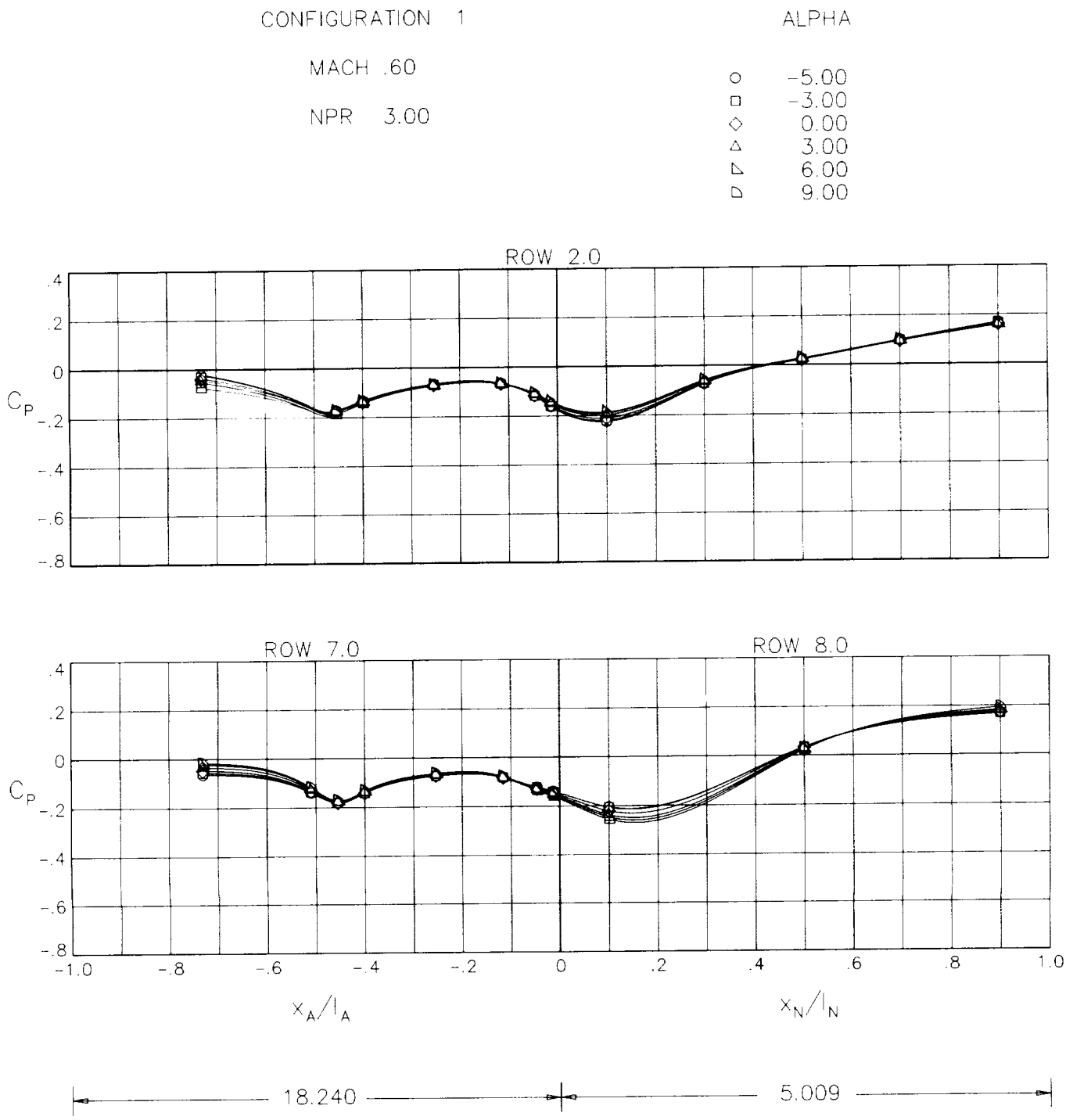

(a) M = 0.60; NPR = 3.0.

Figure 5.- Afterbody/nozzle static-pressure coefficient distributions along upper and lower surface of mid right side for configuration 1.

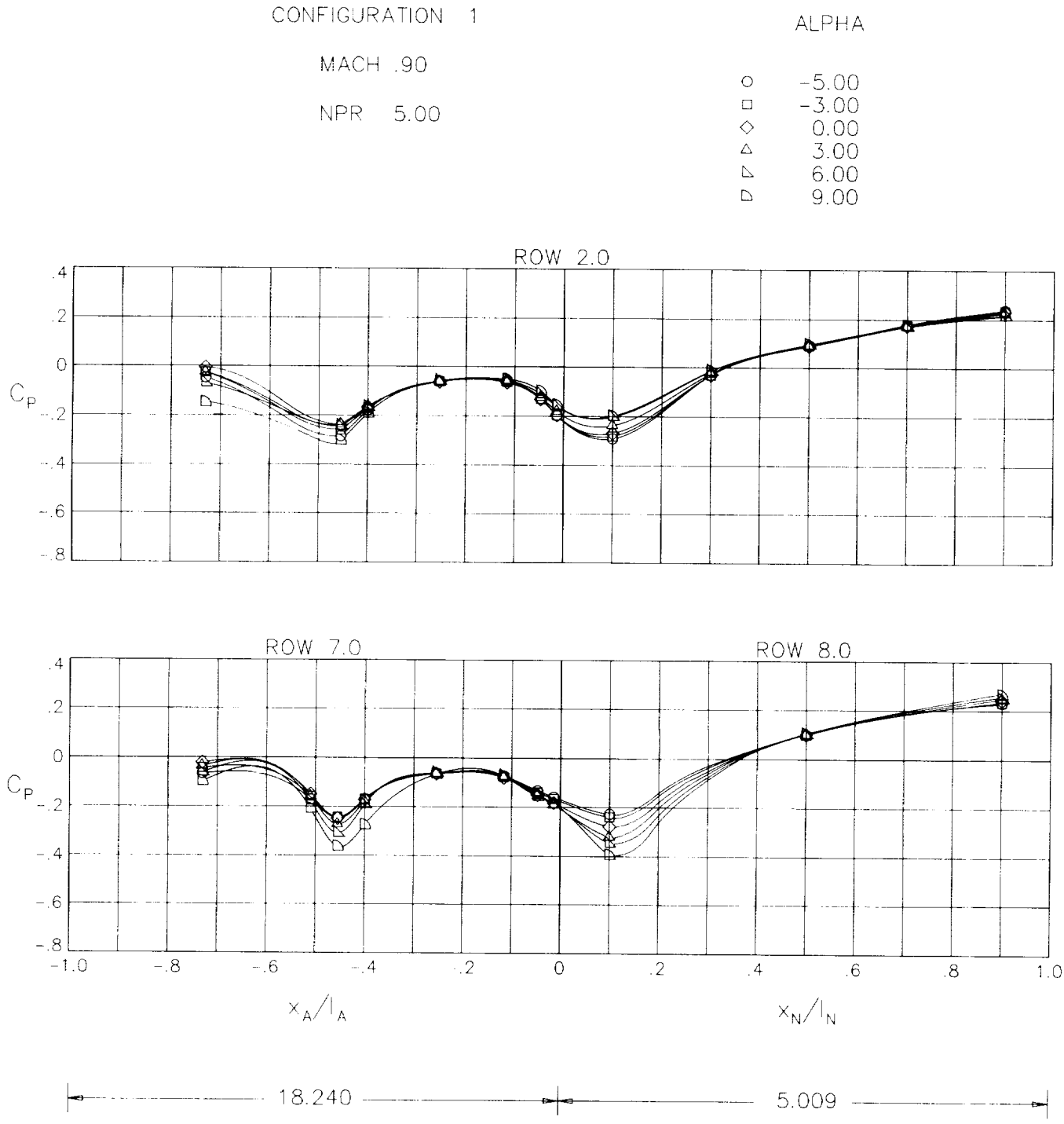

(b) M = 0.90; NPR = 5.0.

Figure 5.- Continued.

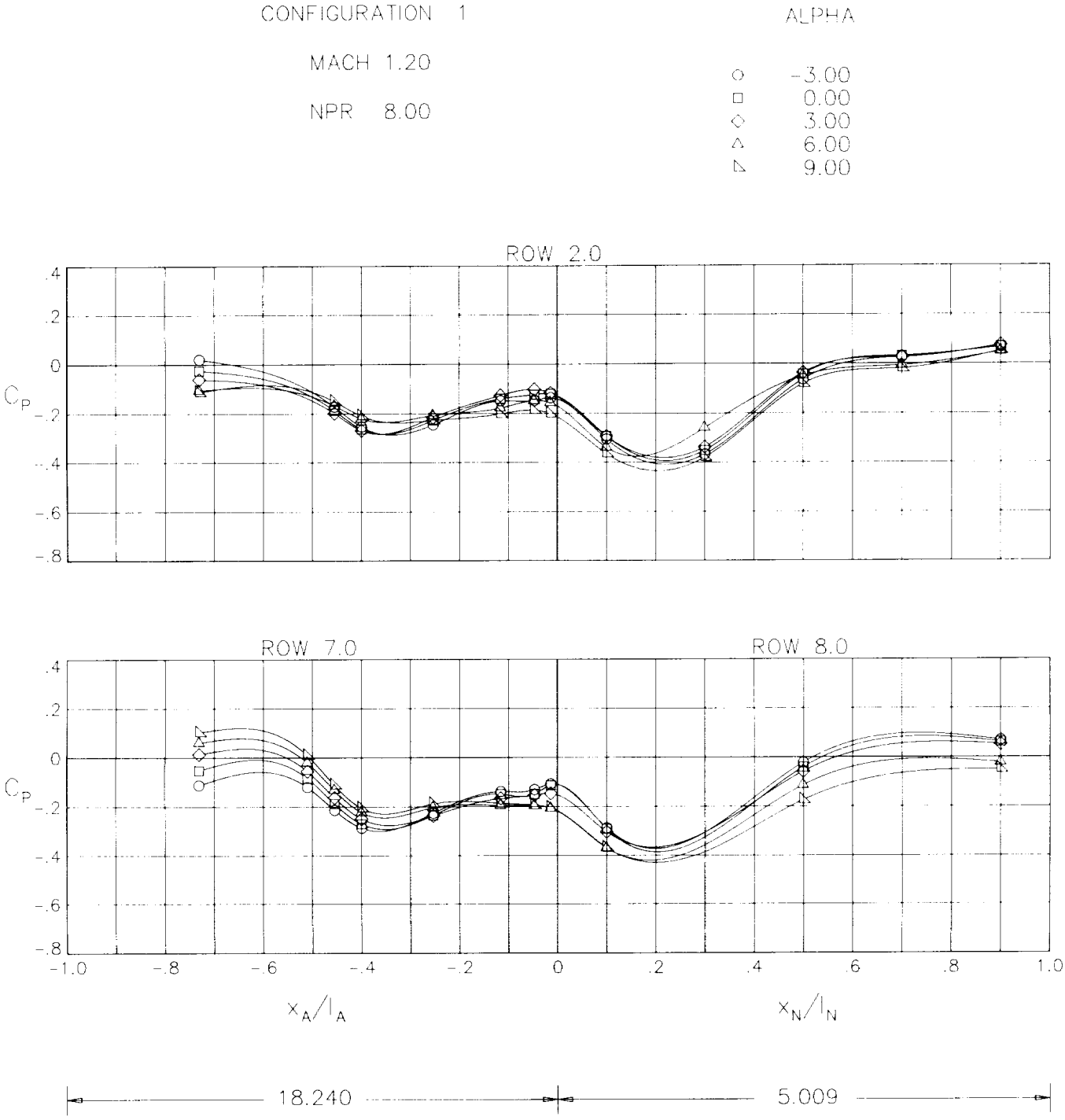

(c) M = 1.20; NPR = 8.0.

Figure 5.- Concluded.

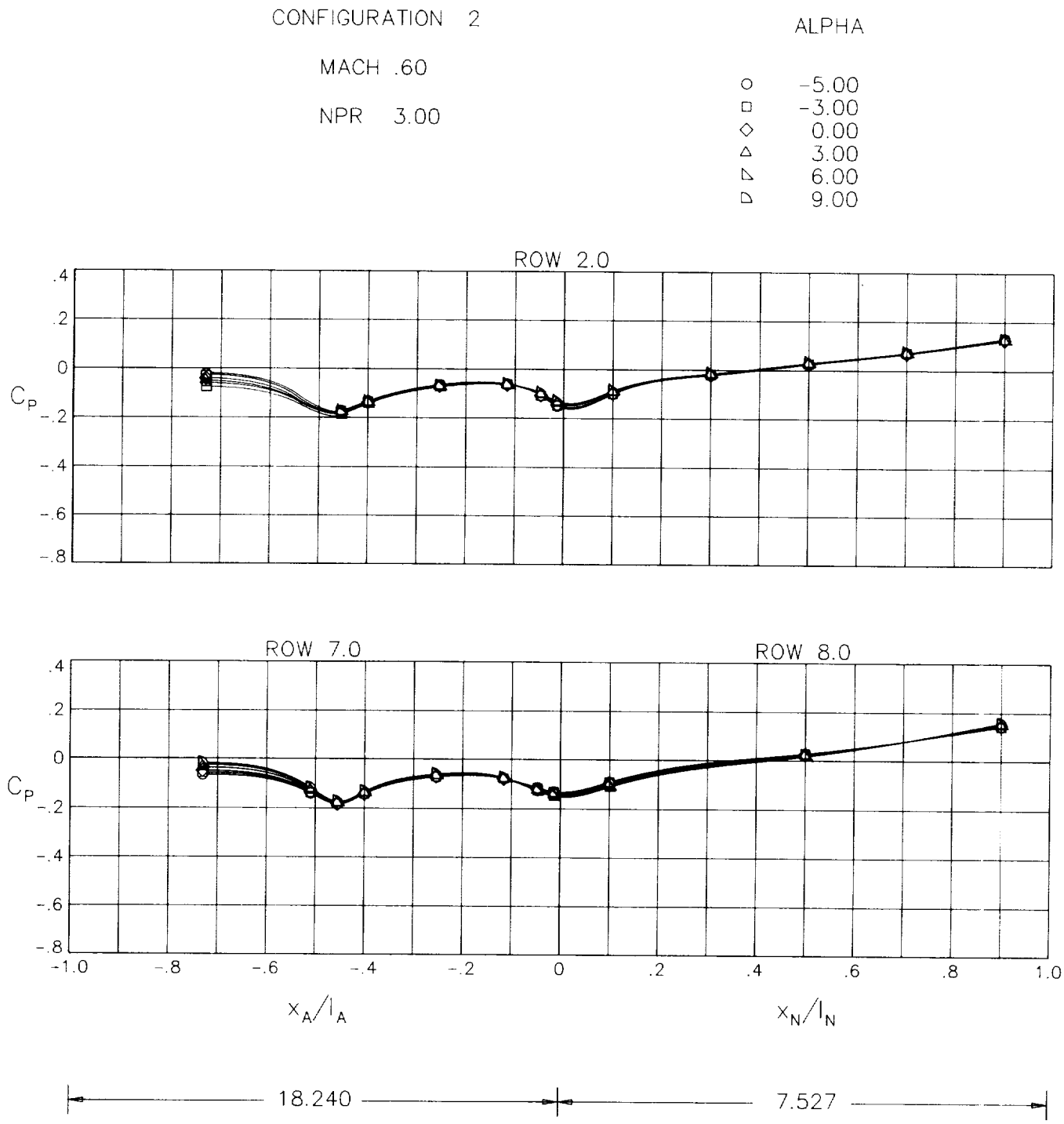

(a) M = 0.60; NPR = 3.0.

Figure 6.- Afterbody/nozzle static-pressure coefficient distributions along upper and lower surface of mid right side for configuration 2.

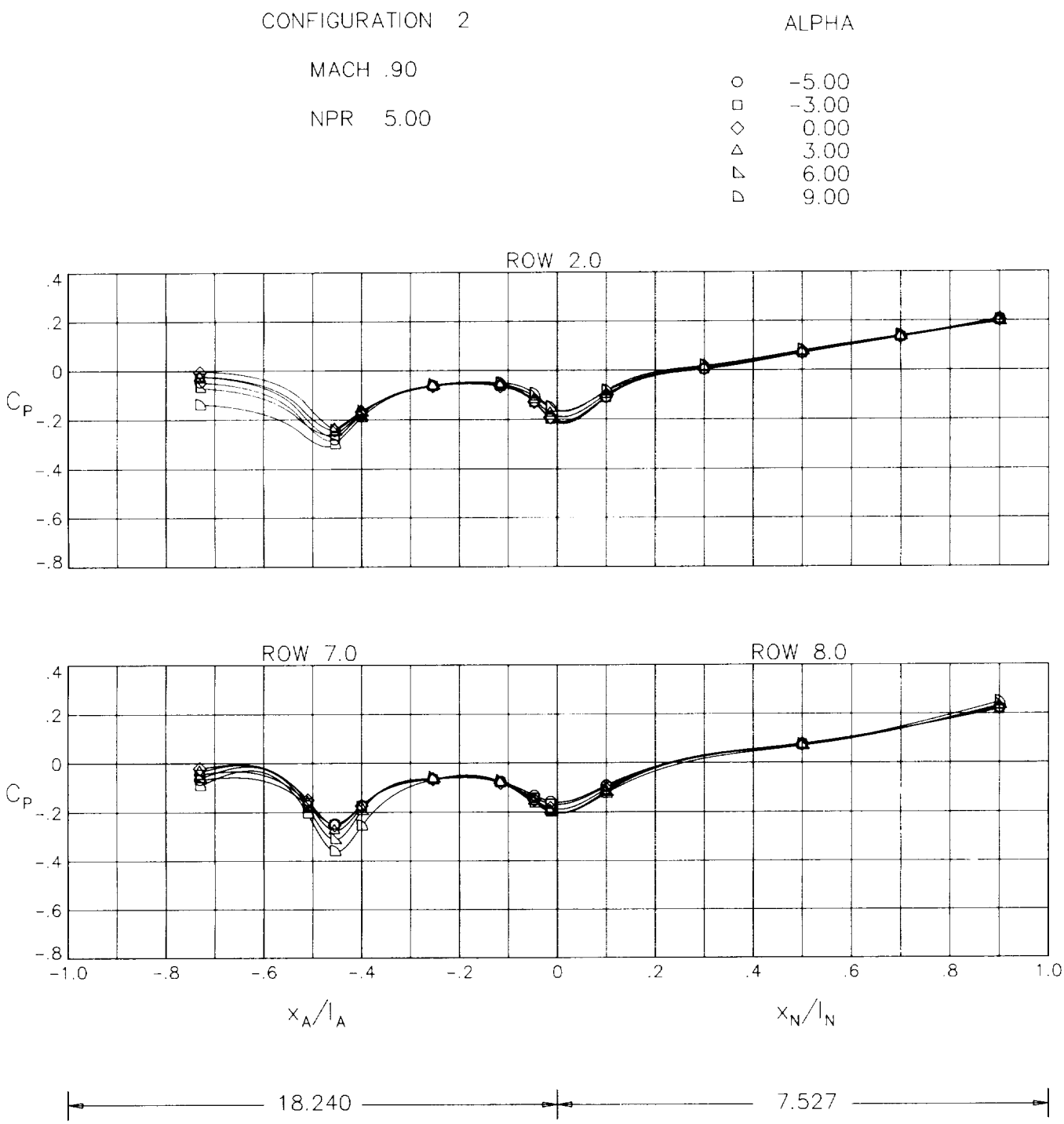

(b) M = 0.90; NPR = 5.0.

Figure 6.- Continued.

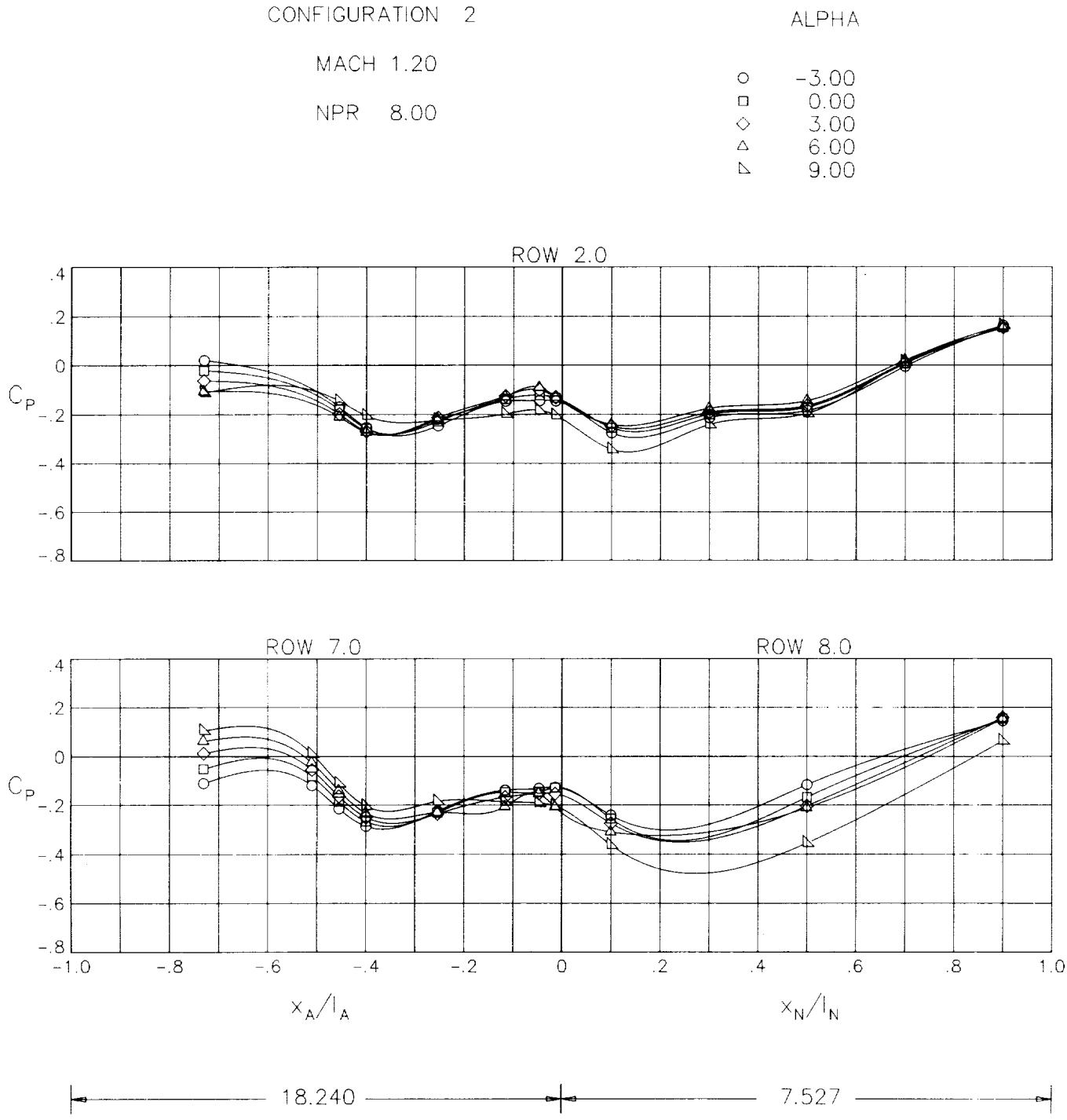

(c) M = 1.20; NPR = 8.0.

Figure 6.- Concluded.

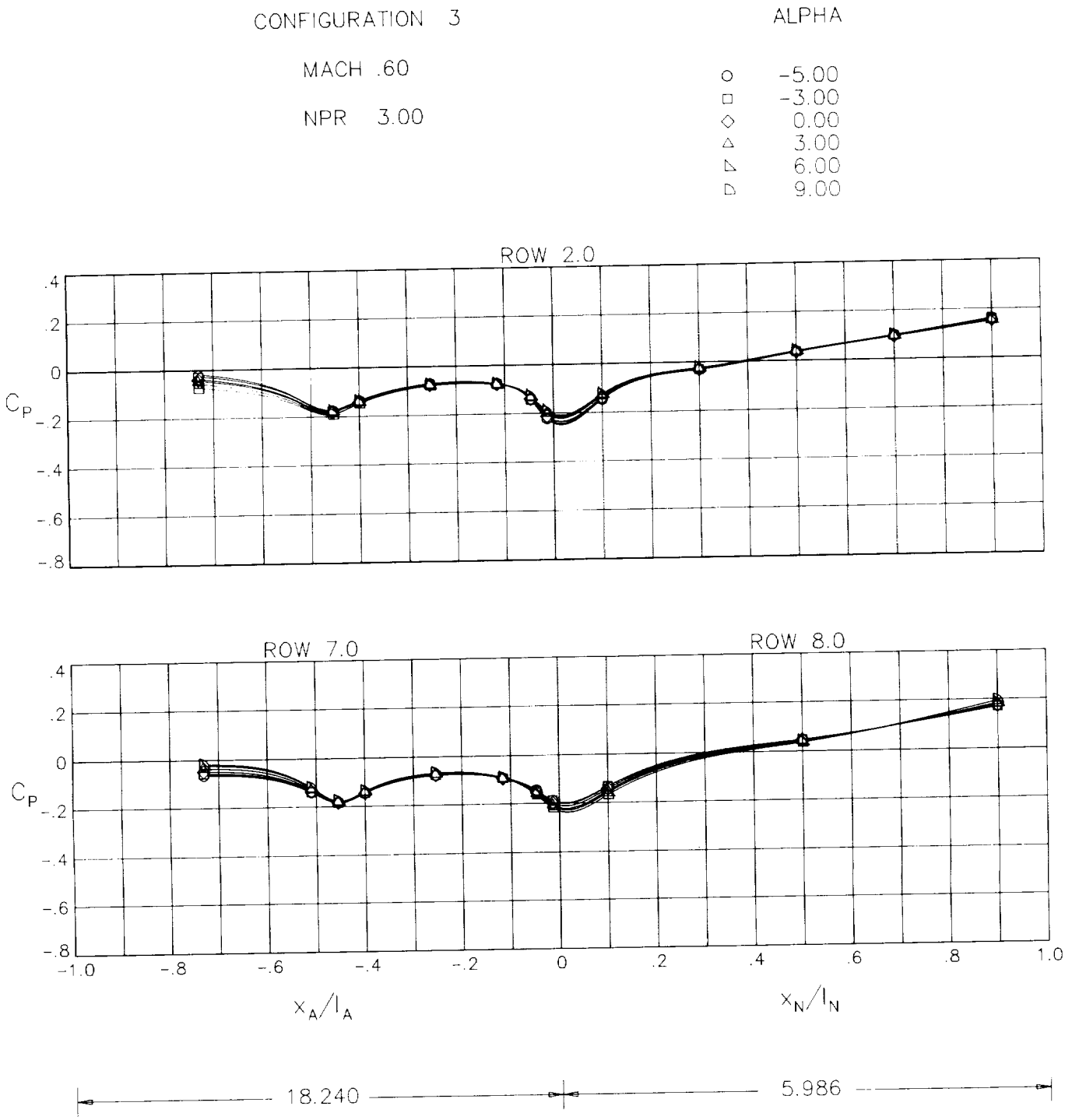

(a) M = 0.60; NPR = 3.0.

Figure 7.- Afterbody/nozzle static-pressure coefficient distributions along upper and lower surface of mid right side for configuration 3.

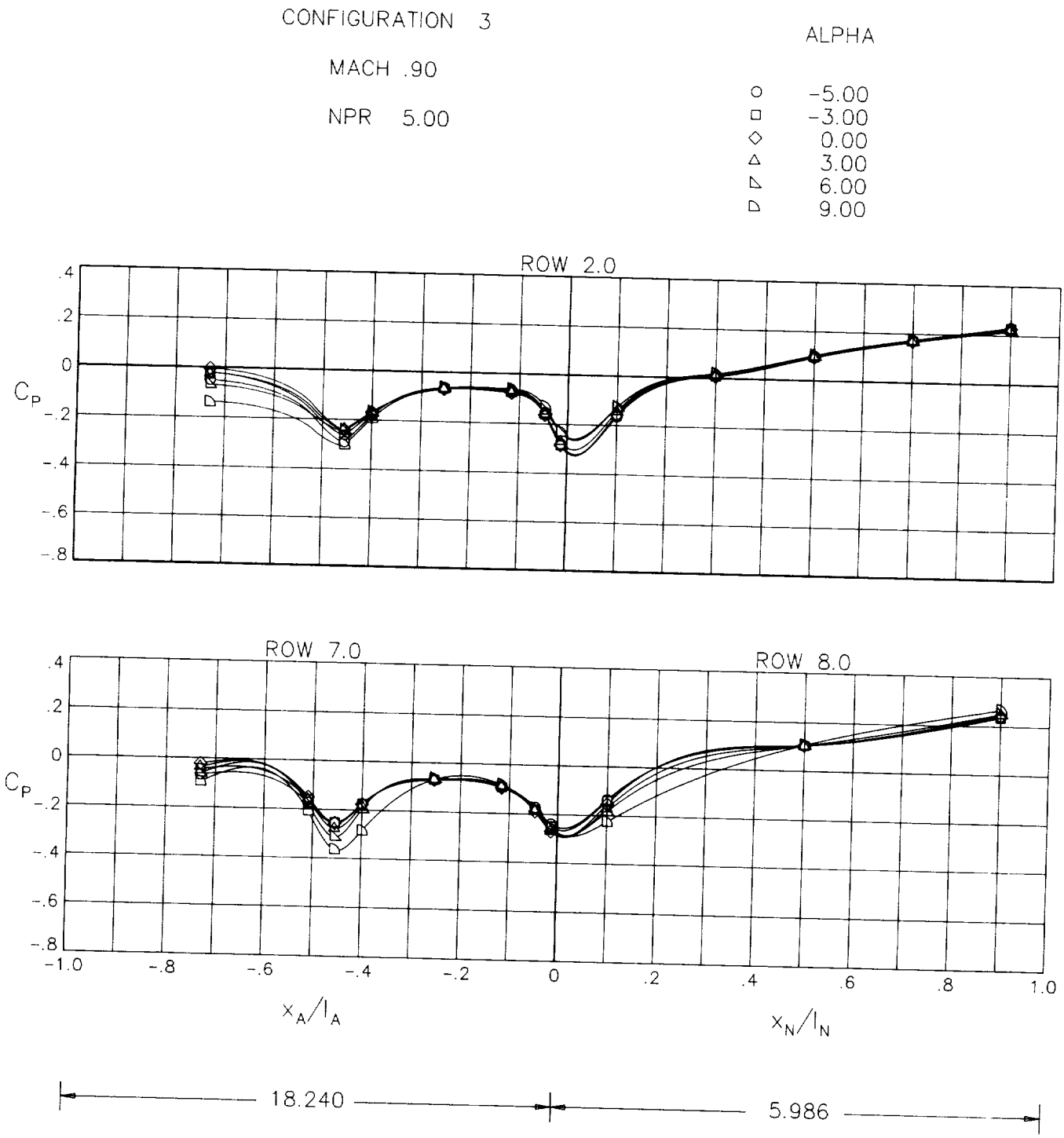

(b) M = 0.90; NPR = 5.0.

Figure 7.- Continued.

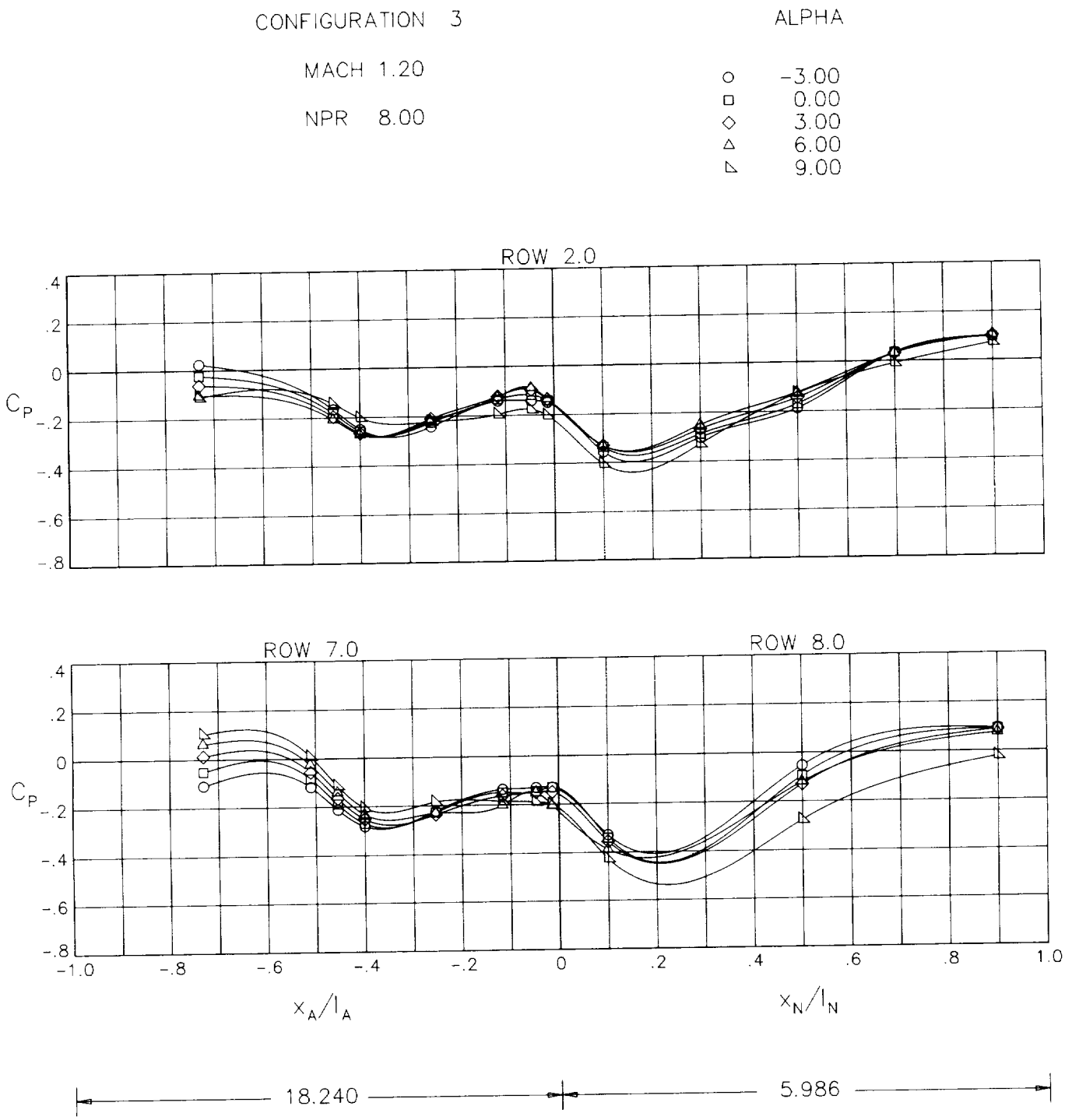

(c) M = 1.20; NPR = 8.0.

Figure 7.- Concluded.

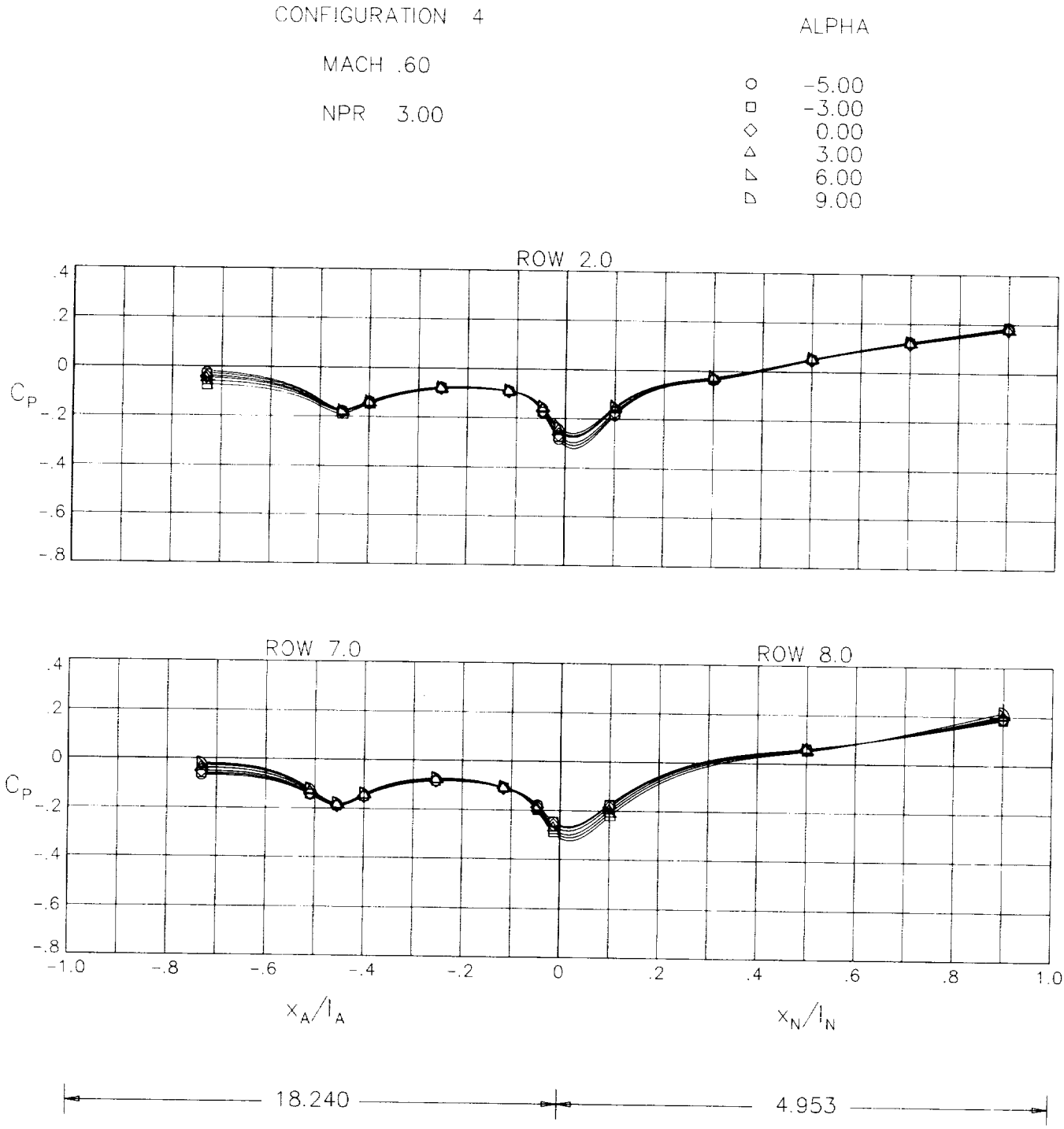

(a) M = 0.60; NPR = 3.0.

Figure 8.- Afterbody/nozzle static-pressure coefficient distributions along upper and lower surface of mid right side for configuration 4.

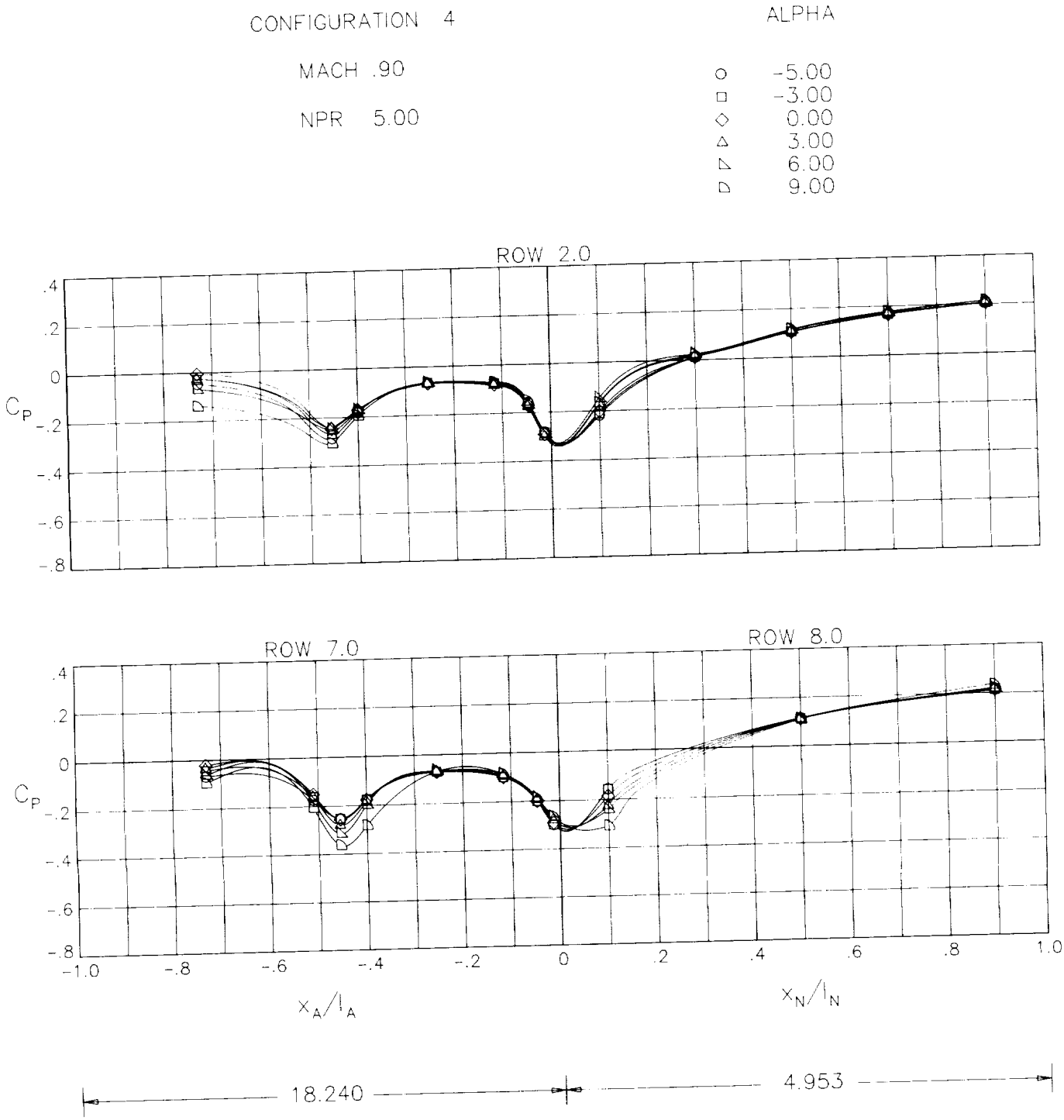

(b) M = 0.90; NPR = 5.0.

Figure 8.- Continued.

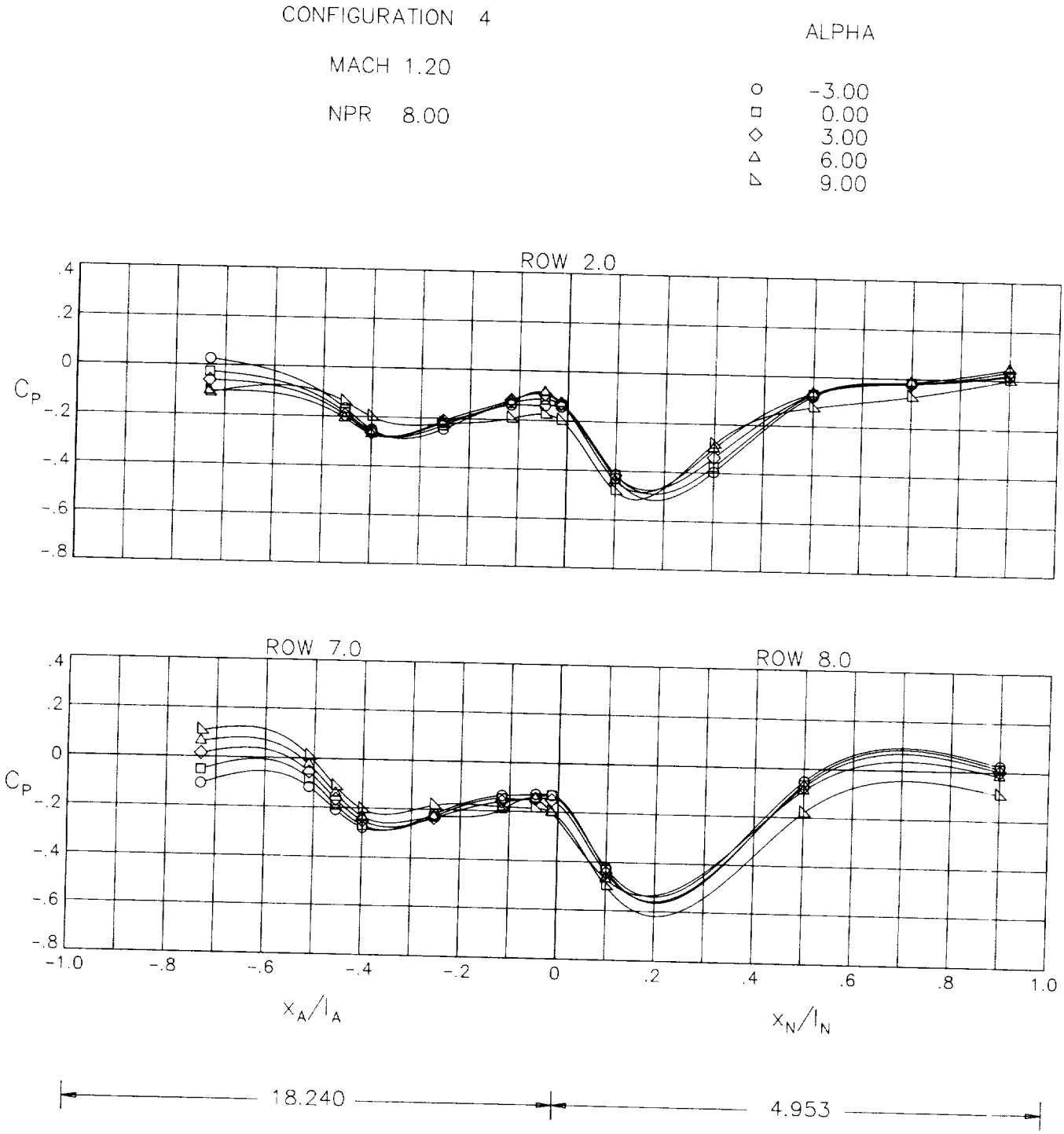

(c) M = 1.20; NPR = 8.0.

Figure 8.- Concluded.

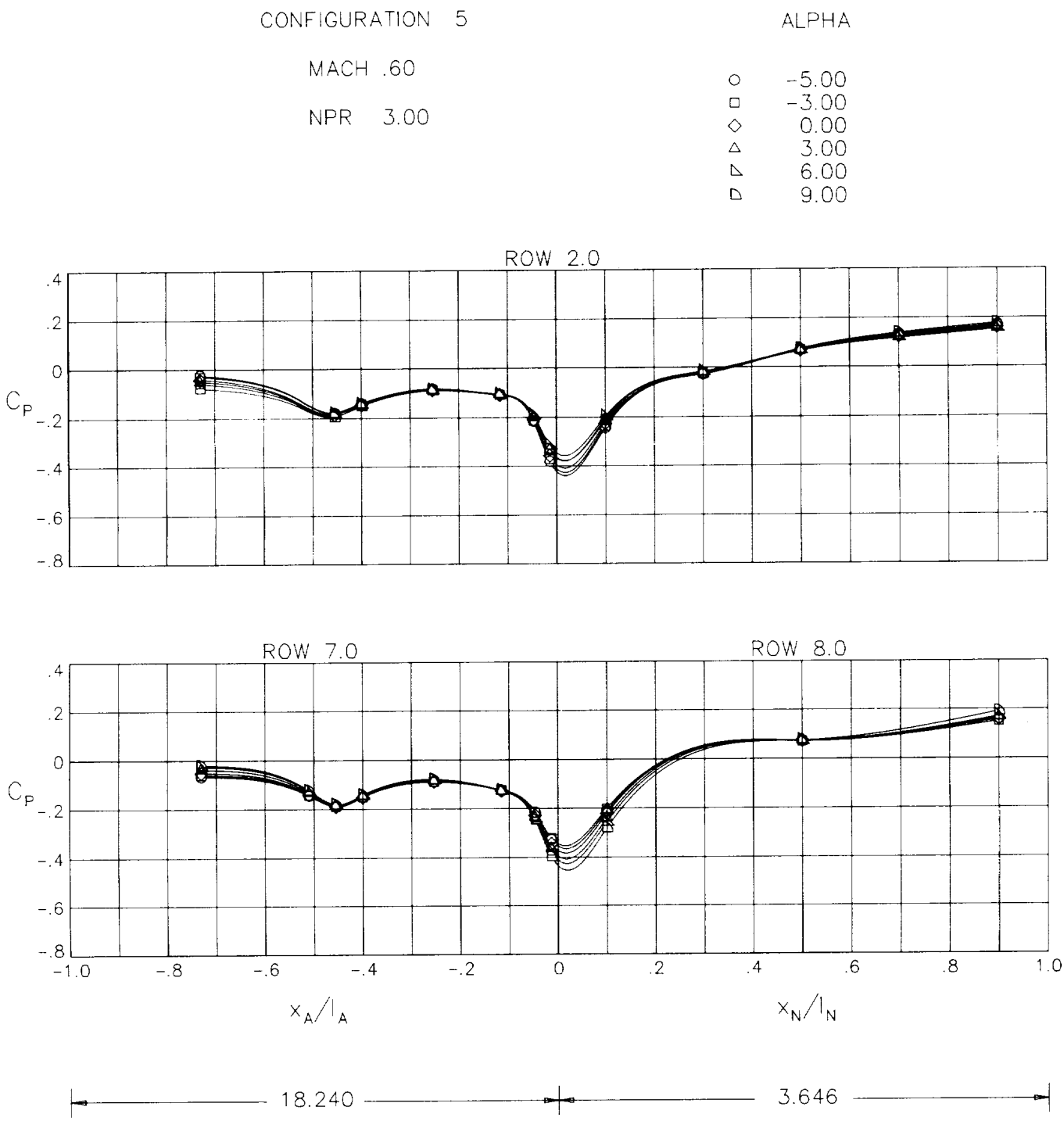

(a) M = 0.60; NPR = 3.0.

Figure 9.- Afterbody-nozzle static-pressure coefficient distributions along upper and lower surface of mid right side for configuration 5.

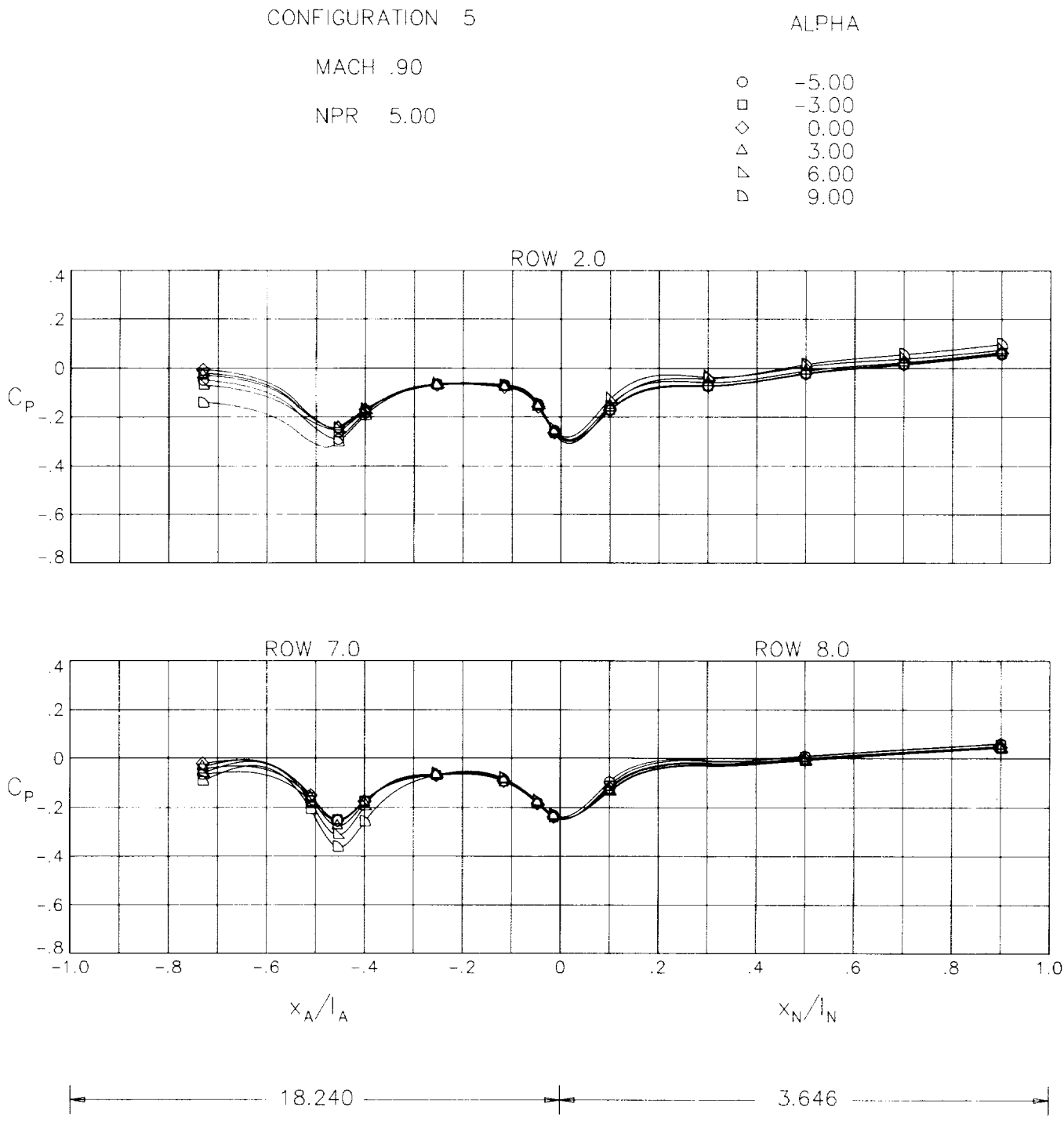

(b) M = 0.90; NPR = 5.0.

Figure 9.- Continued.

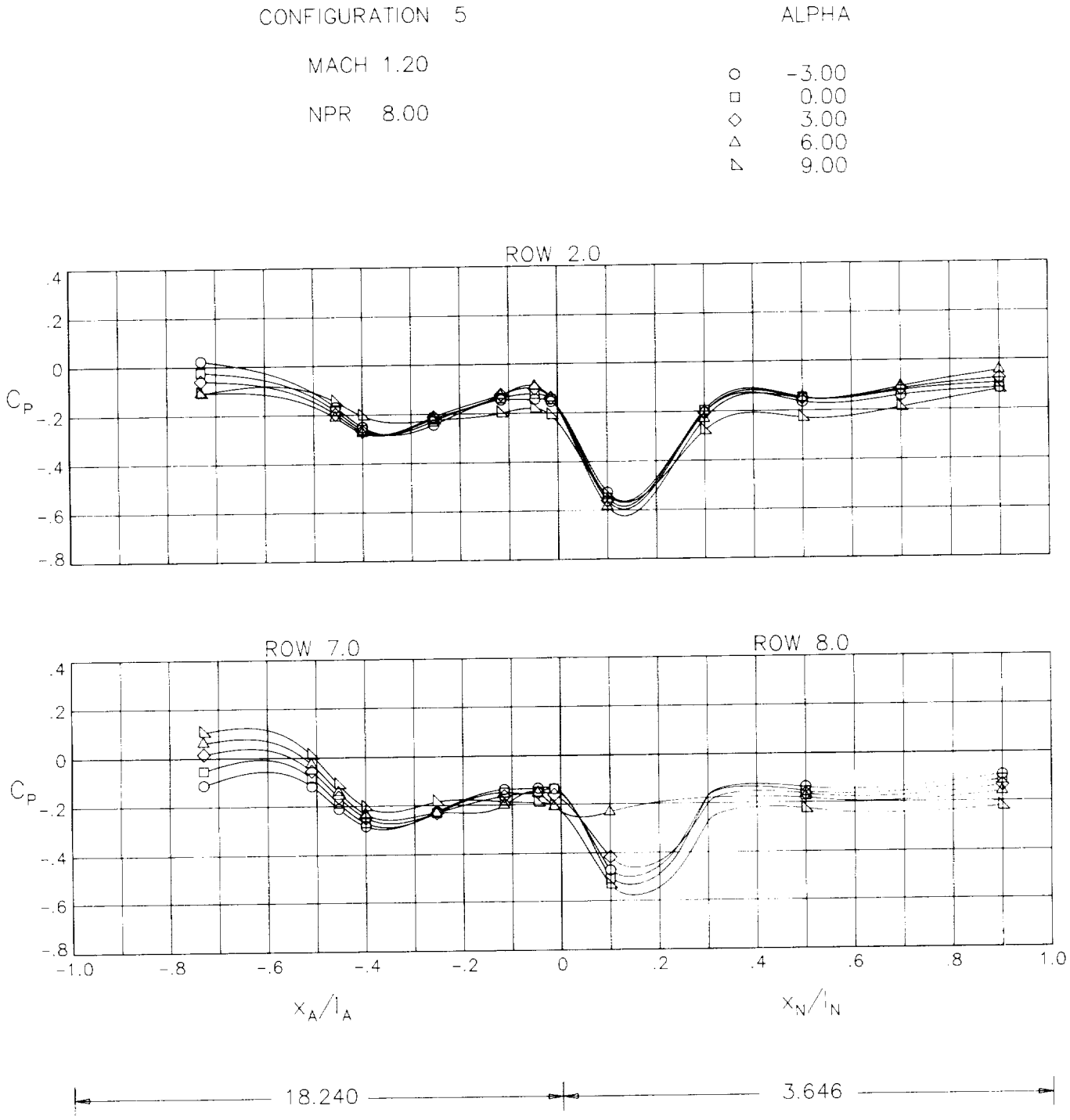

(c) M = 1.20; NPR = 8.0.

Figure 9.- Concluded.

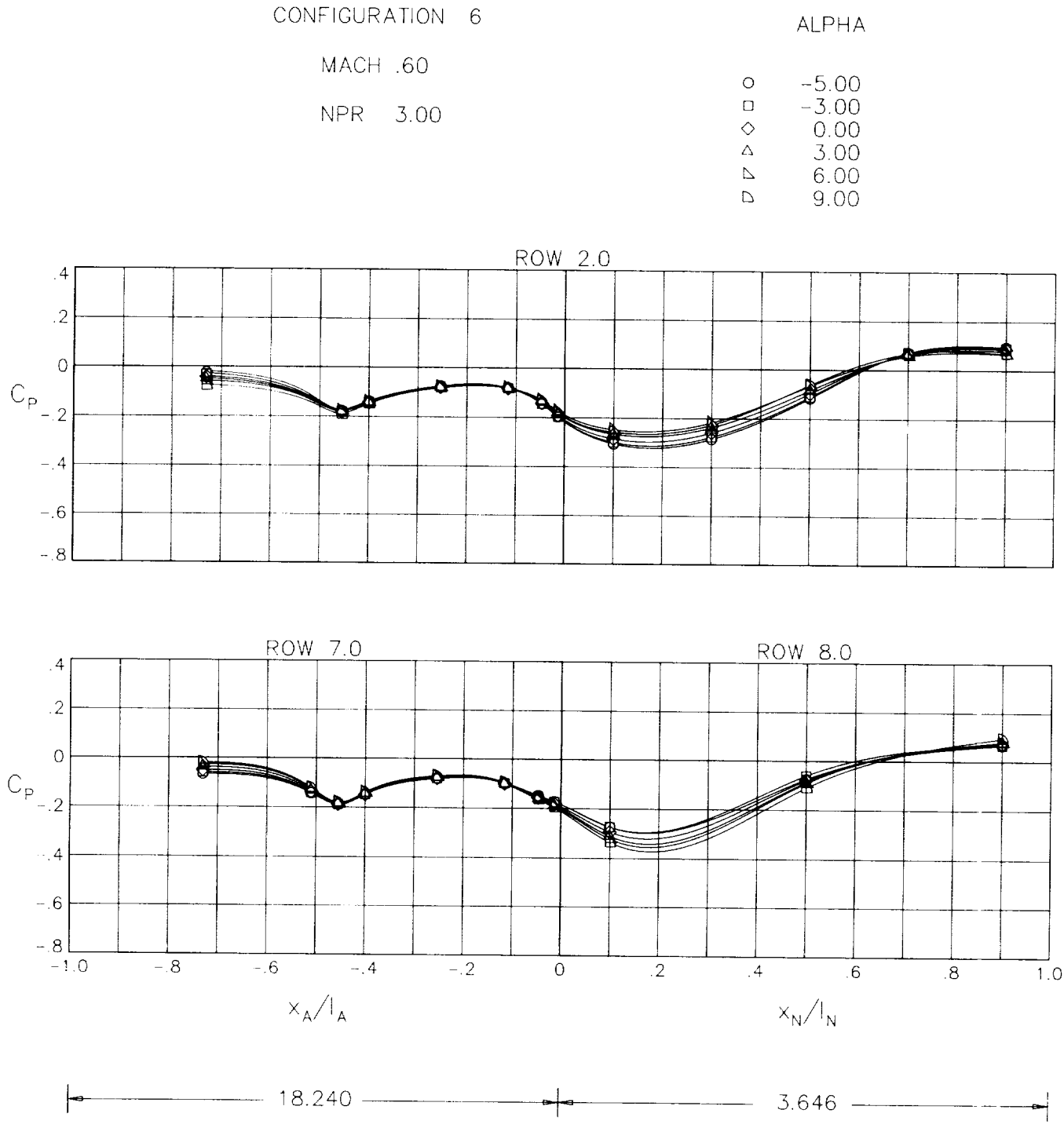

(a) M = 0.60; NPR = 3.0.

Figure 10.- Afterbody/nozzle static-pressure coefficient distributions along upper and lower surface of mid right side for configuration 6.

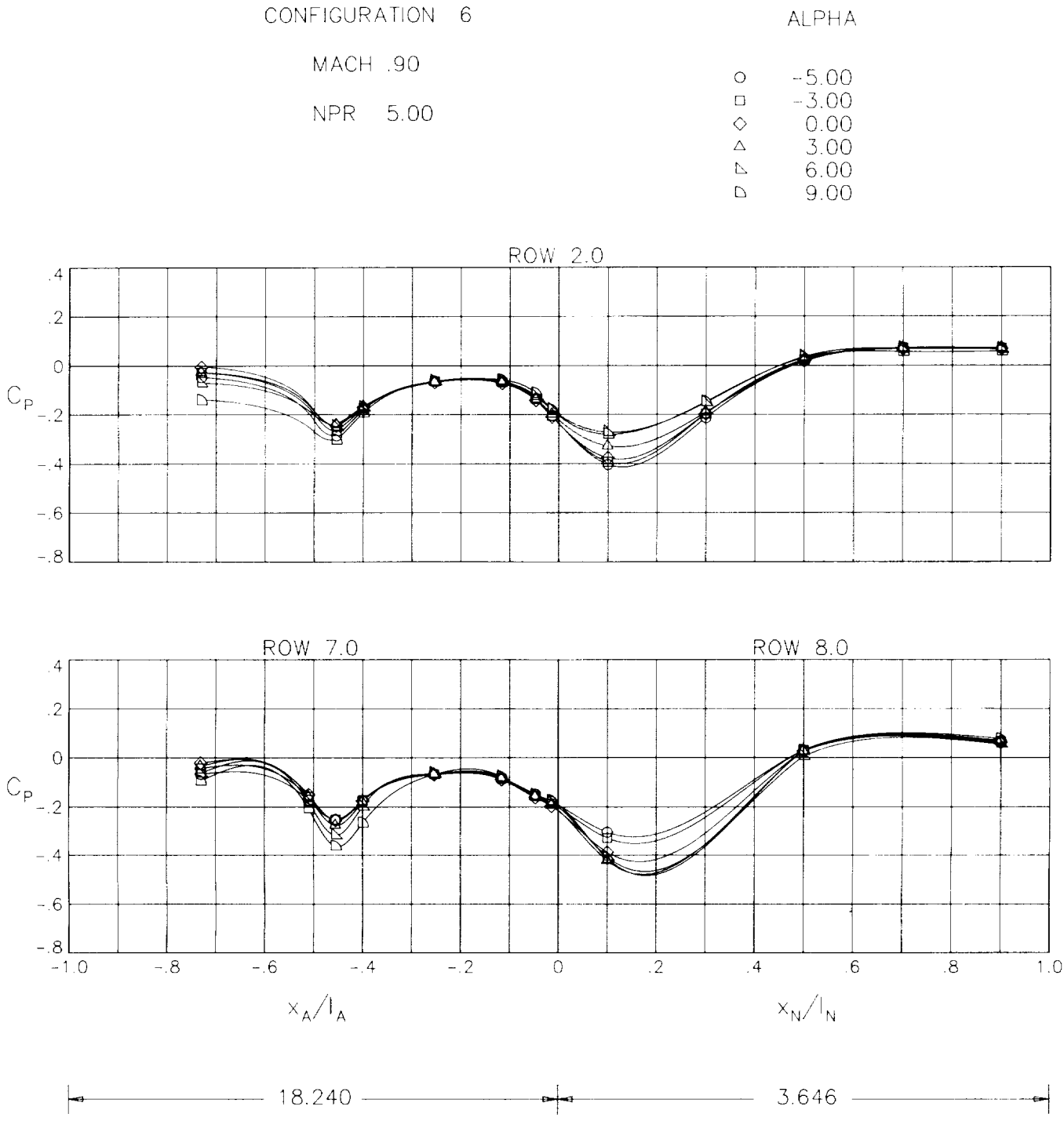

(b) M = 0.90; NPR = 5.0.

Figure 10.- Continued.

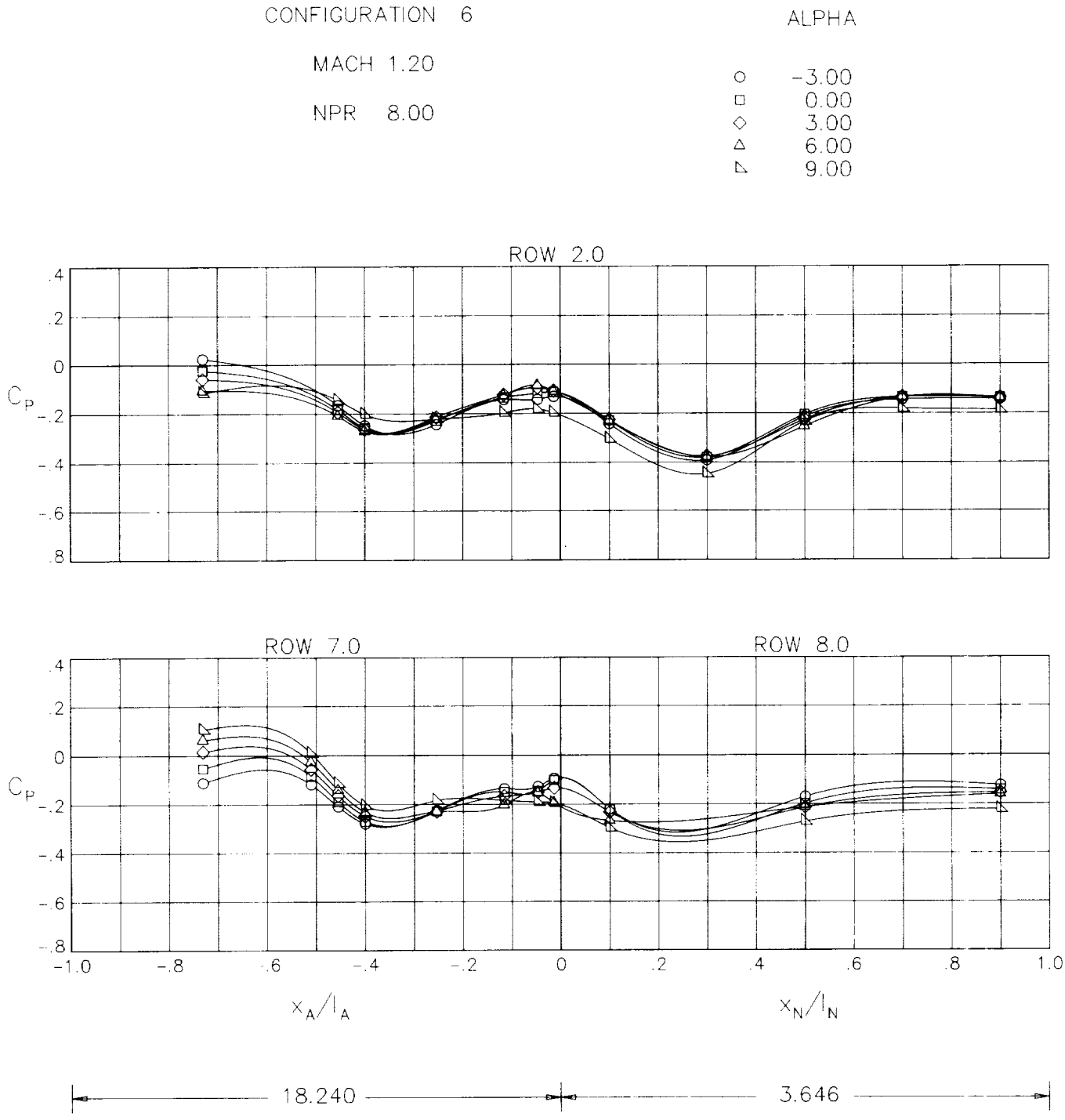

(c) M = 1.20; NPR = 8.0.

Figure 10.- Concluded.

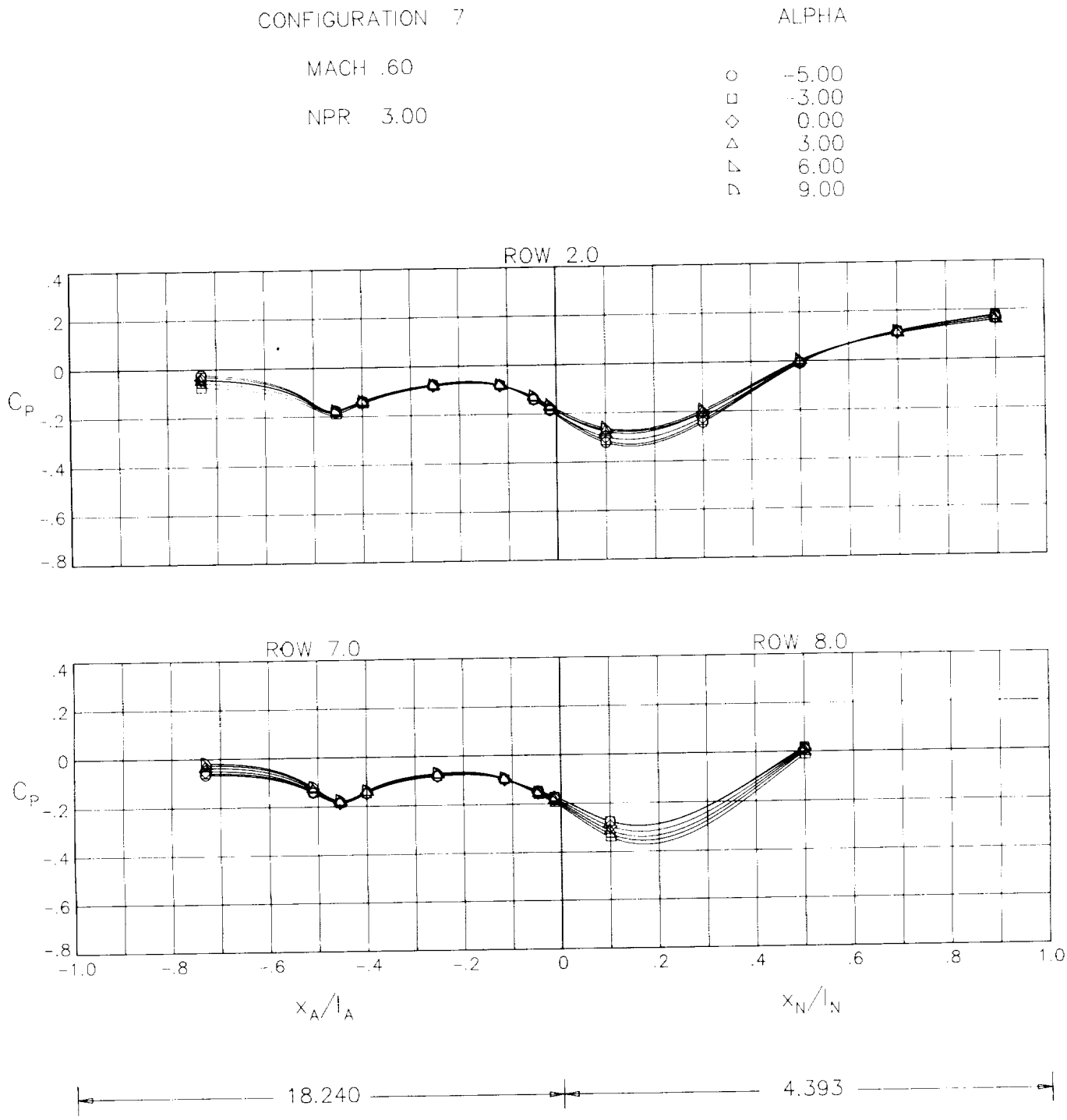

(a) M = 0.60; NPR = 3.0.

Figure 11.- Afterbody/nozzle static-pressure coefficient distributions along upper and lower surface of mid right side for configuration 7.

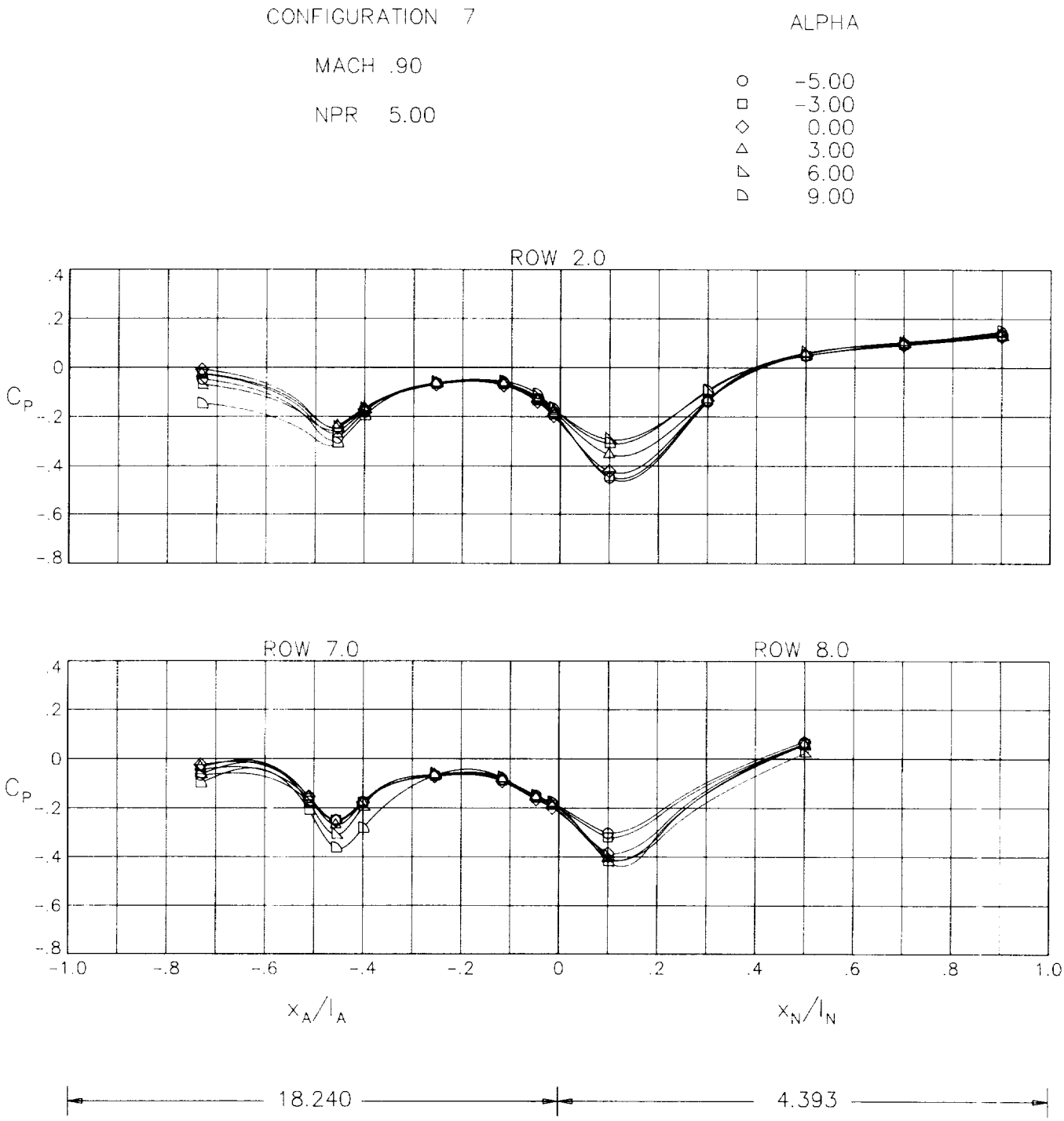

(b) M = 0.90; NPR = 5.0.

Figure 11.- Continued.

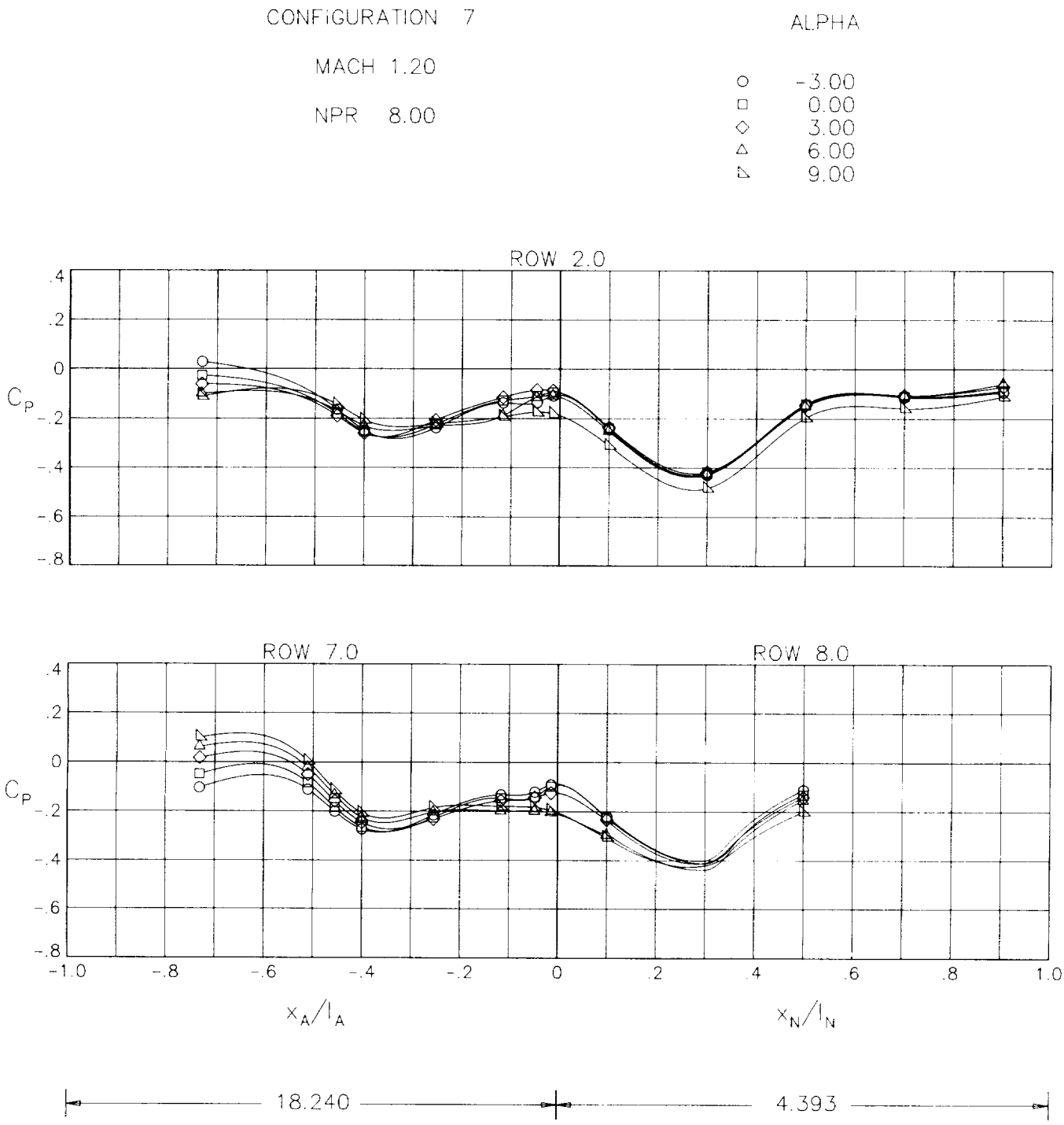

(c) M = 1.20; NPR = 8.0.

Figure 11.- Concluded.

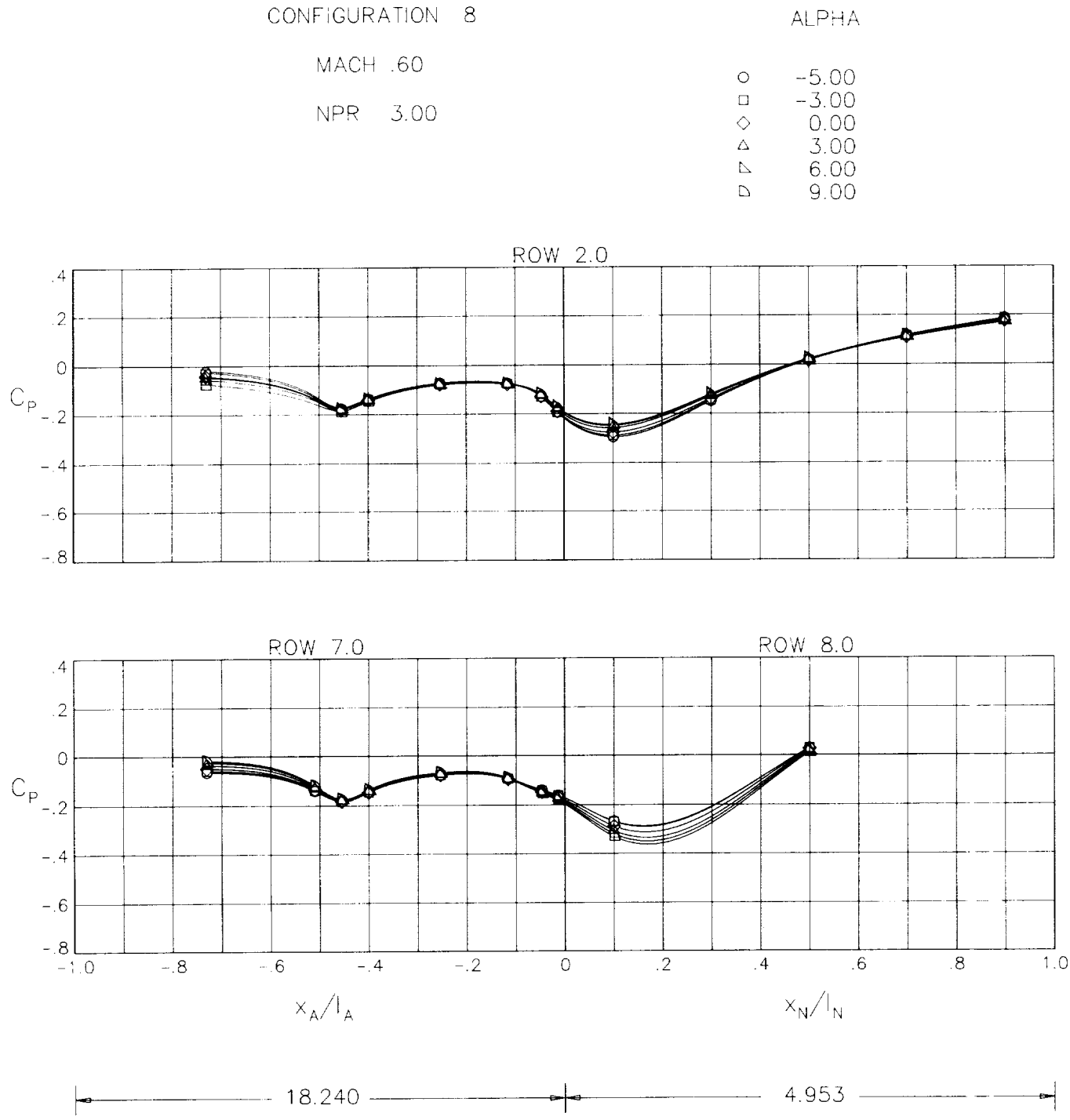

(a) M = 0.60; NPR = 3.0.

Figure 12.- Afterbody/nozzle static-pressure coefficient distributions along upper and lower surface of mid right side for configuration 8.

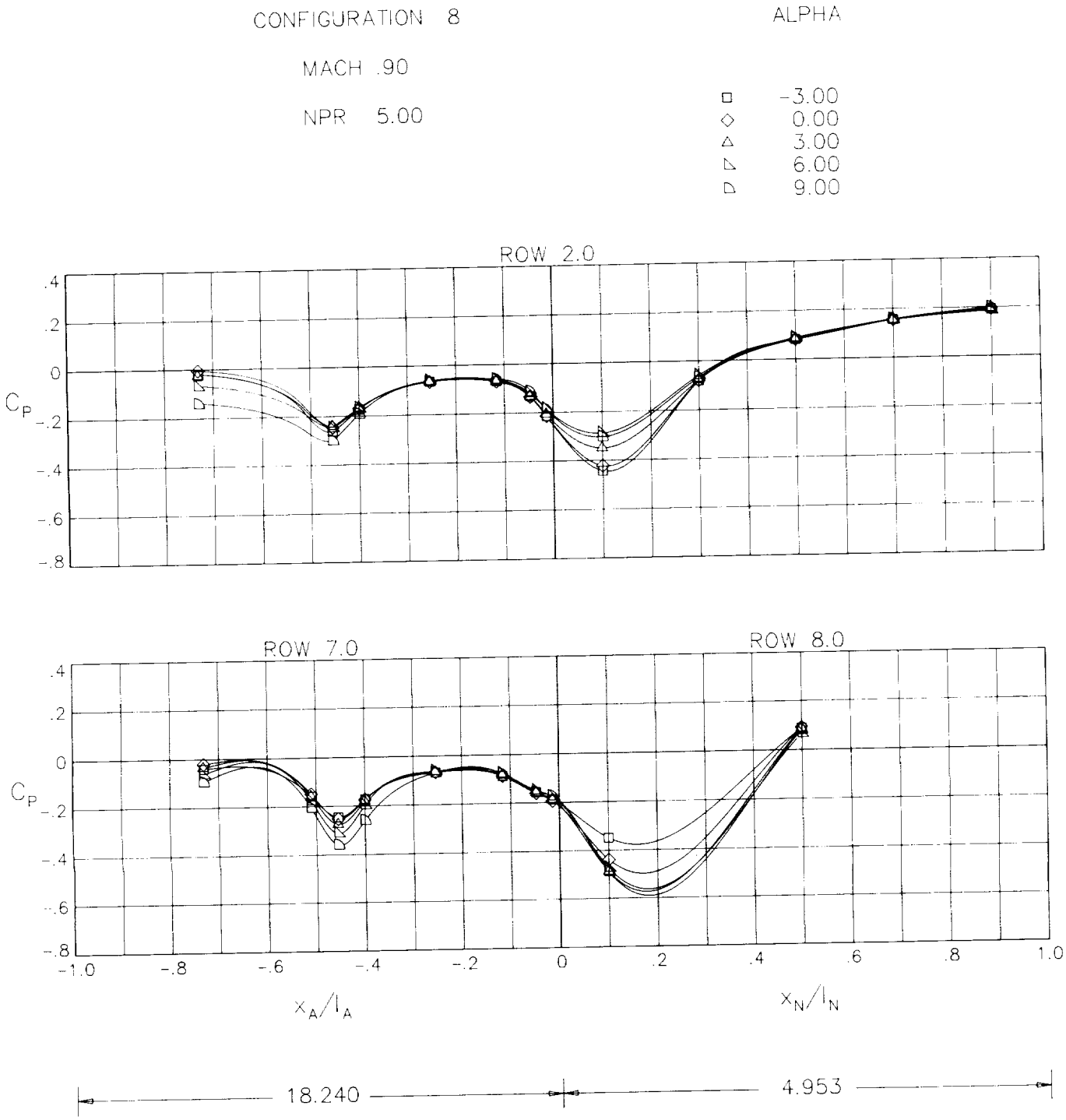

(b) M = 0.90; NPR = 5.0.

Figure 12.- Continued.

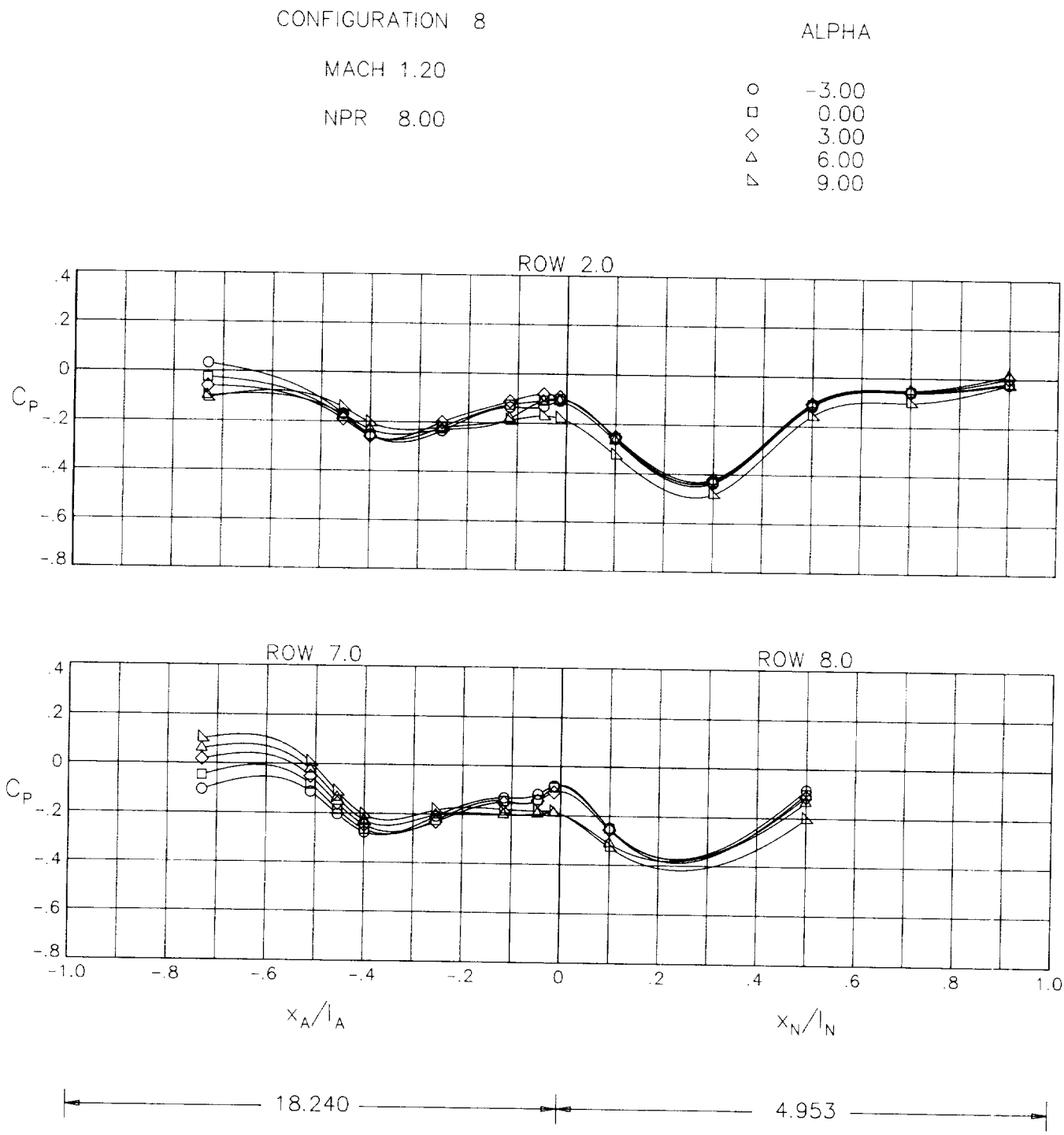

(c) M = 1.20; NPR = 8.0.

Figure 12.- Concluded.

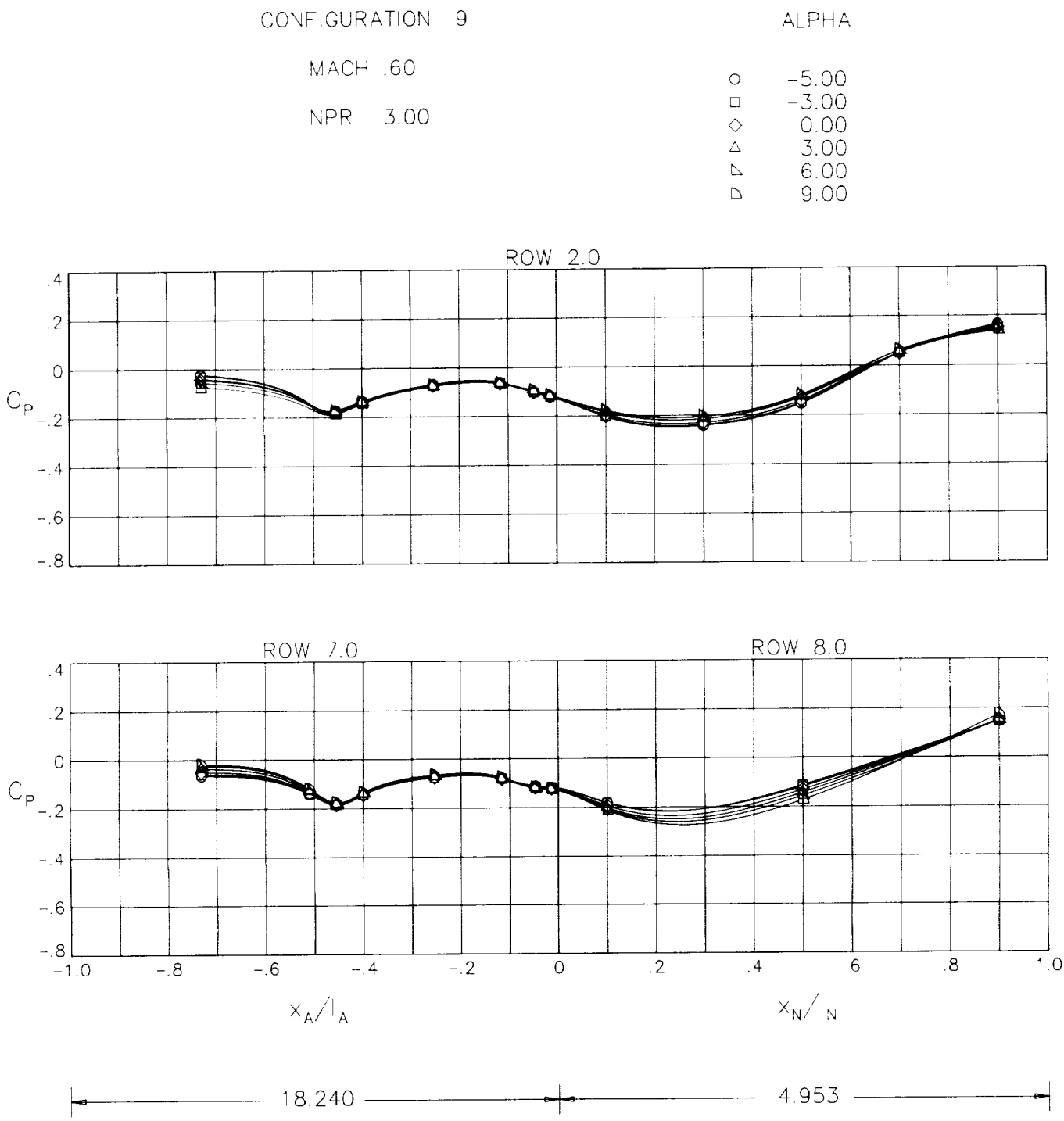

(a) M = 0.60; NPR = 3.0.

Figure 13.- Afterbody/nozzle static-pressure coefficient distributions along upper and lower surface of mid right side for configuration 9.

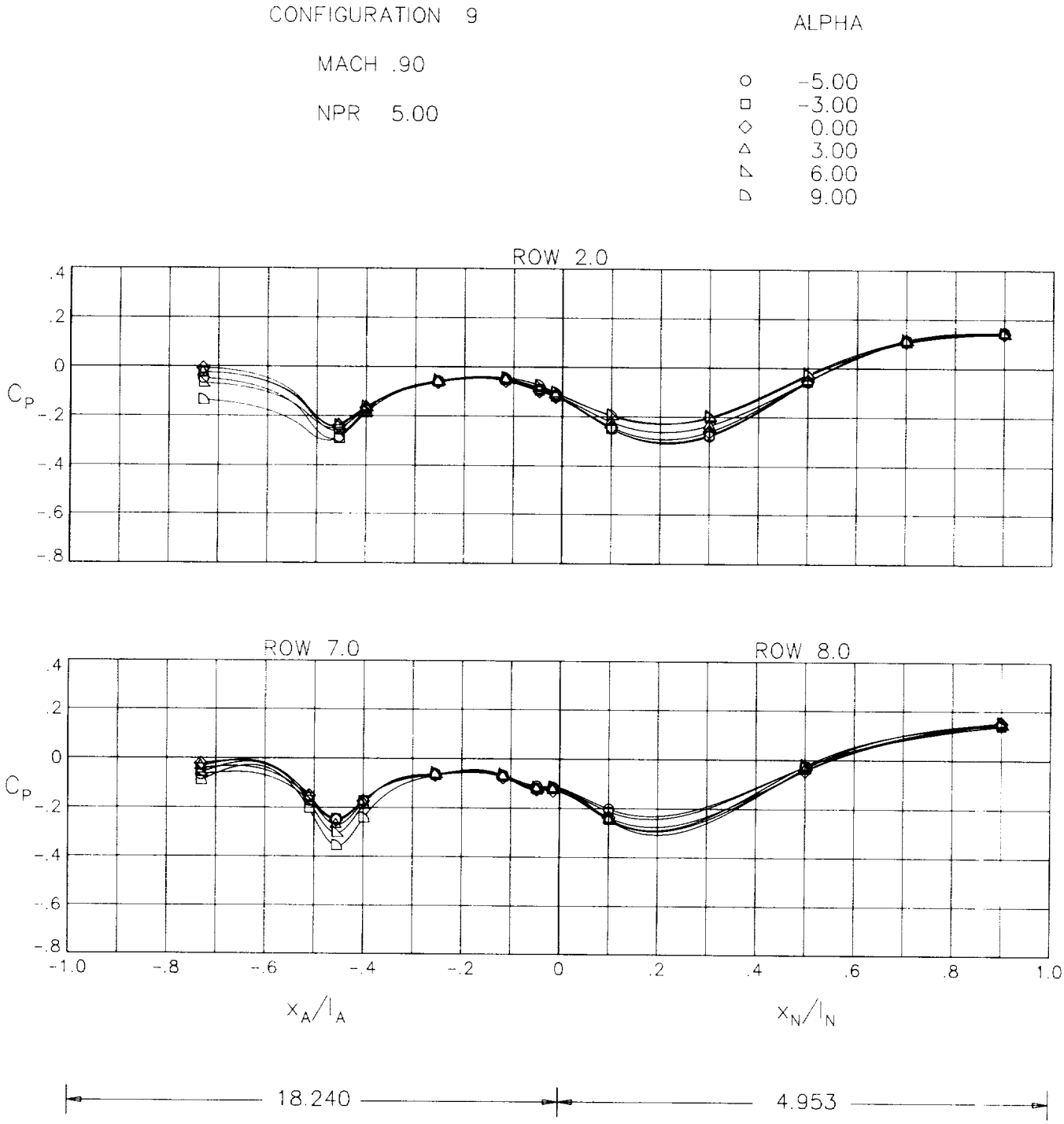

(b) M = 0.90; NPR = 5.0.

Figure 13.- Continued.

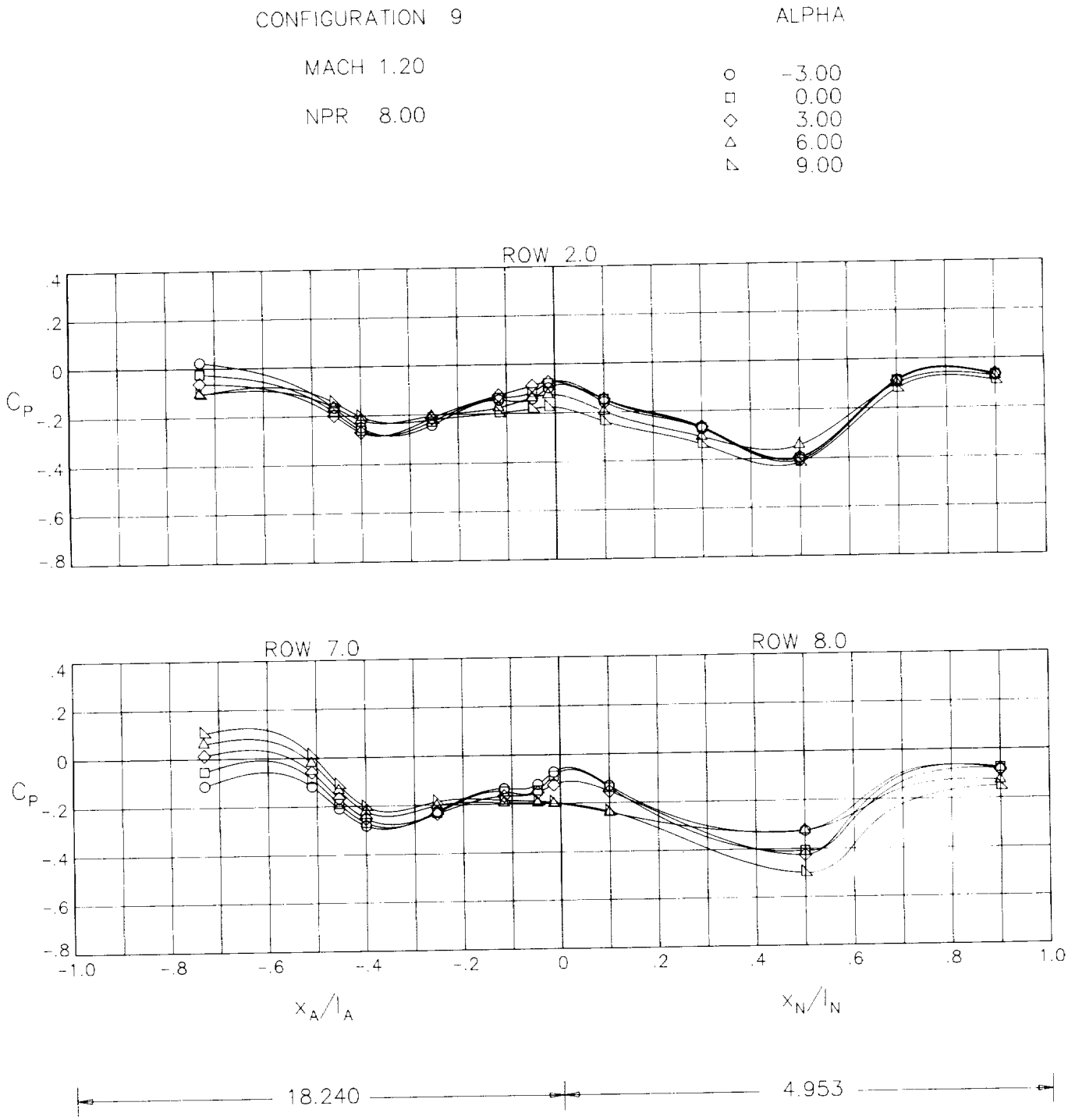

(c) M = 1.20; NPR = 8.0.

Figure 13.- Concluded.

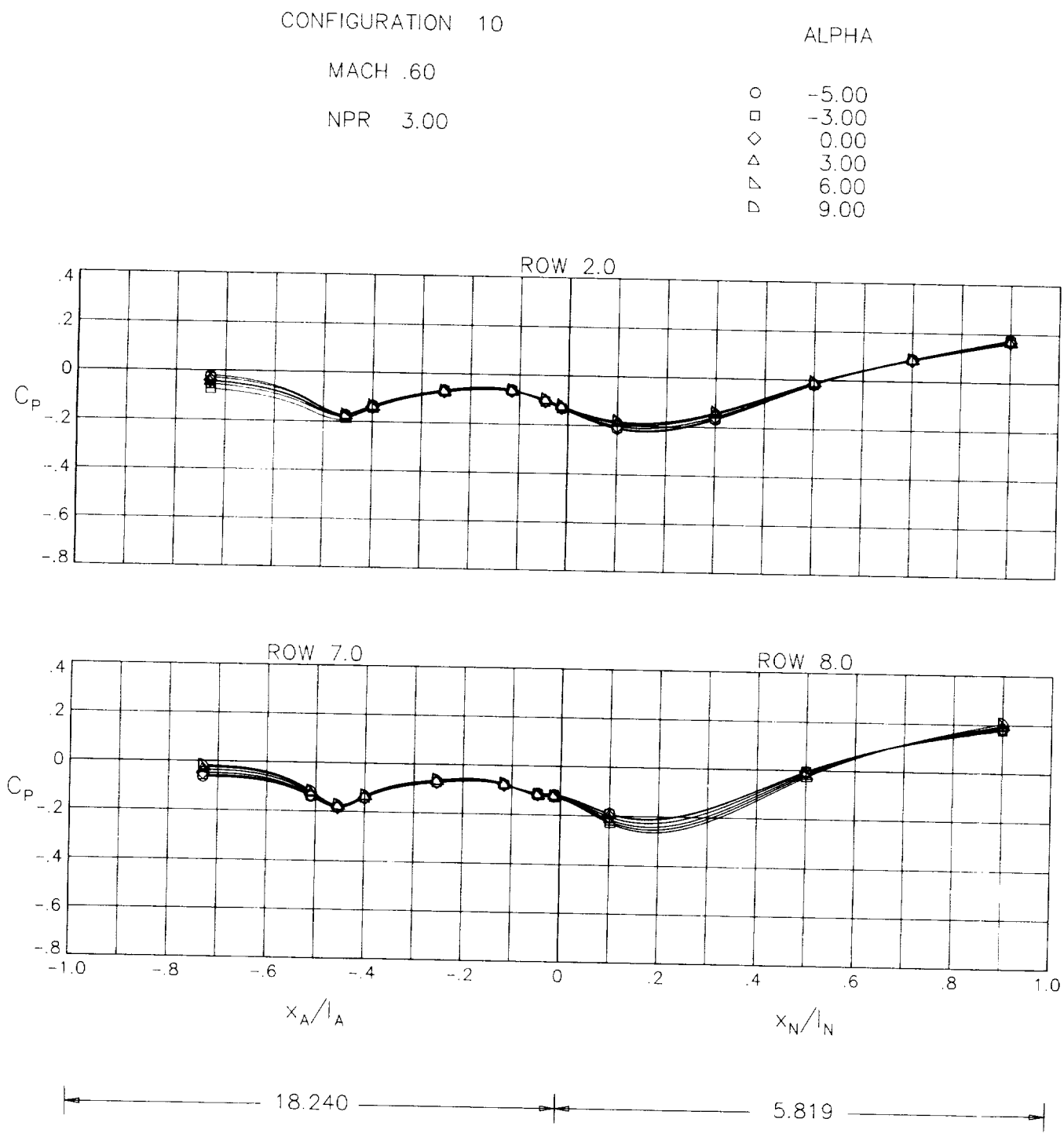

(a) M = 0.60; NPR = 3.0.

Figure 14.- Afterbody/nozzle static-pressure coefficient distributions along upper and lower surface of mid right side for configuration 10.

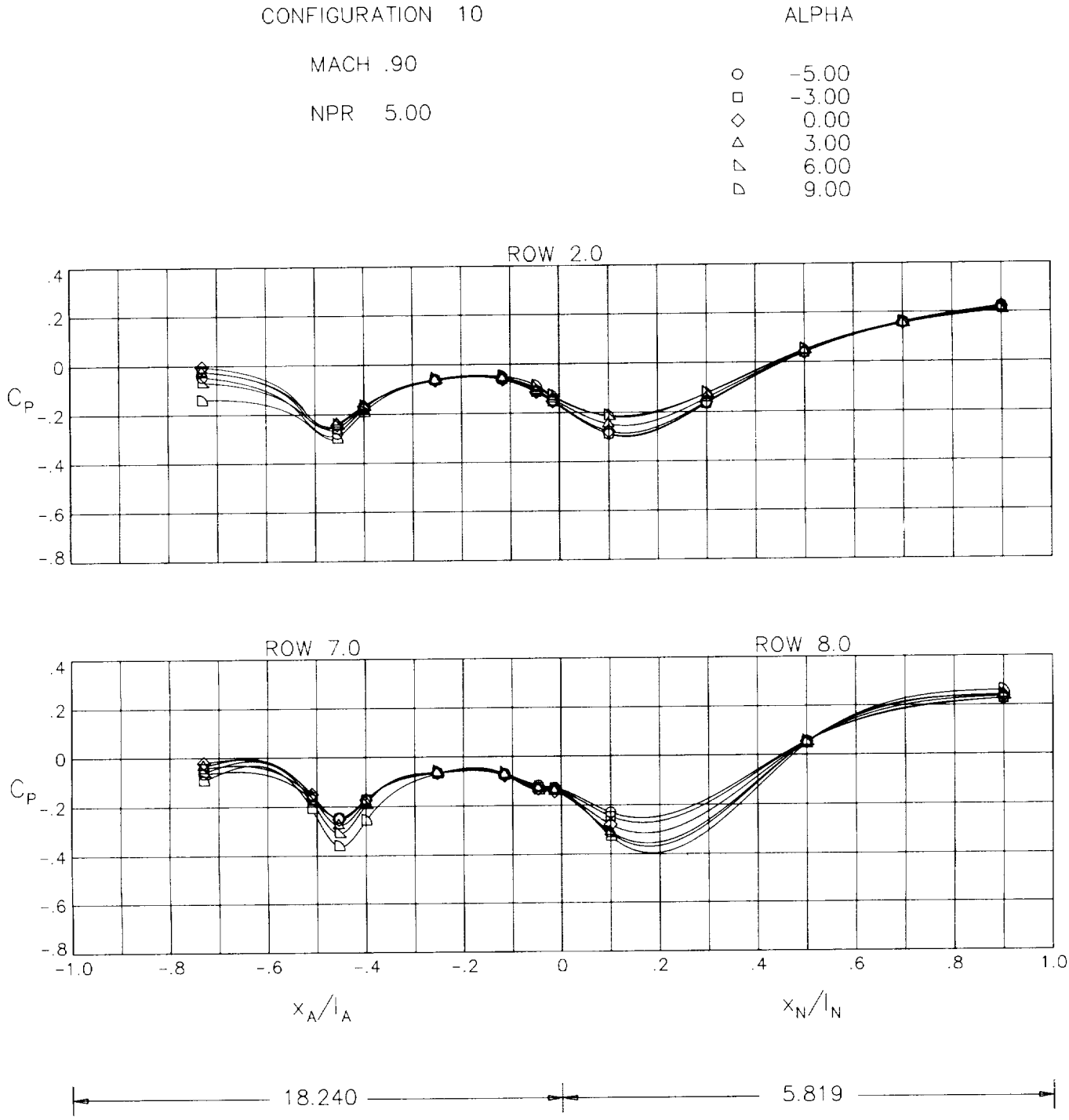

(b) M = 0.90; NPR = 5.0.

Figure 14.- Continued.

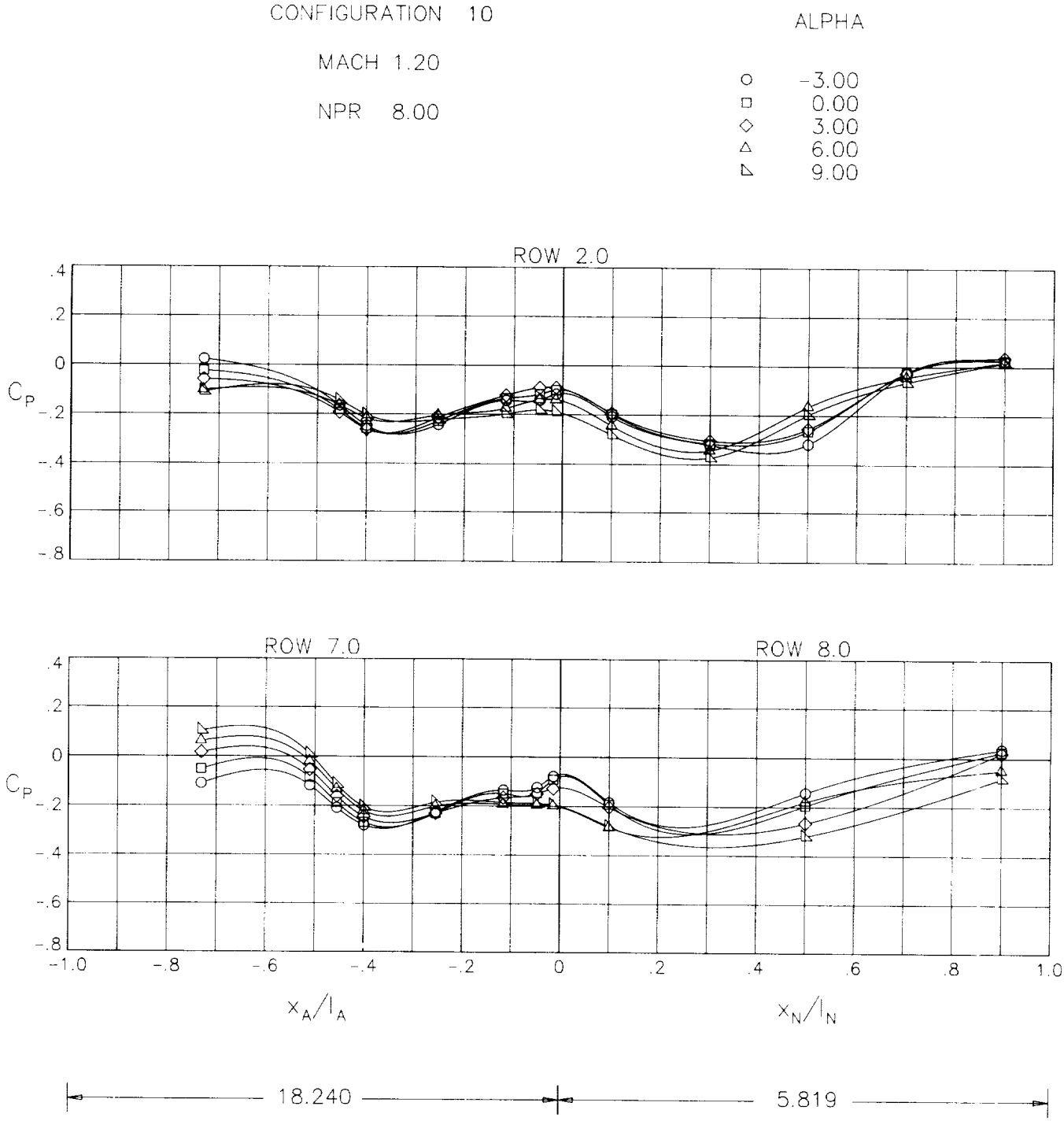

(c) M = 1.20; NPR = 8.0.

Figure 14.- Concluded.

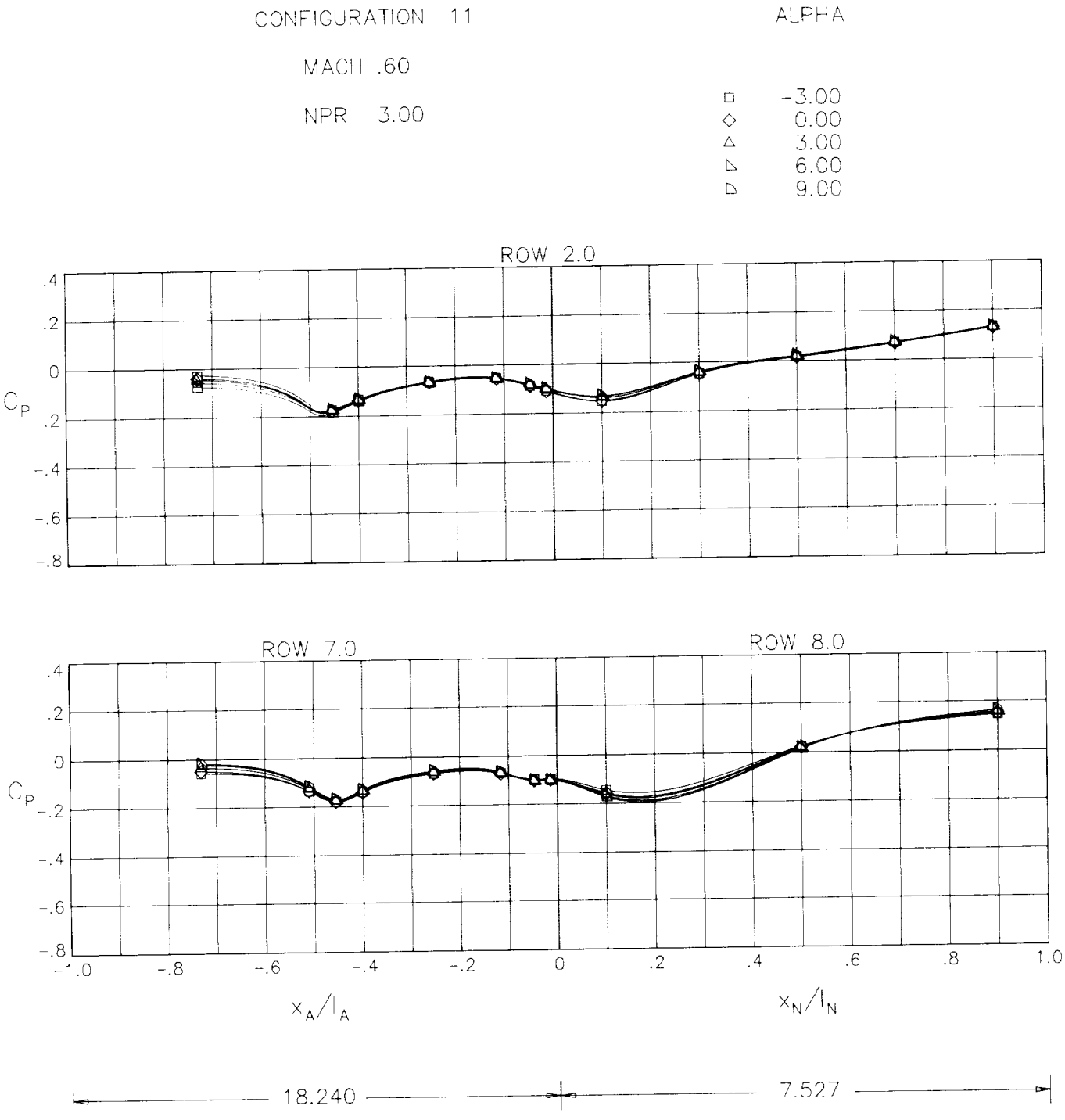

(a) M = 0.60; NPR = 3.0.

Figure 15.- Afterbody/nozzle static-pressure coefficient distributions along upper and lower surface of mid right side for configuration 11.

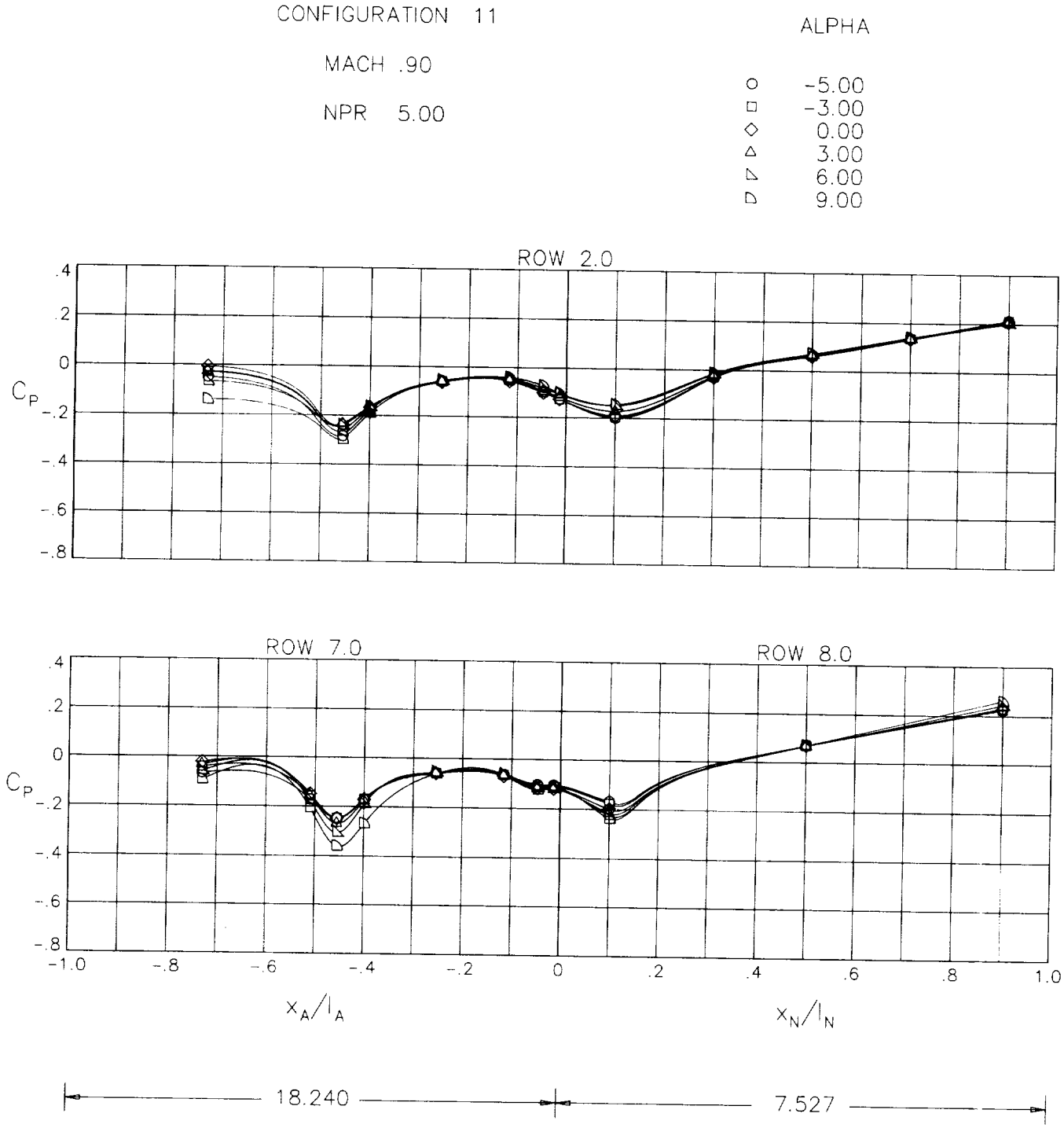

(b) M = 0.90; NPR = 5.0.

Figure 15.- Continued.

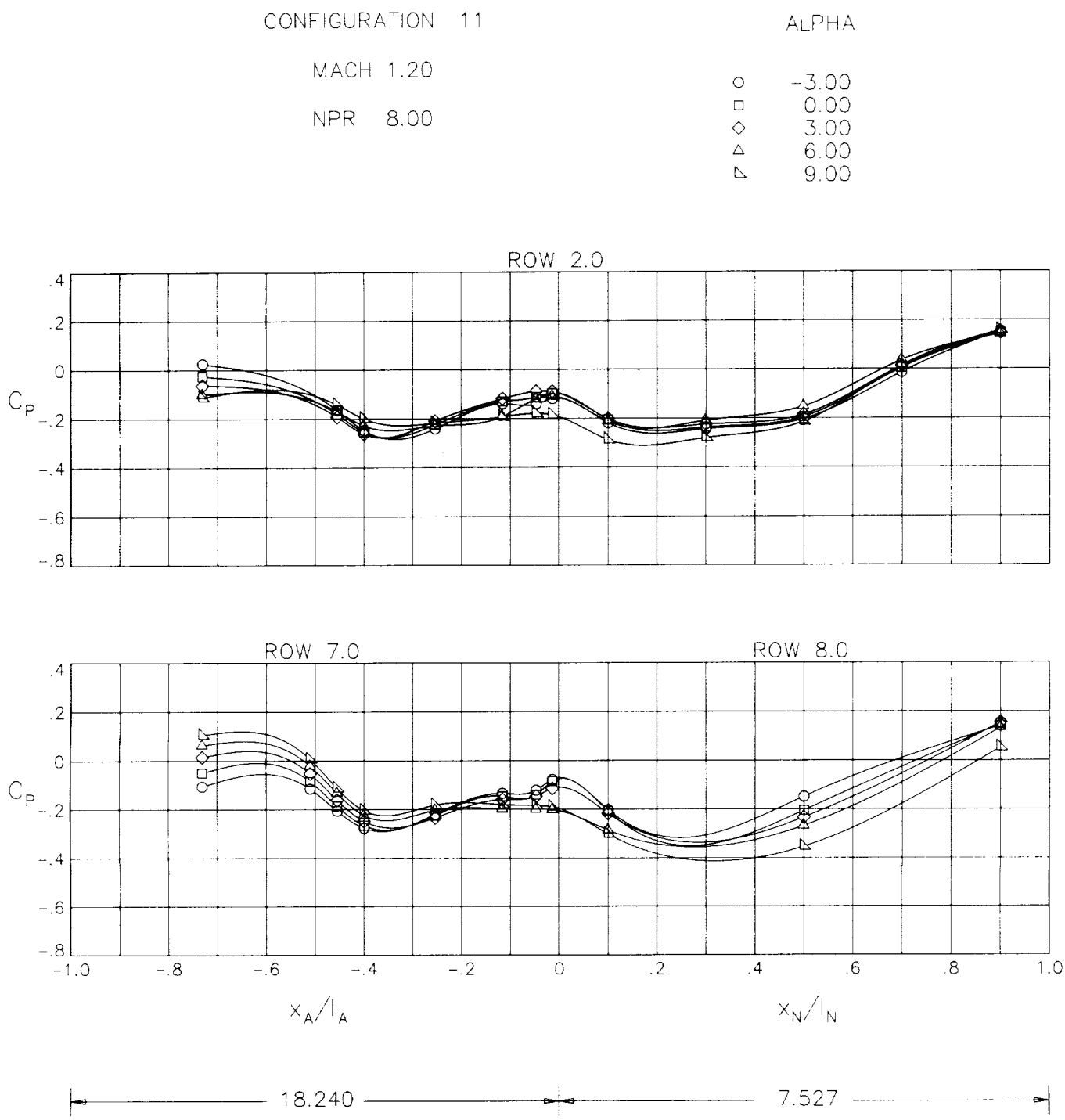

(c) M = 1.20; NPR = 8.0.

Figure 15.- Concluded.

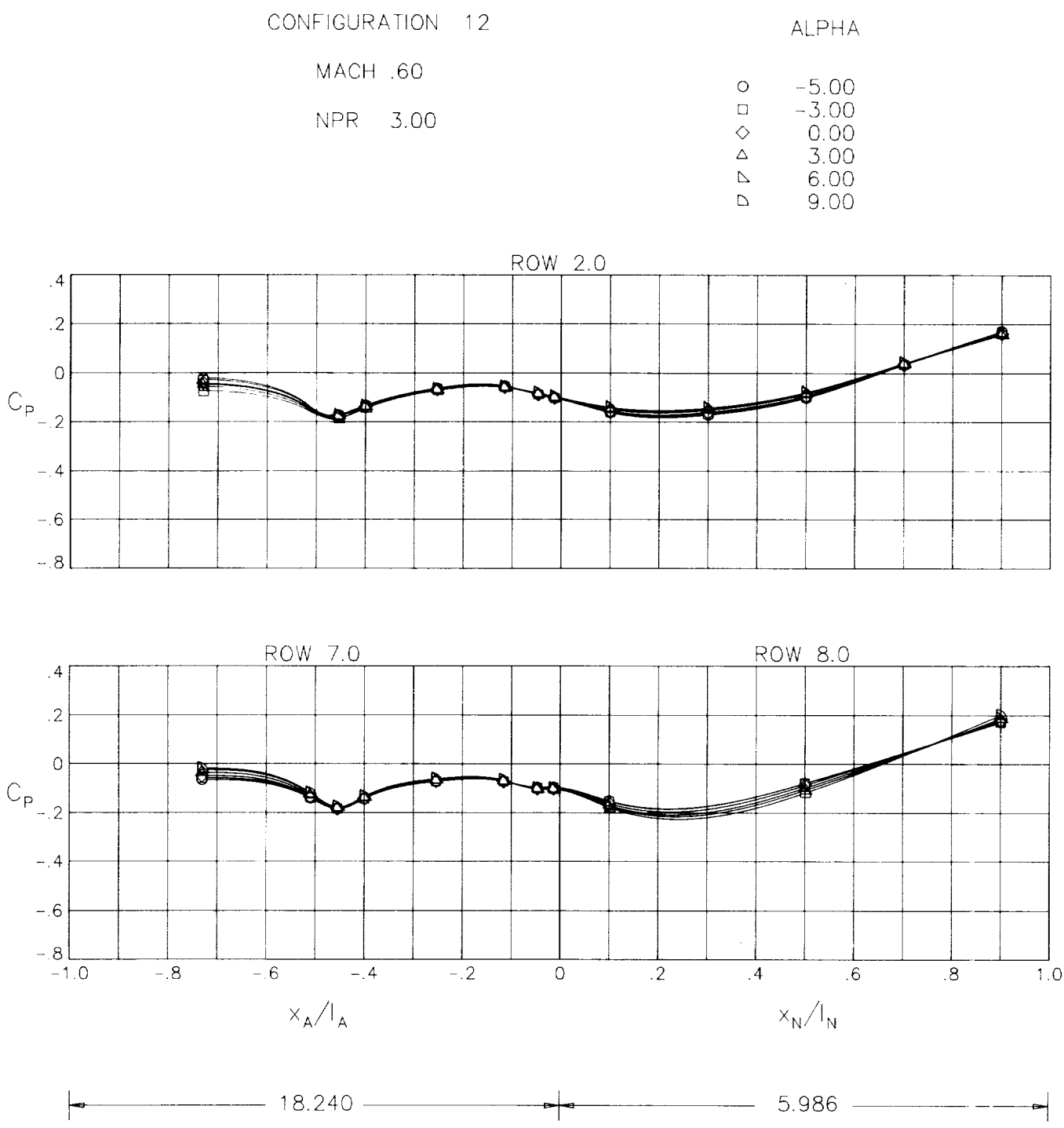

(a) M = 0.60; NPR = 3.0.

Figure 16.- Afterbody/nozzle static-pressure coefficient distributions along upper and lower surface of mid right side for configuration 12.

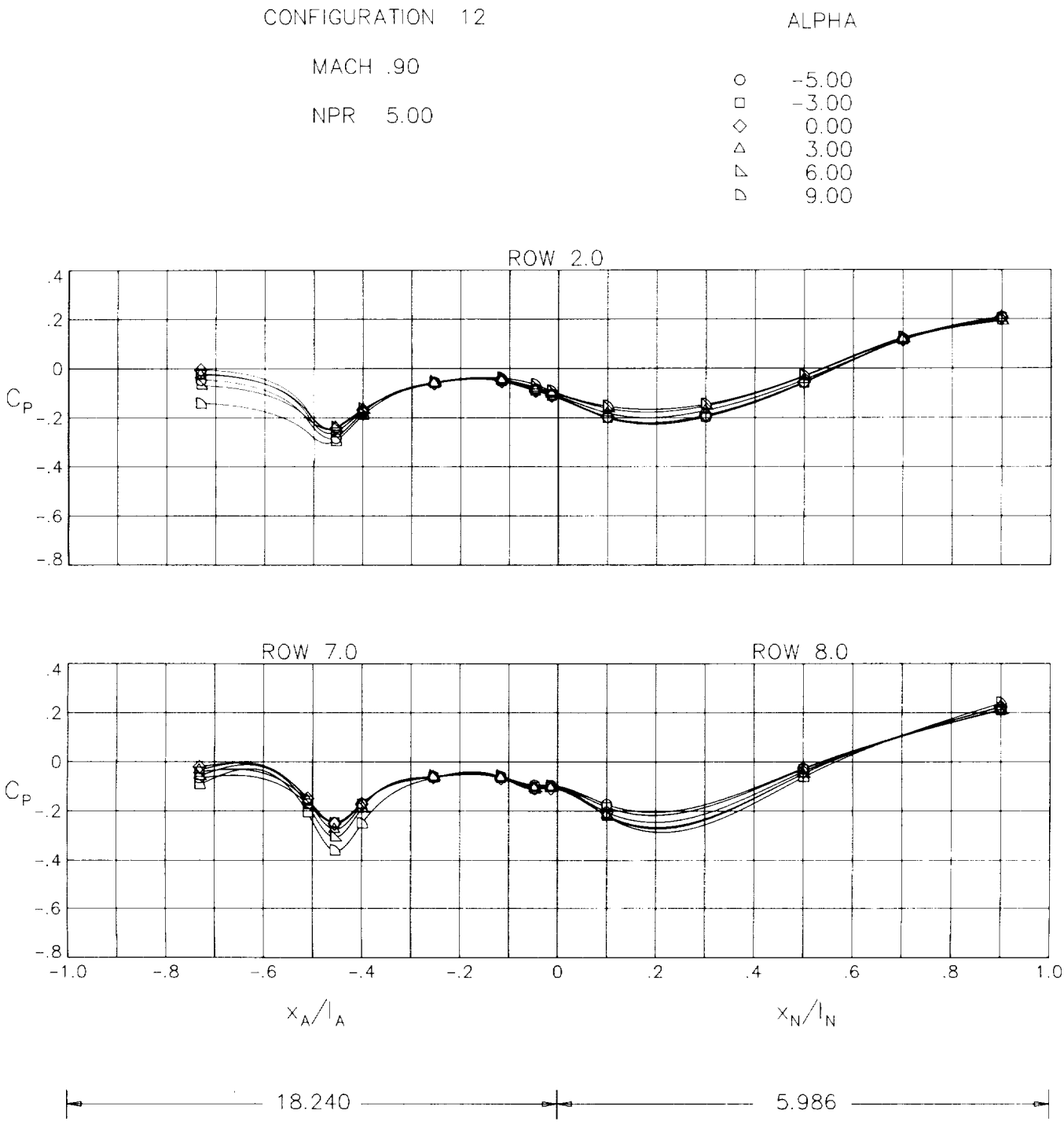

(b) M = 0.90; NPR = 5.0.

Figure 16.- Continued.

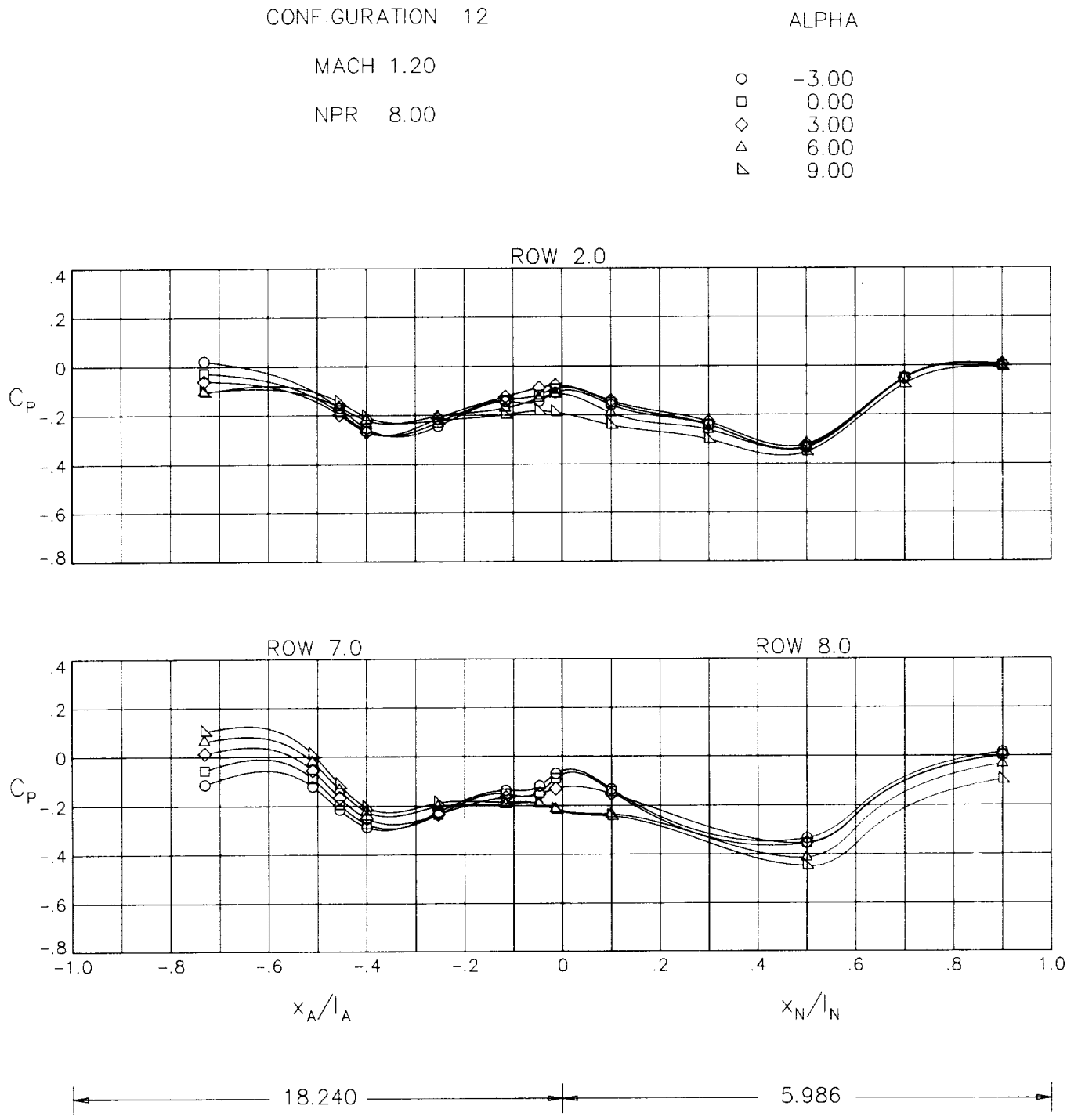

(c) M = 1.20; NPR = 8.0.

Figure 16.- Concluded.

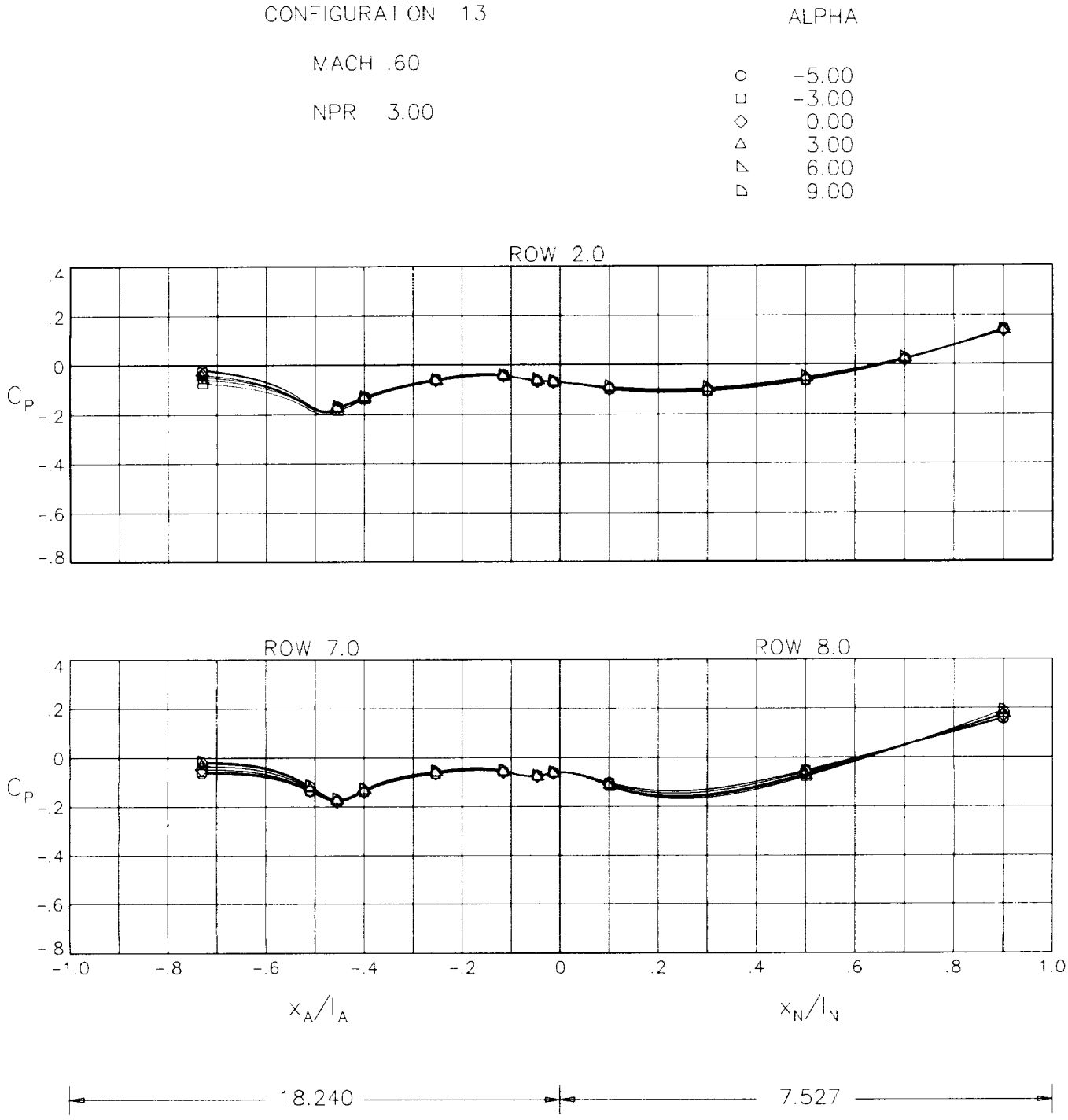

(a) M = 0.60; NPR = 3.0.

Figure 17.- Afterbody/nozzle static-pressure coefficient distributions along upper and lower surface of mid right side for configuration 13.

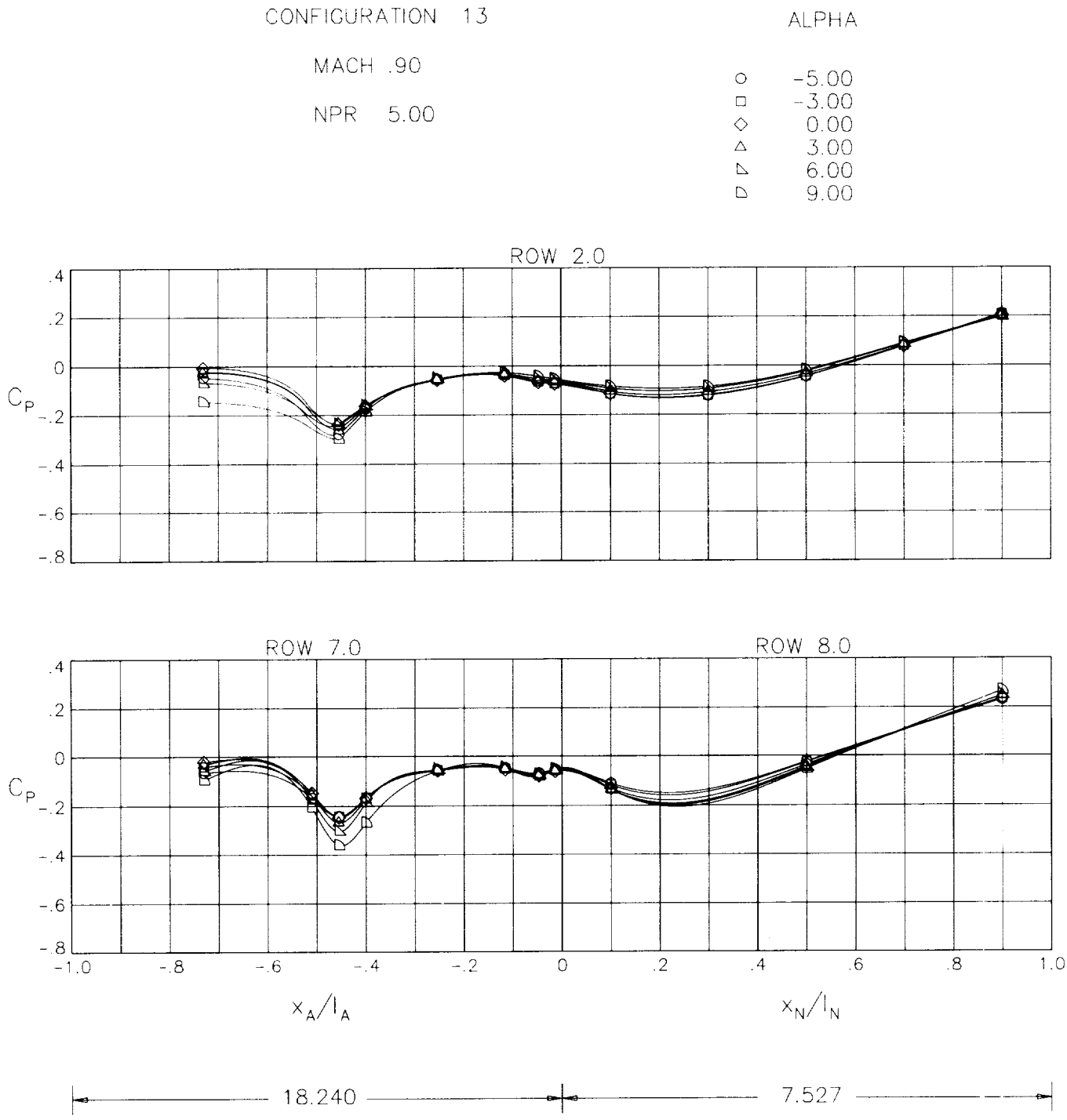

(b) M = 0.90; NPR = 5.0.

Figure 17.- Continued.

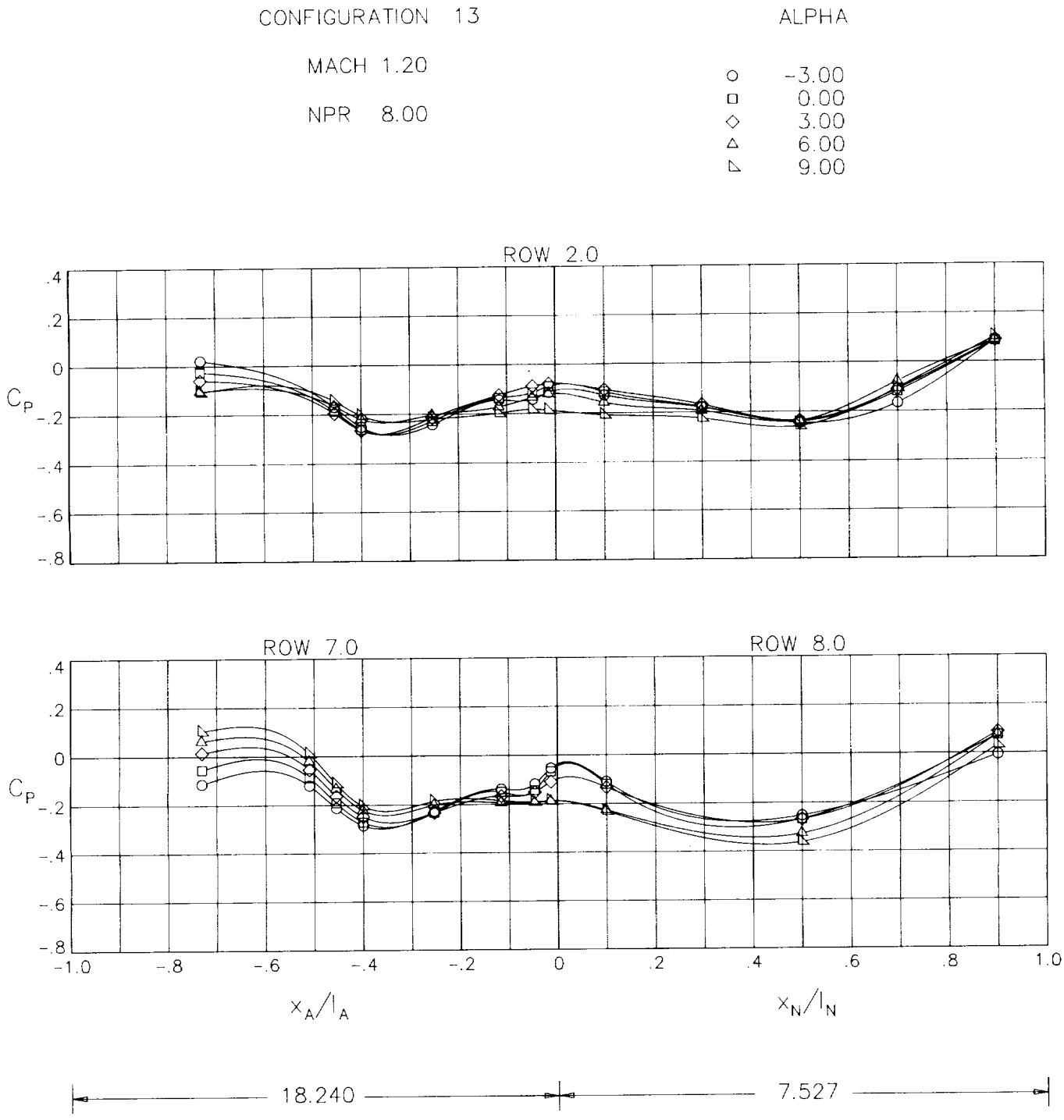

(c) M = 1.20; NPR = 8.0.

Figure 17.- Concluded.

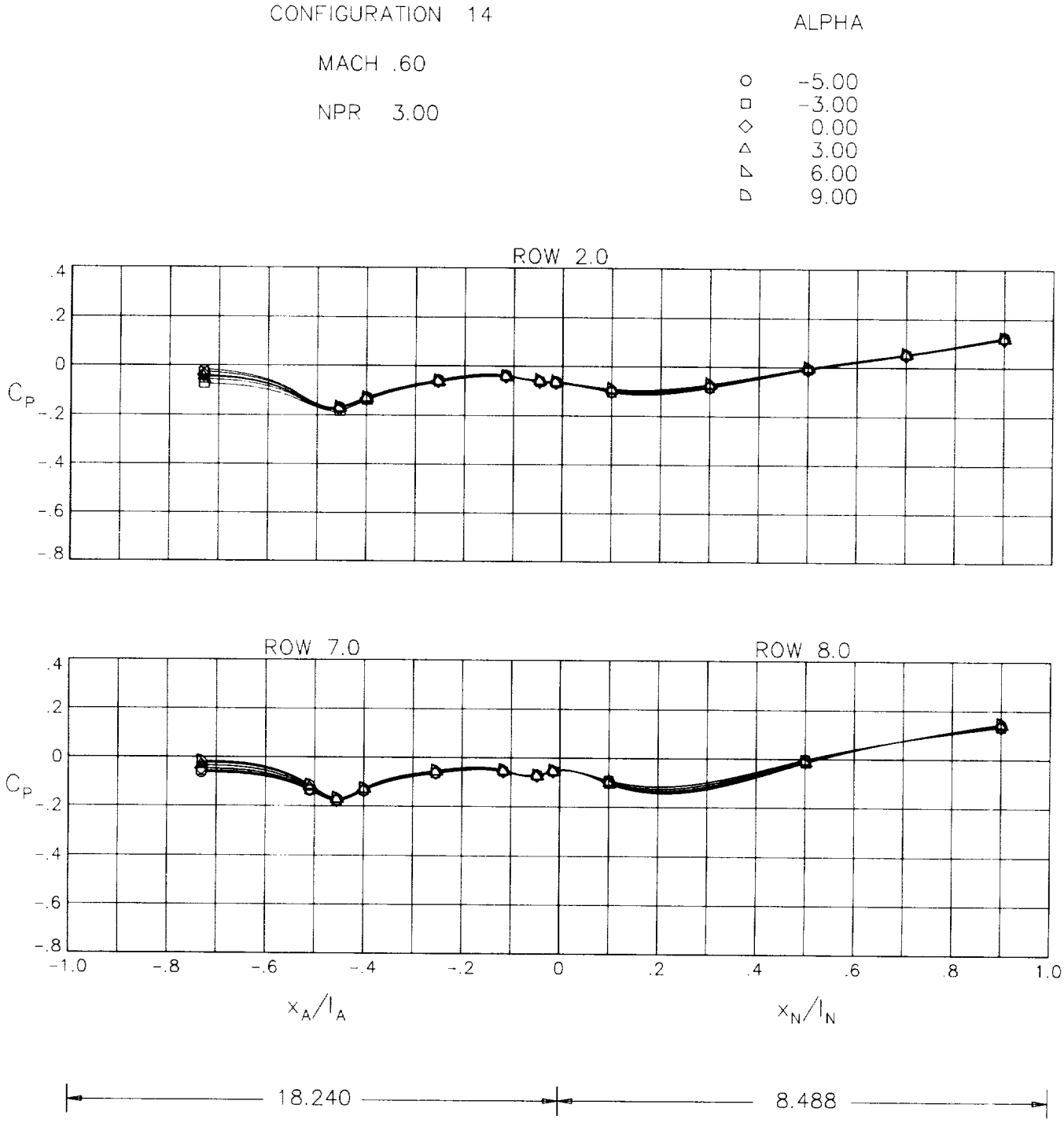

(a) M = 0.60; NPR = 3.0.

Figure 18.- Afterbody/nozzle static-pressure coefficient distributions along upper and lower surface of mid right side for configuration 14.

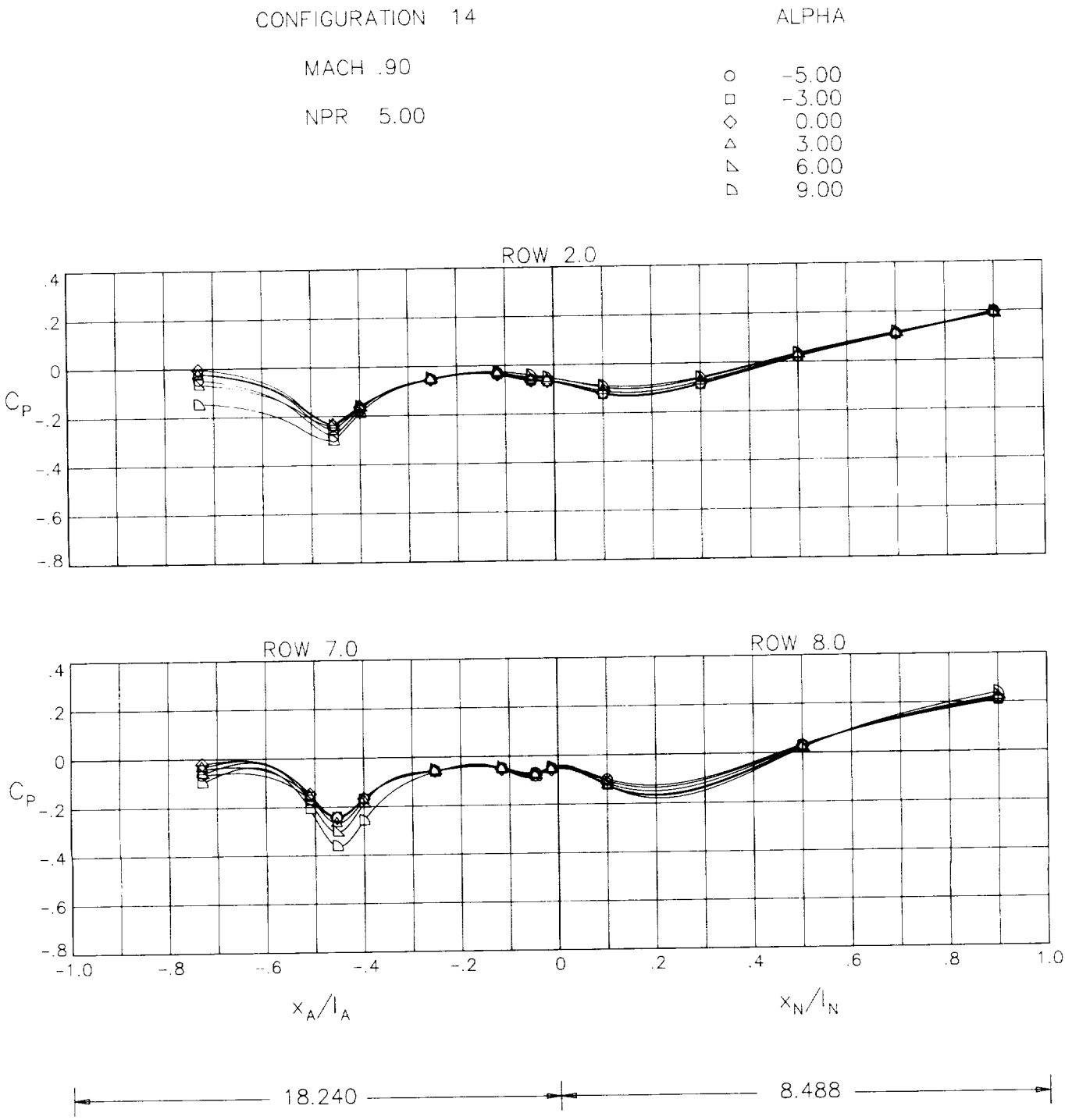

(b) M = 0.90; NPR = 5.0.

Figure 18.- Continued.

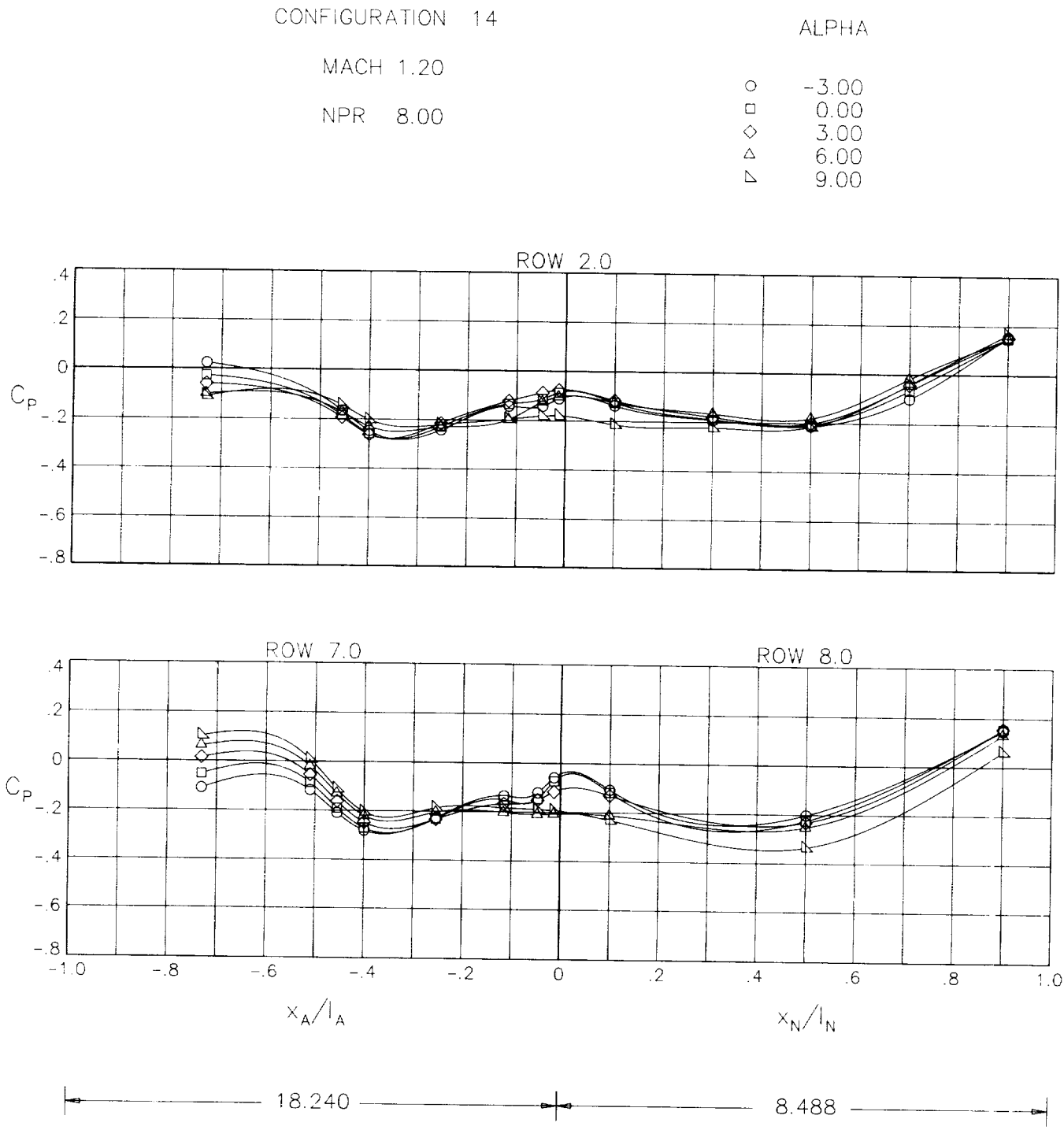

(c) M = 1.20; NPR = 8.0.

Figure 18.- Concluded.

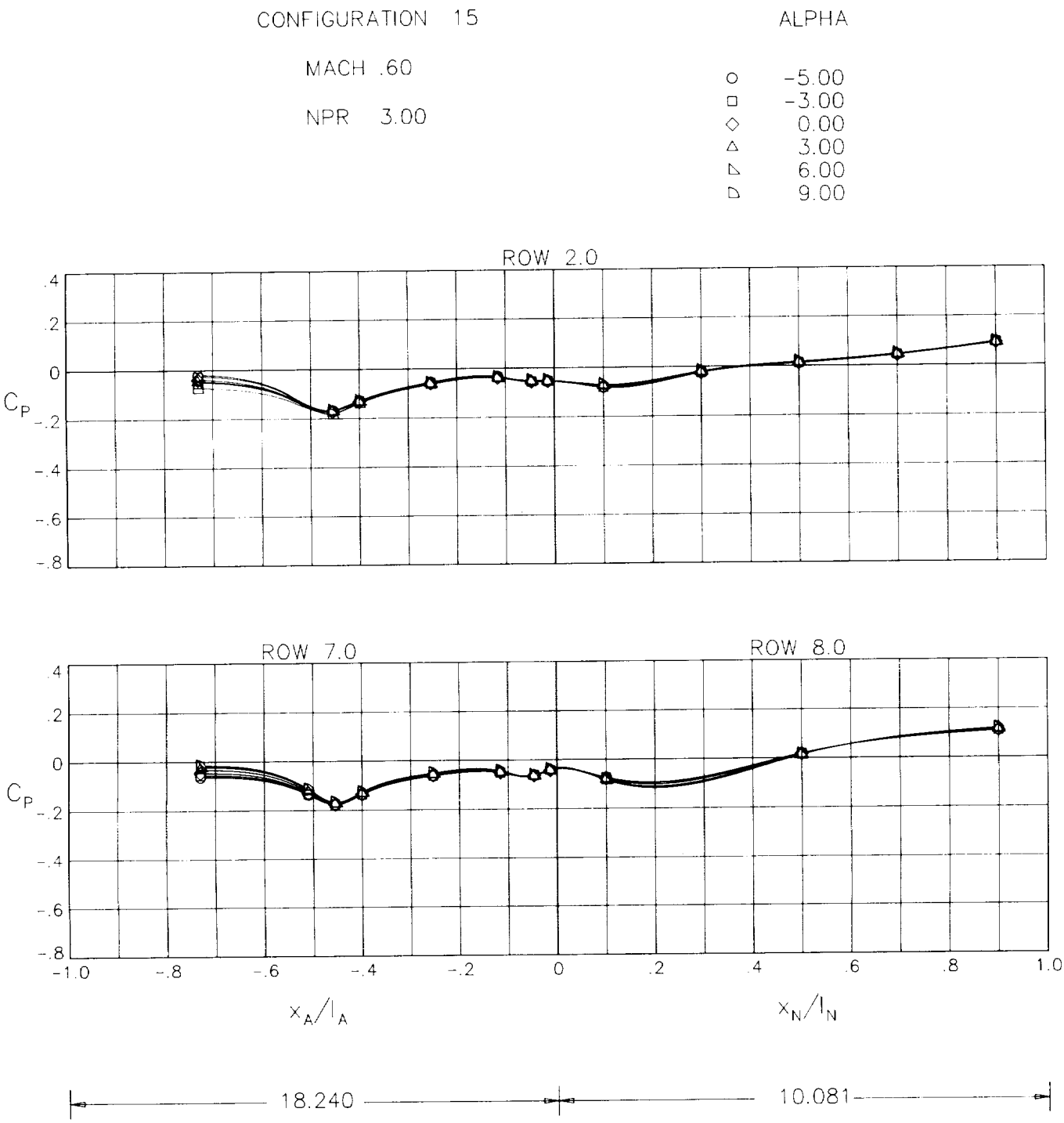

(a) M = 0.60; NPR = 3.0.

Figure 19.- Afterbody/nozzle static-pressure coefficient distributions along upper and lower surface of mid right side for configuration 15.

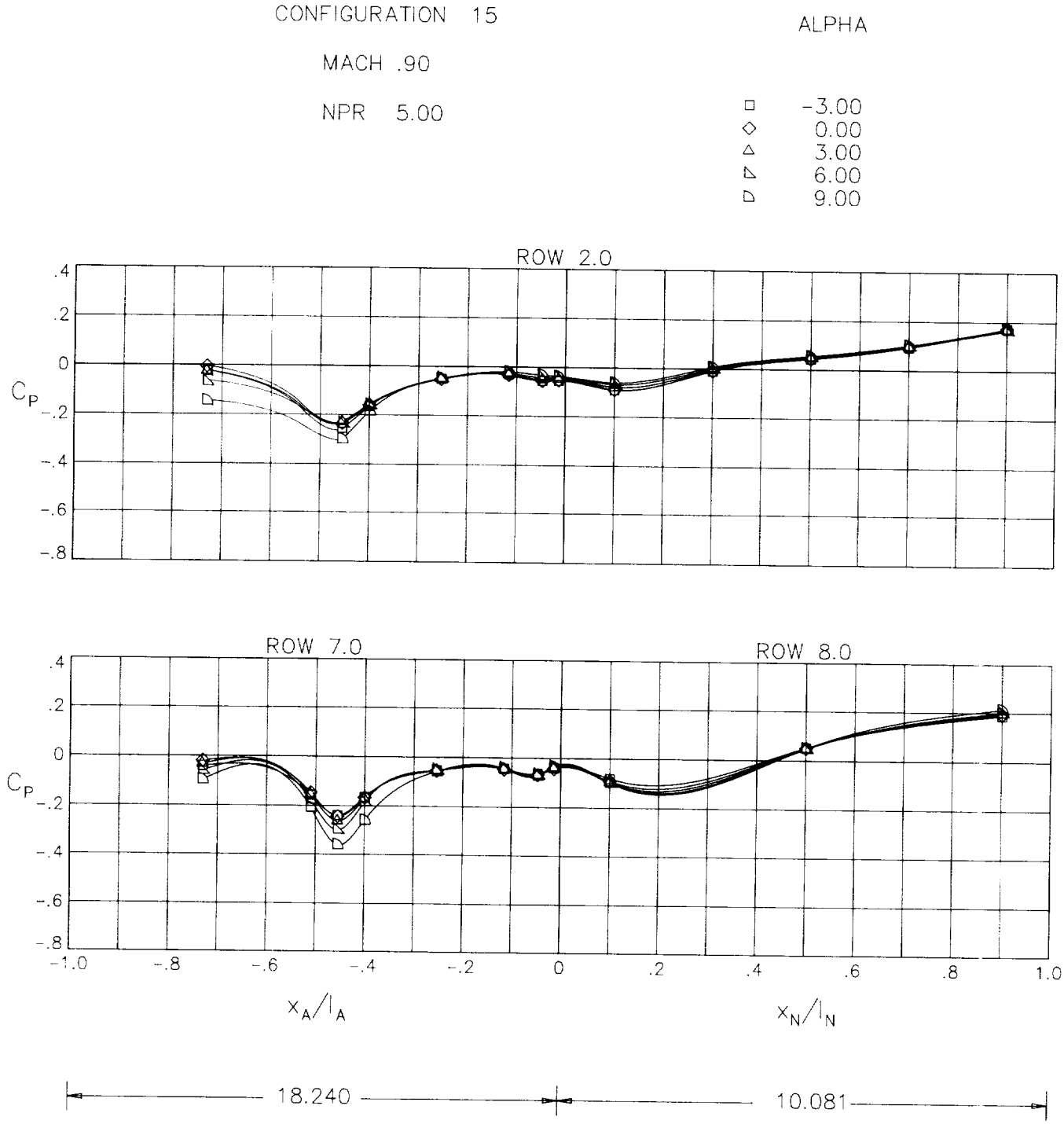

(b) M = 0.90; NPR = 5.0.

Figure 19.- Continued.

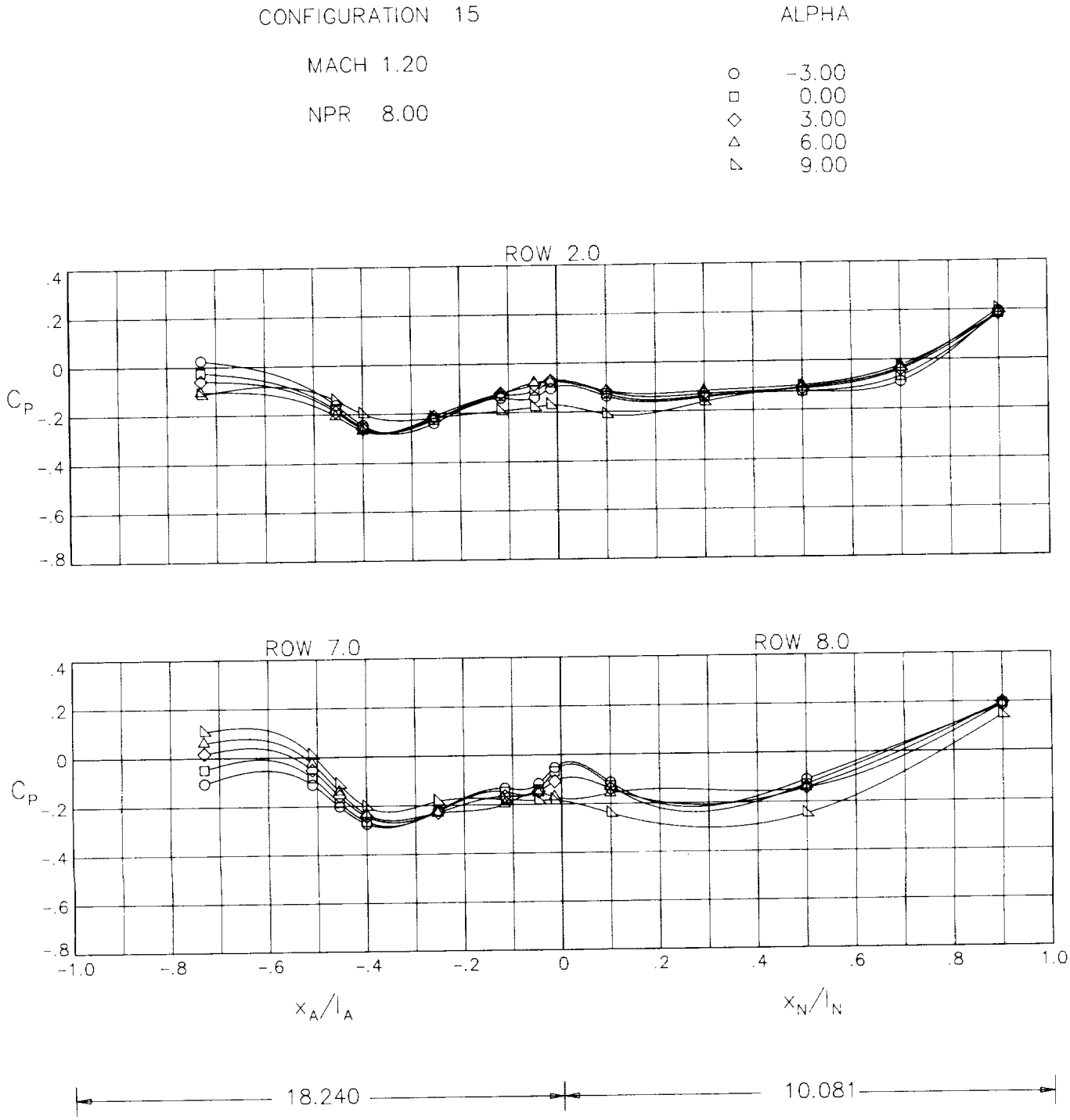

(c) M = 1.20; NPR = 8.0.

Figure 19.- Concluded.

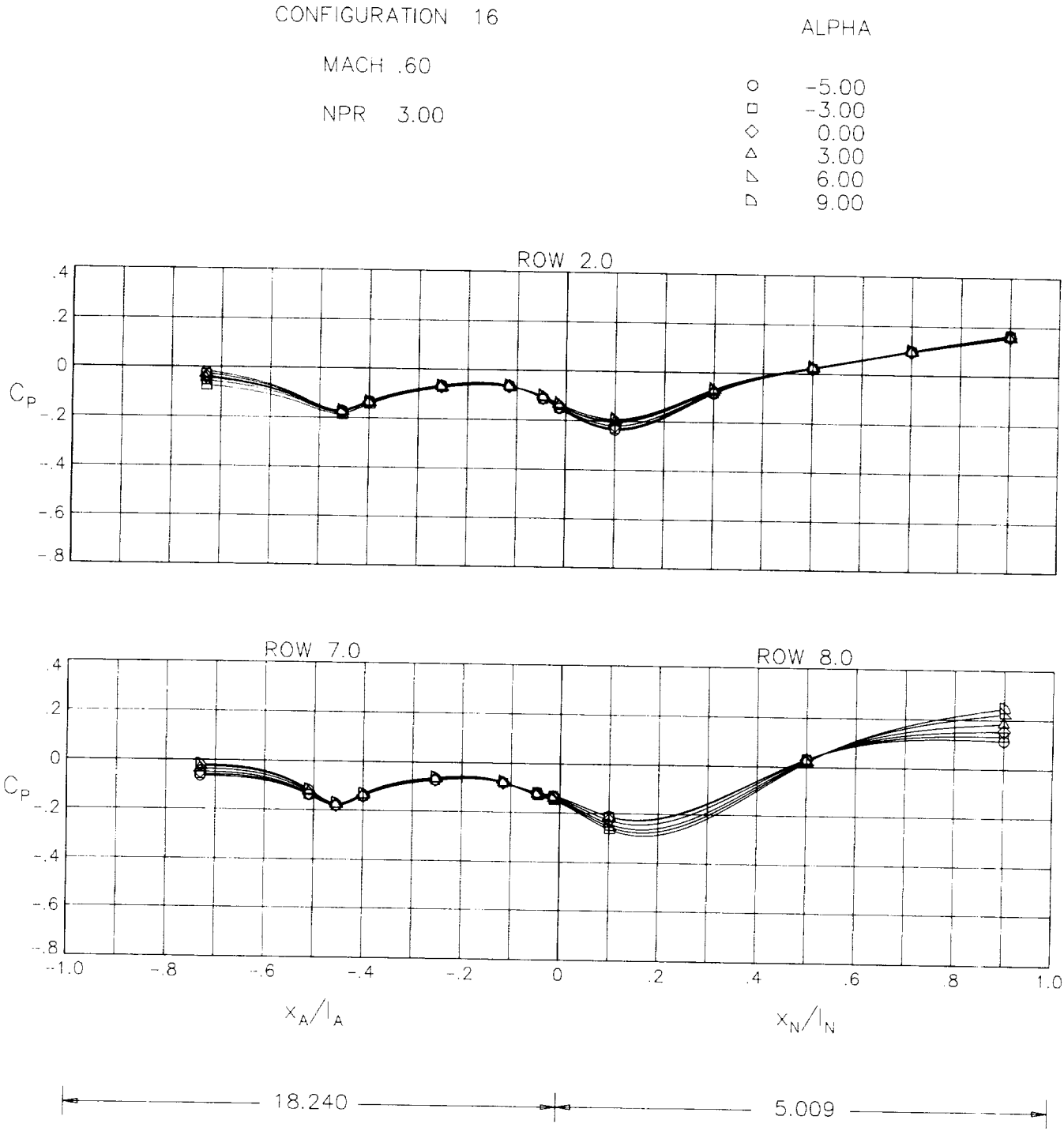

(a) M = 0.60; NPR = 3.0.

Figure 20.- Afterbody/nozzle static-pressure coefficient distributions along upper and lower surface of mid right side for configuration 16.

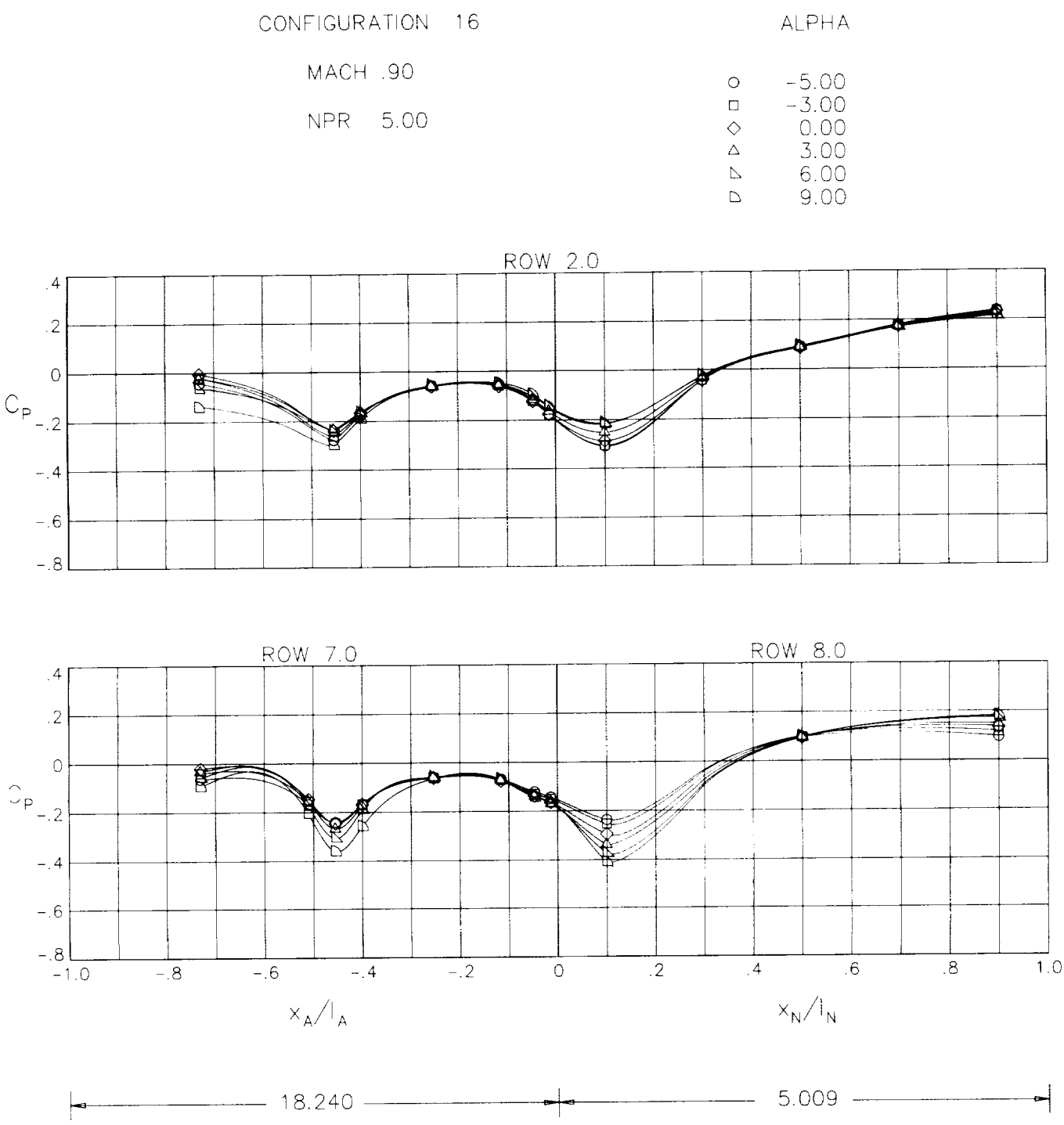

(b) M = 0.90; NPR = 5.0.

Figure 20.- Continued.

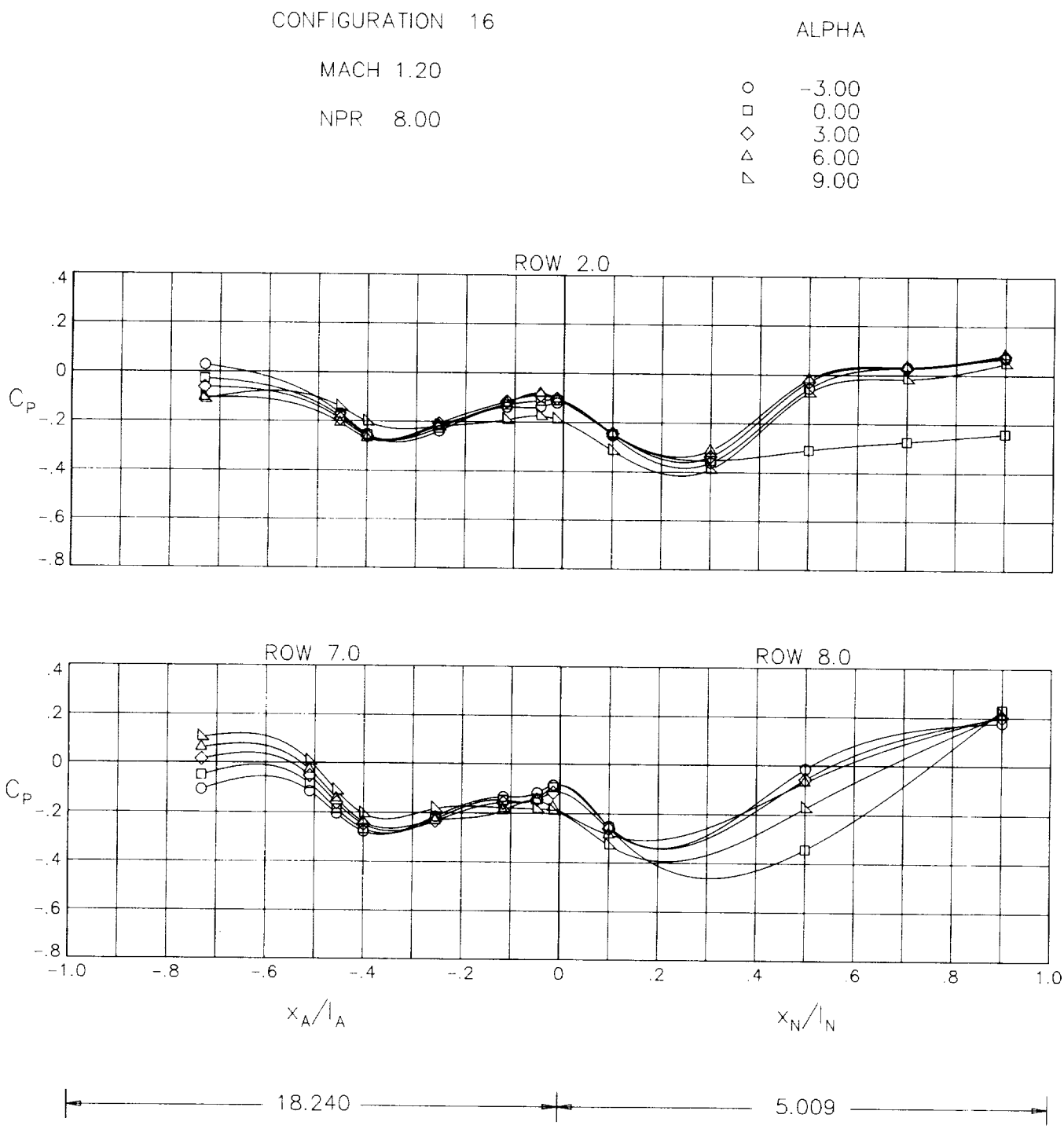

(c) M = 1.20; NPR = 8.0.

Figure 20.- Concluded.

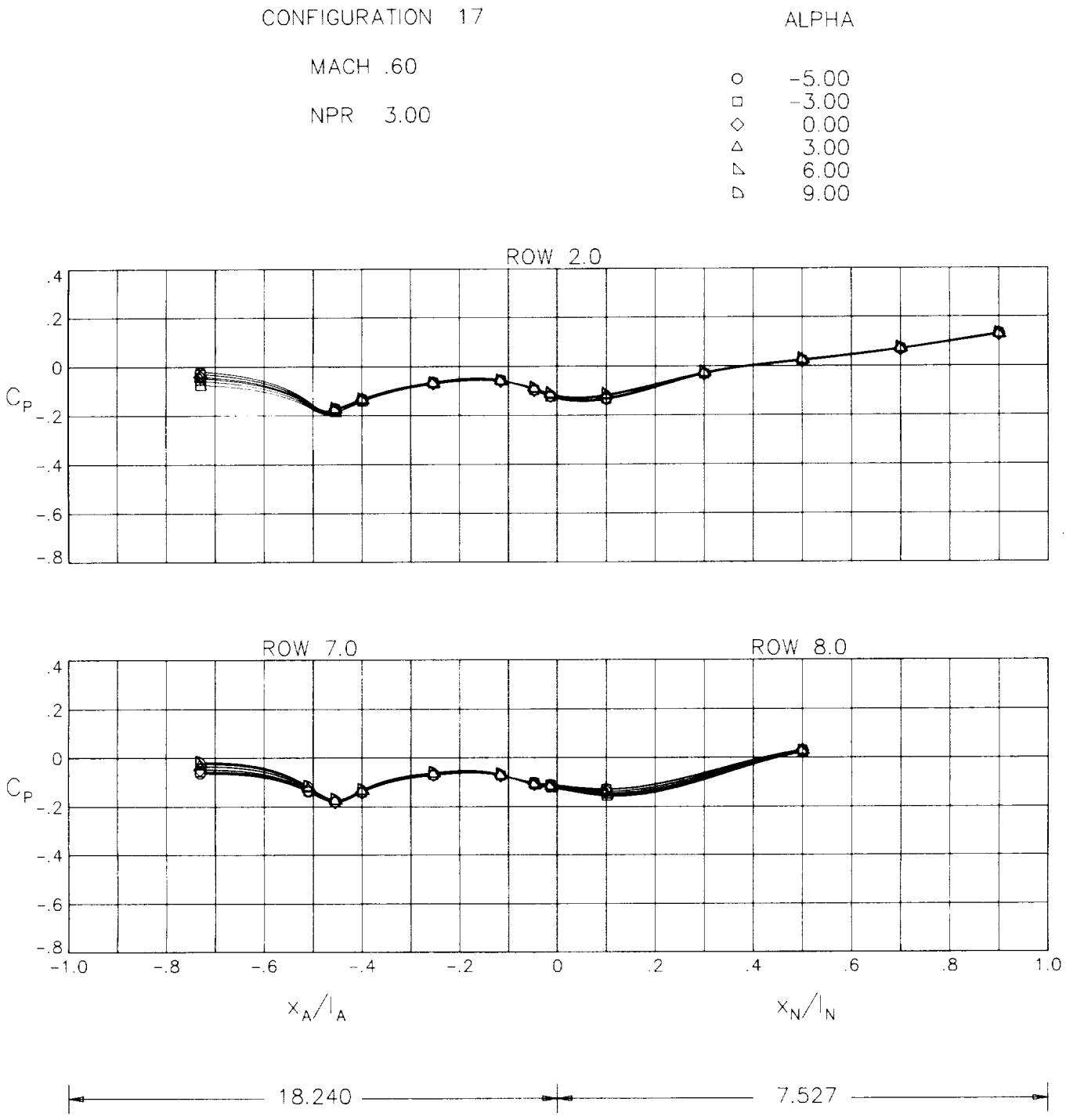

(a) M = 0.60; NPR = 3.0.

Figure 21.- Afterbody/nozzle static-pressure coefficient distributions along upper and lower surface of mid right side for configuration 17.

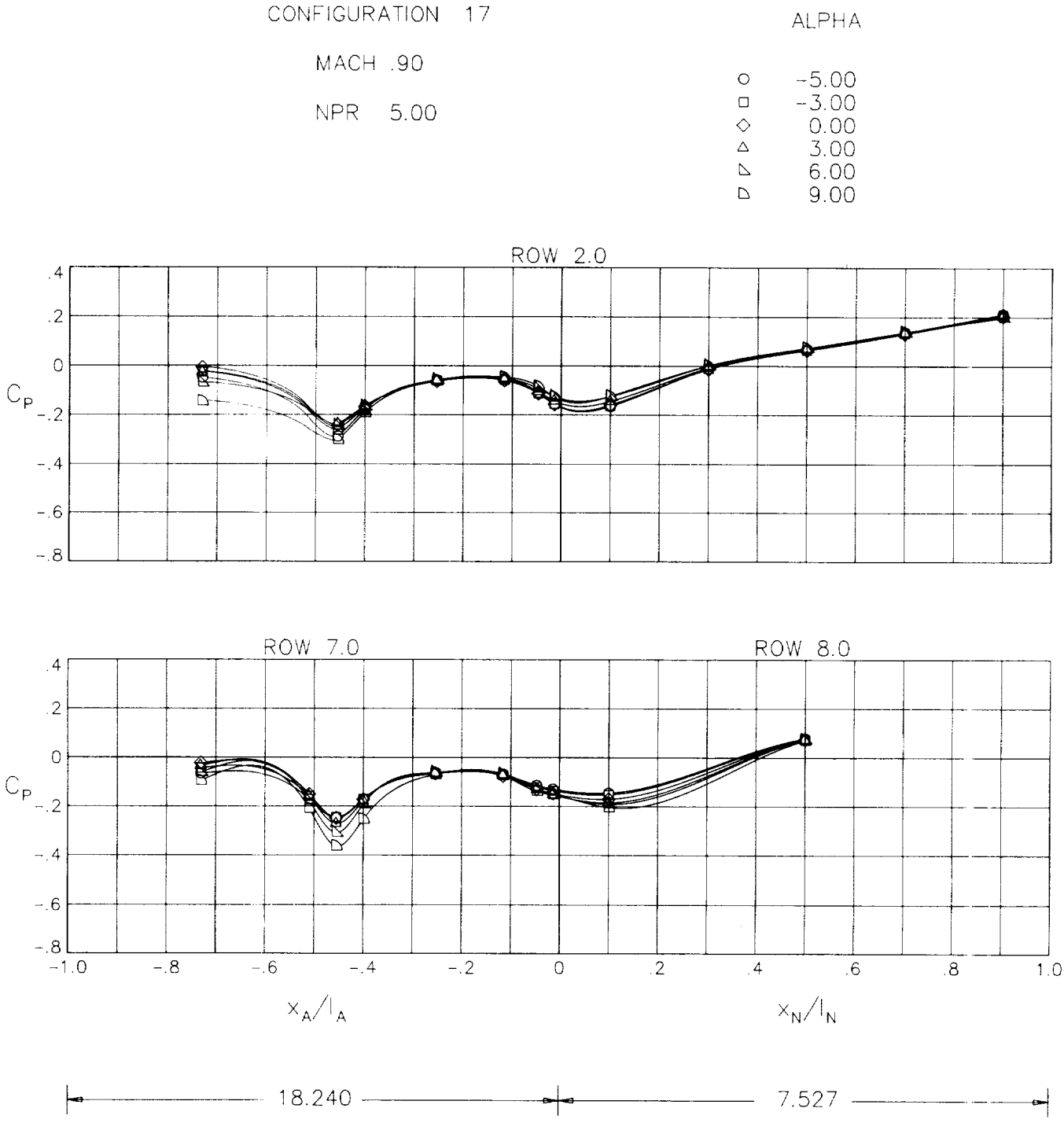

(b) M = 0.90; NPR = 5.0.

Figure 21.- Continued.

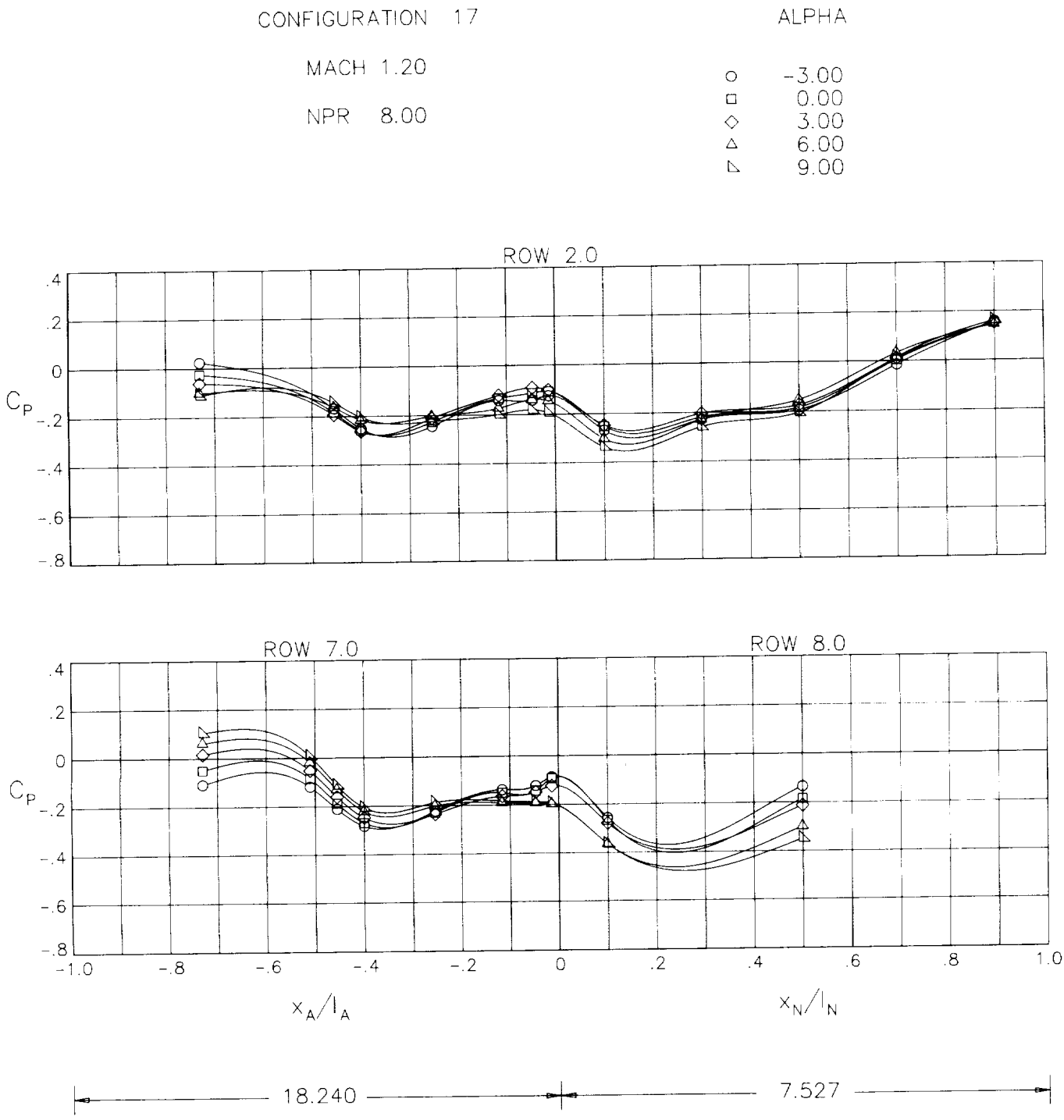

(c) M = 1.20; NPR = 8.0.

Figure 21.- Concluded.

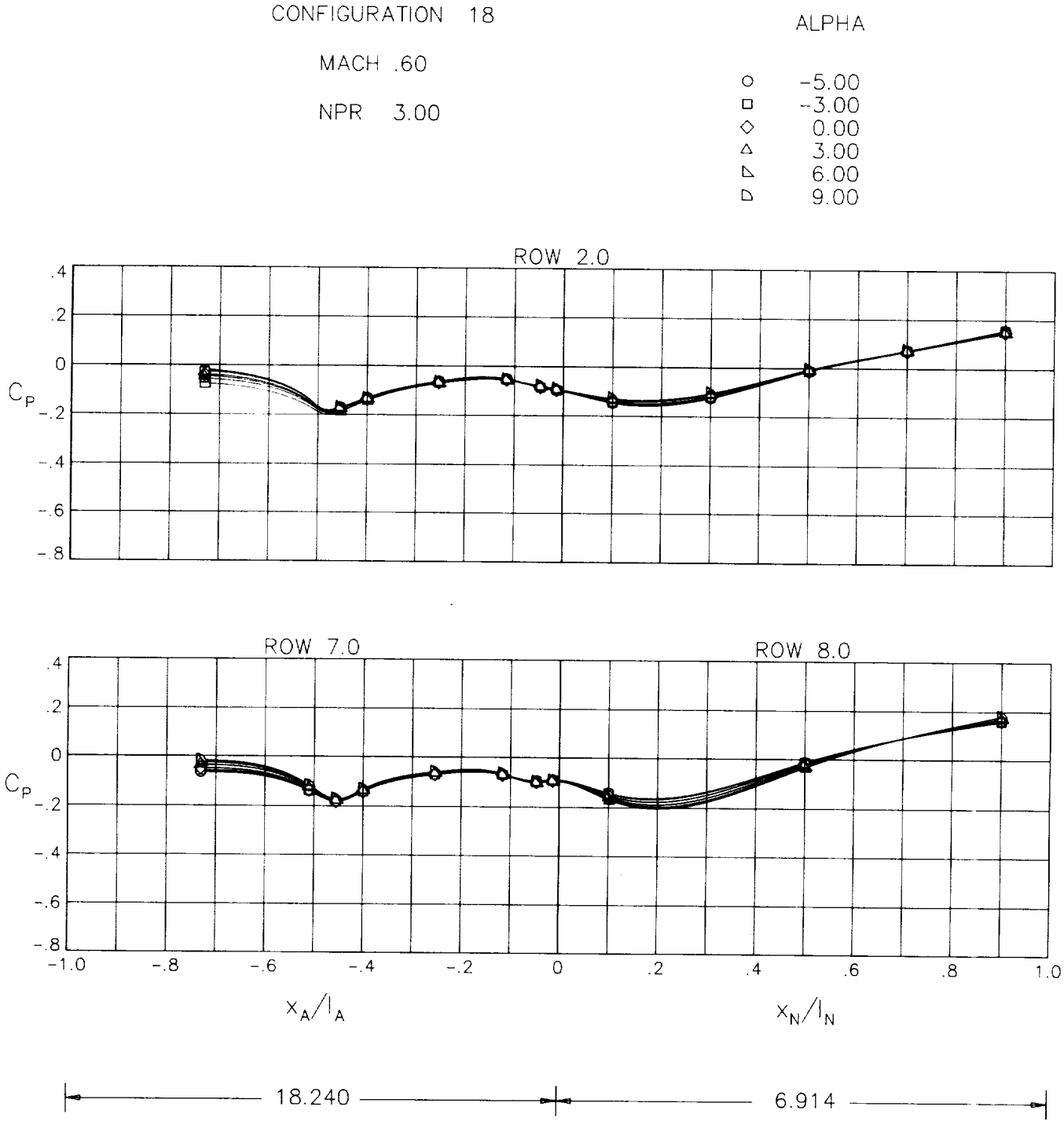

(a) M = 0.60; NPR = 3.0.

Figure 22.- Afterbody/nozzle static-pressure coefficient distributions along upper and lower surface of mid right side for configuration 18.

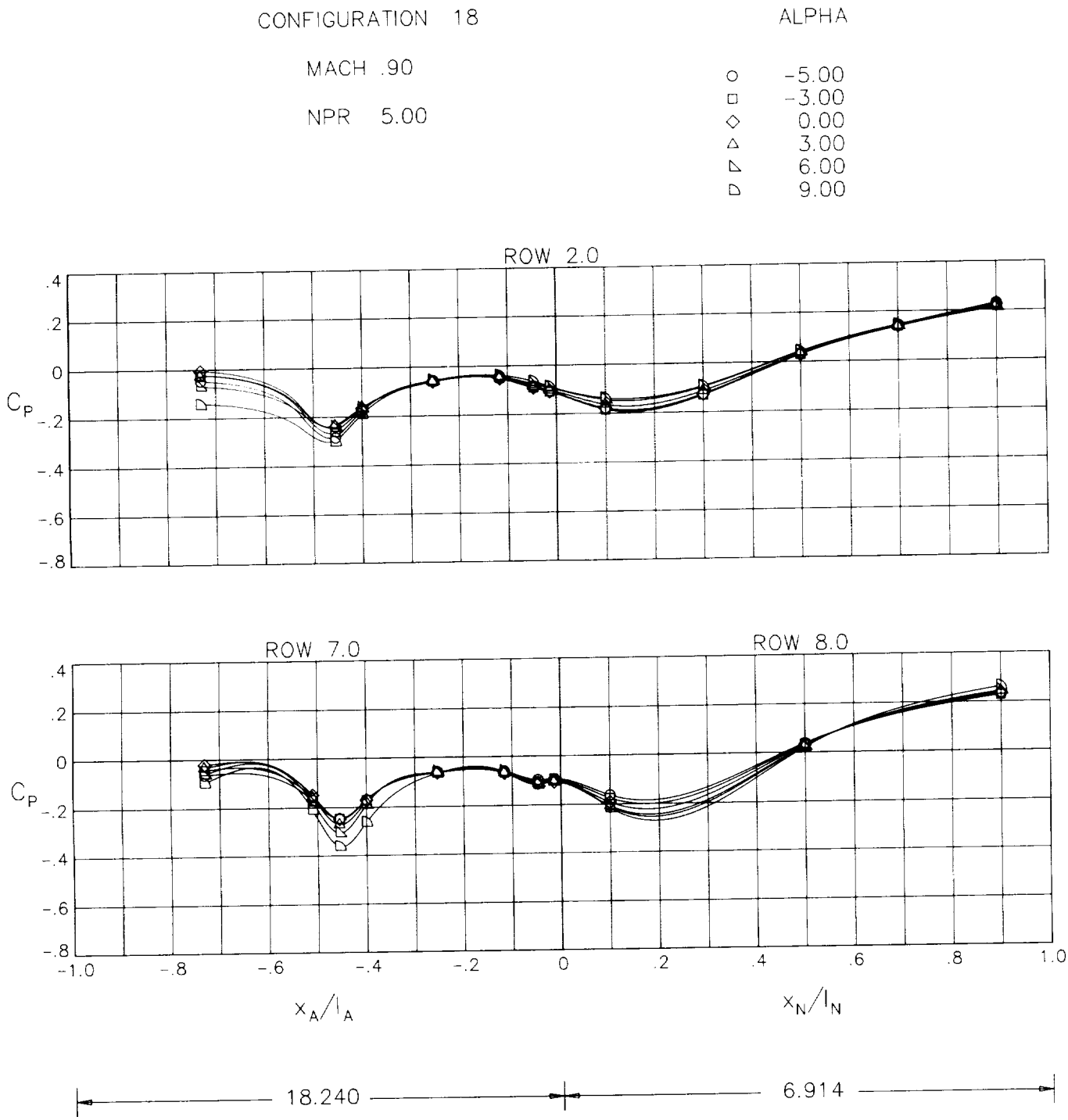

(b) M = 0.90; NPR = 5.0.

Figure 22.- Continued.

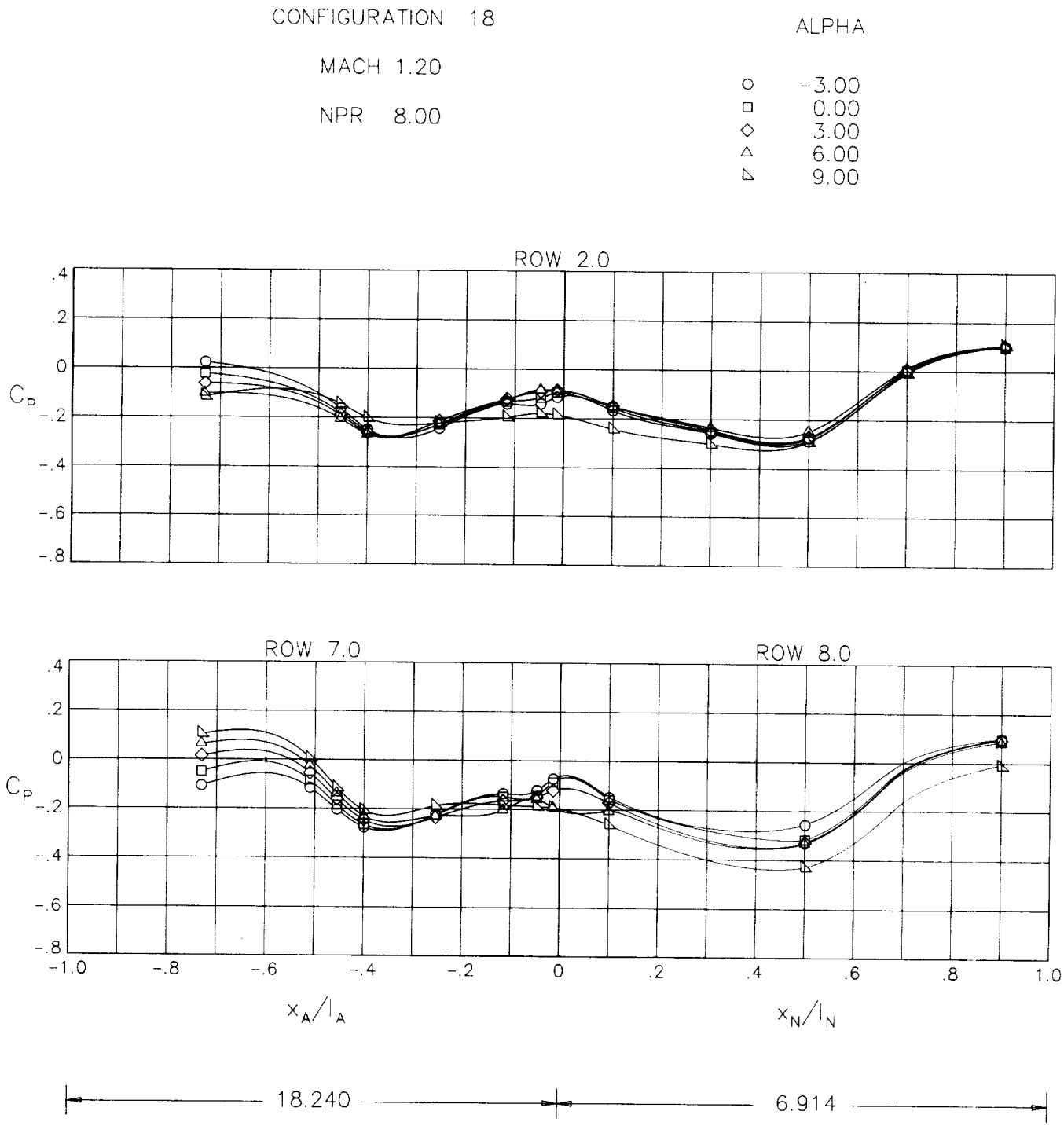

(c) M = 1.20; NPR = 8.0.

Figure 22.- Concluded.

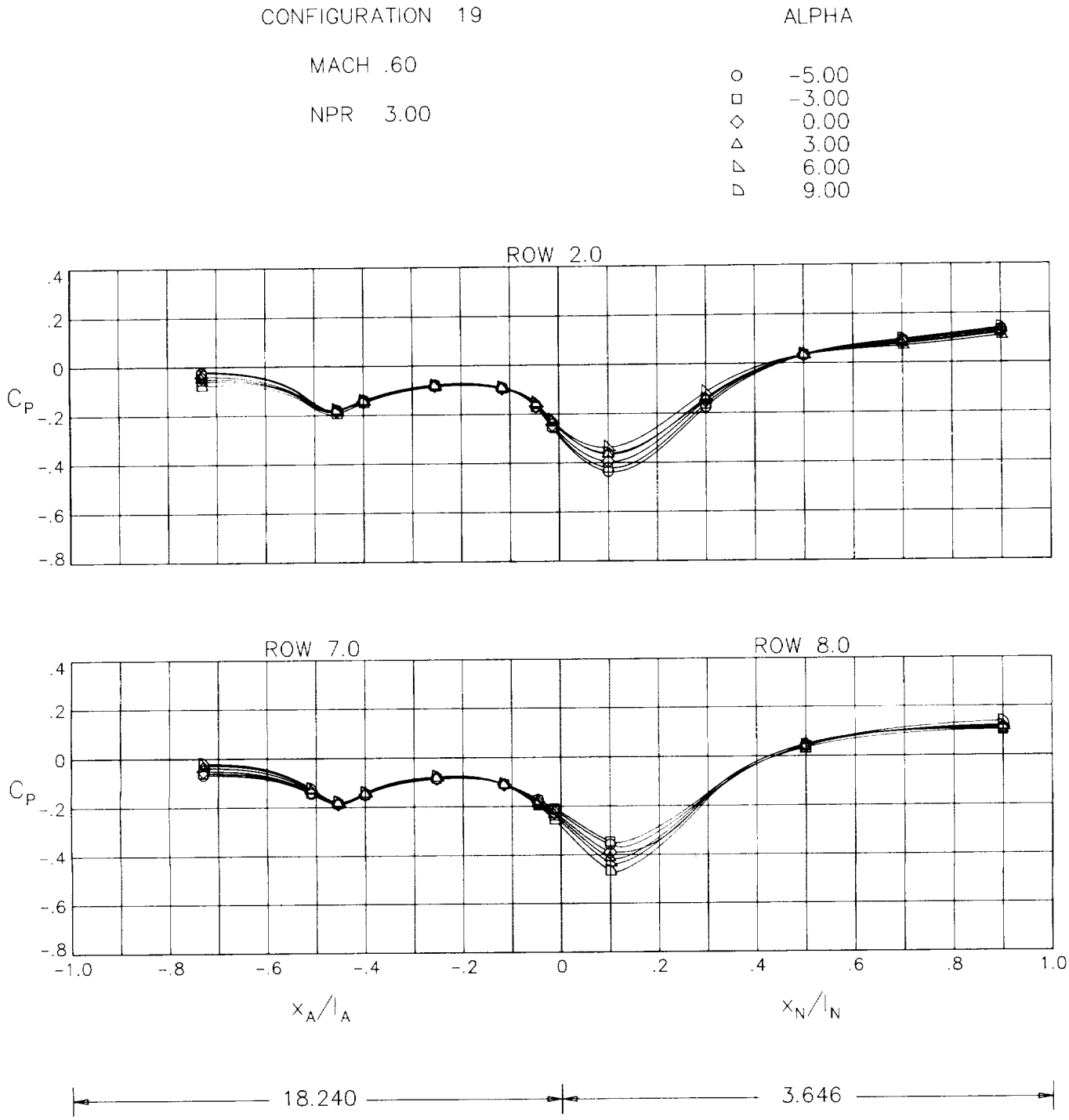

(a) M = 0.60; NPR = 3.0.

Figure 23.- Afterbody/nozzle static-pressure coefficient distributions along upper and lower surface of mid right side for configuration 19.

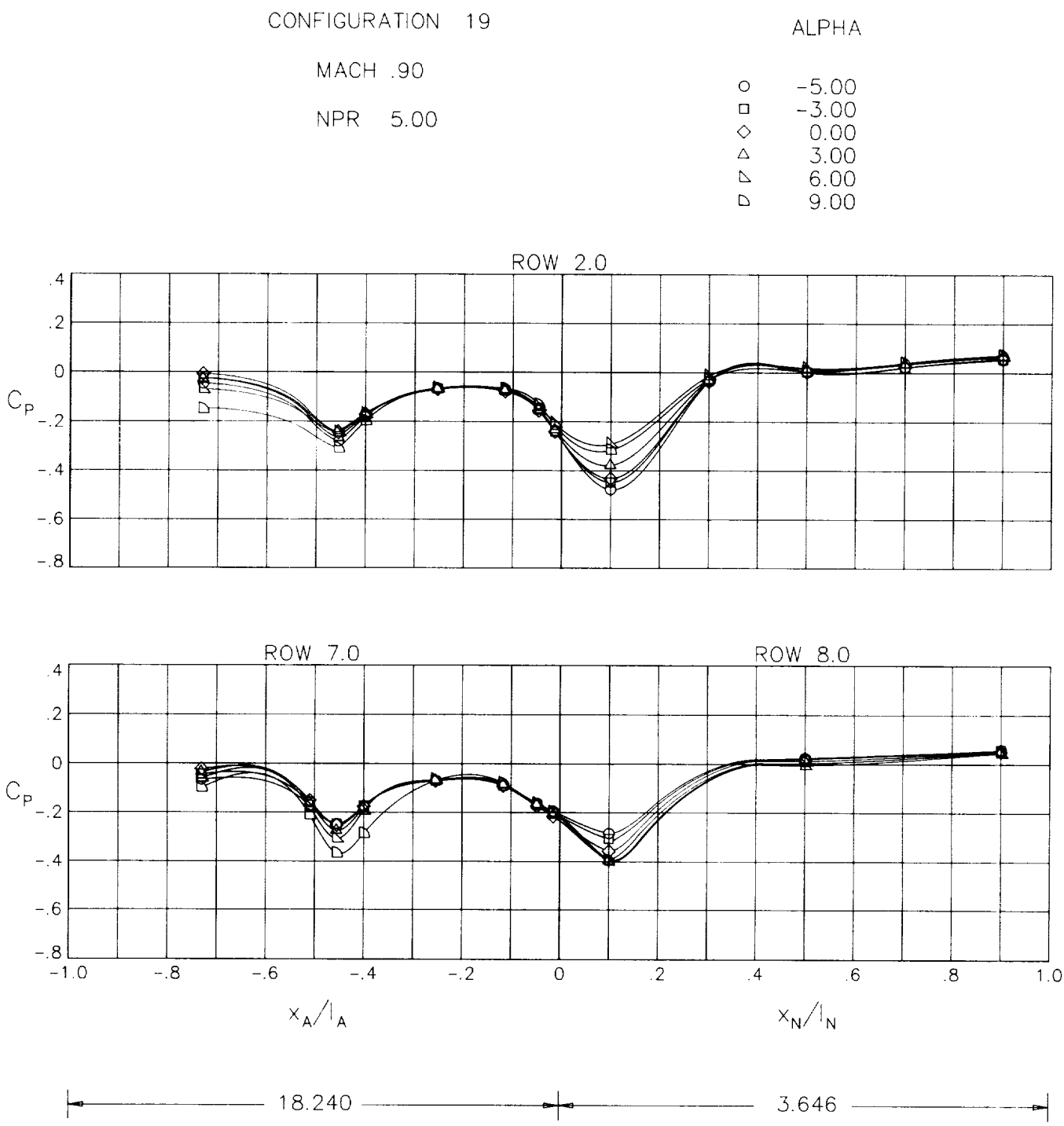

(b) M = 0.90; NPR = 5.0.

Figure 23.- Continued.

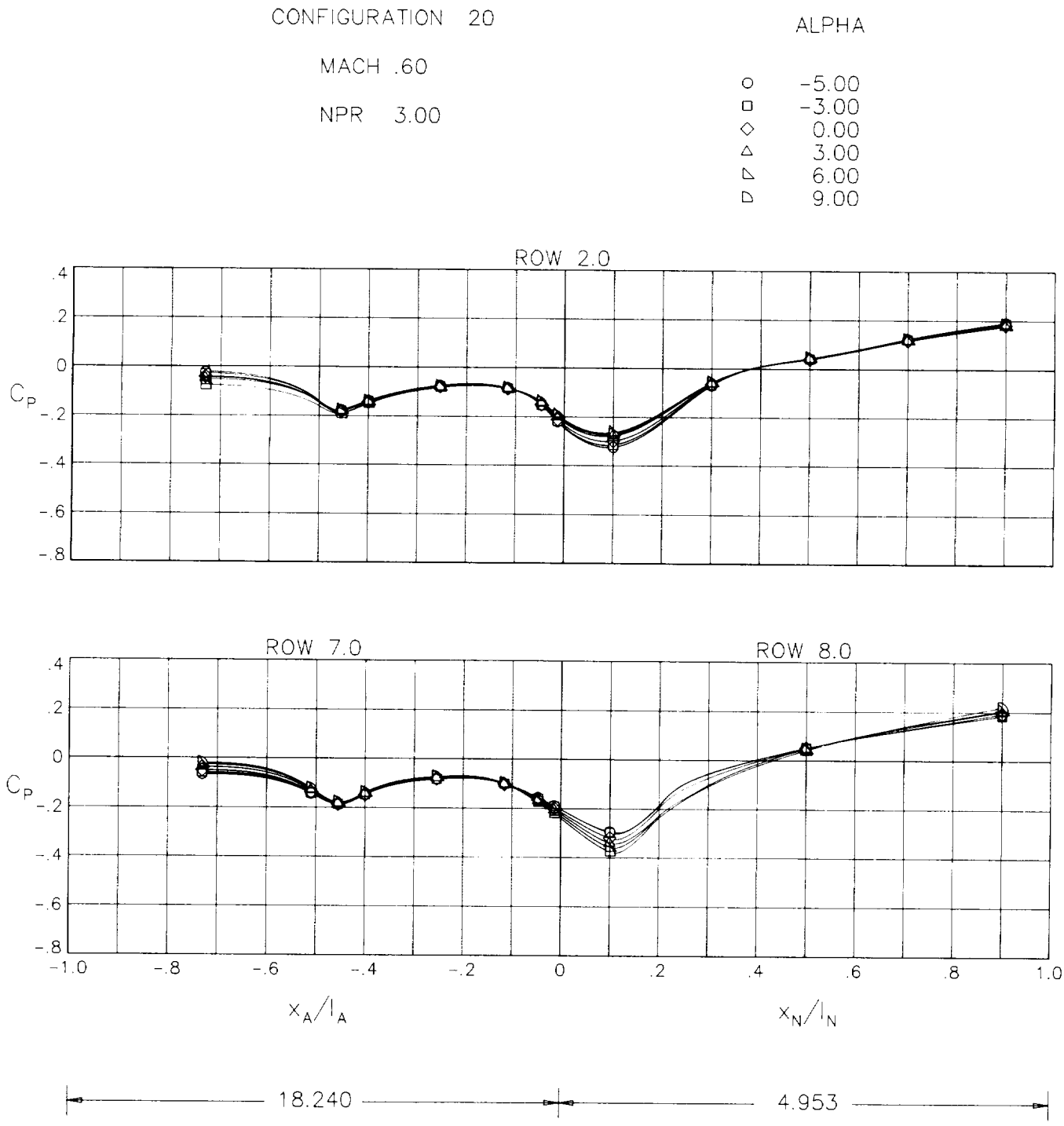

(a) M = 0.60; NPR = 3.0.

Figure 24.- Afterbody/nozzle static-pressure coefficient distributions along upper and lower surface of mid right side for configuration 20.

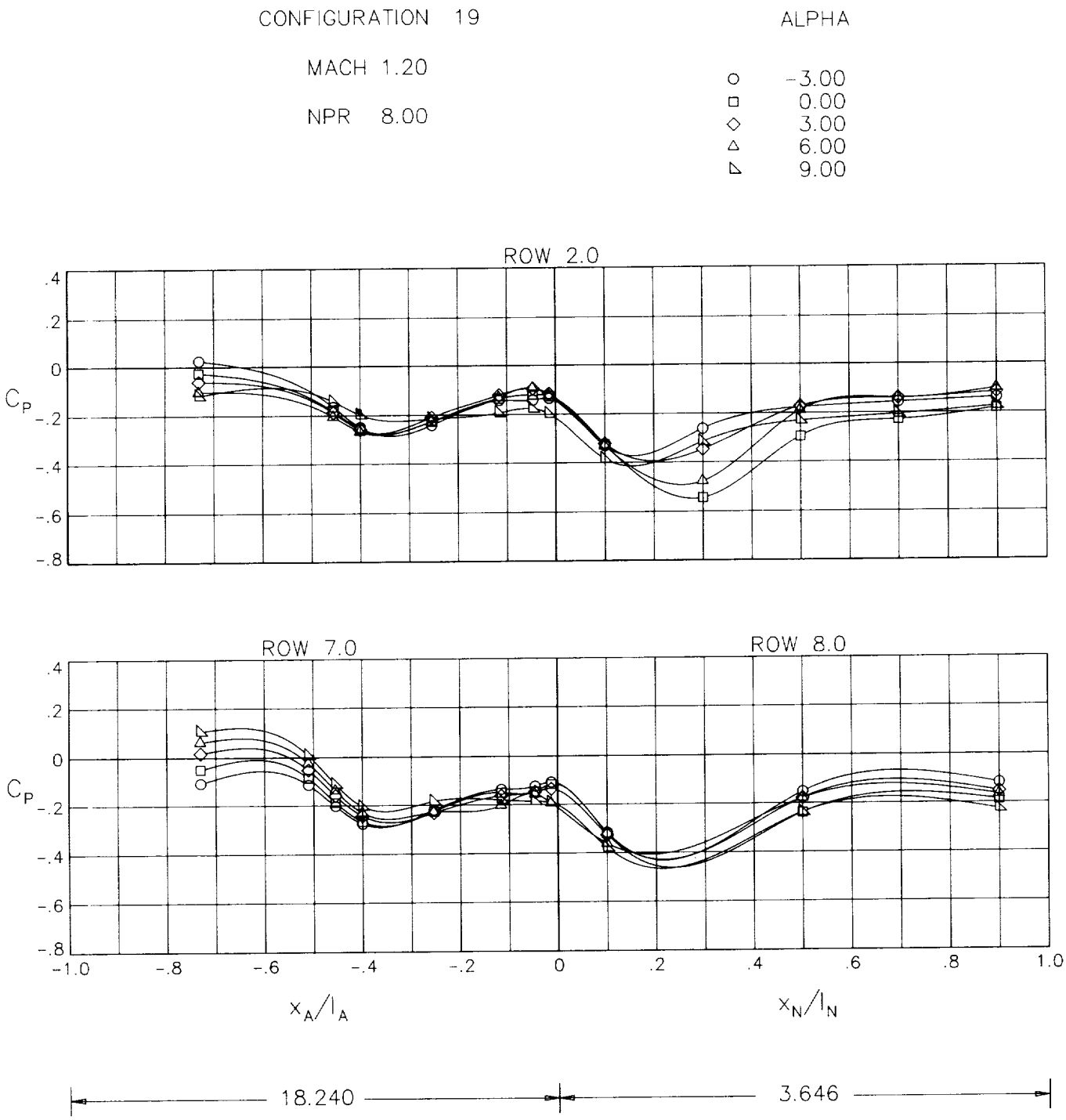

(c) M = 1.20; NPR = 8.0.

Figure 23.- Concluded.

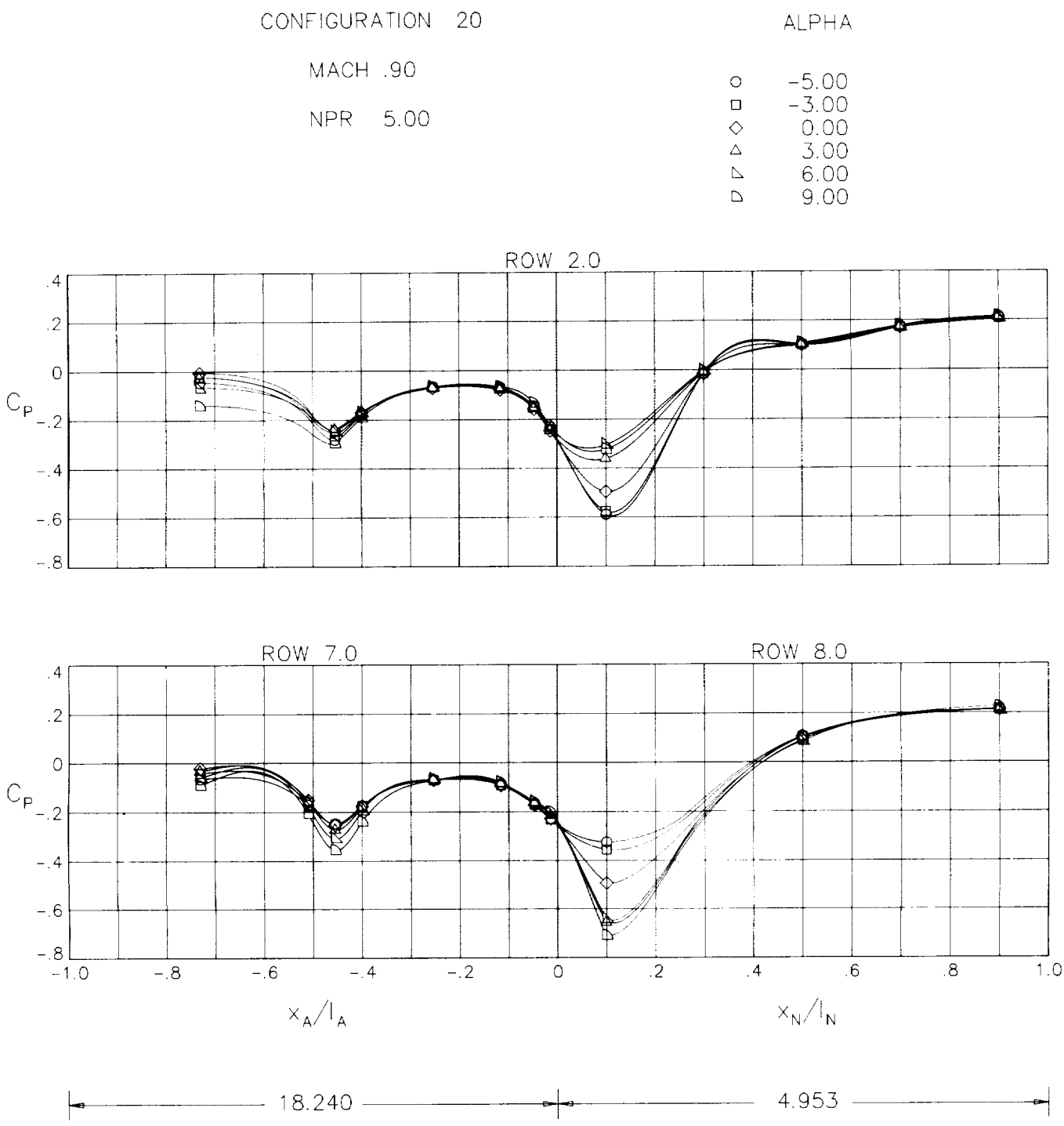

(b) M = 0.90; NPR = 5.0.

Figure 24.- Continued.

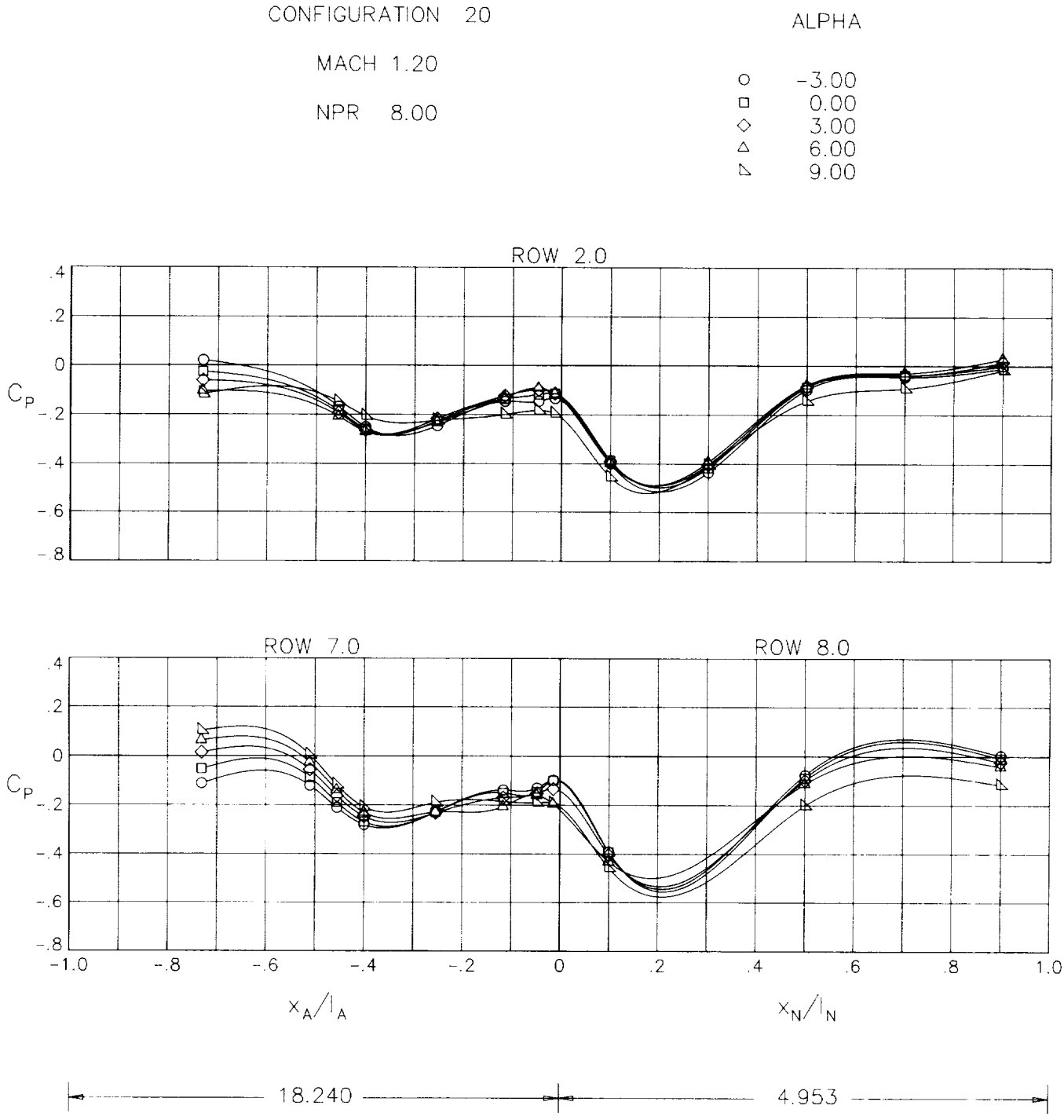

(c) M = 1.20; NPR = 8.0.

Figure 24.- Concluded.

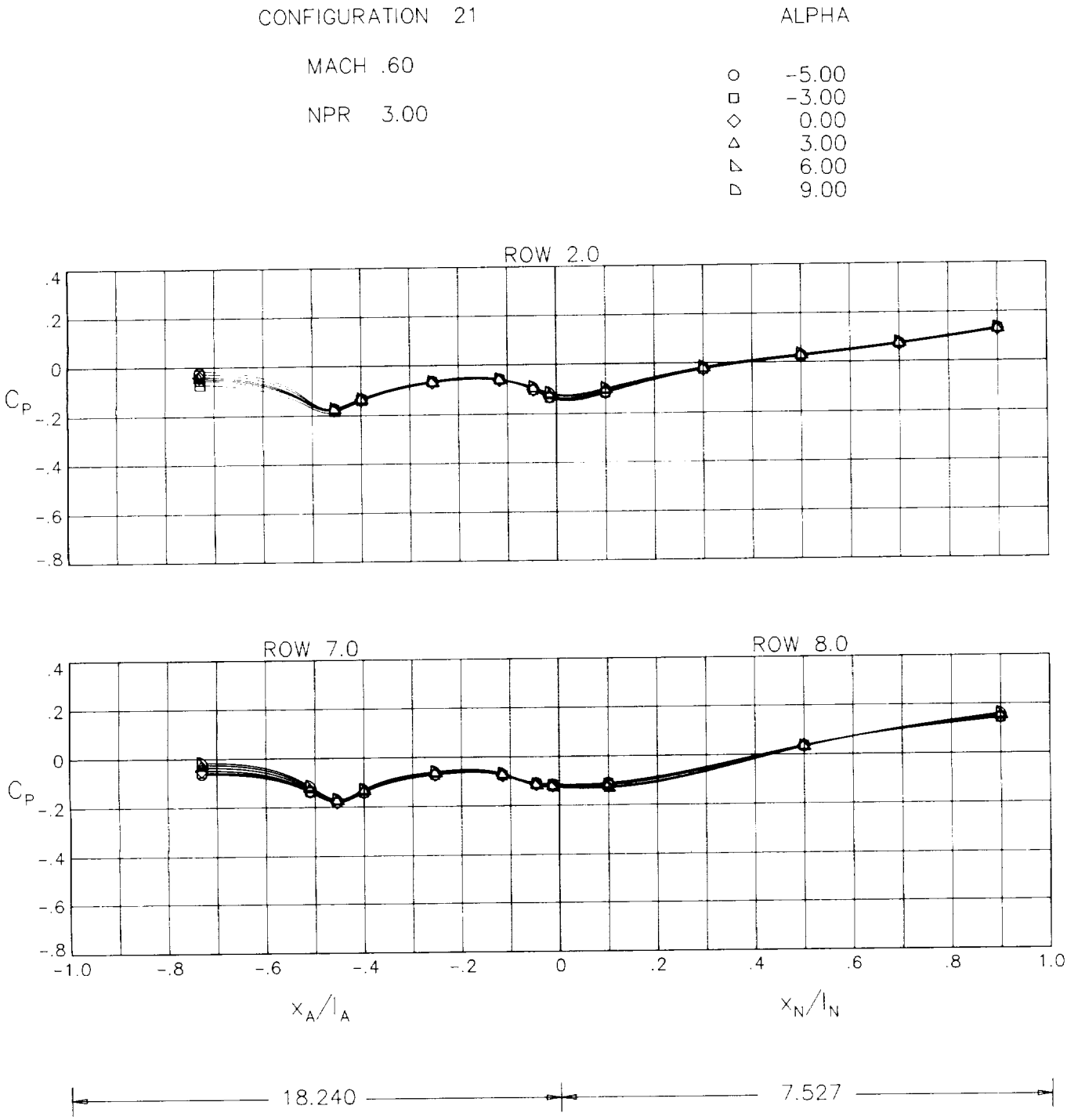

(a) M = 0.60; NPR = 3.0.

Figure 25.- Afterbody/nozzle static-pressure coefficient distributions along upper and lower surface of mid right side for configuration 21.

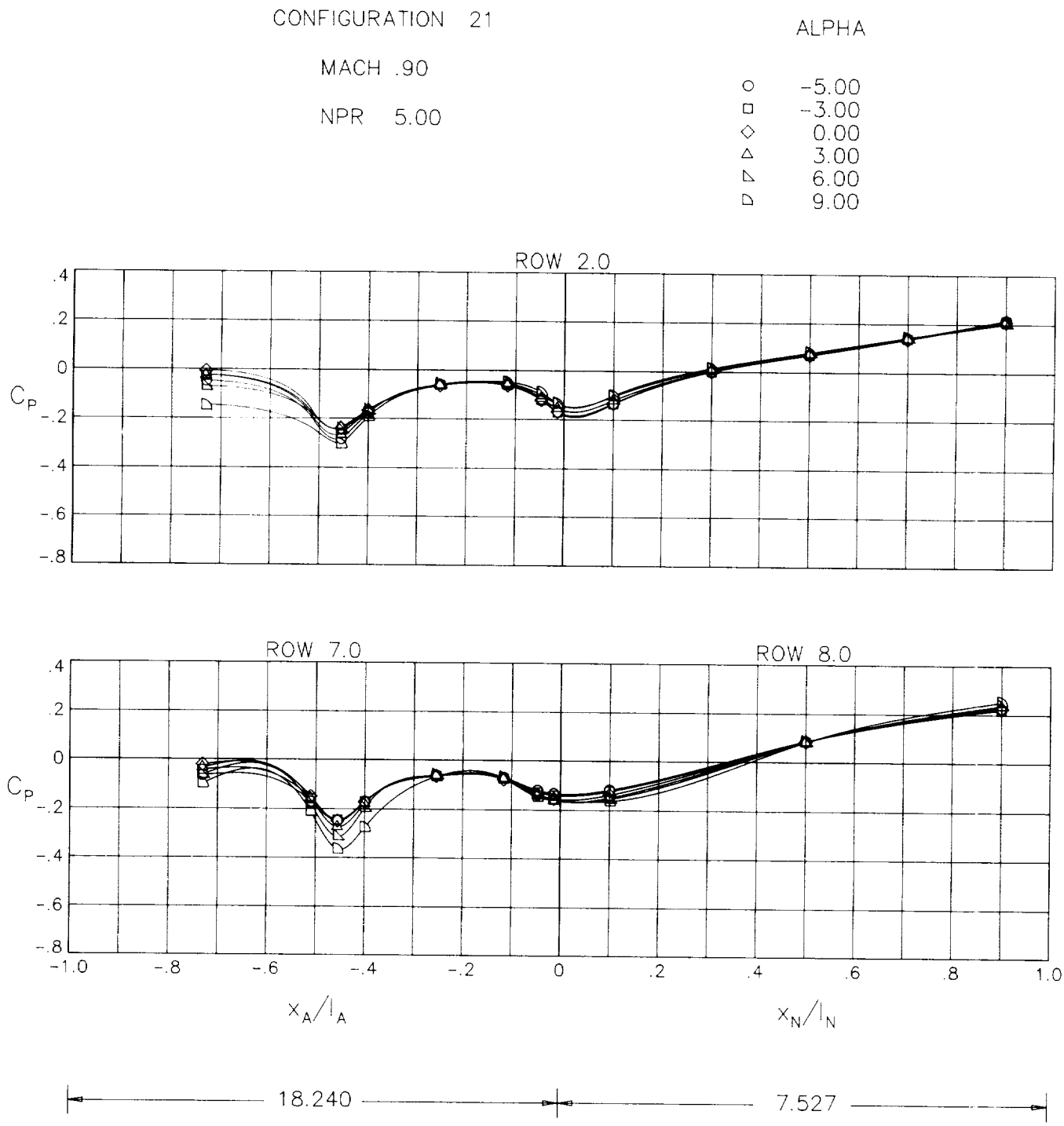

(b) M = 0.90; NPR = 5.0.

Figure 25.- Continued.

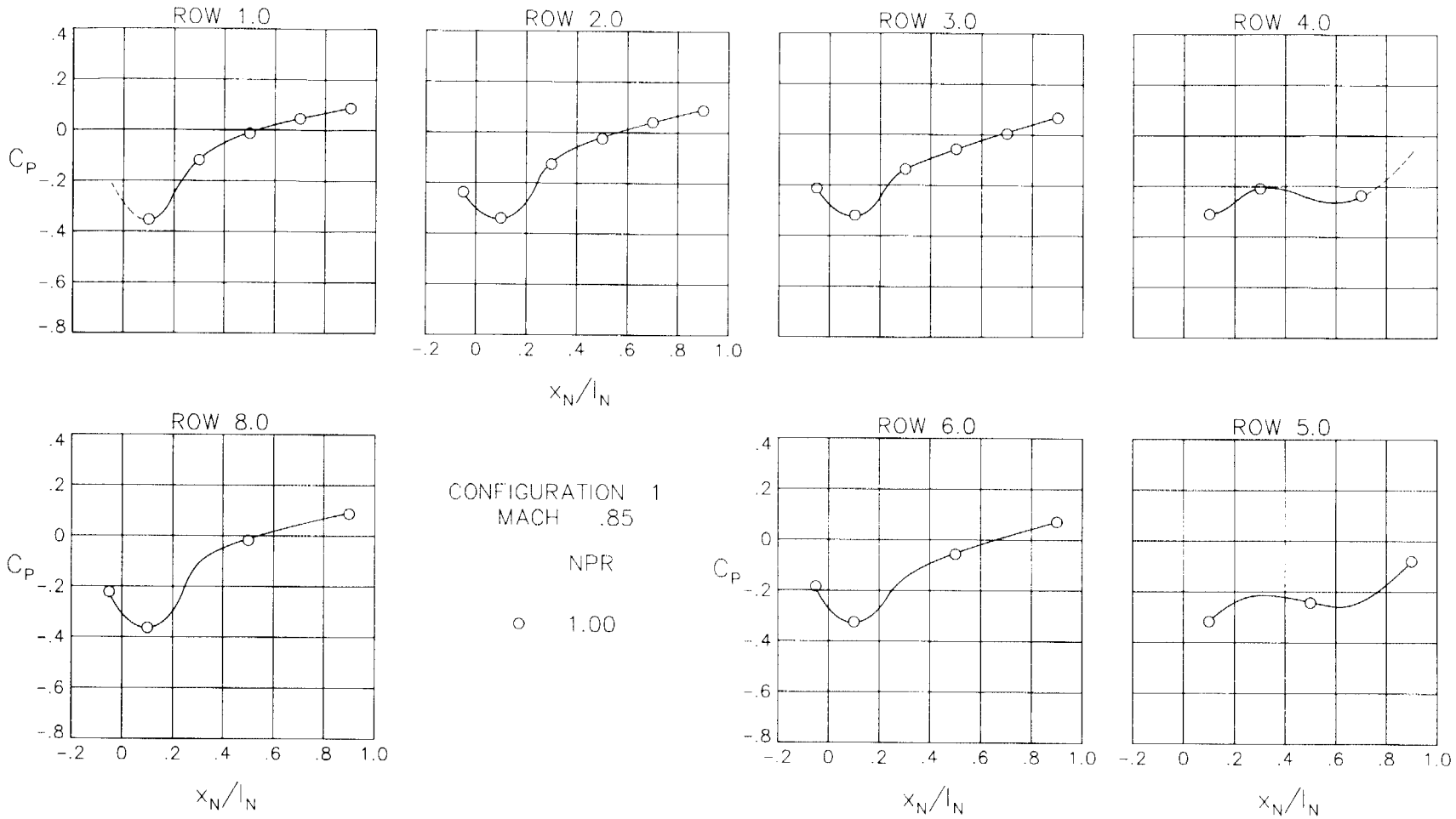

(d) M = 0.85.

Figure 26.- Continued.

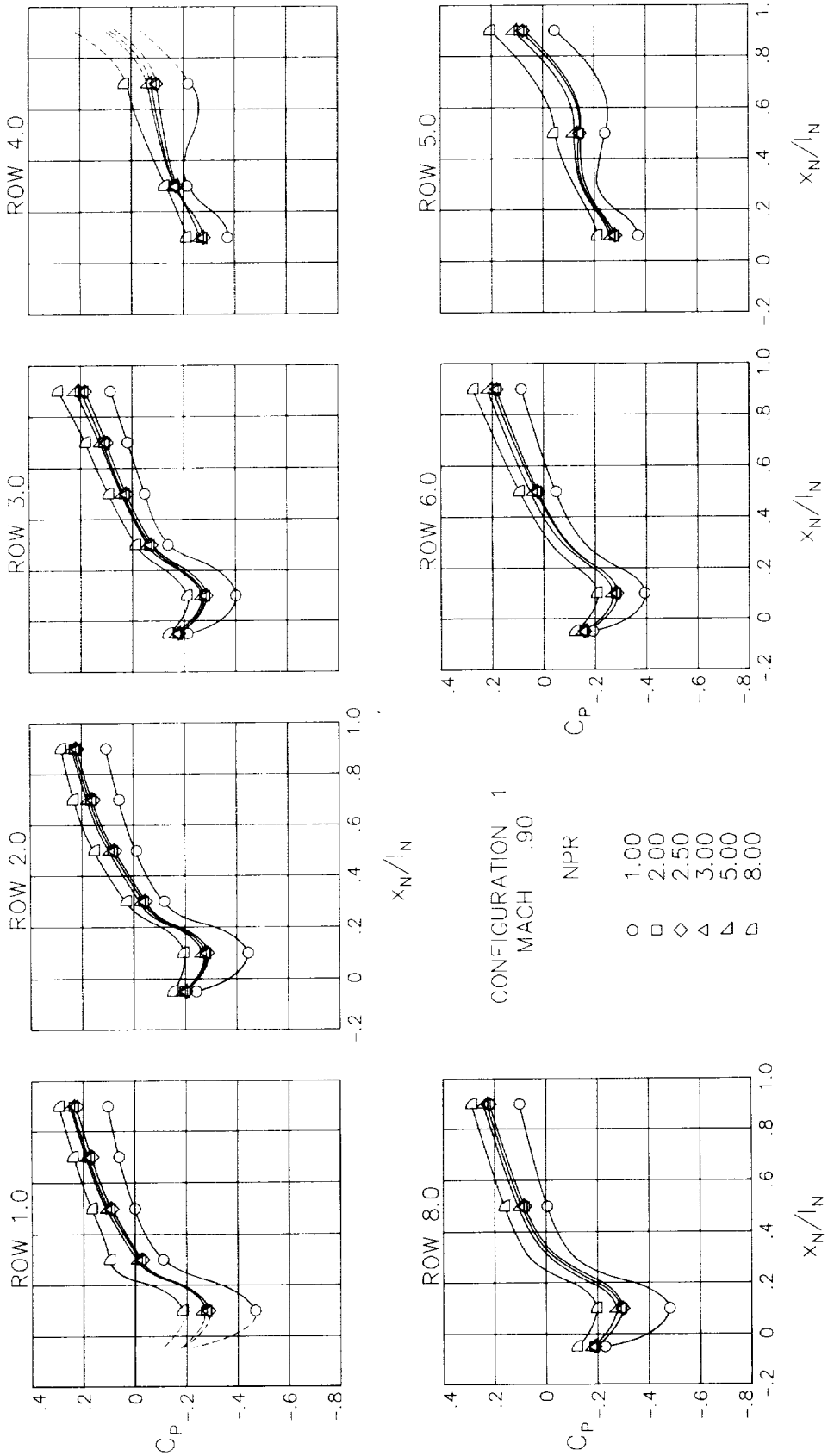

(e) M = 0.90.

Figure 26.- Continued.

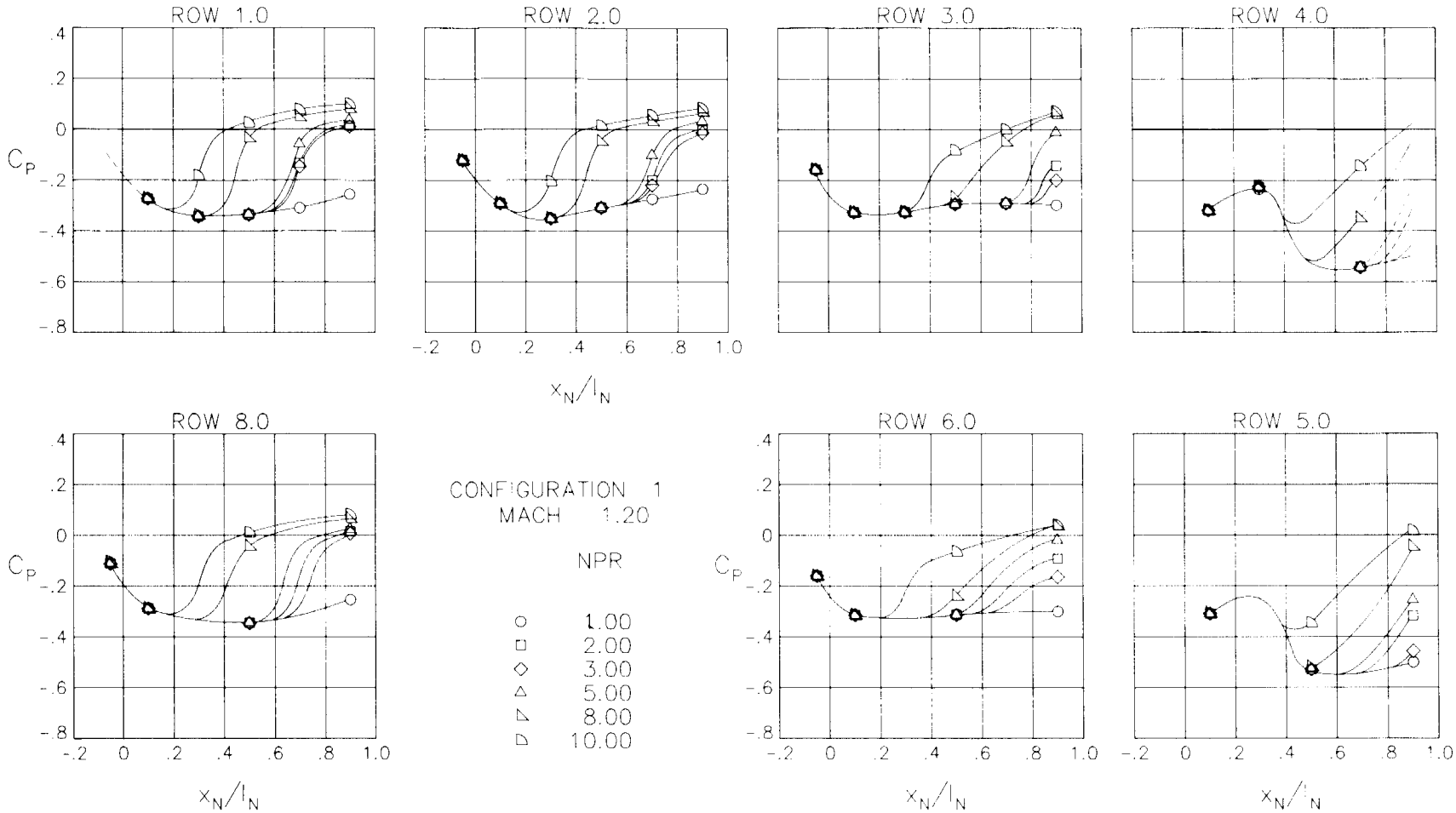

(f) M = 1.20.

Figure 26.- Concluded.

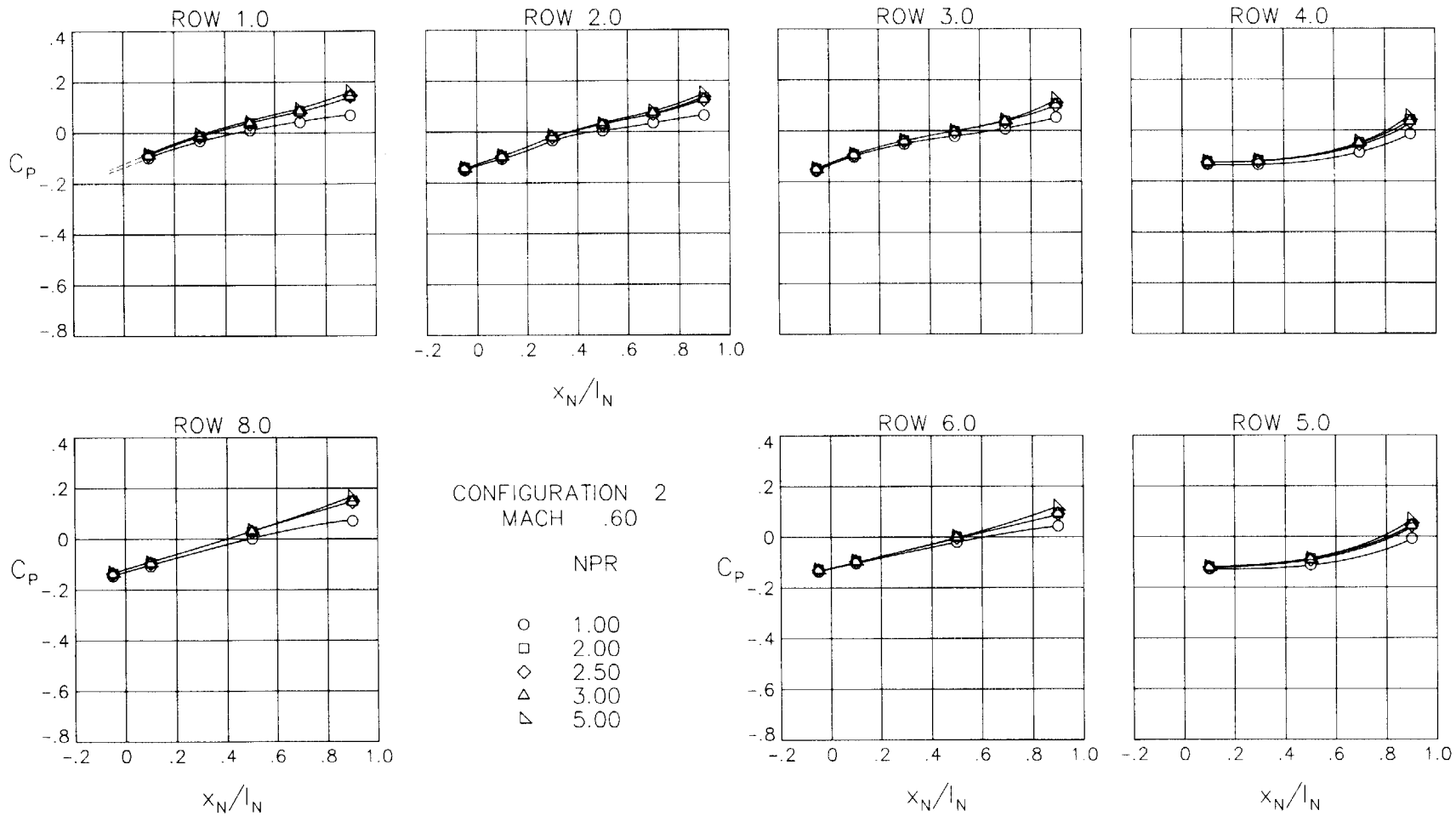

(a) M = 0.60.

Figure 27.- Surface static-pressure coefficient distributions around nozzle for configuration 2. α = 0°.

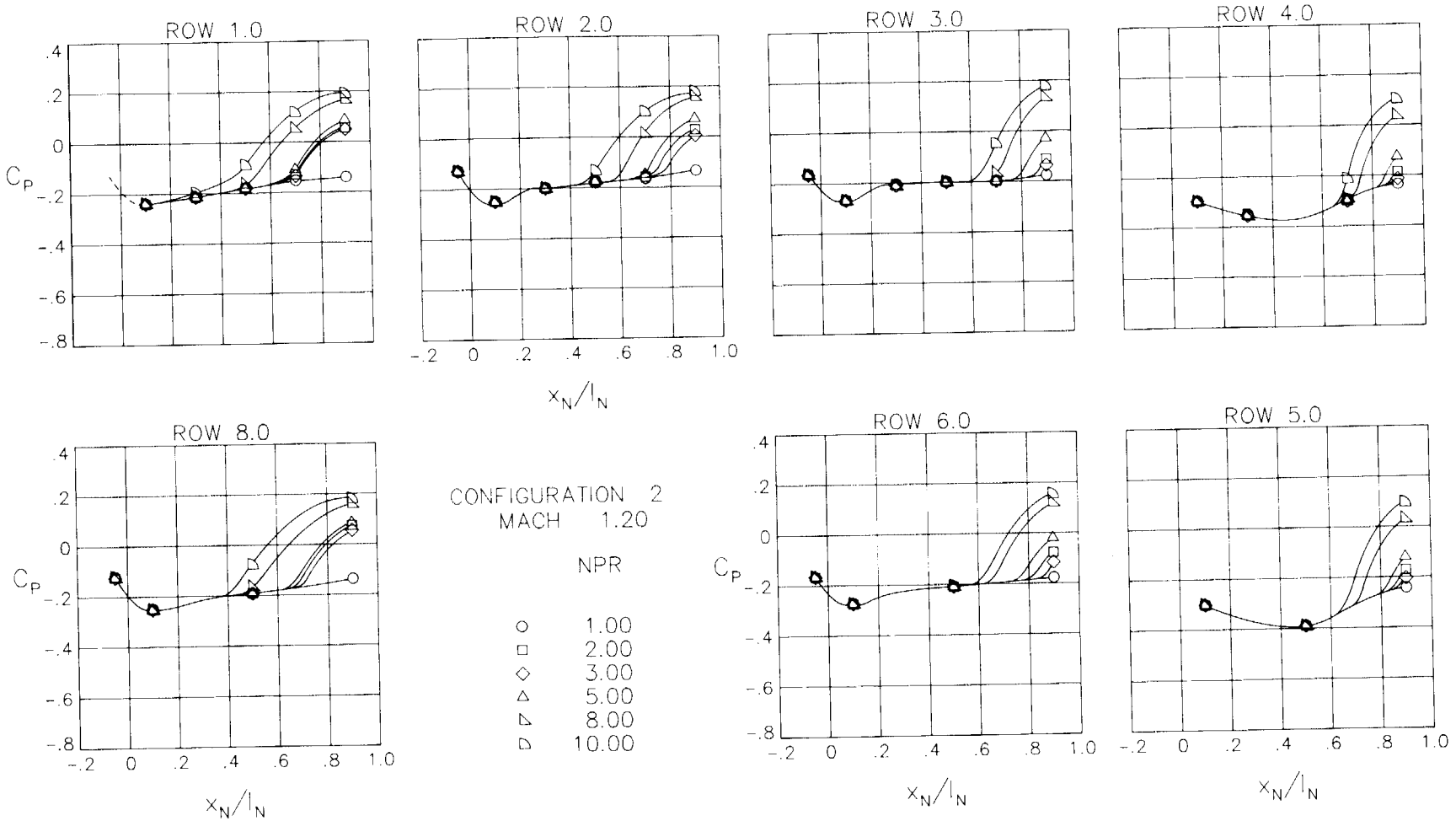

(f) M = 1.20.

Figure 27.- Concluded.

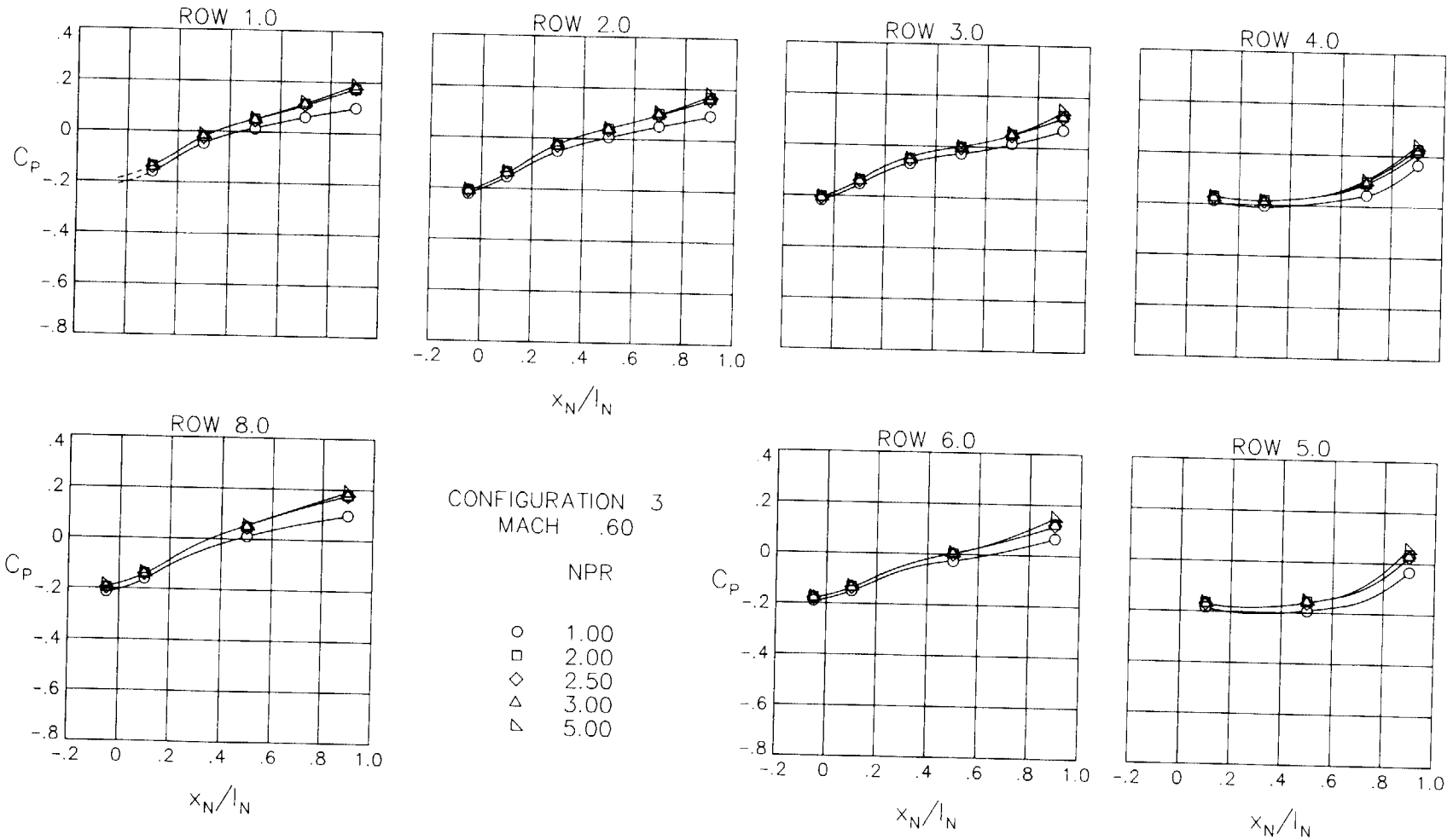

(a) M = 0.60.

Figure 28.- Surface static-pressure coefficient distributions around nozzle for configuration 3. $\alpha = 0°$.

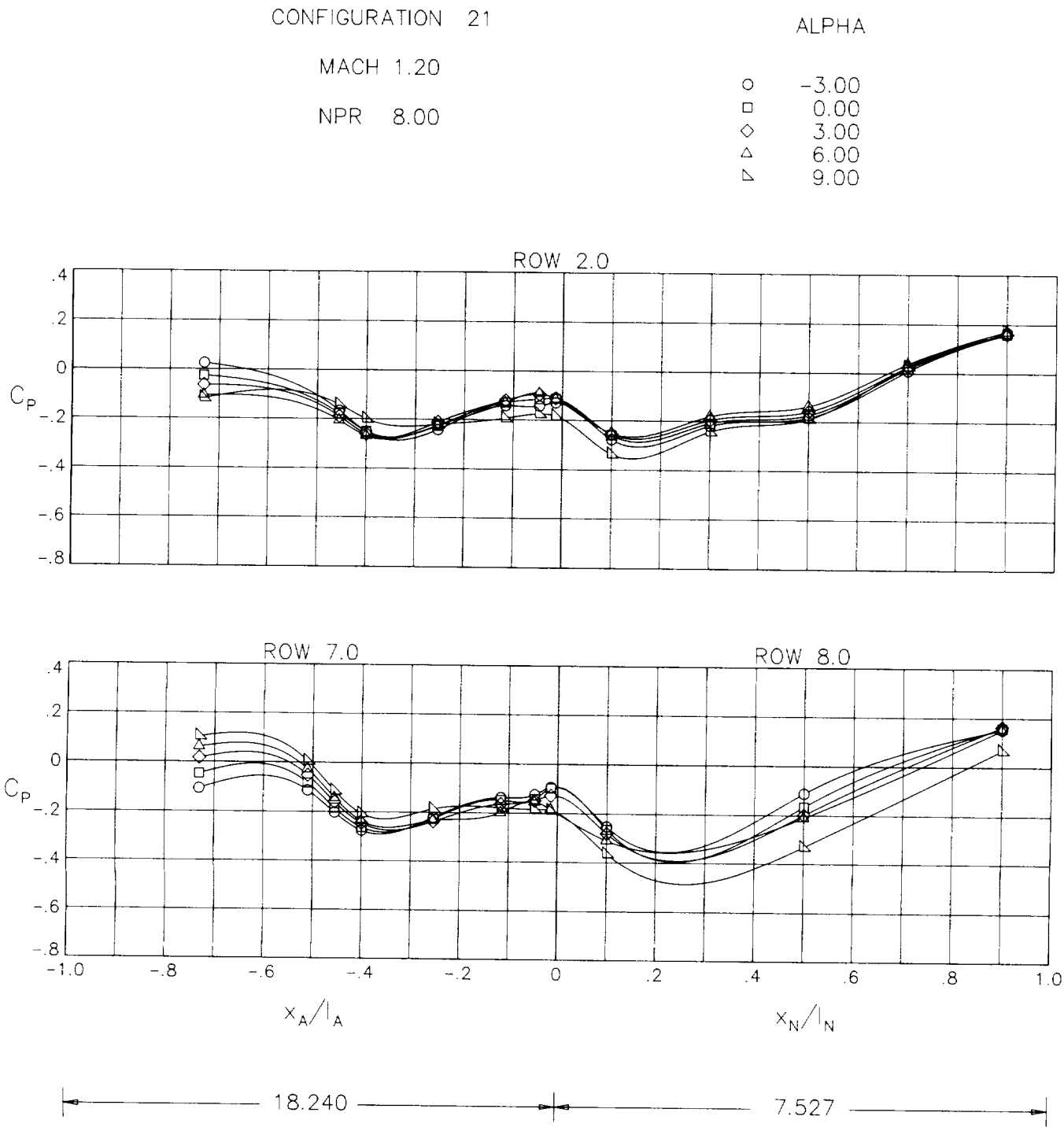

(c) M = 1.20; NPR = 8.0.

Figure 25.- Concluded.

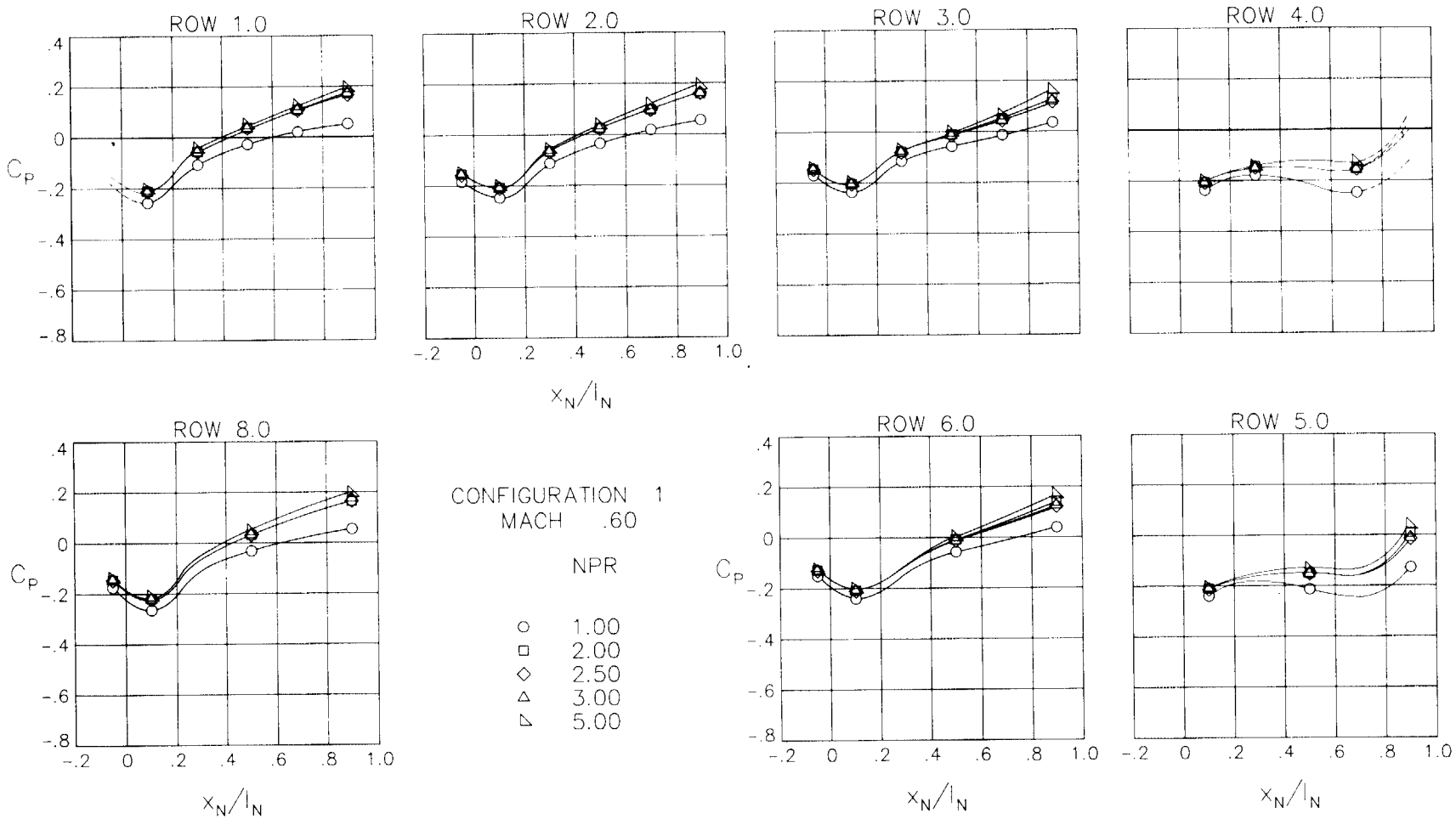

(a) M = 0.60.

Figure 26.- Surface static-pressure coefficient distributions around nozzle for configuration 1. $\alpha = 0°$.

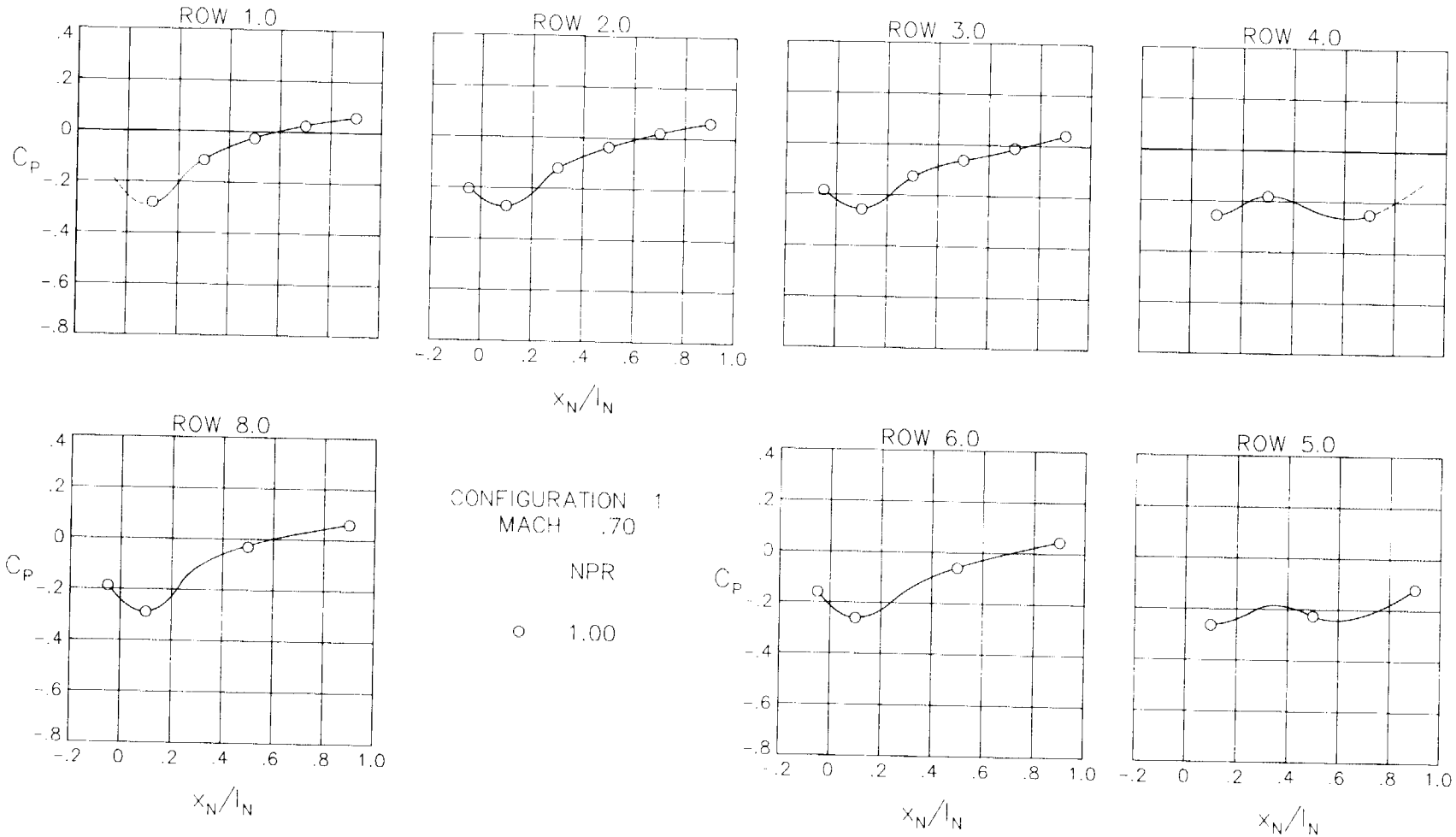

(b) M = 0.70.

Figure 26.- Continued.

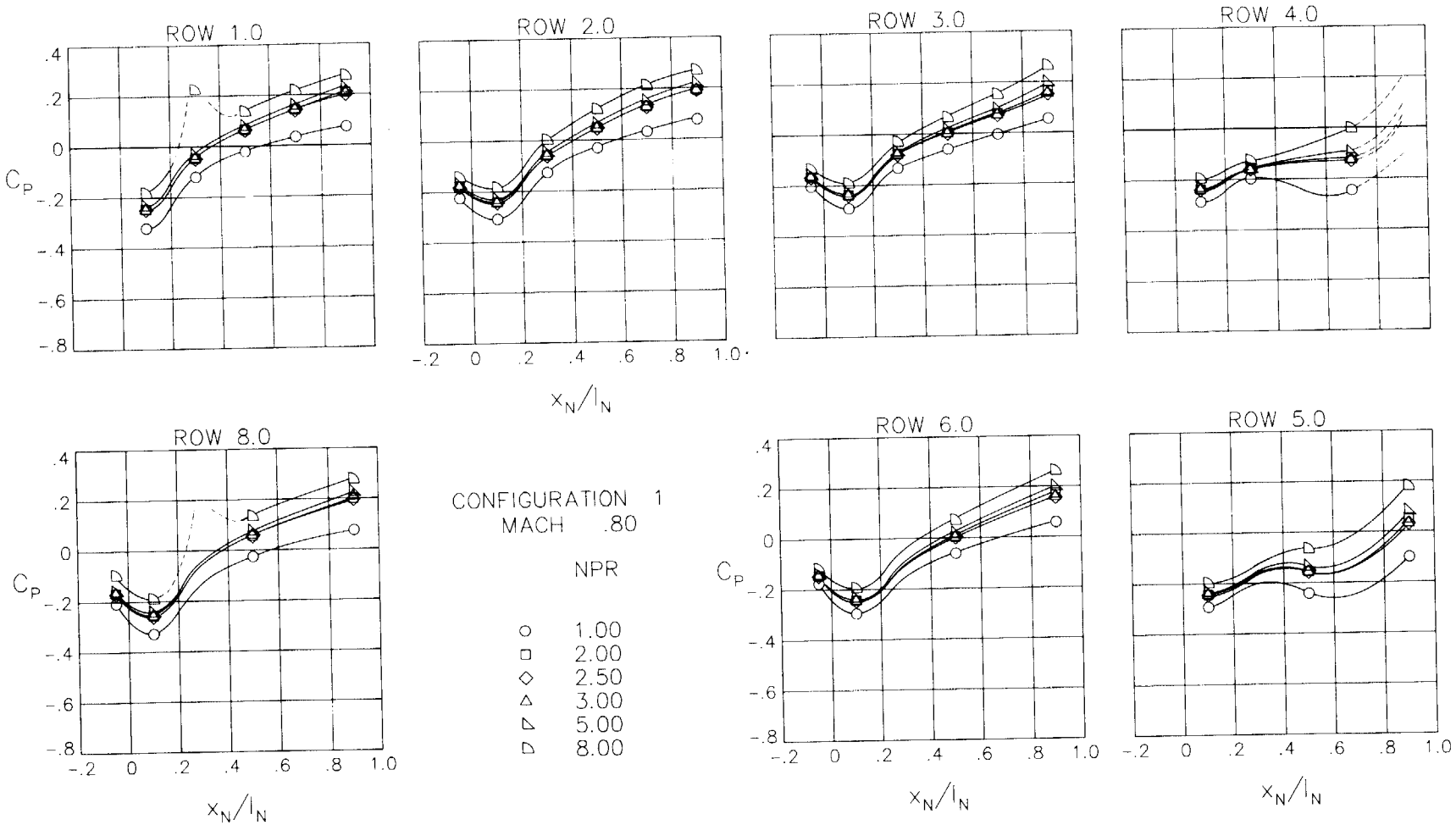

(c) M = 0.80.

Figure 26.- Continued.

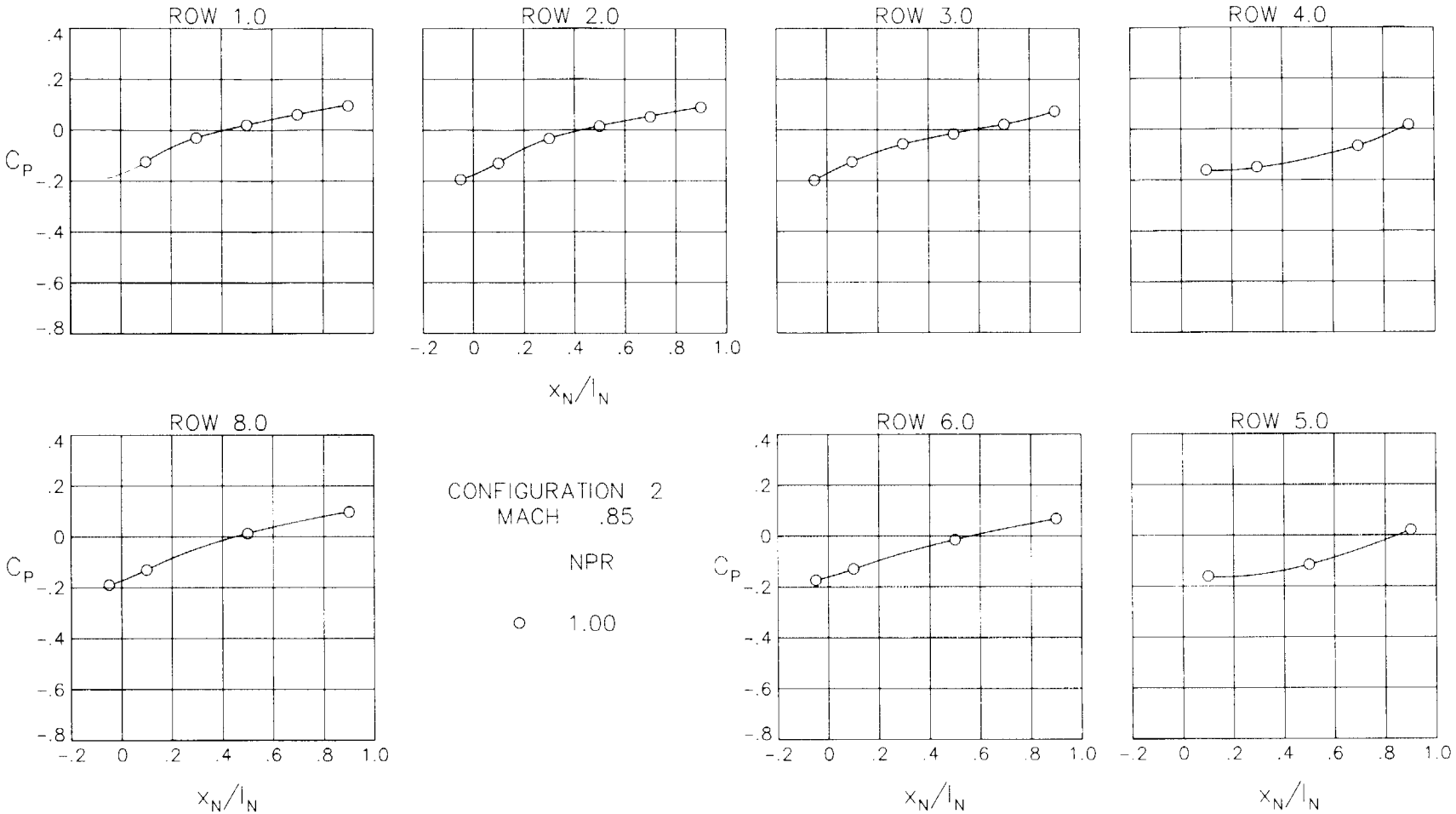

(d) M = 0.85.

Figure 27.- Continued.

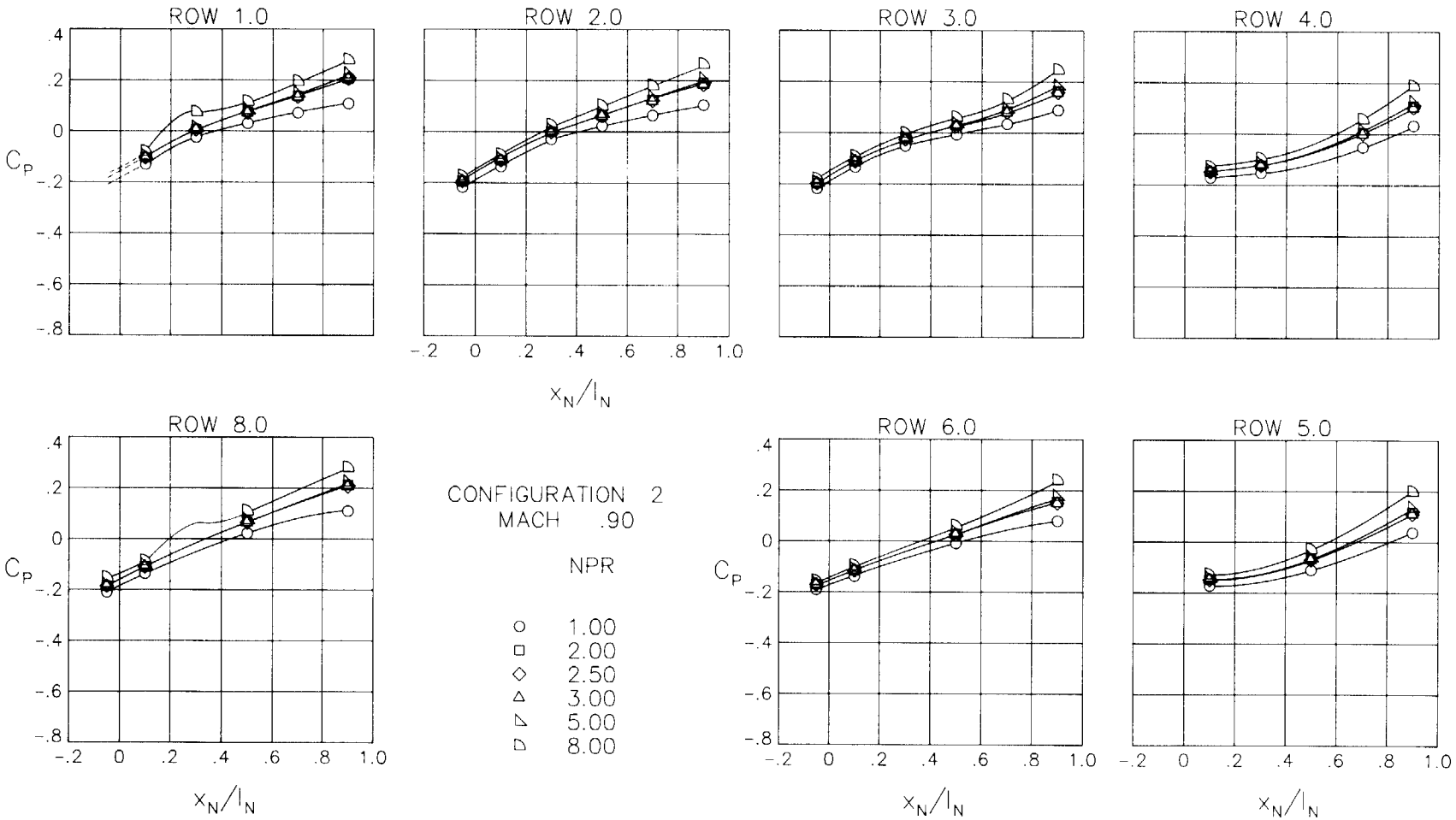

(e) M = 0.90.

Figure 27.- Continued.

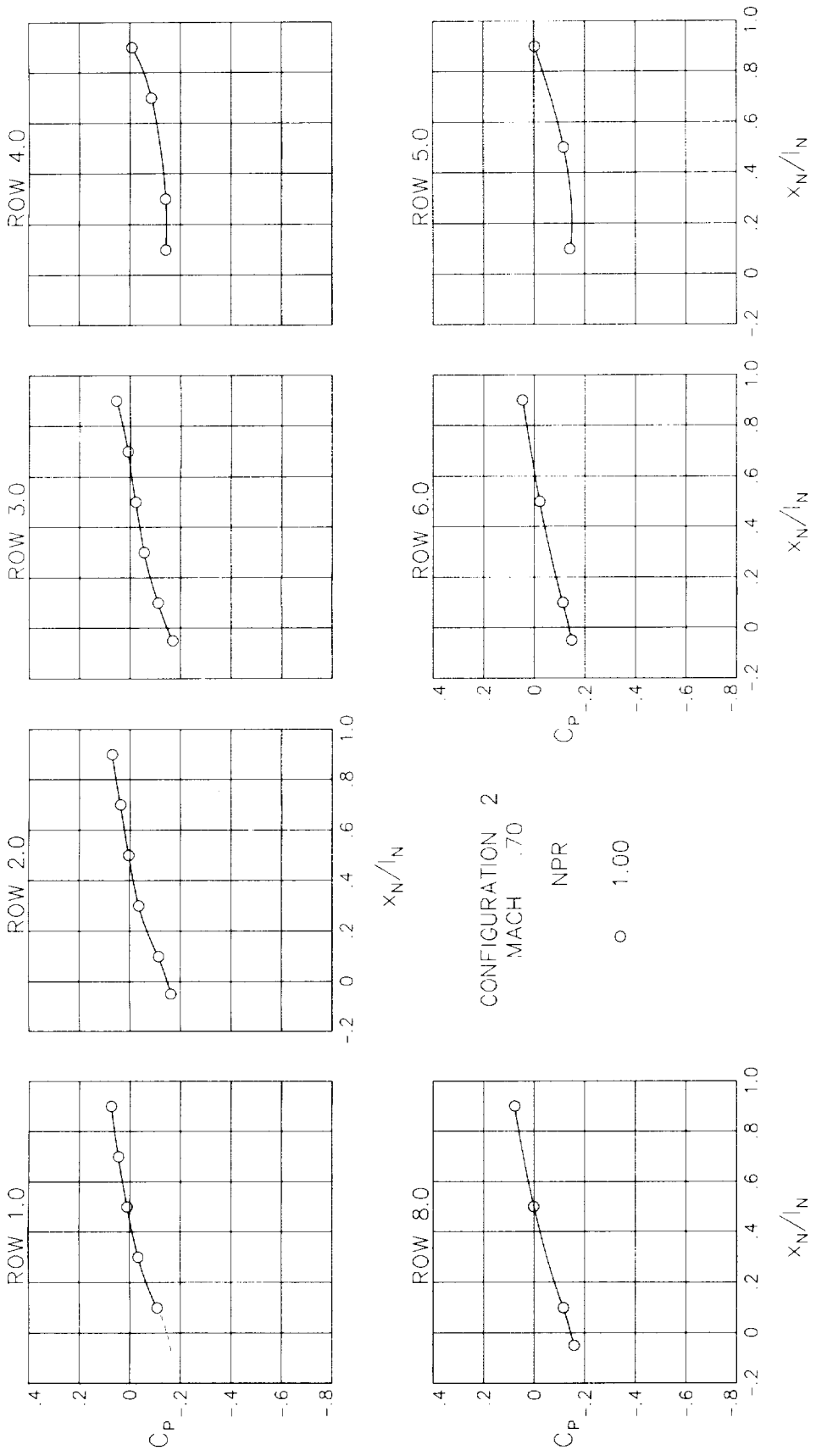

(b) M = 0.70.

Figure 27.- Continued.

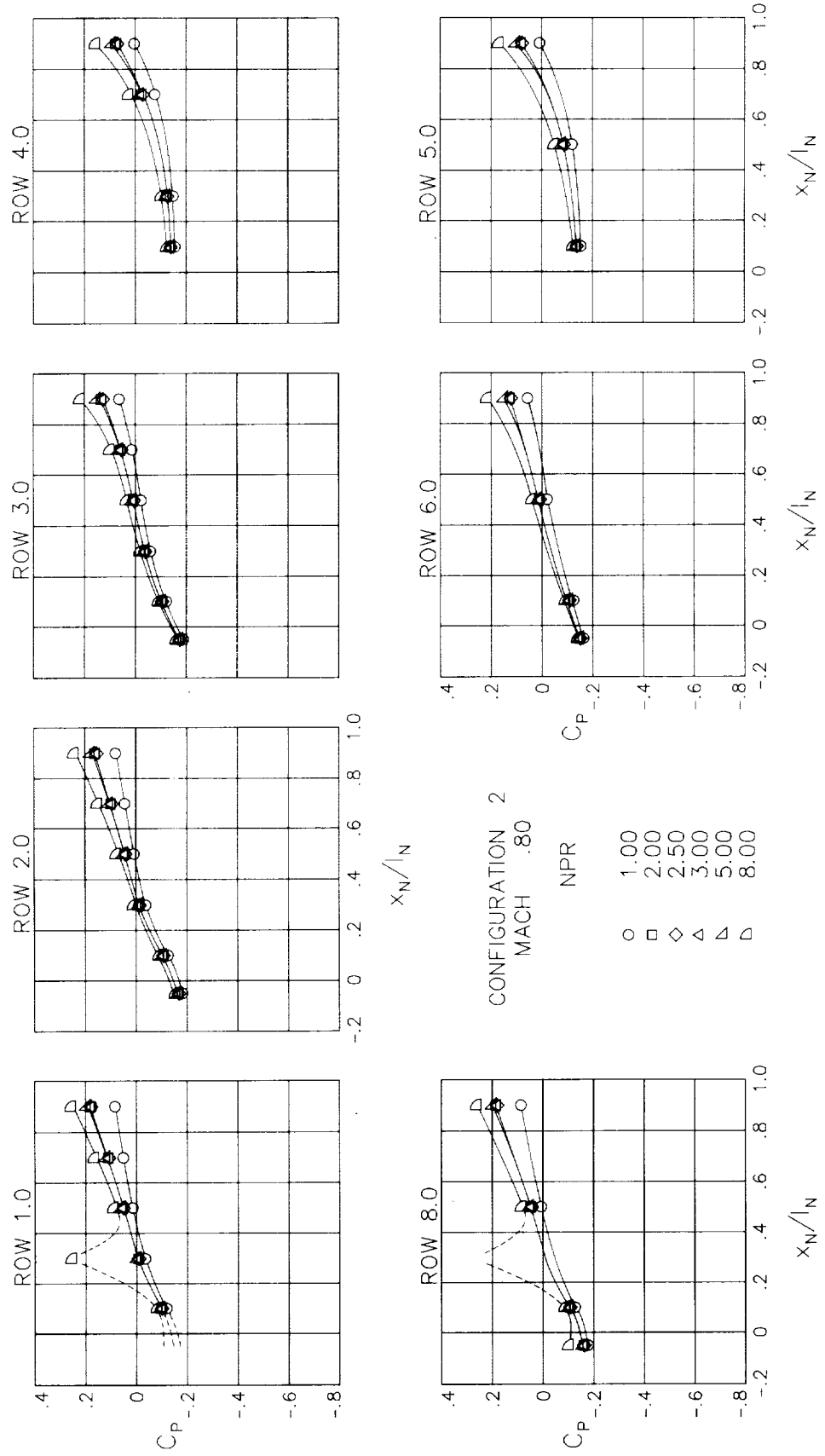

(c) M = 0.80.

Figure 27.- Continued.

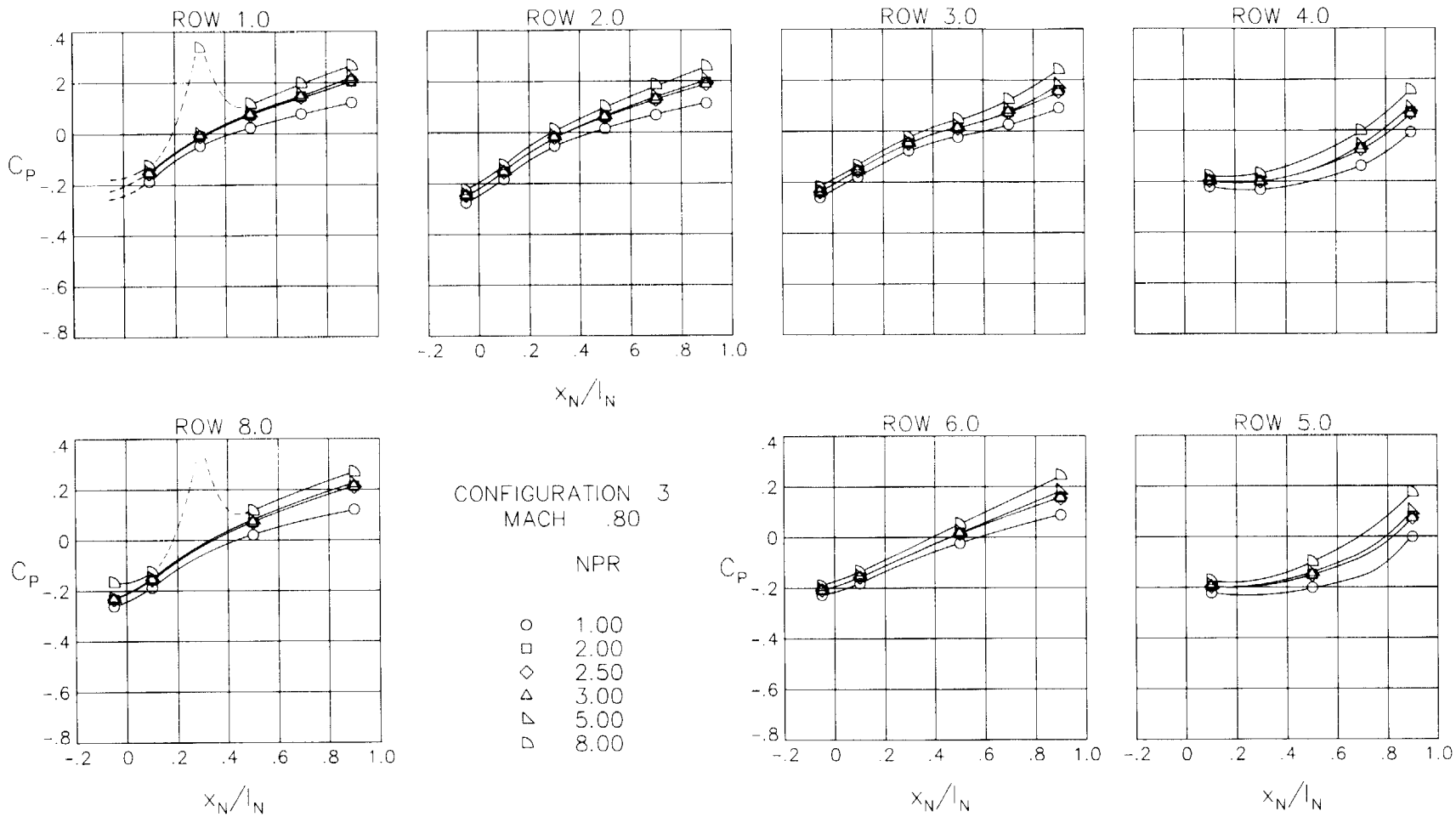

(c) M = 0.80.

Figure 28.- Continued.

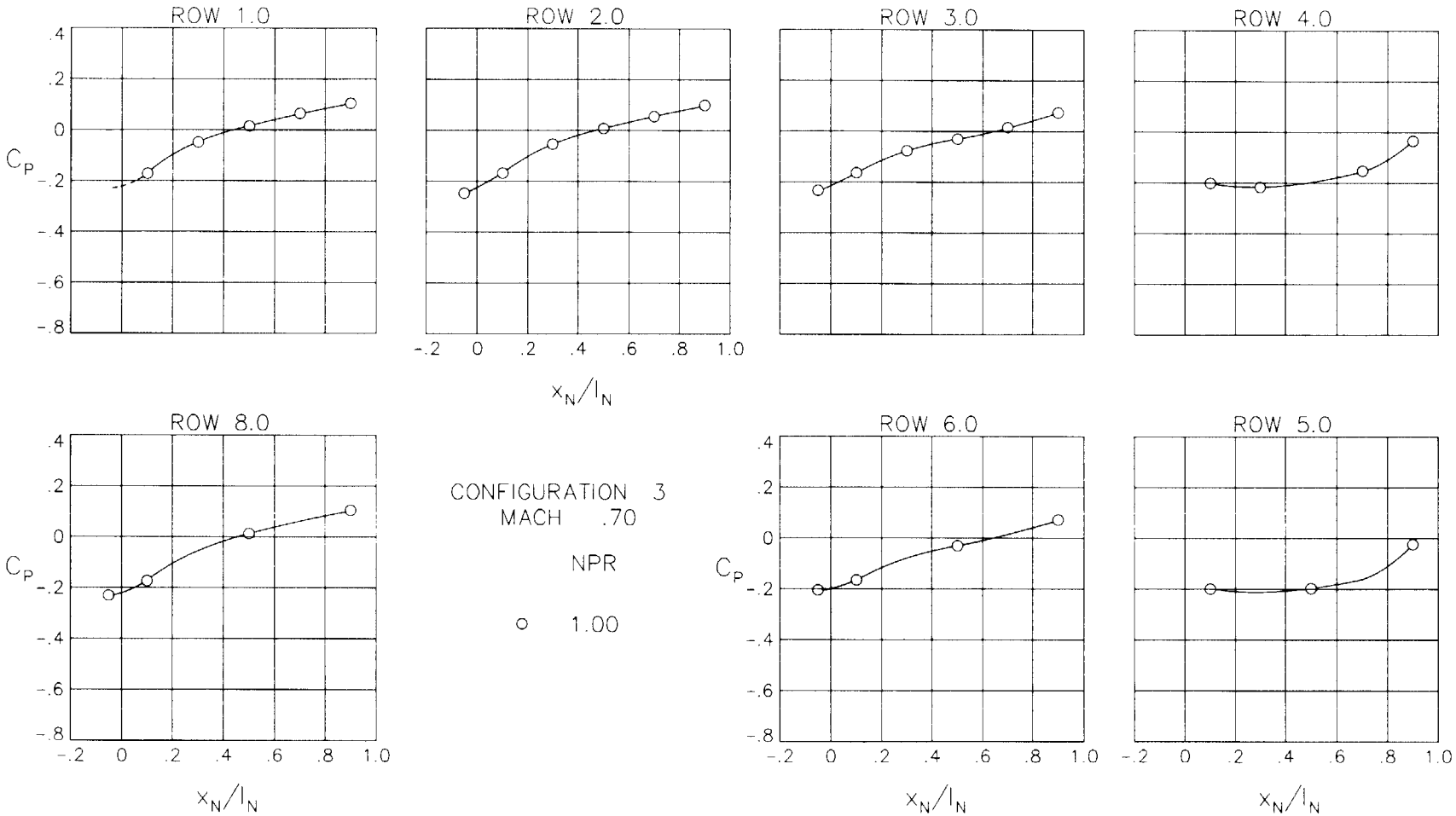

(b) M = 0.70.

Figure 28.- Continued.

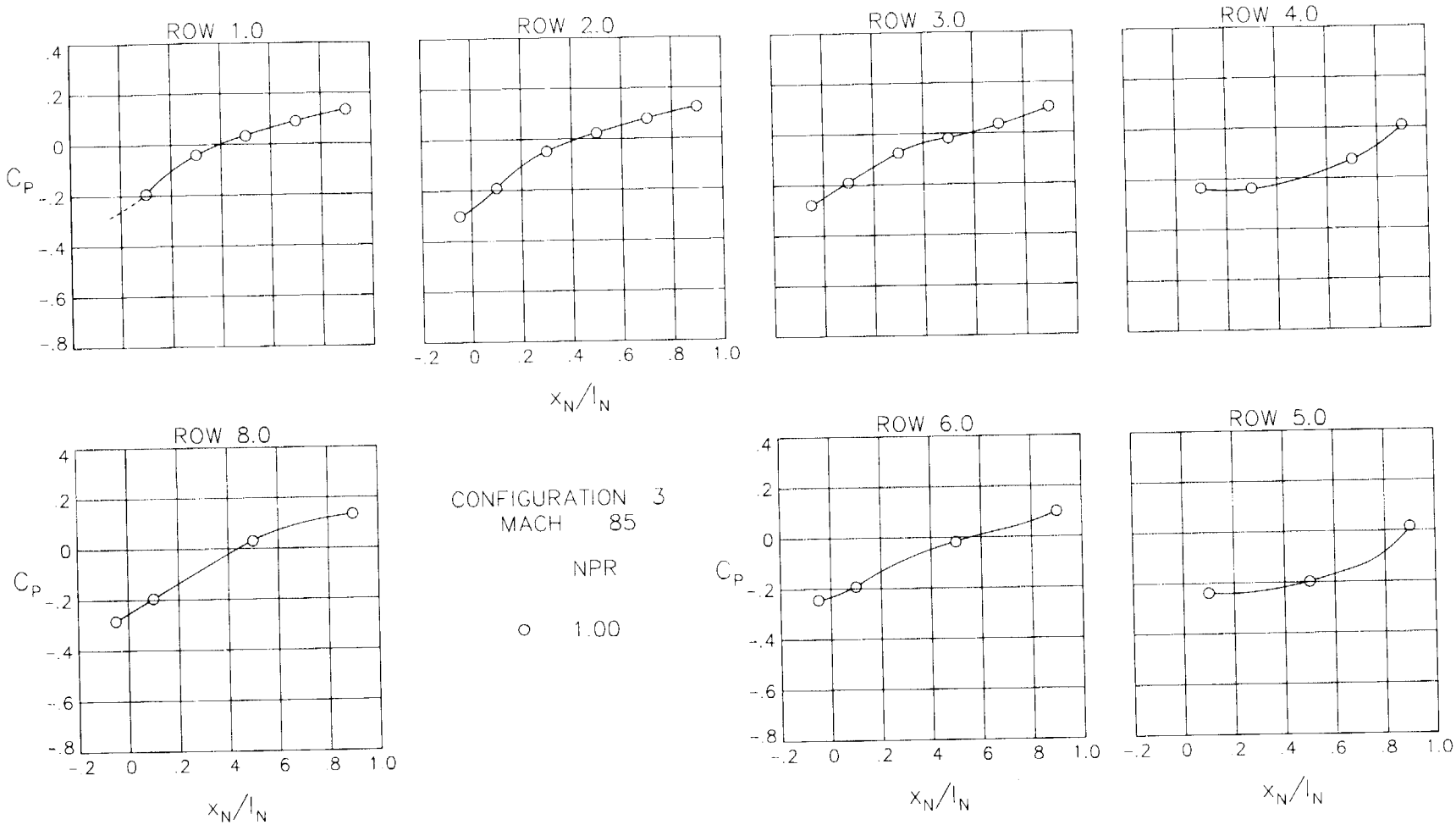

(d) M = 0.85.

Figure 28.- Continued.

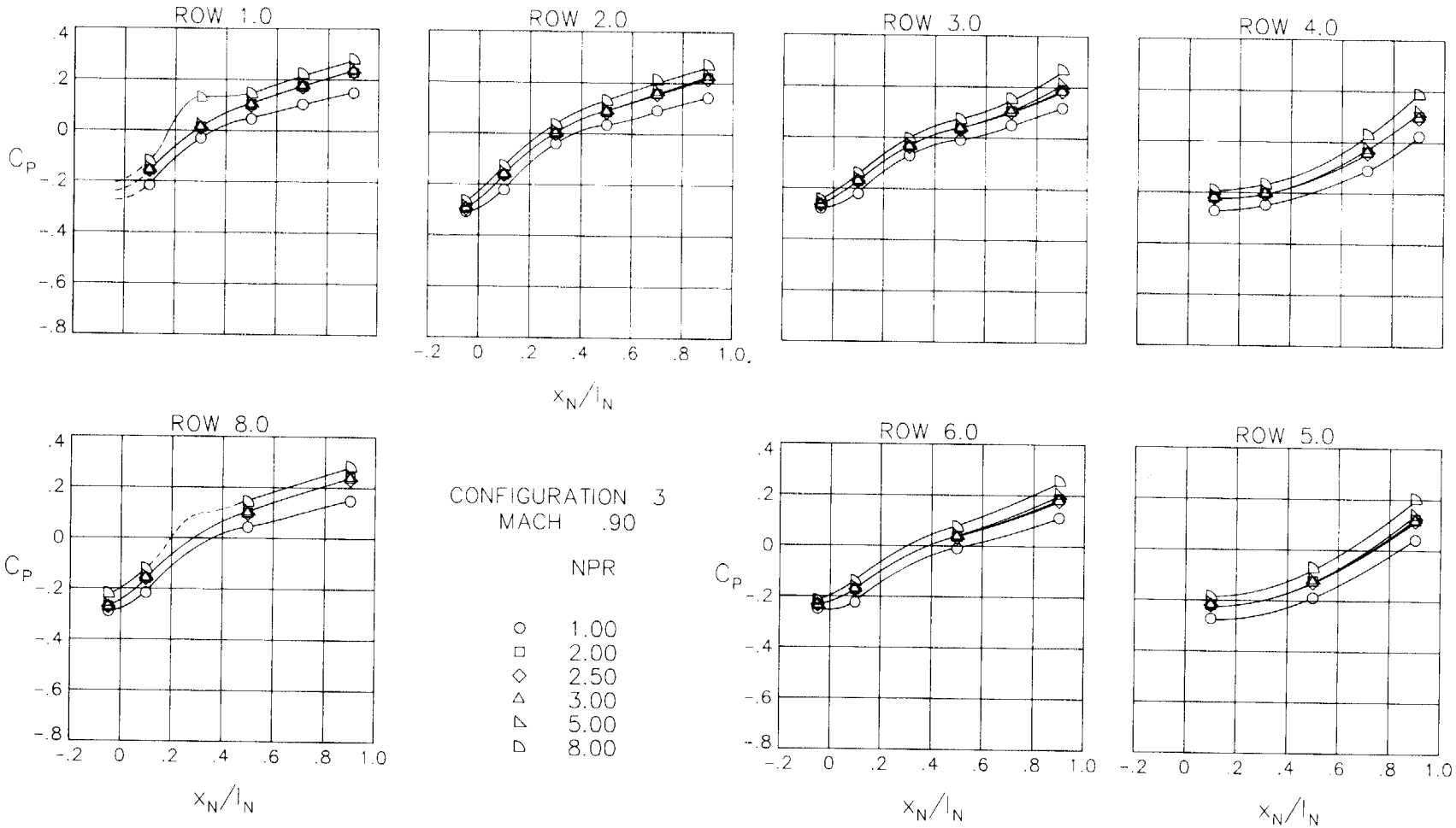

(e) M = 0.90.

Figure 28.- Continued.

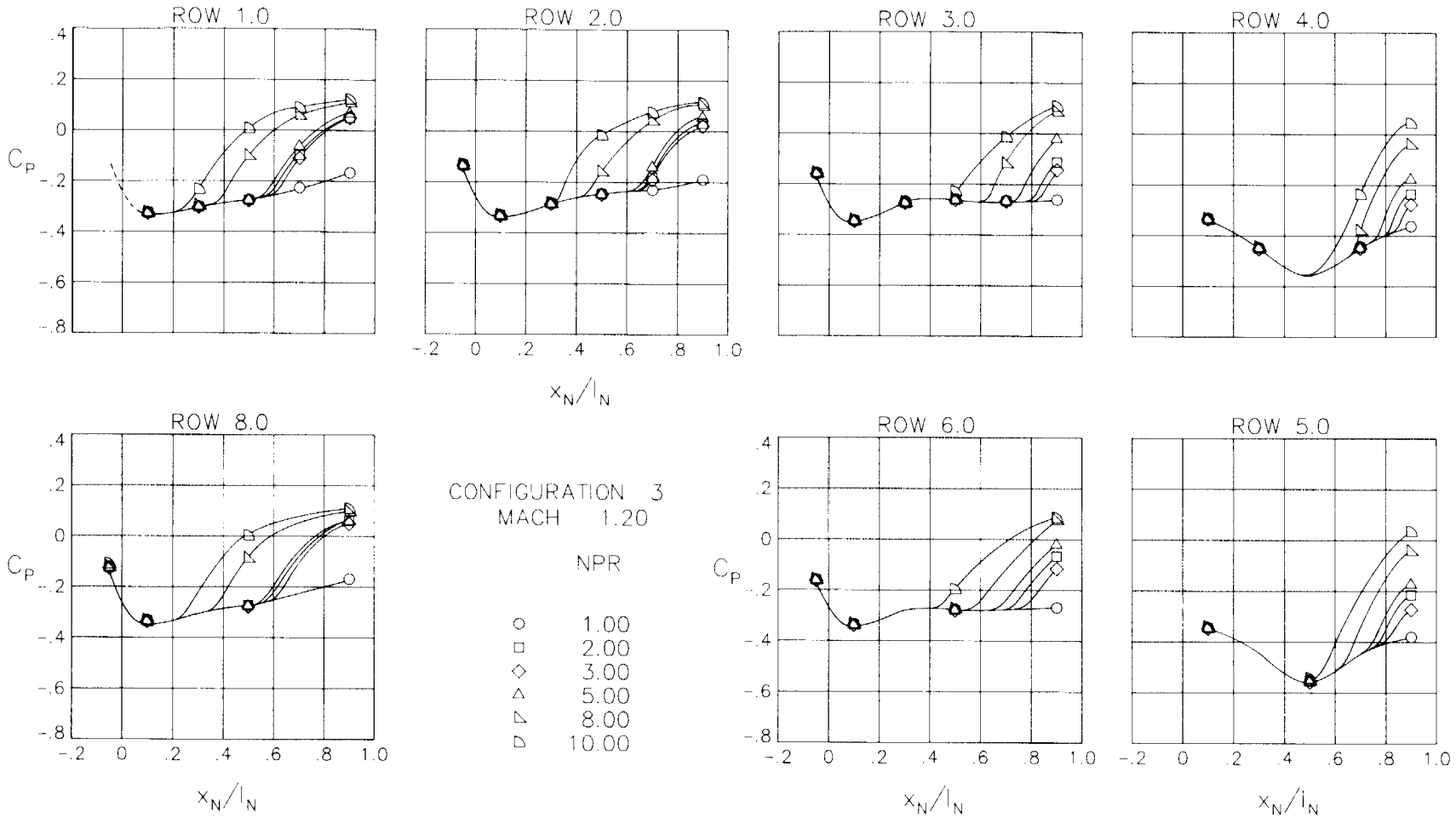

(f) M = 1.20.

Figure 28.- Concluded.

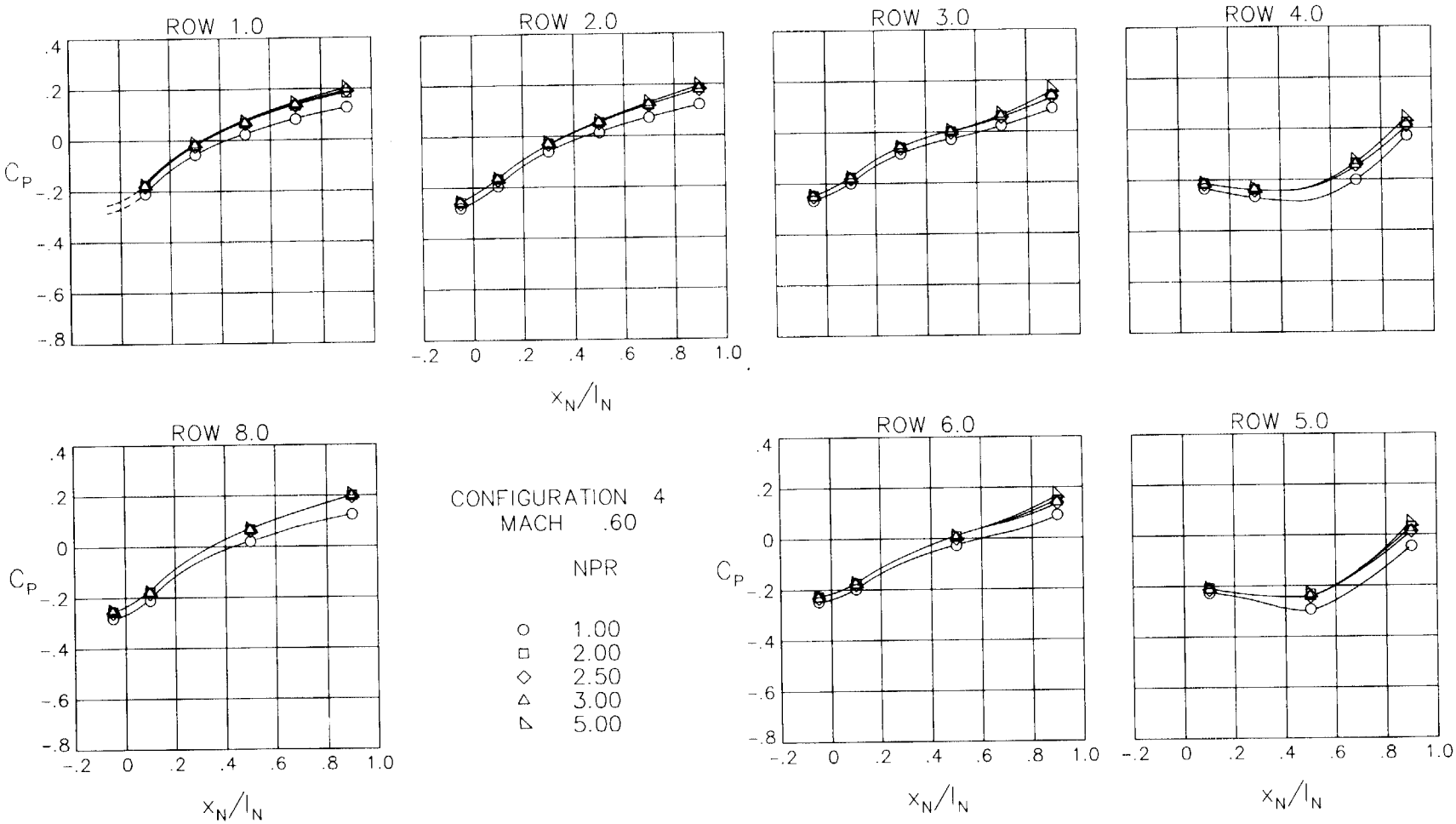

(a) M = 0.60.

Figure 29.- Surface static-pressure coefficient distributions around nozzle for configuration 4. $\alpha = 0°$.

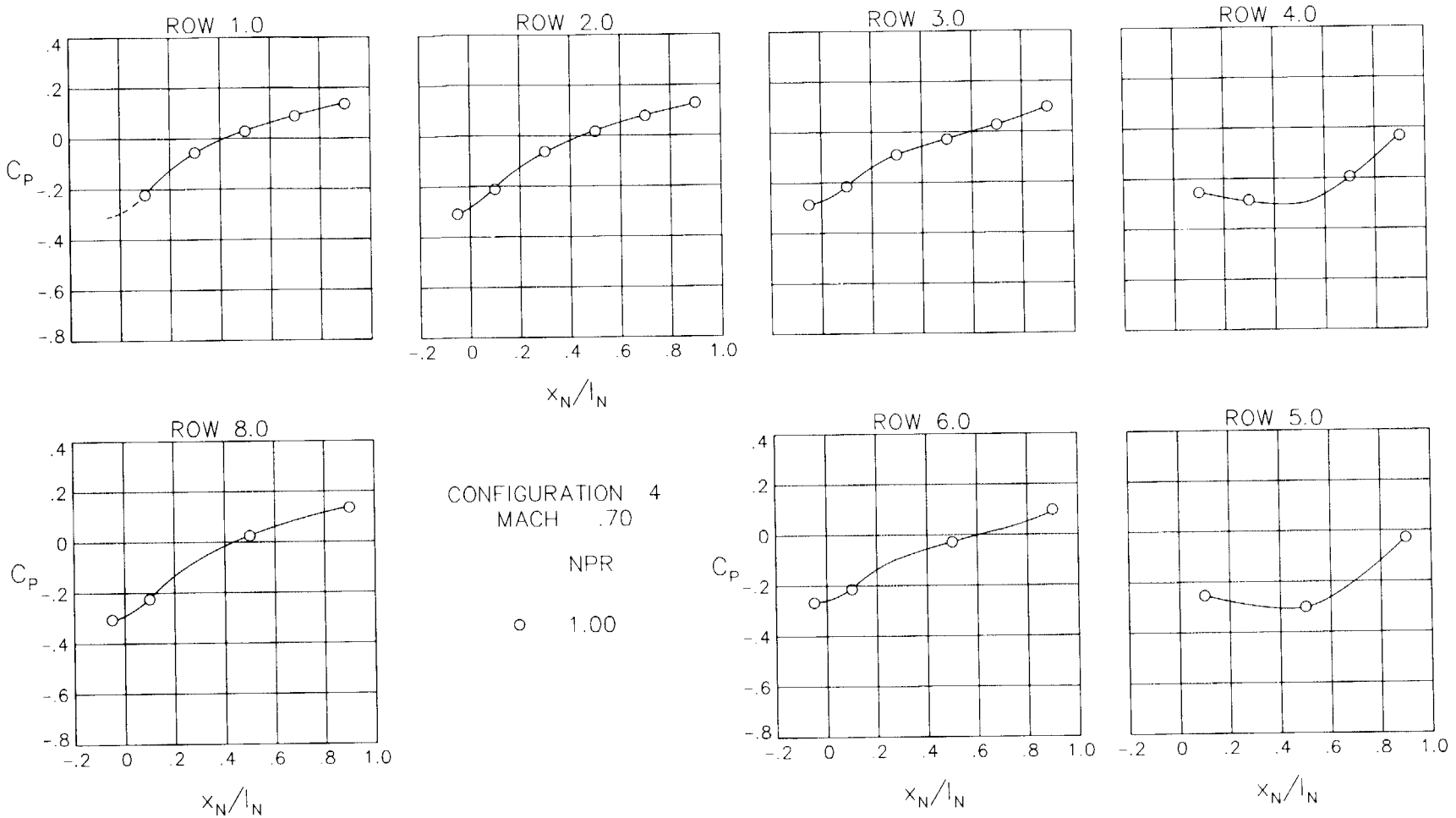

(b) M = 0.70.

Figure 29.- Continued.

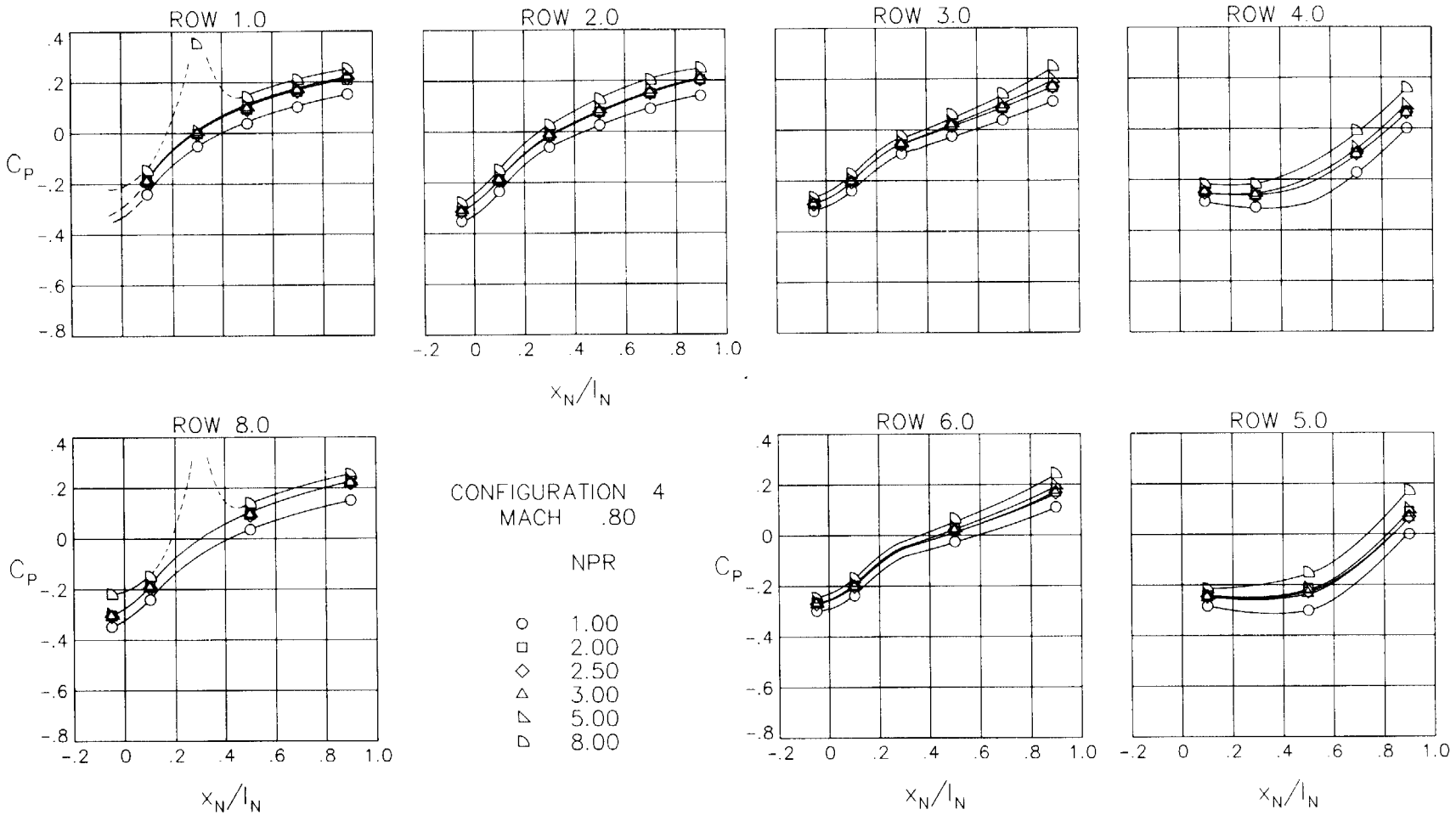

(c) M = 0.80.

Figure 29.- Continued.

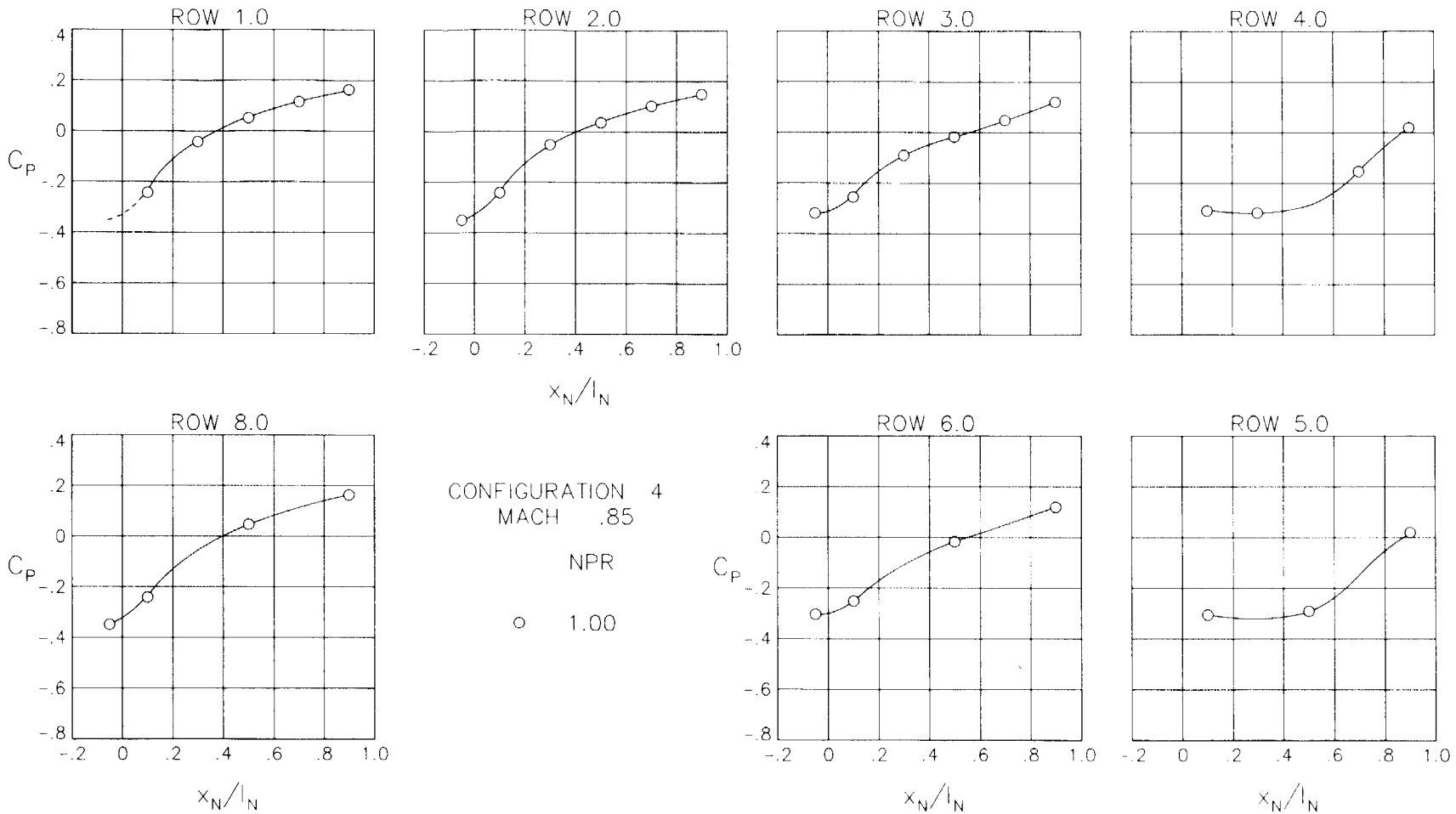

(d) M = 0.85.

Figure 29.- Continued.

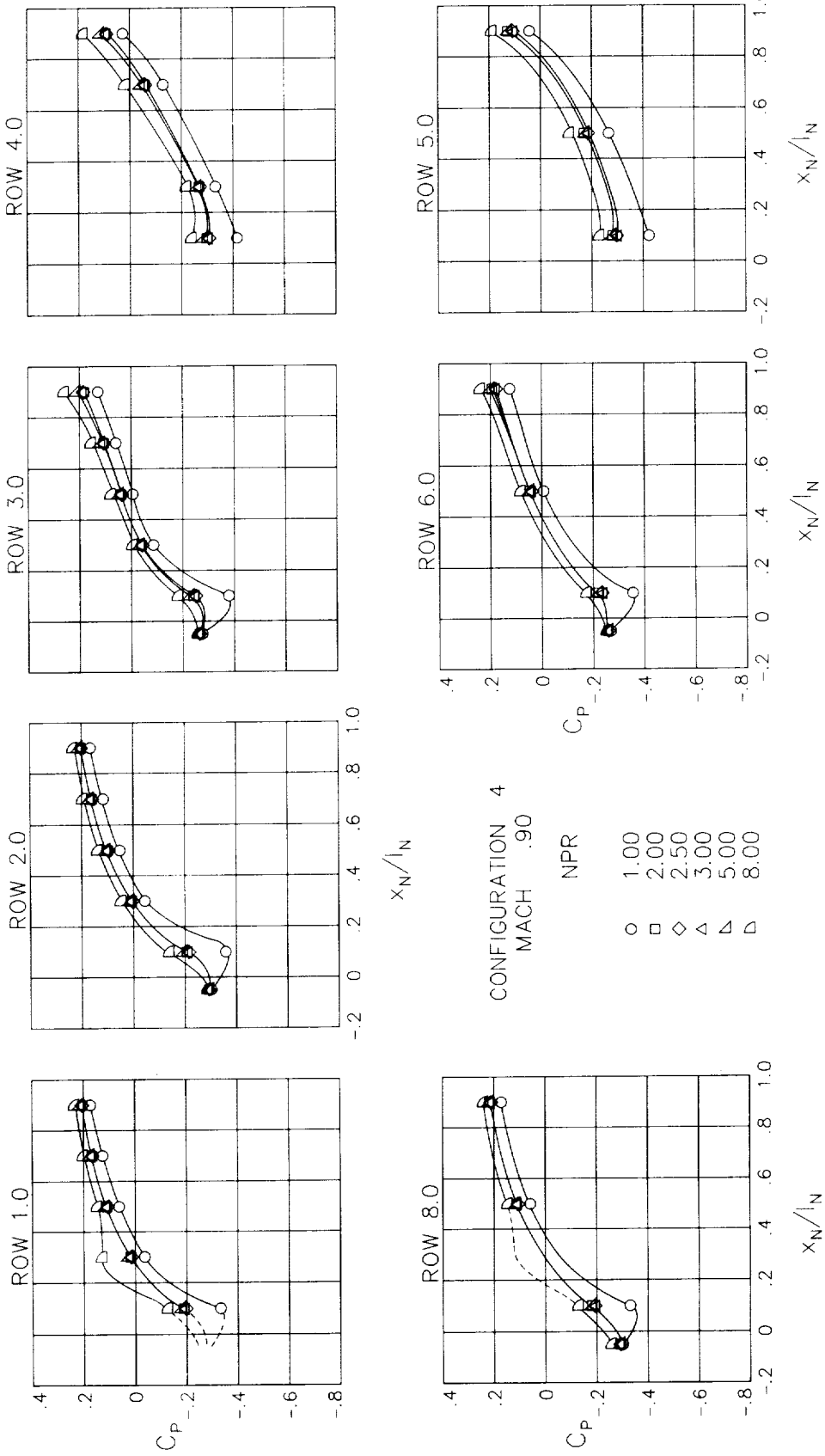

(e) M = 0.90.

Figure 29.- Continued.

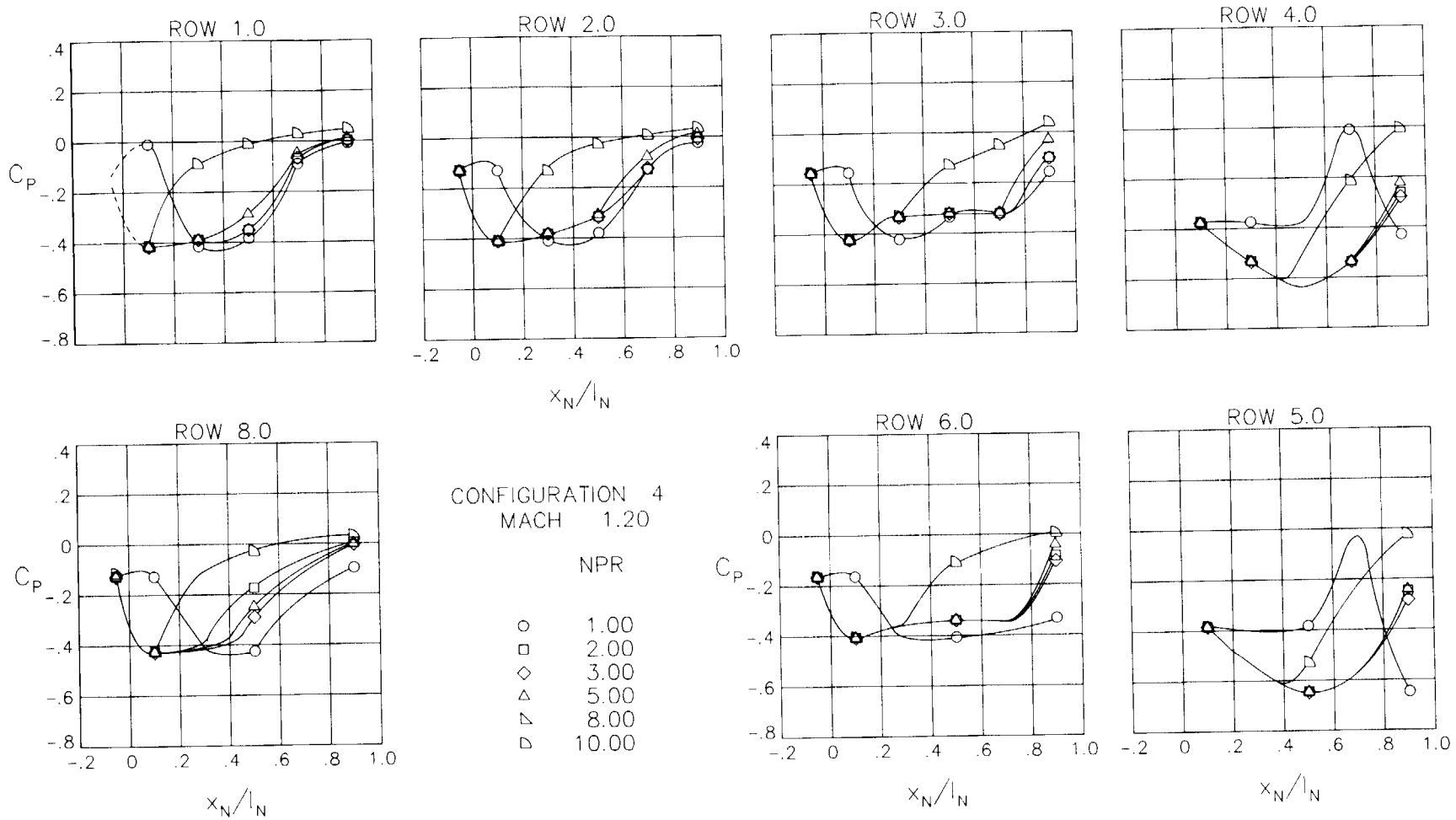

(f) M = 1.20.

Figure 29.- Concluded.

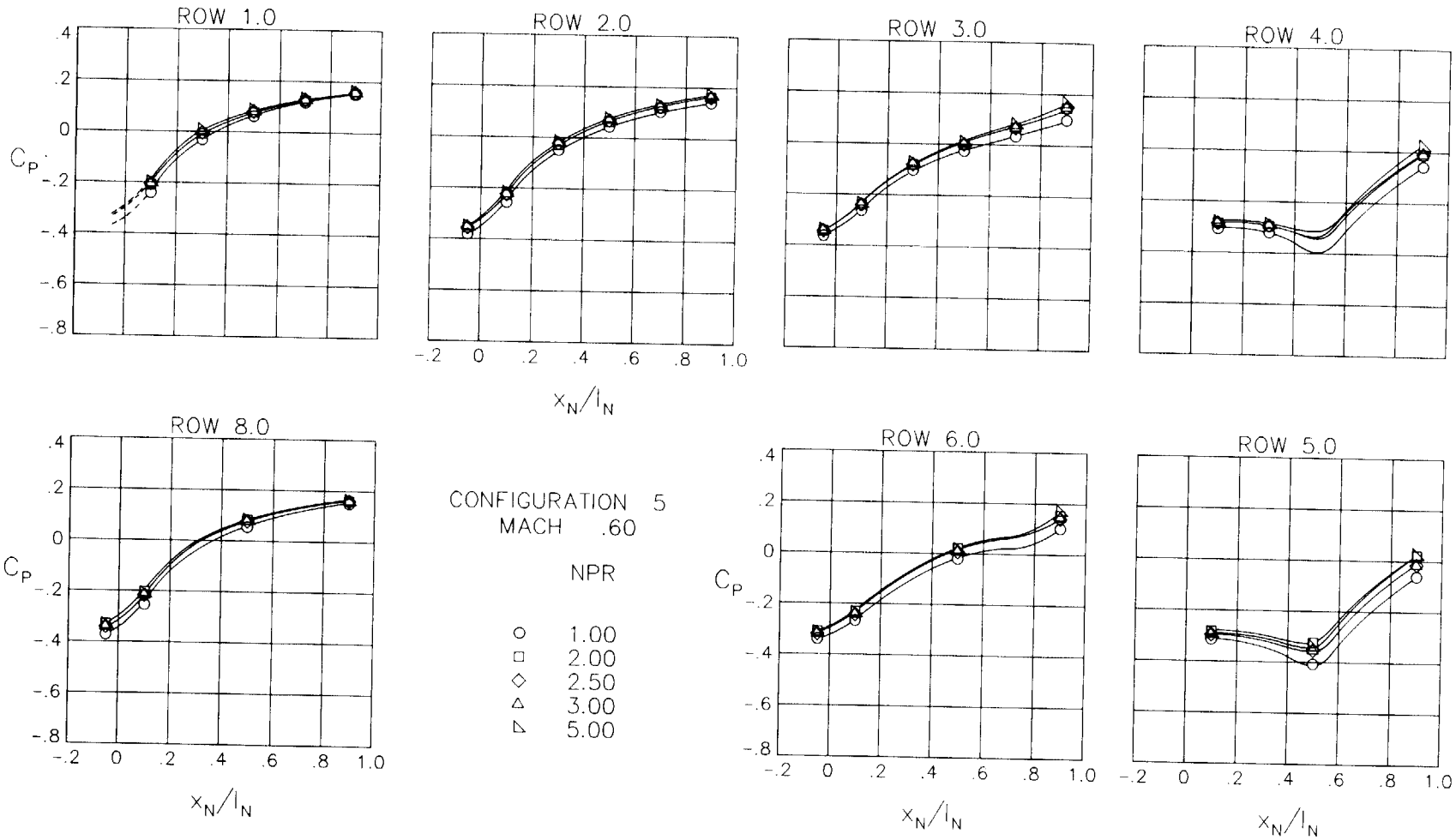

(a) M = 0.60.

Figure 30.- Surface static-pressure coefficient distributions around nozzle for configuration 5. $\alpha = 0°$.

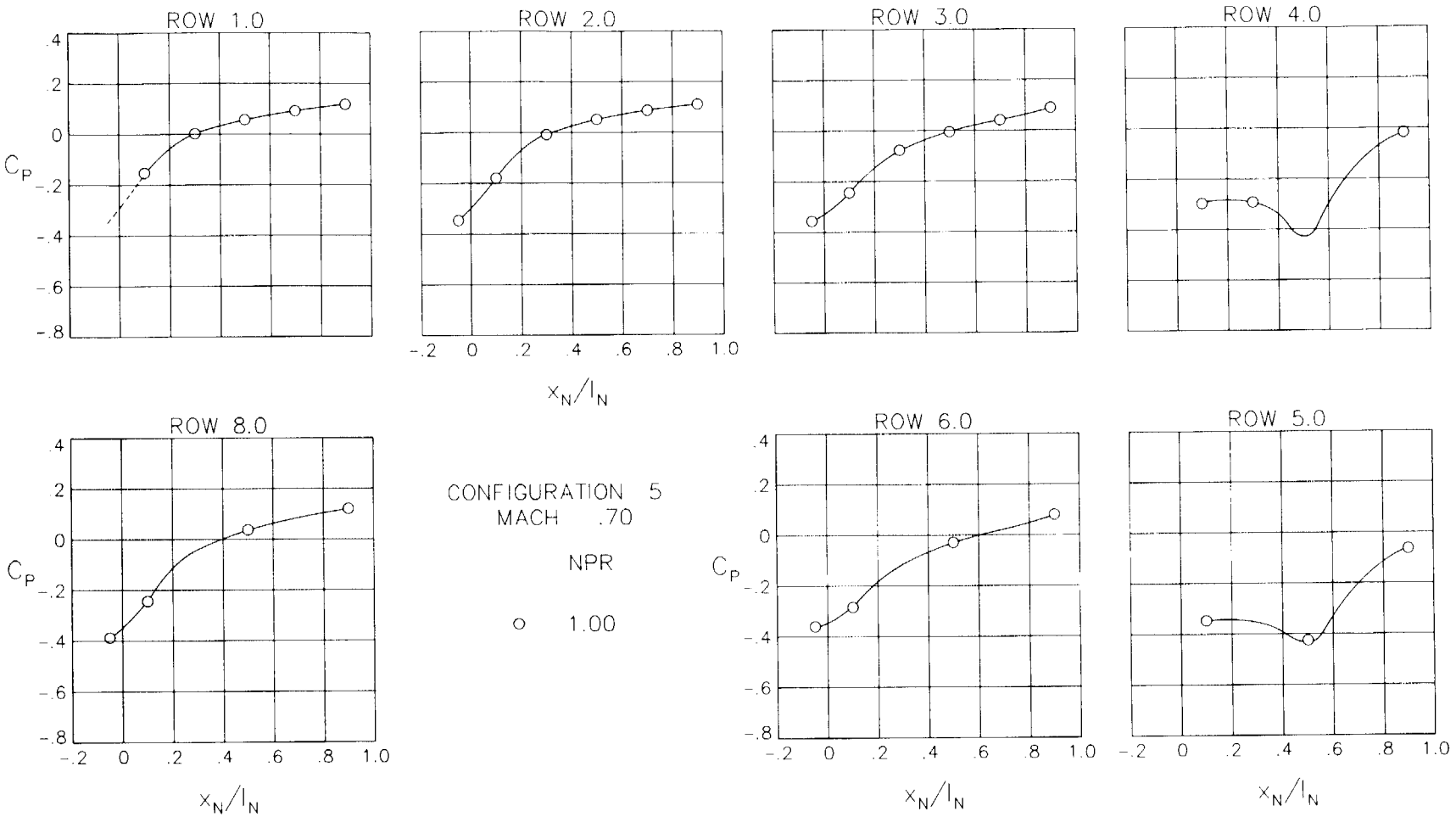

(b) M = 0.70.

Figure 30.- Continued.

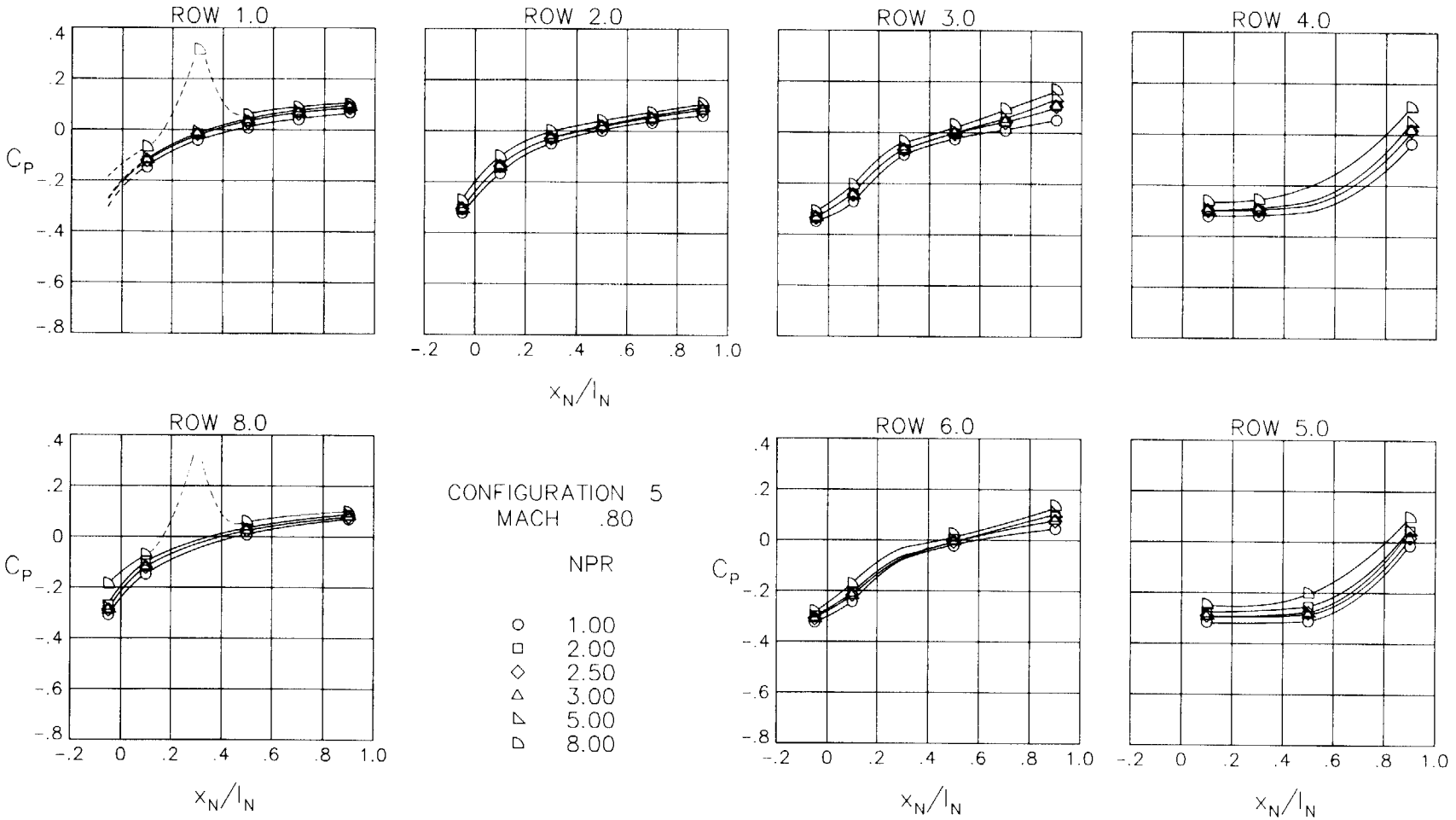

(c) M = 0.80.

Figure 30.- Continued.

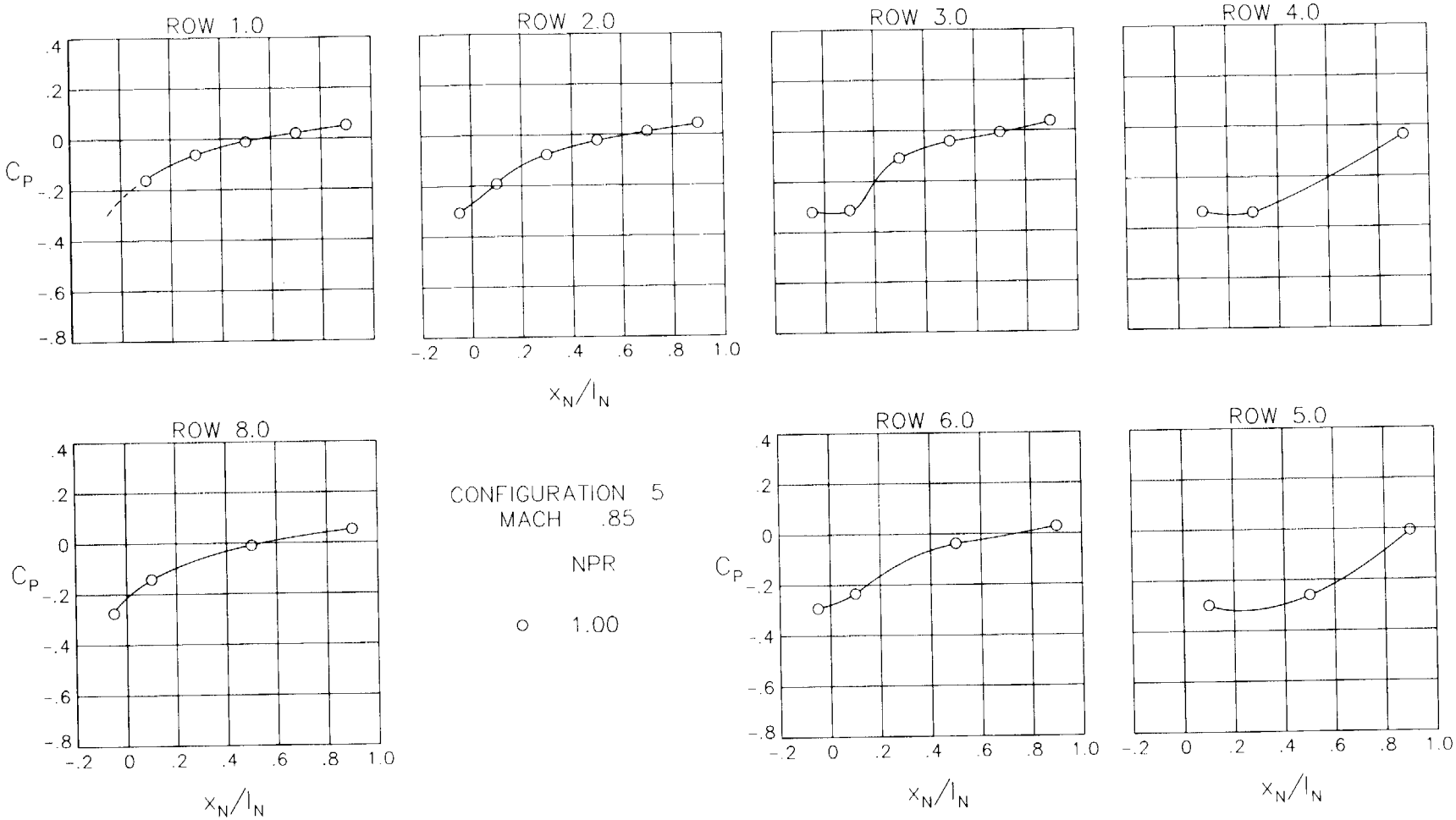

(d) M = 0.85.

Figure 30.- Continued.

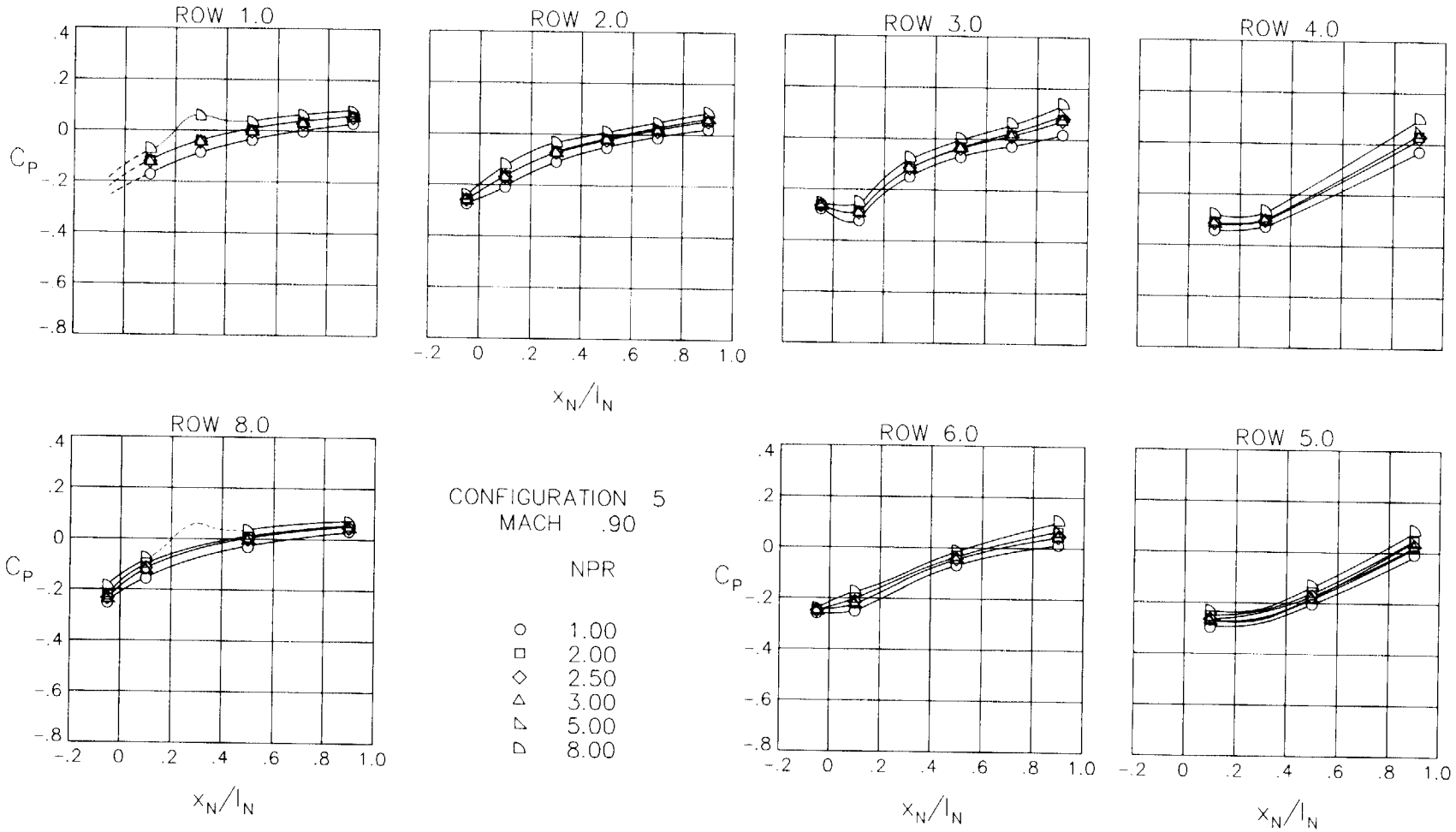

(e) M = 0.90.

Figure 30.- Continued.

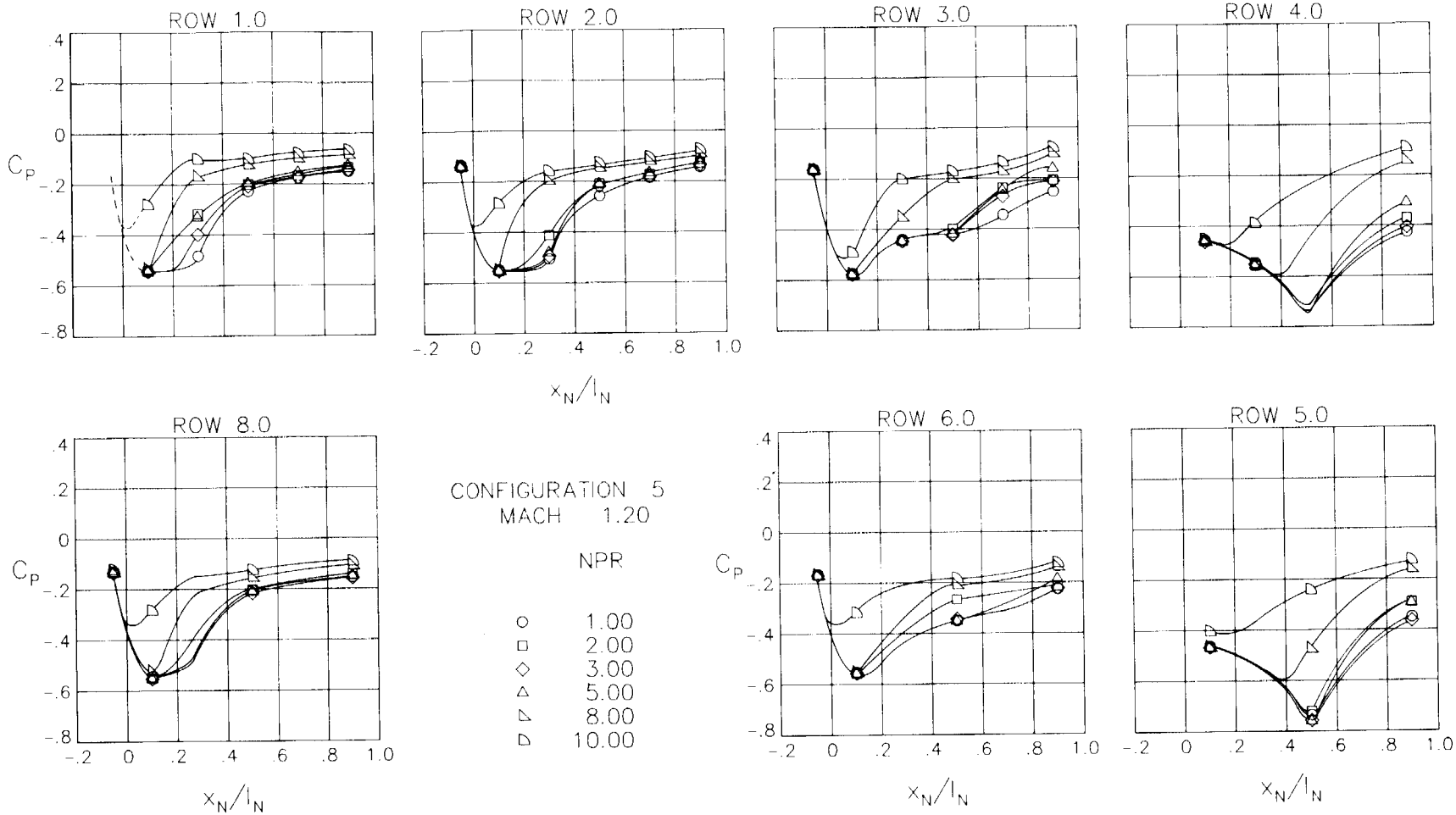

(f) M = 1.20.

Figure 30.- Concluded.

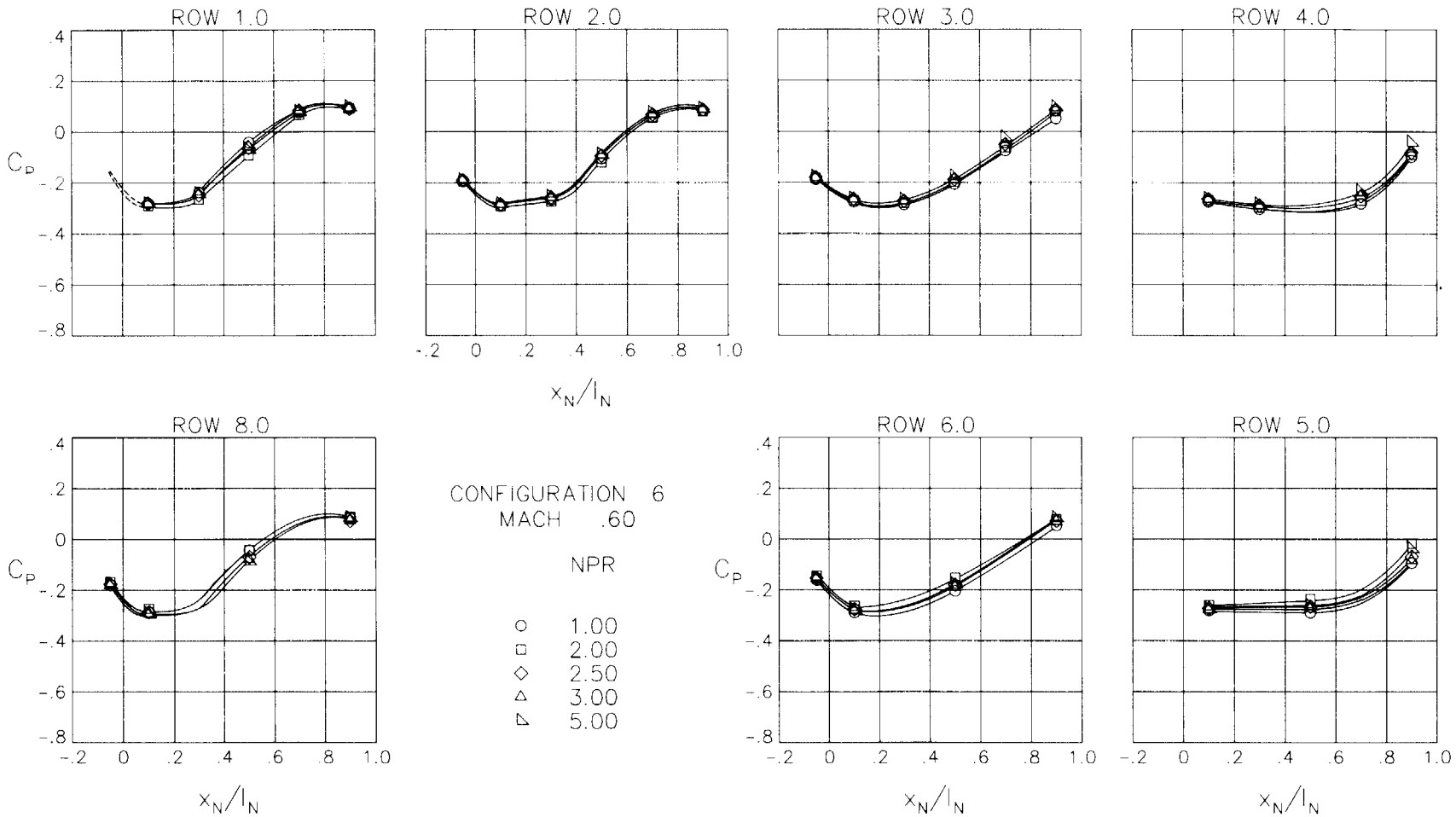

(a) M = 0.60.

Figure 31.- Surface static-pressure coefficient distributions around nozzle for configuration 6. α = 0°.

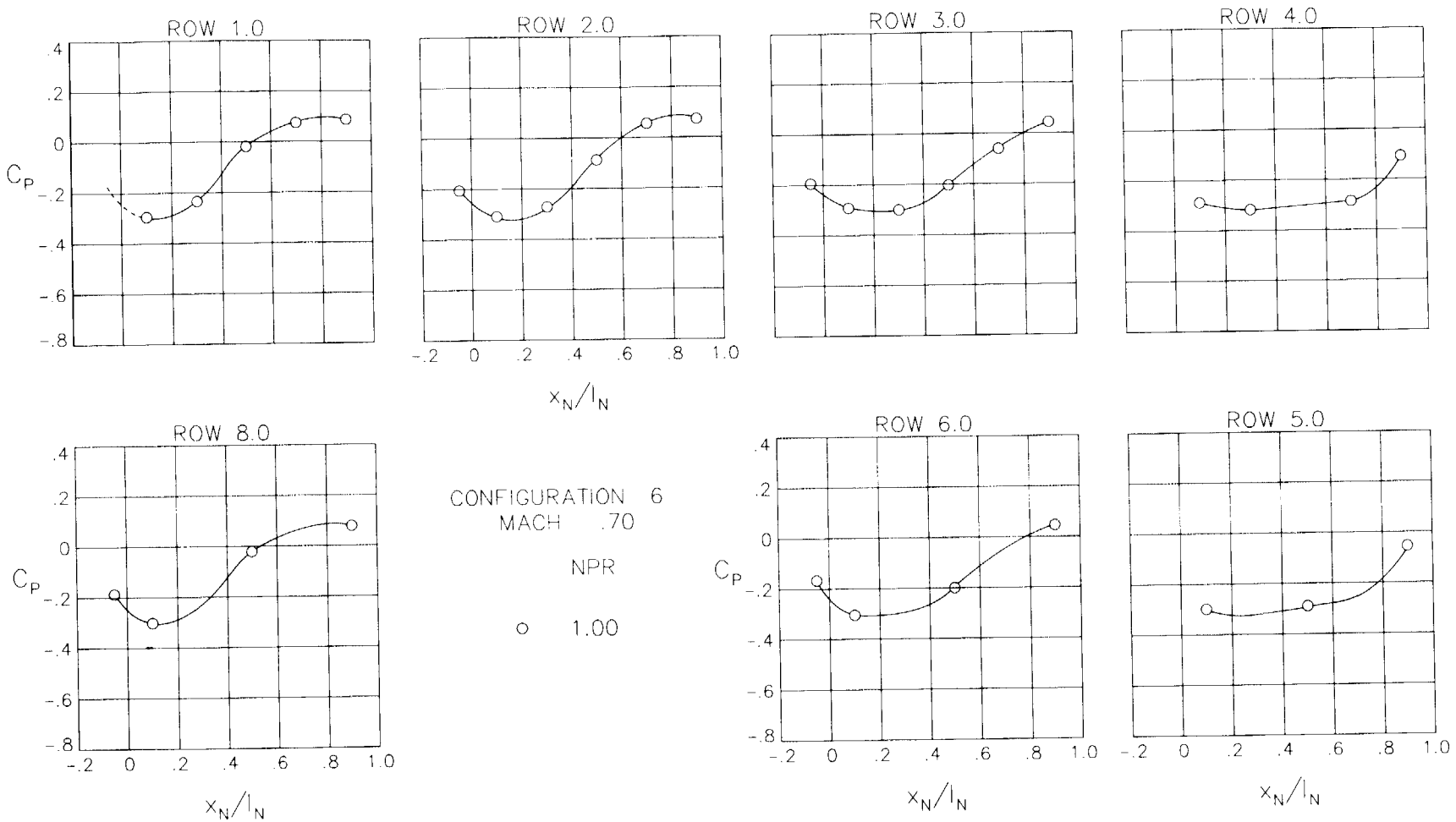

(b) M = 0.70.

Figure 31.- Continued.

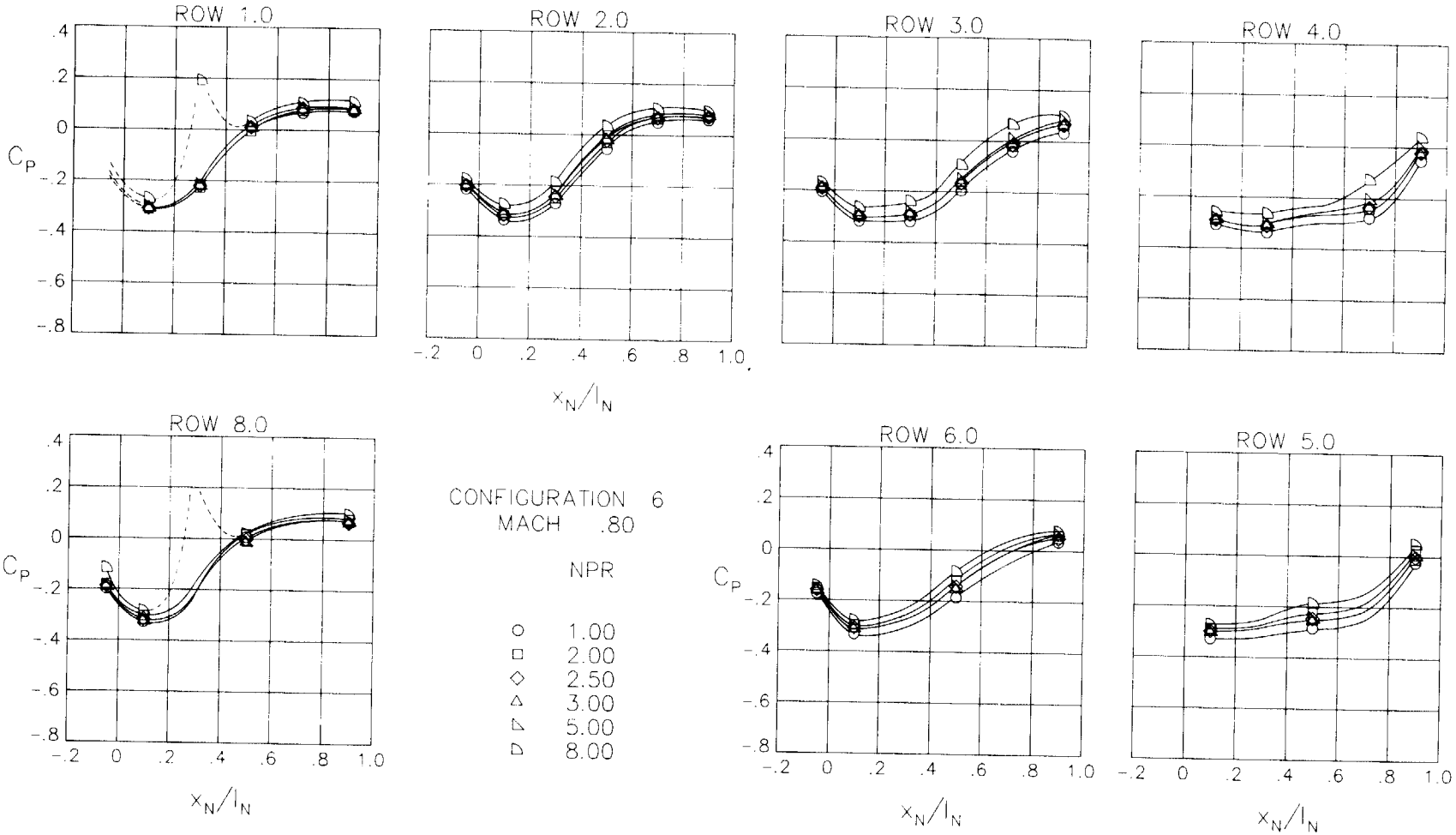

(c) M = 0.80.

Figure 31.- Continued.

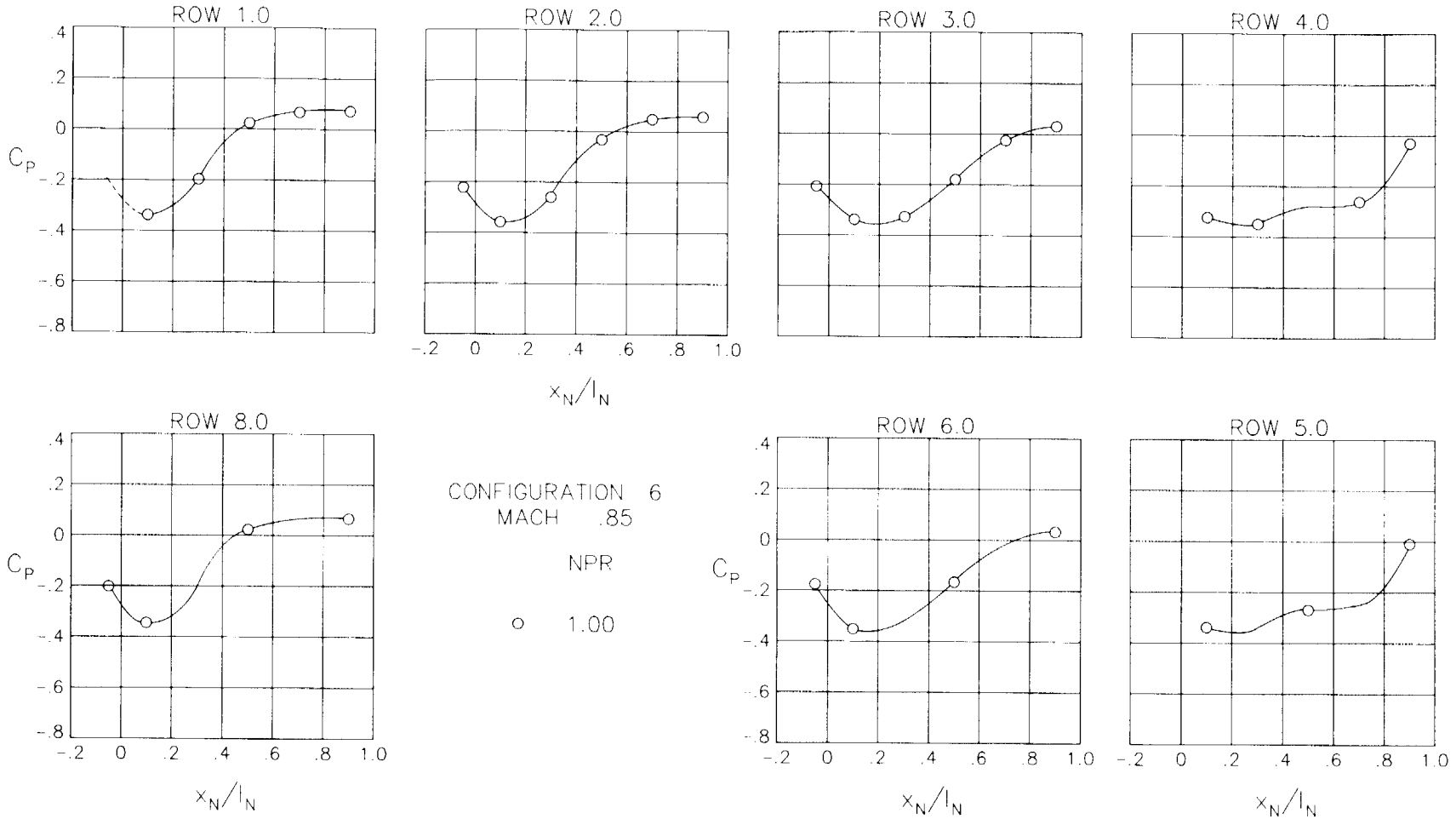

(d) M = 0.85.

Figure 31.- Continued.

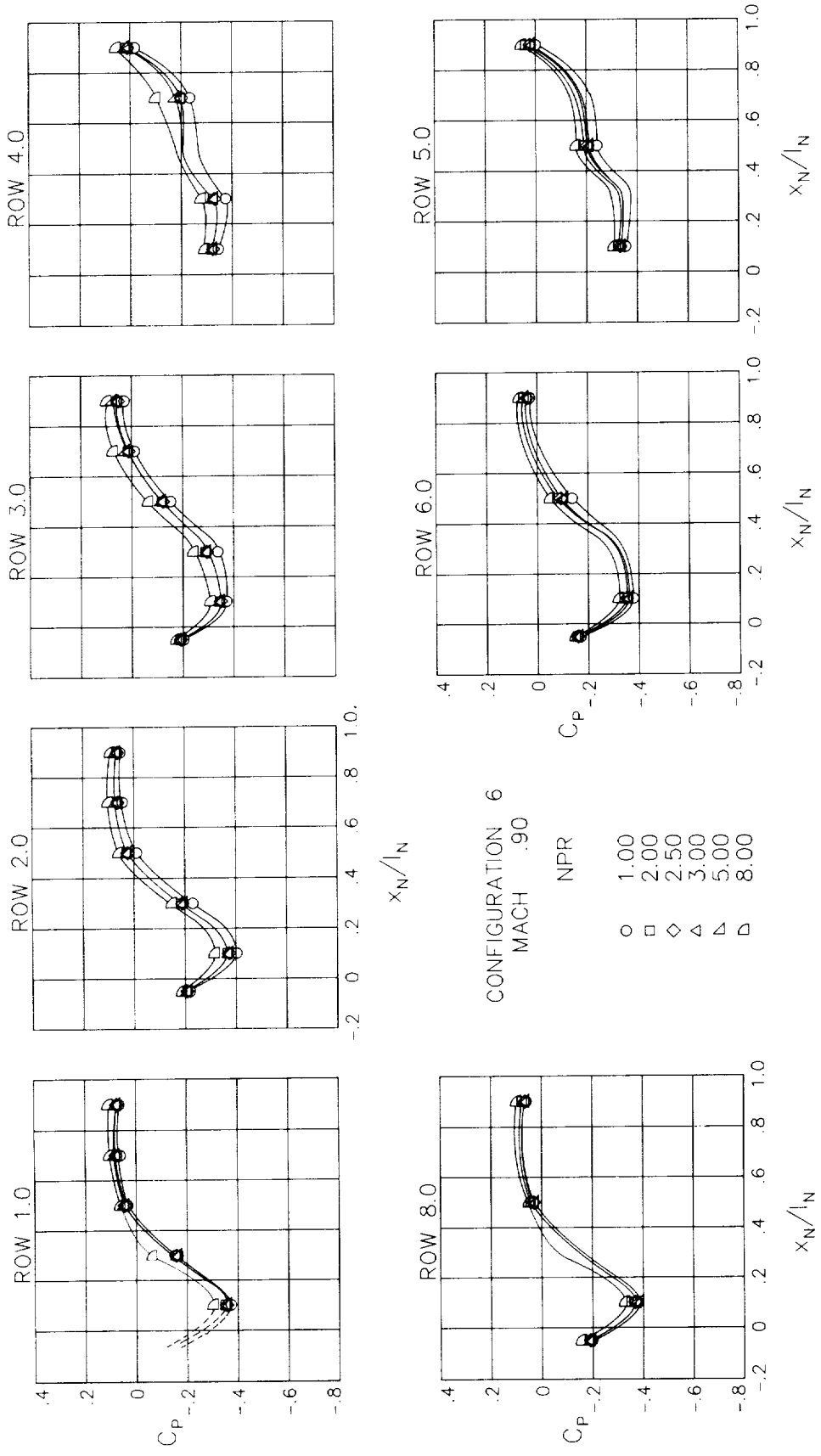

(e) M = 0.90.

Figure 31.- Continued.

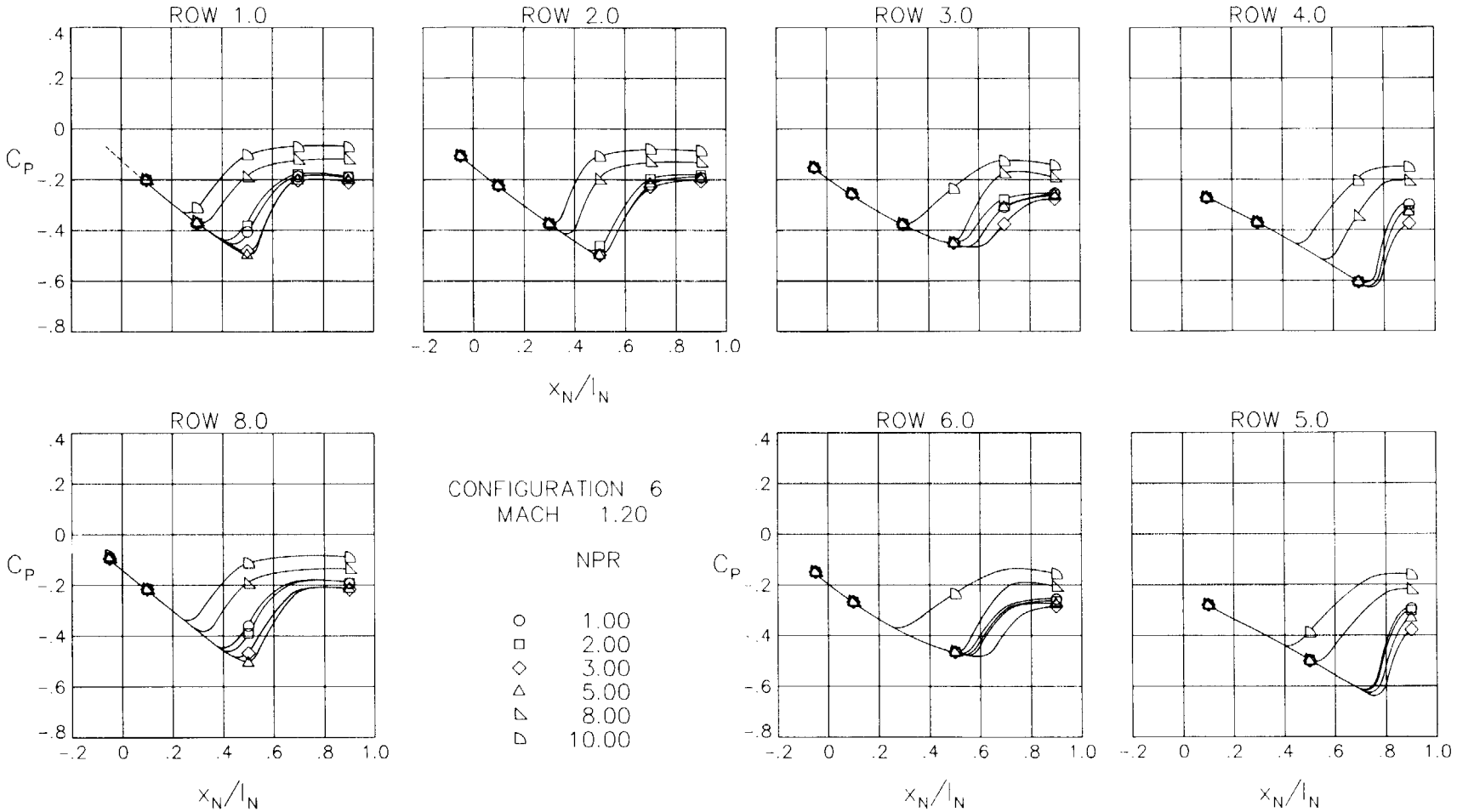

(f) M = 1.20.

Figure 31.- Concluded.

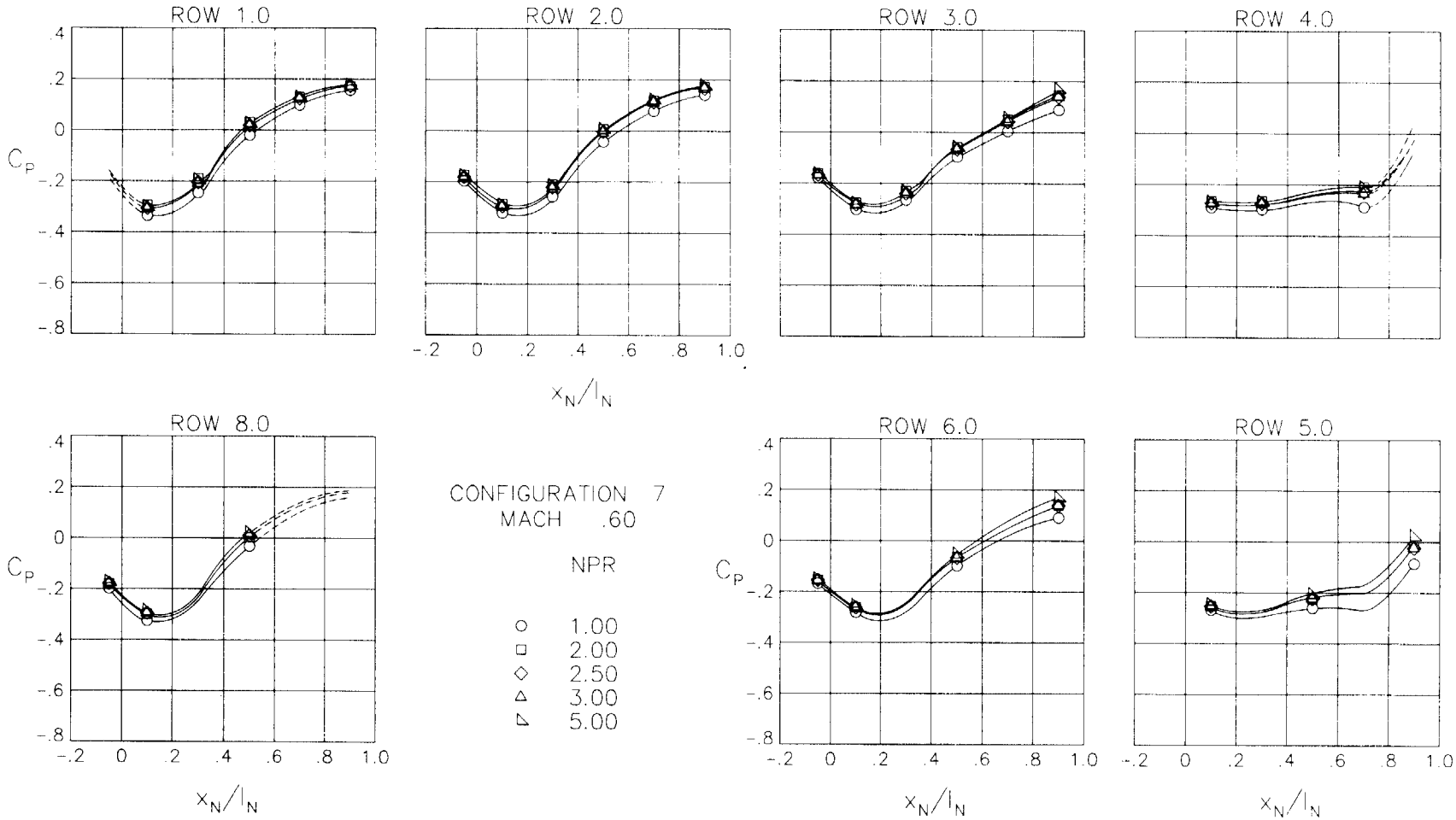

(a) M = 0.60.

Figure 32.- Surface static-pressure coefficient distributions around nozzle for configuration 7. $\alpha = 0°$.

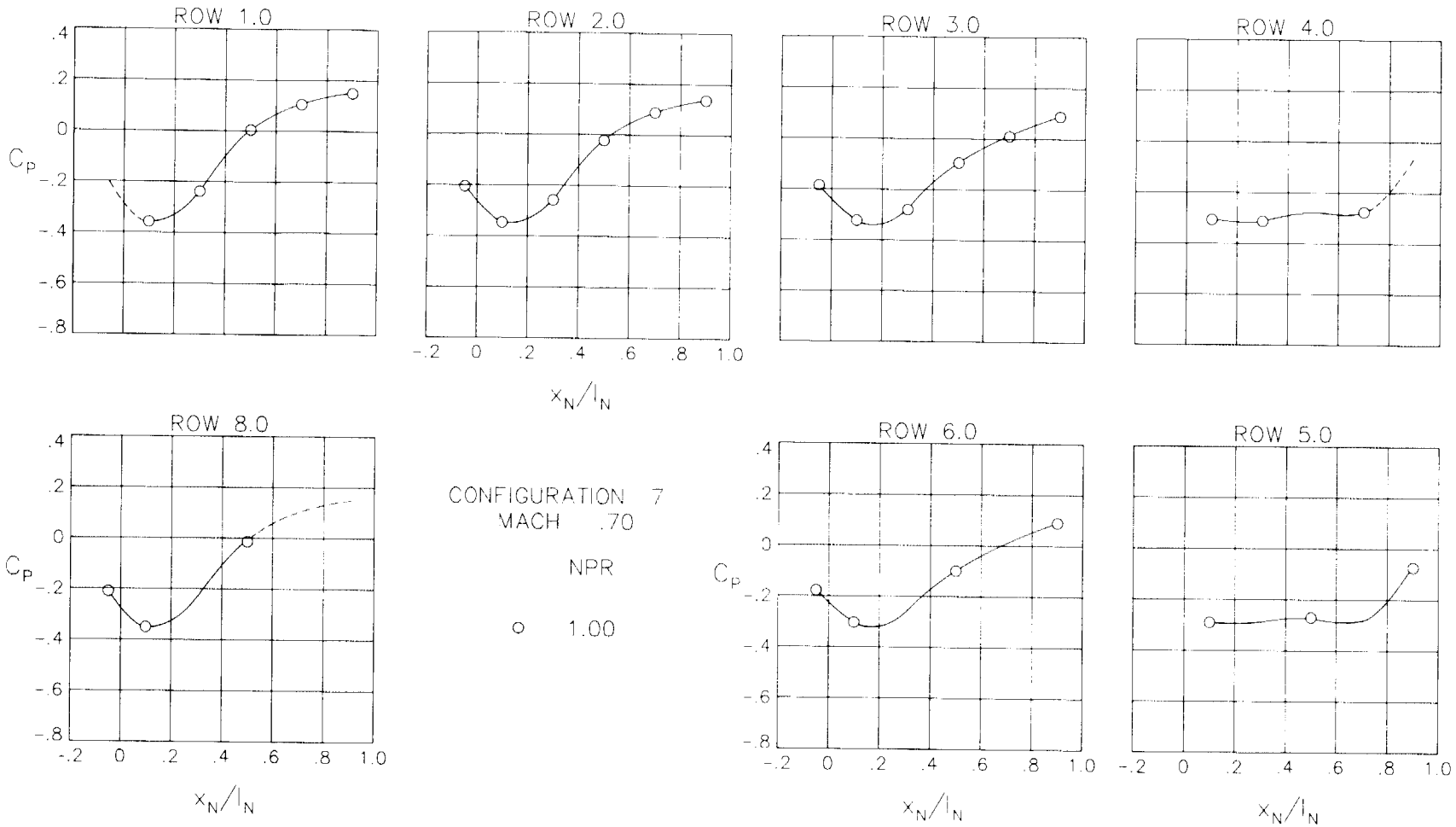

(b) M = 0.70.

Figure 32.- Continued.

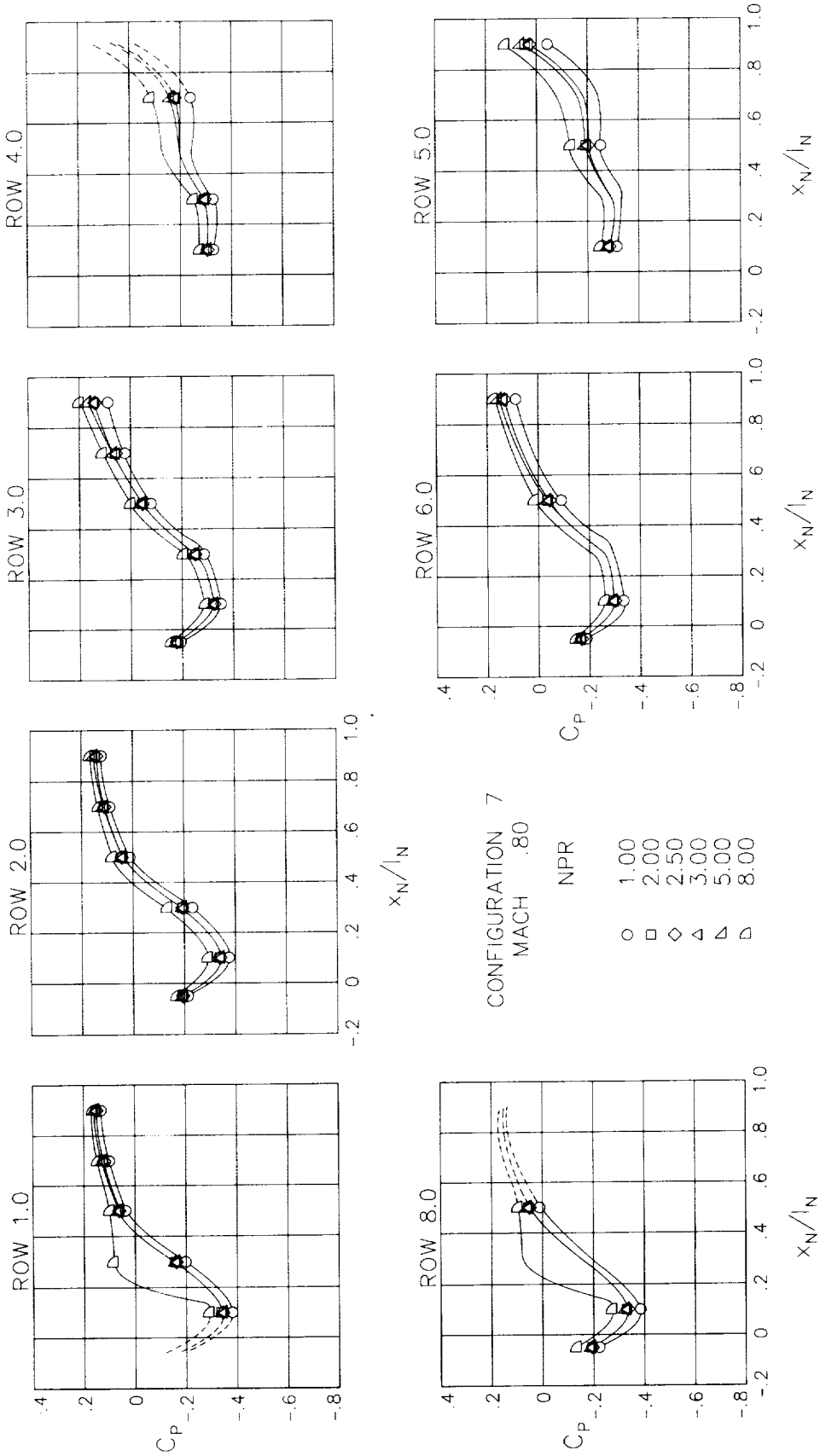

(c) M = 0.80.

Figure 32.- Continued.

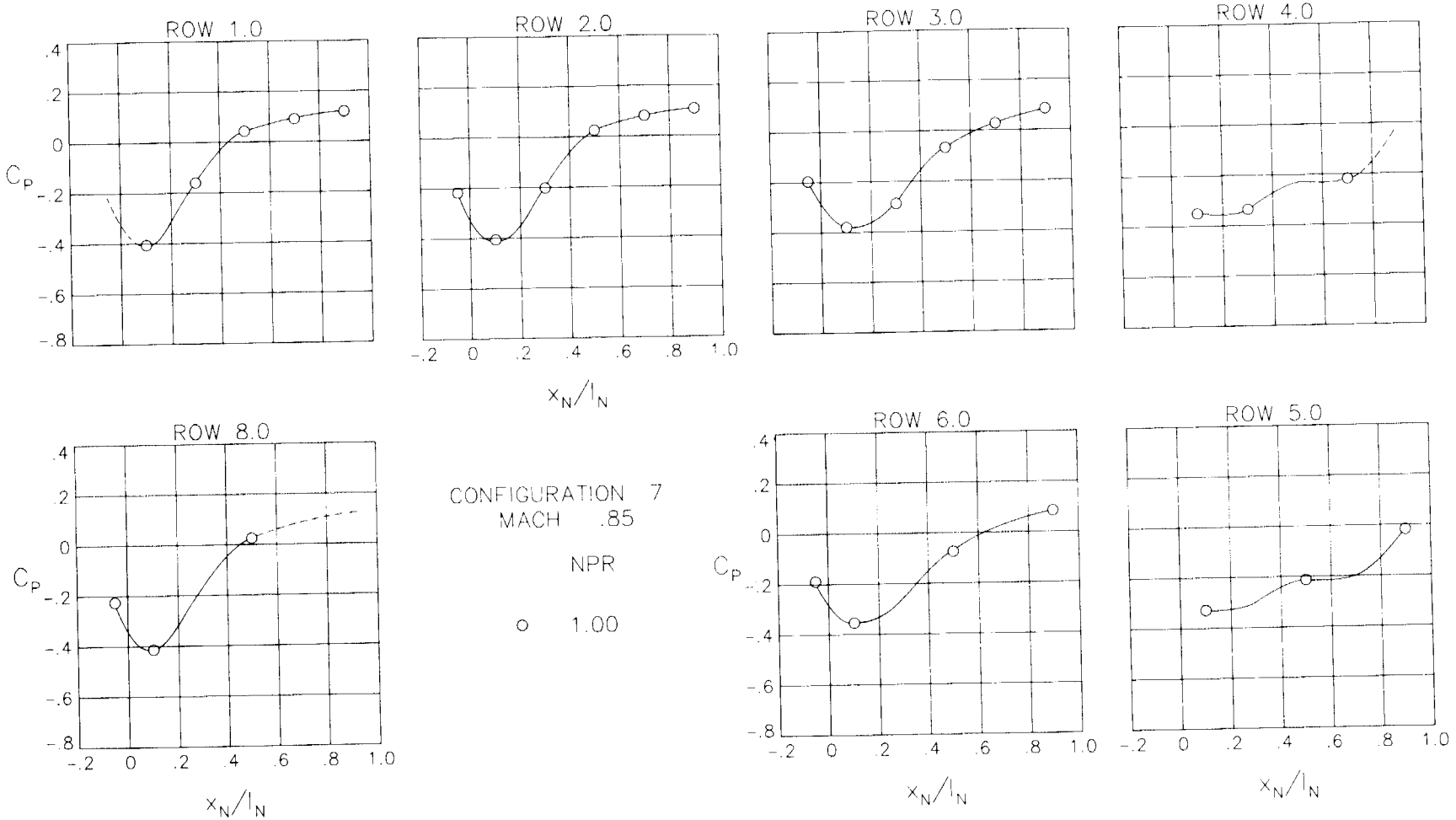

(d) M = 0.85.

Figure 32.- Continued.

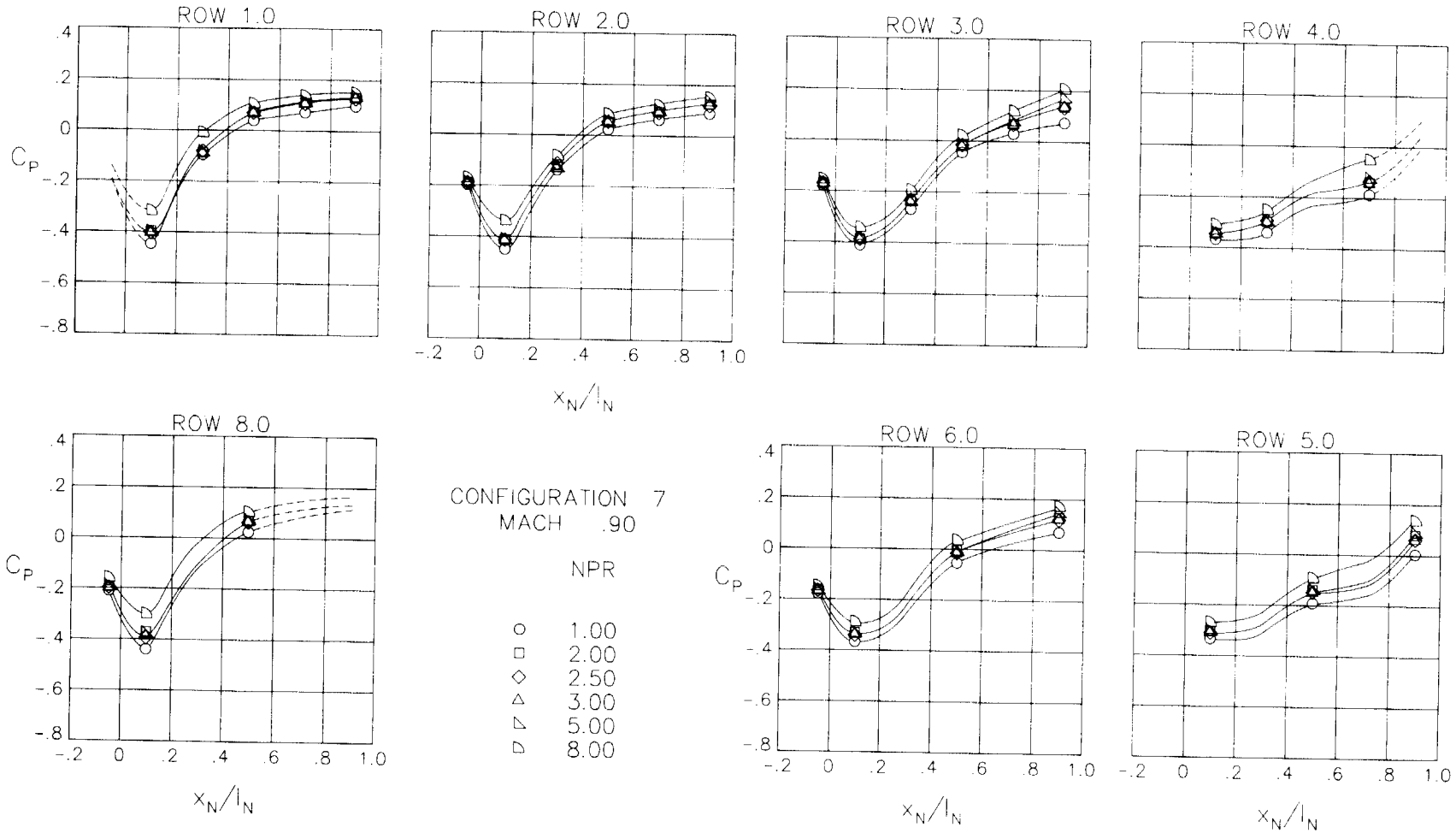

(e) M = 0.90.

Figure 32.- Continued.

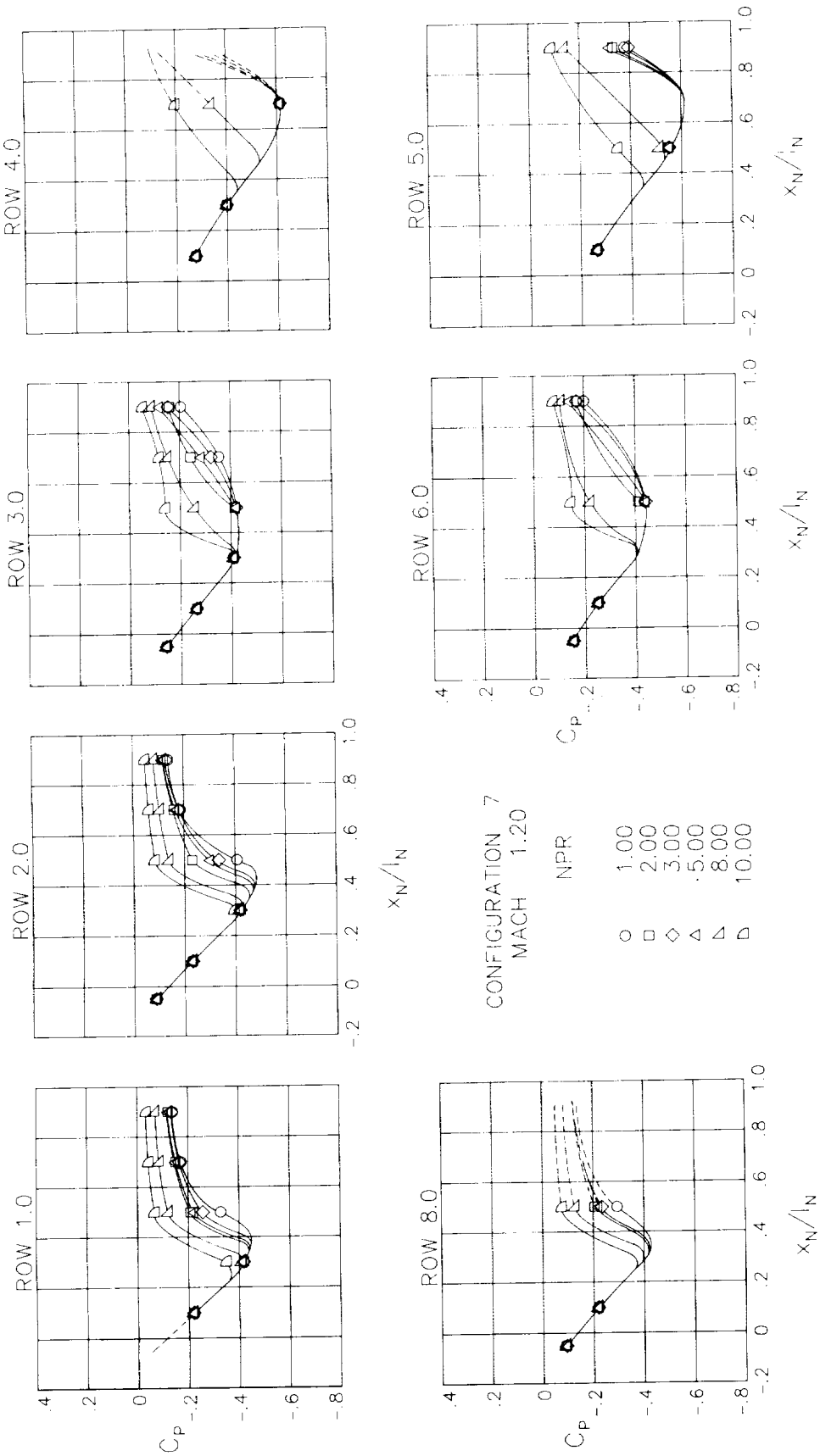

(f) M = 1.20.

Figure 32.- Concluded.

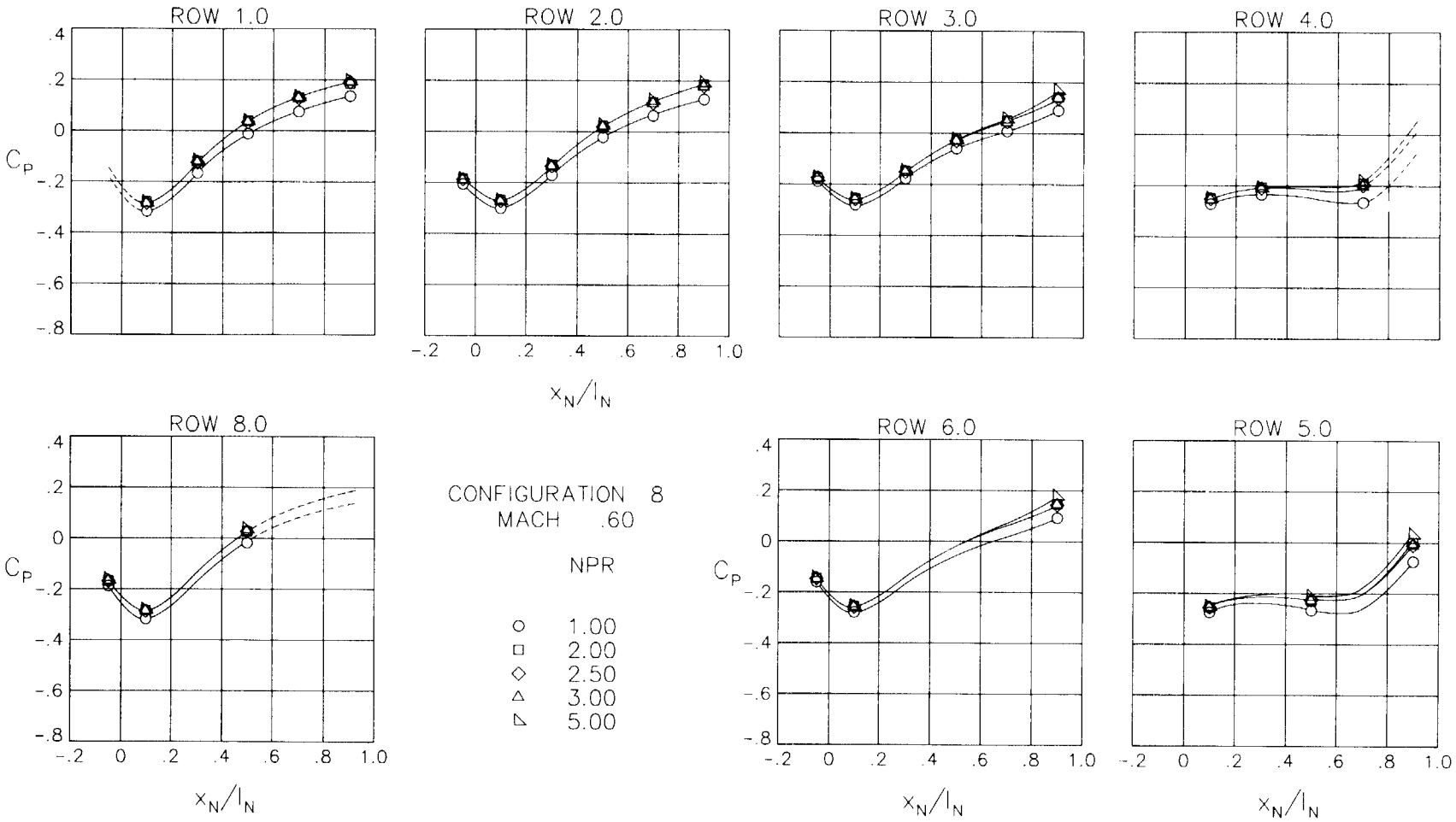

(a) M = 0.60.

Figure 33.- Surface static-pressure coefficient distributions around nozzle for configuration 8. $\alpha = 0°$.

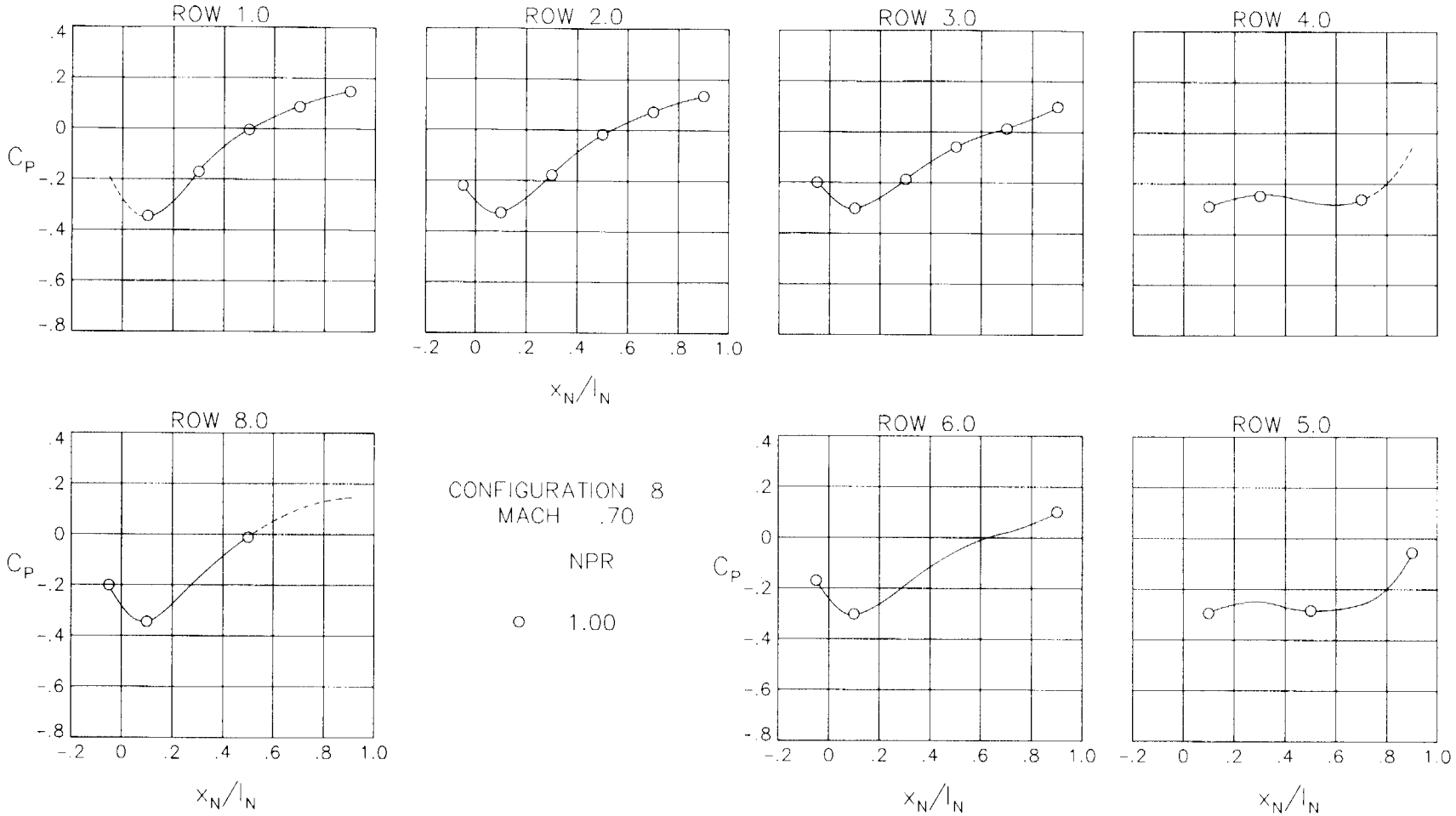

(b) M = 0.70.

Figure 33.- Continued.

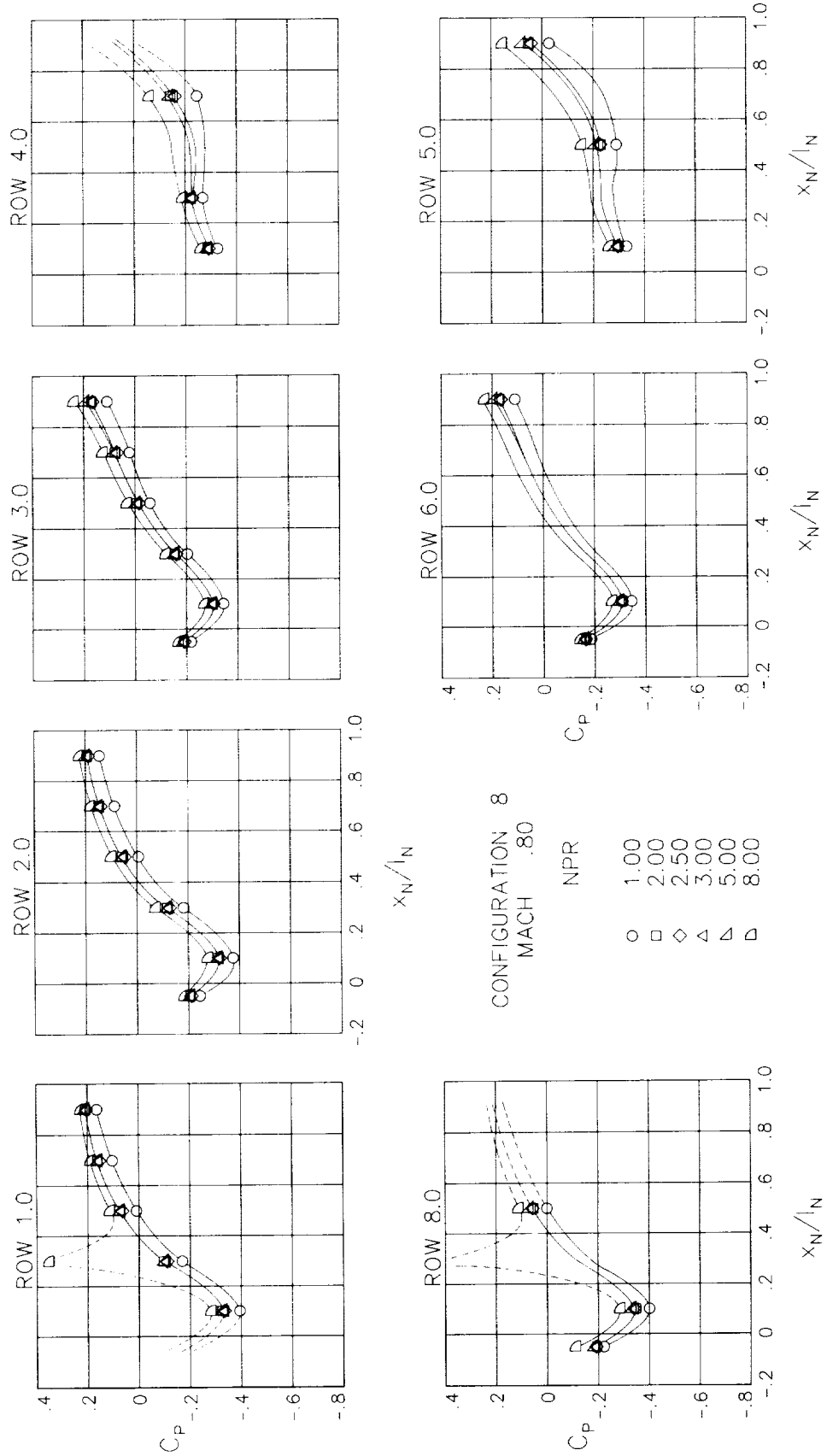

(c) M = 0.80.

Figure 33.- Continued.

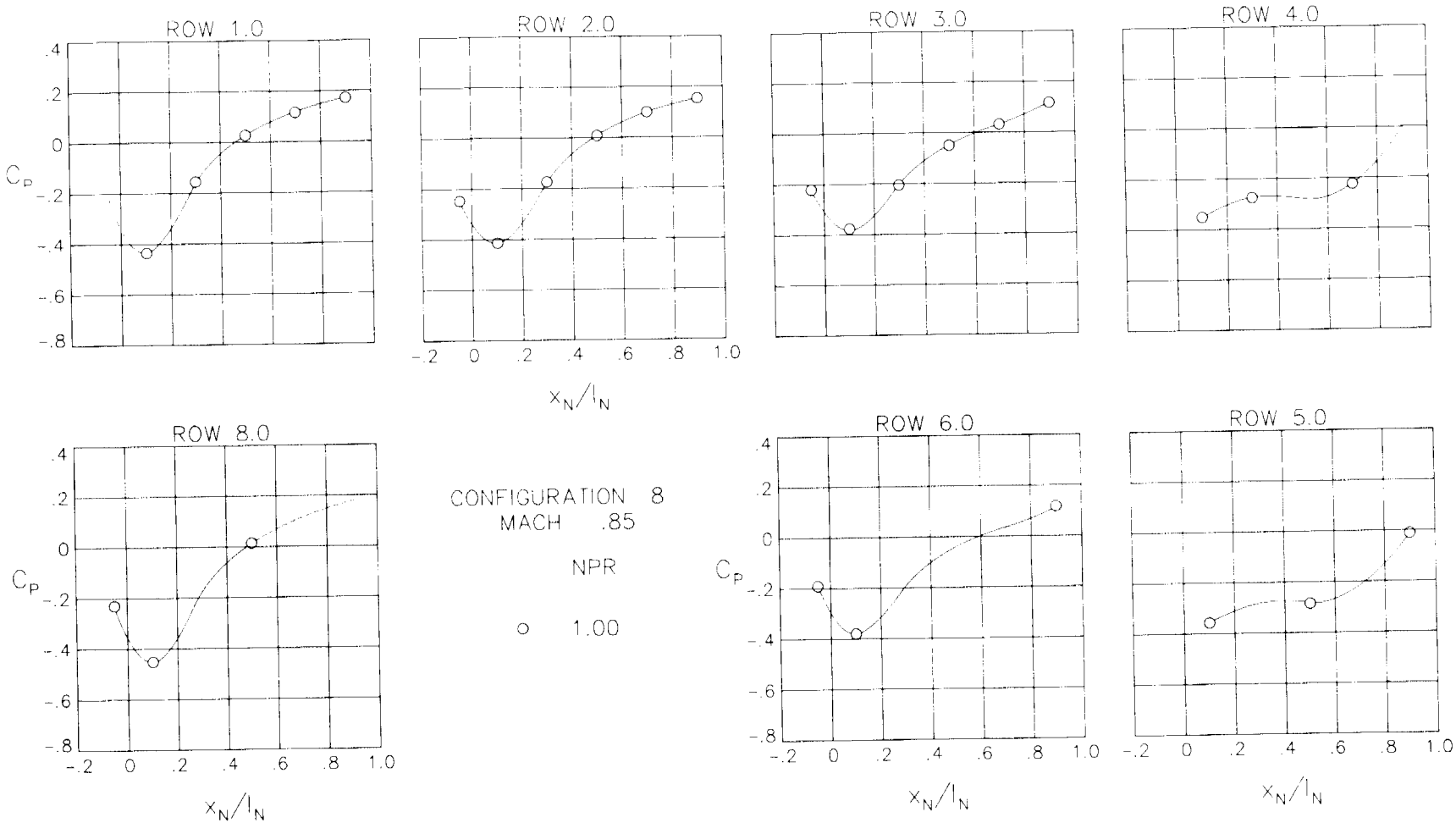

(d) M = 0.85.

Figure 33.- Continued.

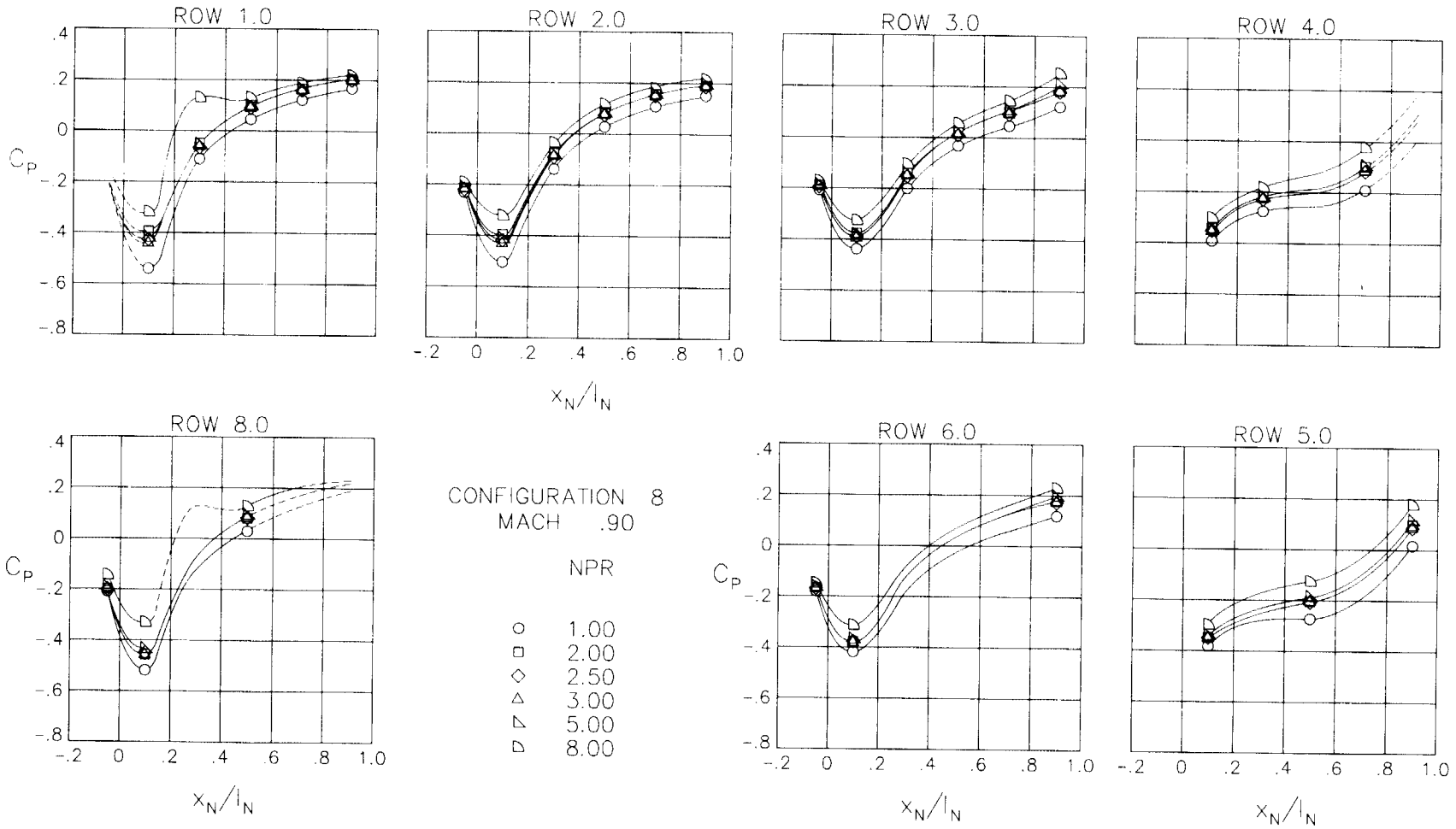

(e) M = 0.90.

Figure 33.- Continued.

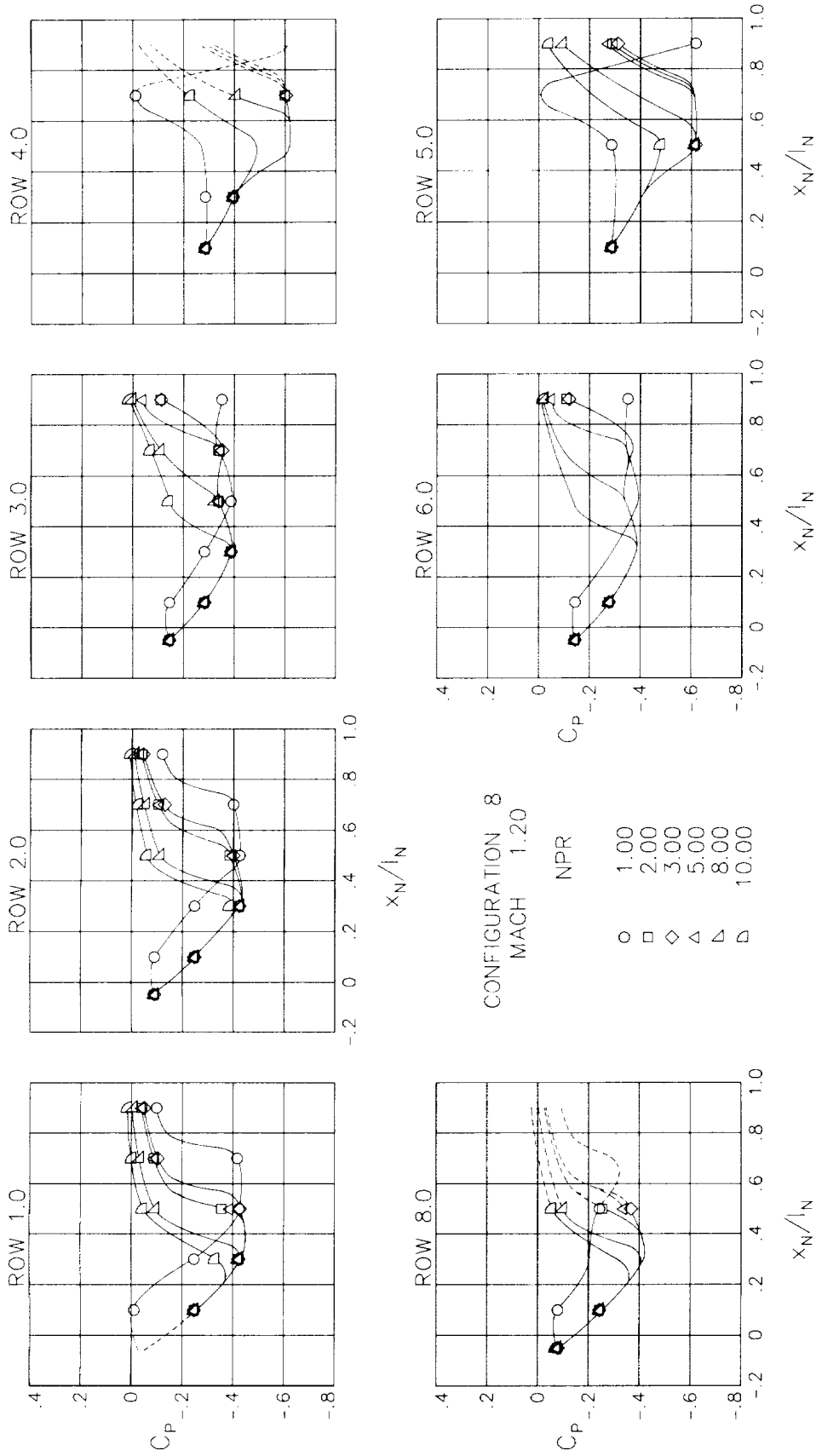

(f) M = 1.20.

Figure 33.- Concluded.

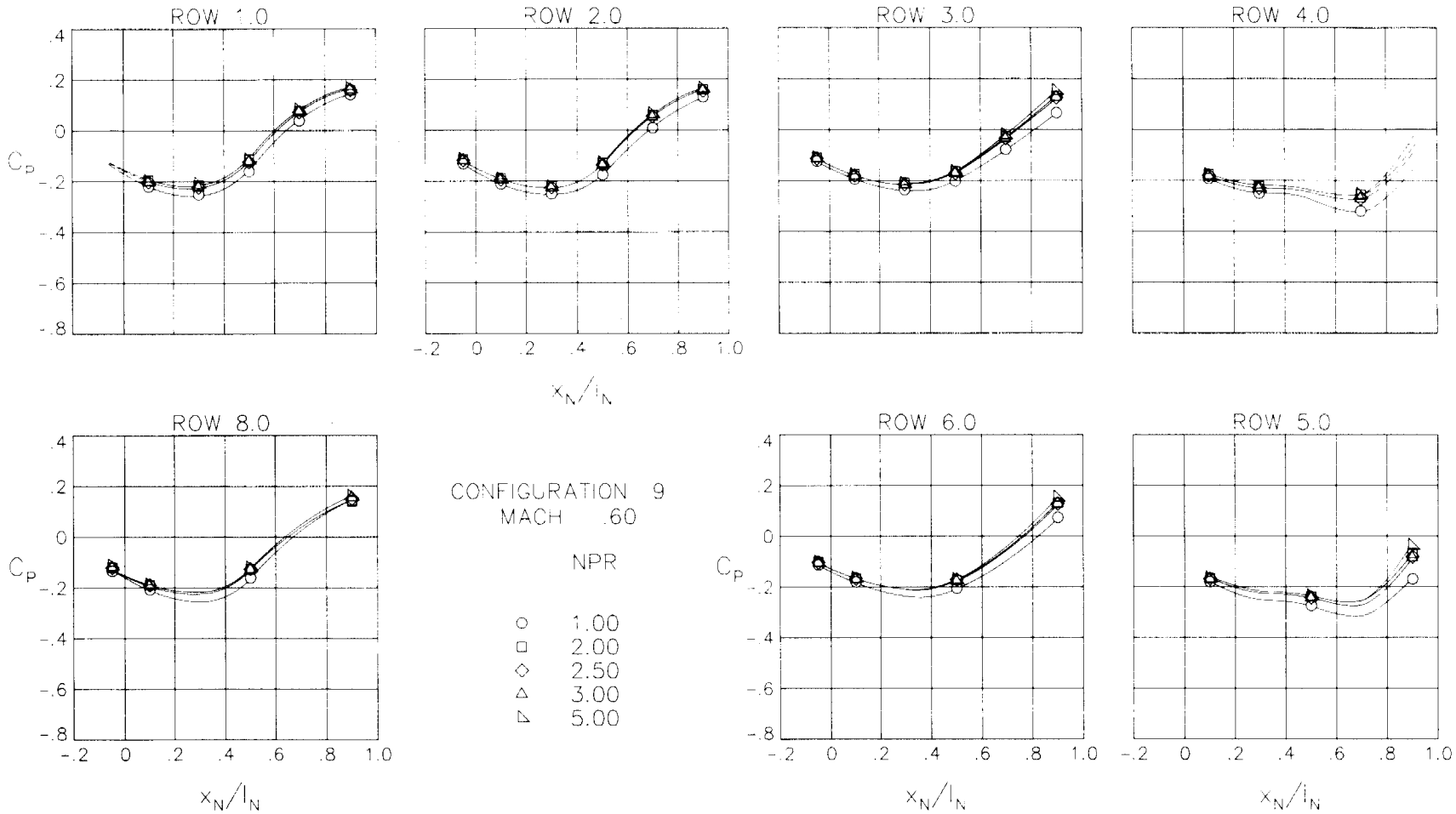

(a) M = 0.60.

Figure 34.- Surface static-pressure coefficient distributions around nozzle for configuration 9. $\alpha = 0°$.

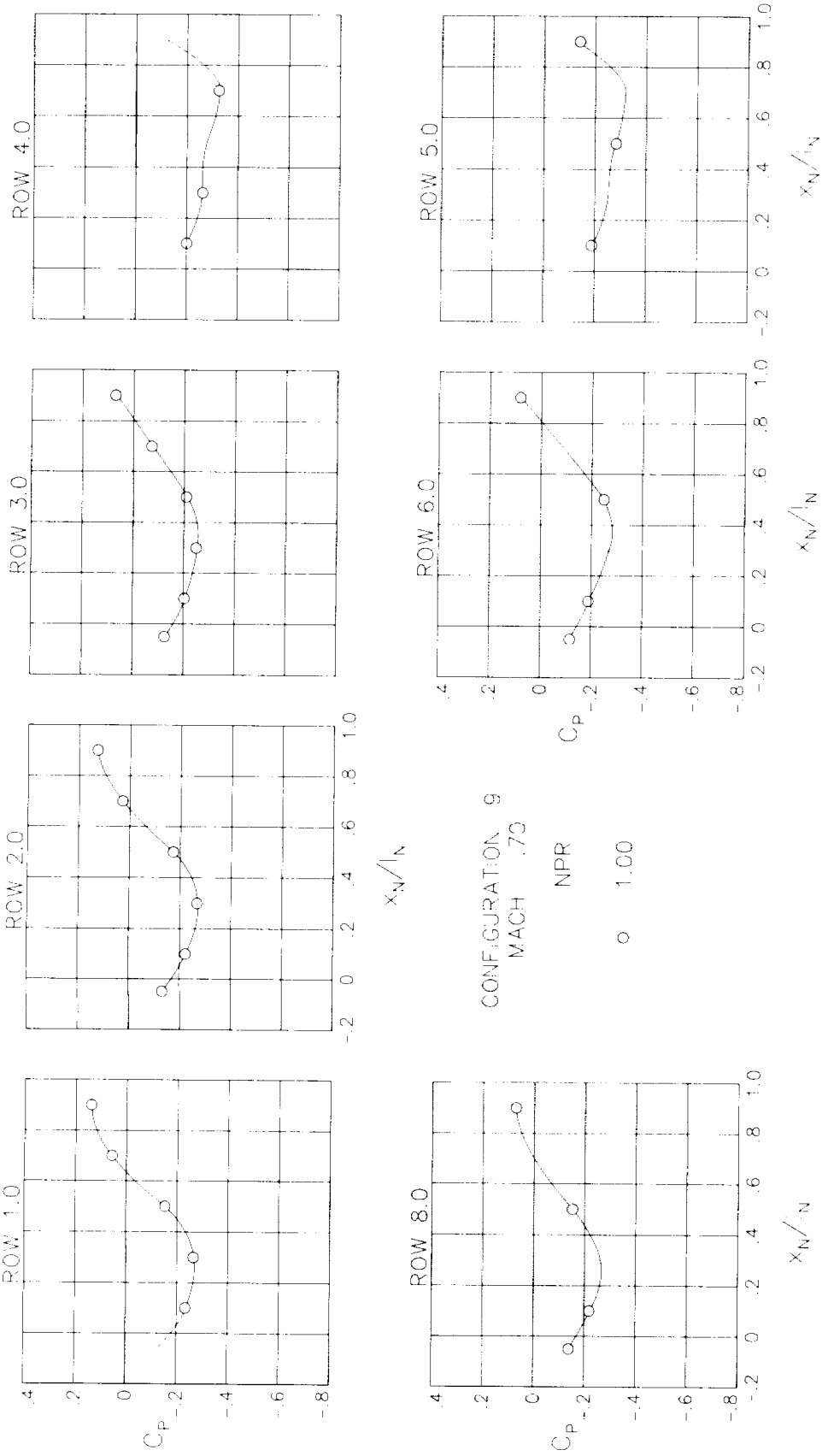

(b) M = 0.70.

Figure 34.- Continued.

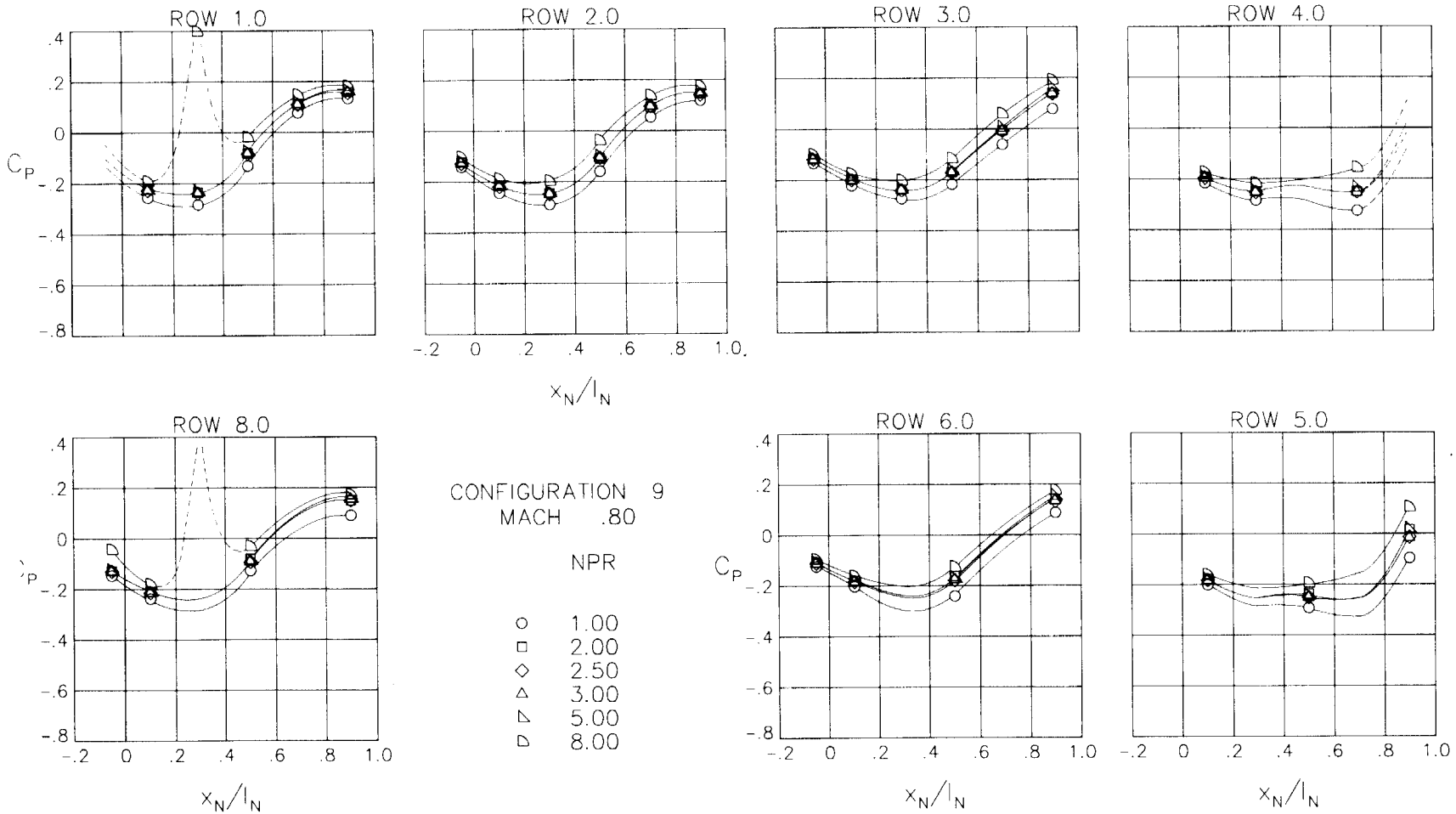

(c) M = 0.80.

Figure 34.- Continued.

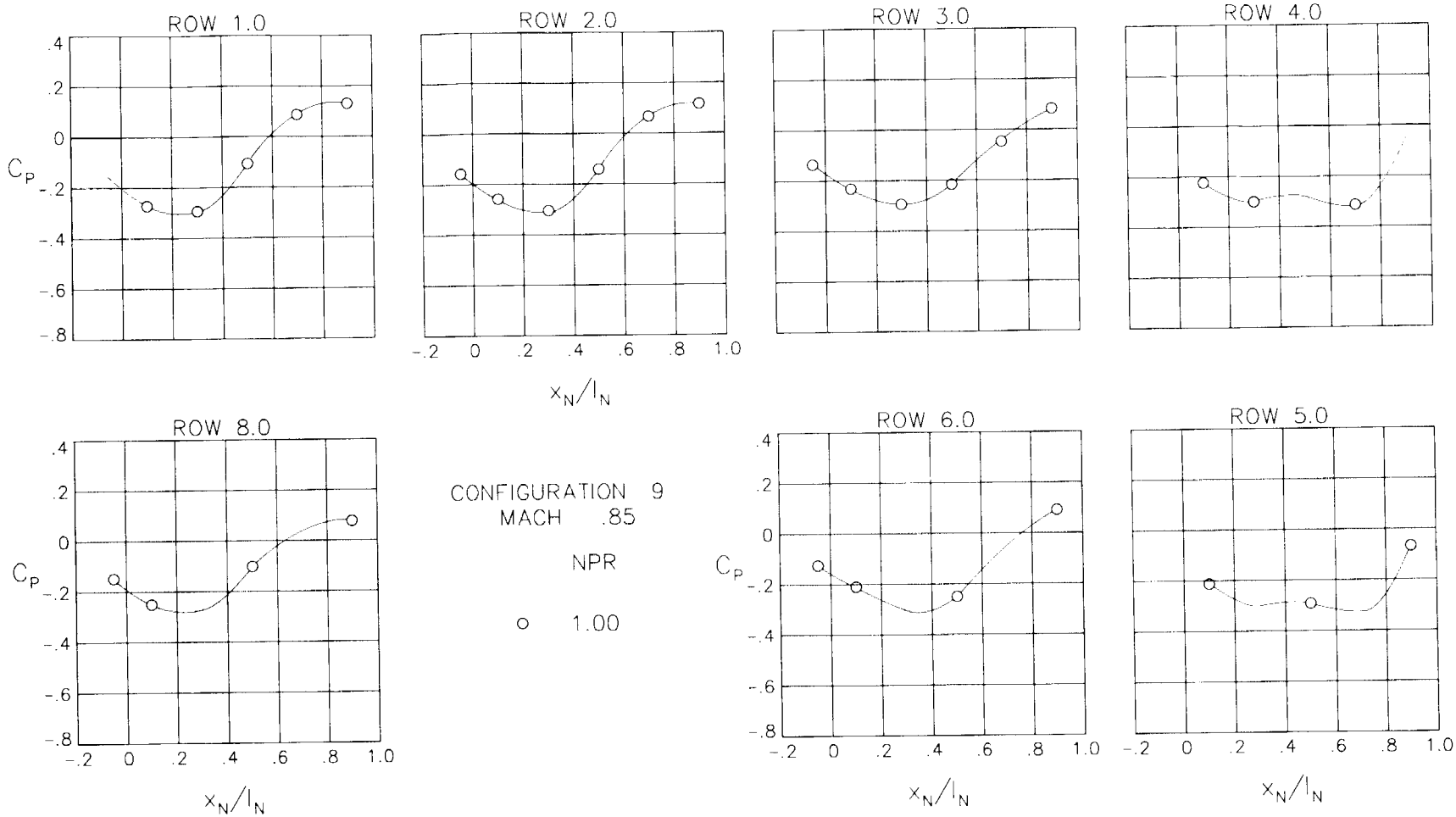

(d) M = 0.85.

Figure 34.- Continued.

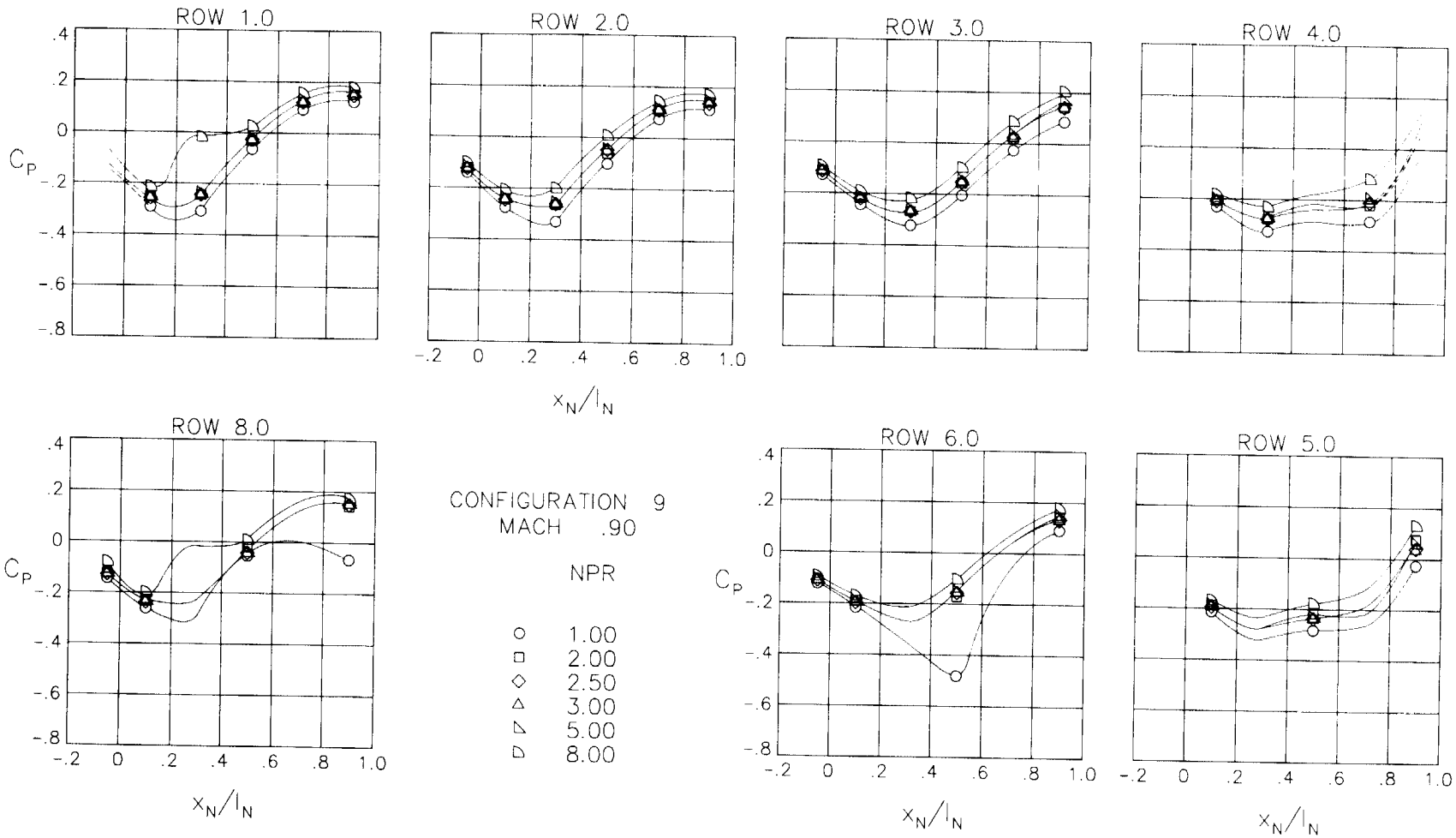

(e) M = 0.90.

Figure 34.- Continued.

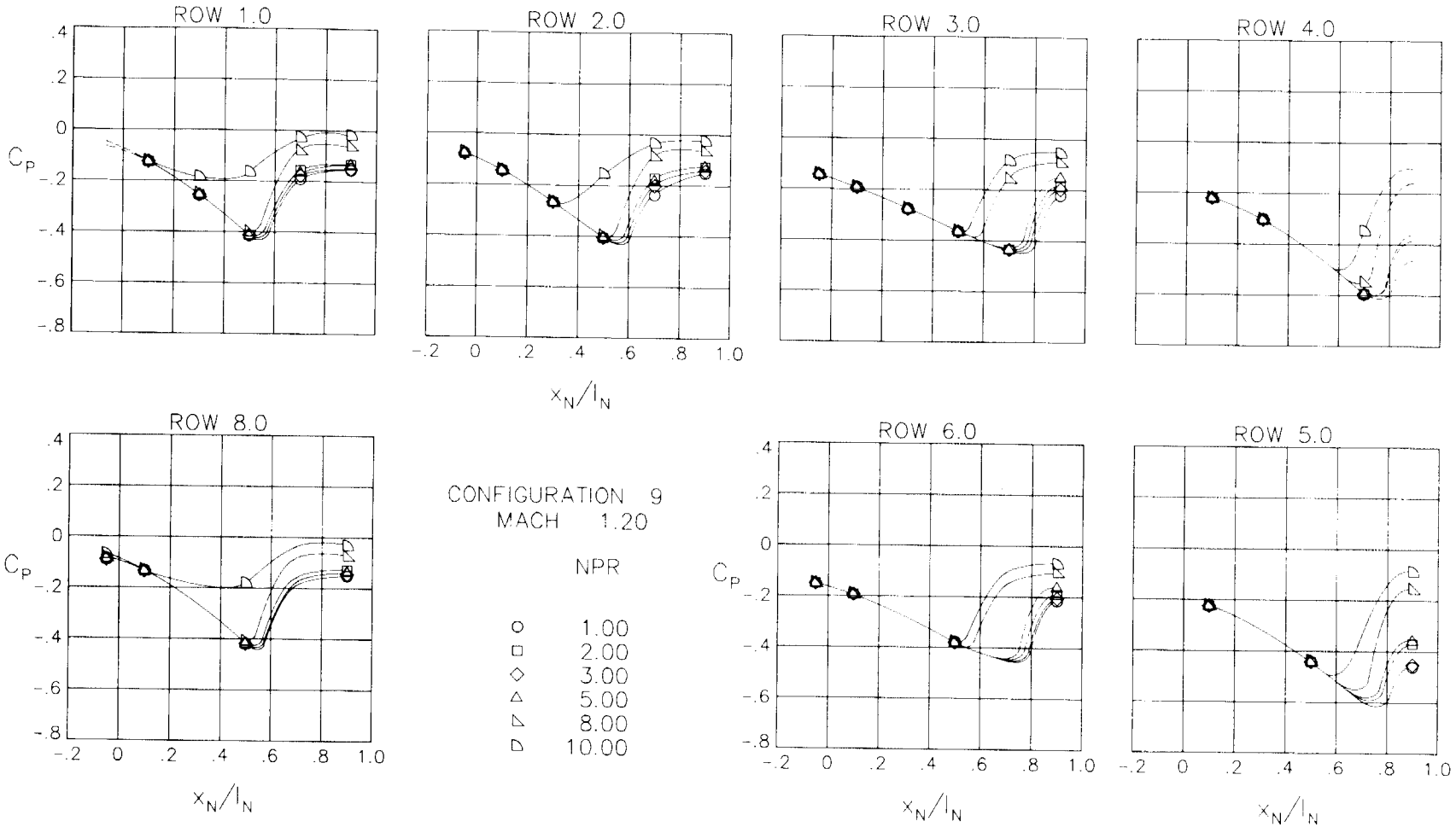

(f) M = 1.20.

Figure 34.- Concluded.

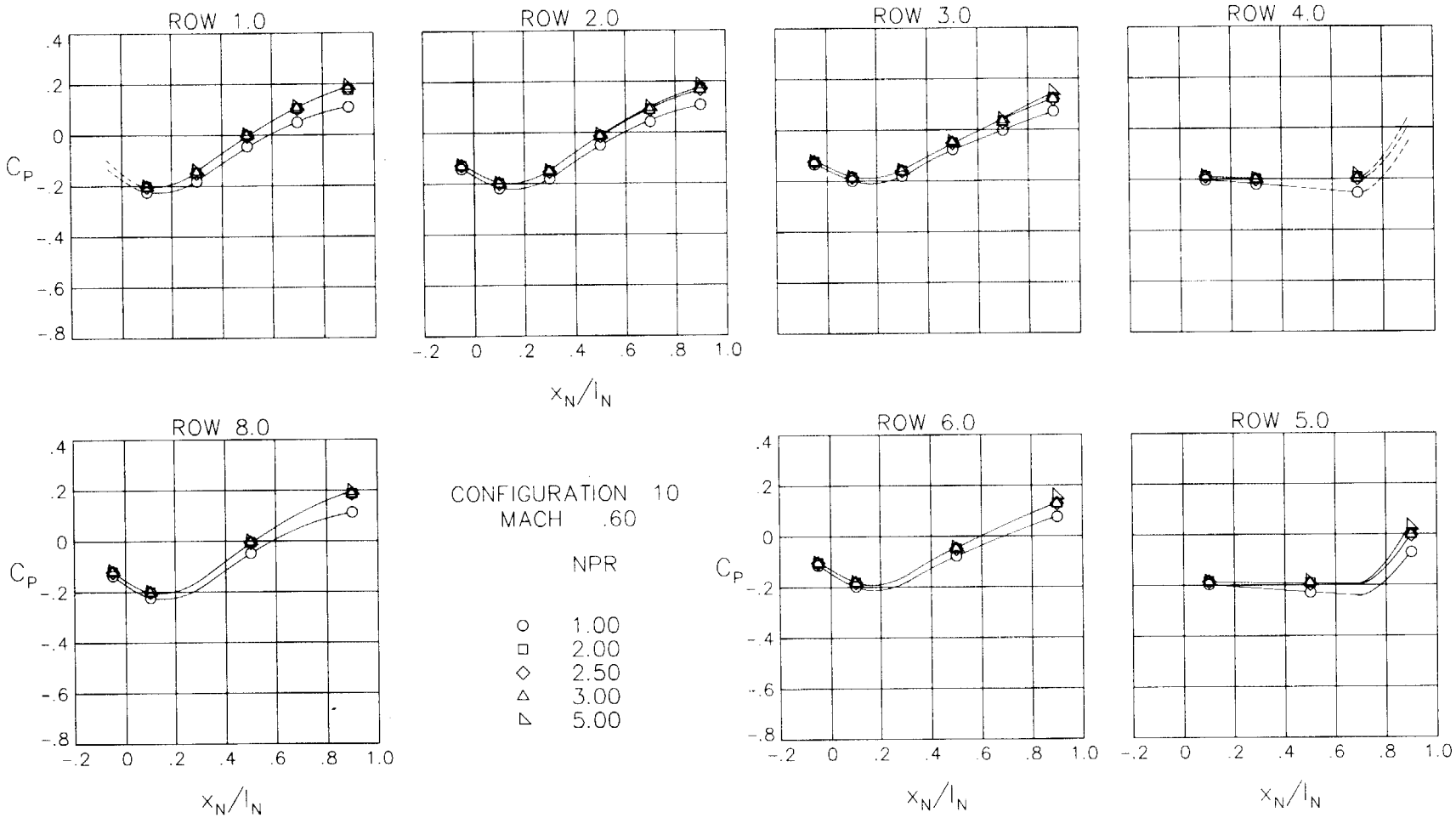

(a) M = 0.60.

Figure 35.- Surface static-pressure coefficient distributions around nozzle for configuration 10. $\alpha = 0°$.

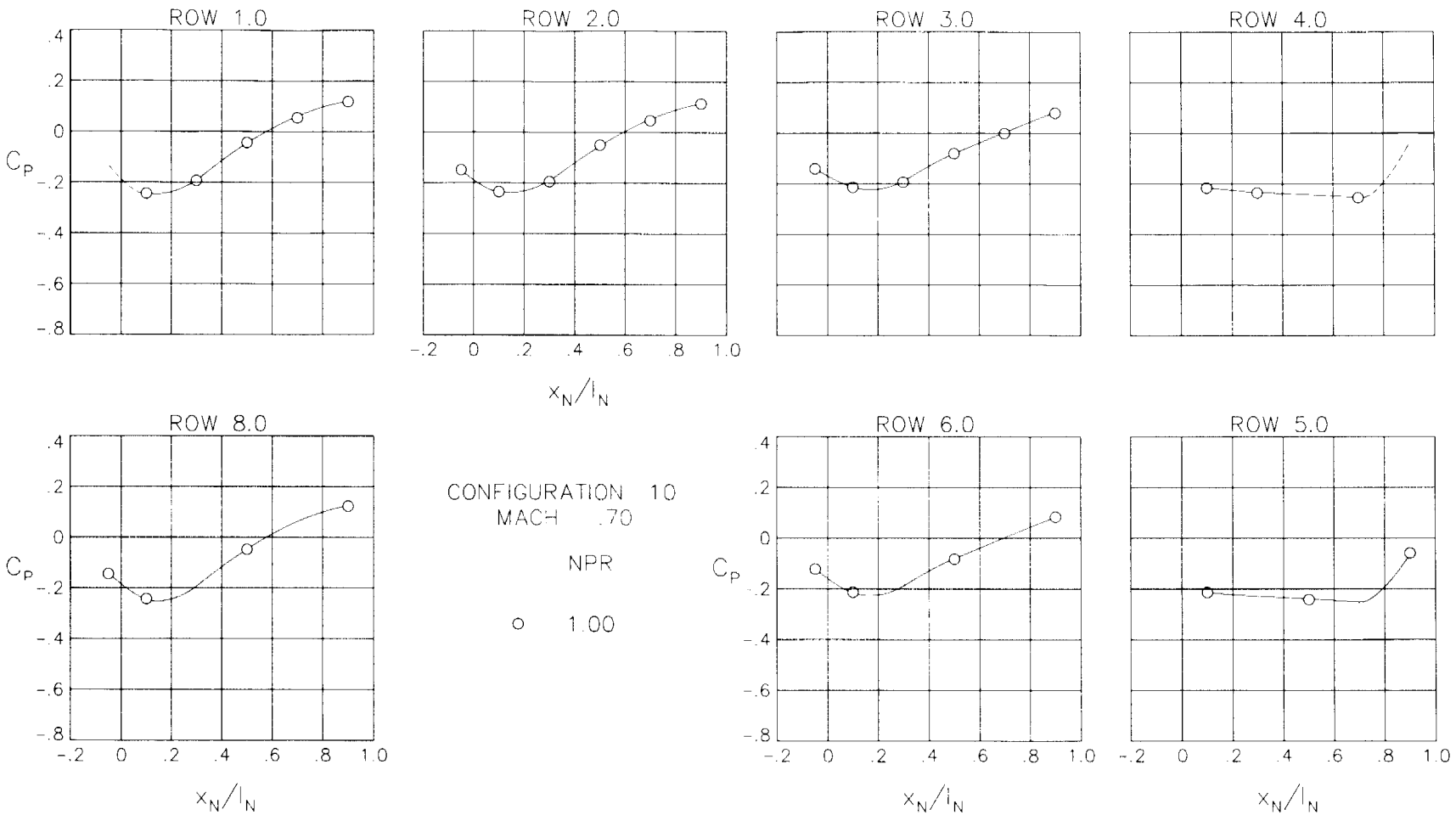

(b) M = 0.70.

Figure 35.- Continued.

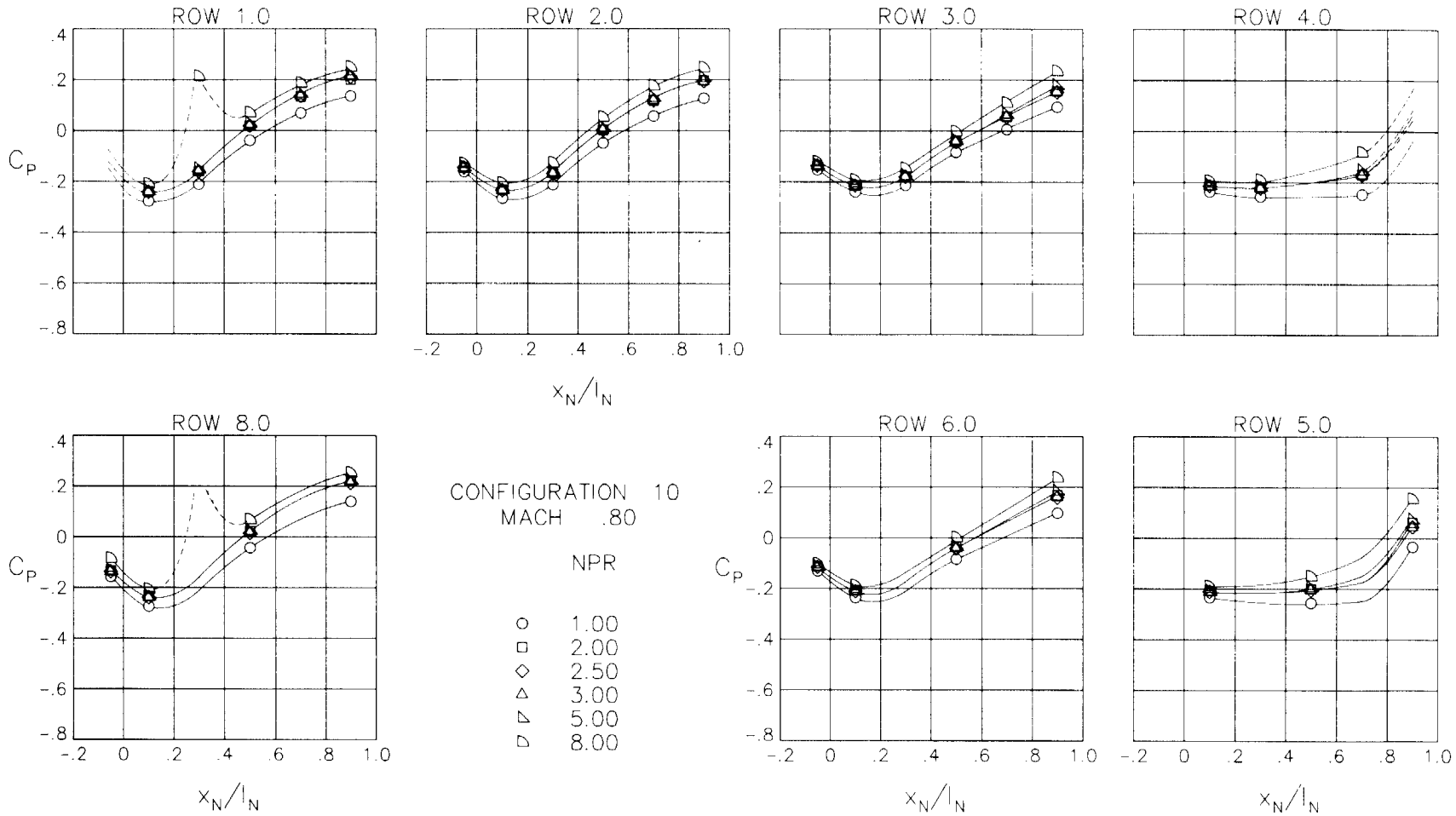

(c) M = 0.80.

Figure 35.- Continued.

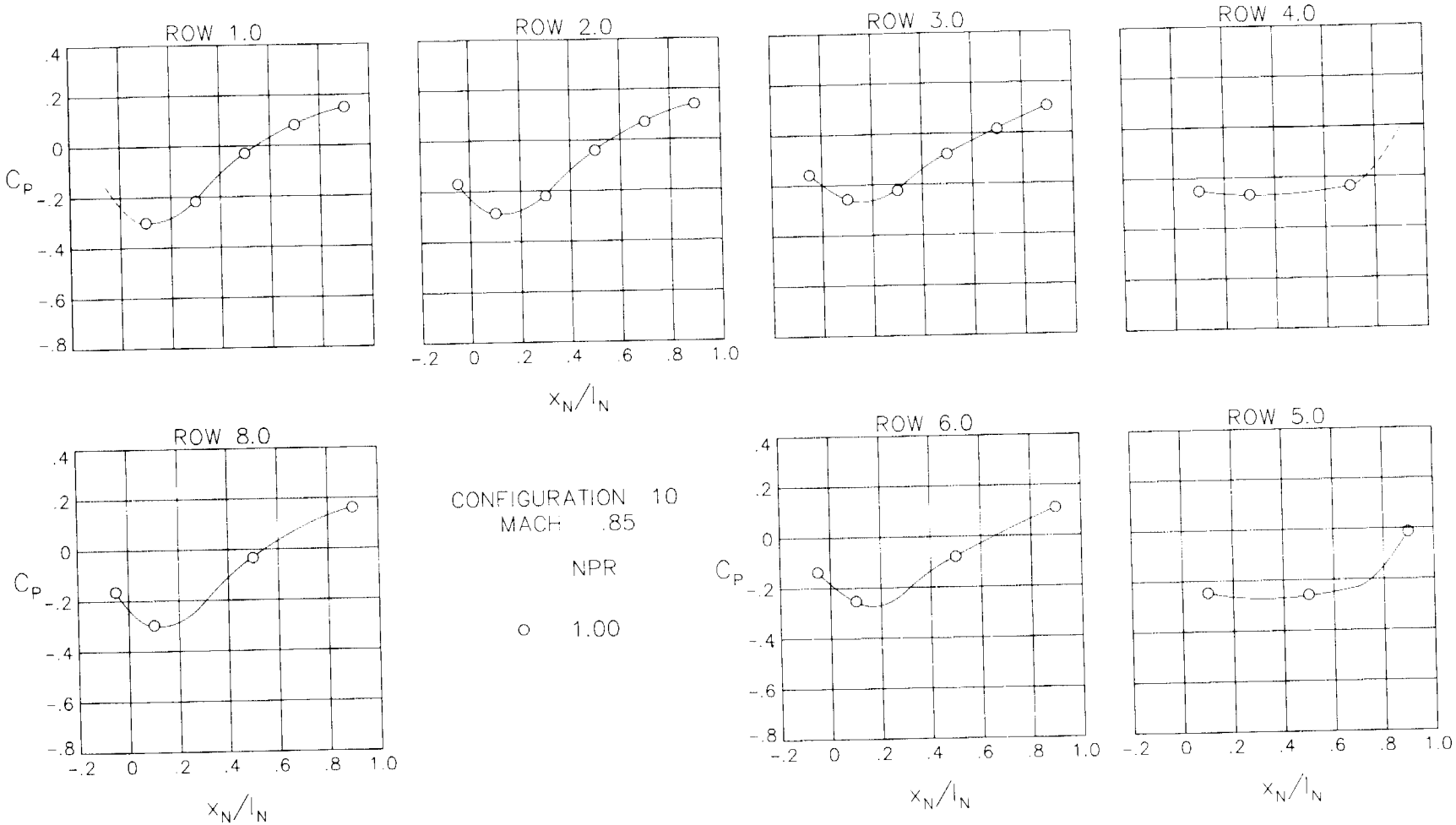

(d) M = 0.85.

Figure 35.- Continued.

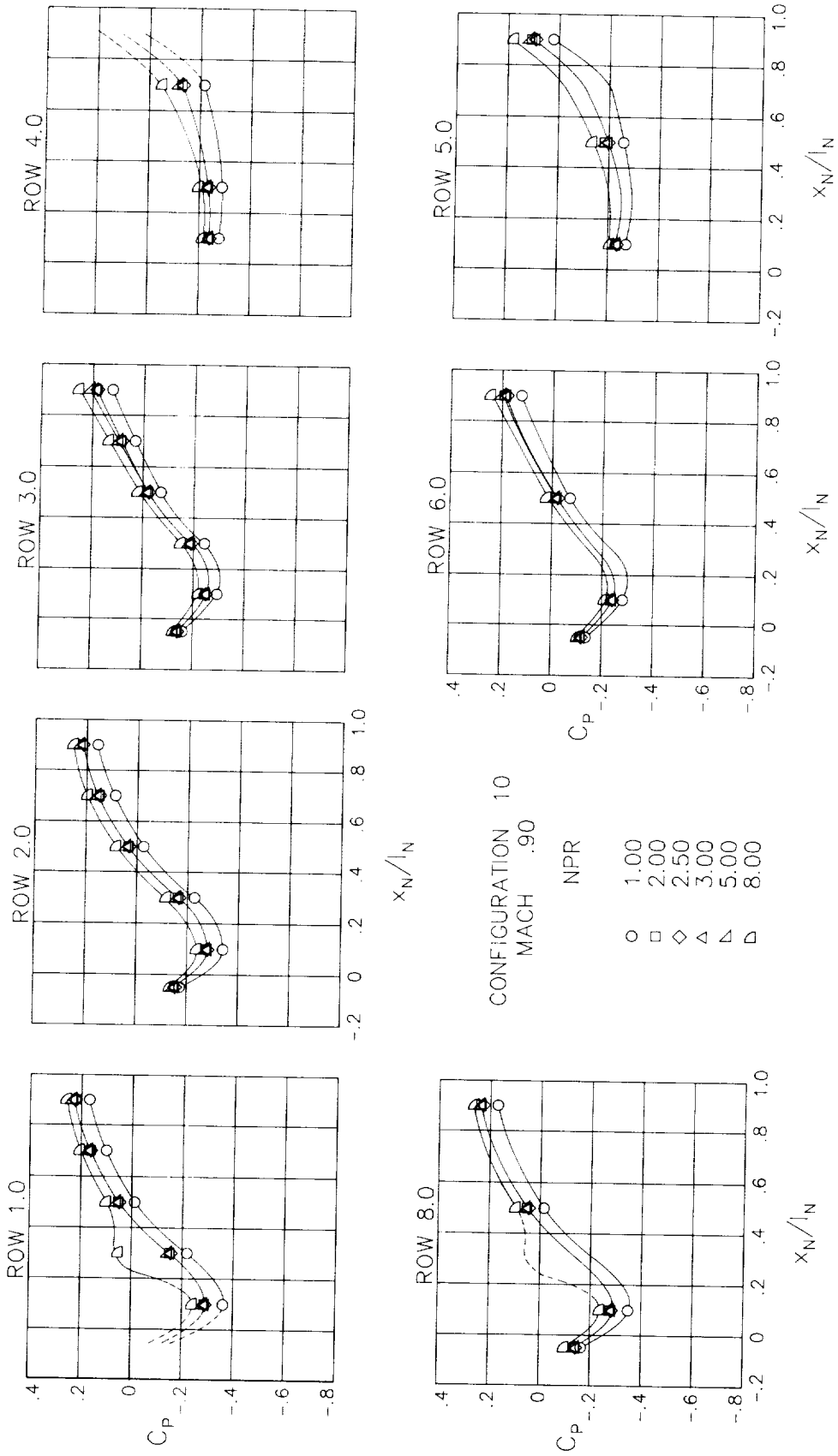

(e) M = 0.90.

Figure 35.- Continued.

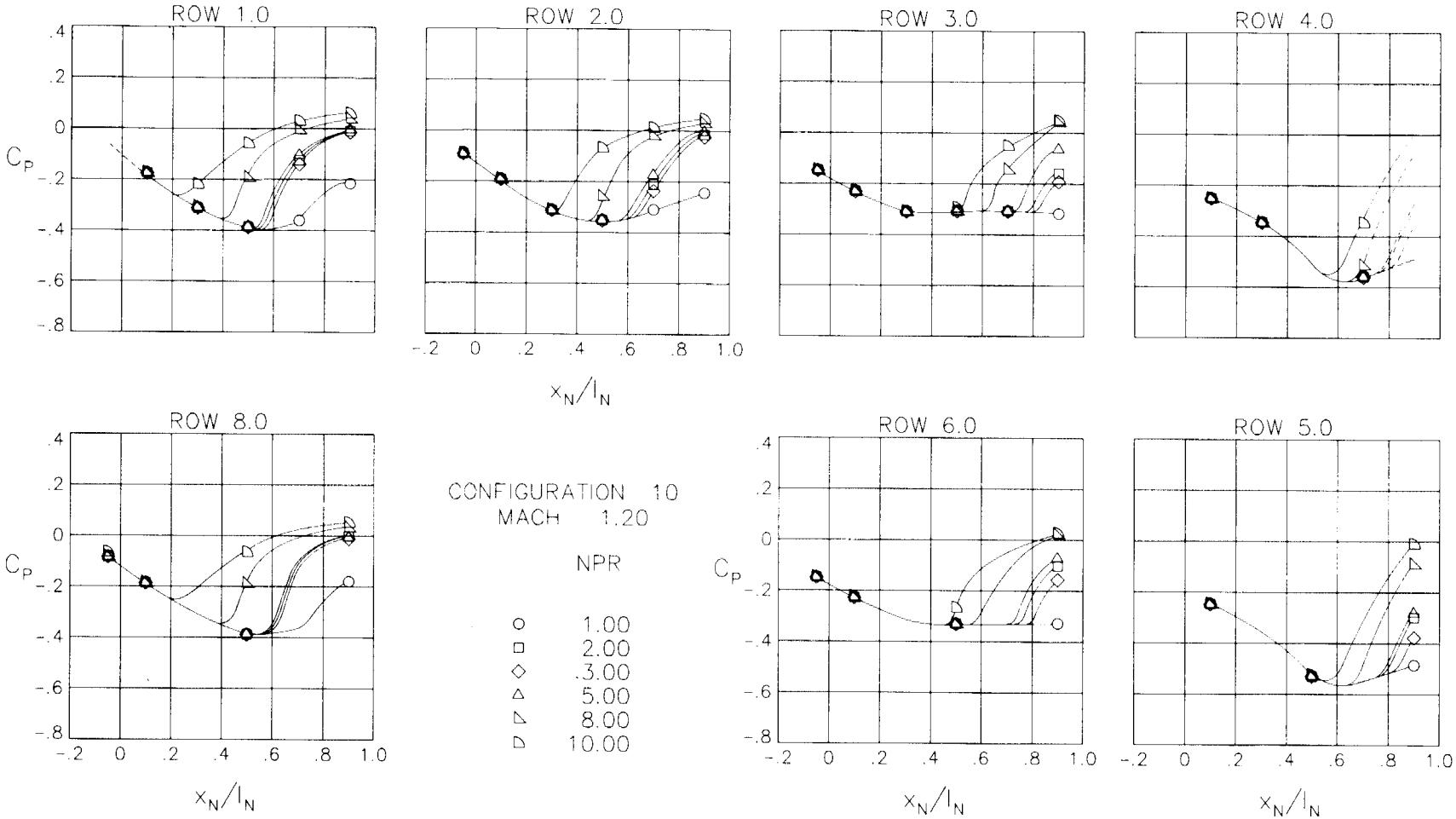

(f) M = 1.20.

Figure 35.- Concluded.

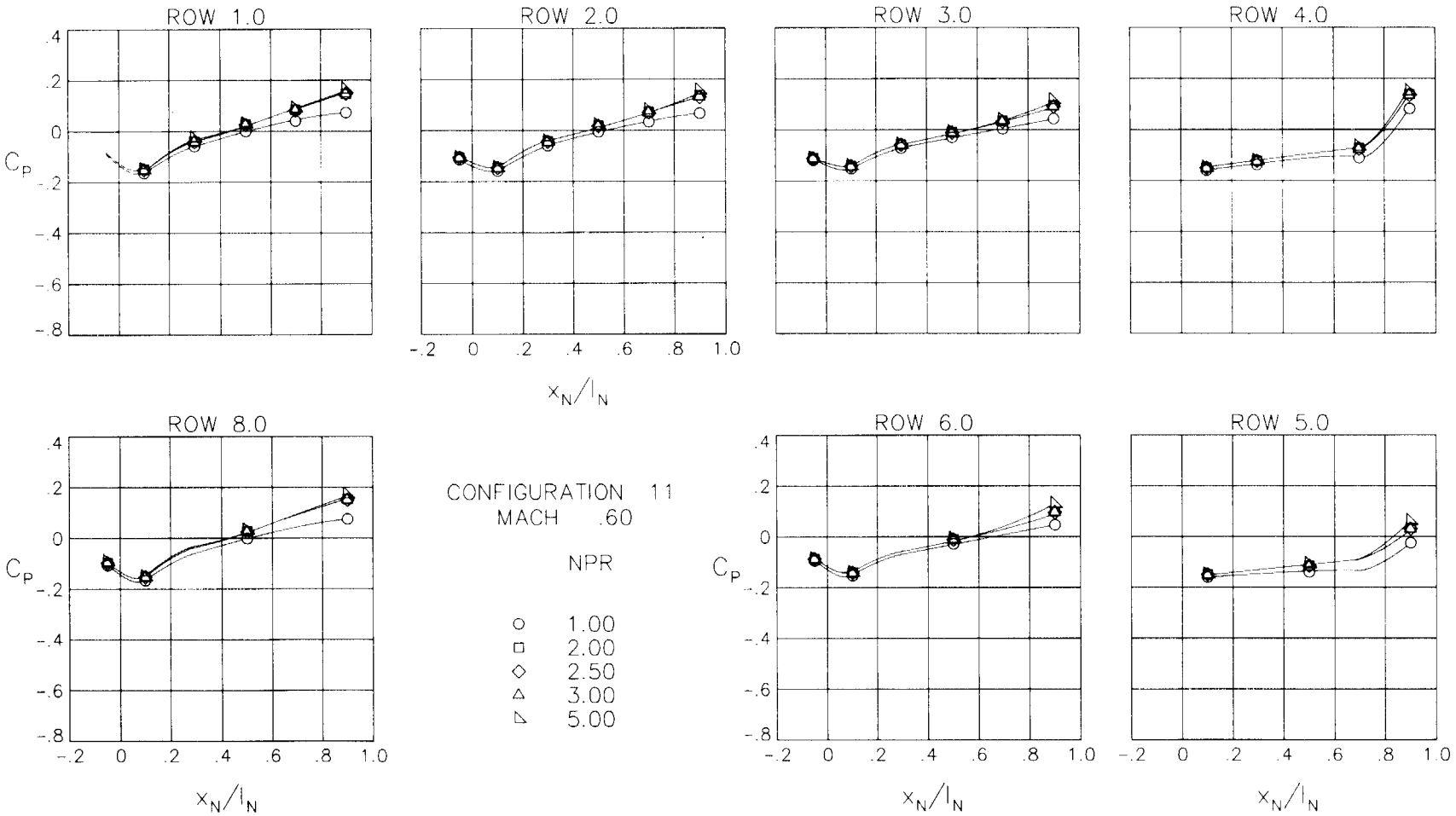

(a) M = 0.60.

Figure 36.- Surface static-pressure coefficient distributions around nozzle for configuration 11. $\alpha = 0°$.

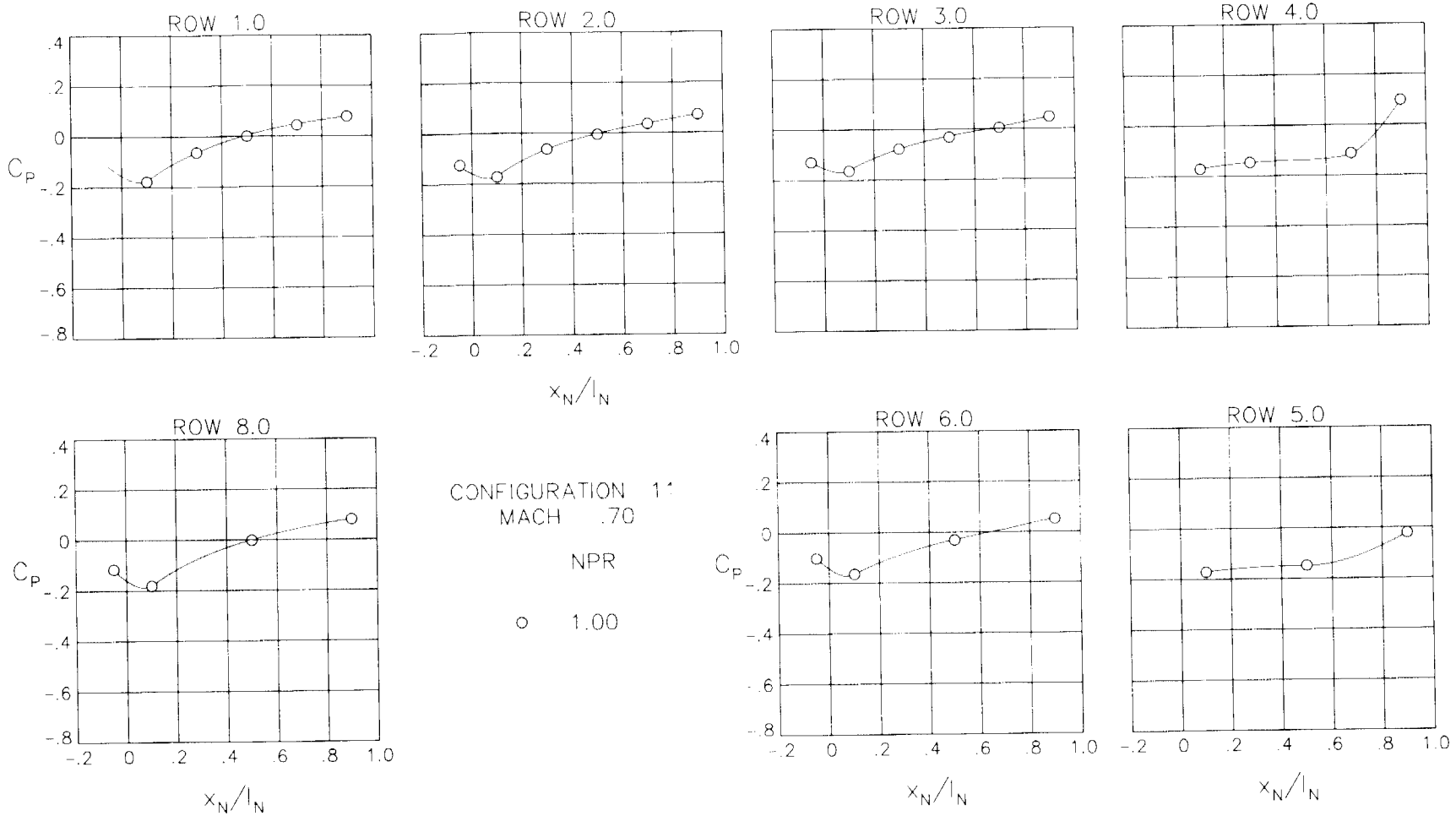

(b) M = 0.70.

Figure 36.- Continued.

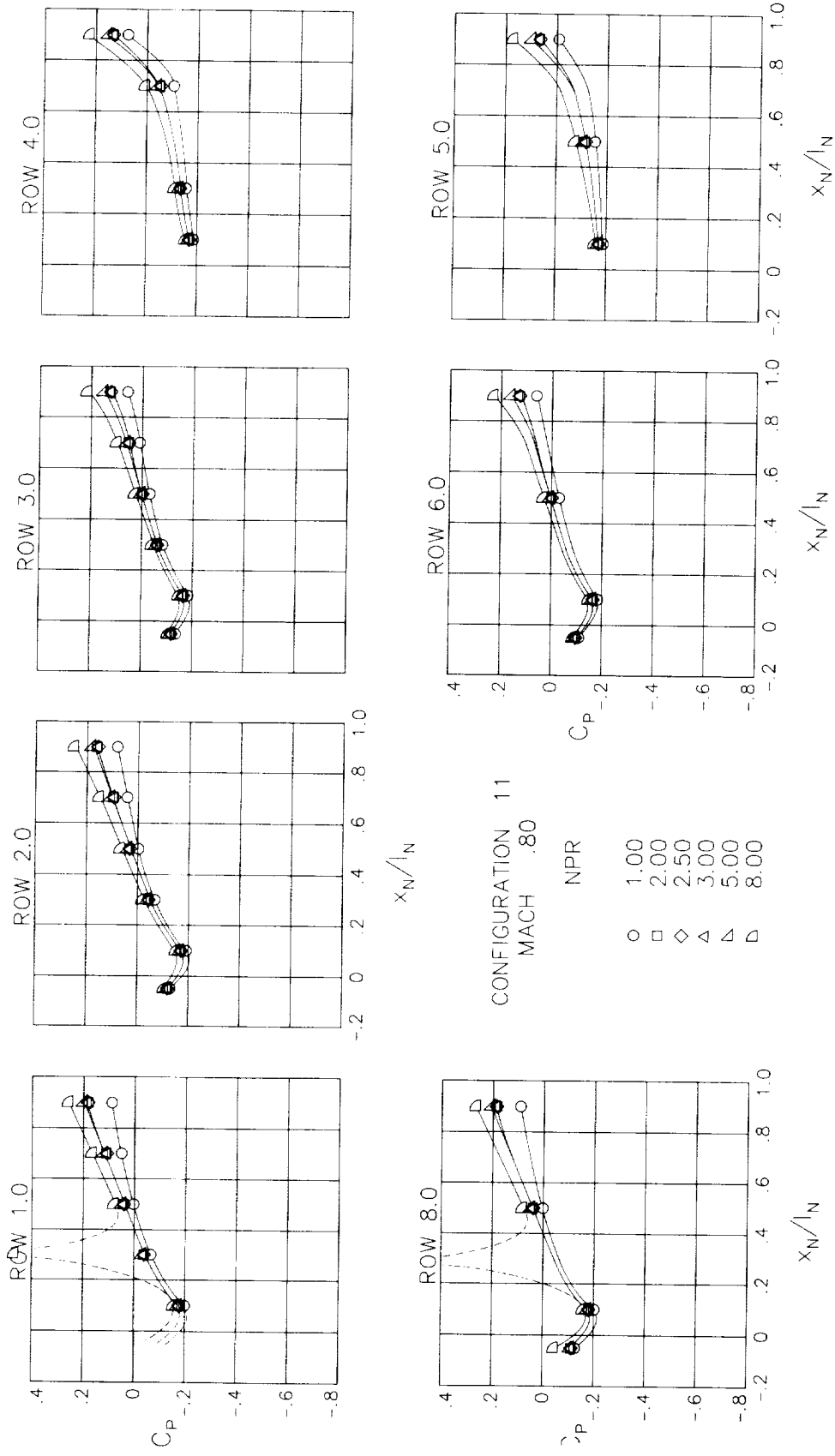

(c) M = 0.80.

Figure 36.- Continued.

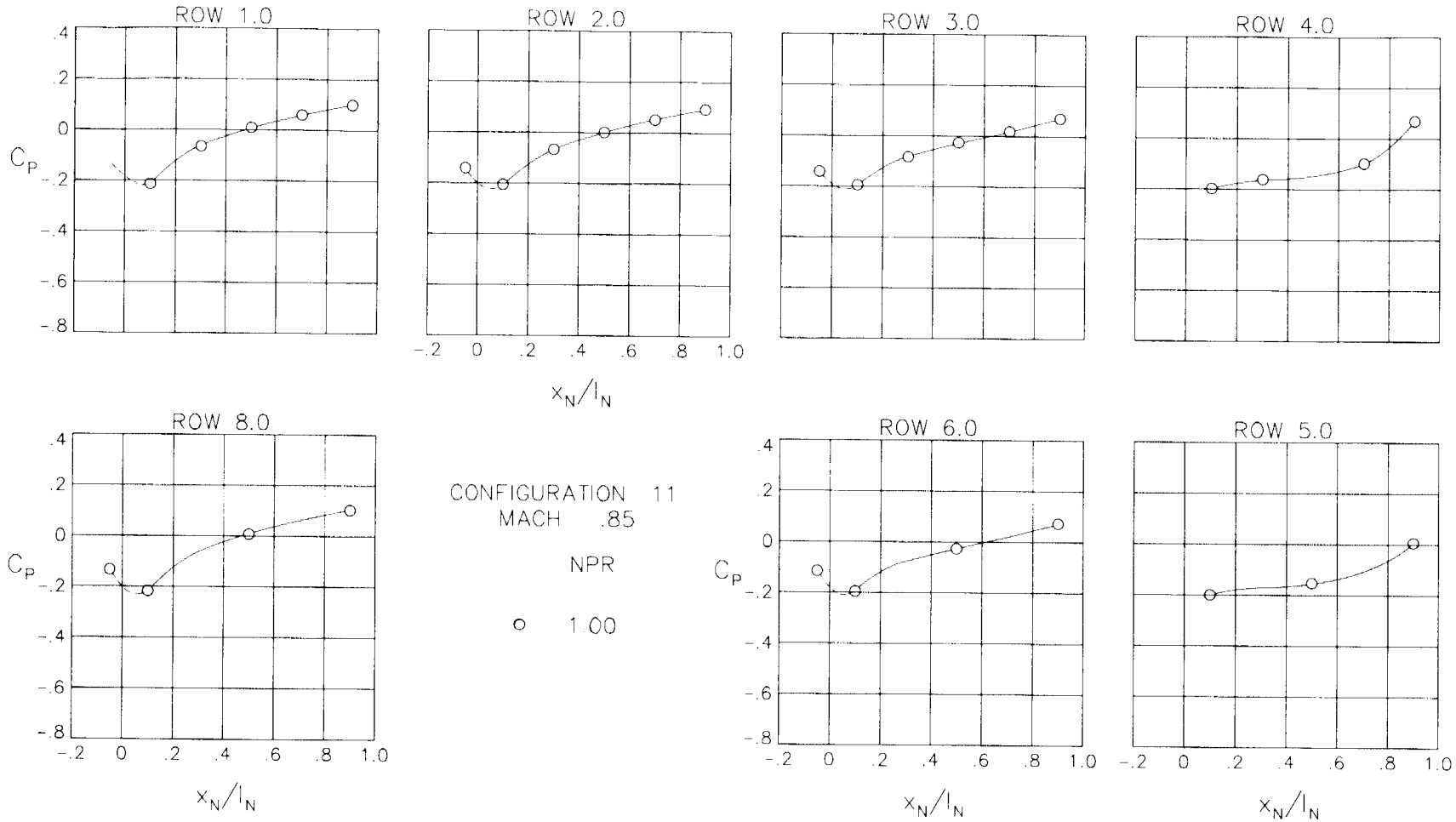

(d) M = 0.85.

Figure 36.- Continued.

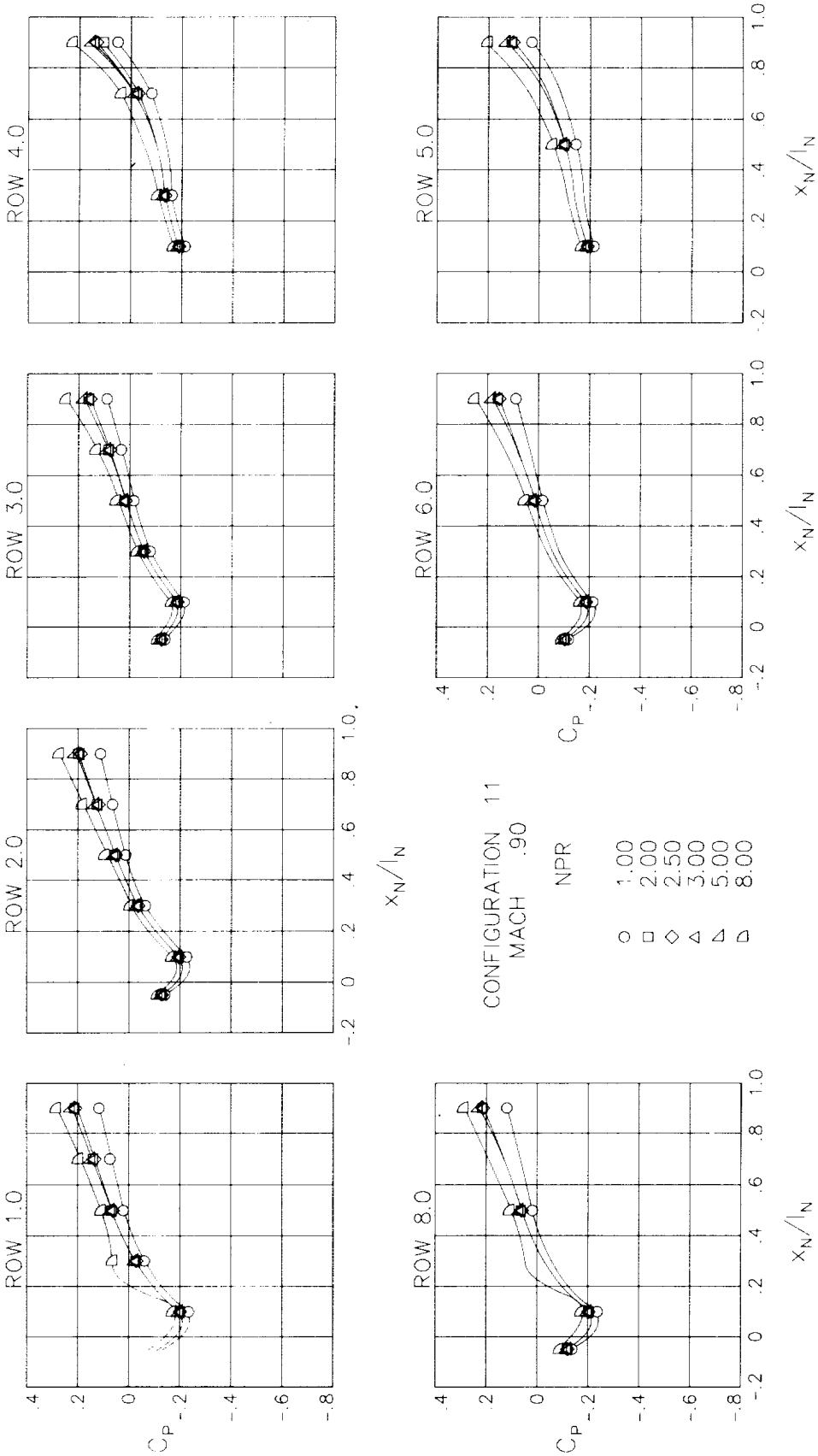

(e) M = 0.90.

Figure 36.- Continued.

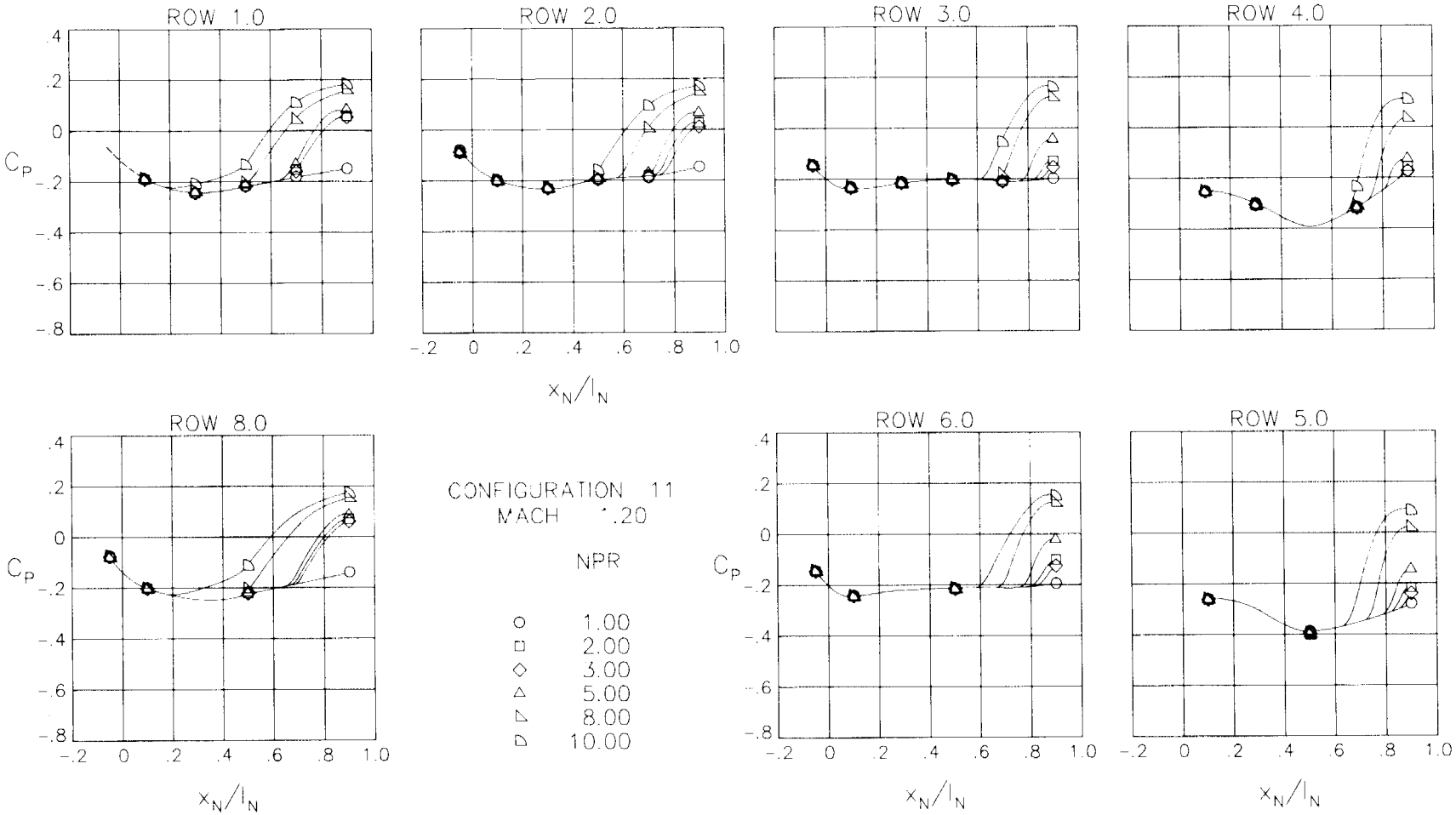

(f) M = 1.20.

Figure 36.- Concluded.

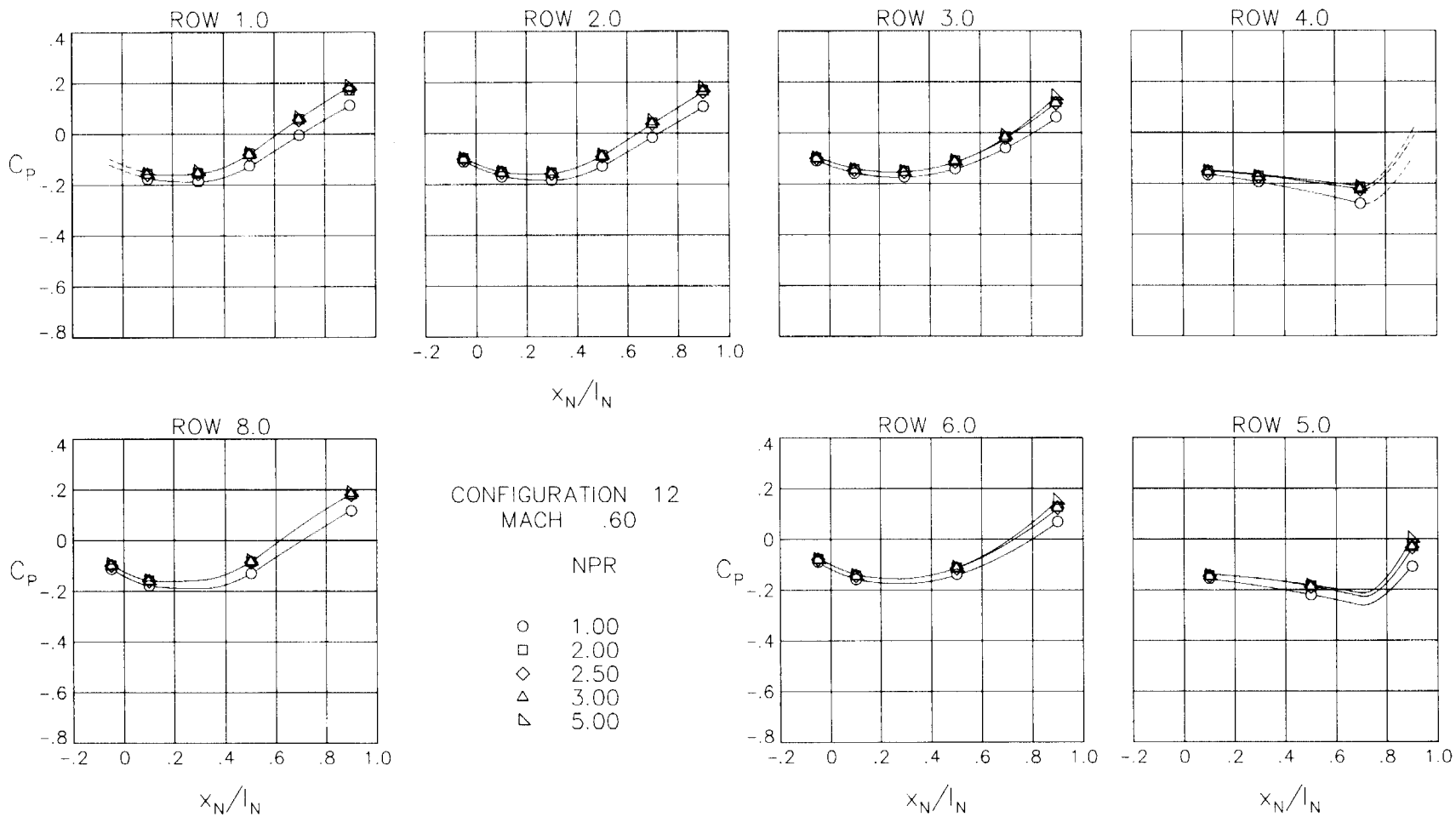

(a) M = 0.60.

Figure 37.- Surface static-pressure coefficient distributions around nozzle for configuration 12. α = 0°.

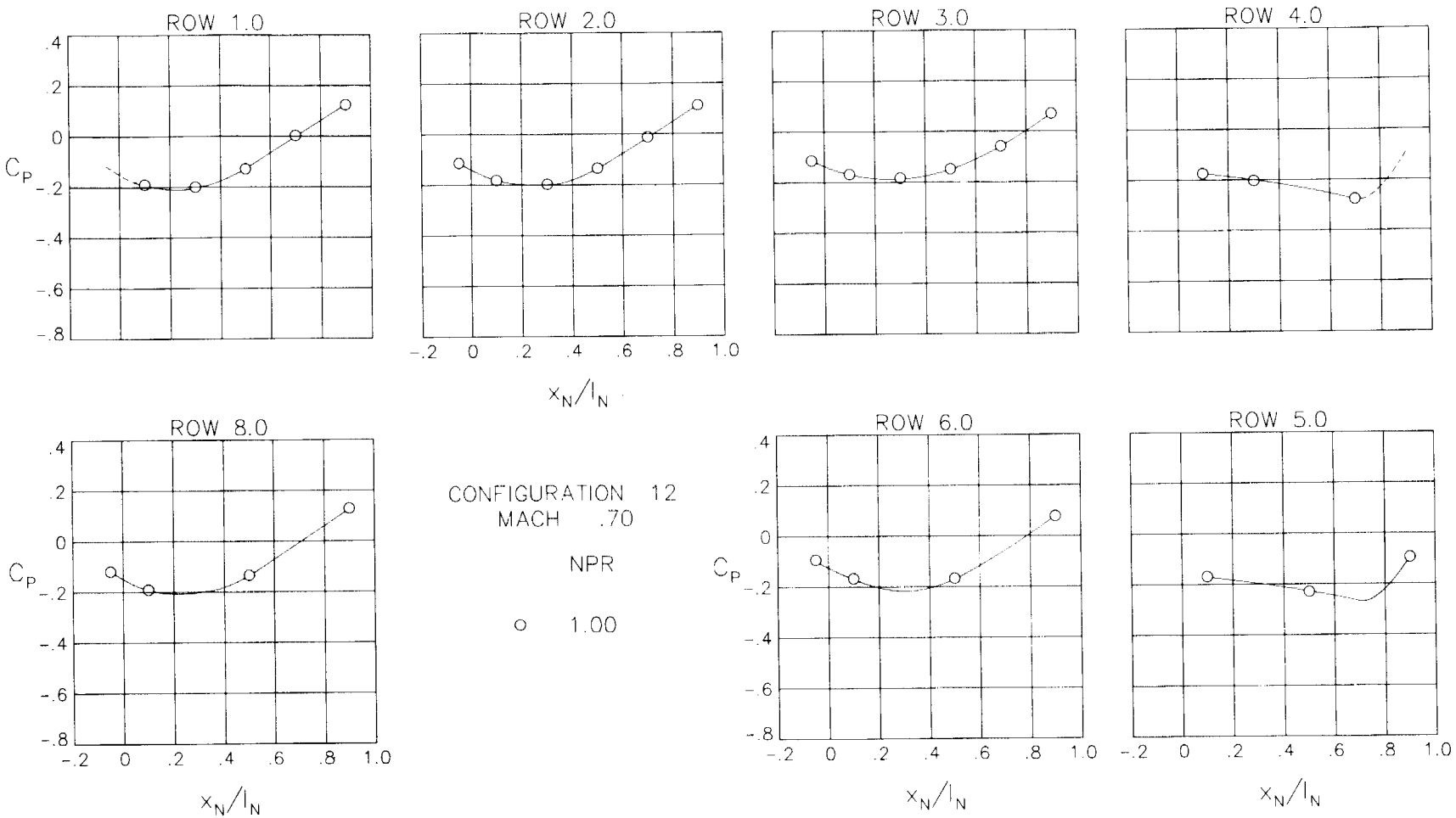

(b) M = 0.70.

Figure 37.- Continued.

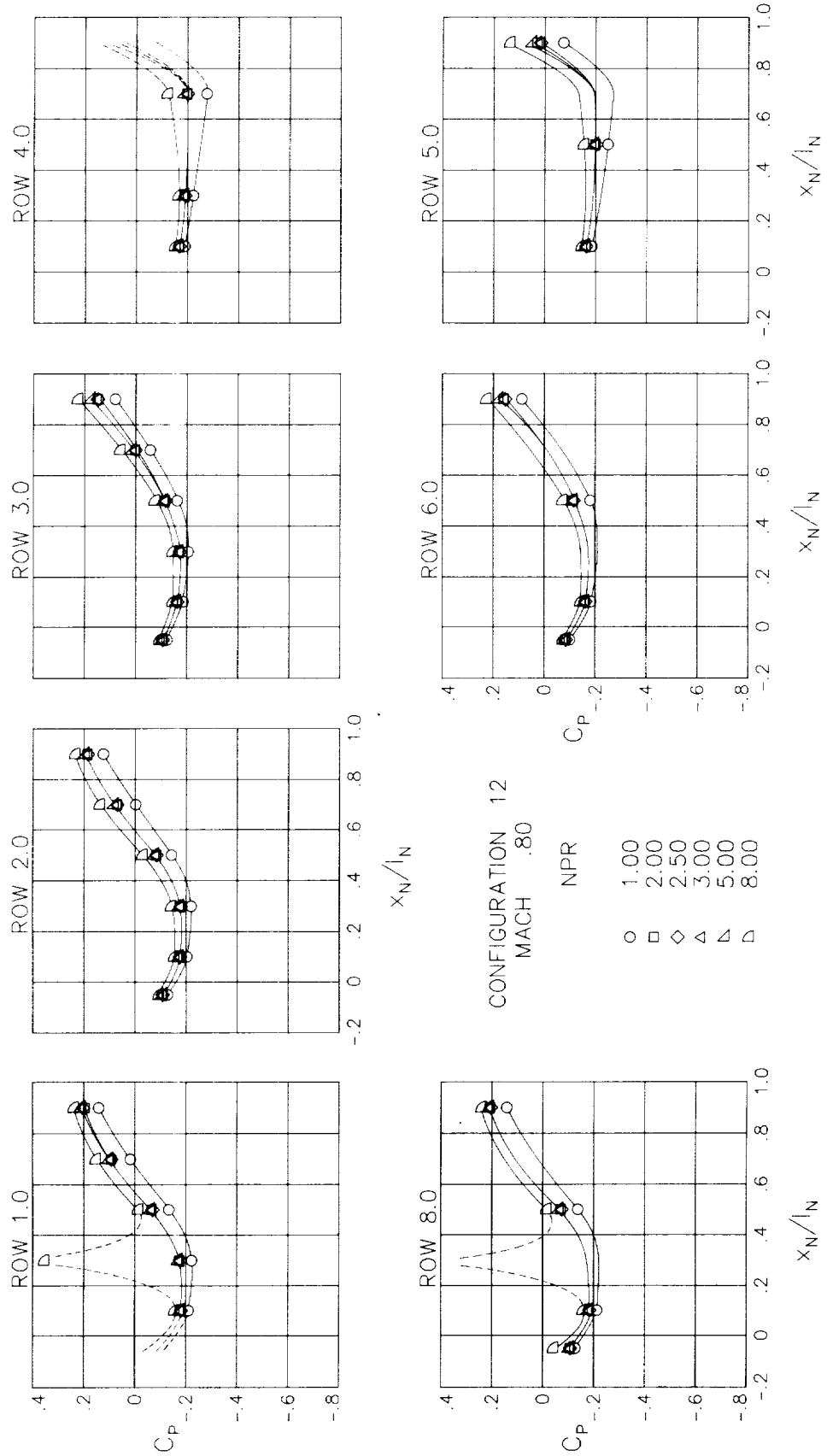

(c) M = 0.80.

Figure 37.- Continued.

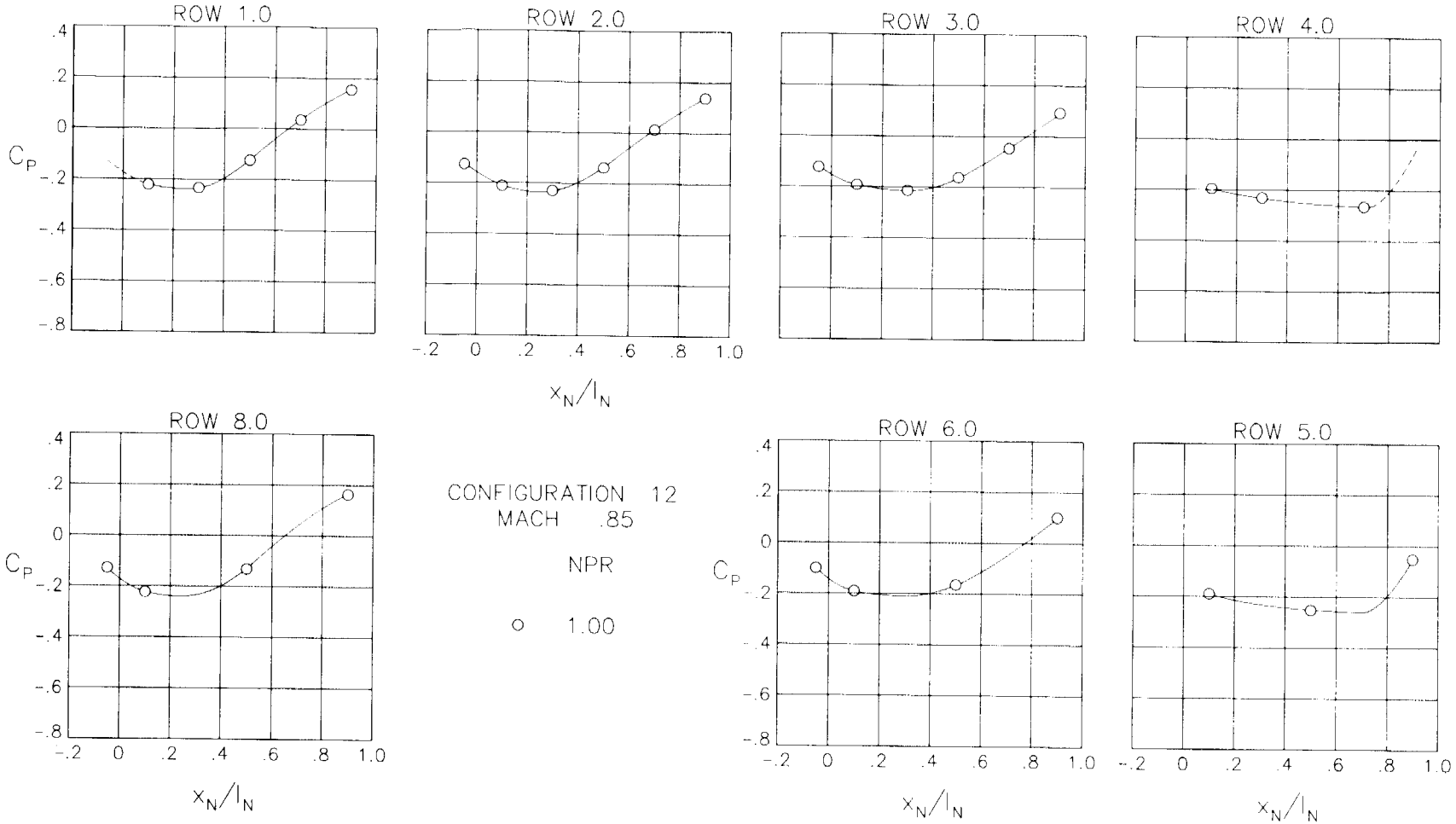

(d) M = 0.85.

Figure 37.- Continued.

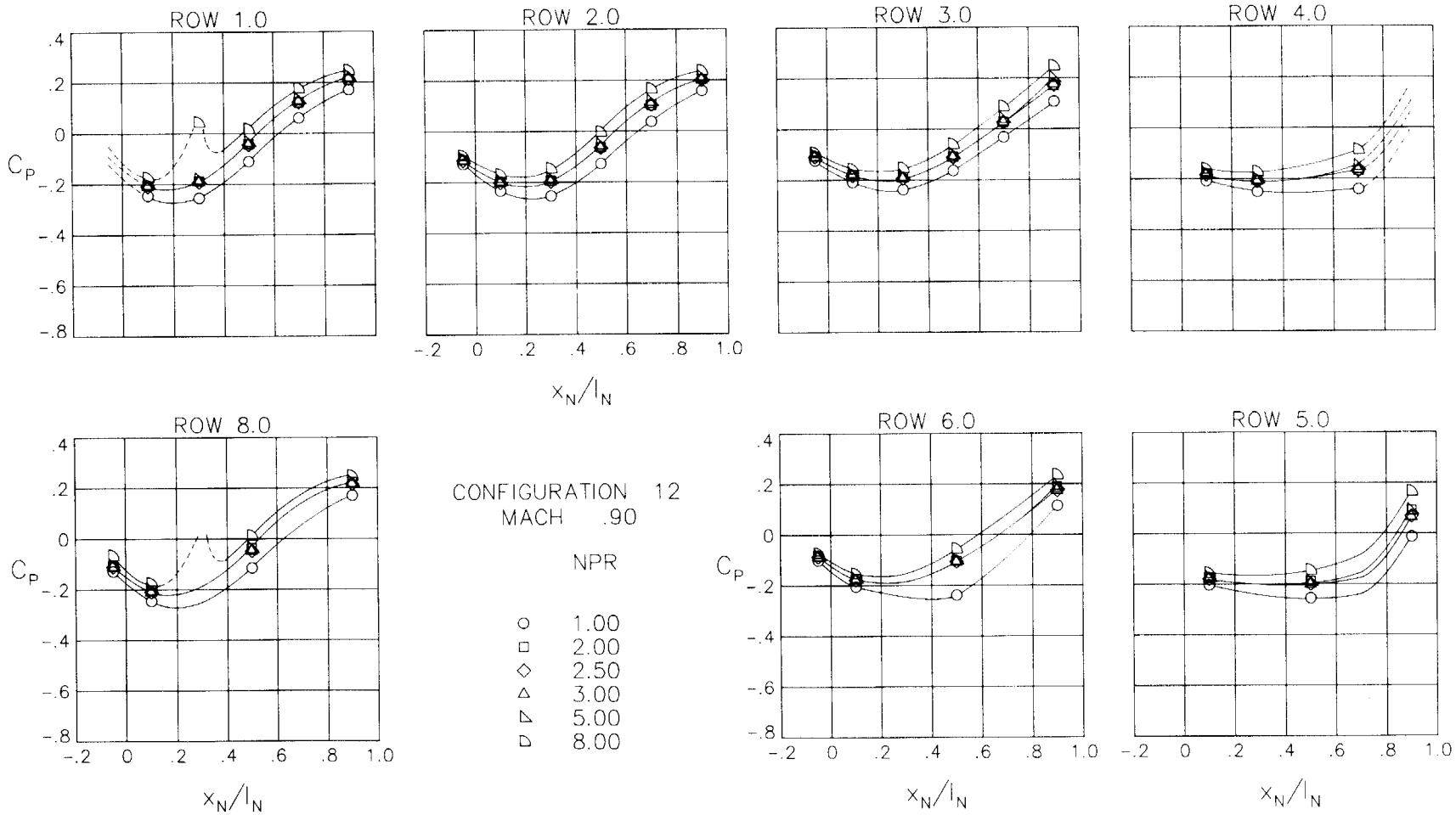

(e) M = 0.90.

Figure 37.- Continued.

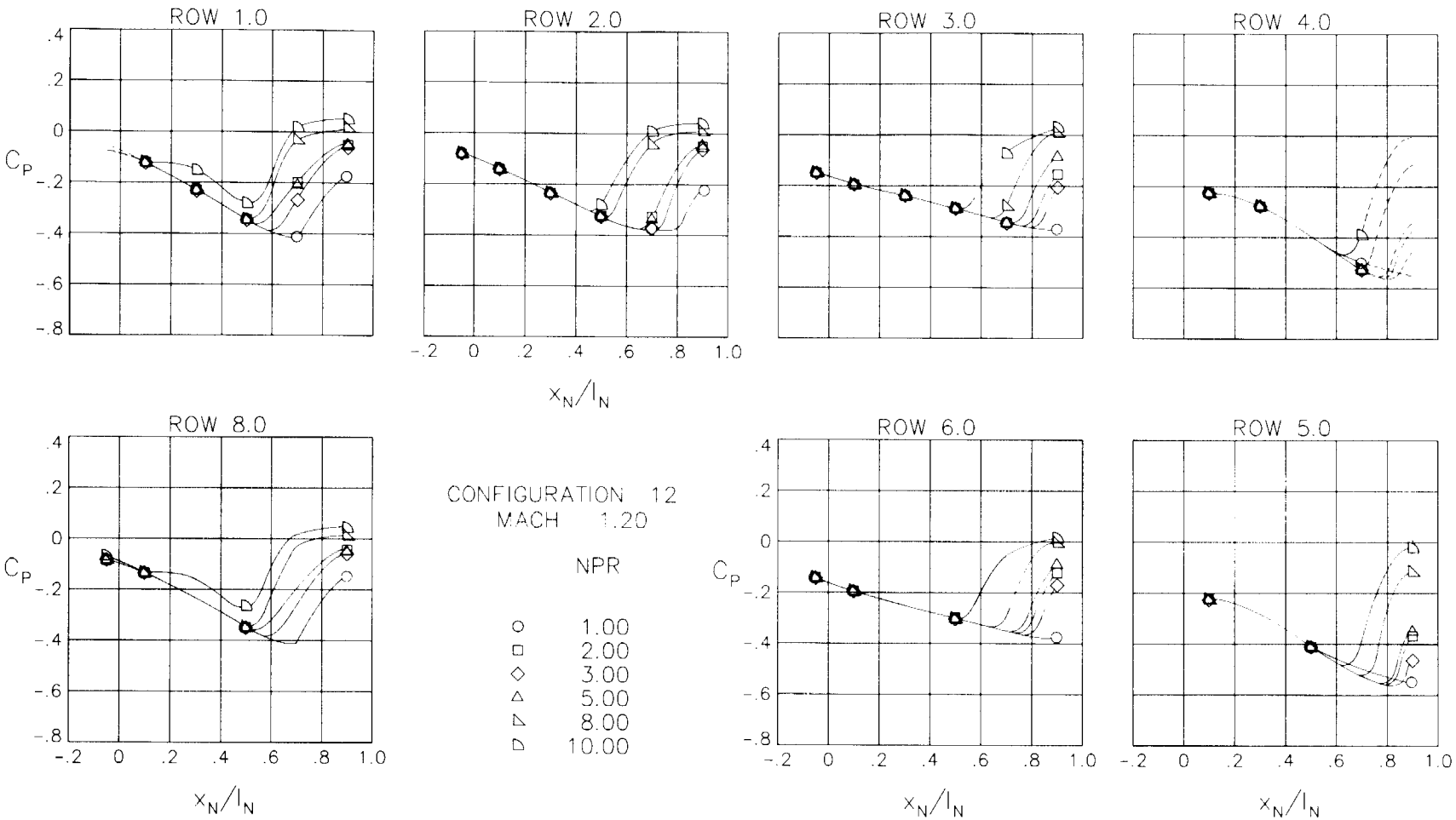

(f) M = 1.20.

Figure 37.- Concluded.

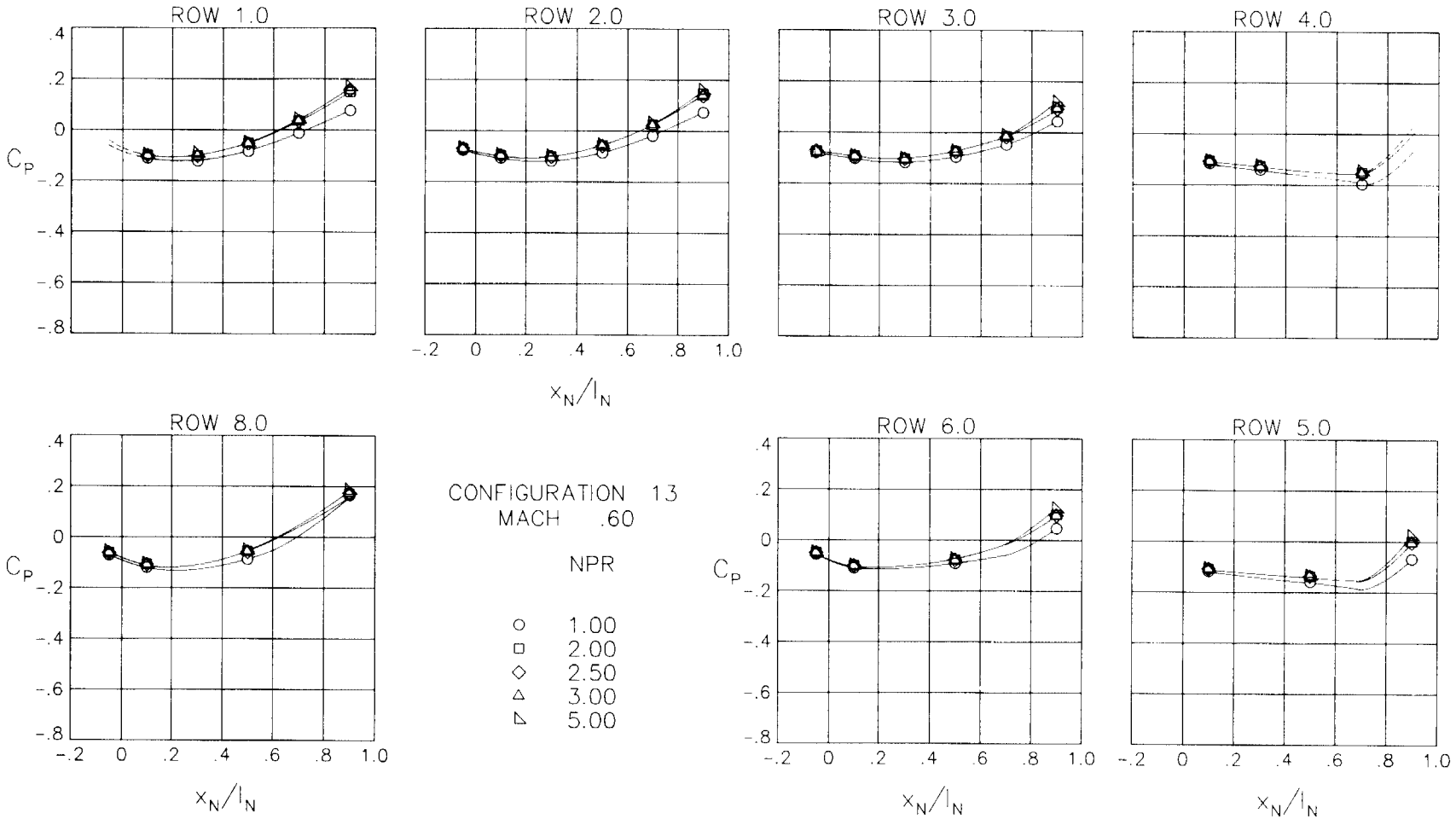

(a) M = 0.60.

Figure 38.- Surface static-pressure coefficient distributions around nozzle for configuration 13. α = 0°.

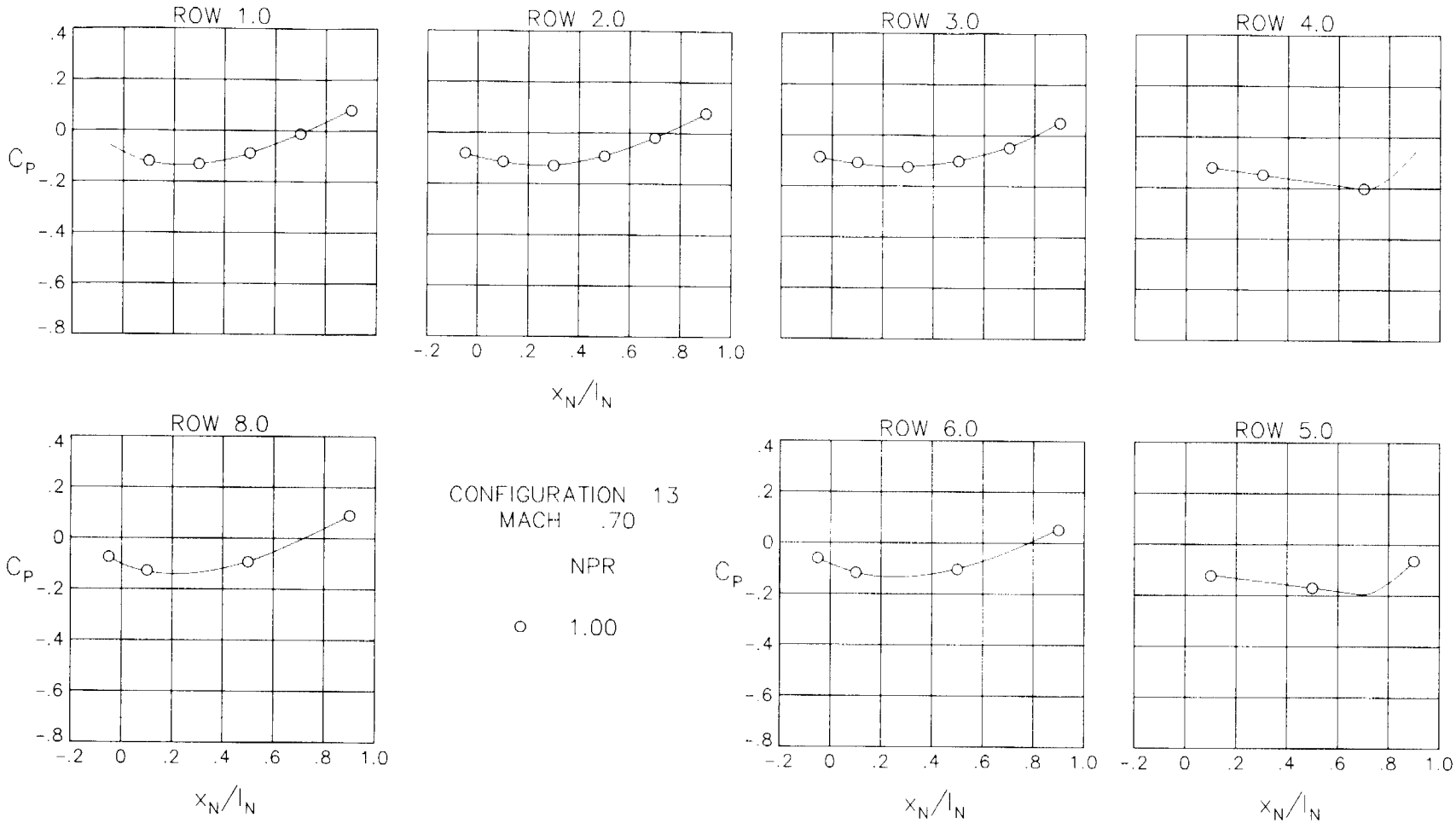

(b) M = 0.70.

Figure 38.- Continued.

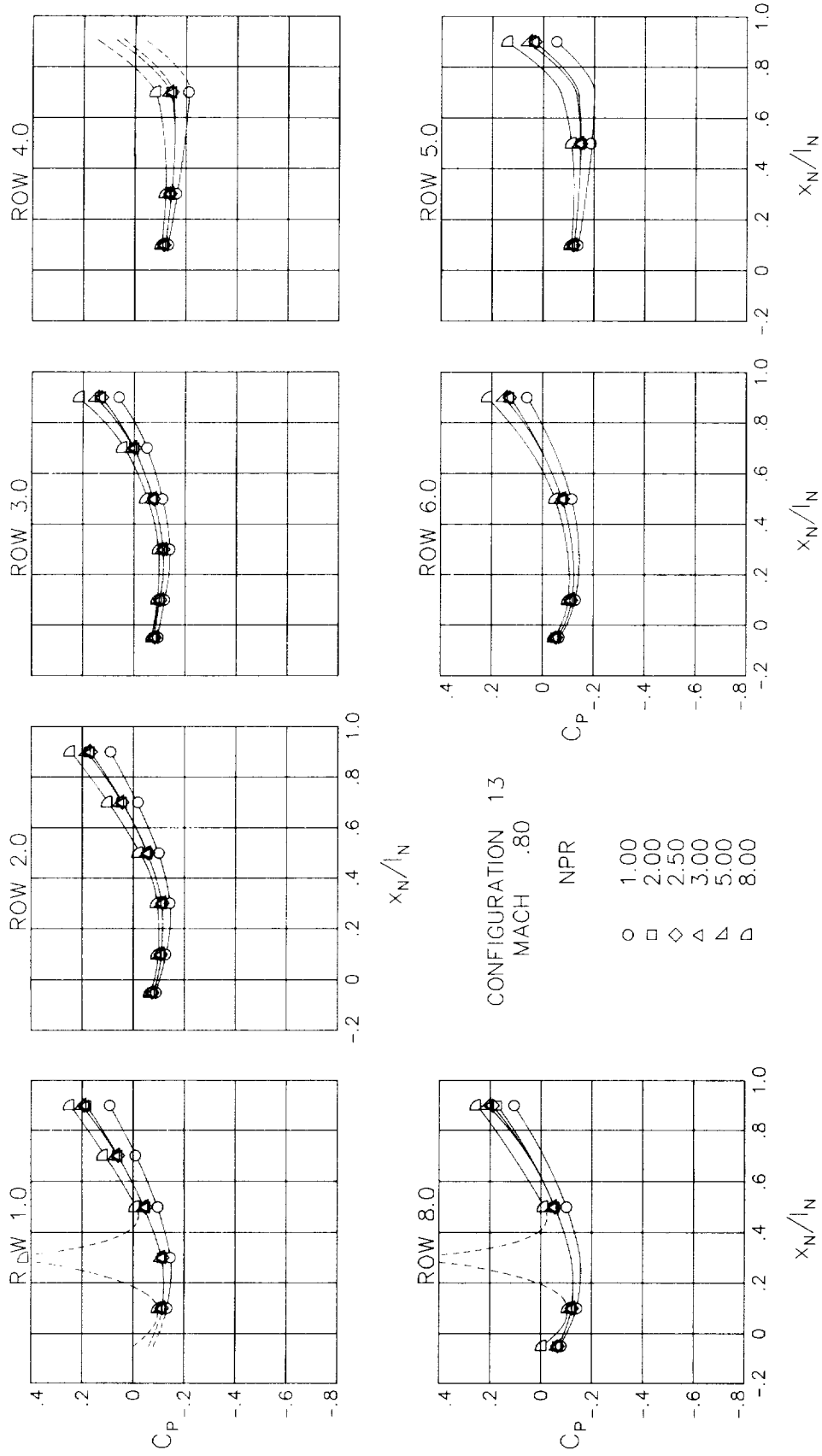

(c) M = 0.80.

Figure 38.- Continued.

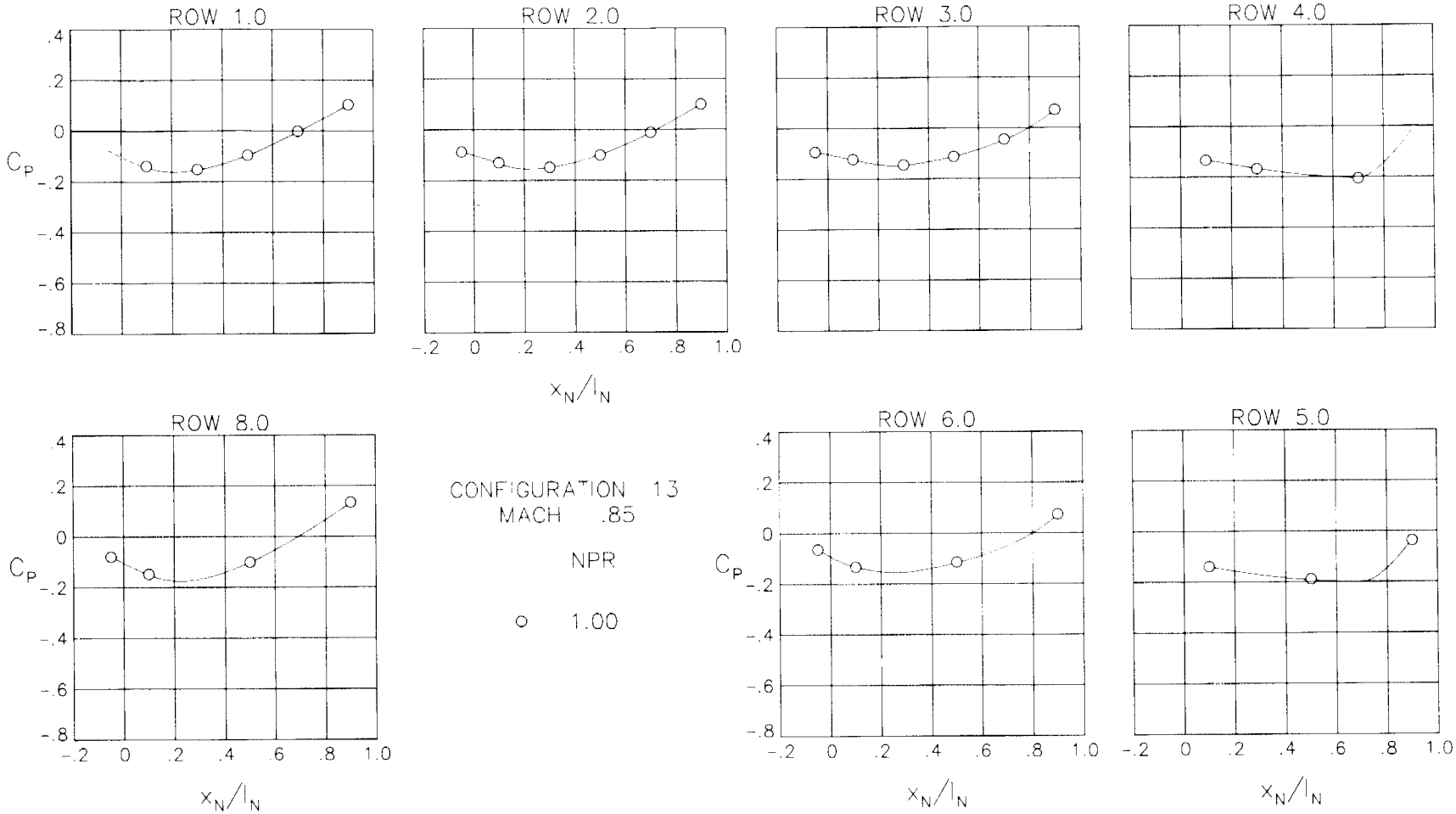

(d) M = 0.85.

Figure 38.- Continued.

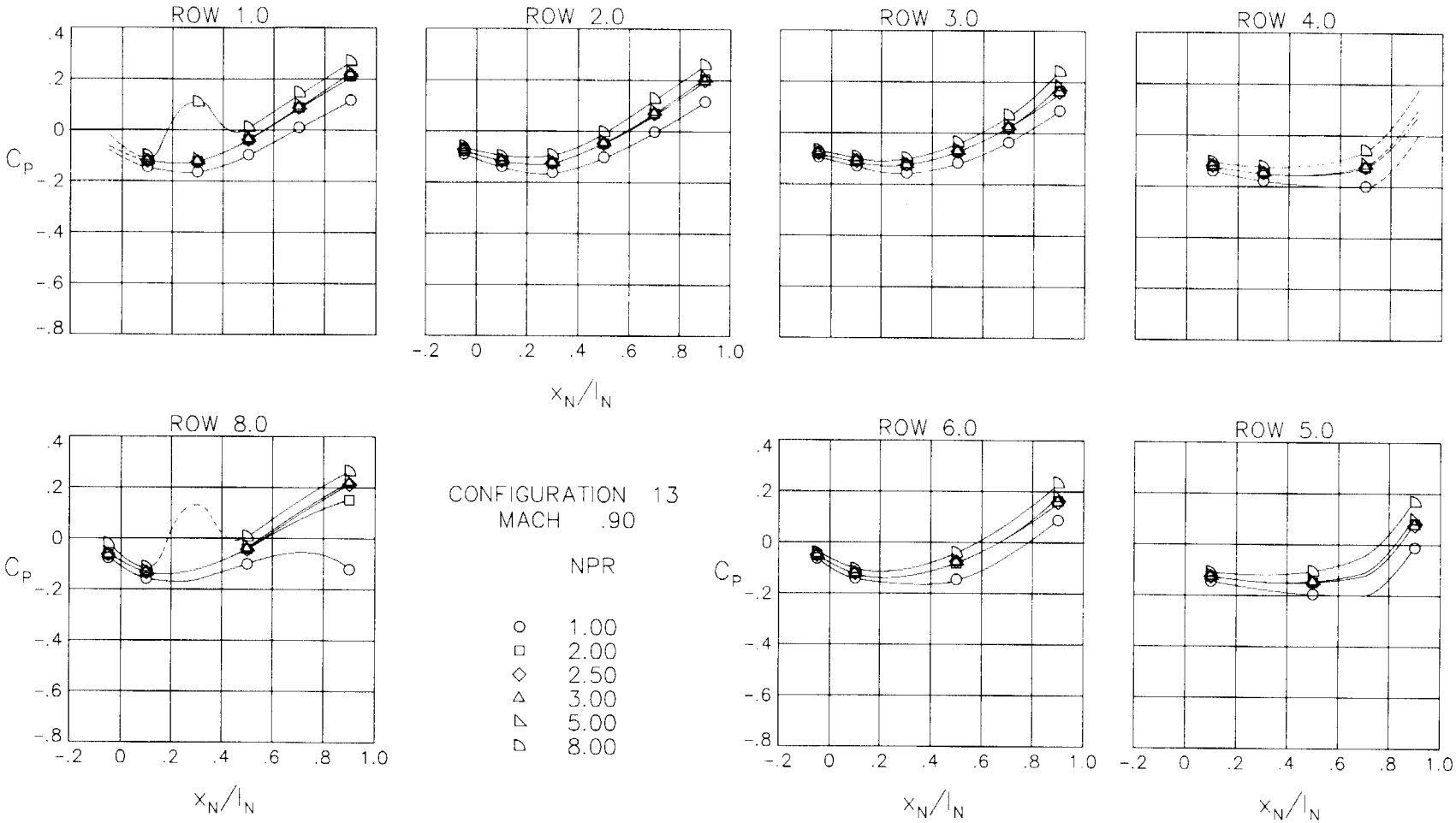

(e) M = 0.90.

Figure 38.- Continued.

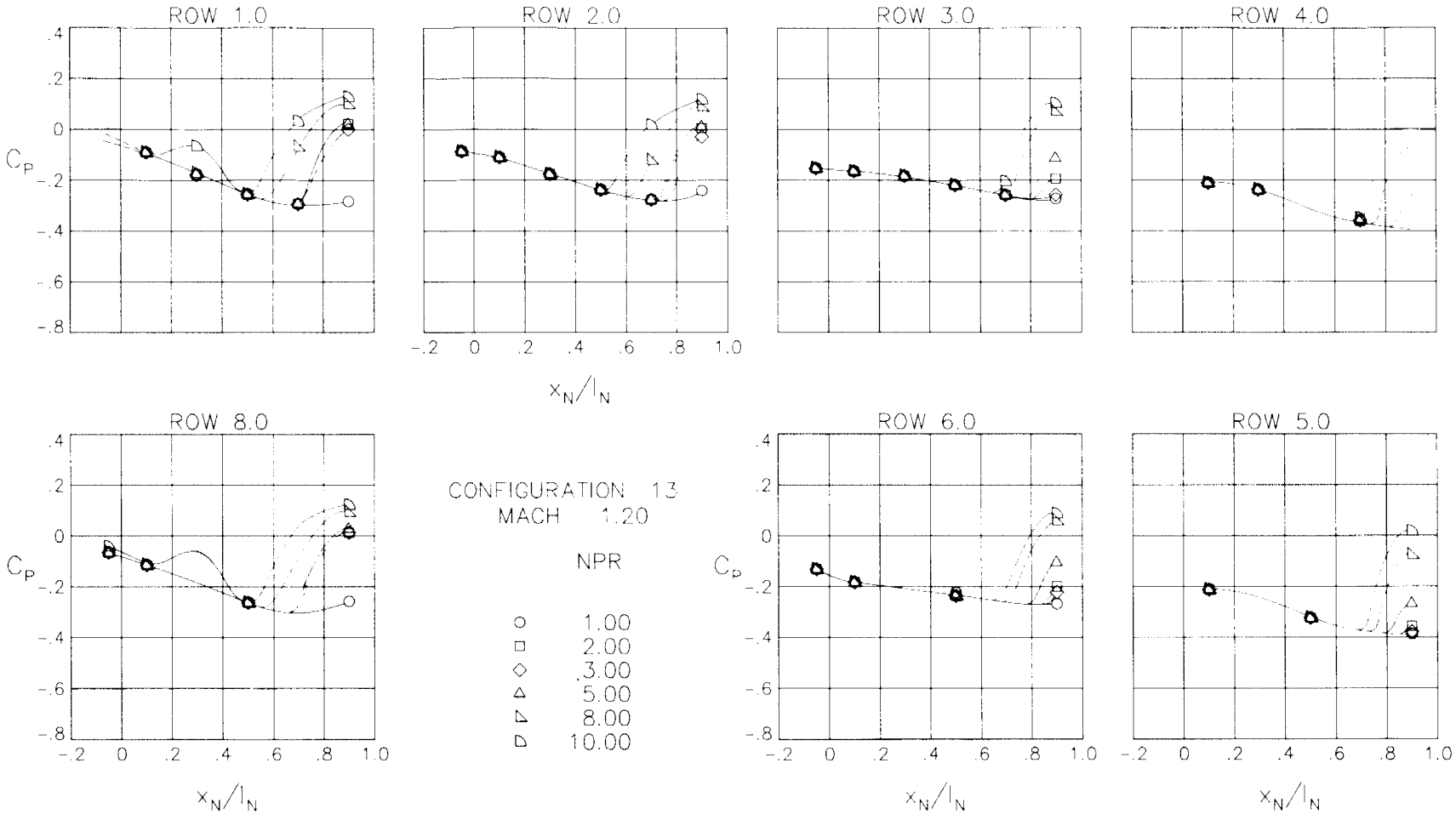

(f) M = 1.20.

Figure 38.- Concluded.

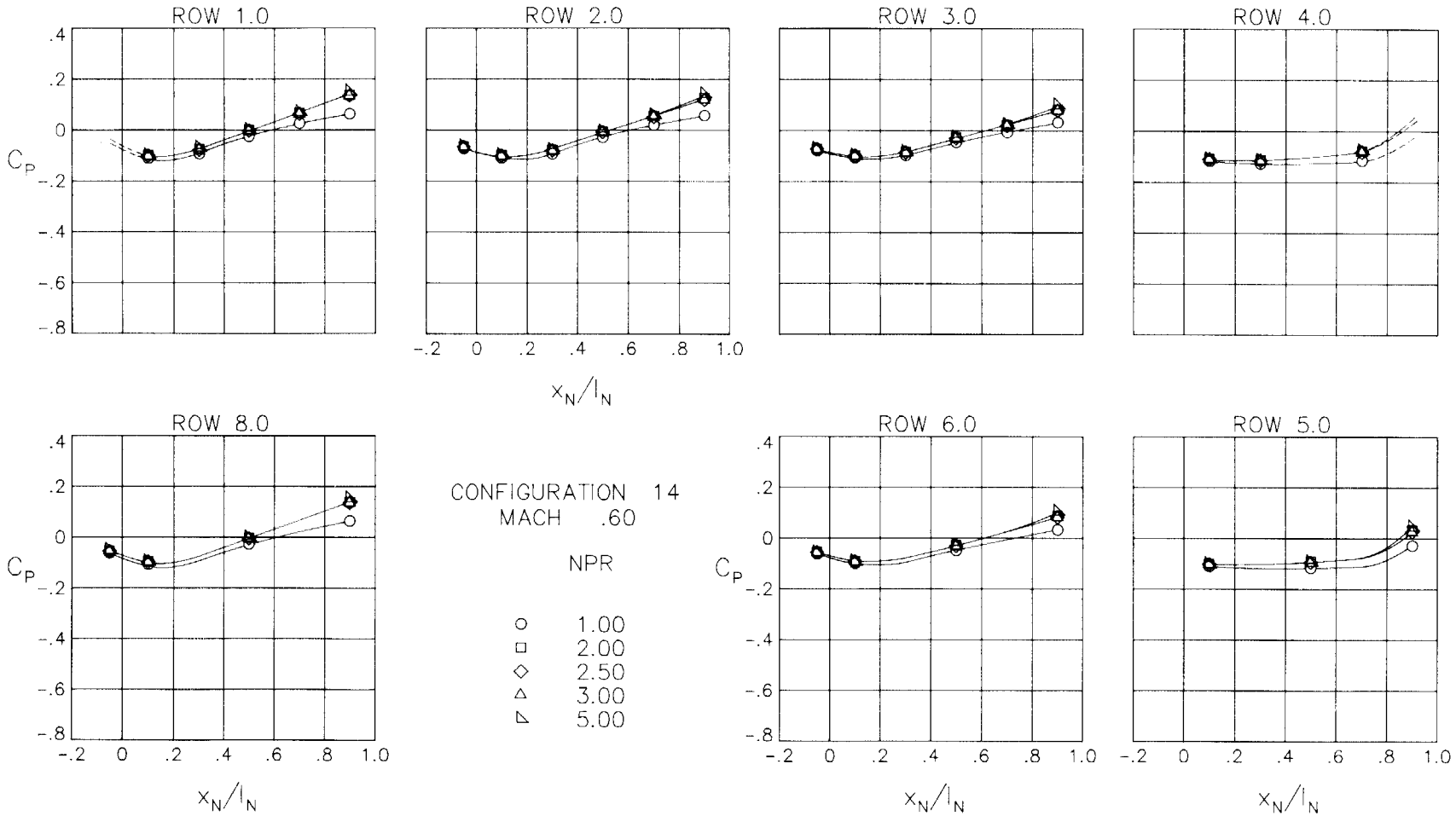

(a) M = 0.60.

Figure 39.- Surface static-pressure coefficient distributions around nozzle for configuration 14. α = 0°.

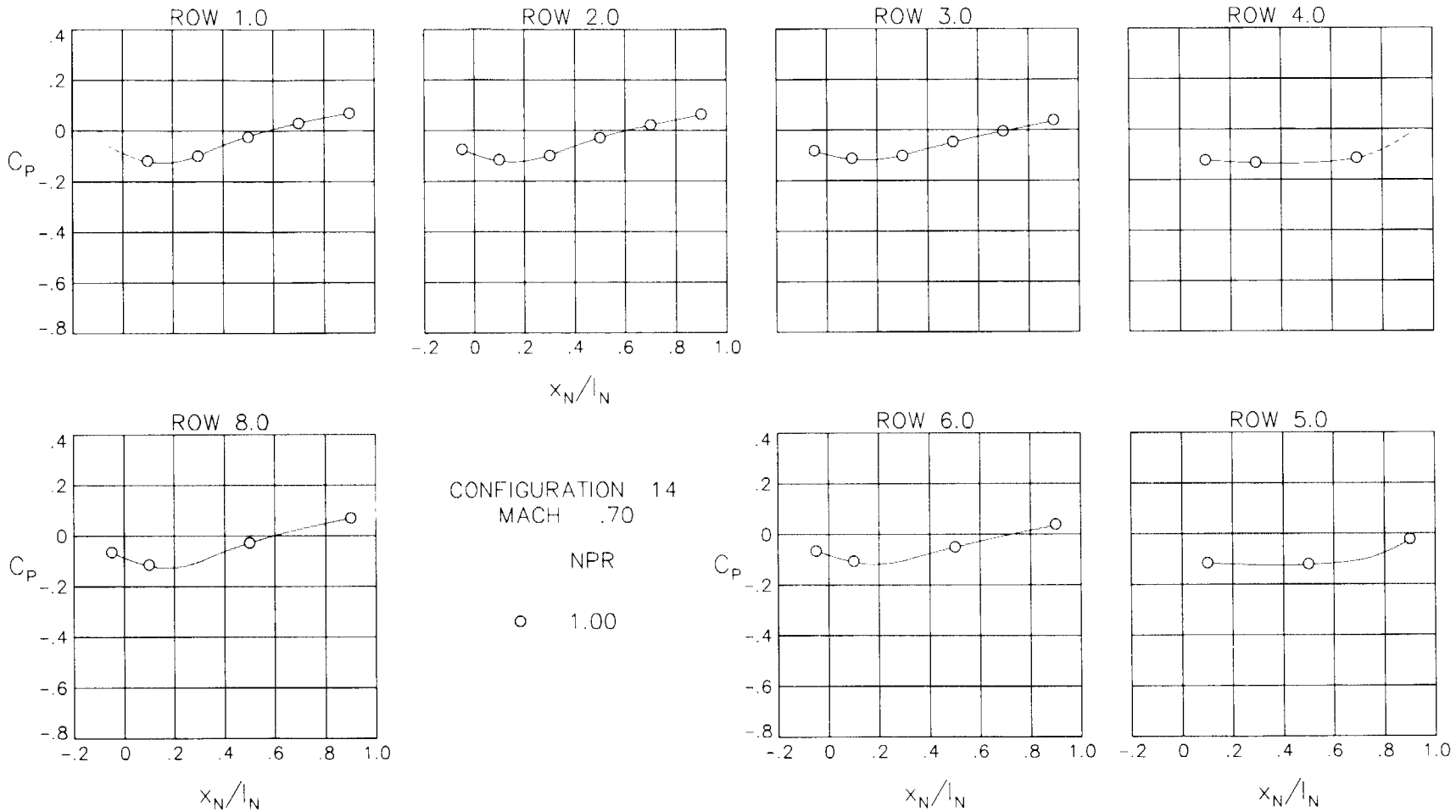

(b) M = 0.70.

Figure 39.- Continued.

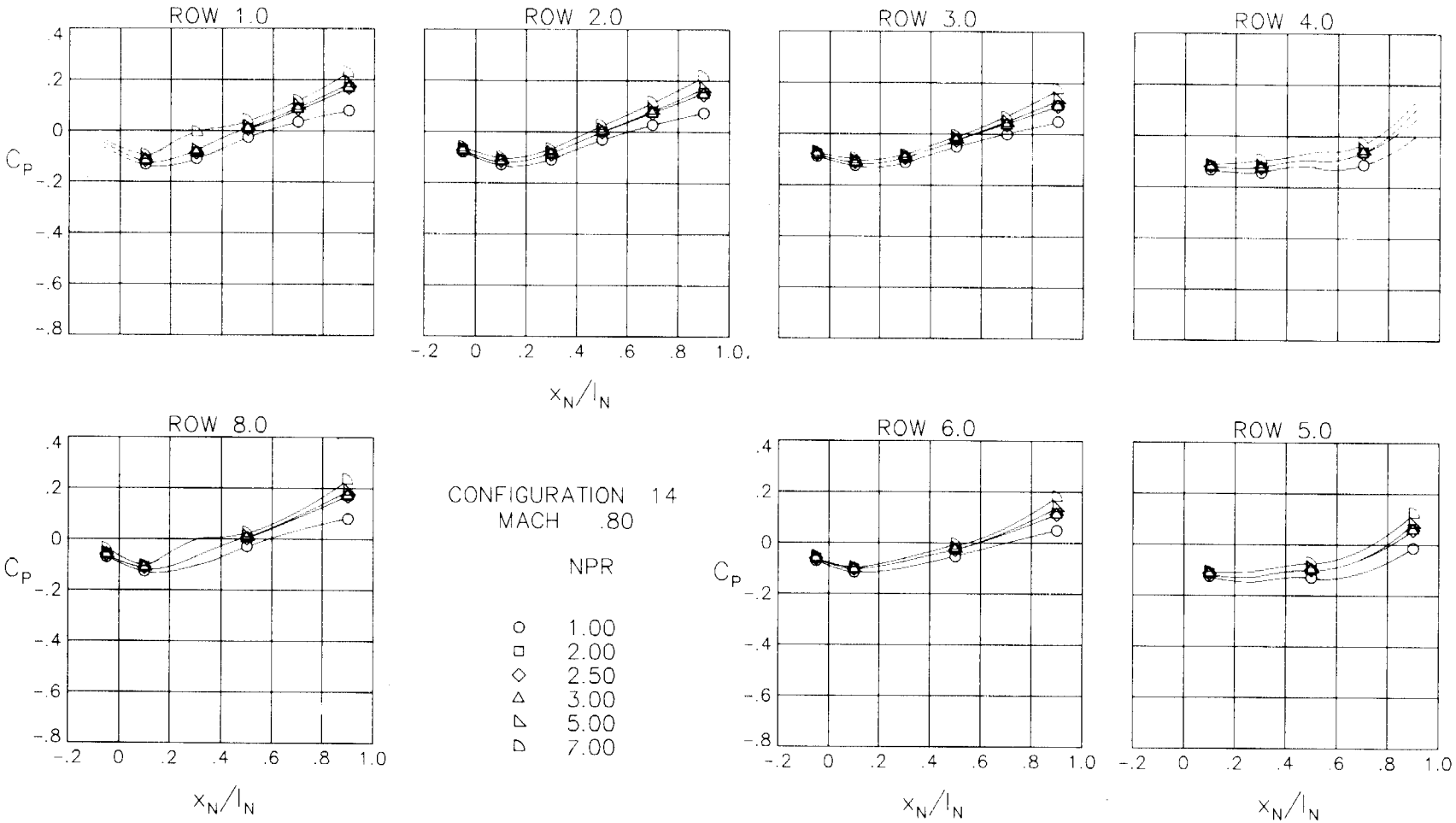

(c) M = 0.80.

Figure 39.- Continued.

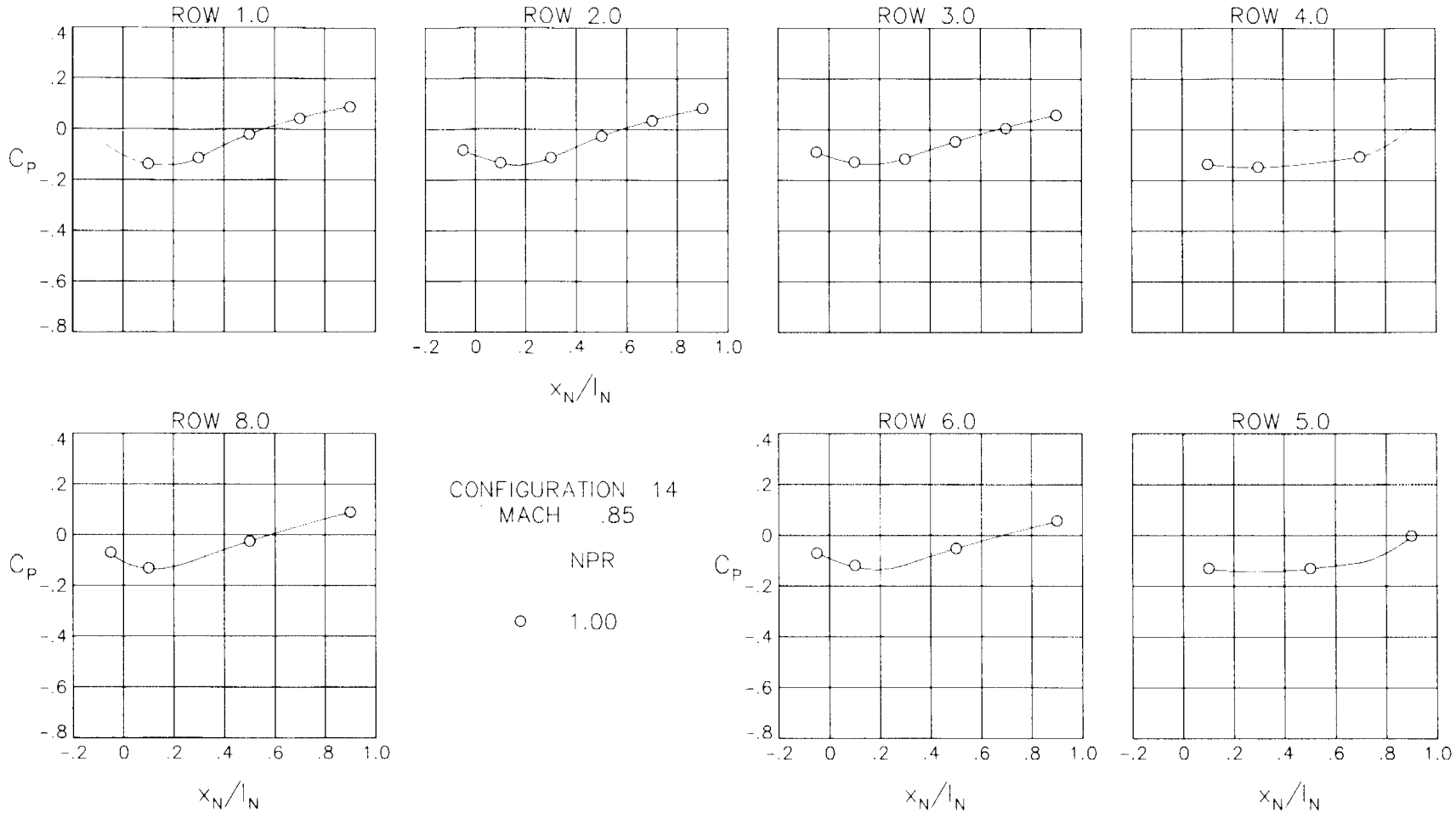

(d) M = 0.85.

Figure 39.- Continued.

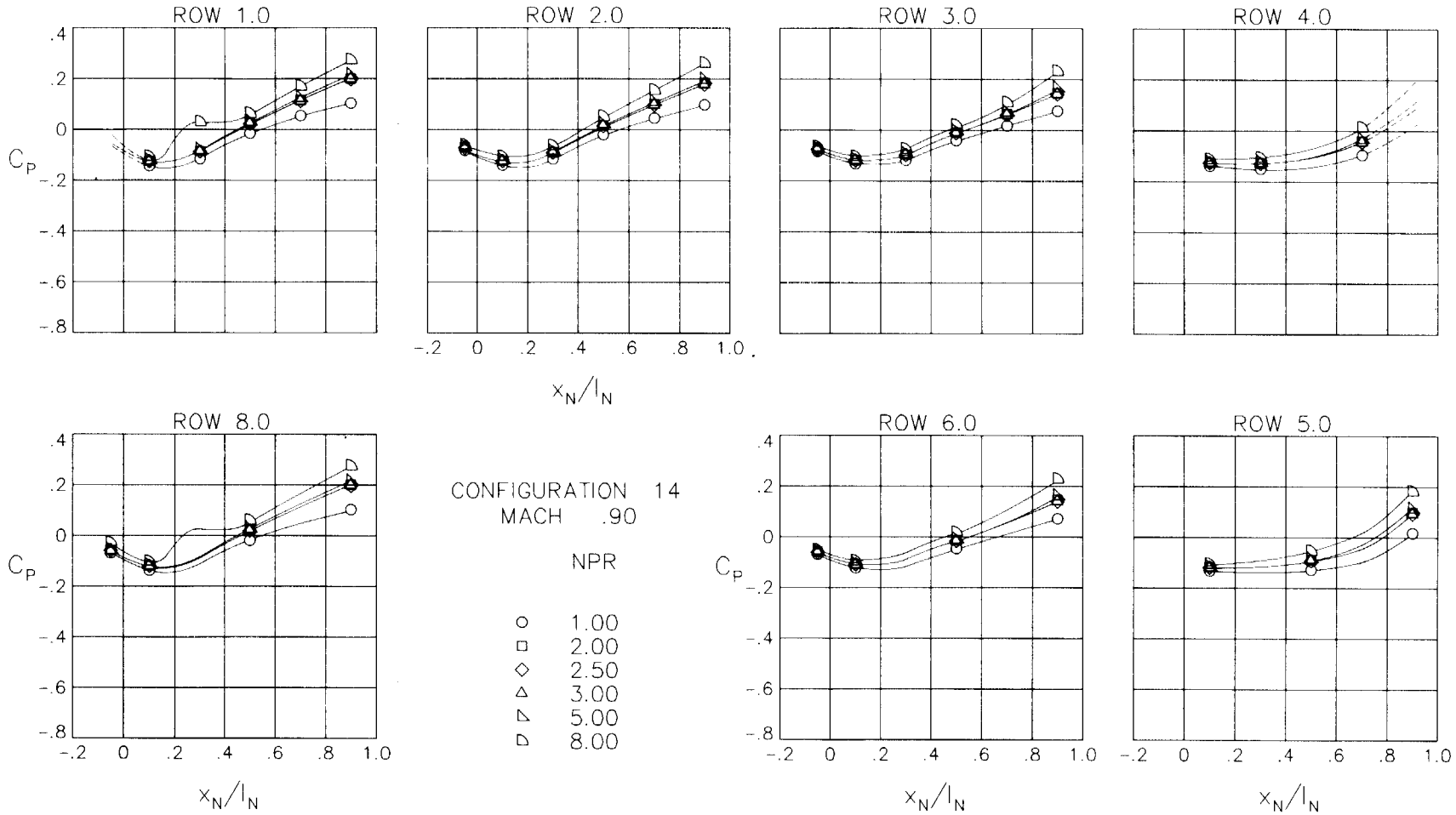

(e) M = 0.90.

Figure 39.- Continued.

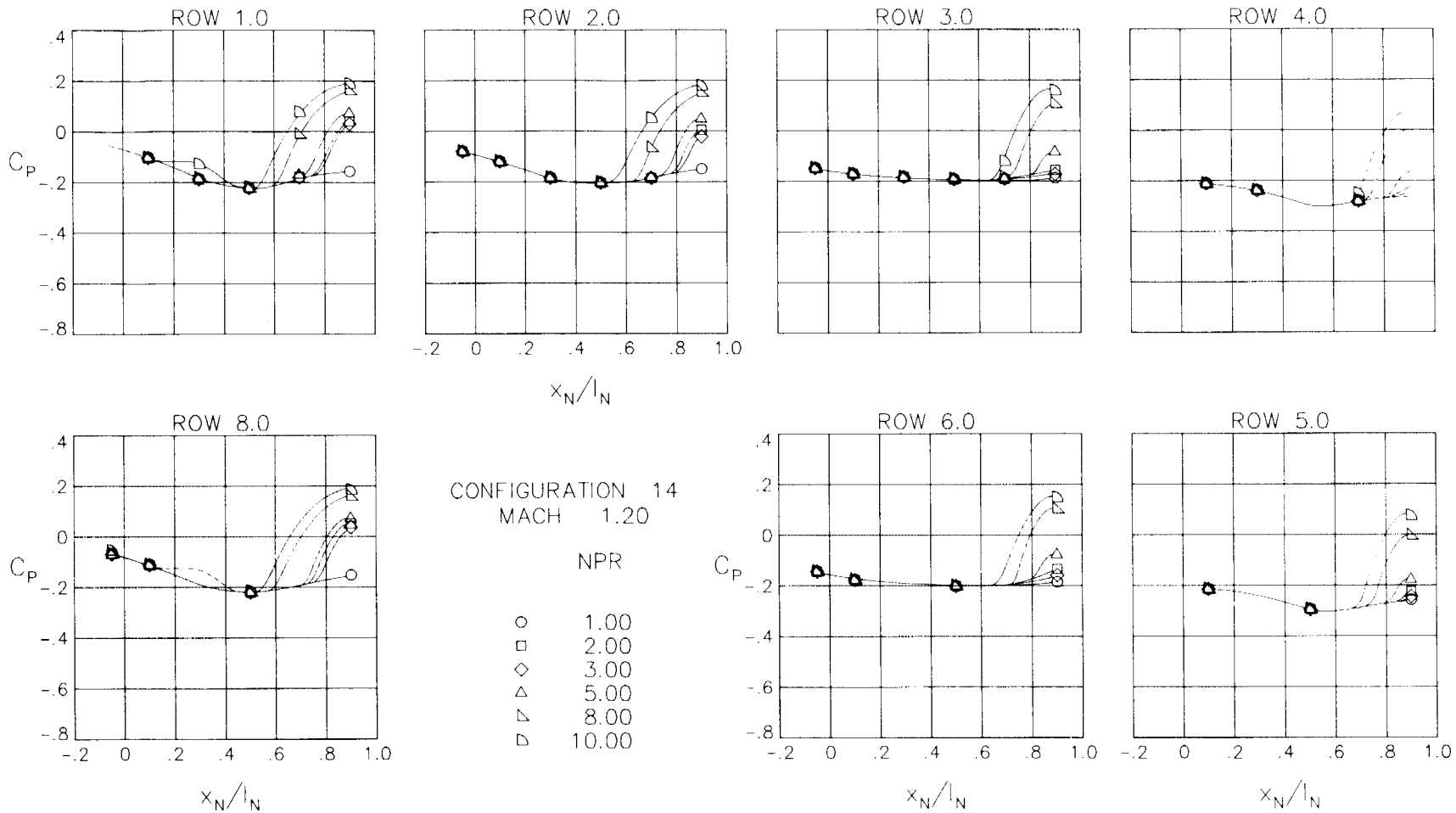

(f) M = 1.20.

Figure 39.- Concluded.

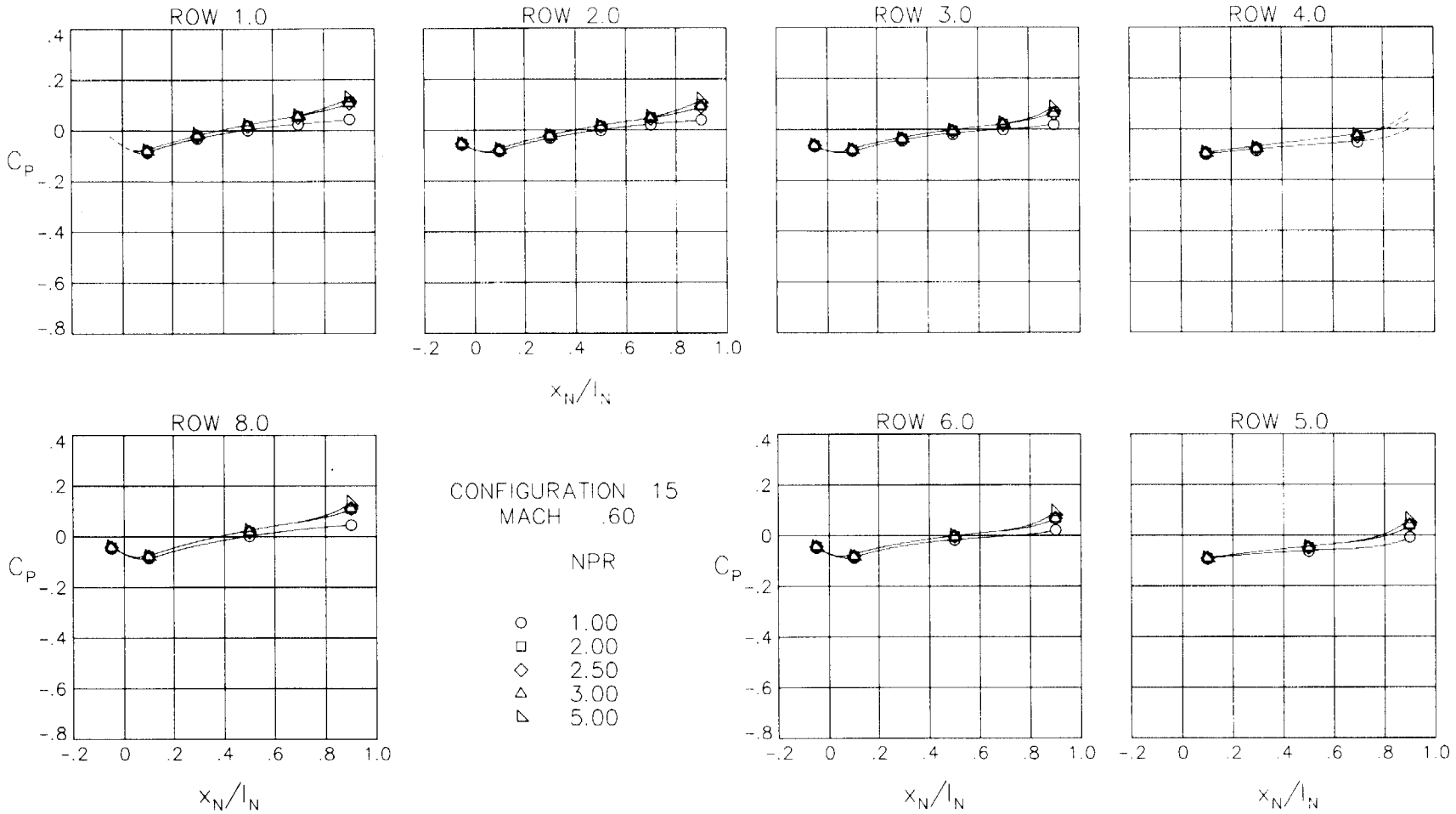

(a) M = 0.60.

Figure 40.- Surface static-pressure coefficient distributions around nozzle for configuration 15. $\alpha = 0°$.

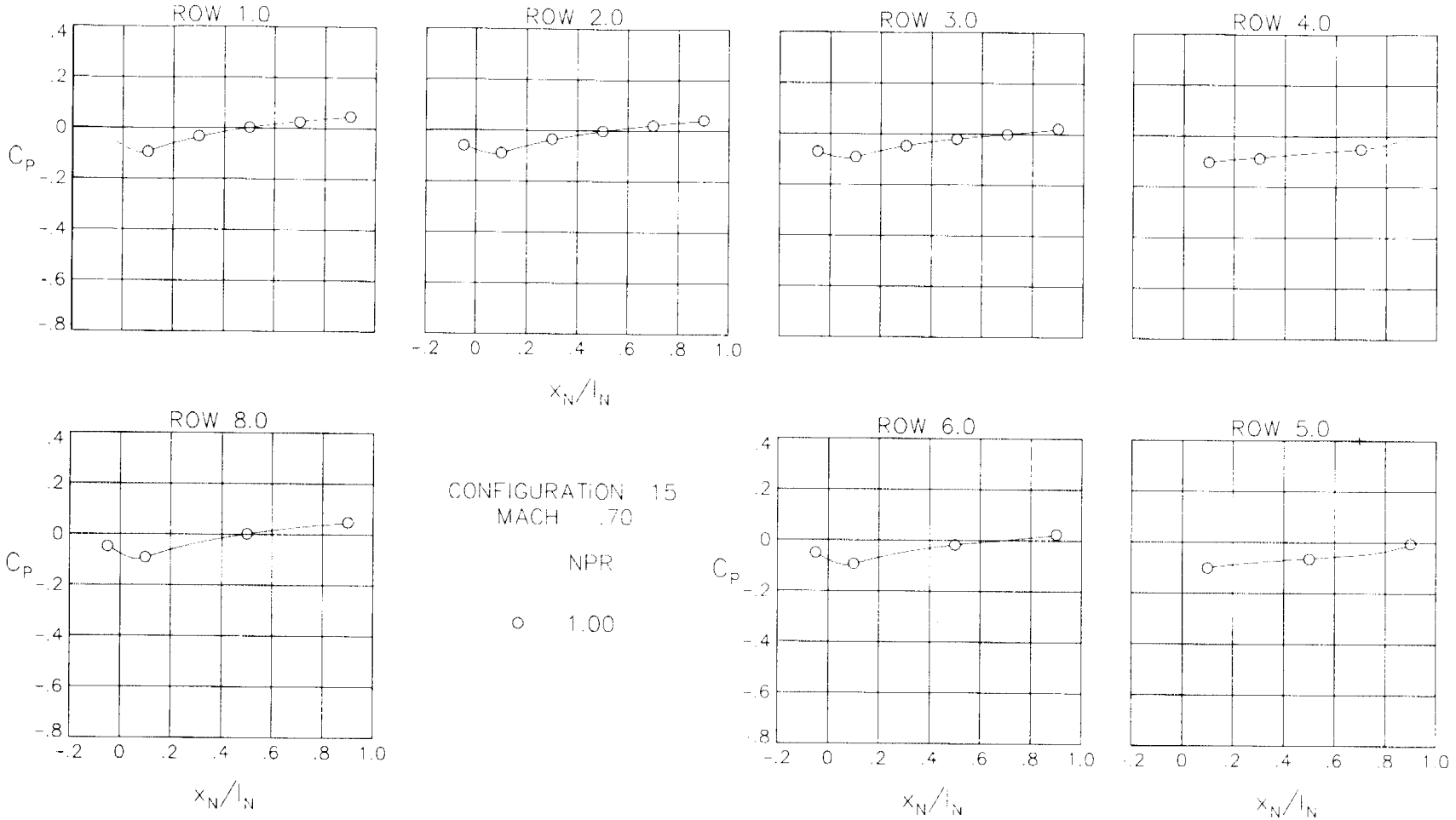

(b) M = 0.70.

Figure 40.- Continued.

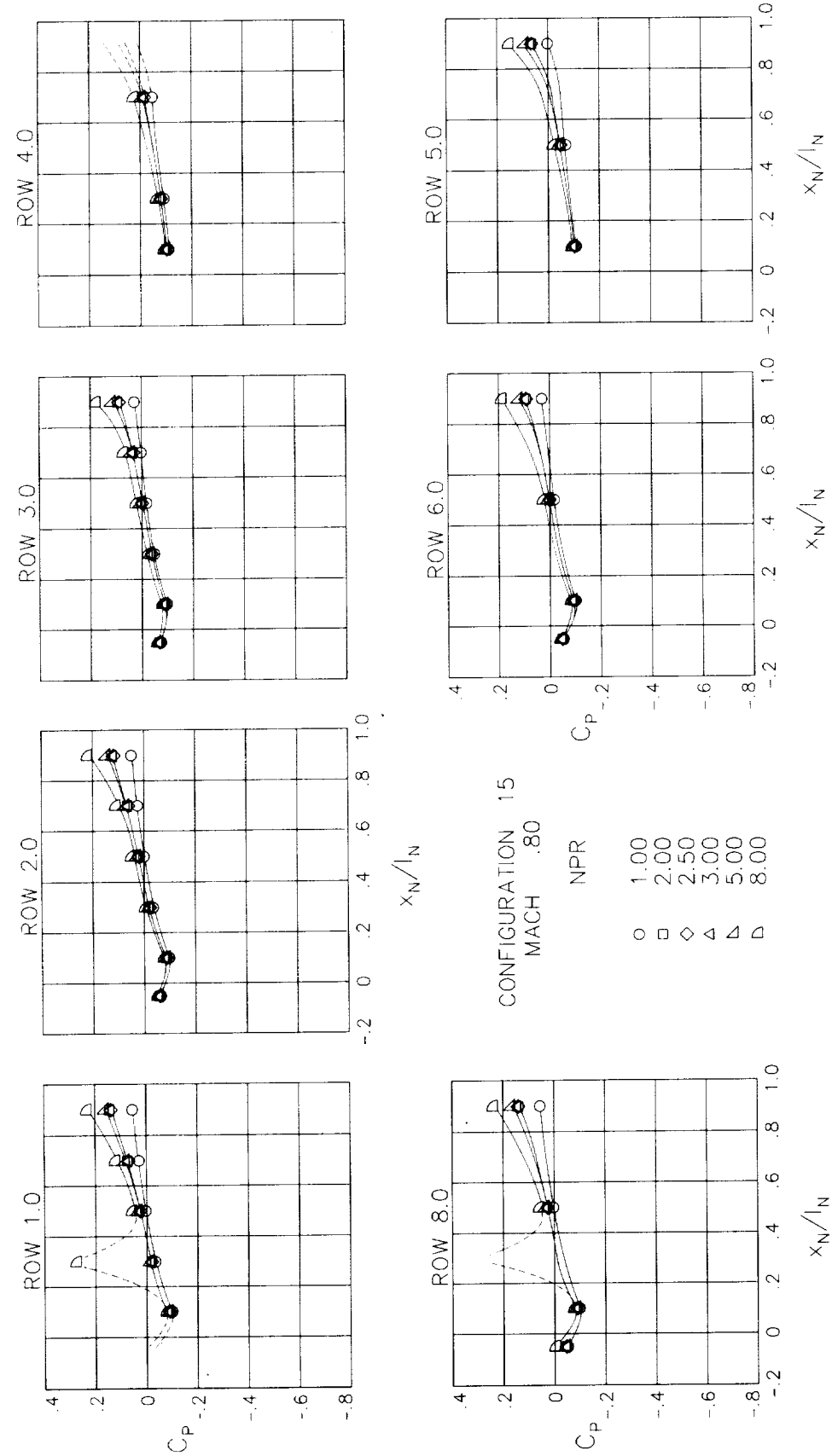

(c) M = 0.80.

Figure 40.- Continued.

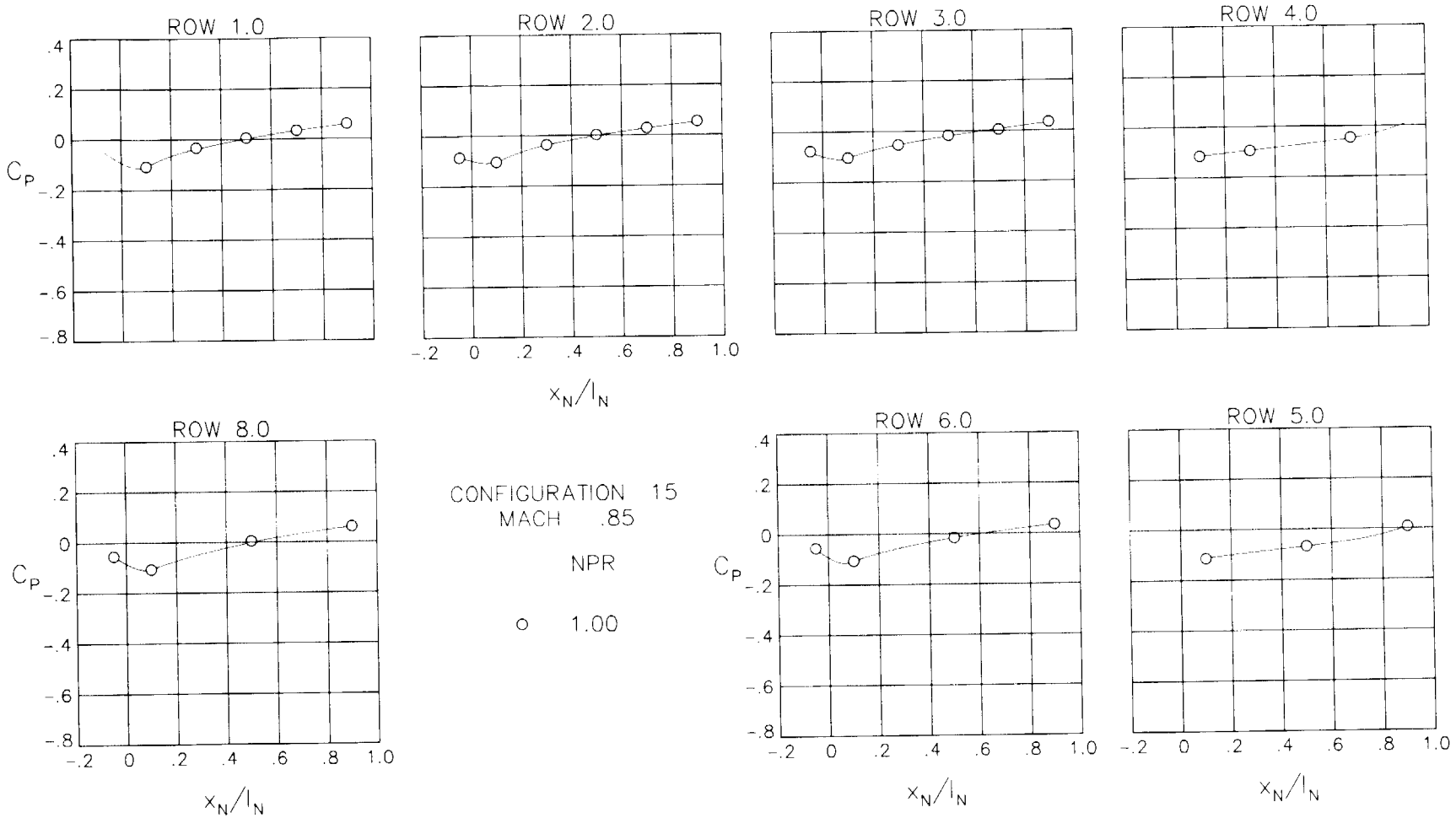

(d) M = 0.85.

Figure 40.- Continued.

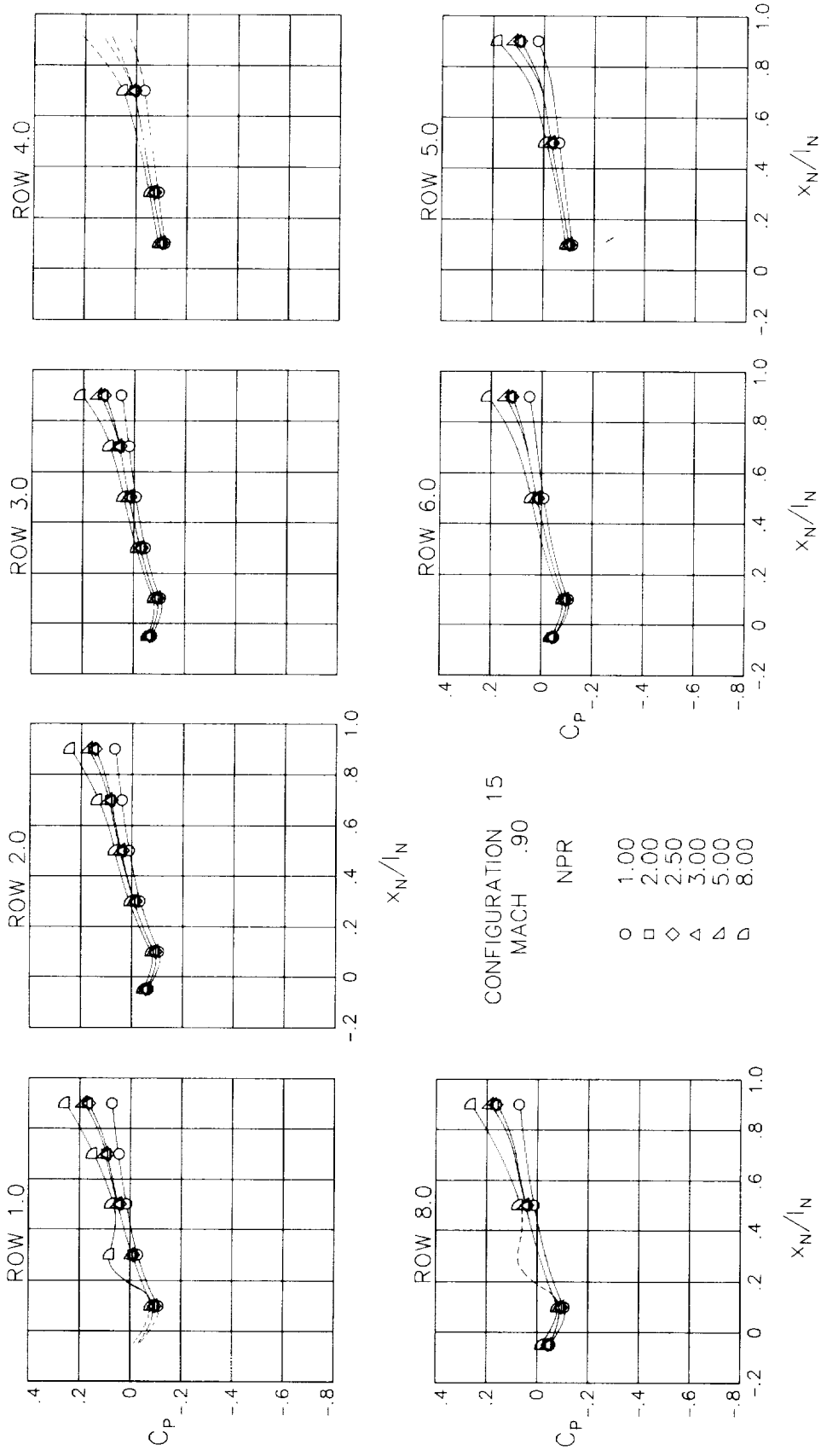

(e) M = 0.90.

Figure 40.- Continued.

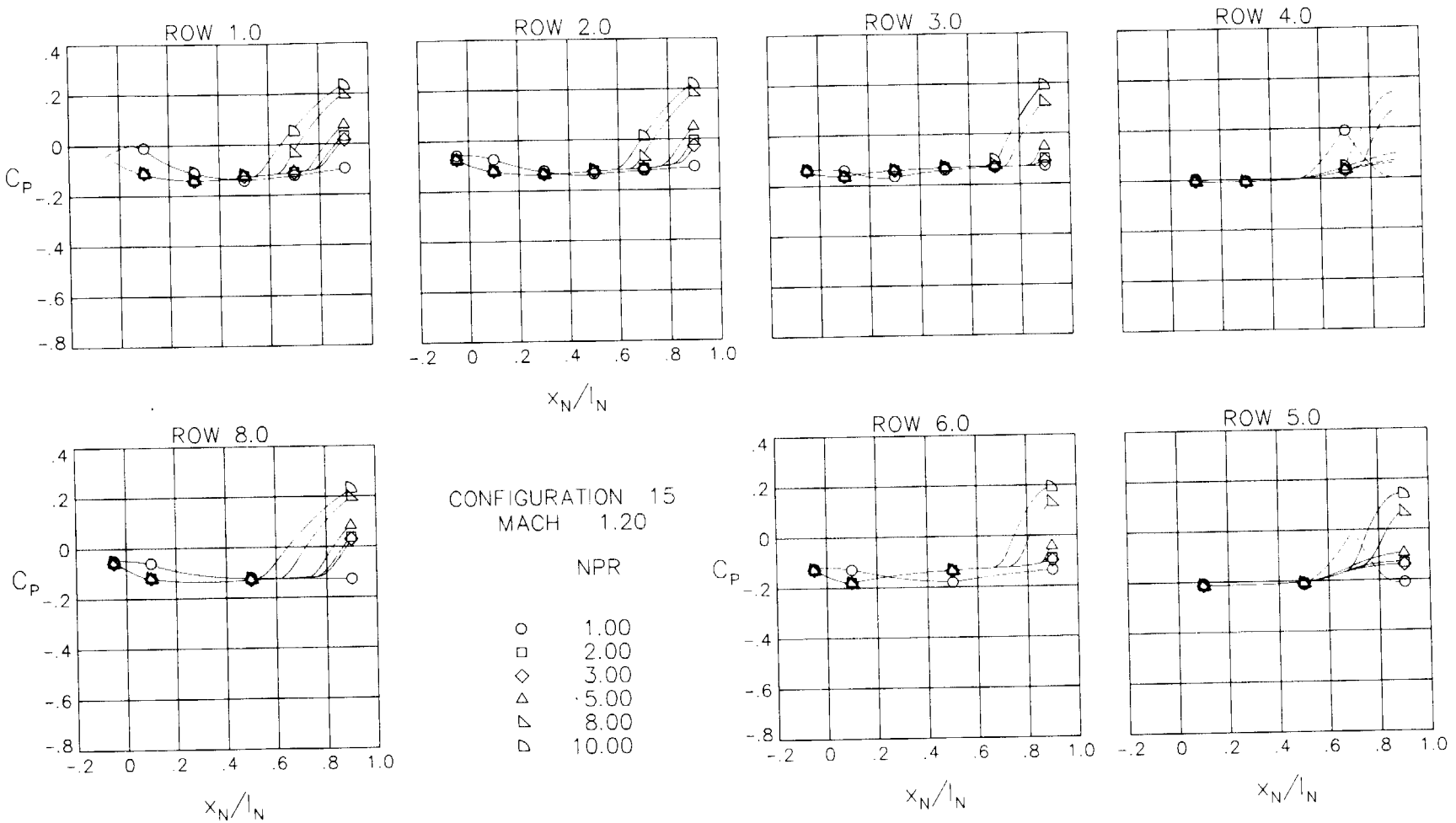

(f) M = 1.20.

Figure 40.- Concluded.

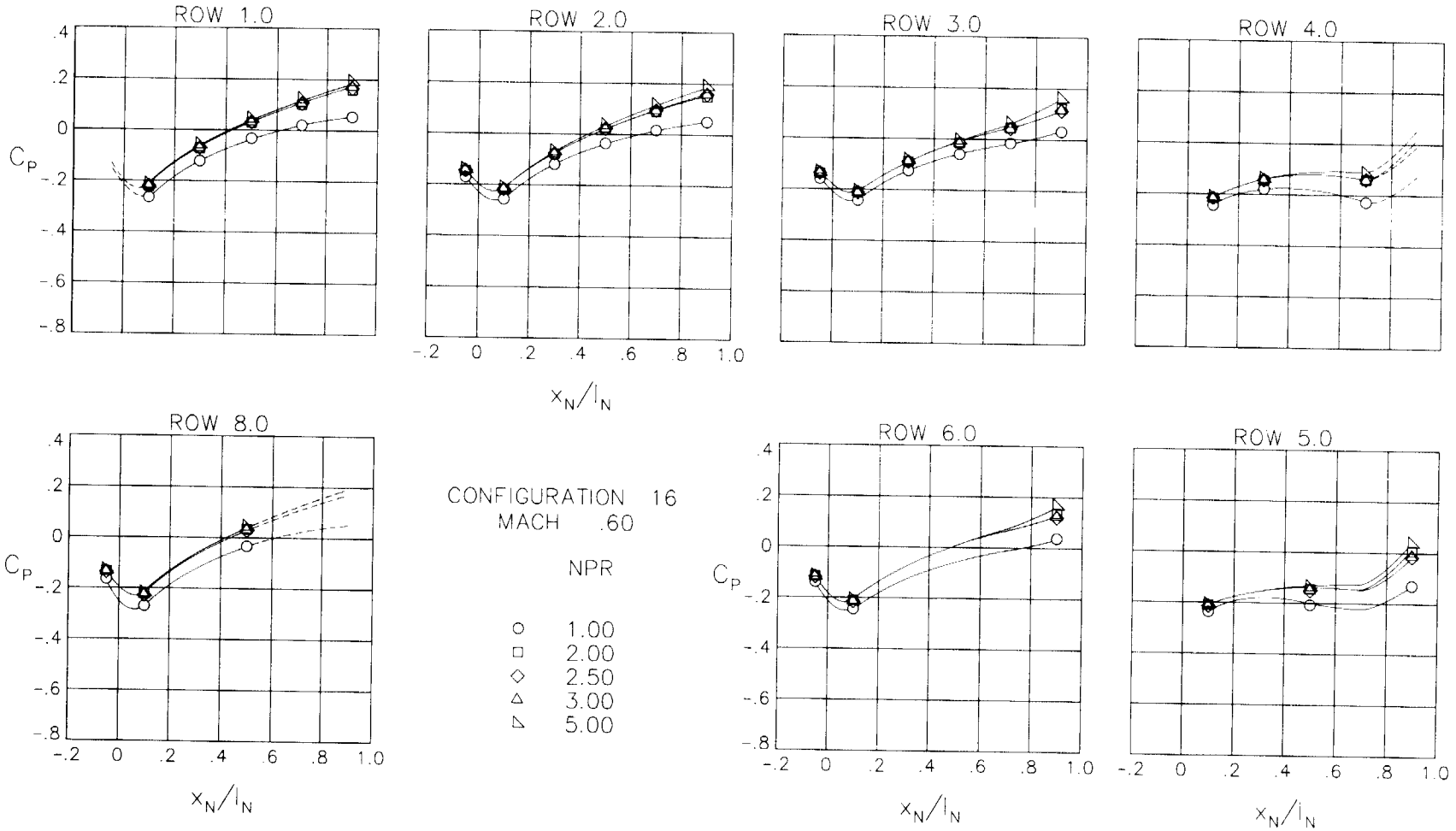

(a) M = 0.60.

Figure 41.- Surface static-pressure coefficient distributions around nozzle for configuration 16. $\alpha = 0°$.

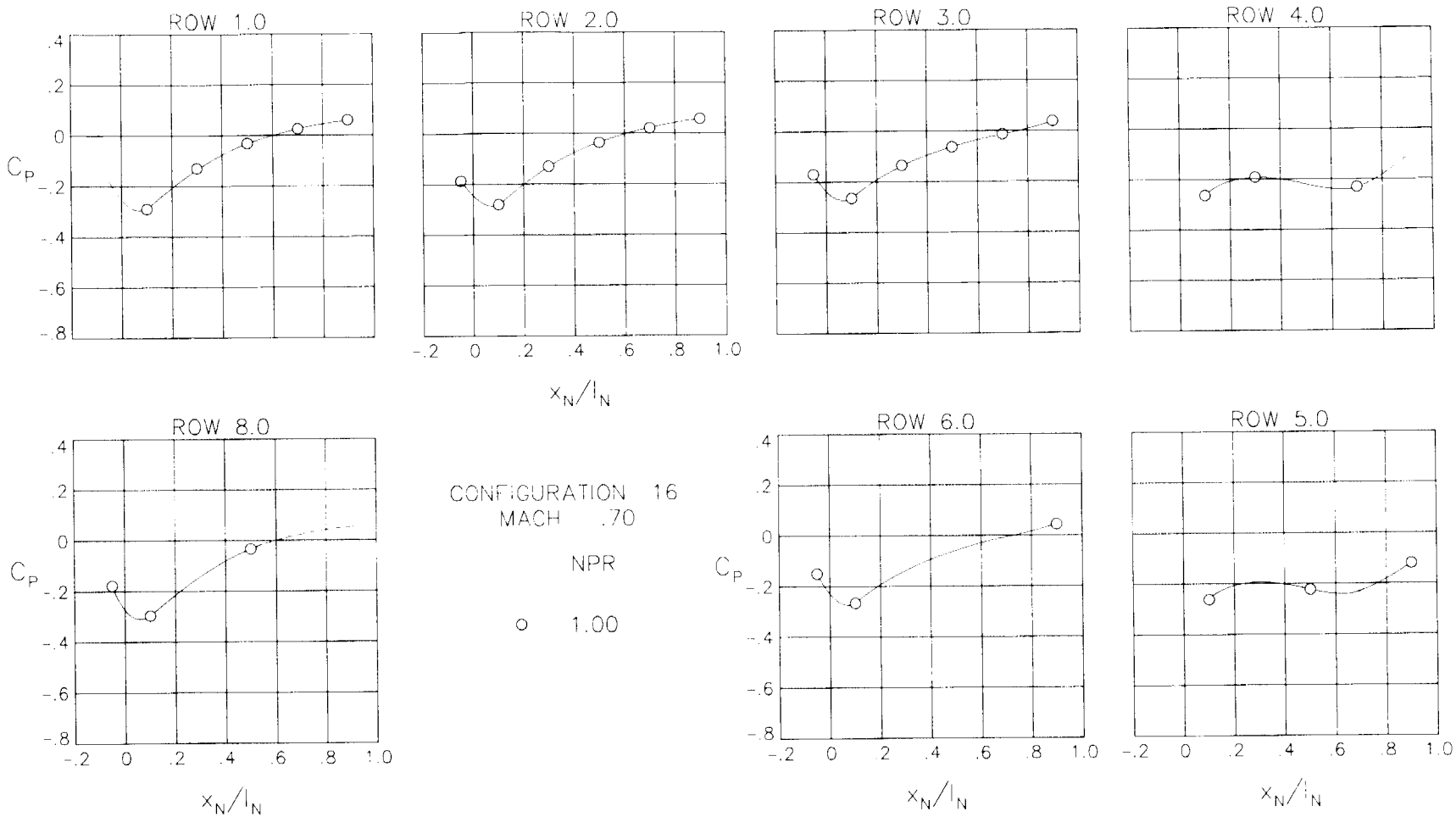

(b) M = 0.70.

Figure 41.- Continued.

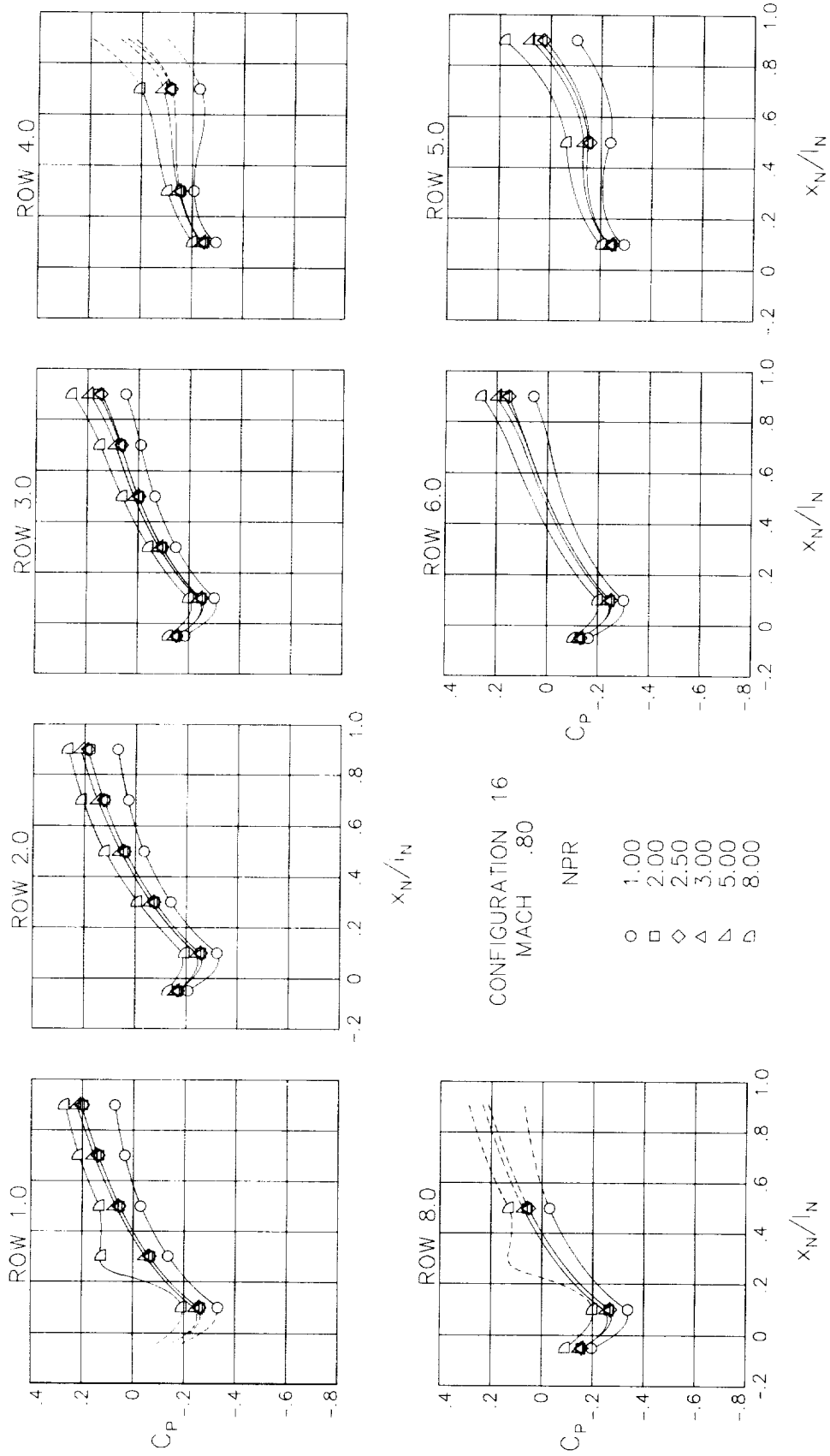

(c) M = 0.80.

Figure 41.- Continued.

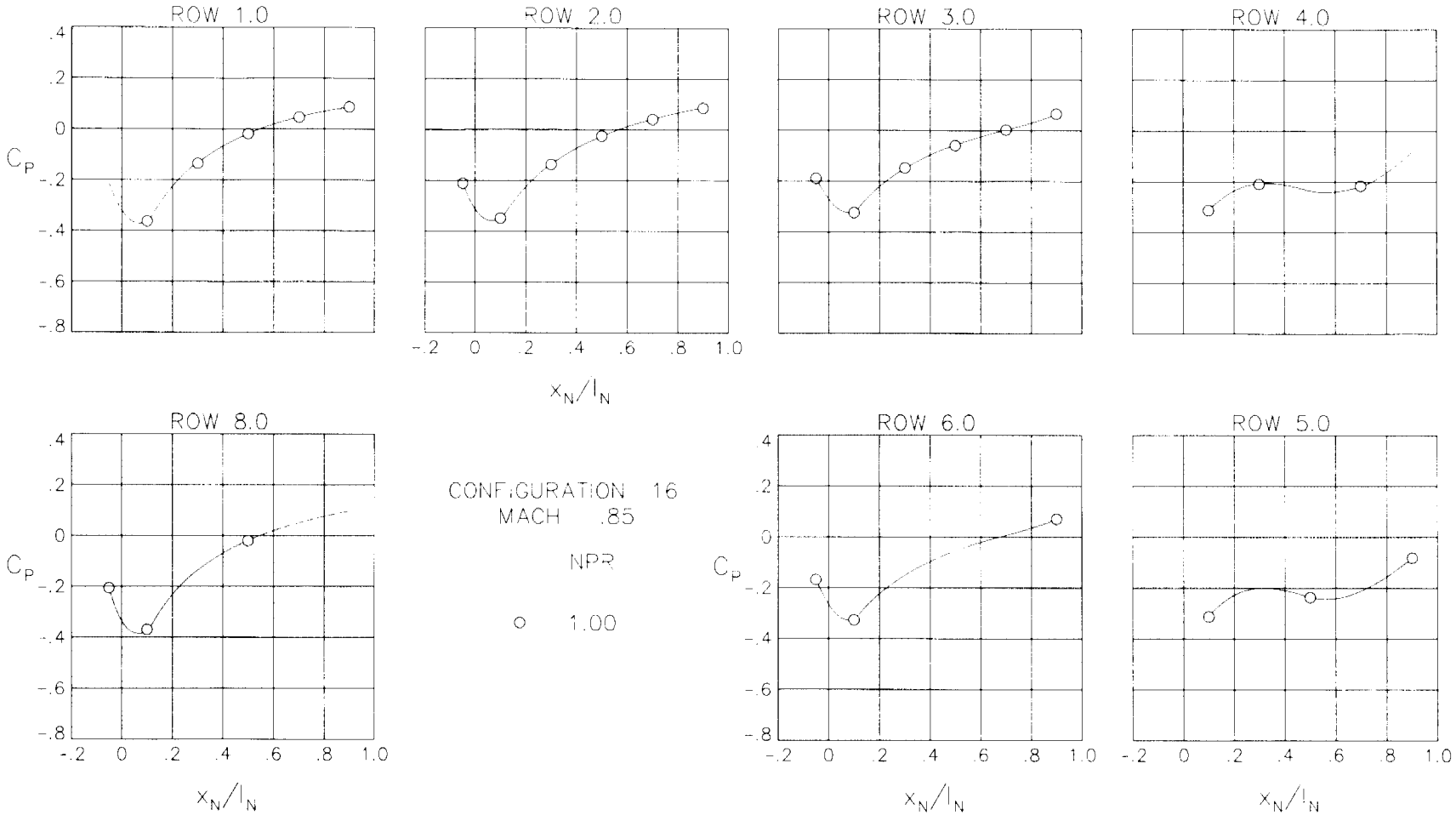

(d) M = 0.85.

Figure 41.- Continued.

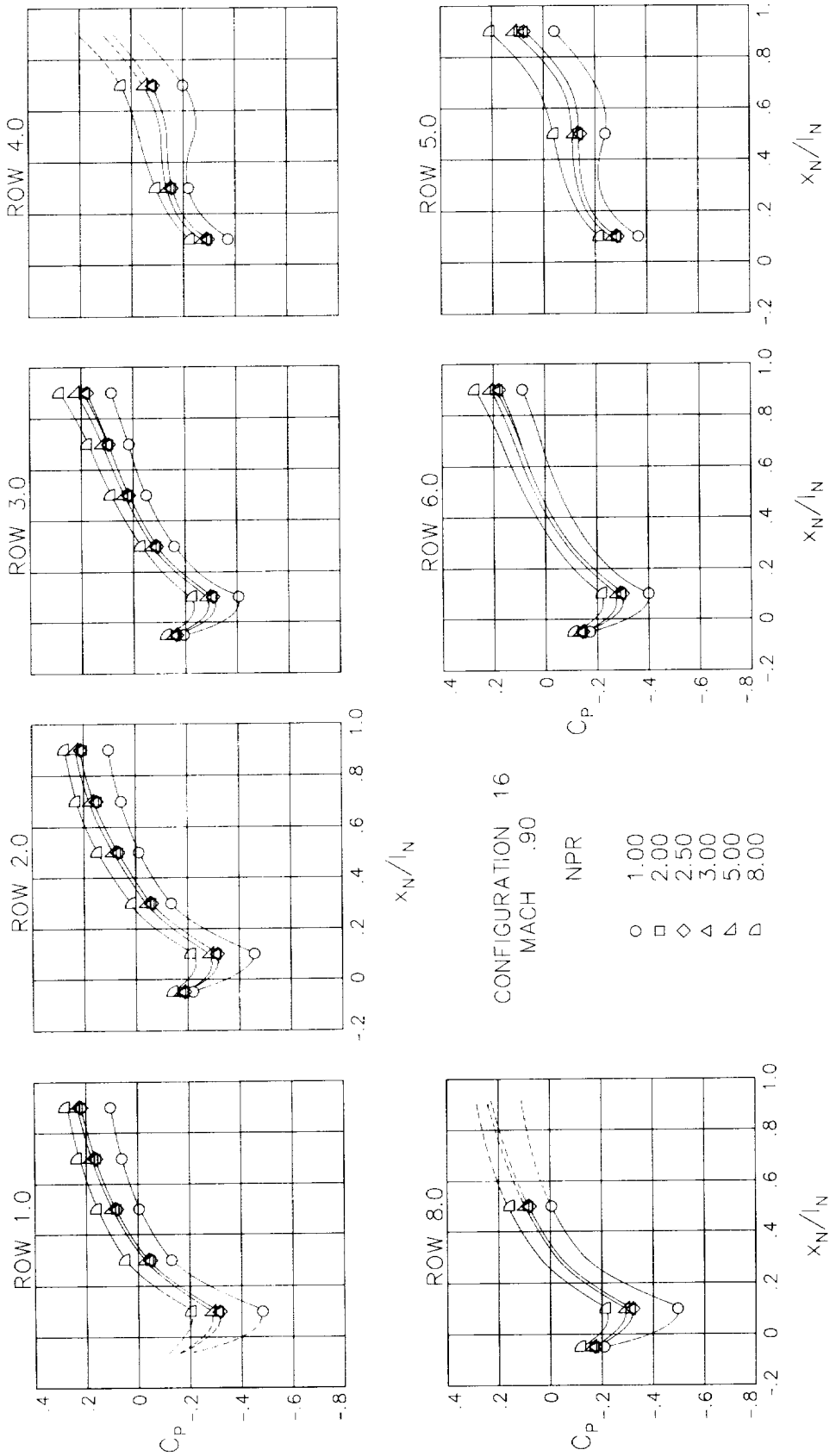

(e) M = 0.90.

Figure 41.- Continued.

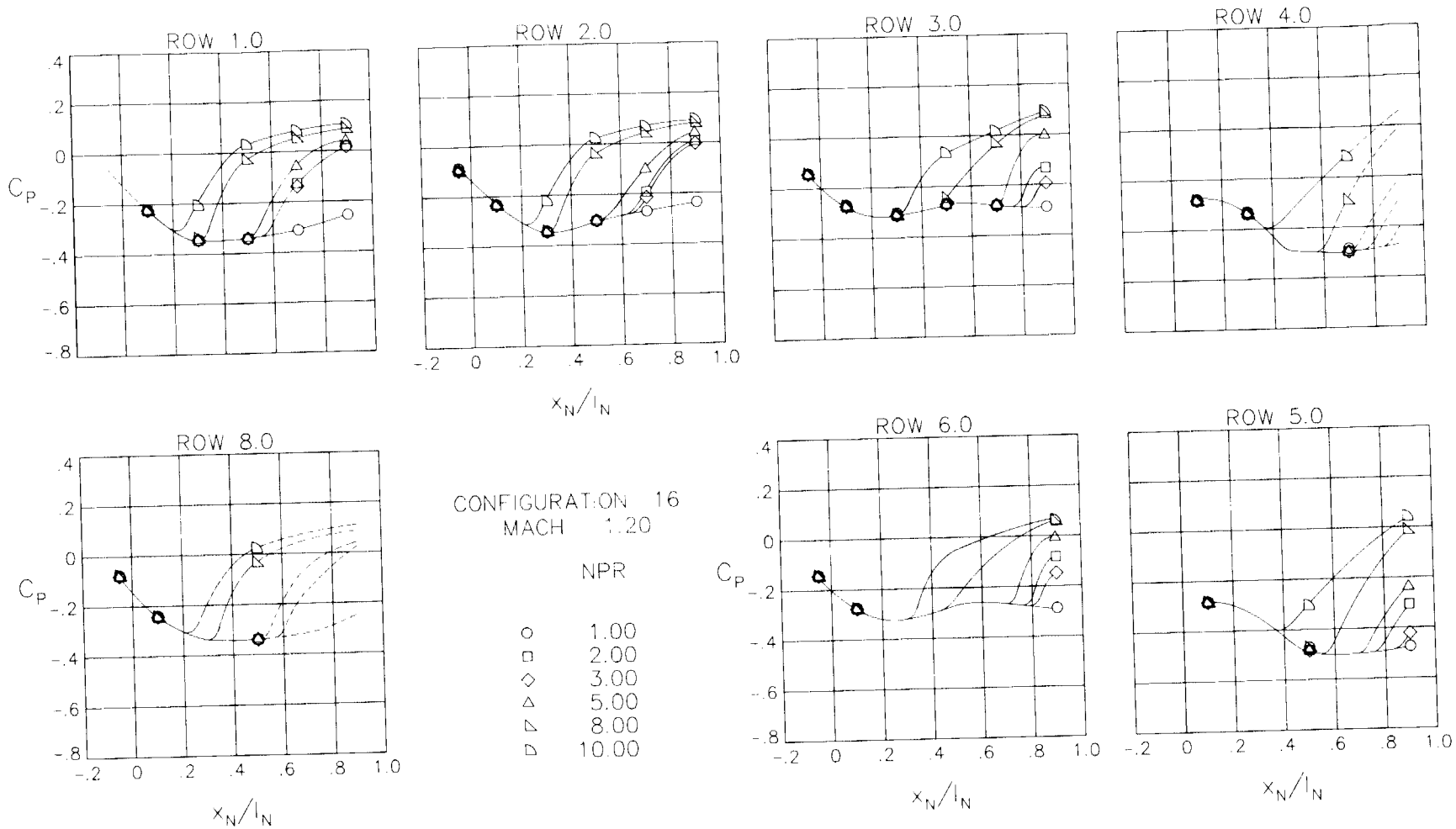

(f) M = 1.20.

Figure 41.- Concluded.

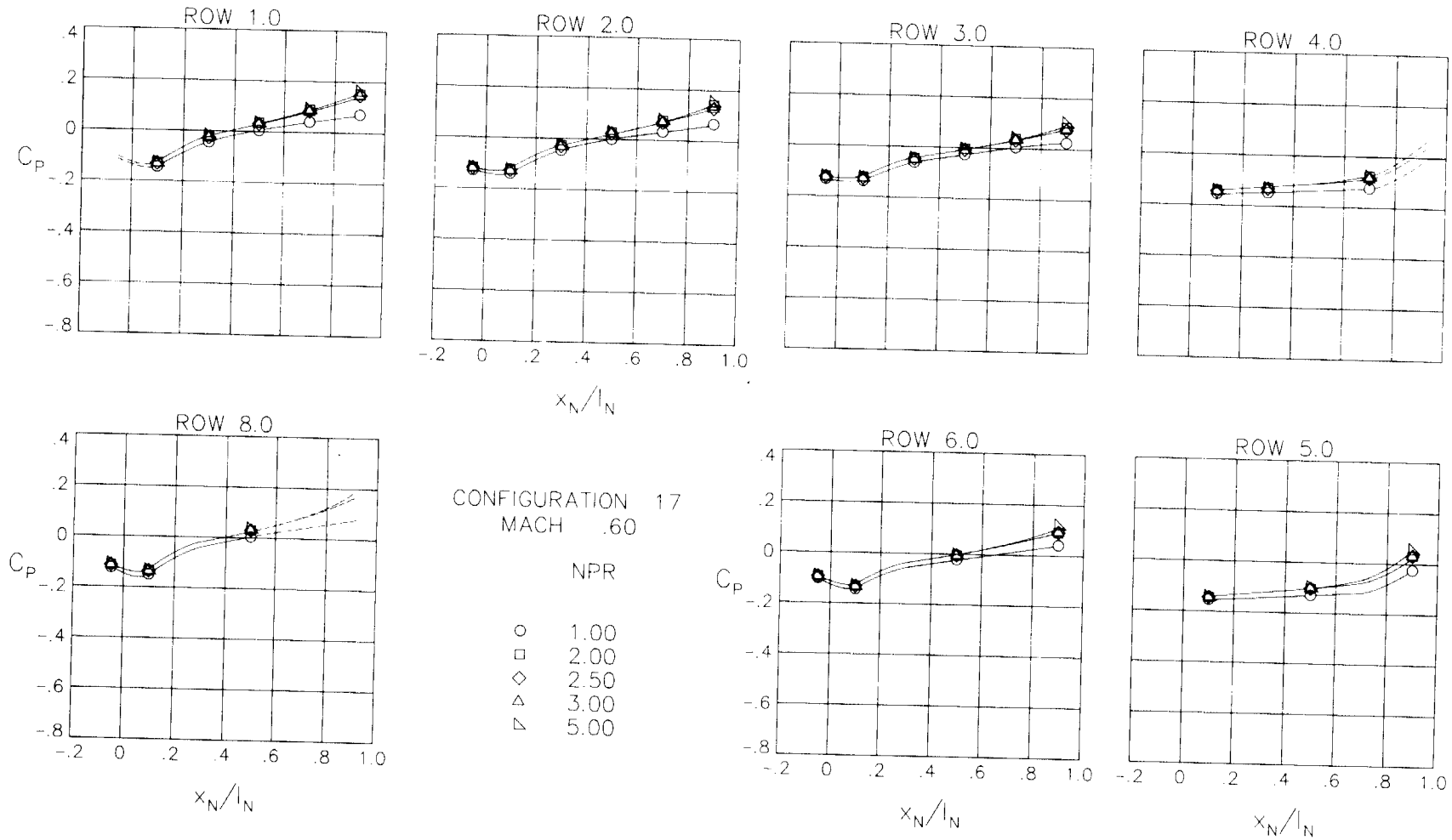

(a) M = 0.60.

Figure 42.- Surface static-pressure coefficient distributions around nozzle for configuration 17. α = 0°.

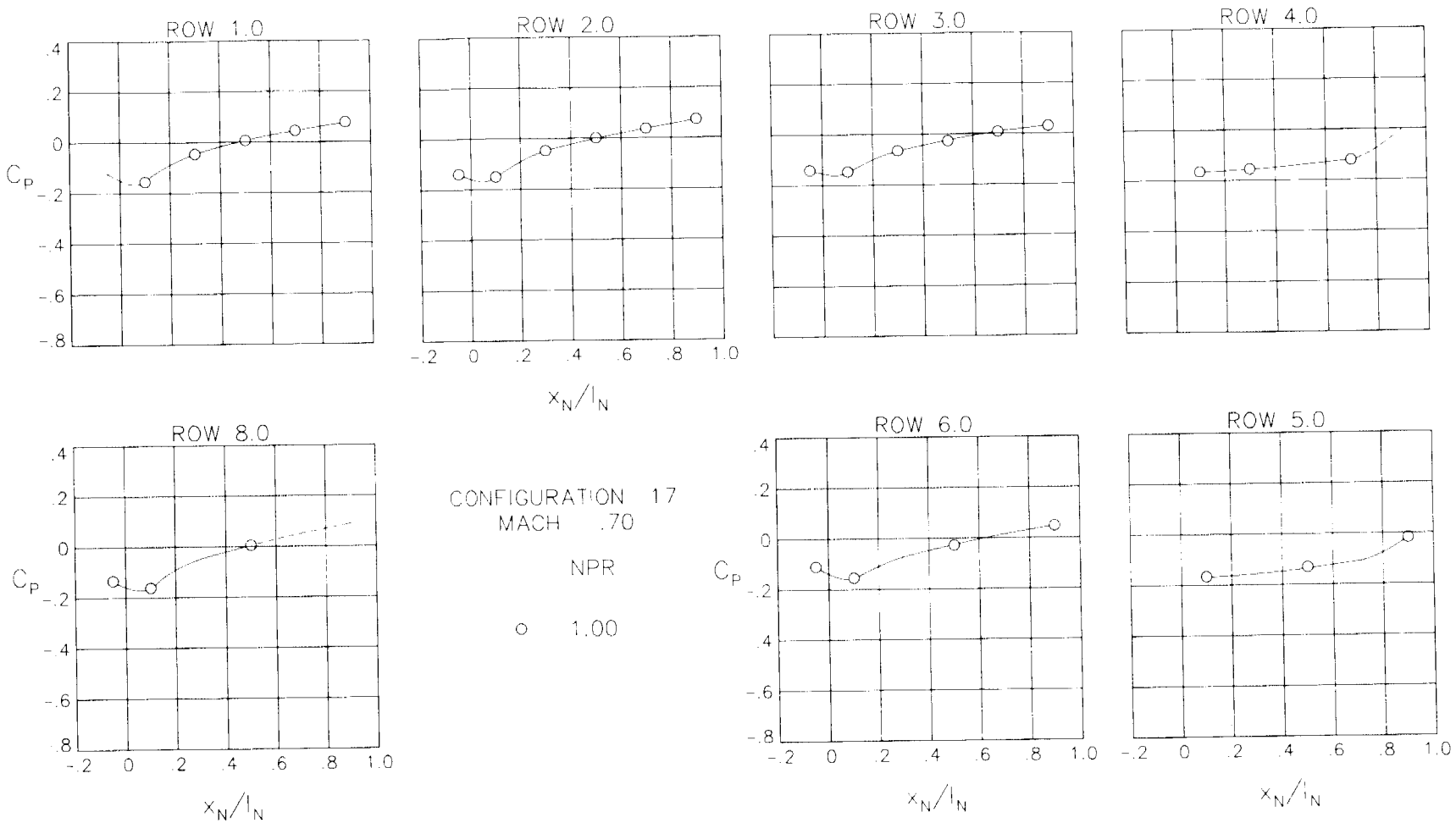

(b) M = 0.70.

Figure 42.- Continued.

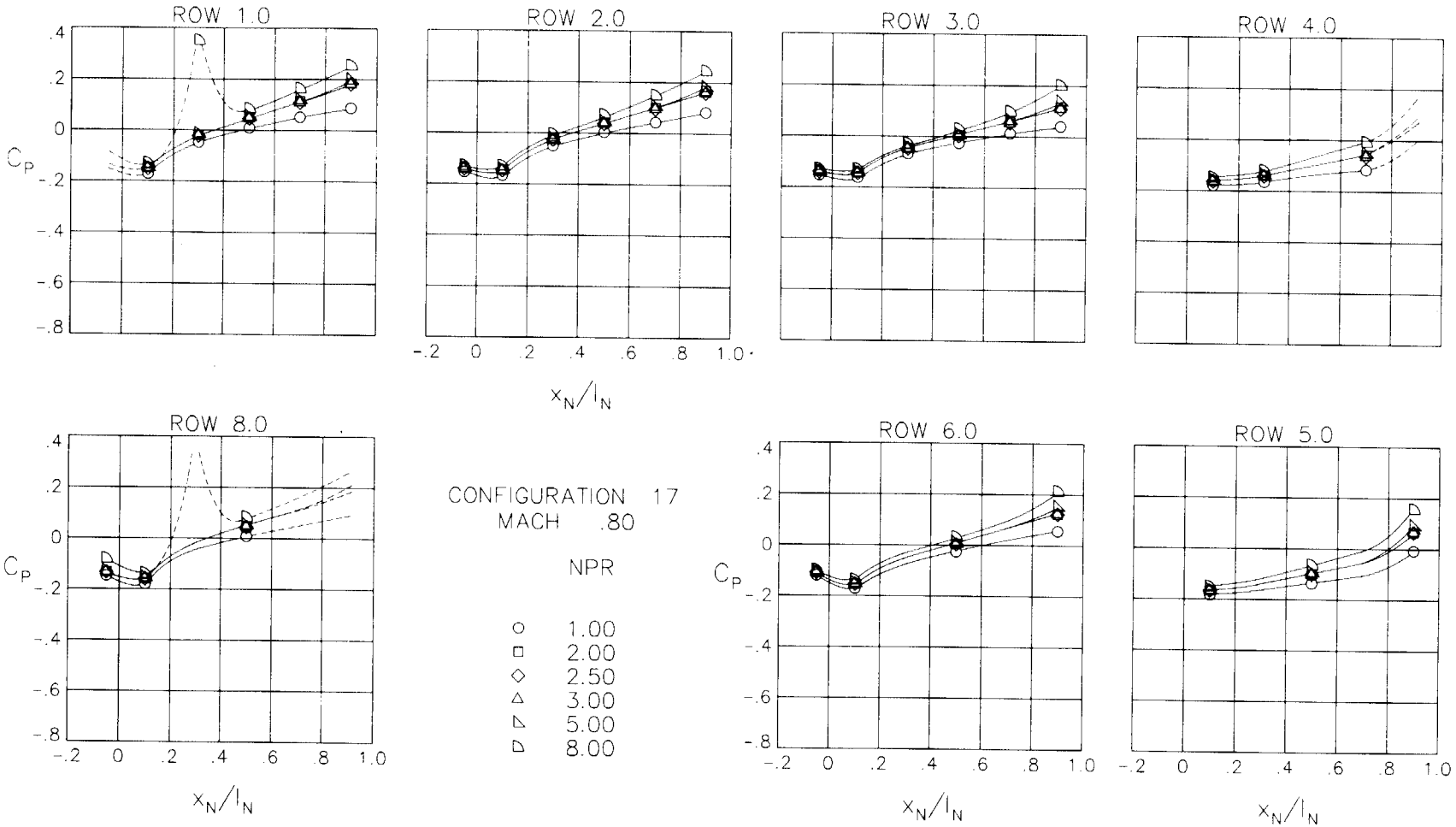

(c) M = 0.80.

Figure 42.- Continued.

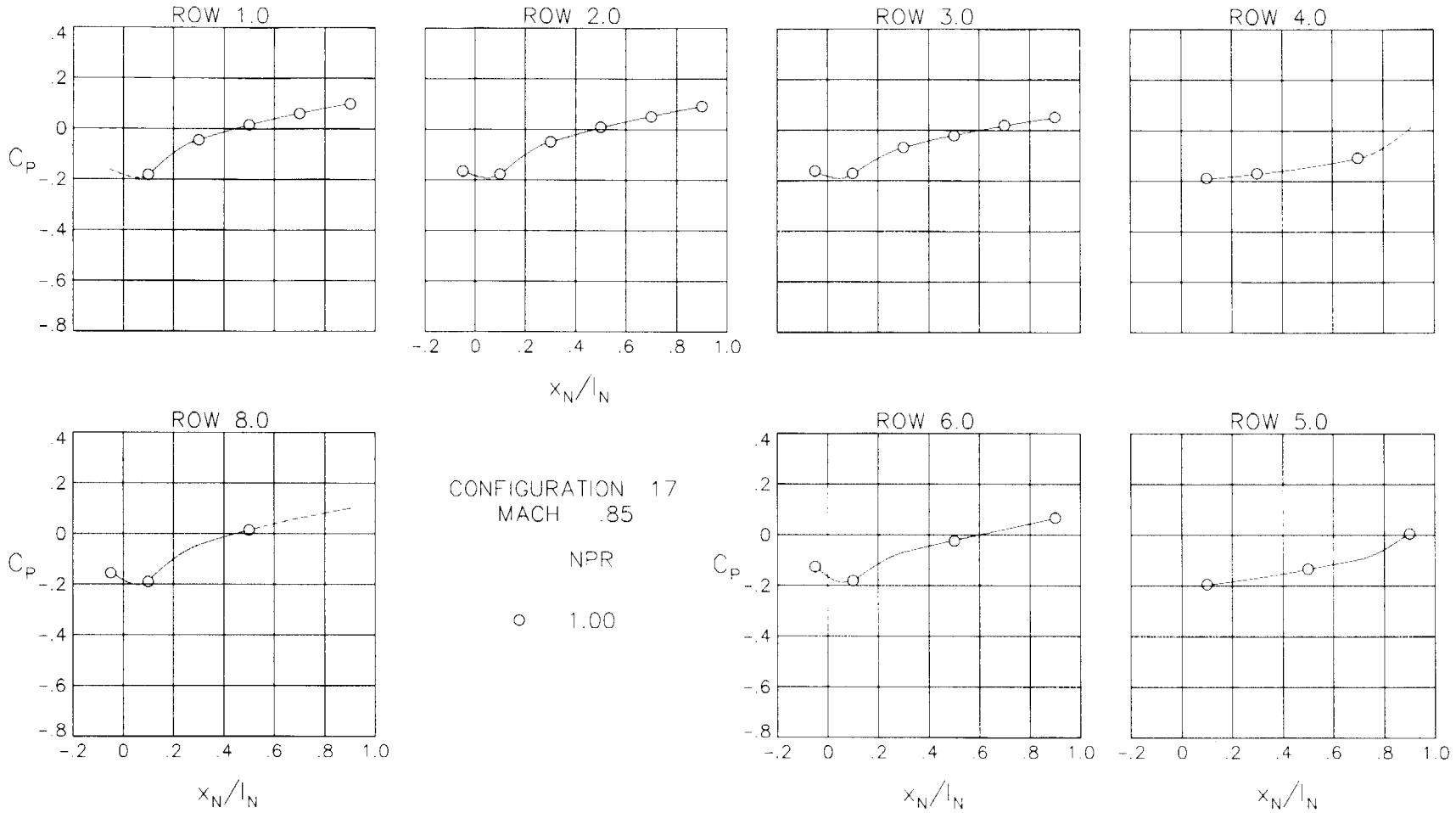

(d) M = 0.85.

Figure 42.- Continued.

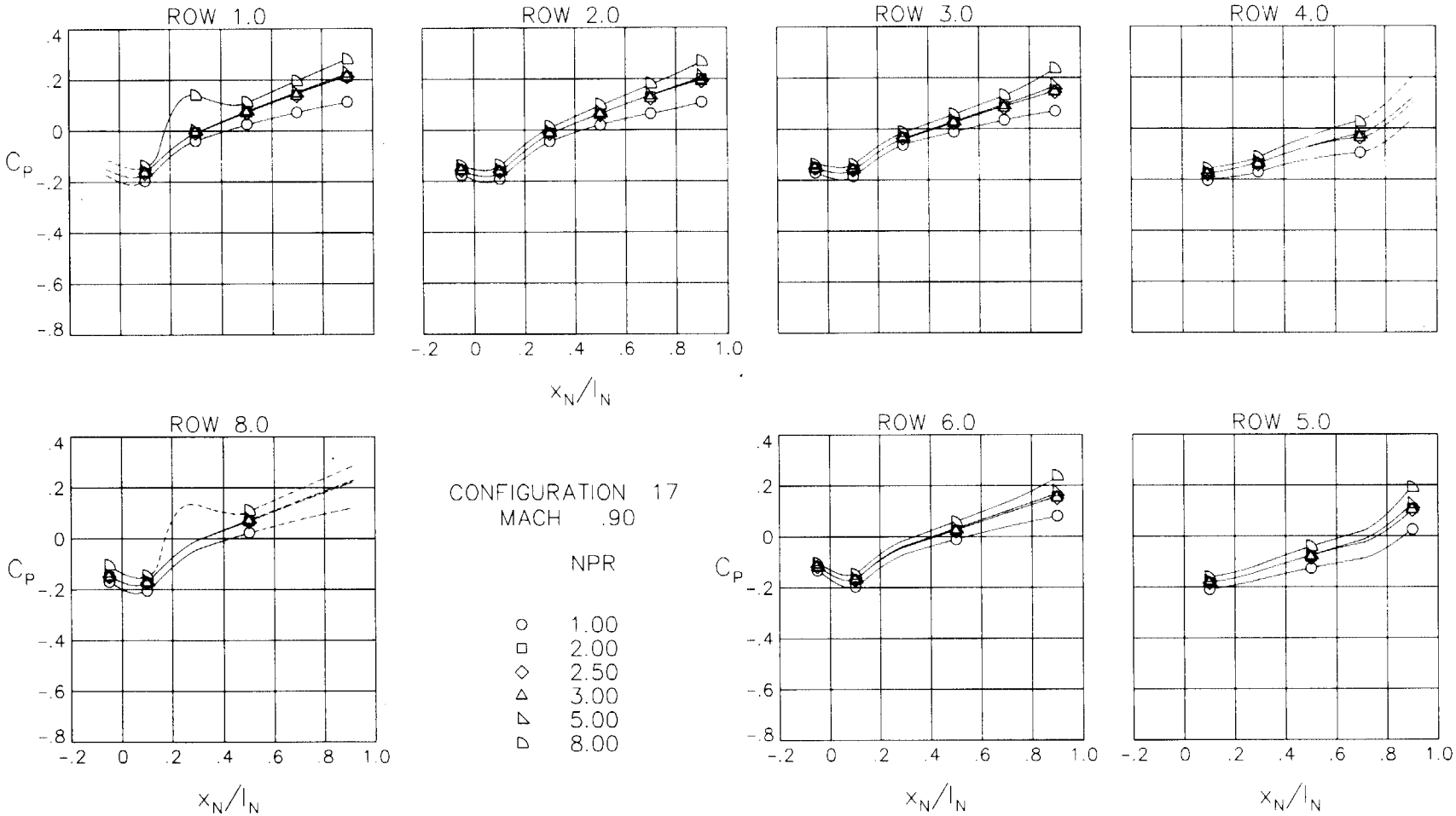

(e) M = 0.90.

Figure 42.- Continued.

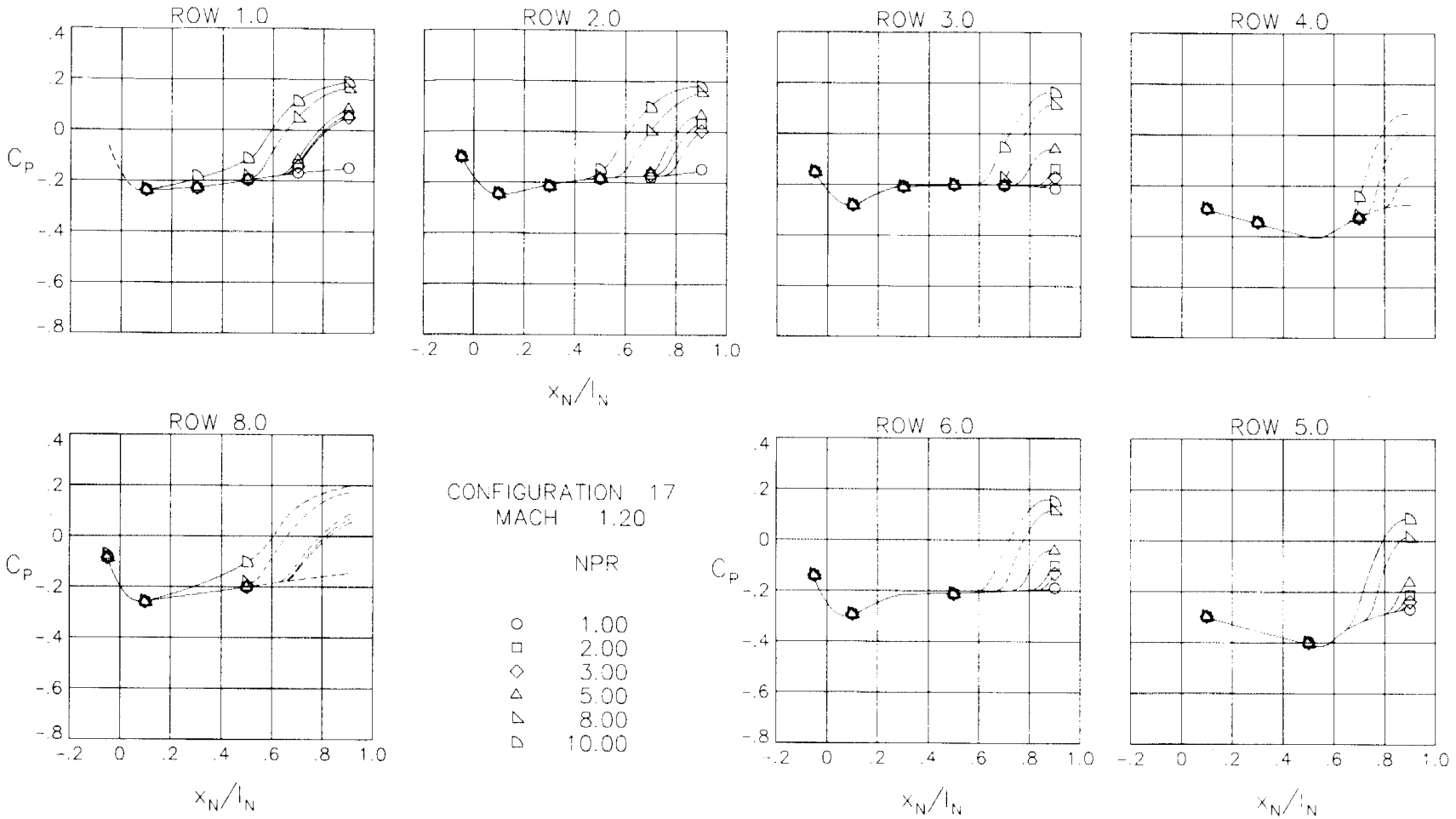

(f) M = 1.20.

Figure 42.- Concluded.

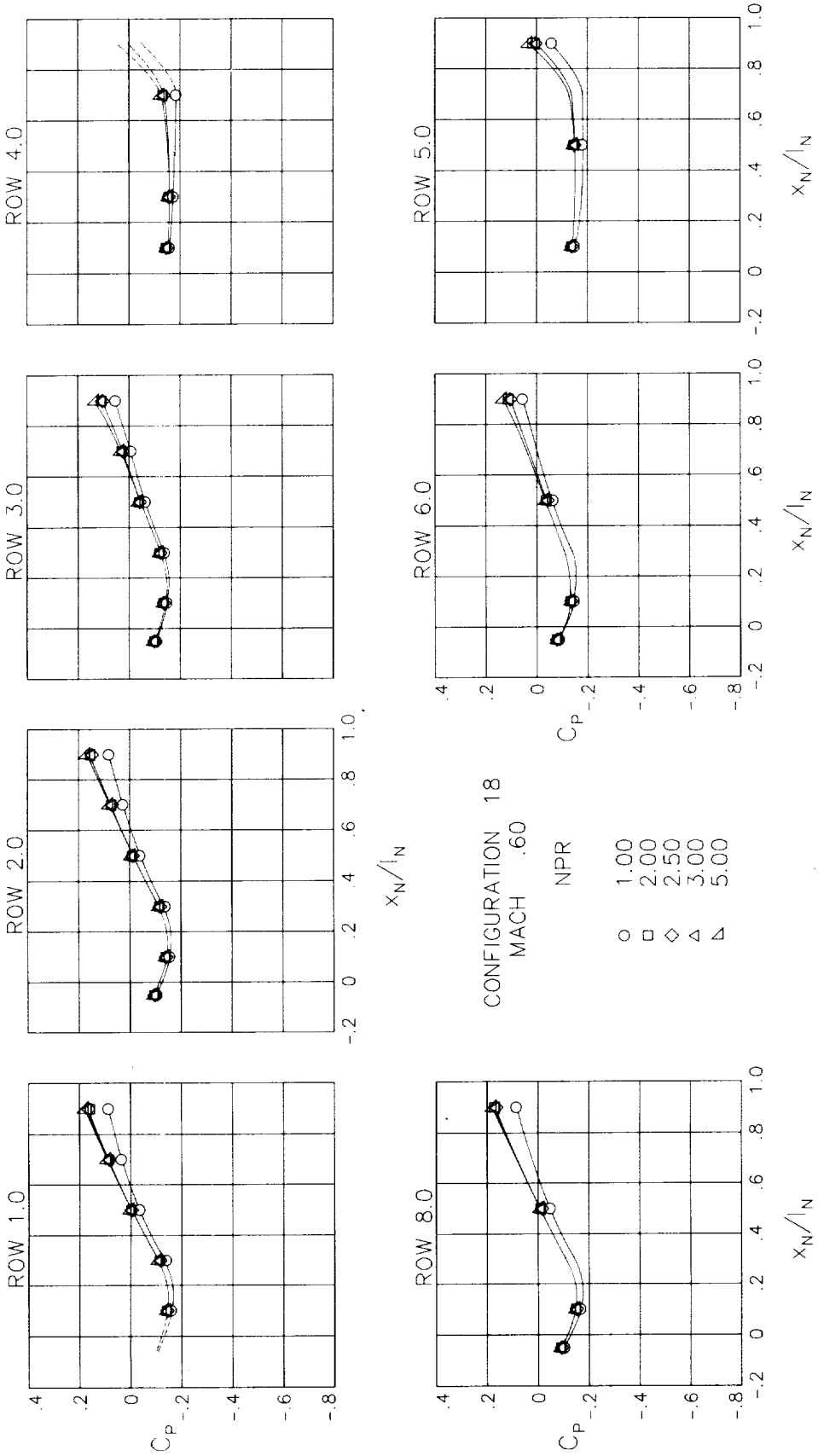

(a) M = 0.60.

Figure 43.- Surface static-pressure coefficient distributions around nozzle for configuration 18. $\alpha = 0°$.

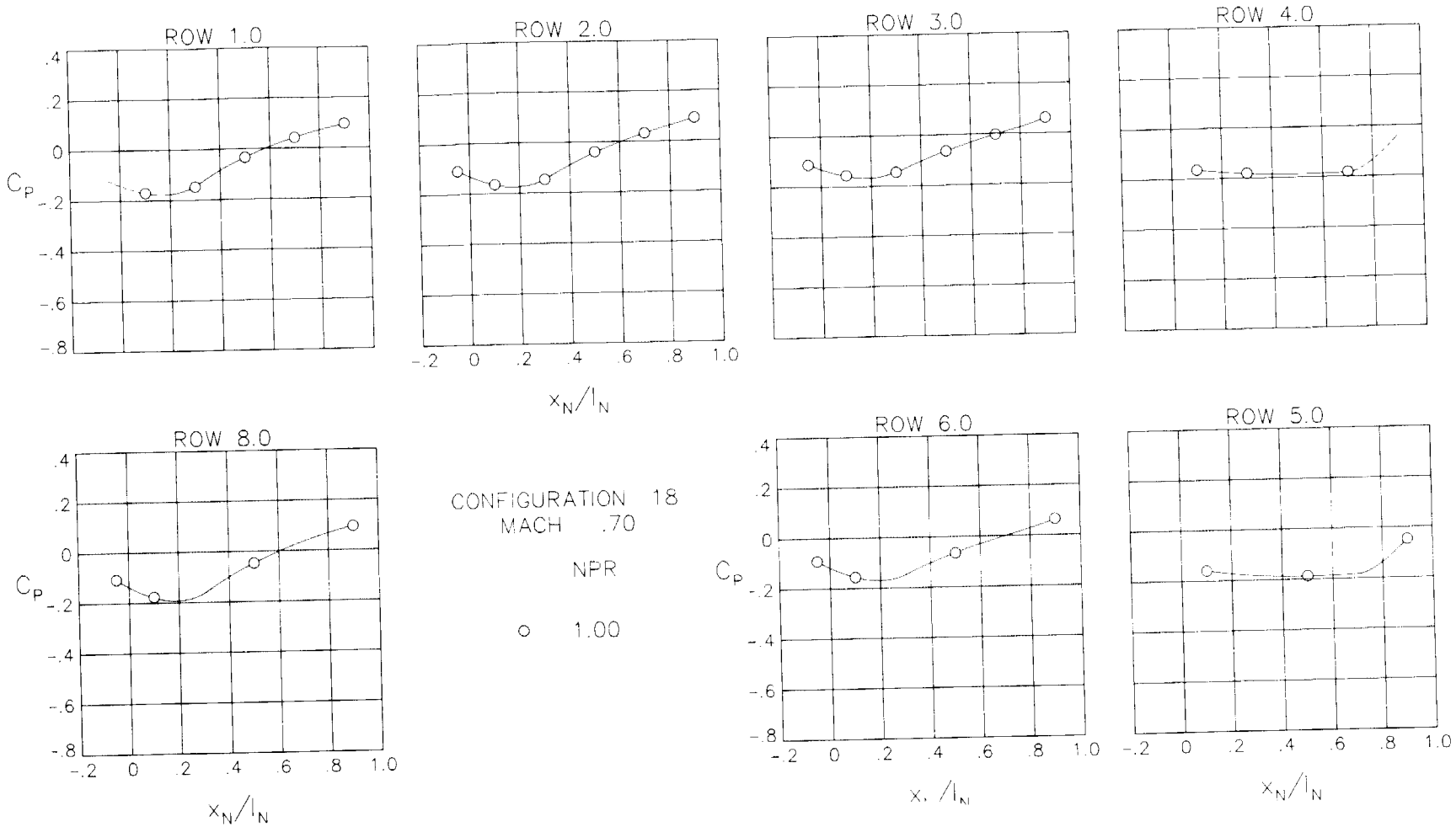

(b) M = 0.70.

Figure 43.- Continued.

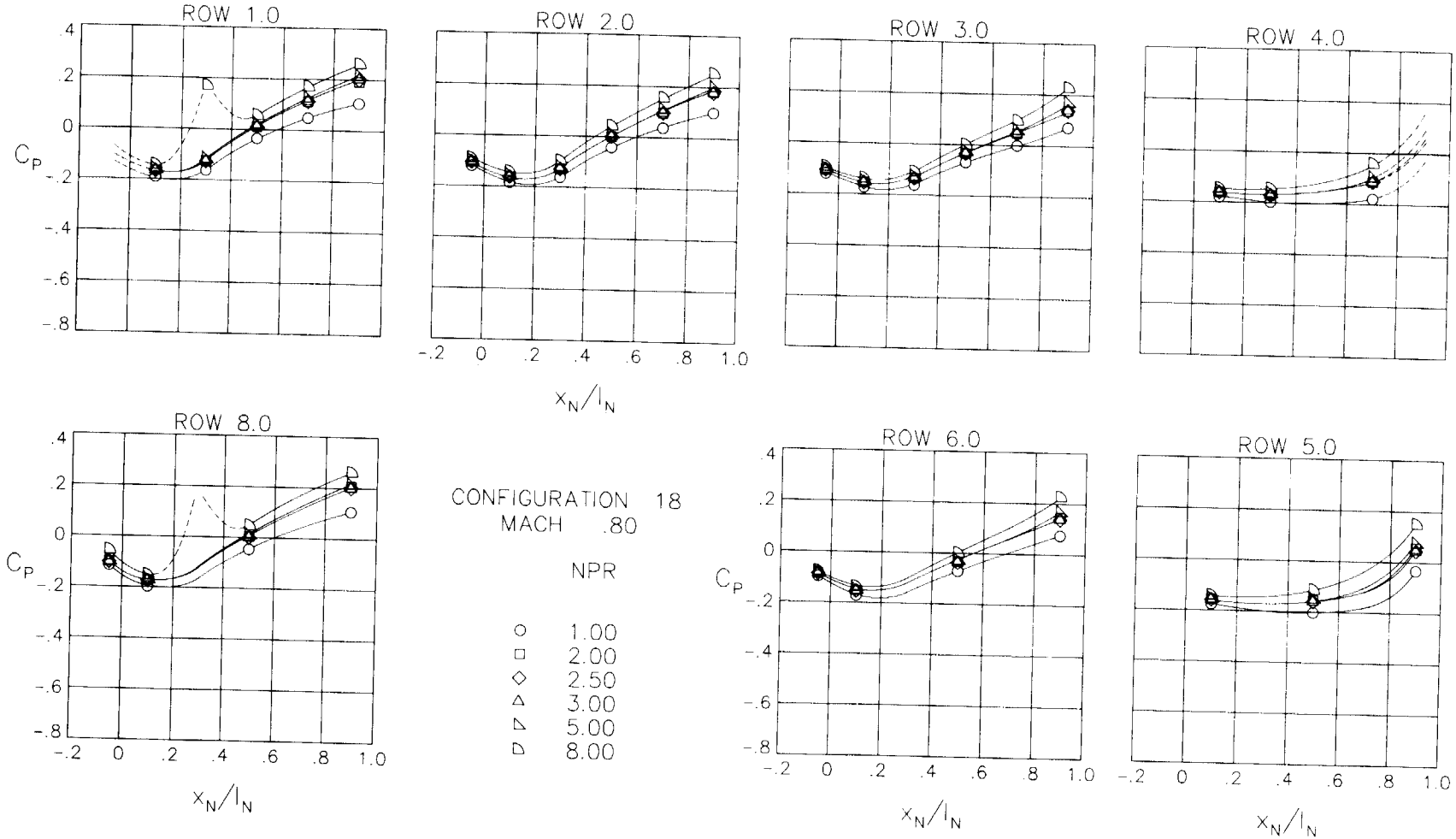

(c) M = 0.80.

Figure 43.- Continued.

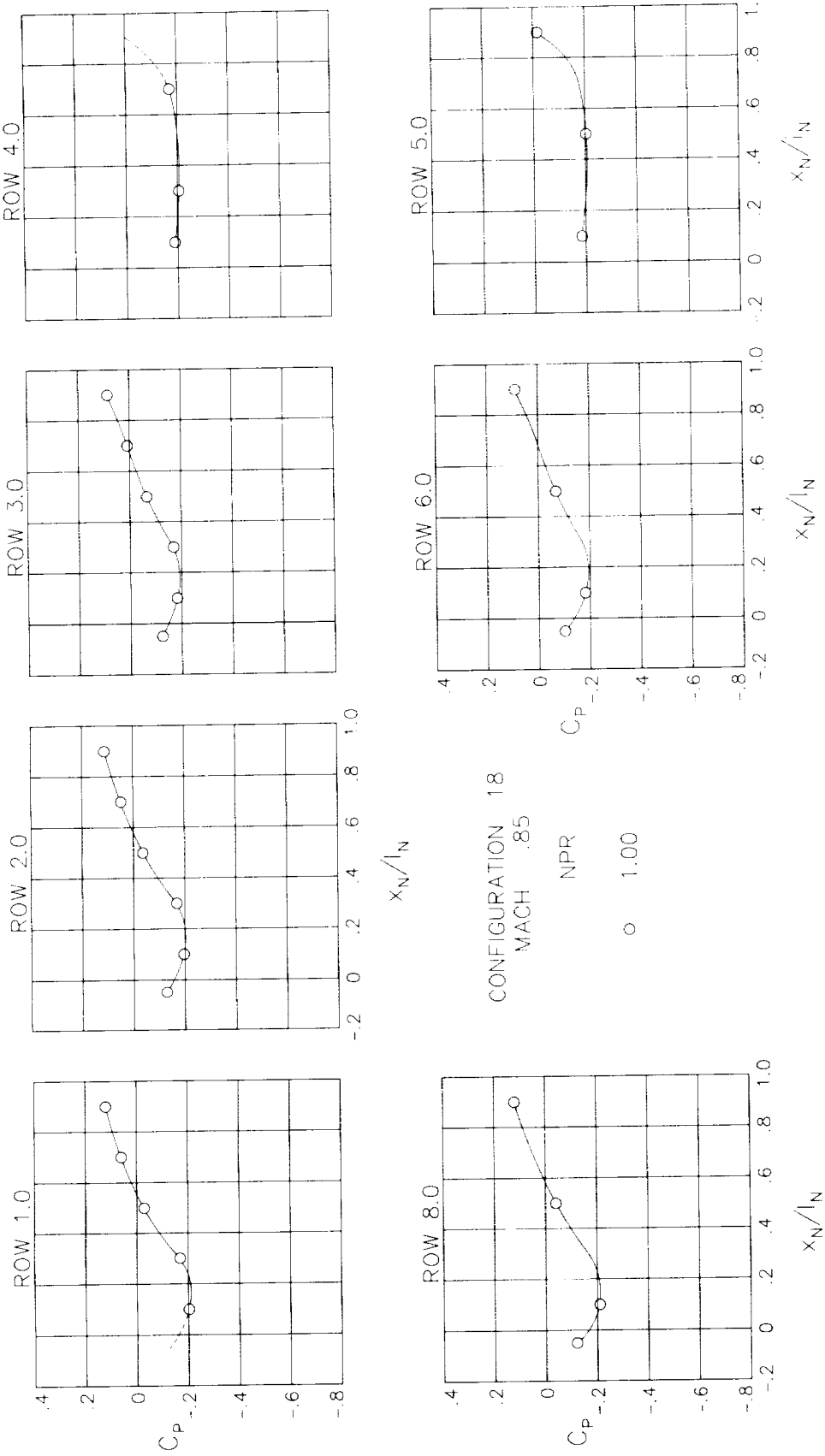

(d) M = 0.85.

Figure 43.- Continued.

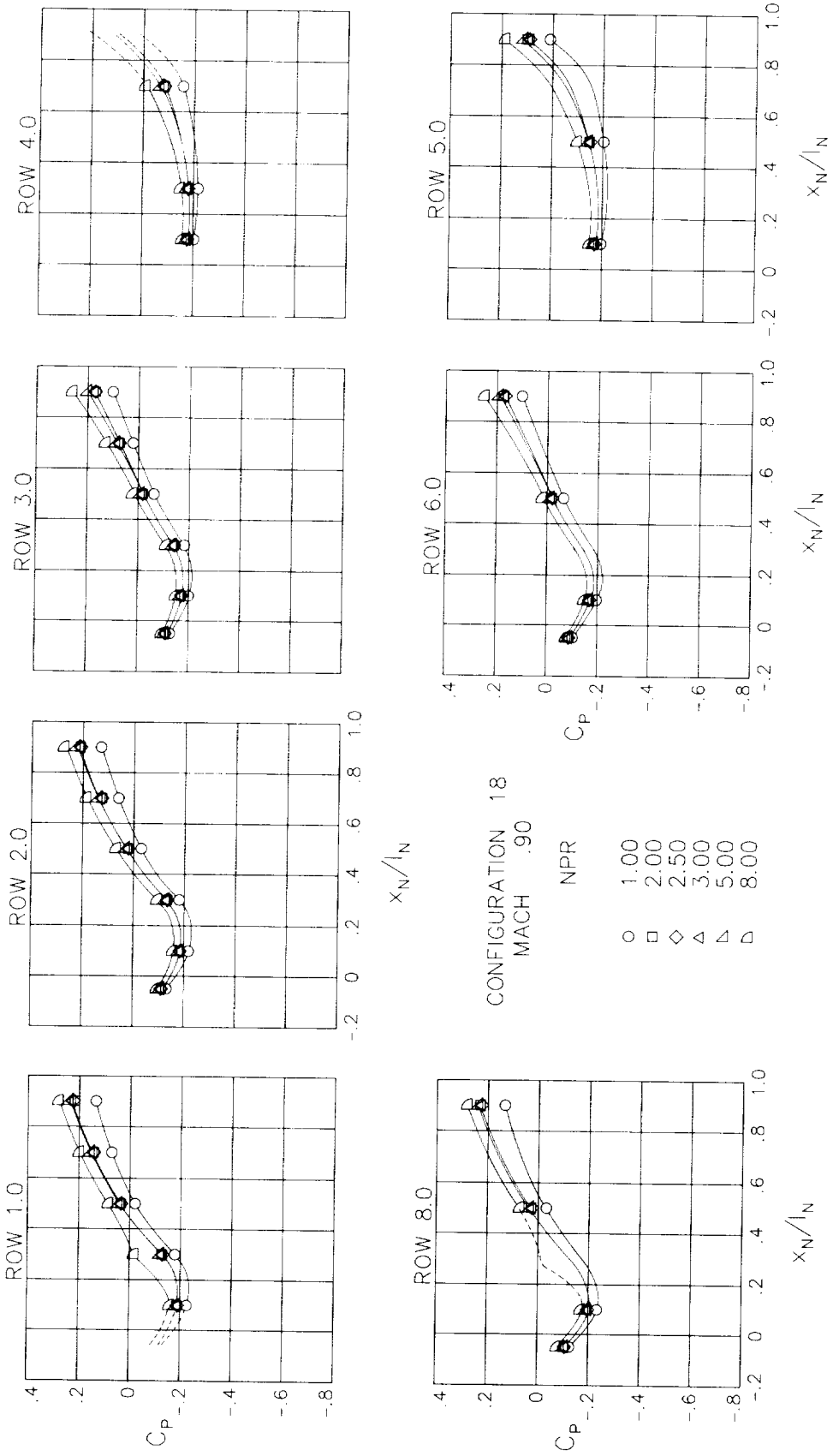

(e) M = 0.90.

Figure 43.- Continued.

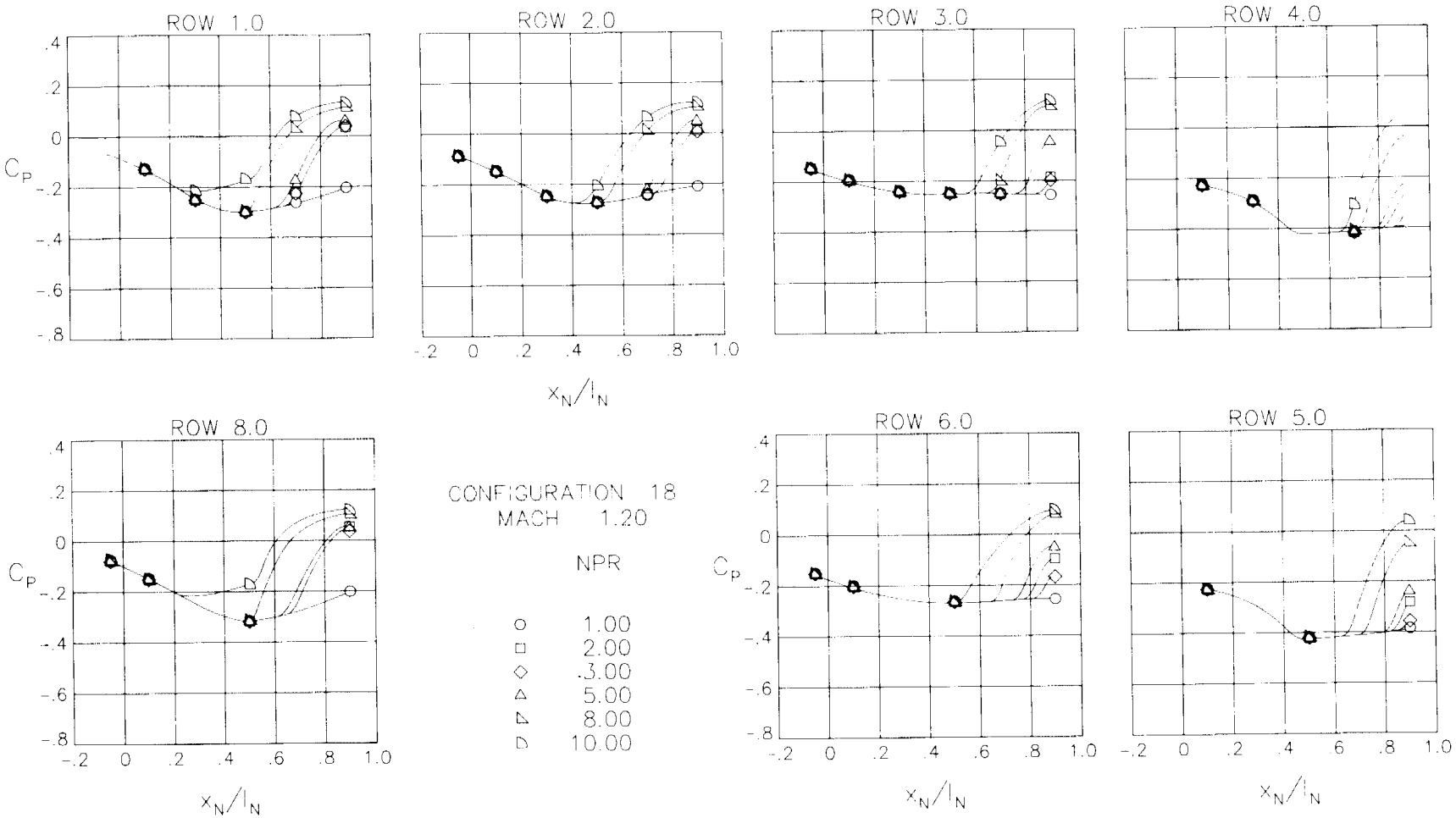

(f) M = 1.20.

Figure 43.- Concluded.

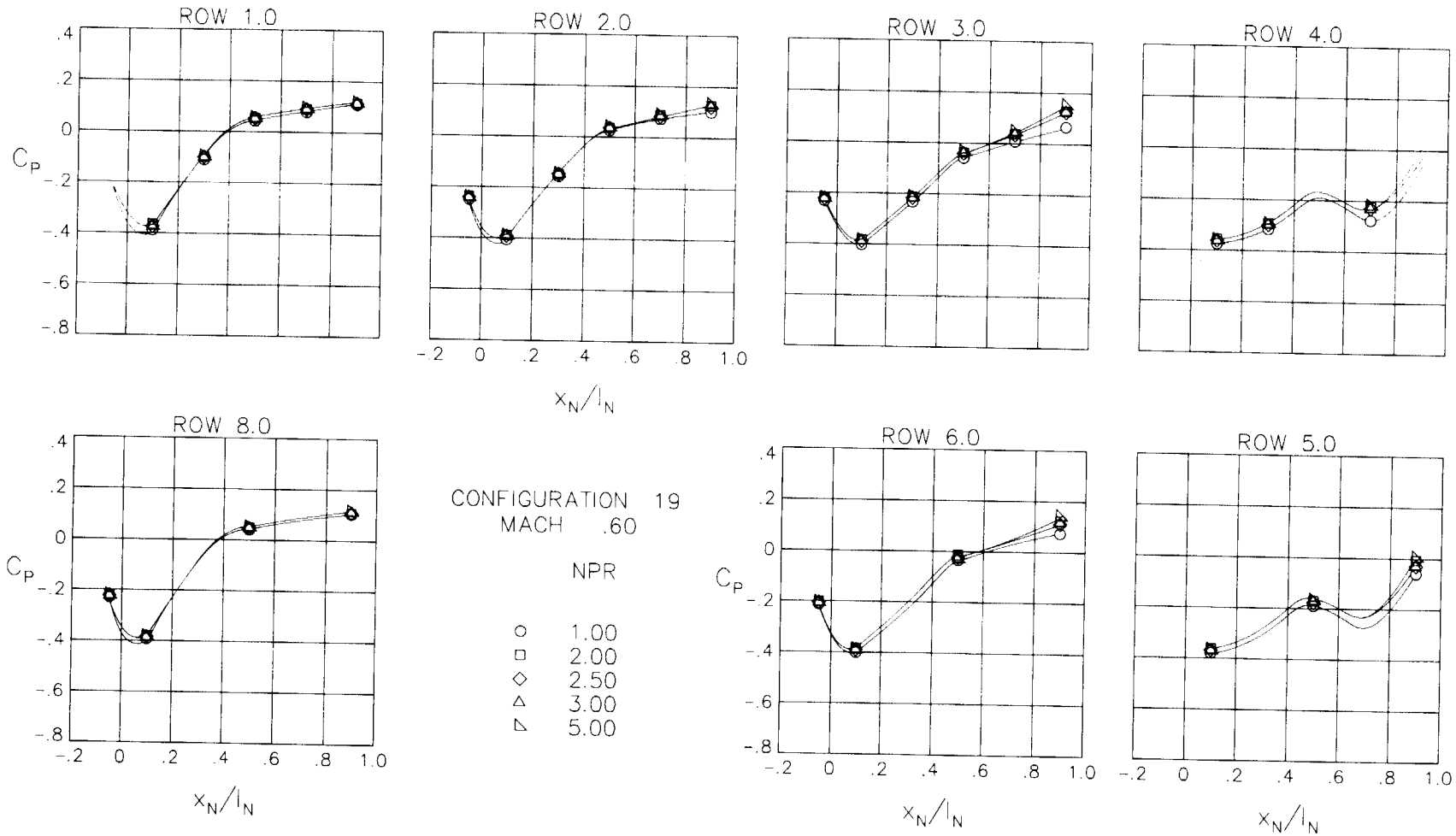

(a) M = 0.60.

Figure 44.- Surface static-pressure coefficient distributions around nozzle for configuration 19. $\alpha = 0°$.

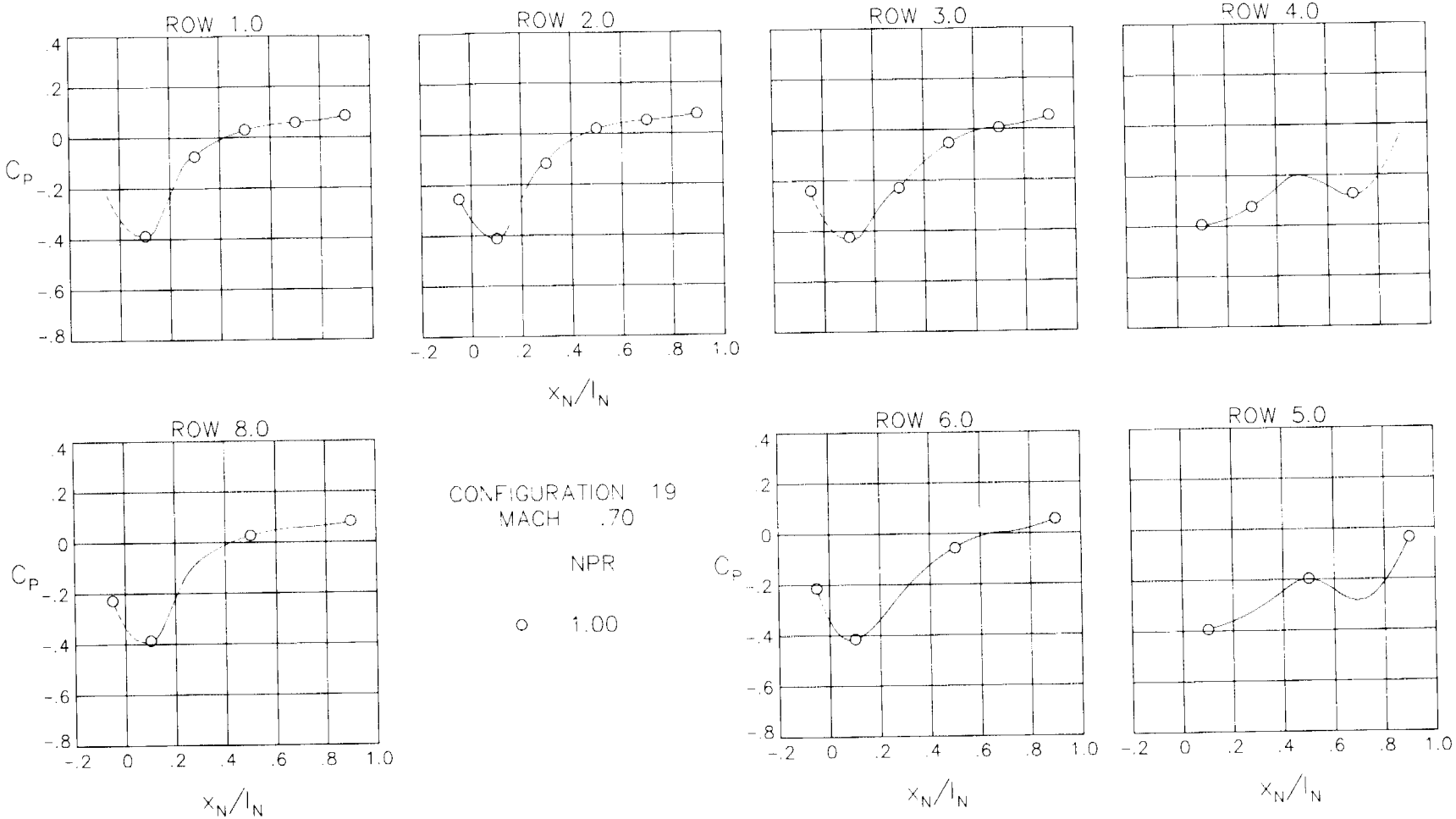

(b) M = 0.70.

Figure 44.- Continued.

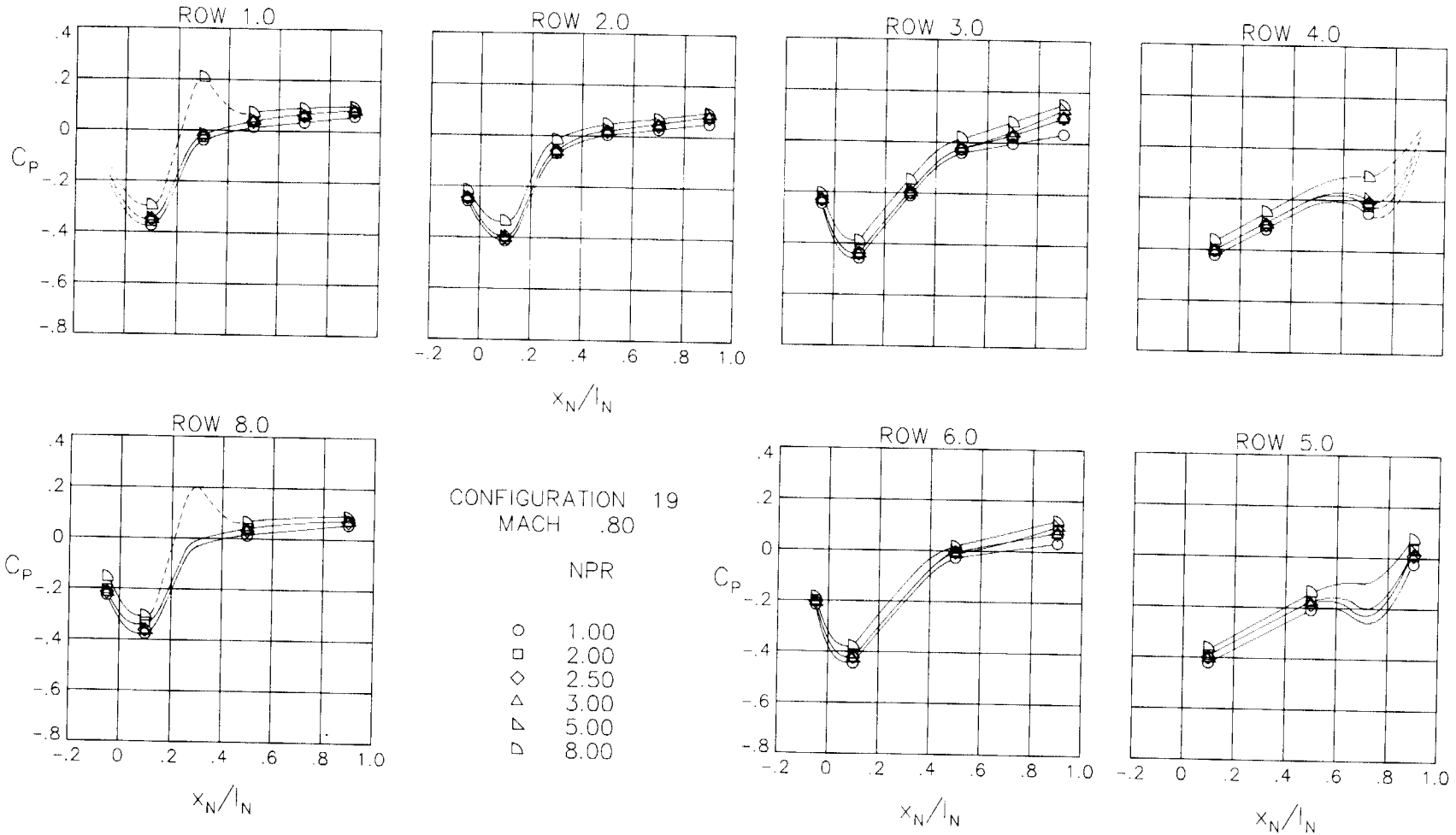

(c) M = 0.80.

Figure 44.- Continued.

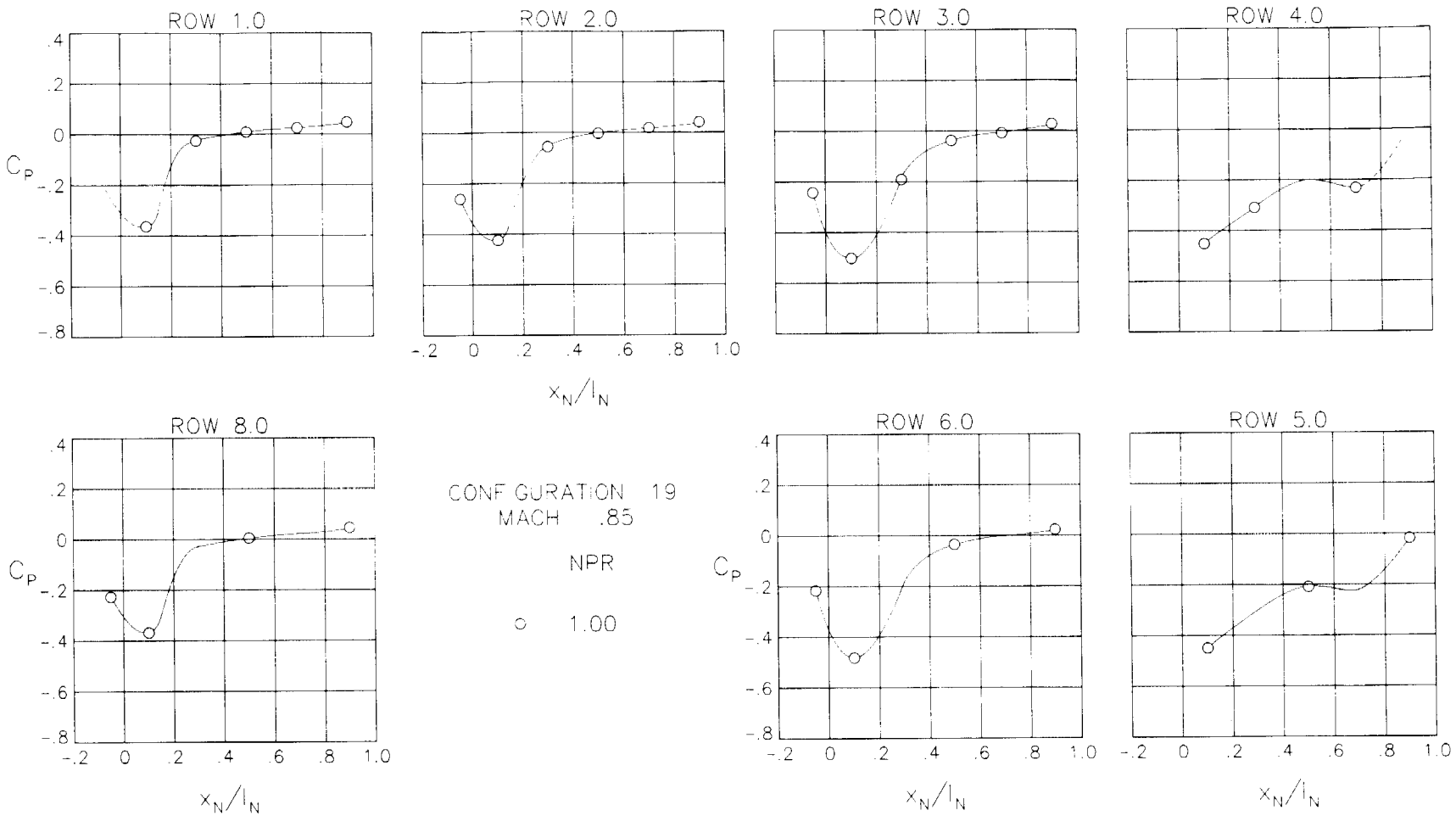

(d) M = 0.85.

Figure 44.- Continued.

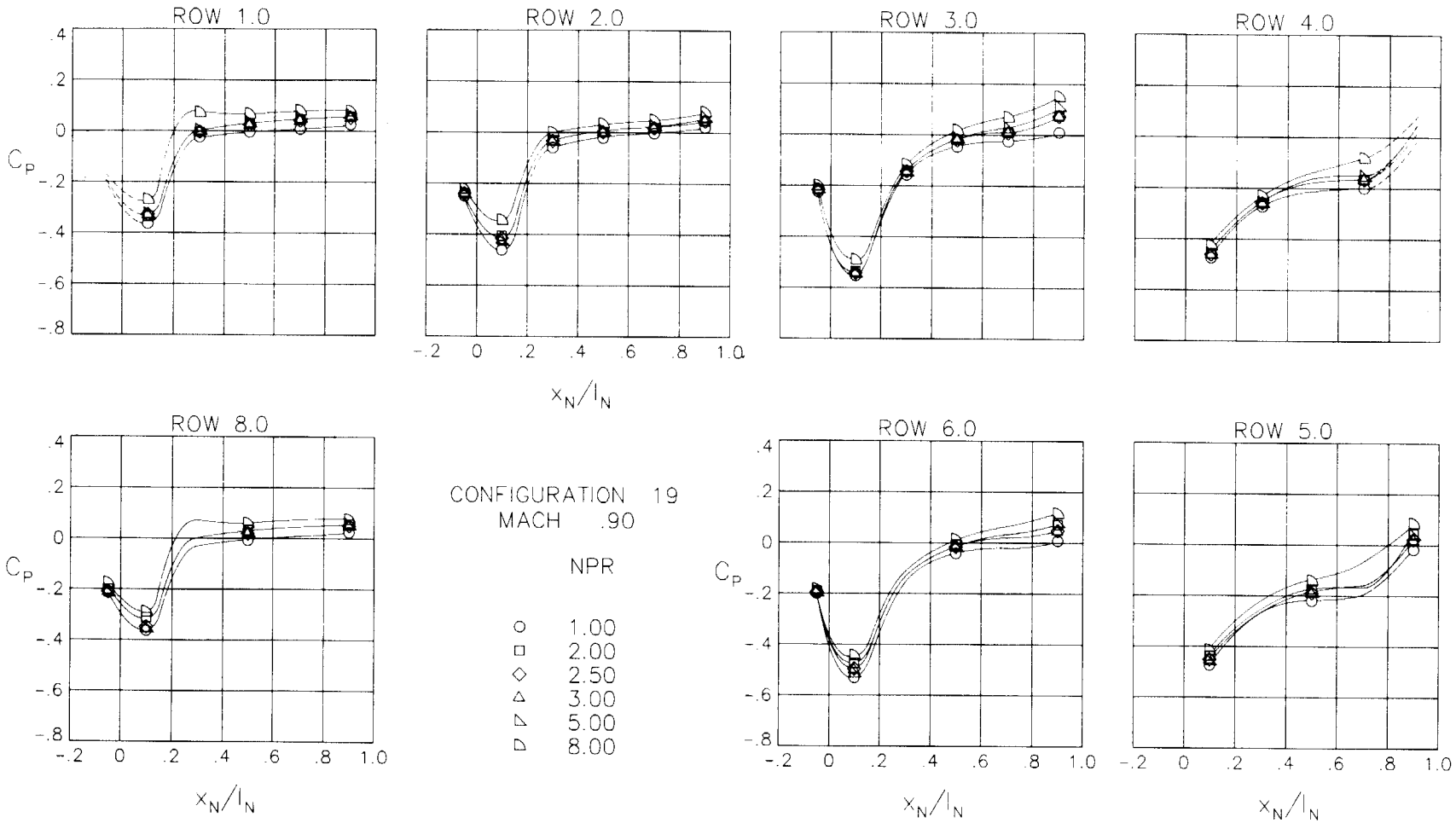

(e) M = 0.90.

Figure 44.- Continued.

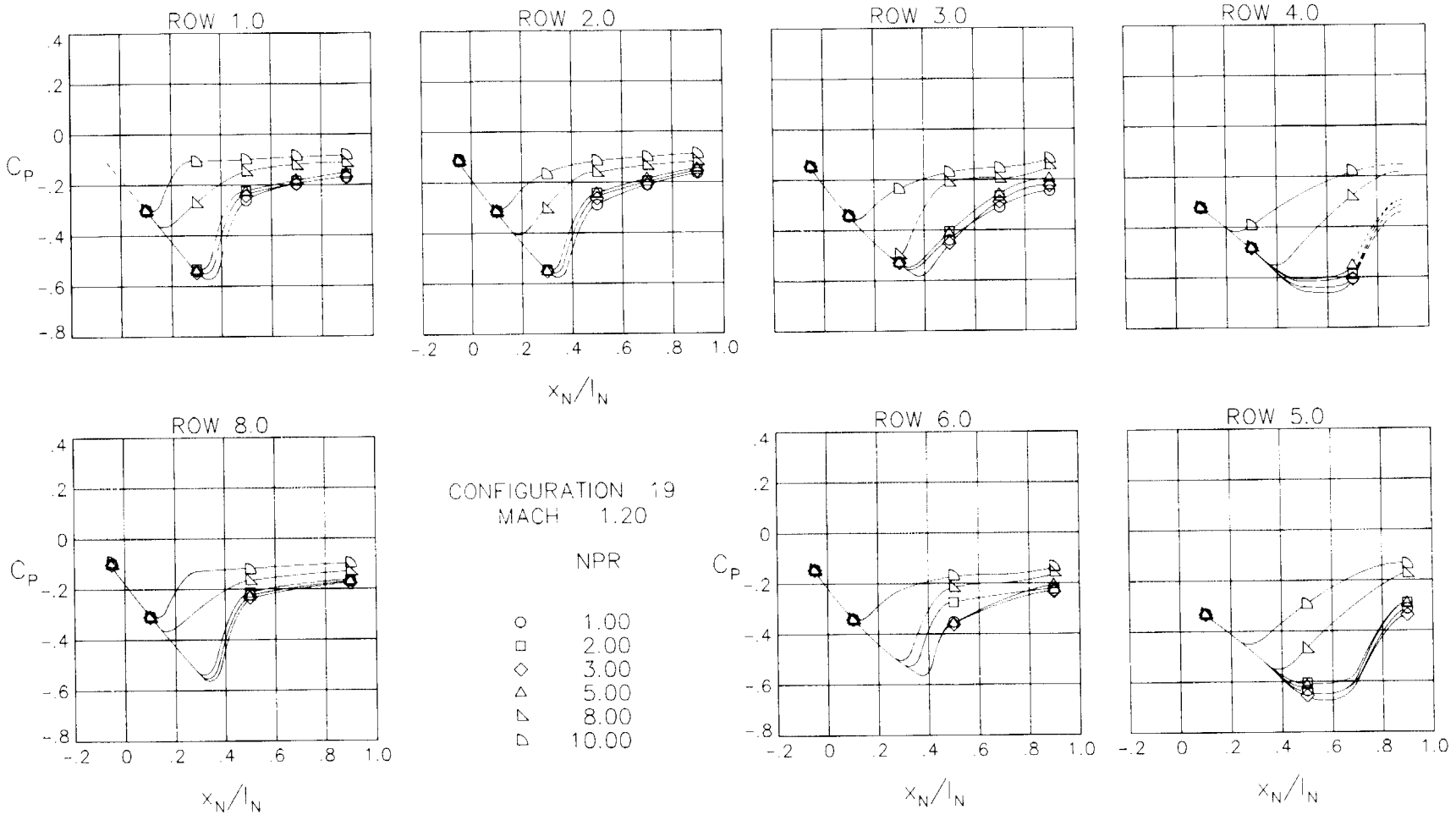

(f) M = 1.20.

Figure 44.- Concluded.

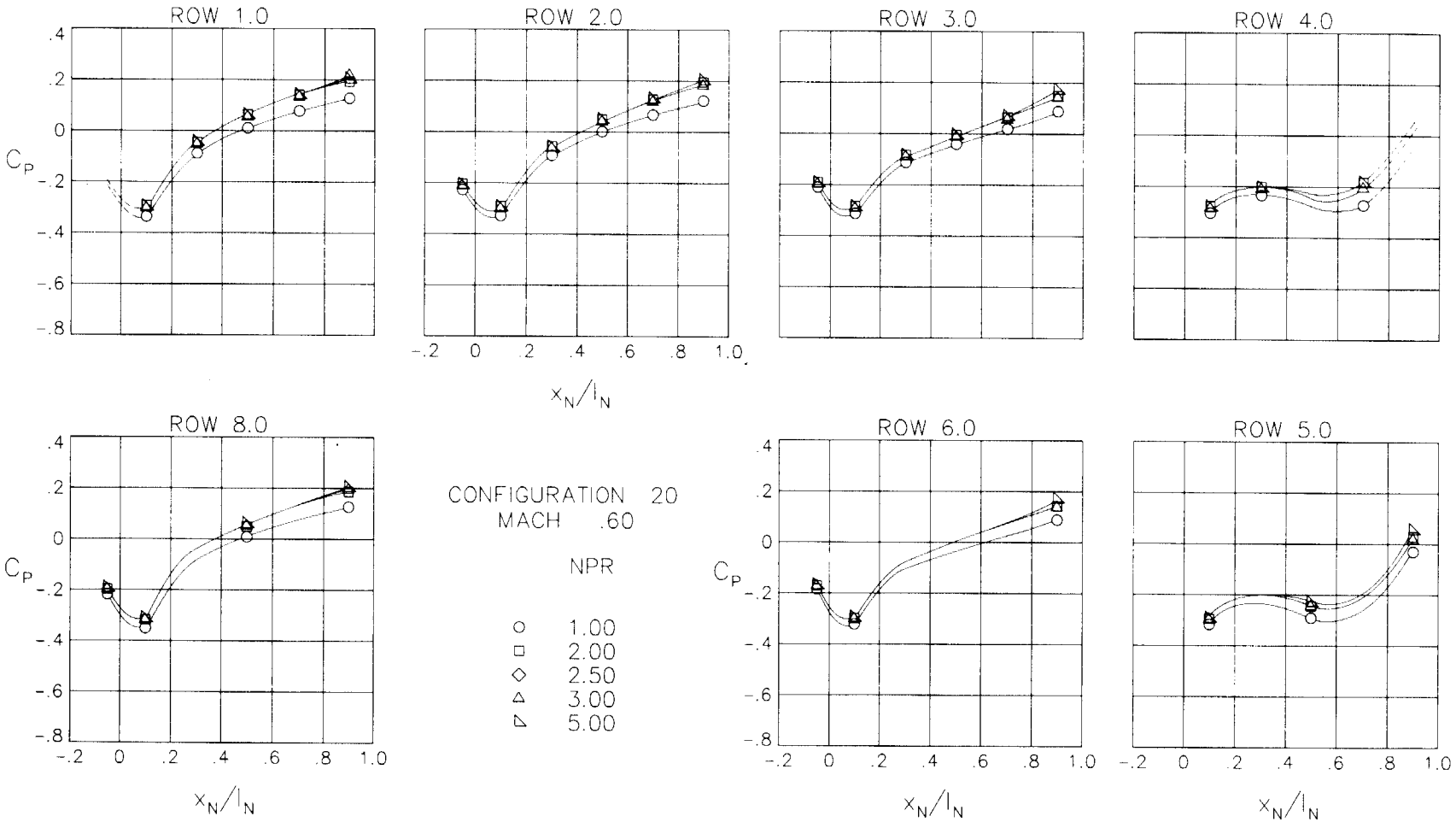

(a) M = 0.60.

Figure 45.- Surface static-pressure coefficient distributions around nozzle for configuration 20. $\alpha = 0°$.

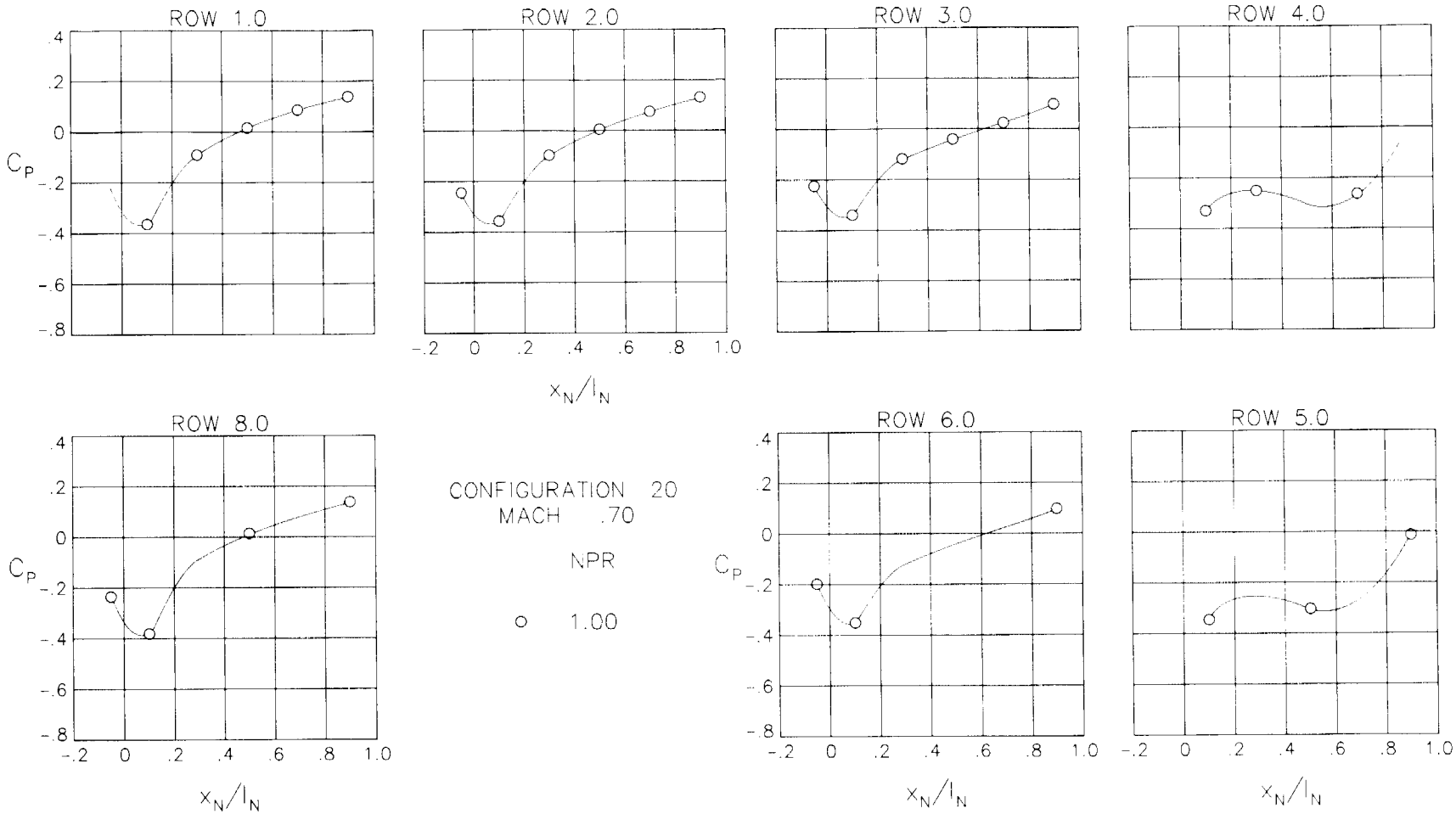

(b) M = 0.70.

Figure 45.- Continued.

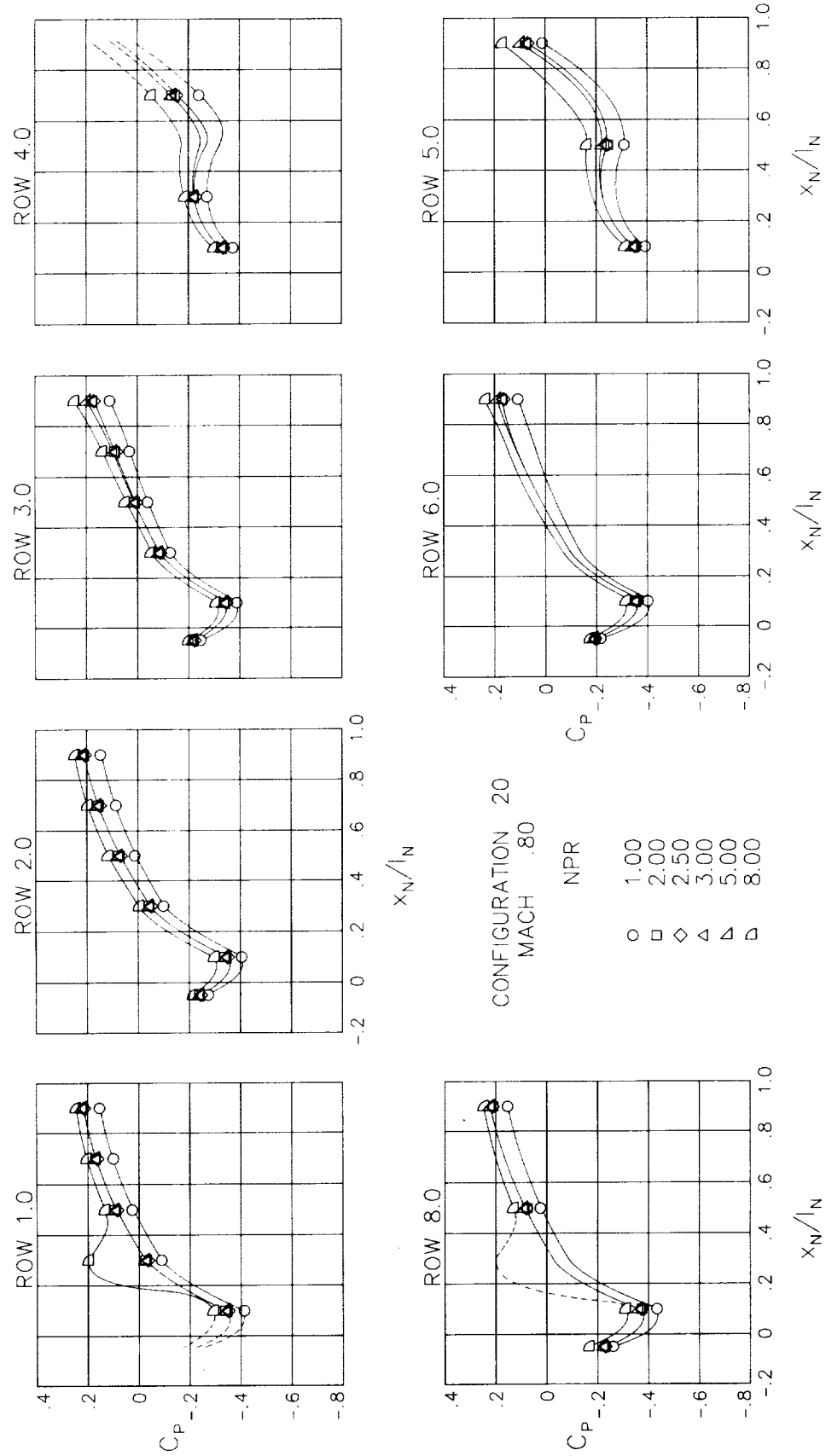

(c) M = 0.80.

Figure 45.- Continued.

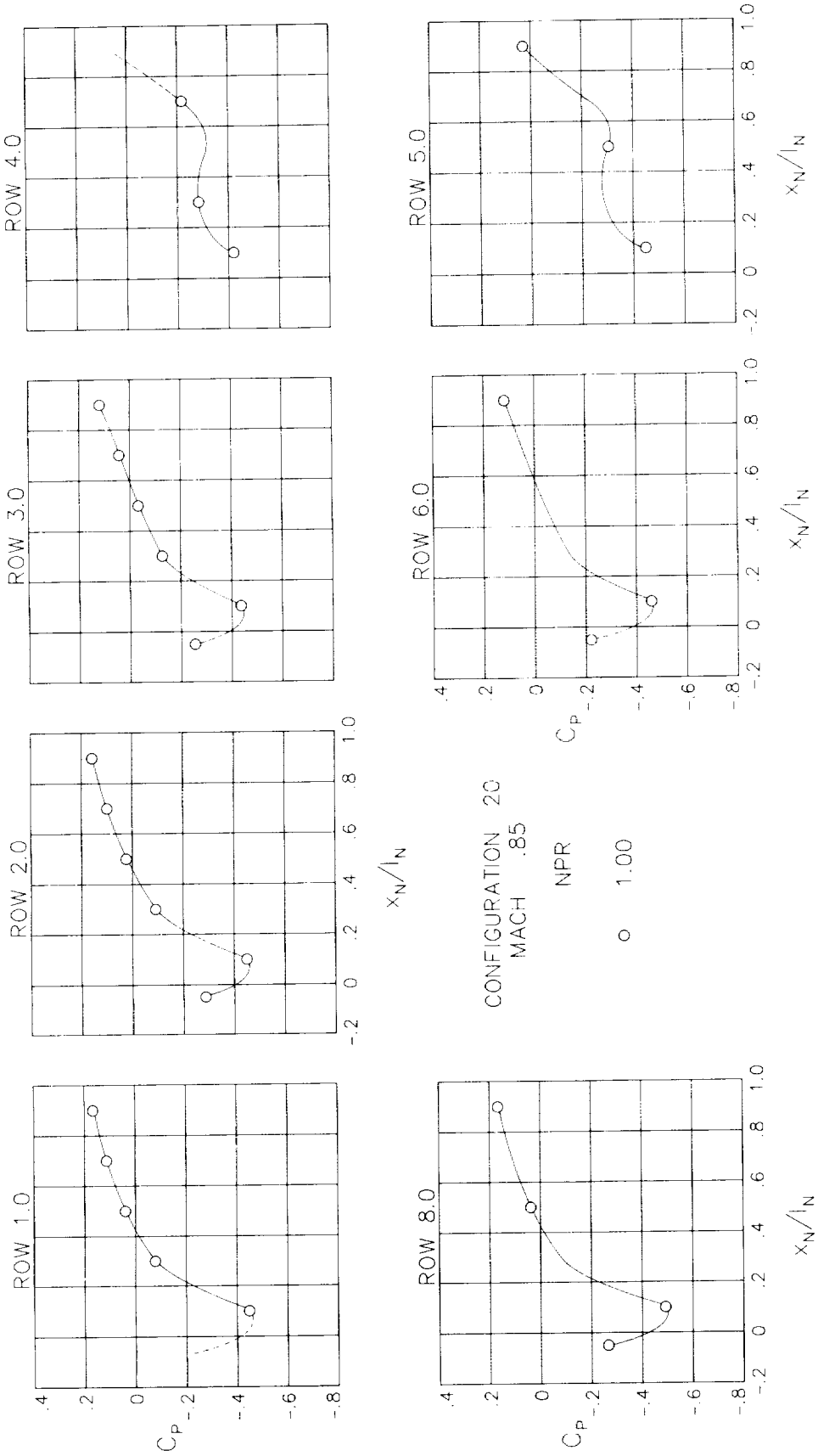

(d) M = 0.85.

Figure 45.- Continued.

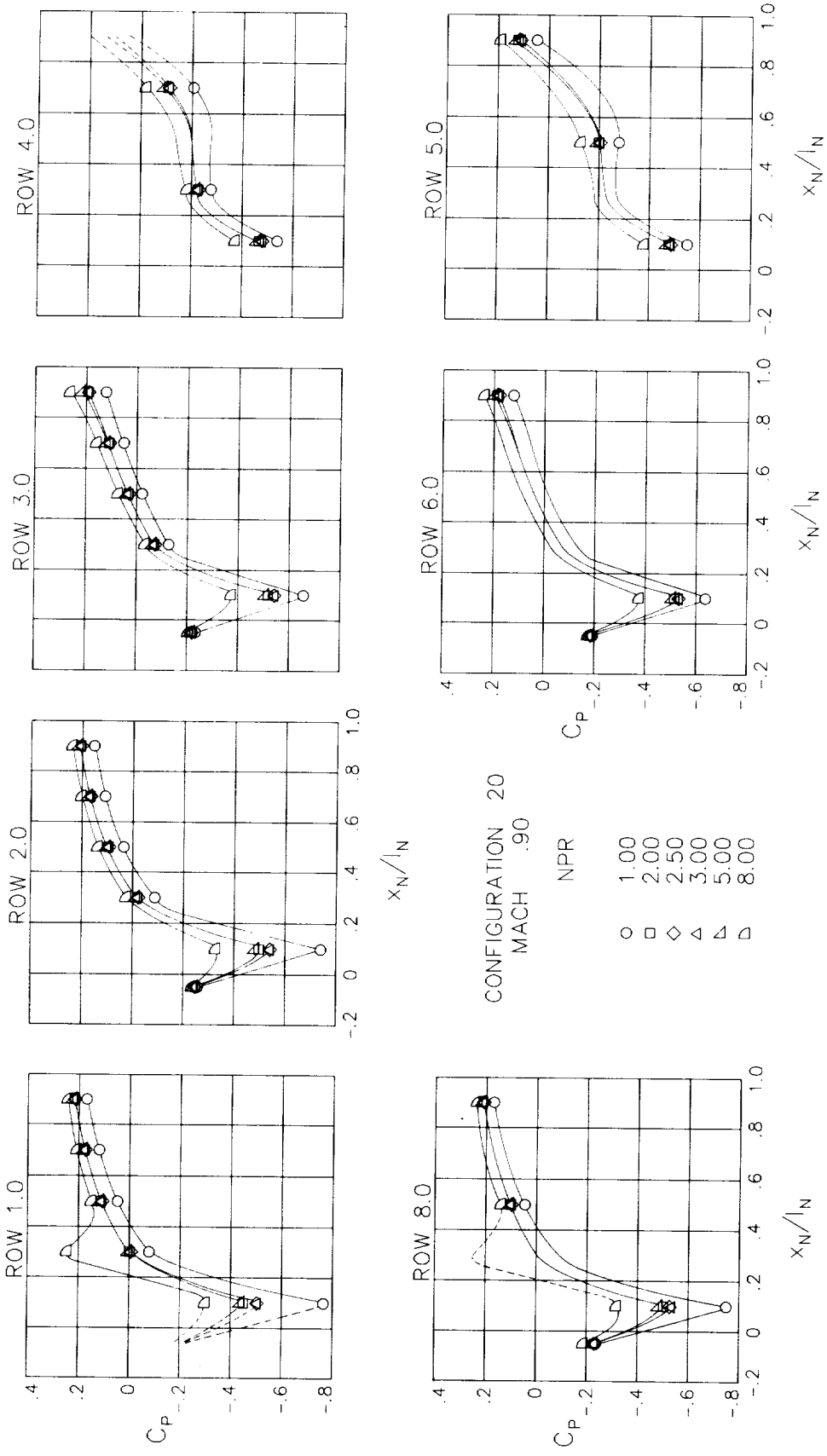

(e) M = 0.90.

Figure 45.- Continued.

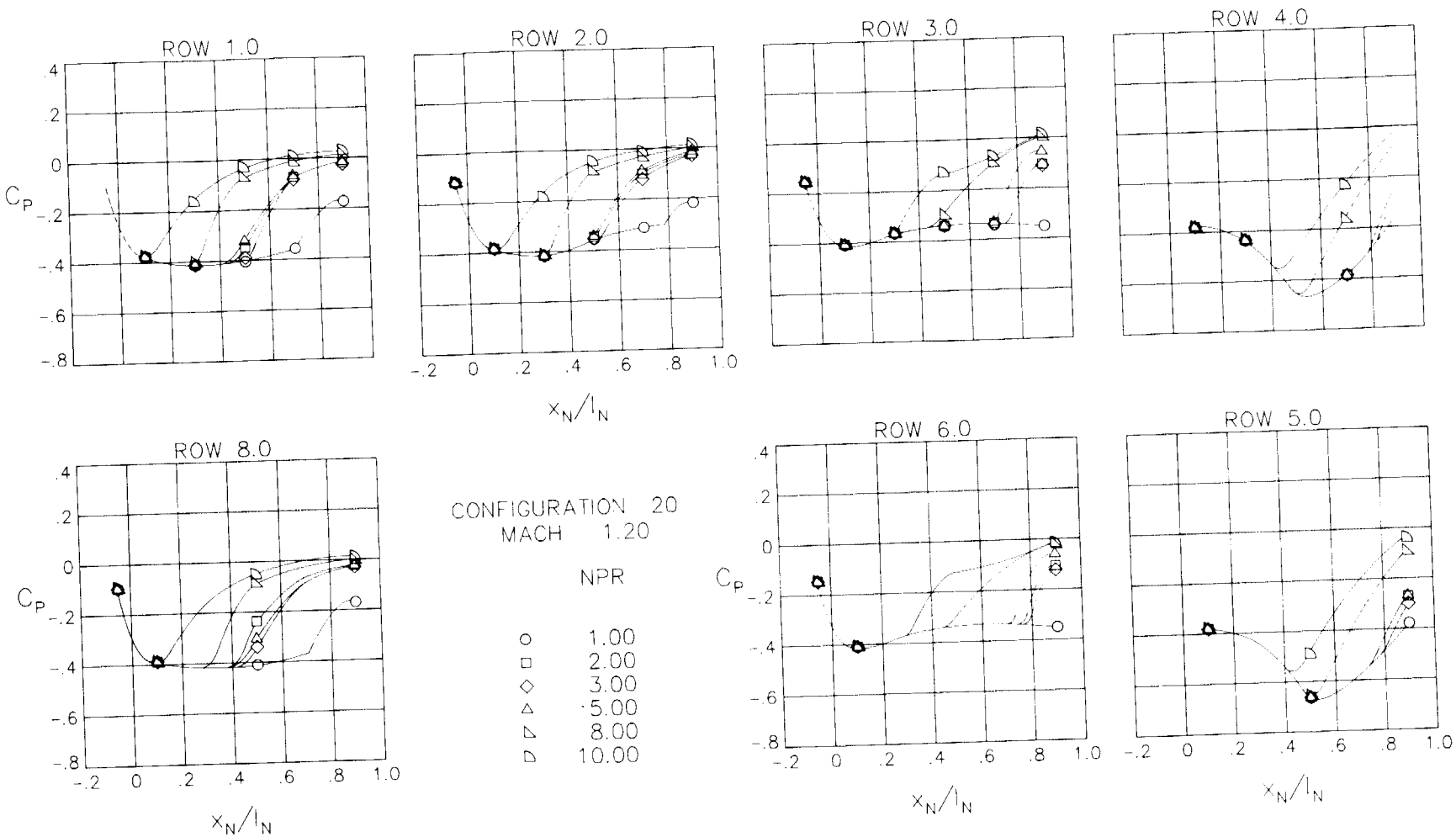

(f) M = 1.20.

Figure 45.- Concluded.

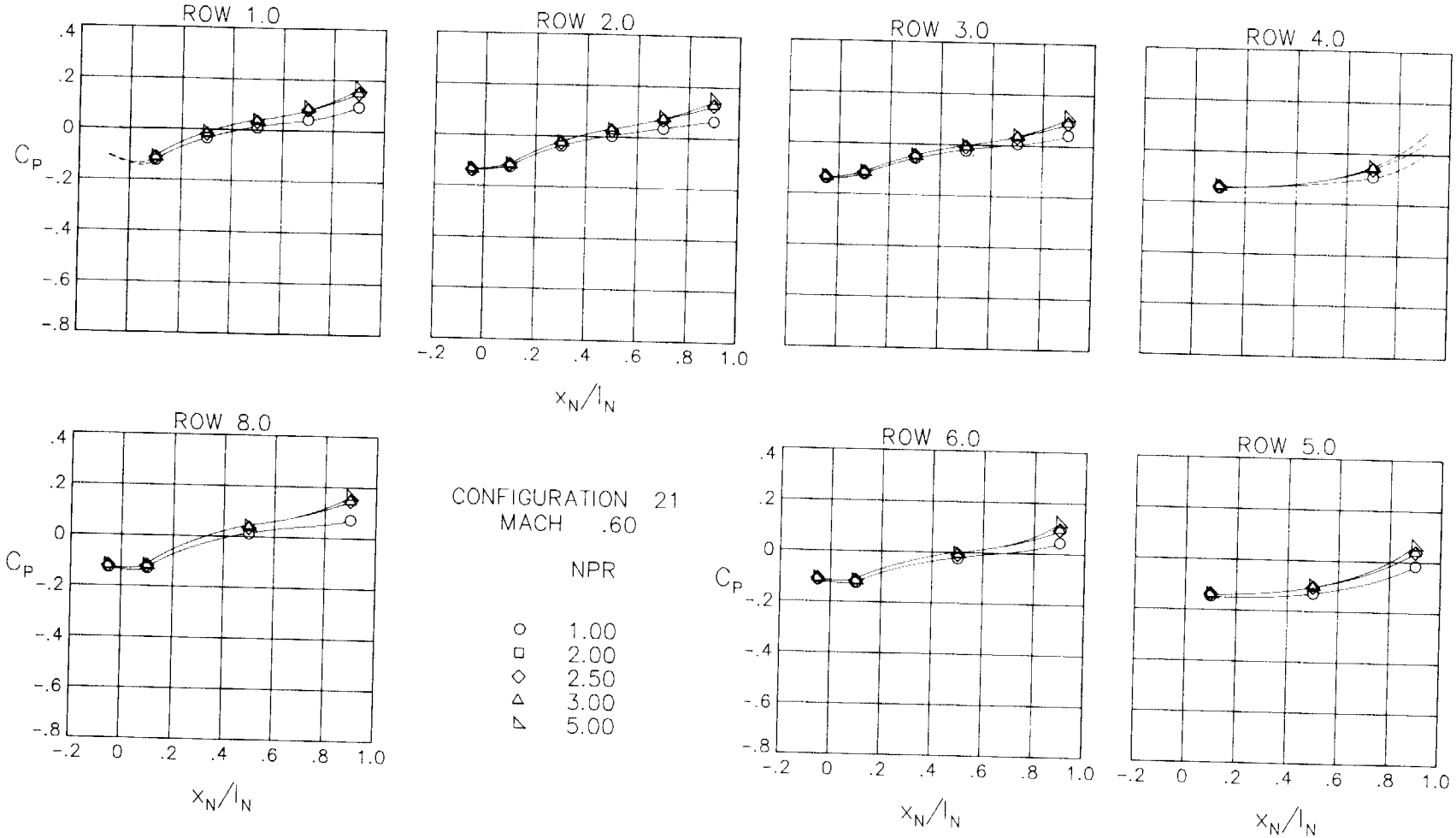

(a) M = 0.60.

Figure 46.- Surface static-pressure coefficient distributions around nozzle for configuration 21. $\alpha = 0°$.

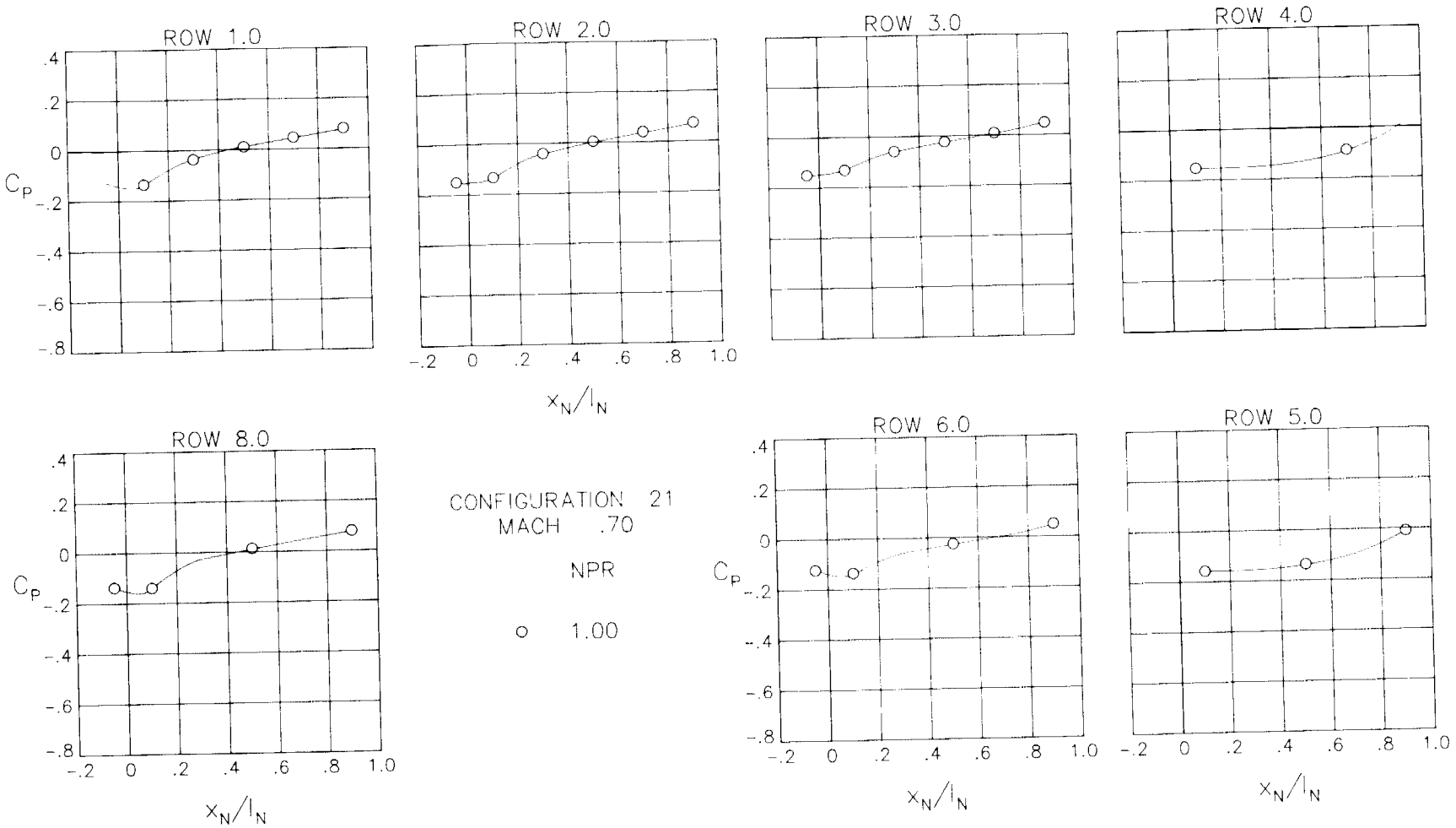

(b) M = 0.70.

Figure 46.- Continued.

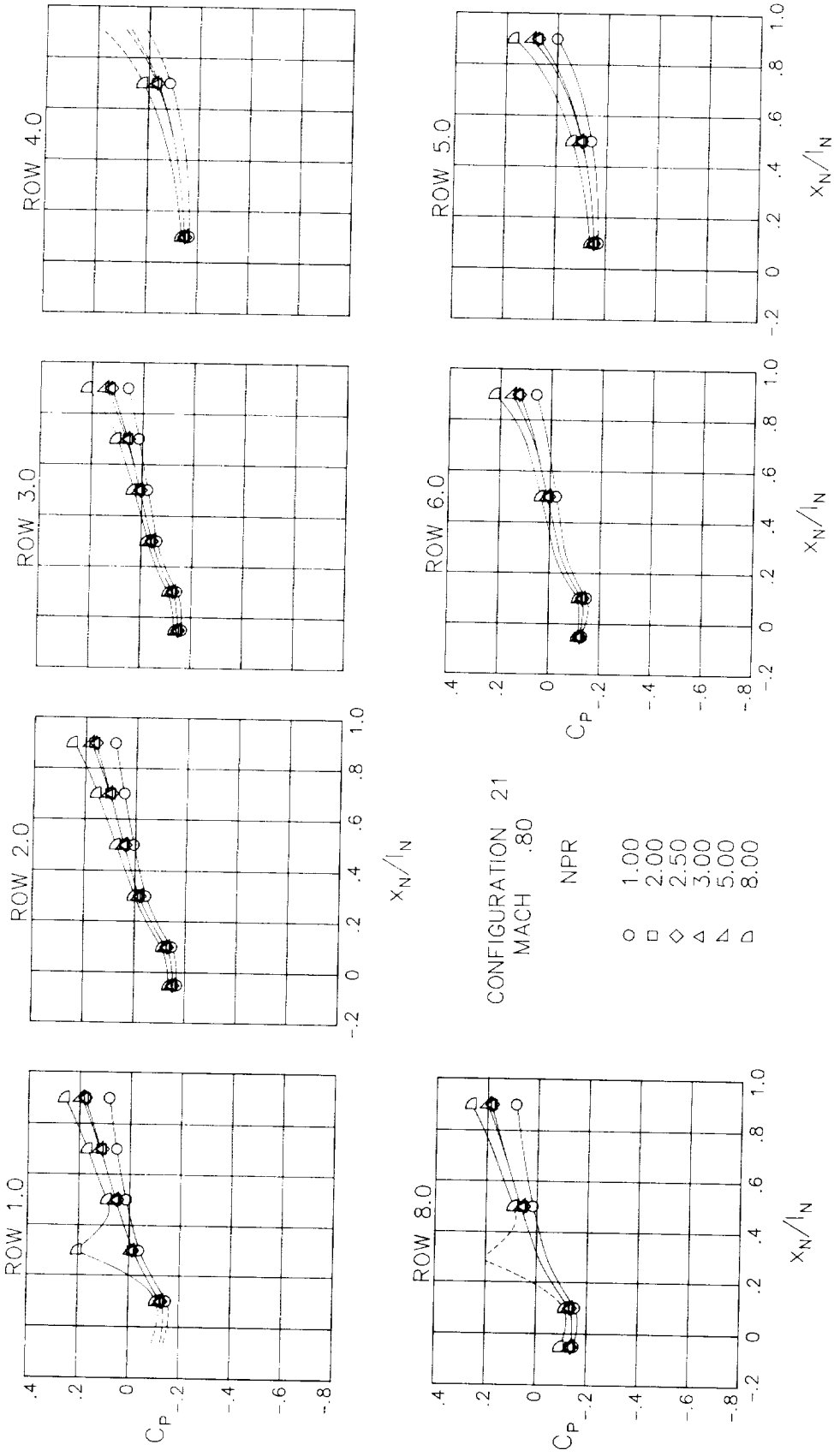

(c) M = 0.80.

Figure 46.- Continued.

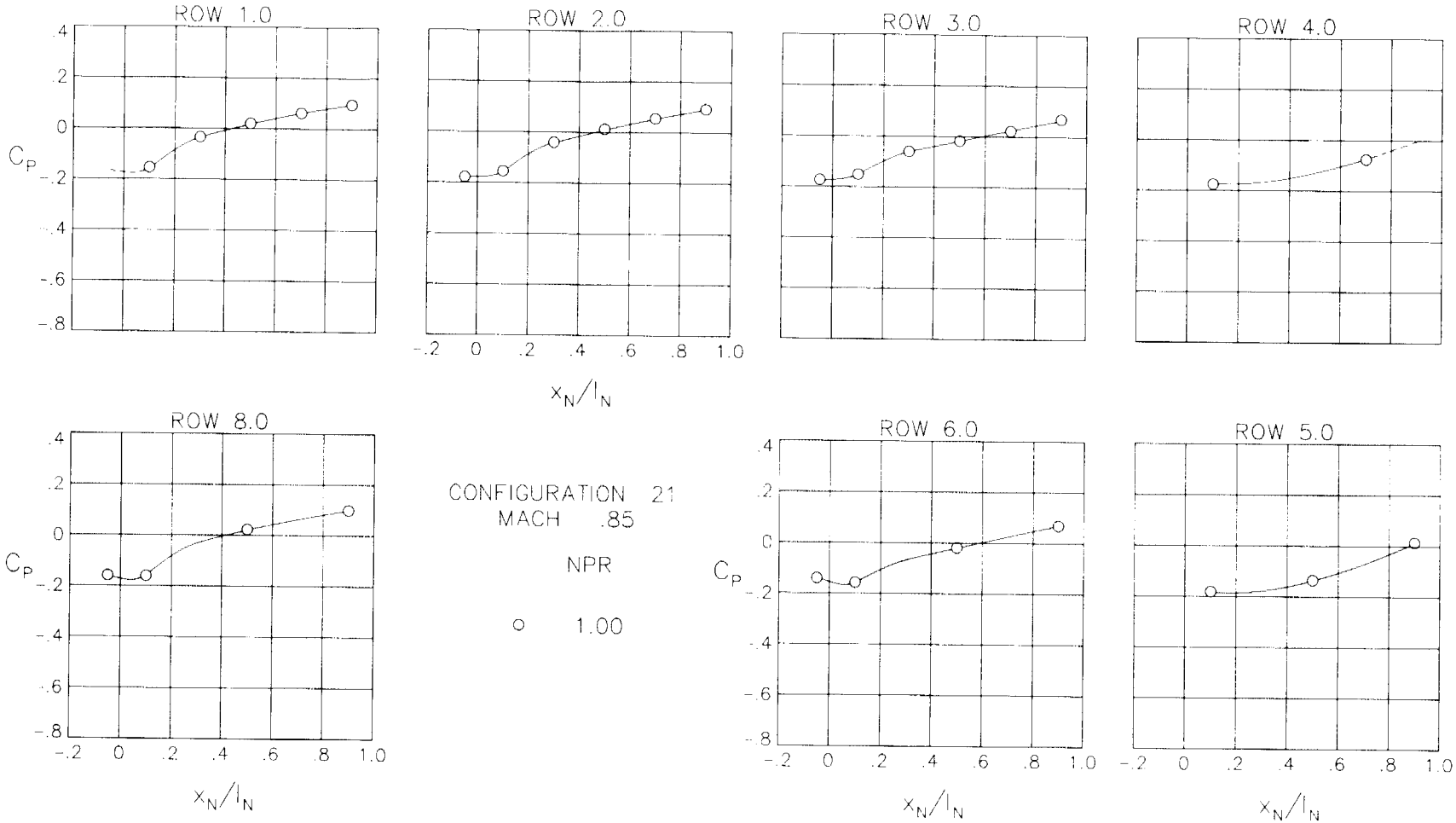

(d) M = 0.85.

Figure 46.- Continued.

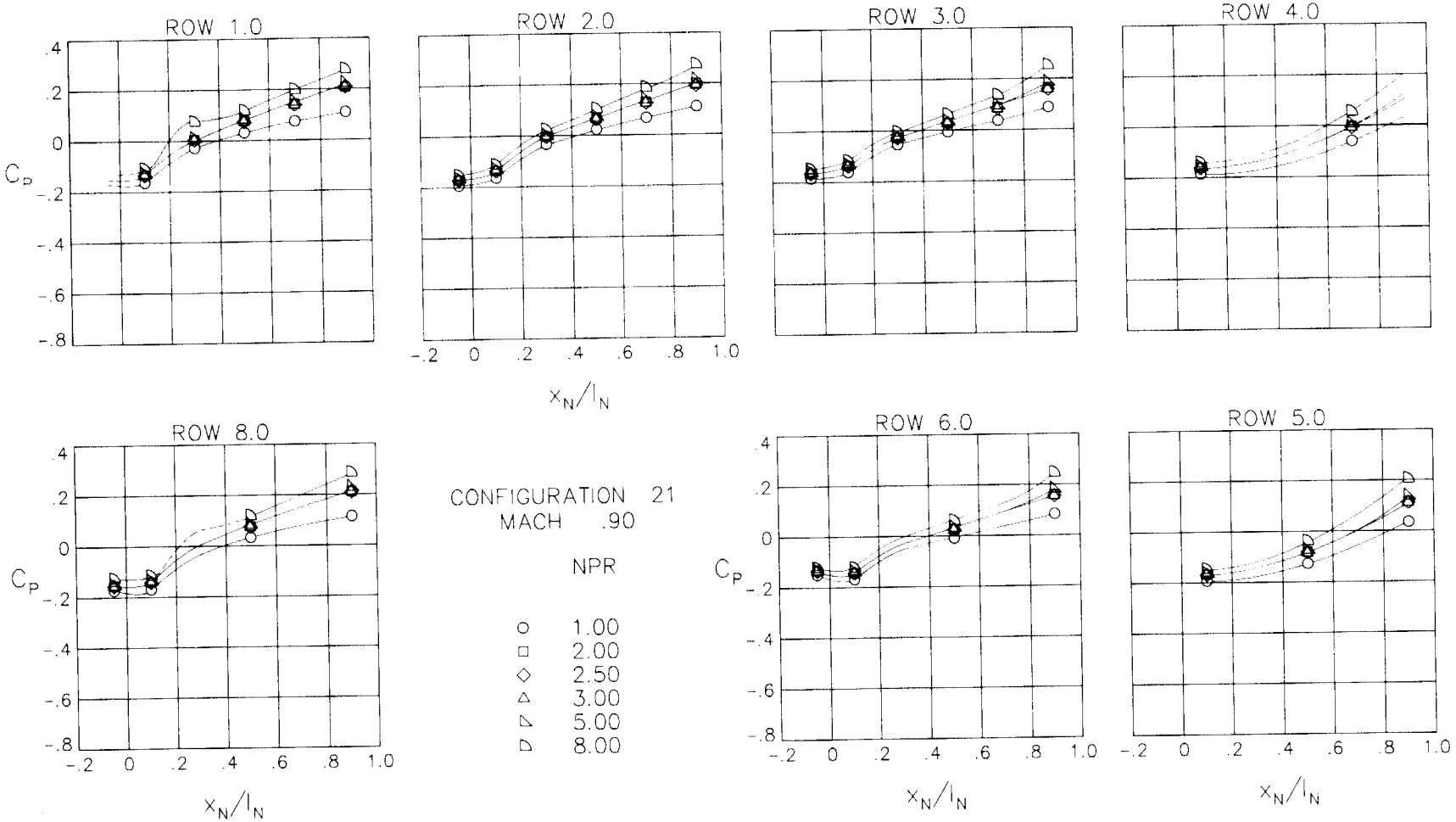

(e) M = 0.90.

Figure 46.- Continued.

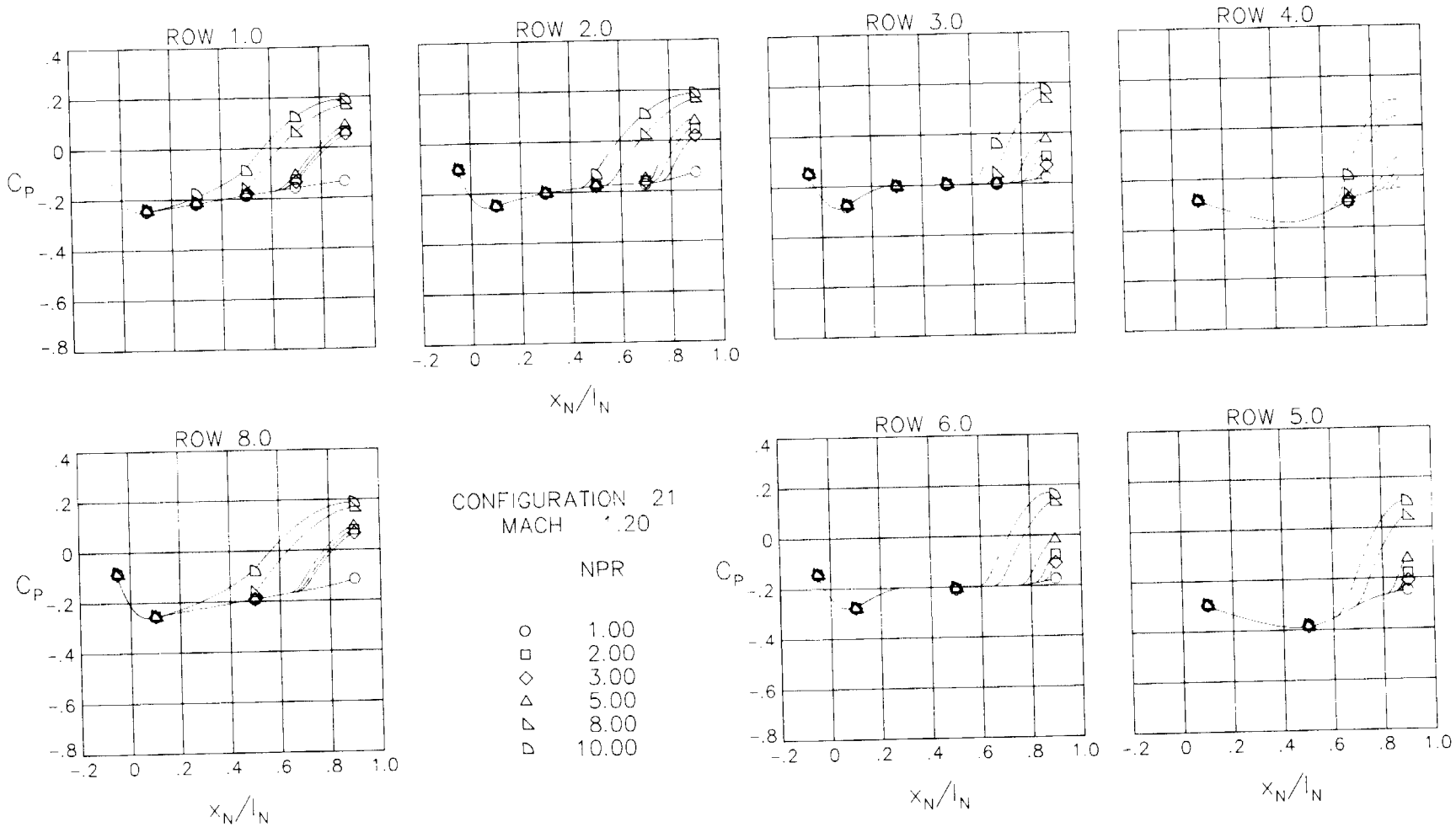

(f) M = 1.20.

Figure 46.- Concluded.

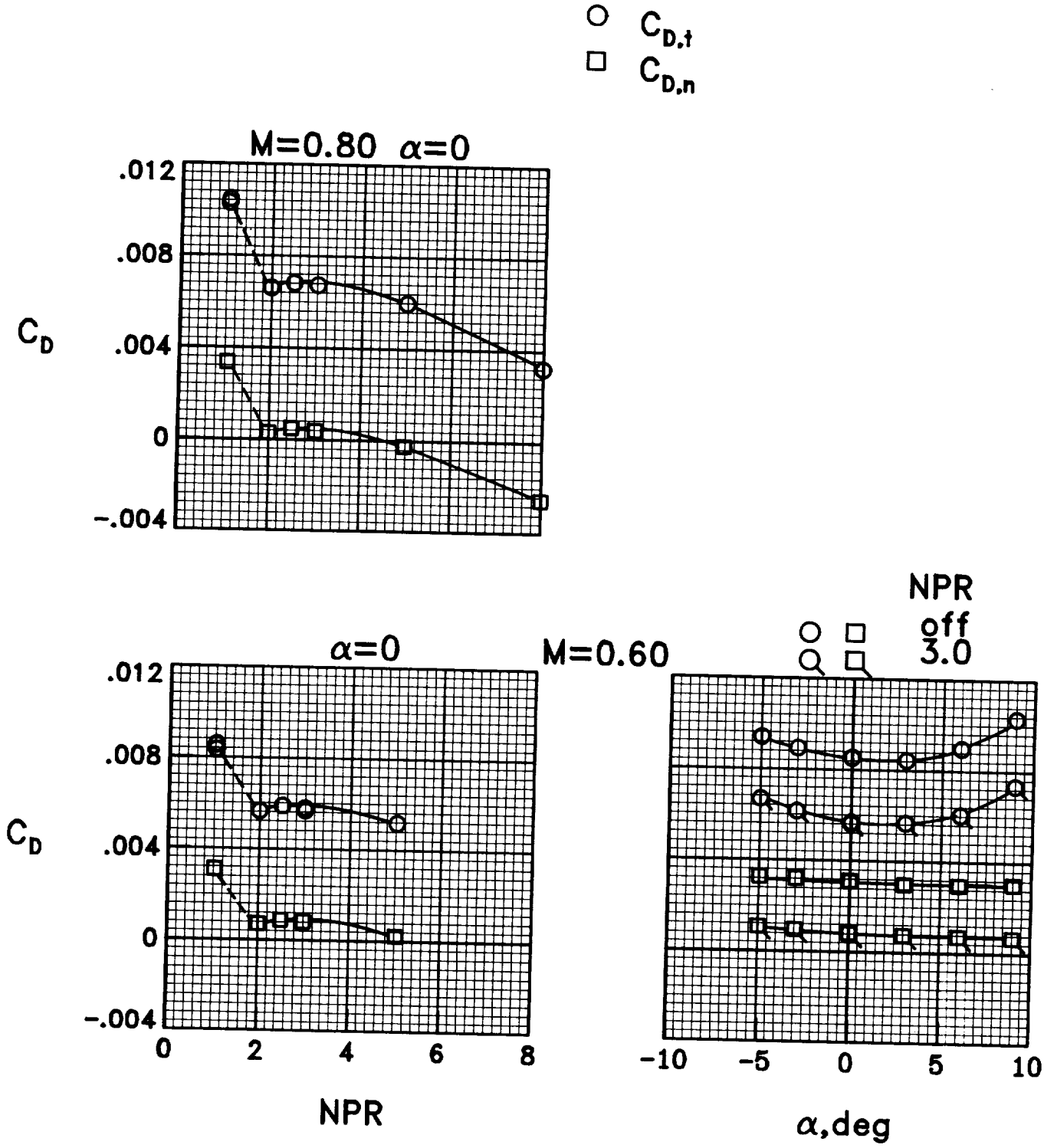

(a) M = 0.60 and 0.80.

Figure 47.- Variation of total drag and nozzle drag coefficients with nozzle pressure ratio and angle of attack for configuration 1.

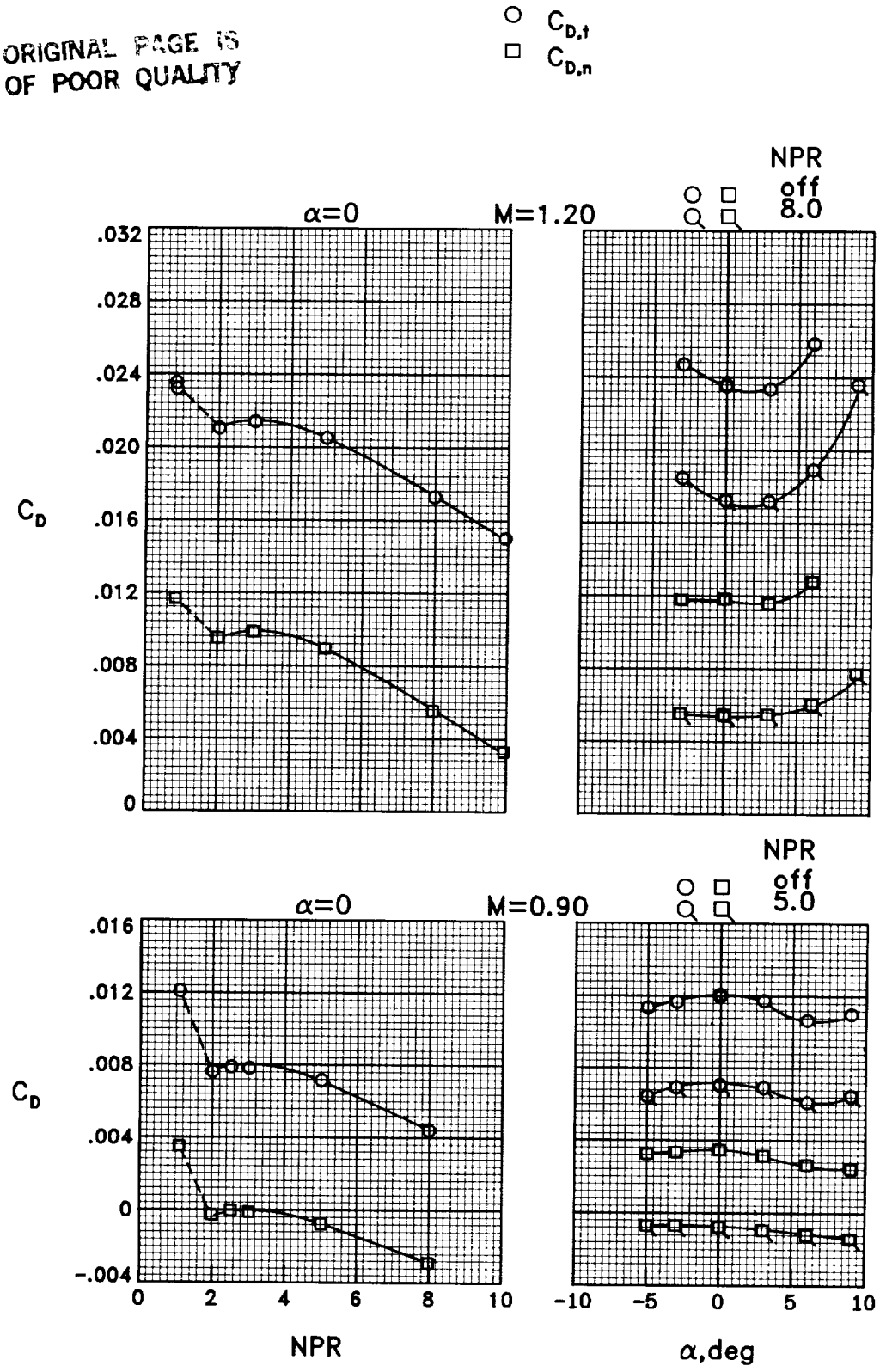

(b) M = 0.90 and 1.20.

Figure 47.- Concluded.

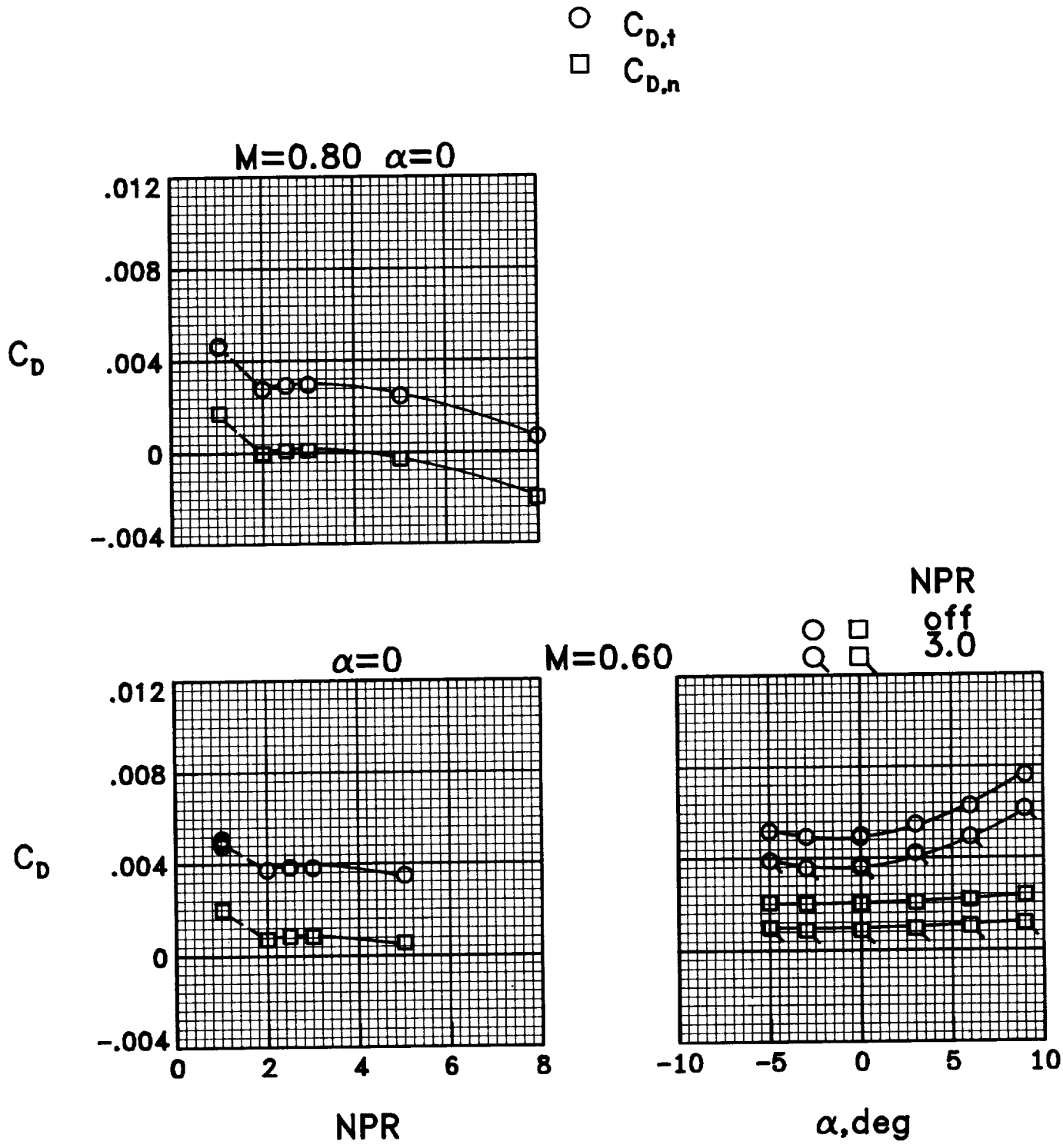

(a) M = 0.60 and 0.80.

Figure 48.- Variation of total drag and nozzle drag coefficients with nozzle pressure ratio and angle of attack for configuration 2.

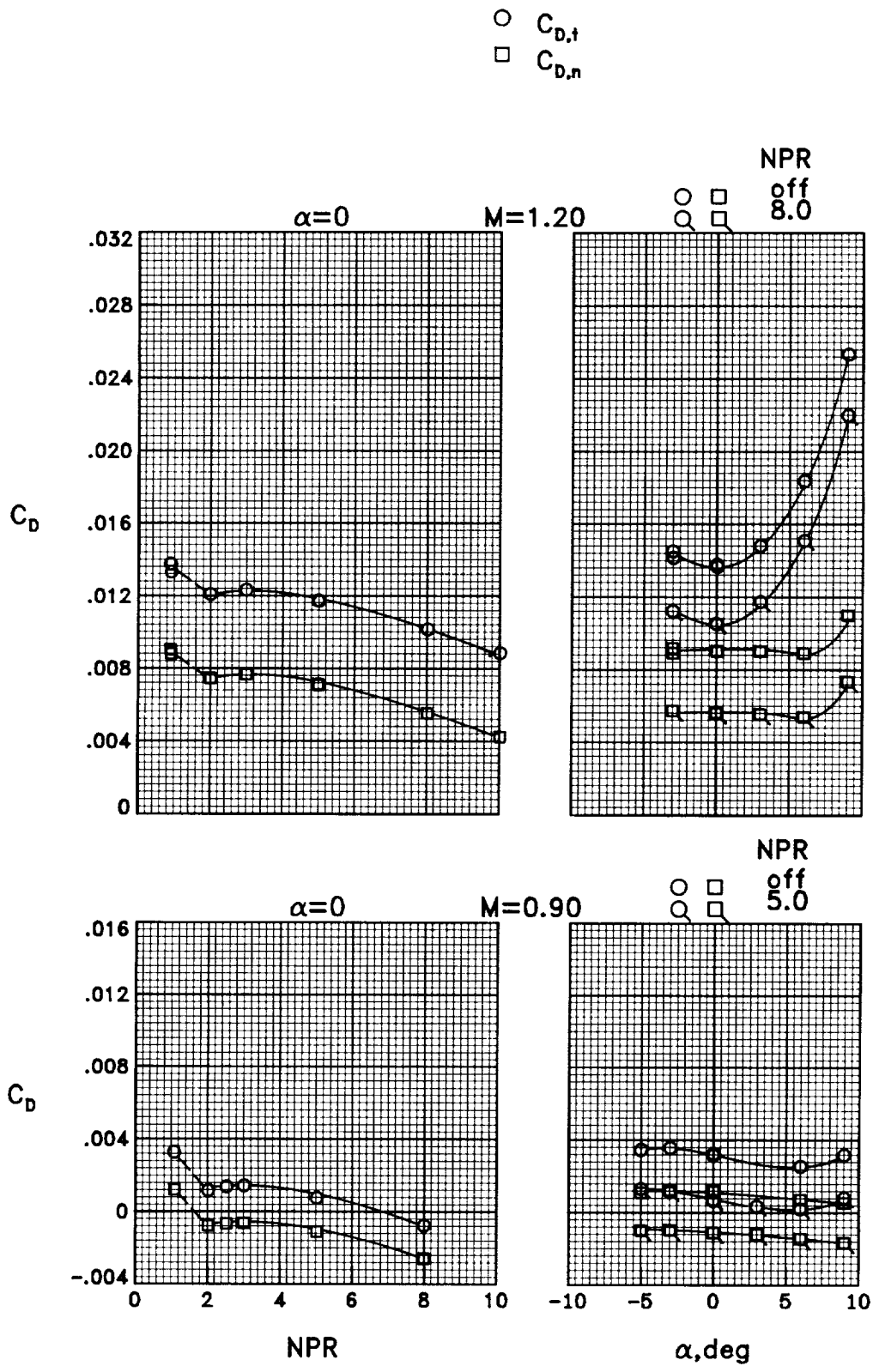

(b) M = 0.90 and 1.20.

Figure 48.- Concluded.

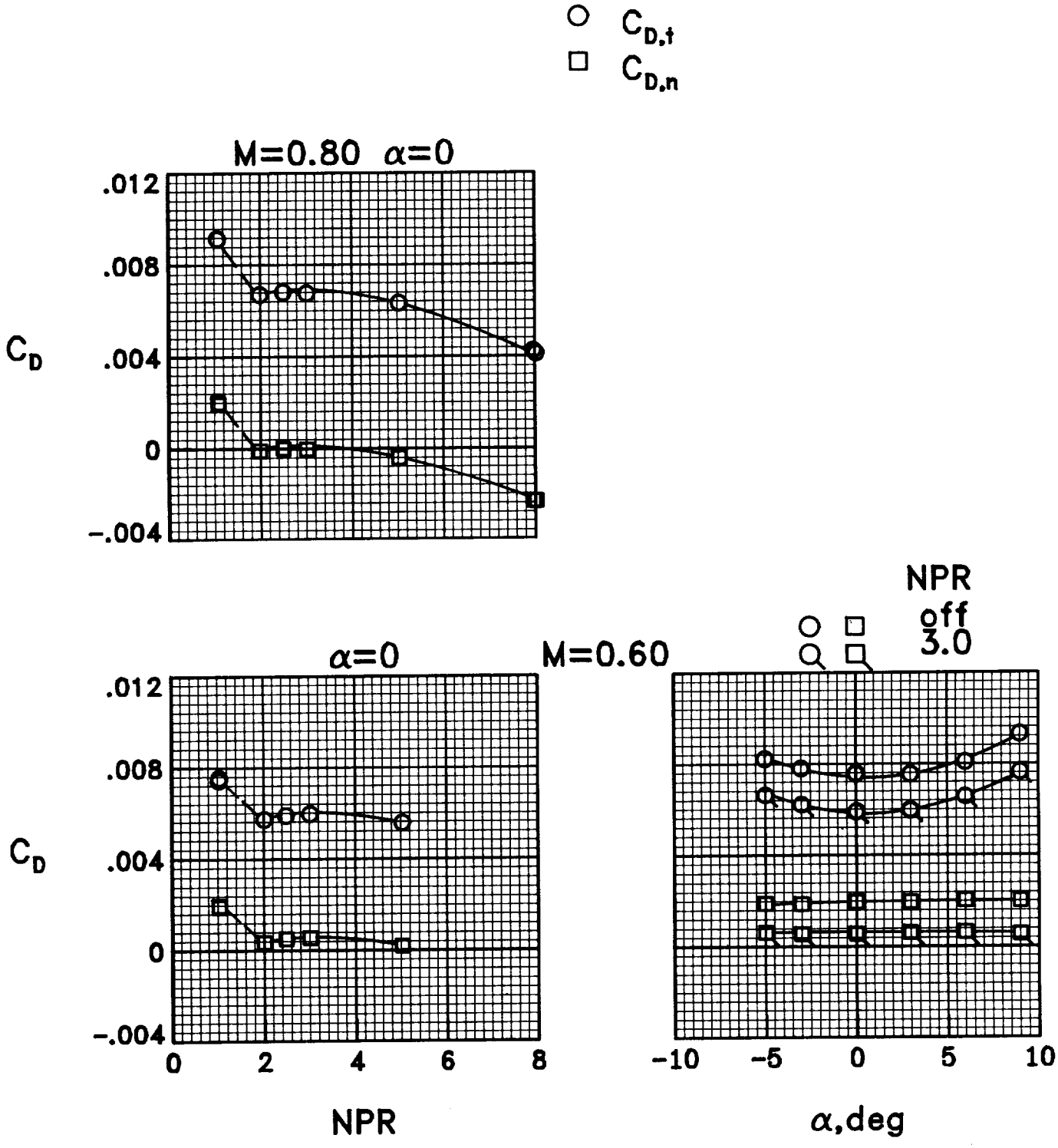

(a) M = 0.60 and 0.80.

Figure 49.- Variation of total drag and nozzle drag coefficients with nozzle pressure ratio and angle of attack for configuration 3.

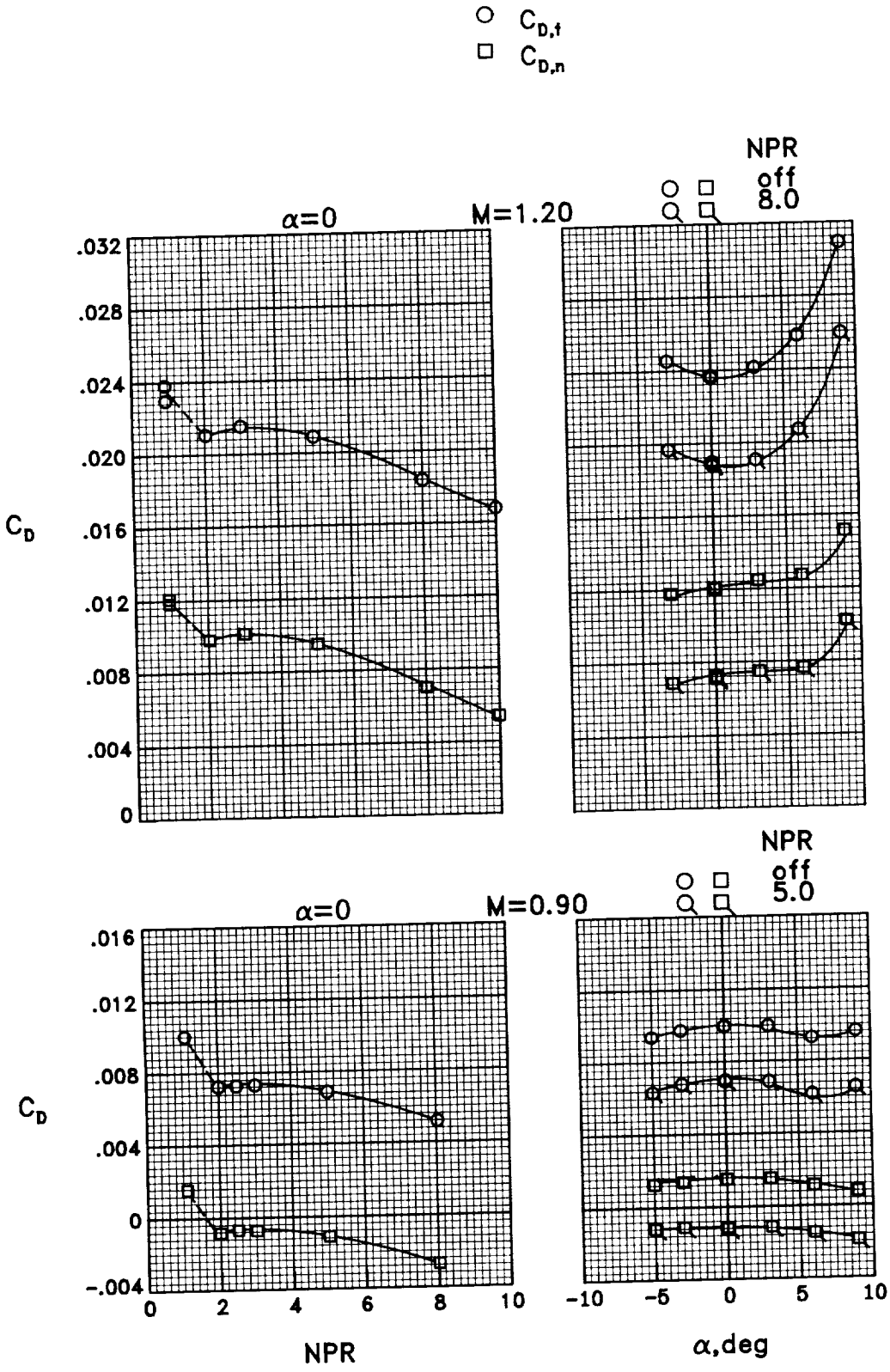

(b) M = 0.90 and 1.20.

Figure 49.- Concluded.

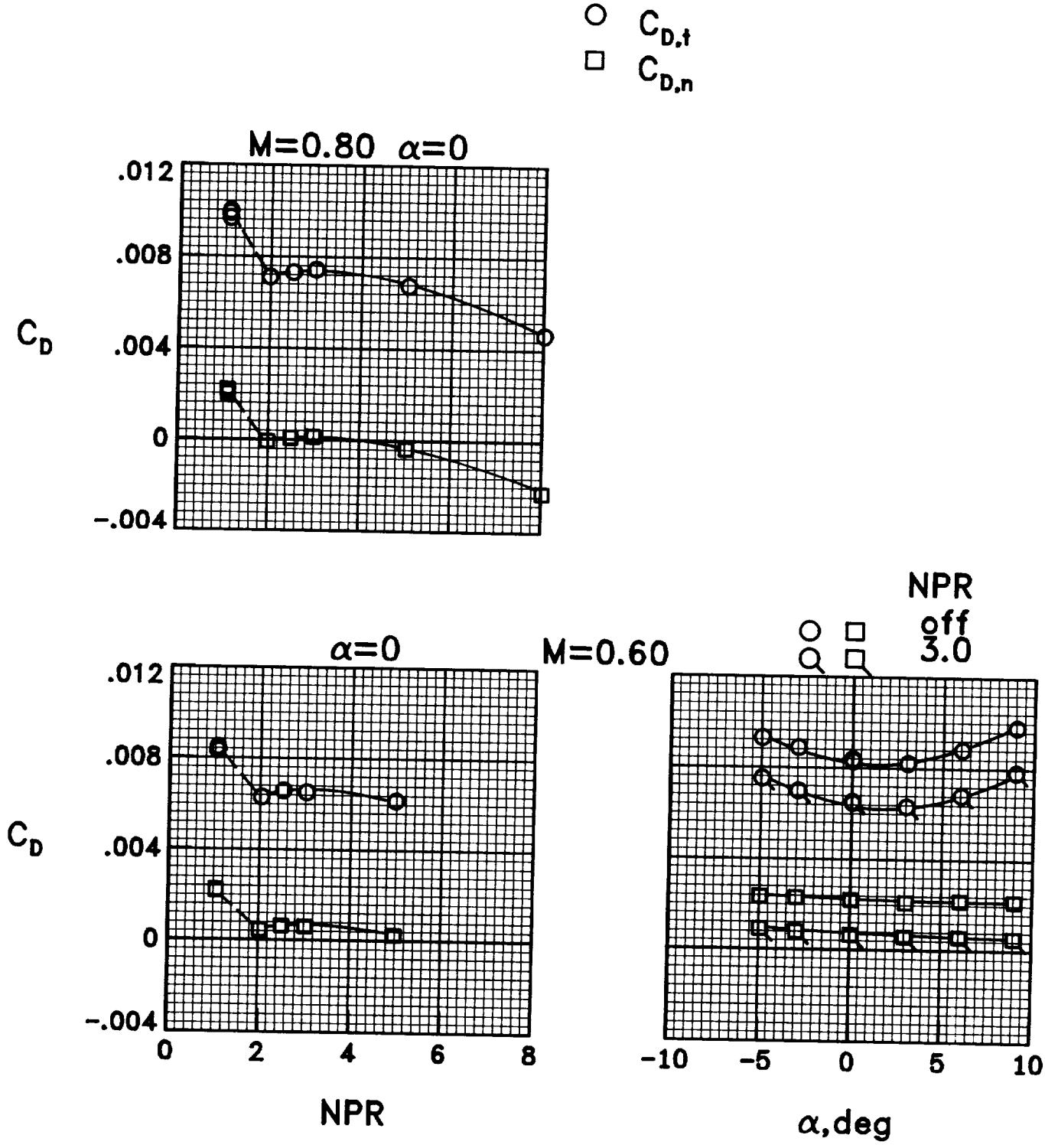

(a) M = 0.60 and 0.80.

Figure 50.- Variation of total drag and nozzle drag coefficients with nozzle pressure ratio and angle of attack for configuration 4.

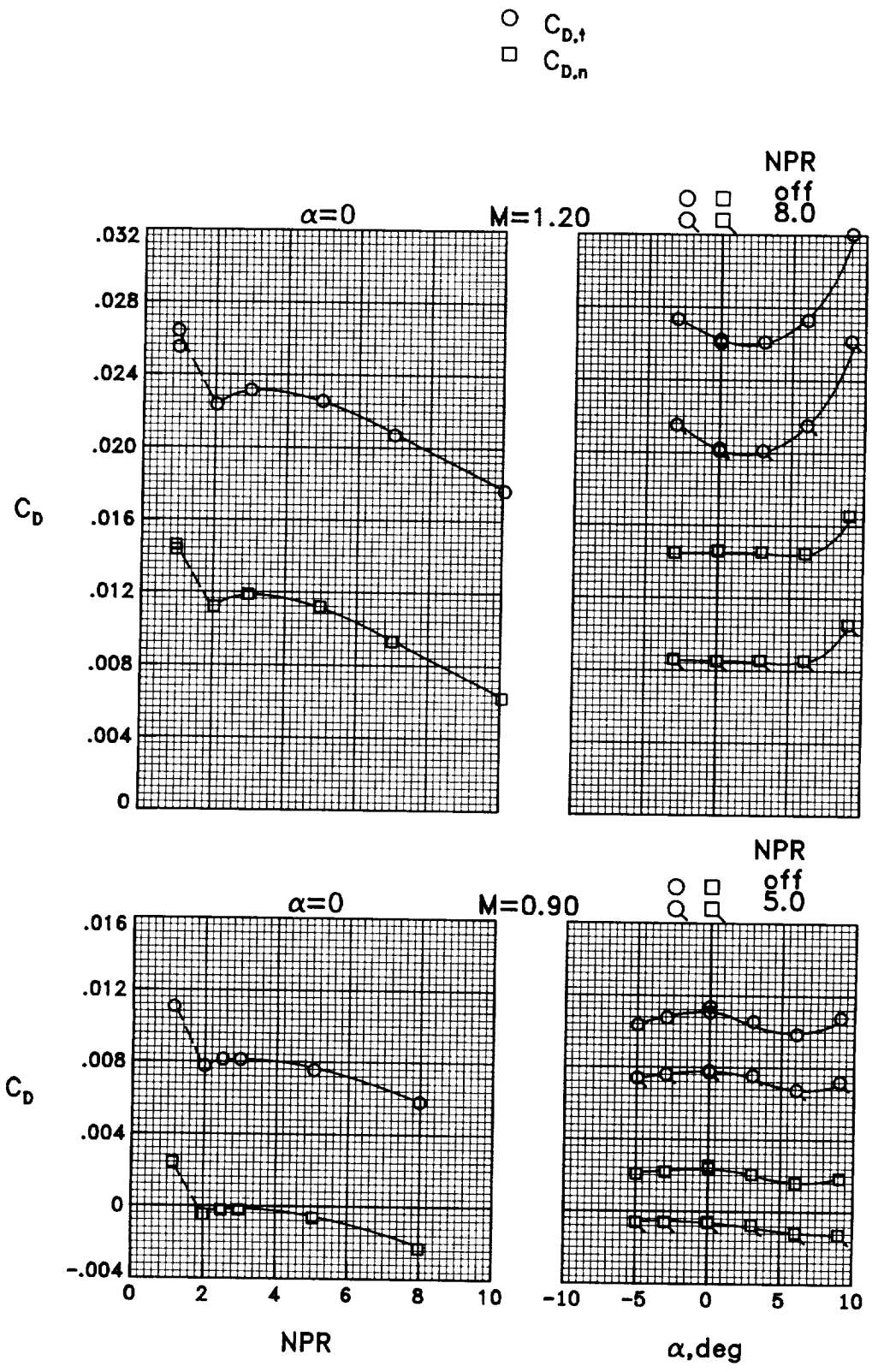

(b) M = 0.90 and 1.20.

Figure 50.- Concluded.

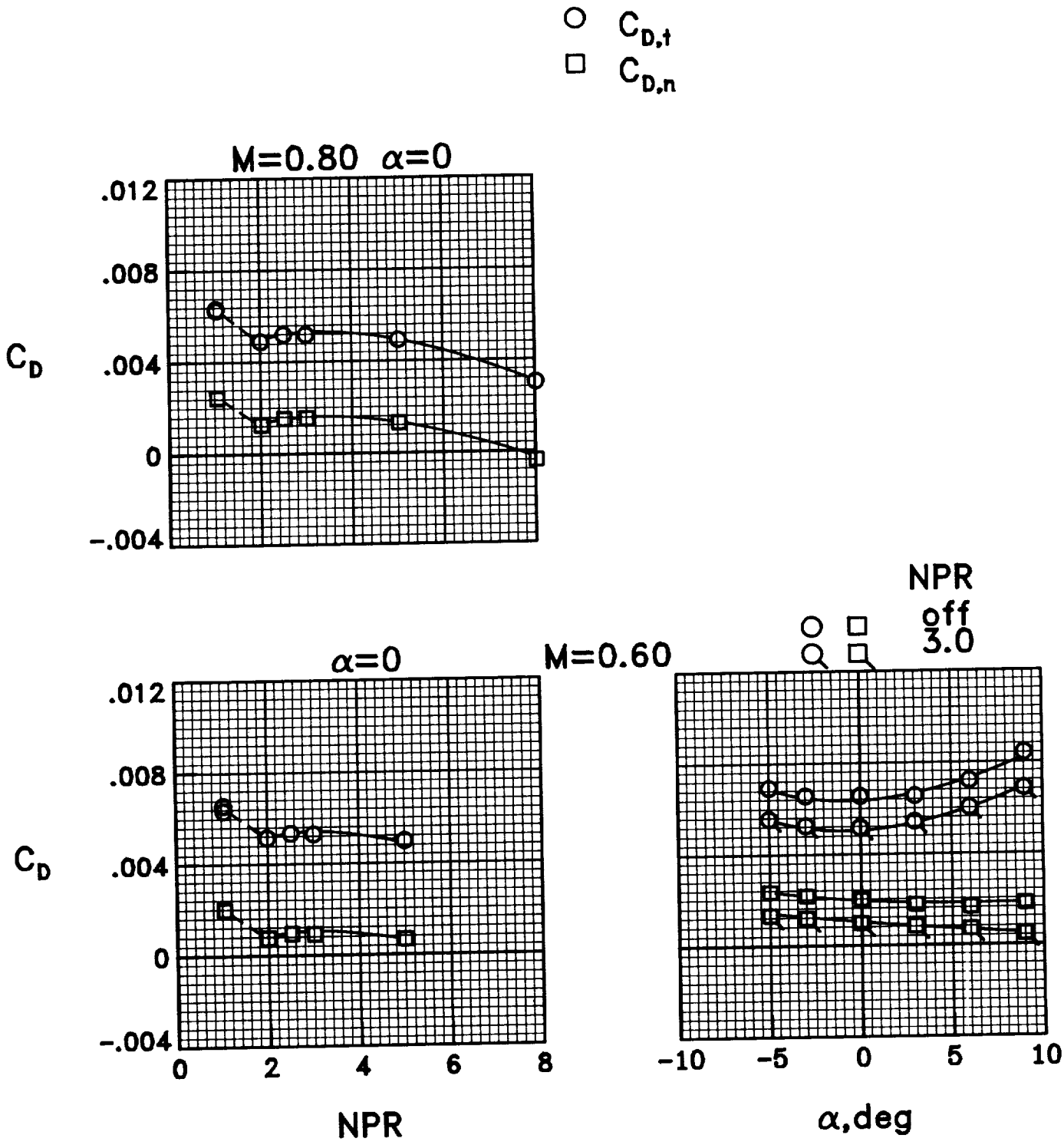

(a) M = 0.60 and 0.80.

Figure 51.- Variation of total drag and nozzle drag coefficients with nozzle pressure ratio and angle of attack for configuration 5.

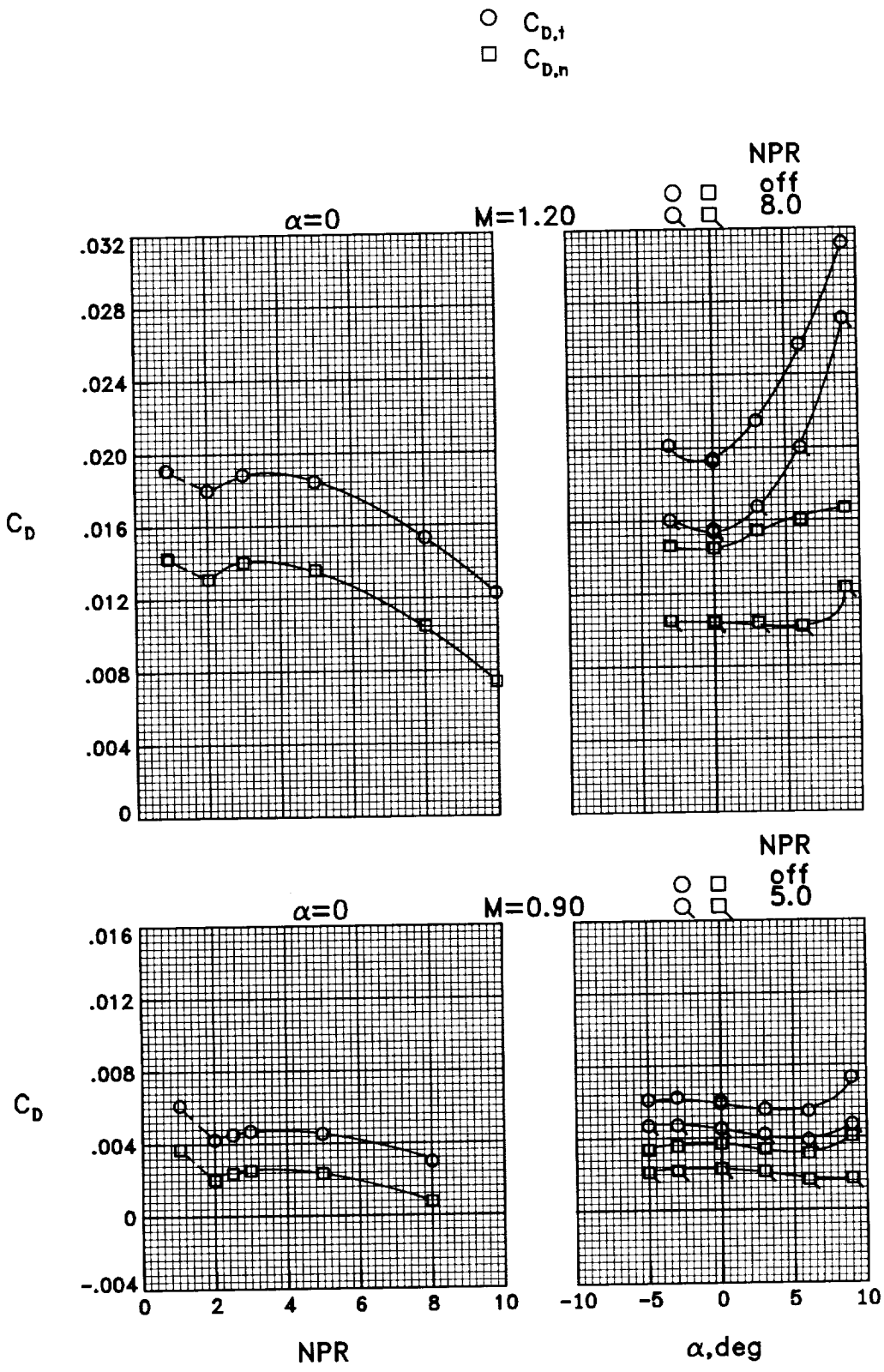

(b) M = 0.90 and 1.20.

Figure 51.- Concluded.

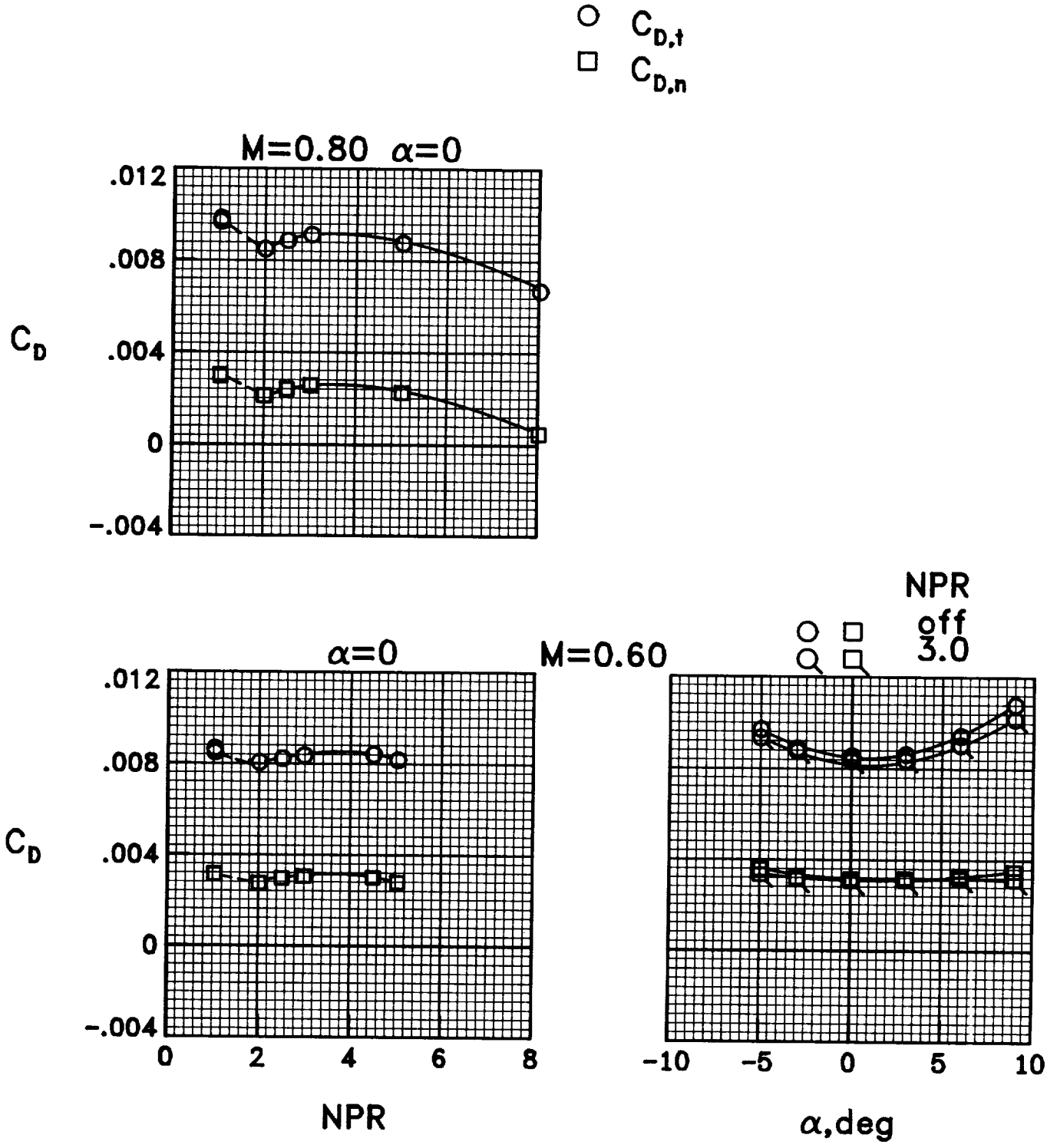

(a) M = 0.60 and 0.80.

Figure 52.- Variation of total drag and nozzle drag coefficients with nozzle pressure ratio and angle of attack for configuration 6.

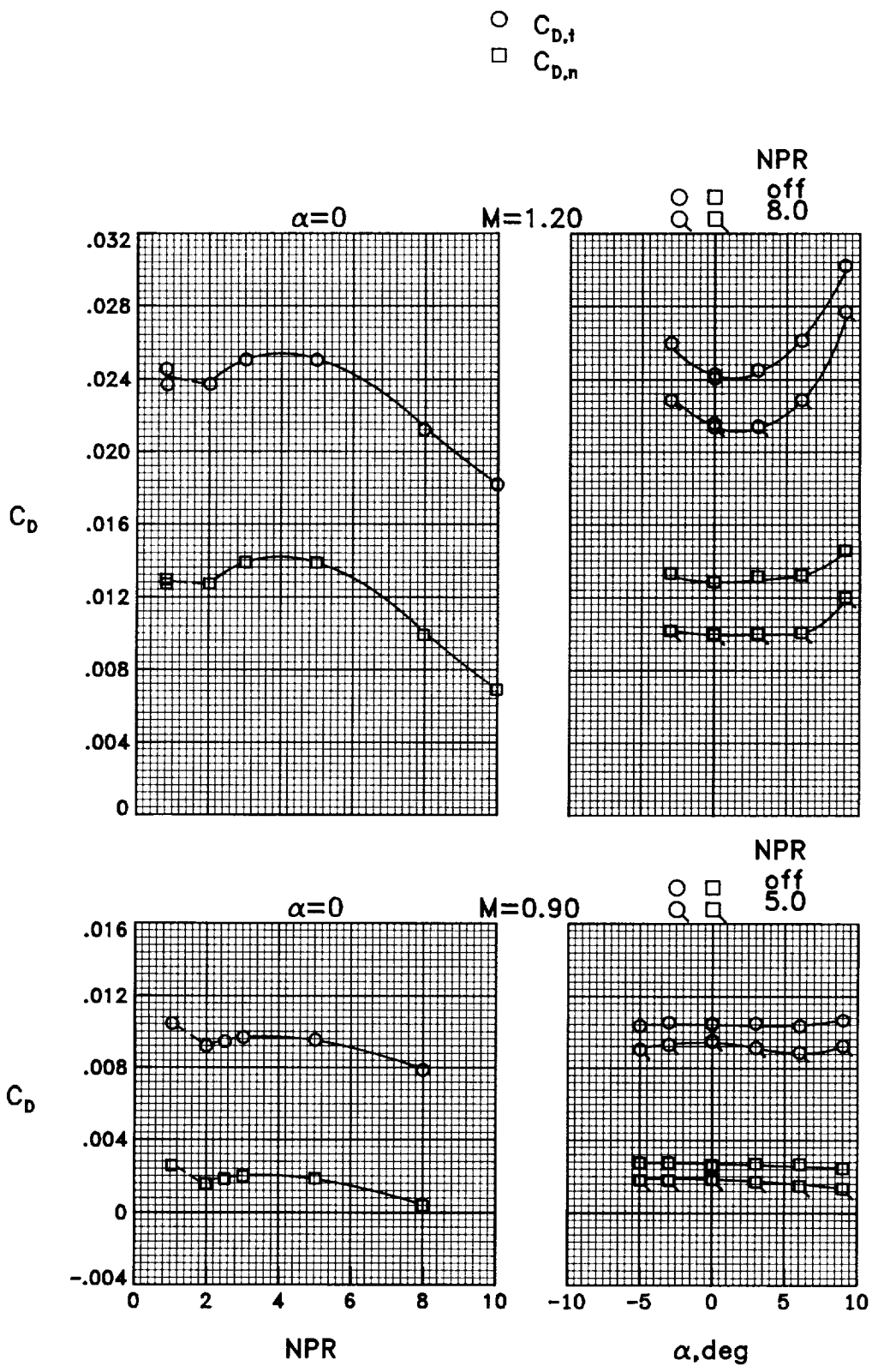

(b) M = 0.90 and 1.20.

Figure 52.- Concluded.

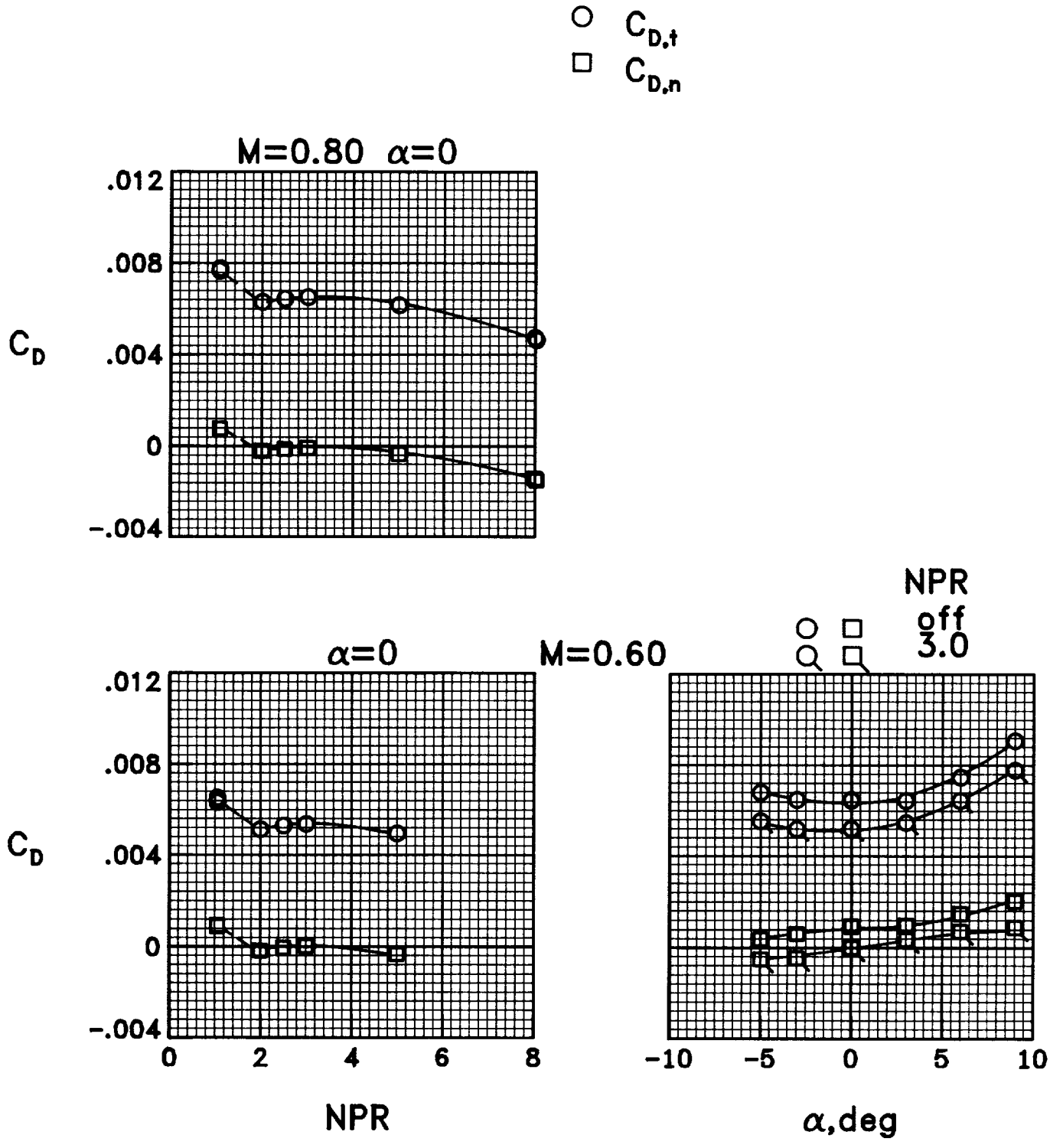

(a) M = 0.60 and 0.80.

Figure 53.- Variation of total drag and nozzle drag coefficients with nozzle pressure ratio and angle of attack for configuration 7.

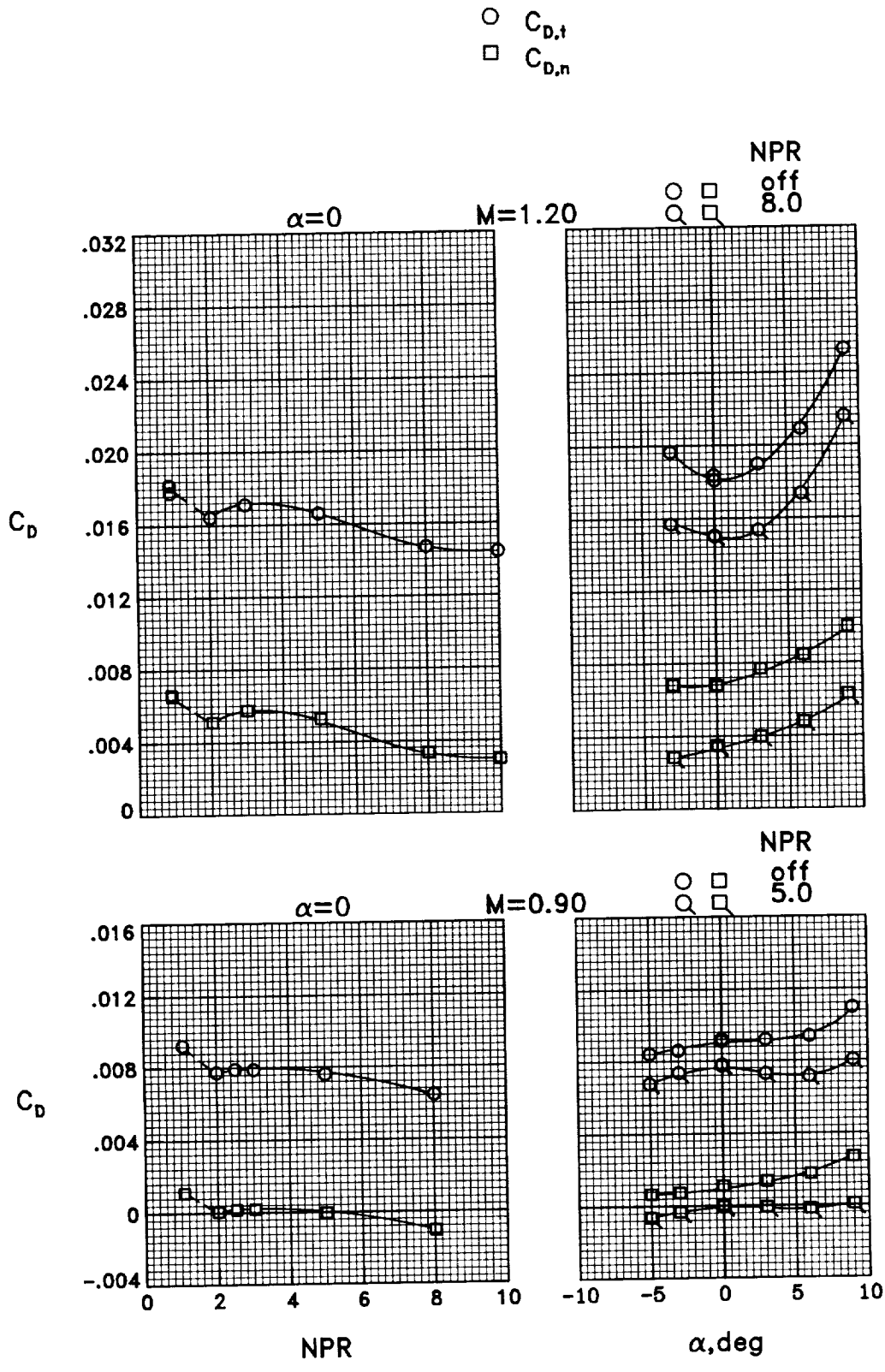

(b) M = 0.90 and 1.20.

Figure 53.- Concluded.

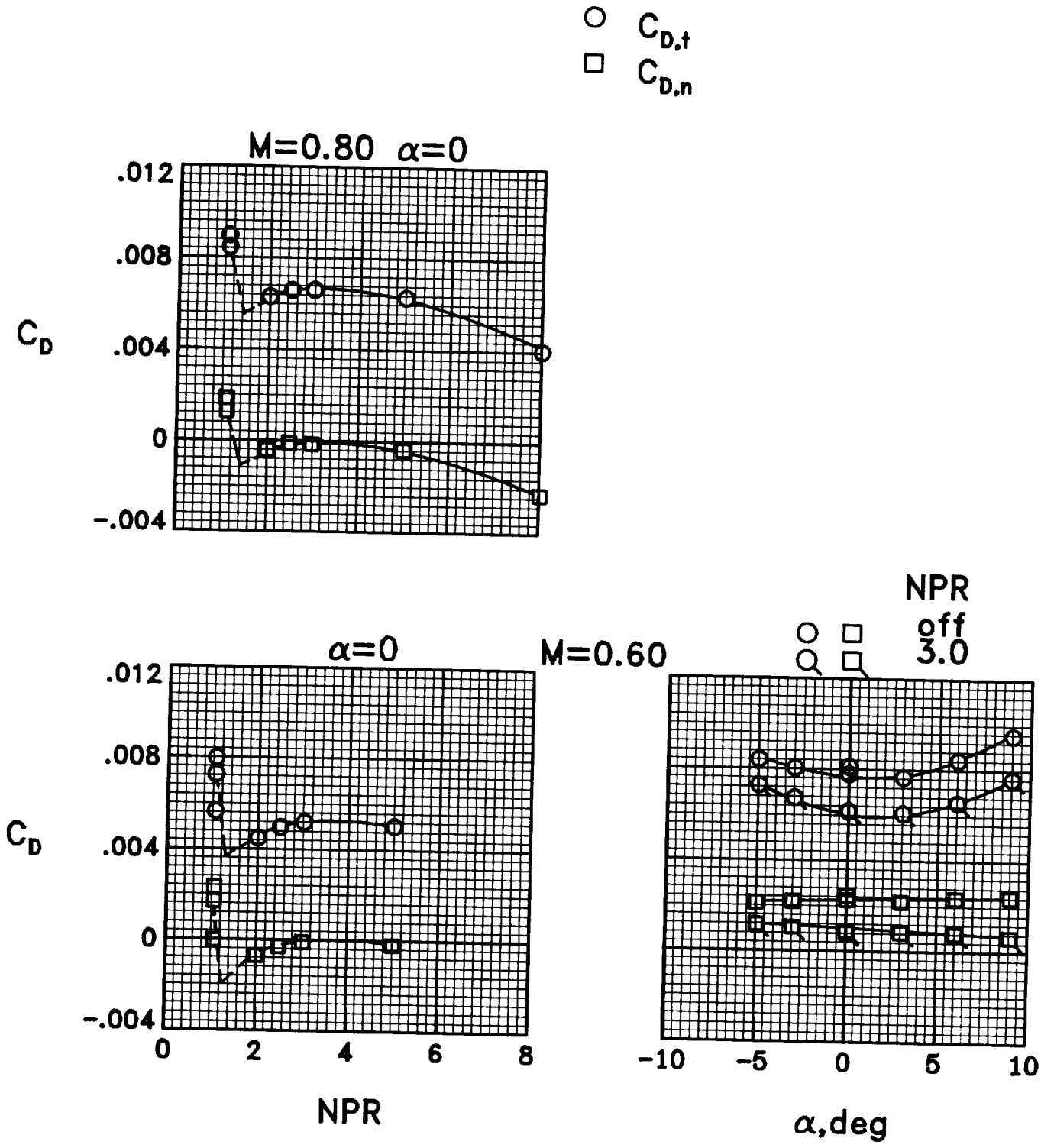

(a) M = 0.60 and 0.80.

Figure 54.- Variation of total drag and nozzle drag coefficients with nozzle pressure ratio and angle of attack for configuration 8.

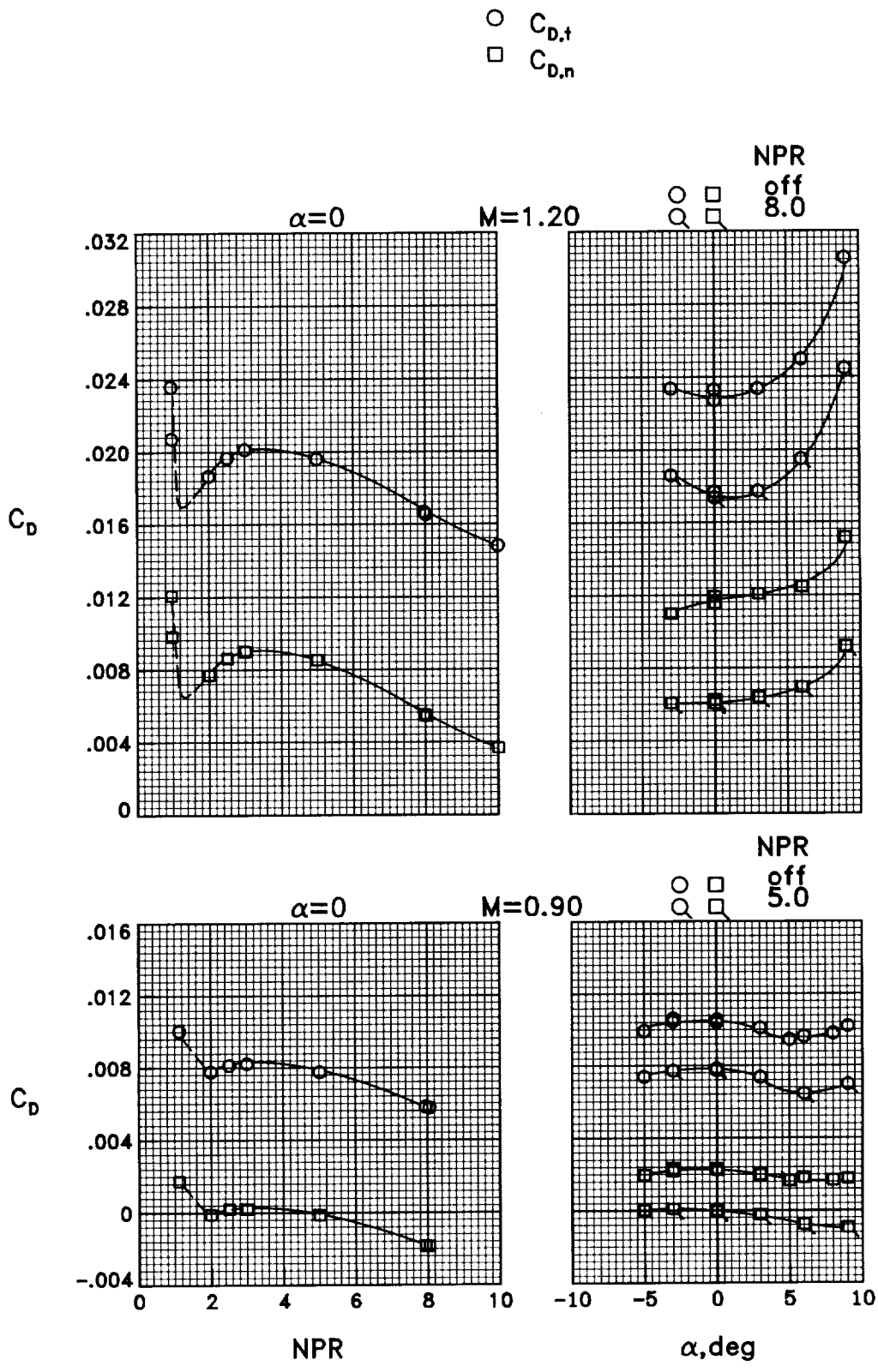

(b) M = 0.90 and 1.20.

Figure 54.- Concluded.

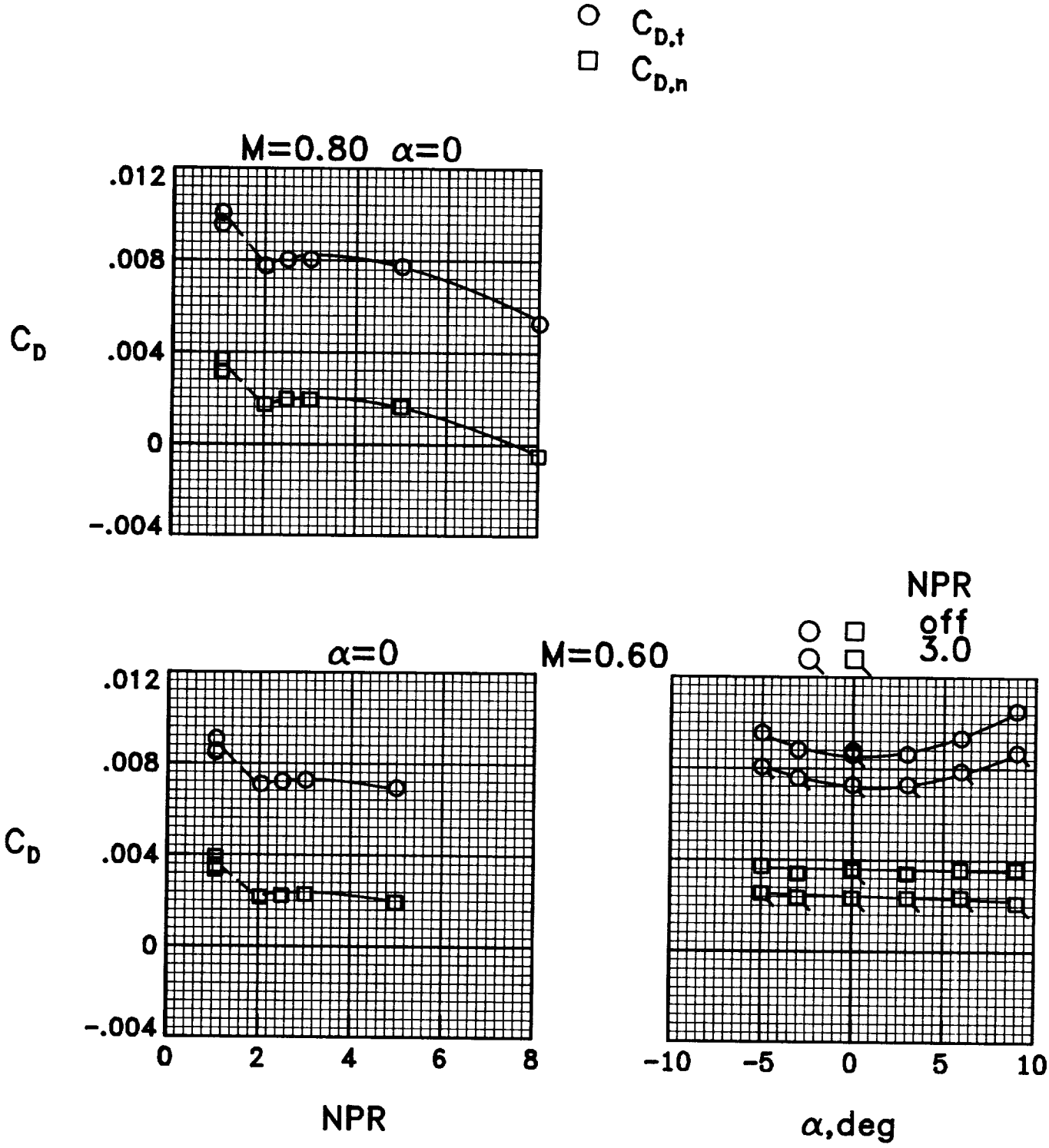

(a) M = 0.60 and 0.80.

Figure 55.- Variation of total drag and nozzle drag coefficients with nozzle pressure ratio and angle of attack for configuration 9.

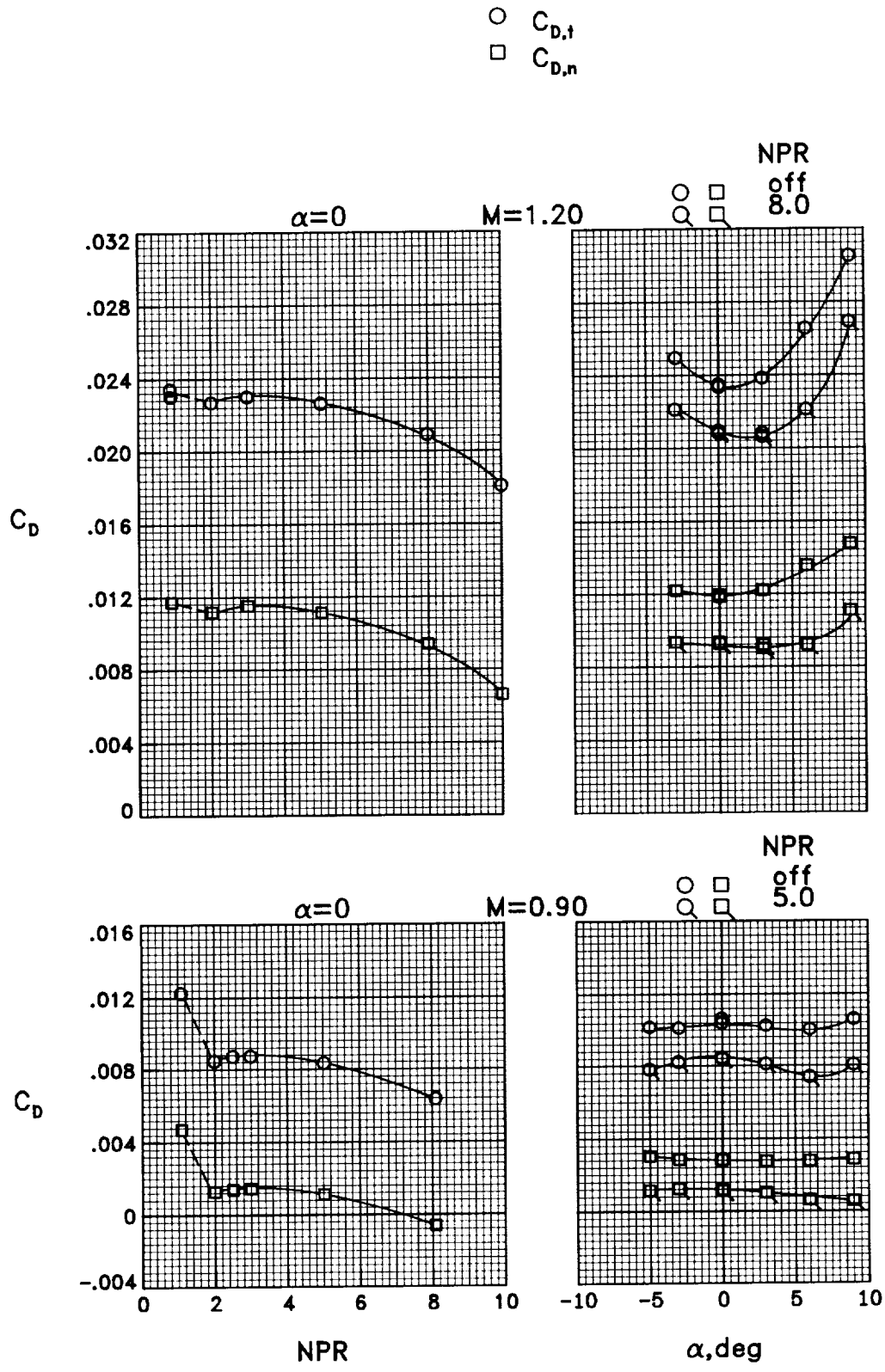

(b) M = 0.90 and 1.20.

Figure 55.- Concluded.

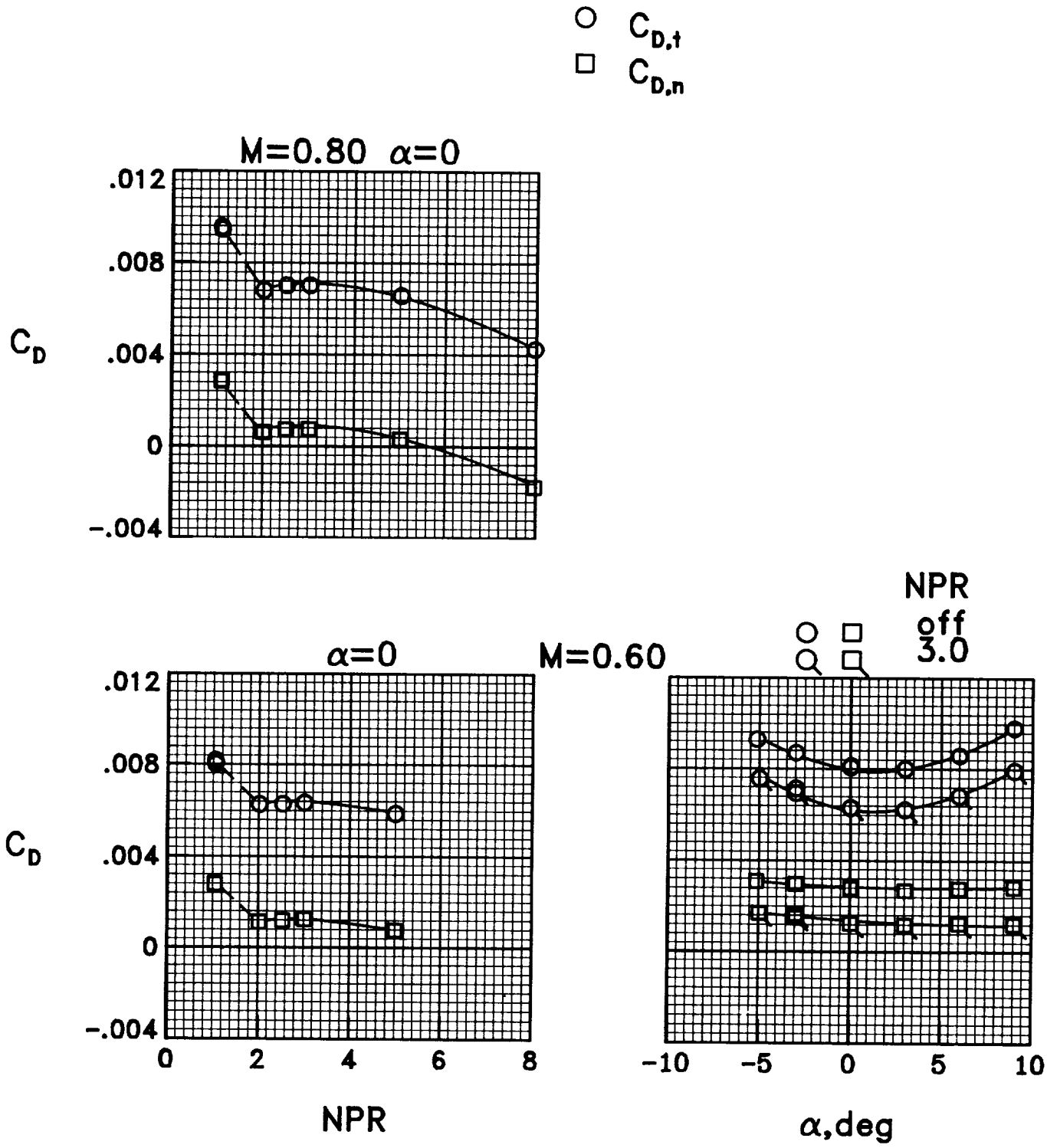

(a) M = 0.60 and 0.80.

Figure 56.- Variation of total drag and nozzle drag coefficients with nozzle pressure ratio and angle of attack for configuration 10.

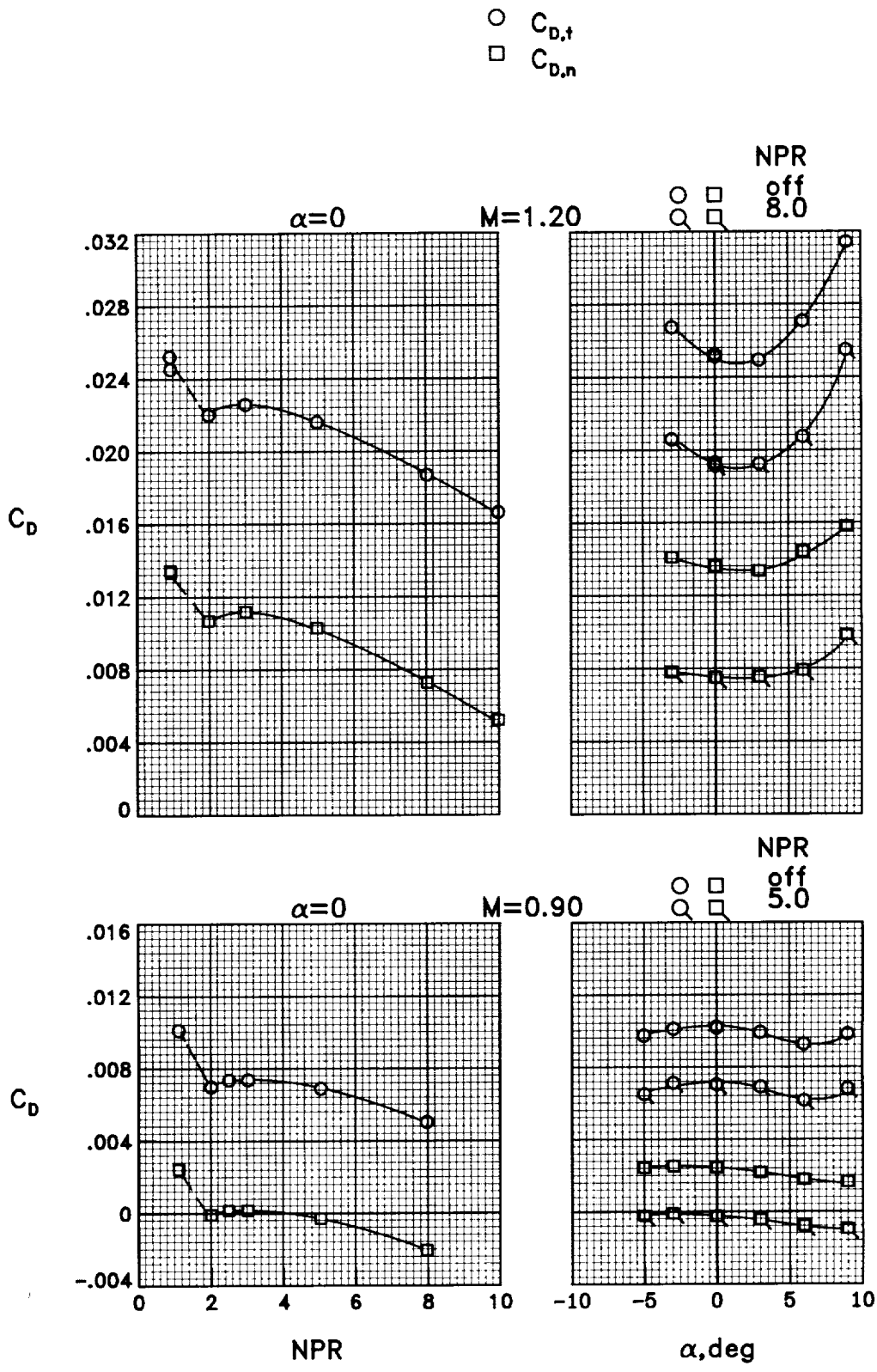

(b) M = 0.90 and 1.20.

Figure 56.- Concluded.

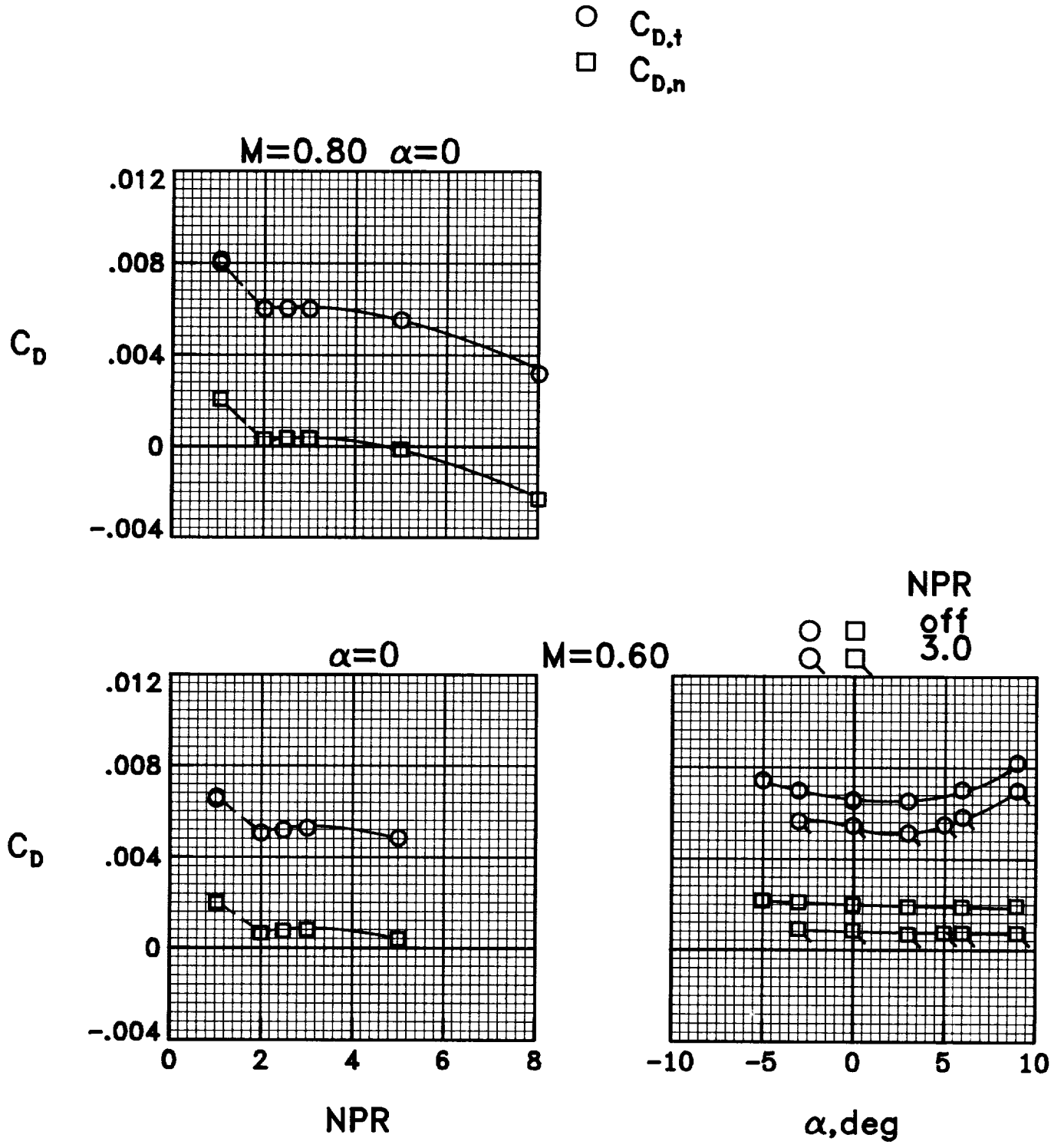

(a) M = 0.60 and 0.80.

Figure 57.- Variation of total drag and nozzle drag coefficients with nozzle pressure ratio and angle of attack for configuration 11.

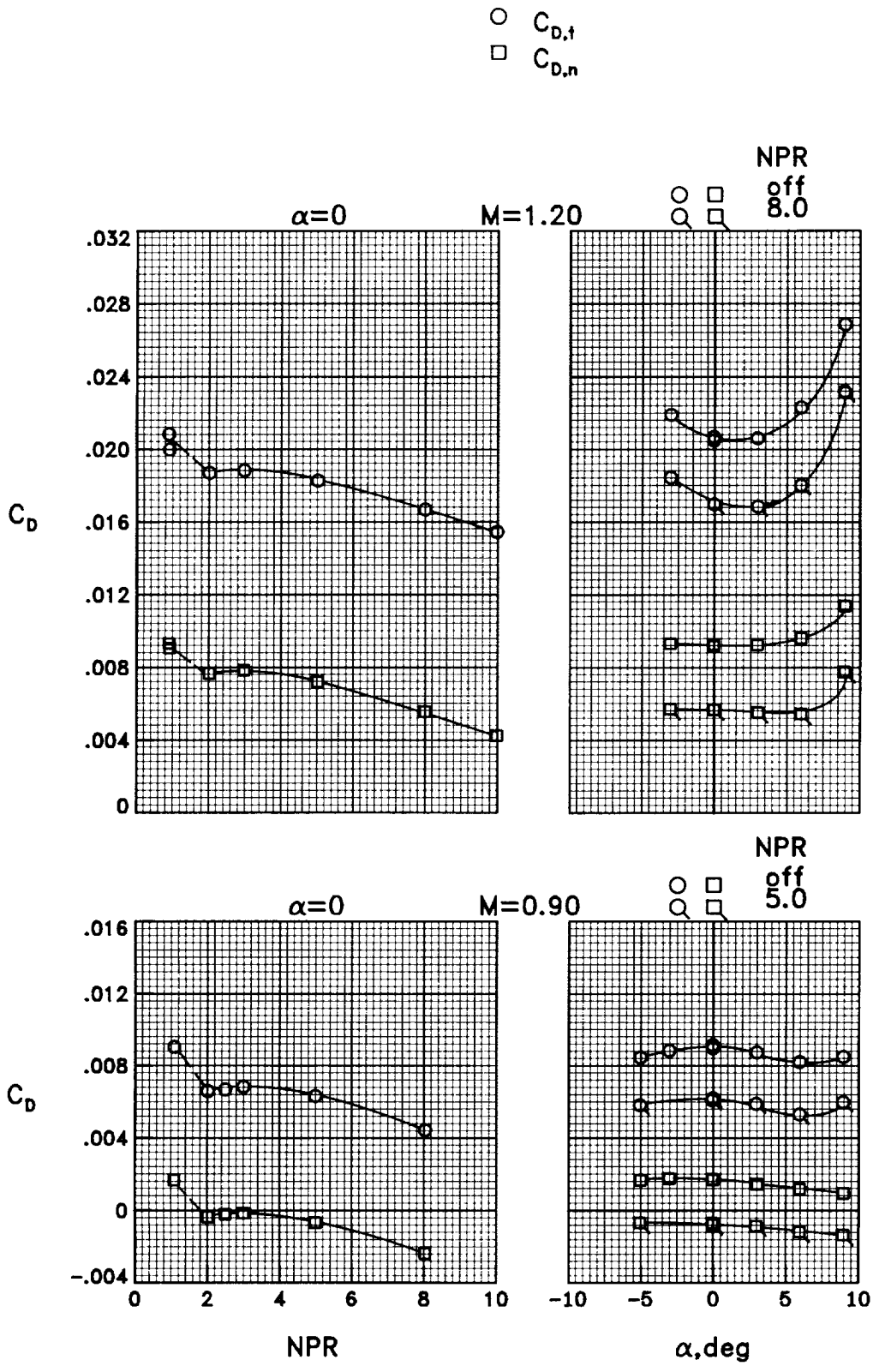

(b) M = 0.90 and 1.20.

Figure 57.- Concluded.

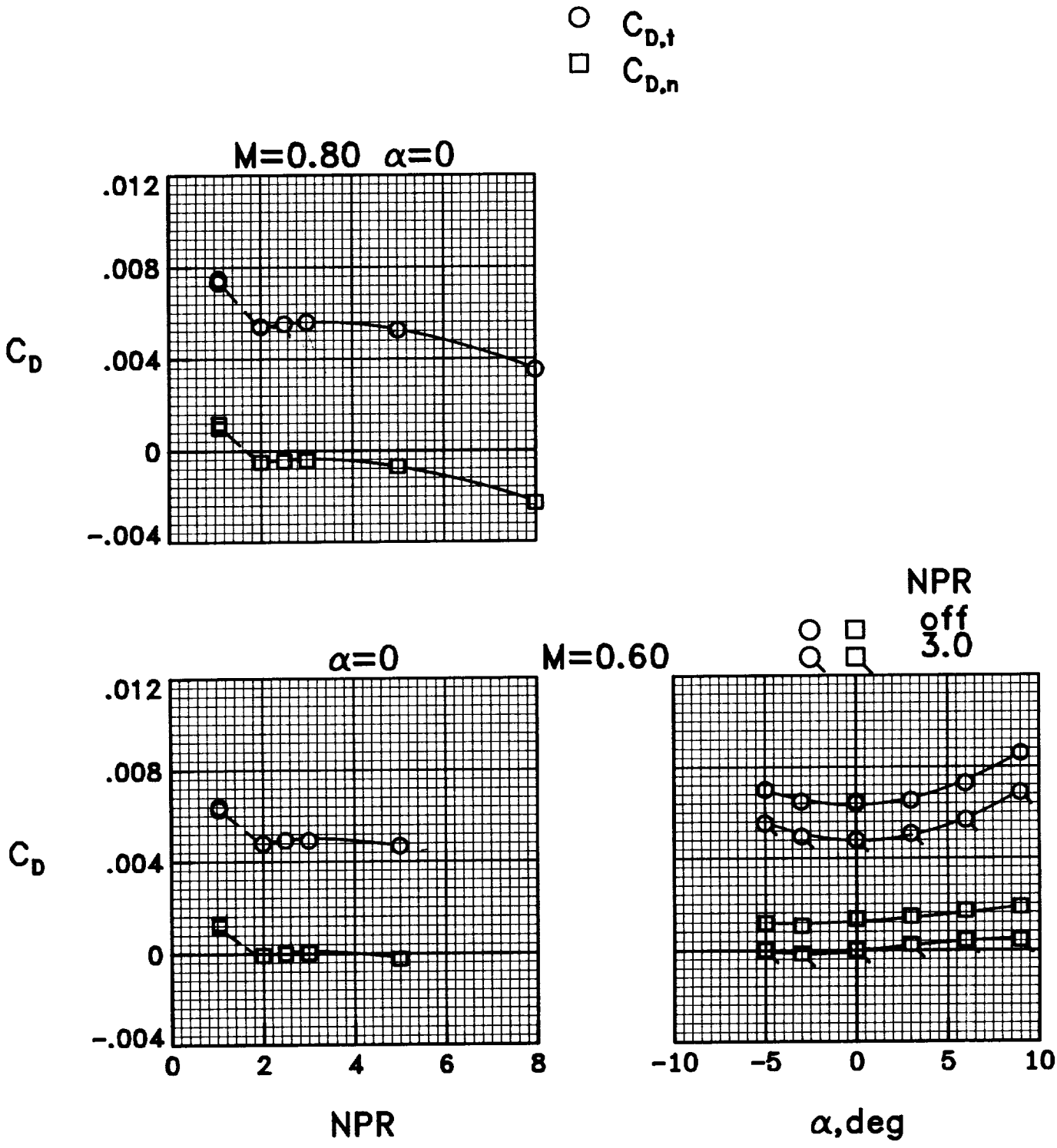

(a) M = 0.60 and 0.80.

Figure 58.- Variation of total drag and nozzle drag coefficients with nozzle pressure ratio and angle of attack for configuration 12.

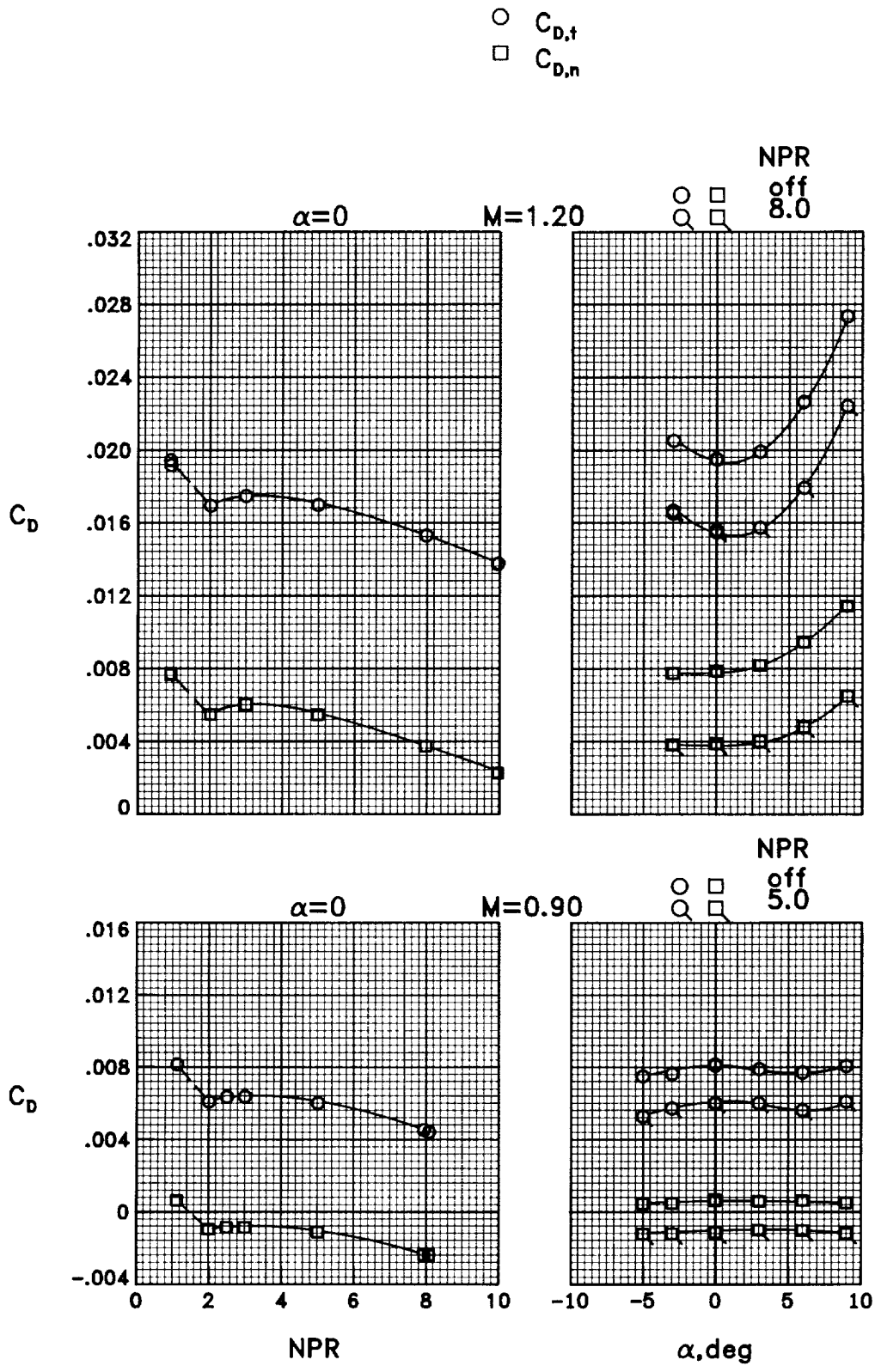

(b) M = 0.90 and 1.20.

Figure 58.- Concluded.

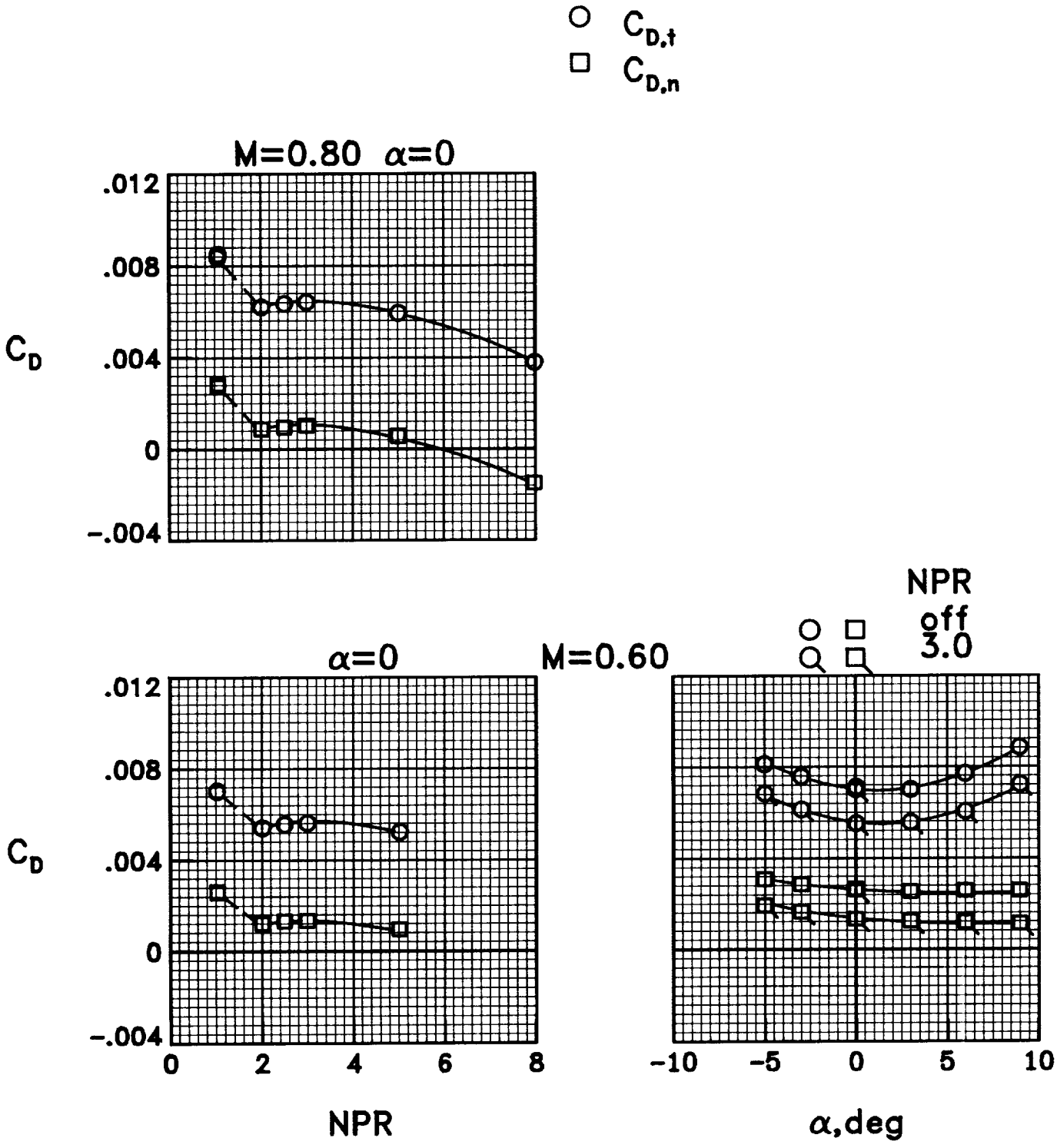

(a) M = 0.60 and 0.80.

Figure 59.- Variation of total drag and nozzle drag coefficients with nozzle pressure ratio and angle of attack for configuration 13.

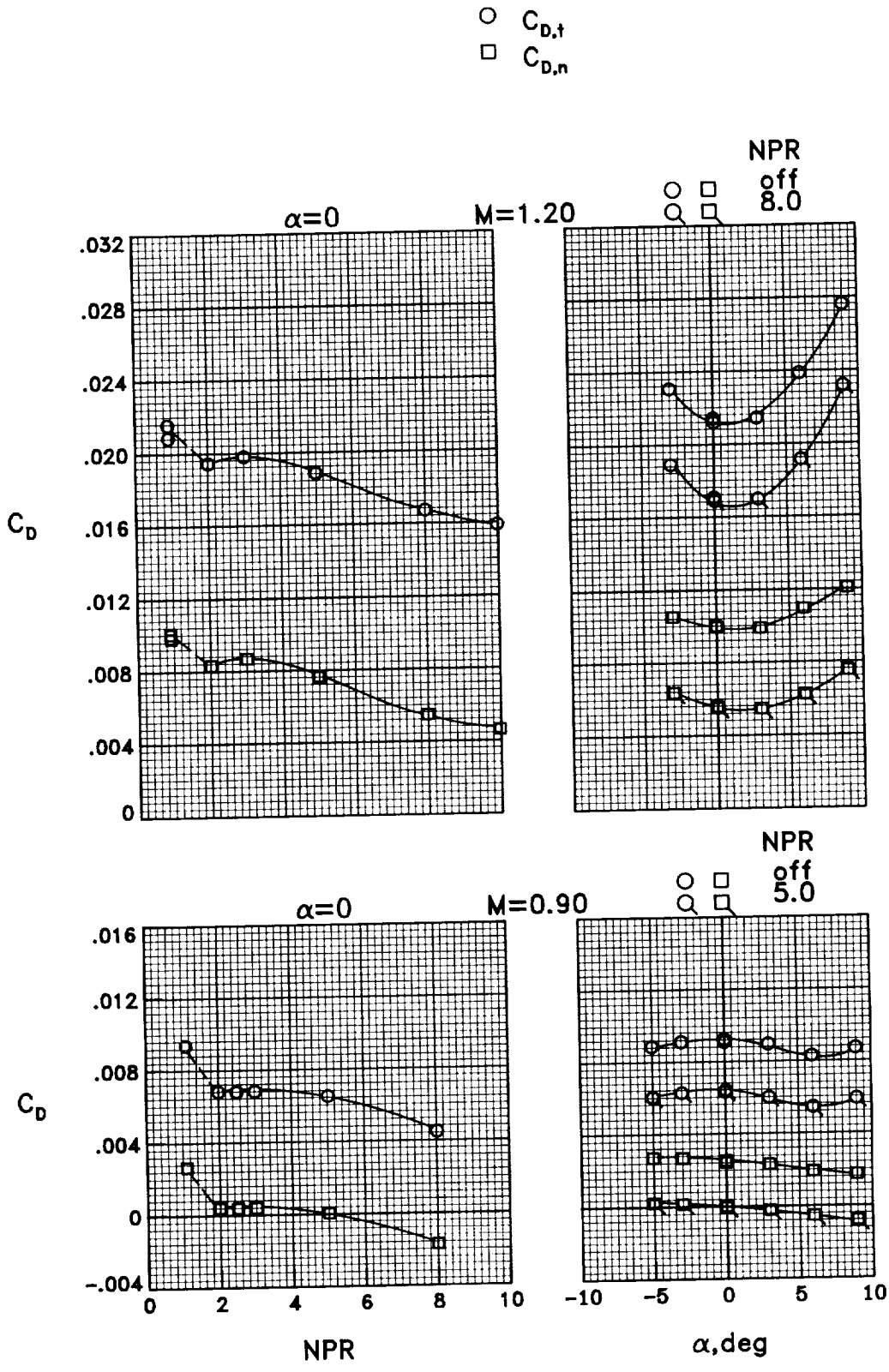

(b) M = 0.90 and 1.20.

Figure 59.- Concluded.

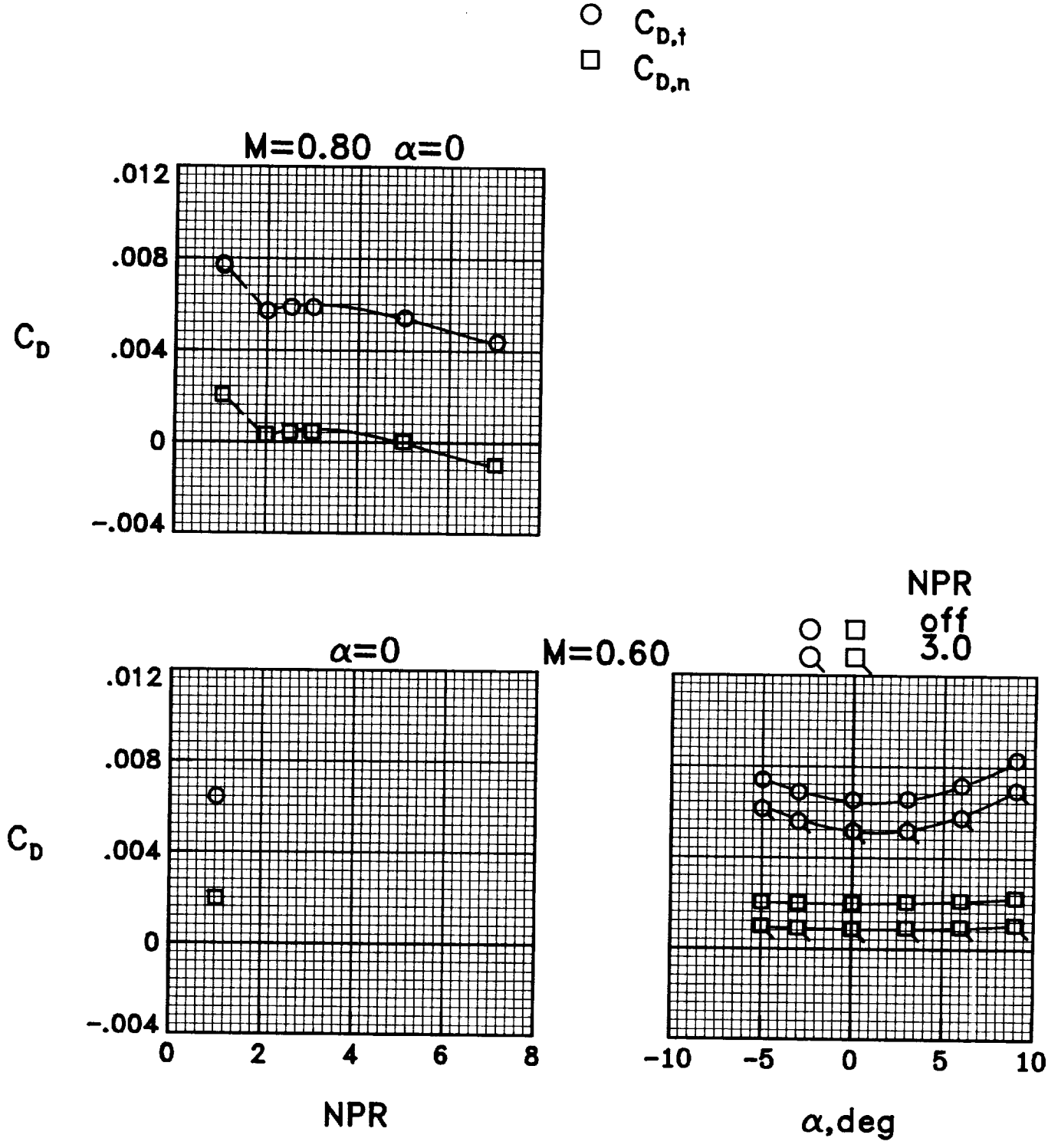

(a) M = 0.60 and 0.80.

Figure 60.- Variation of total drag and nozzle drag coefficients with nozzle pressure ratio and angle of attack for configuration 14.

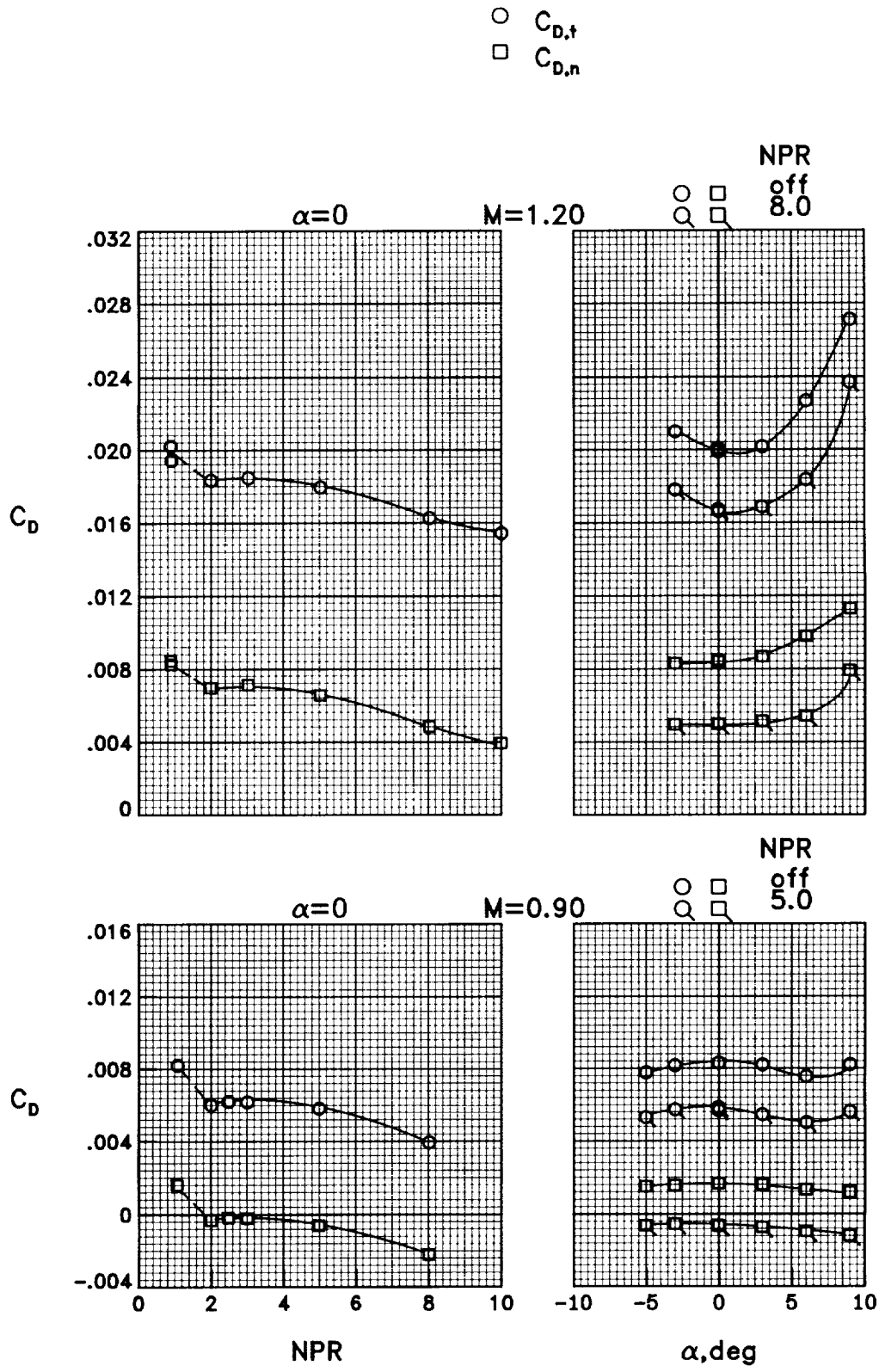

(b) M = 0.90 and 1.20.

Figure 60.- Concluded.

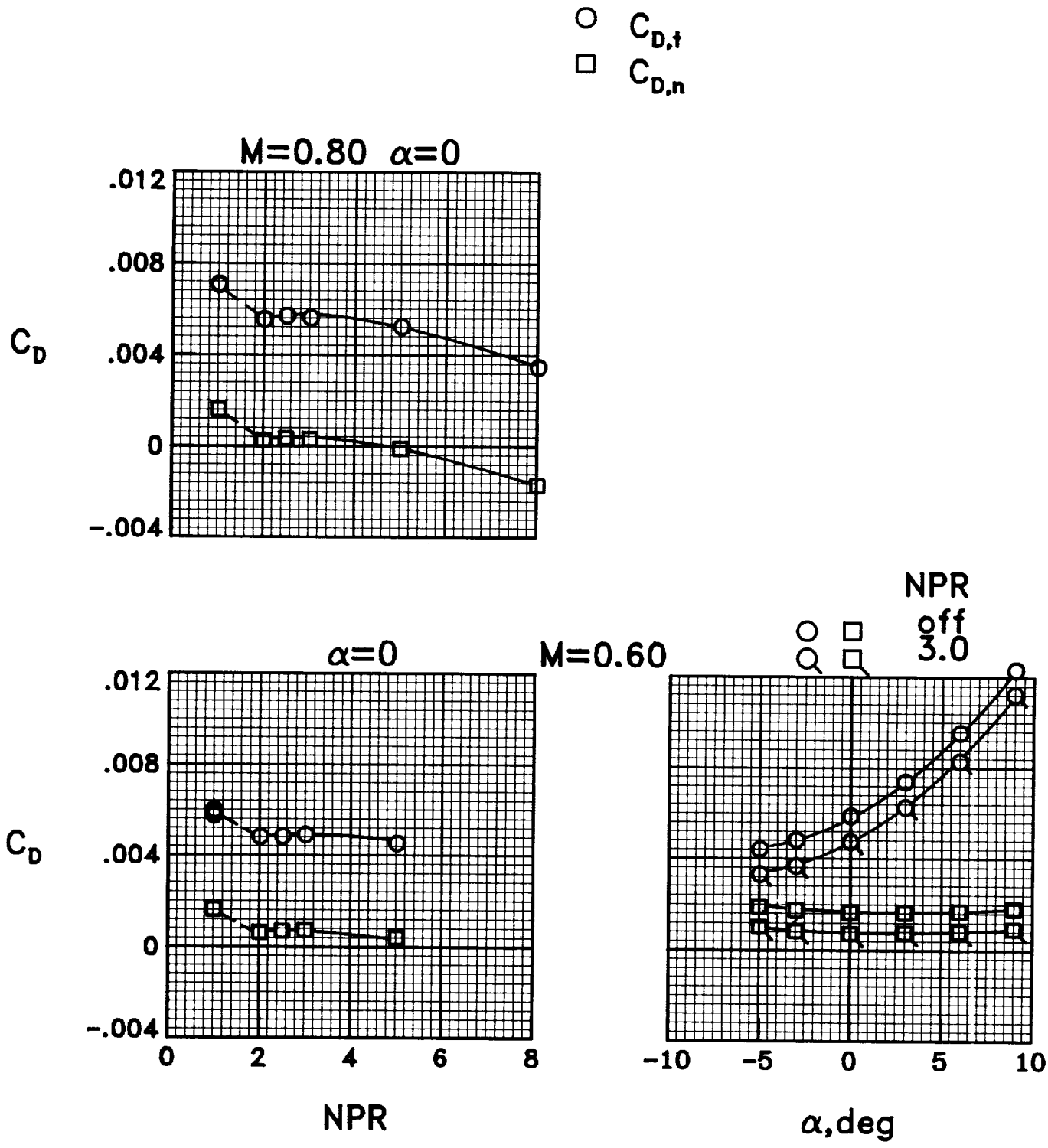

(a) M = 0.60 and 0.80.

Figure 61.- Variation of total drag and nozzle drag coefficients with nozzle pressure ratio and angle of attack for configuration 15.

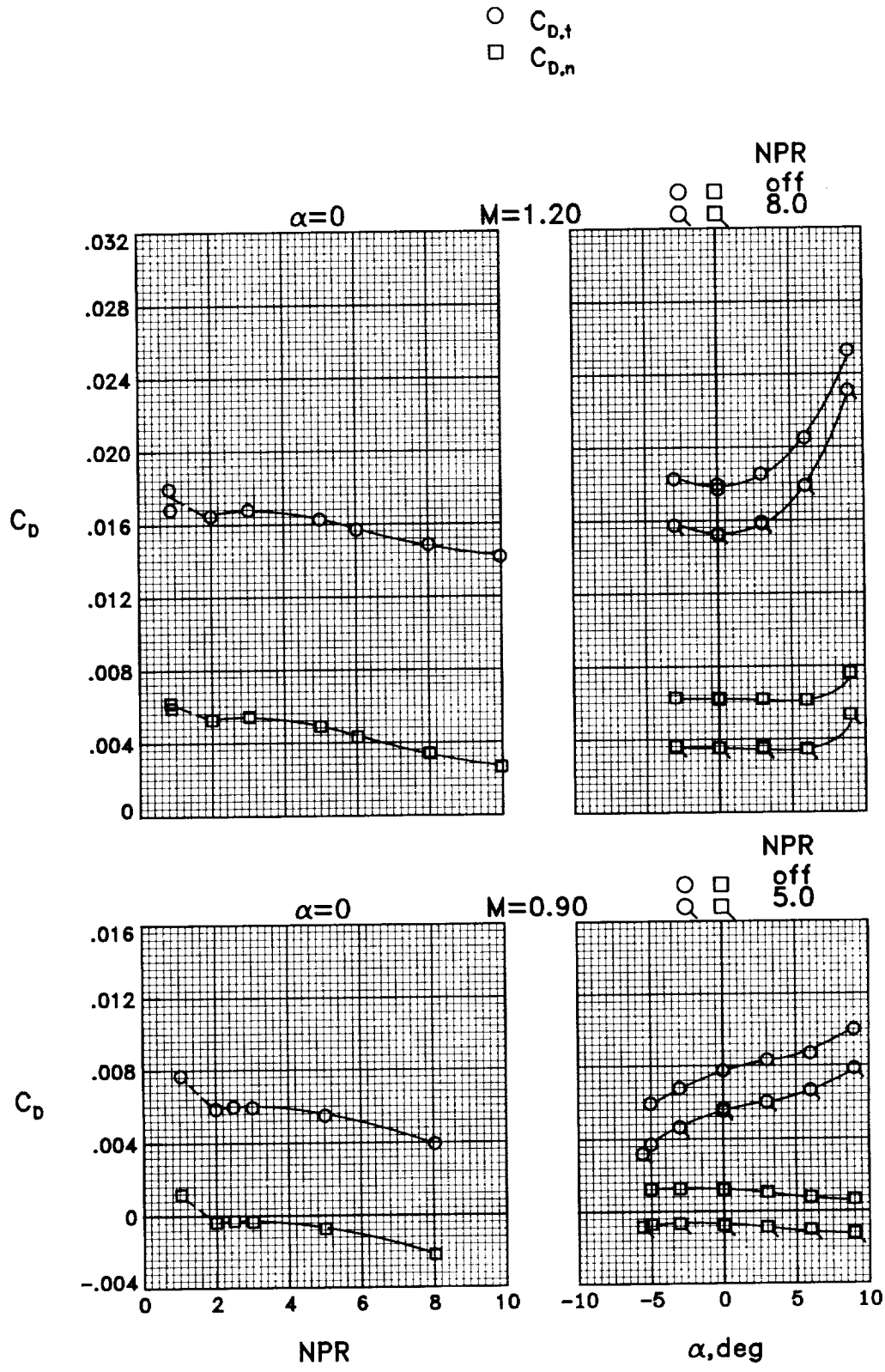

(b) M = 0.90 and 1.20.

Figure 61.- Concluded.

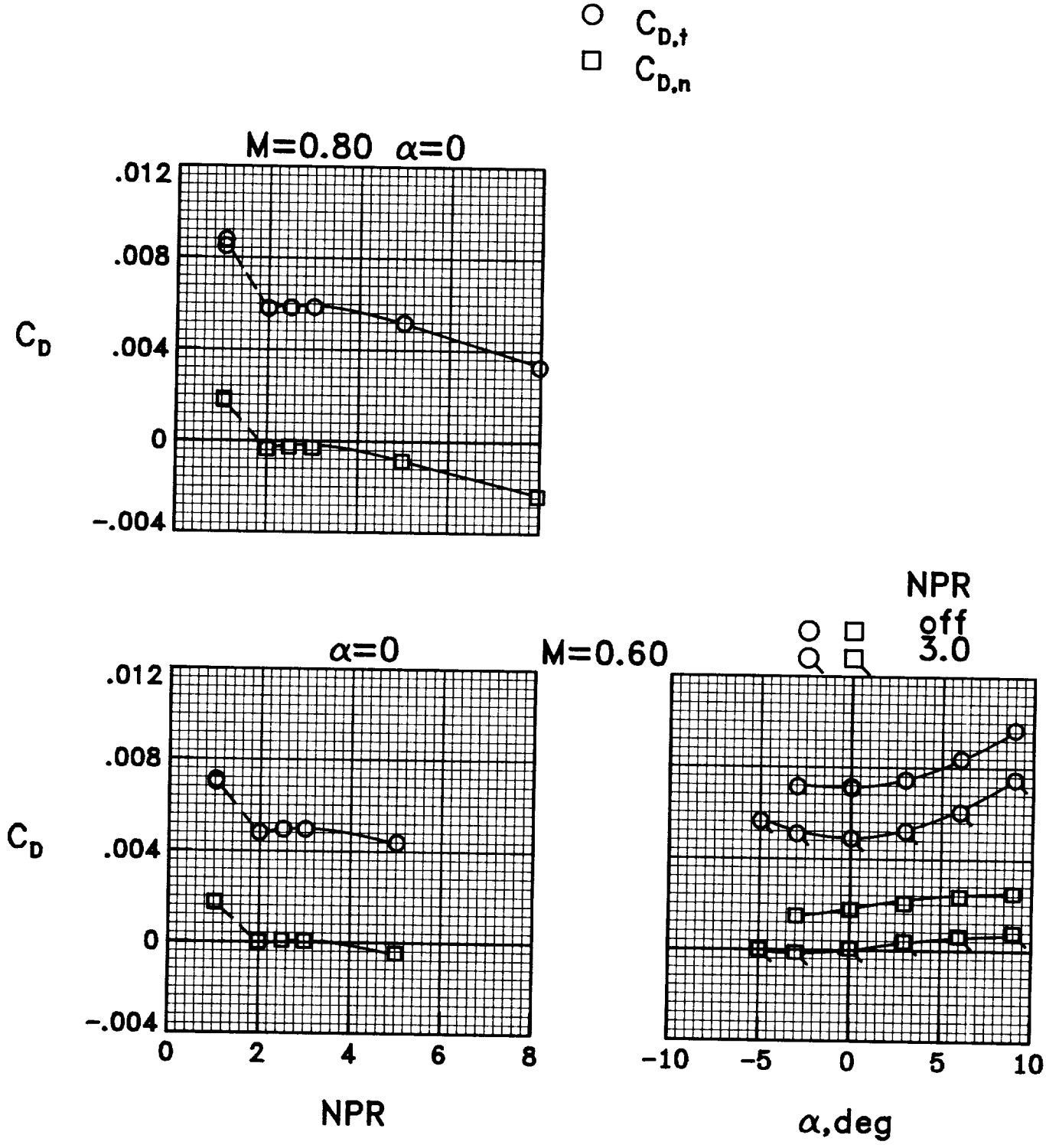

(a) M = 0.60 and 0.80.

Figure 62.- Variation of total drag and nozzle drag coefficients with nozzle pressure ratio and angle of attack for configuration 16.

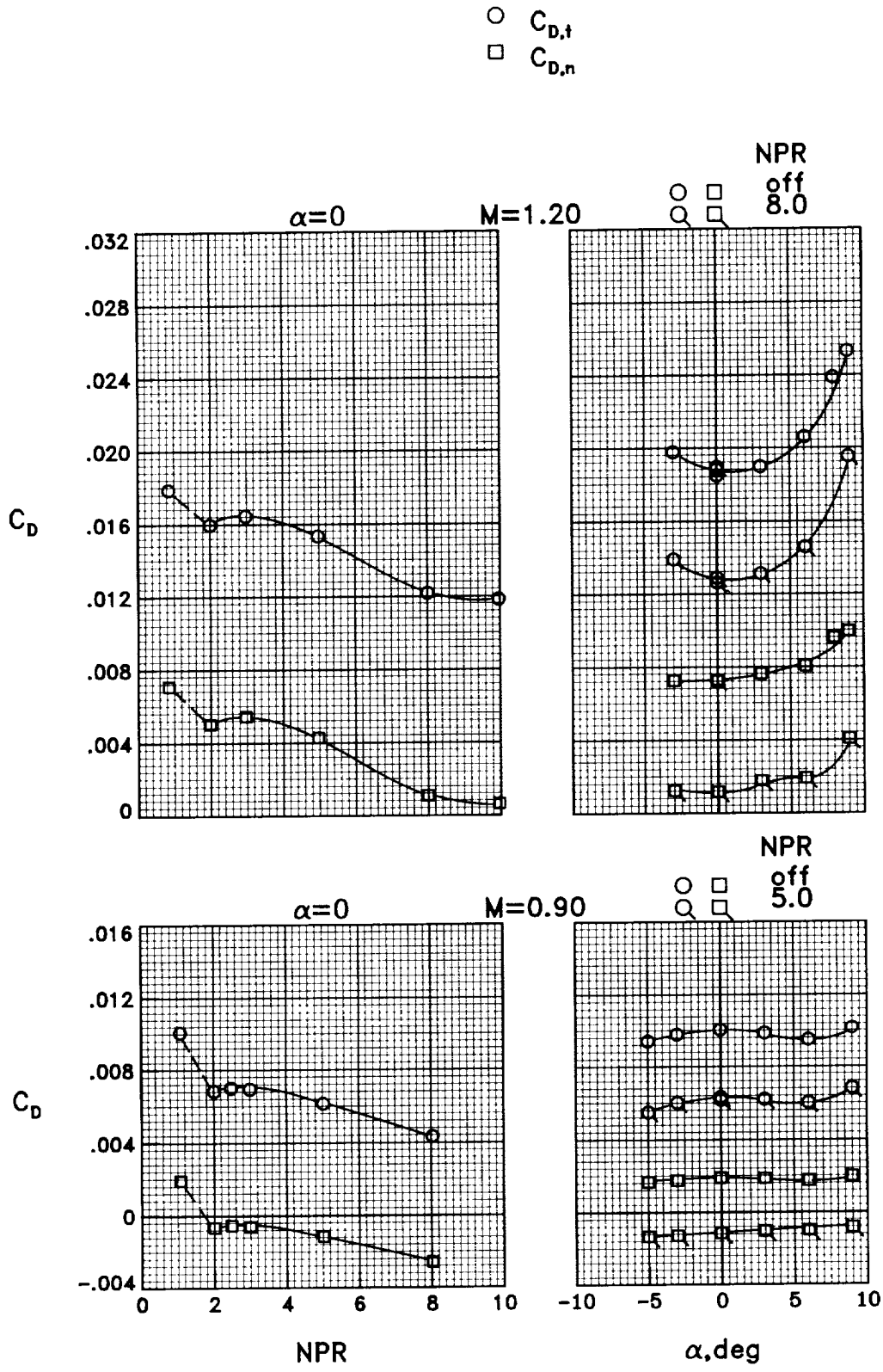

(b) M = 0.90 and 1.20.

Figure 62.- Concluded.

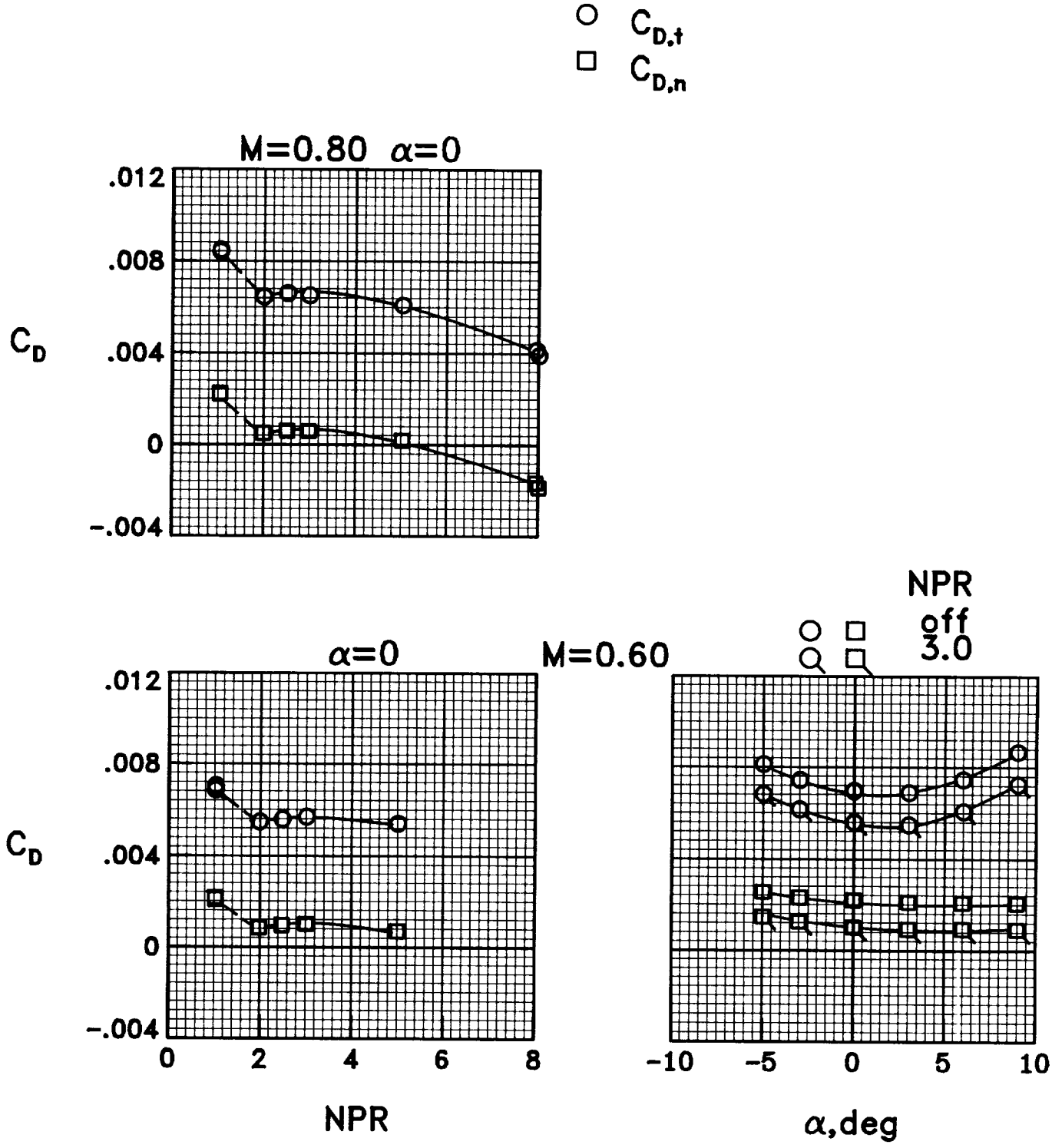

(a) M = 0.60 and 0.80.

Figure 63.- Variation of total drag and nozzle drag coefficients with nozzle pressure ratio and angle of attack for configuration 17.

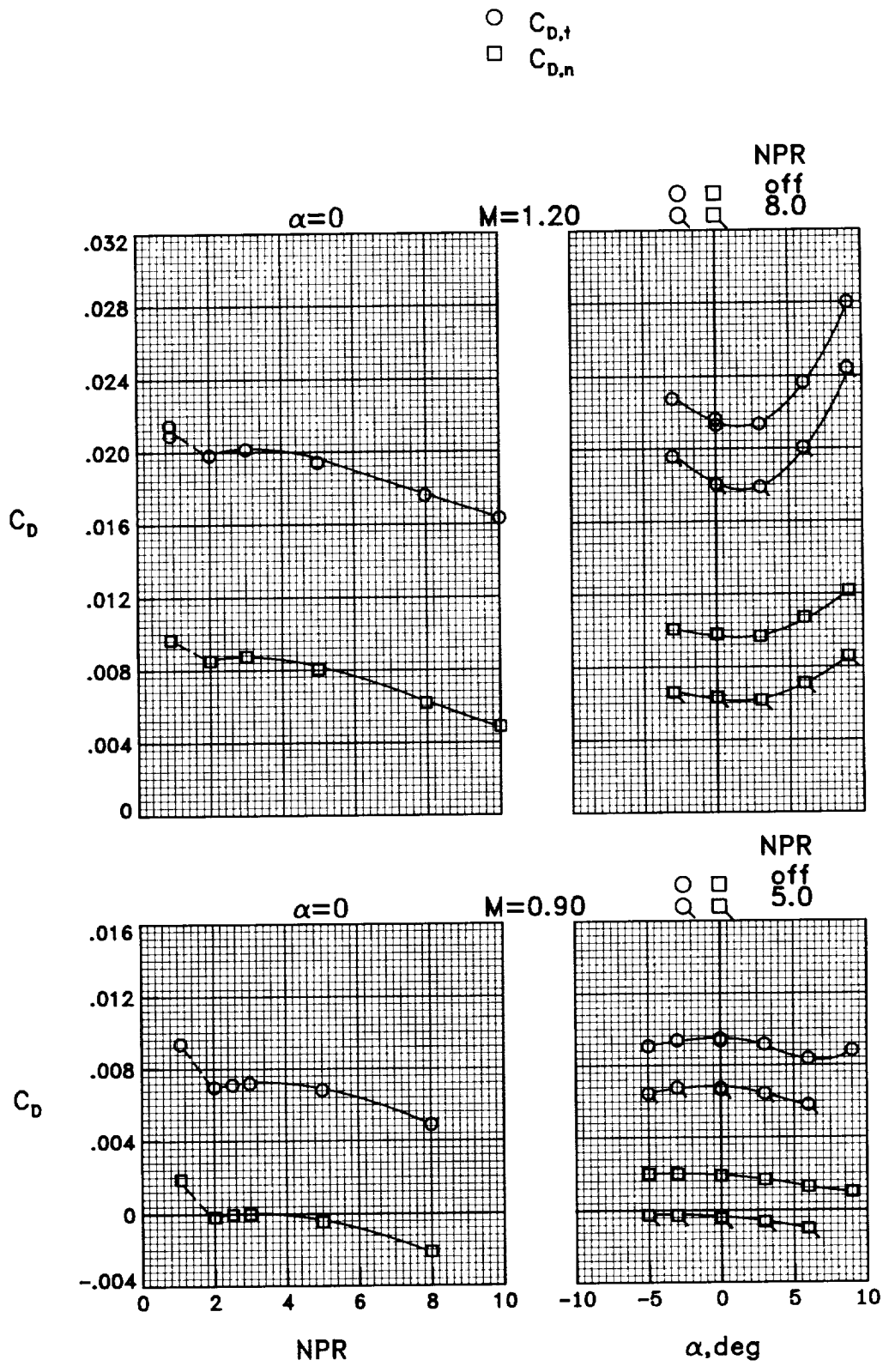

(b) M = 0.90 and 1.20.

Figure 63.- Concluded.

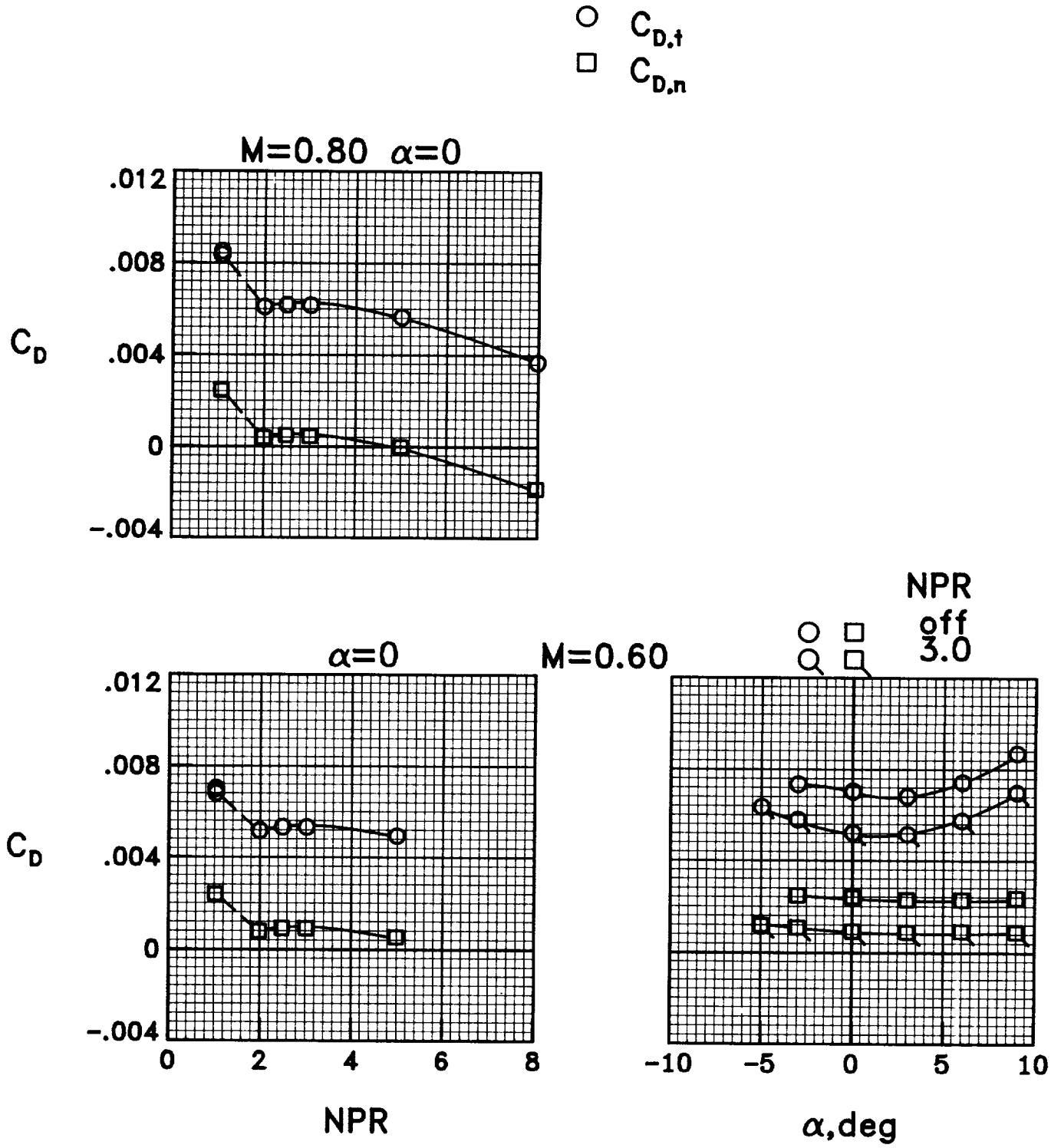

(a) M = 0.60 and 0.80.

Figure 64.- Variation of total drag and nozzle drag coefficients with nozzle pressure ratio and angle of attack for configuration 18.

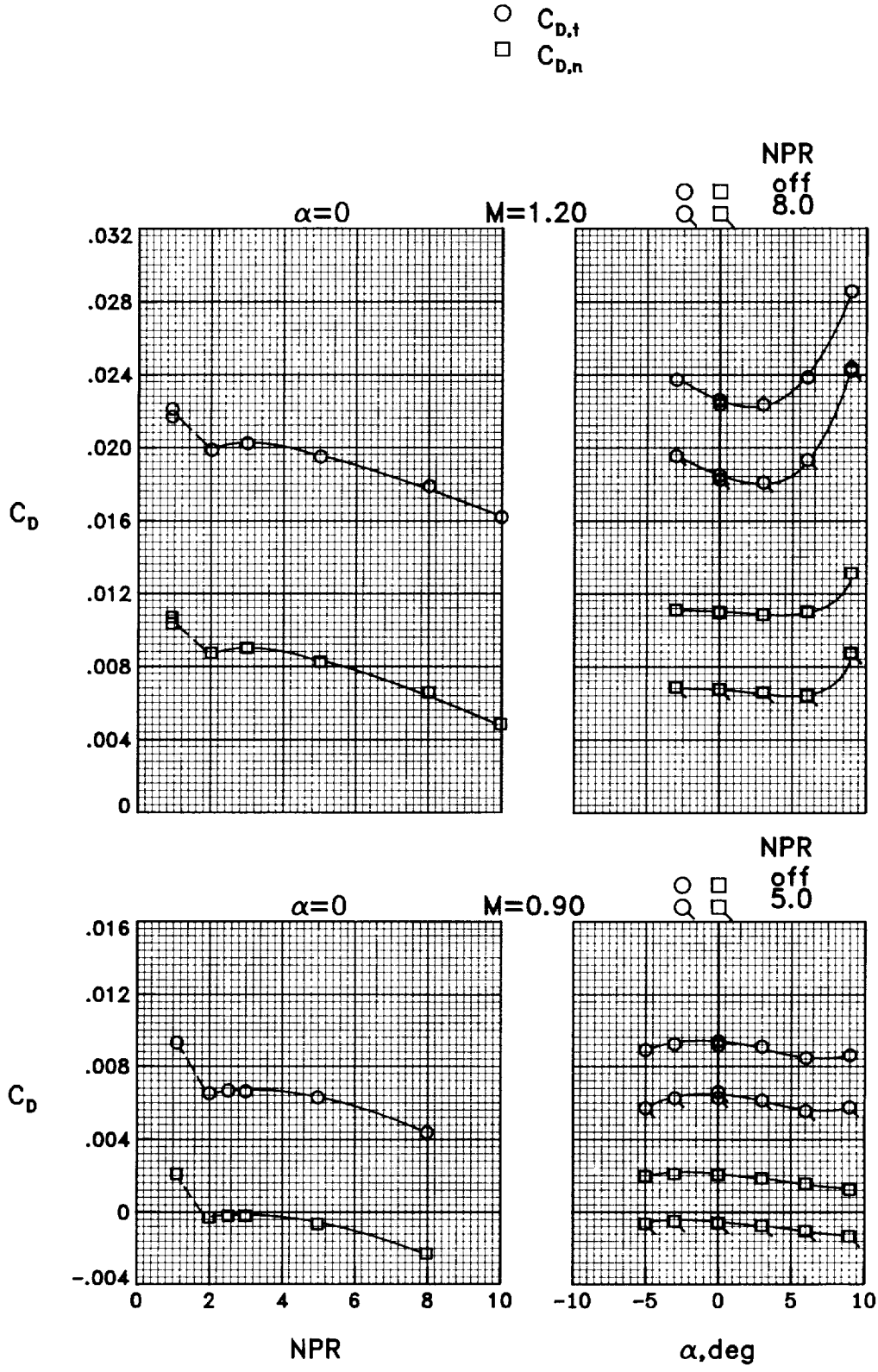

(b) M = 0.90 and 1.20.

Figure 64.- Concluded.

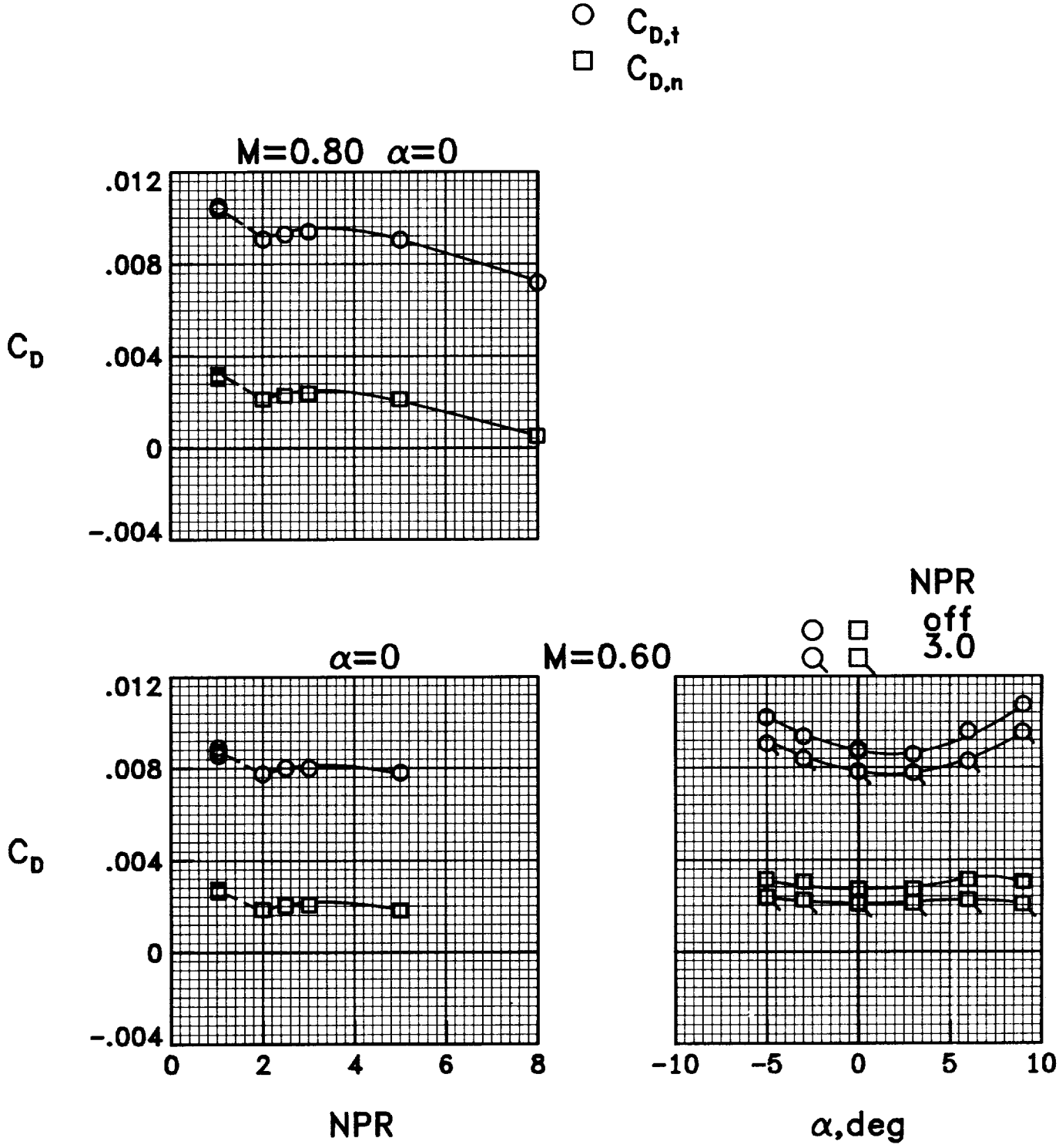

(a) M = 0.60 and 0.80.

Figure 65.- Variation of total drag and nozzle drag coefficients with nozzle pressure ratio and angle of attack for configuration 19.

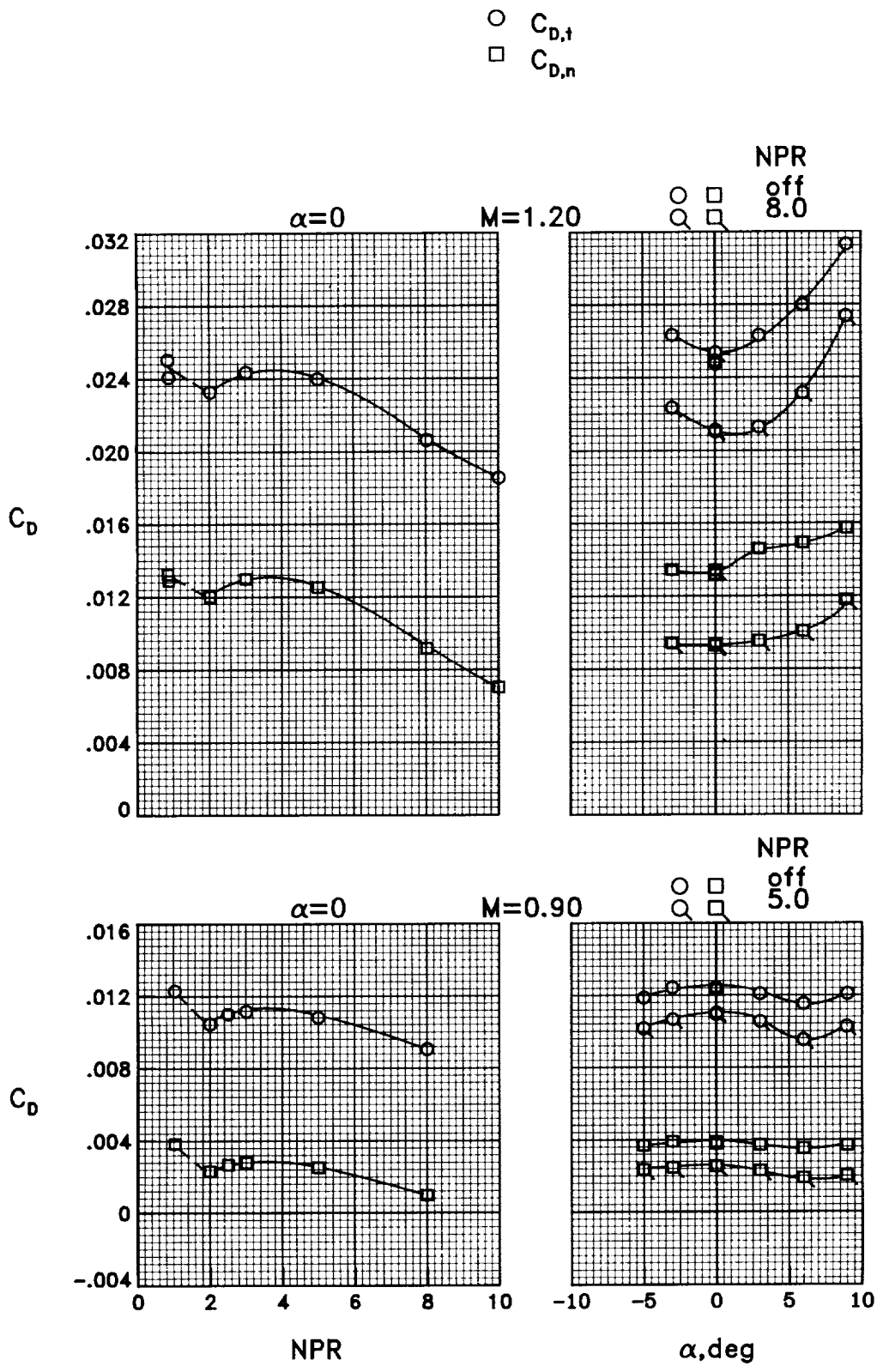

(b) M = 0.90 and 1.20.

Figure 65.- Concluded.

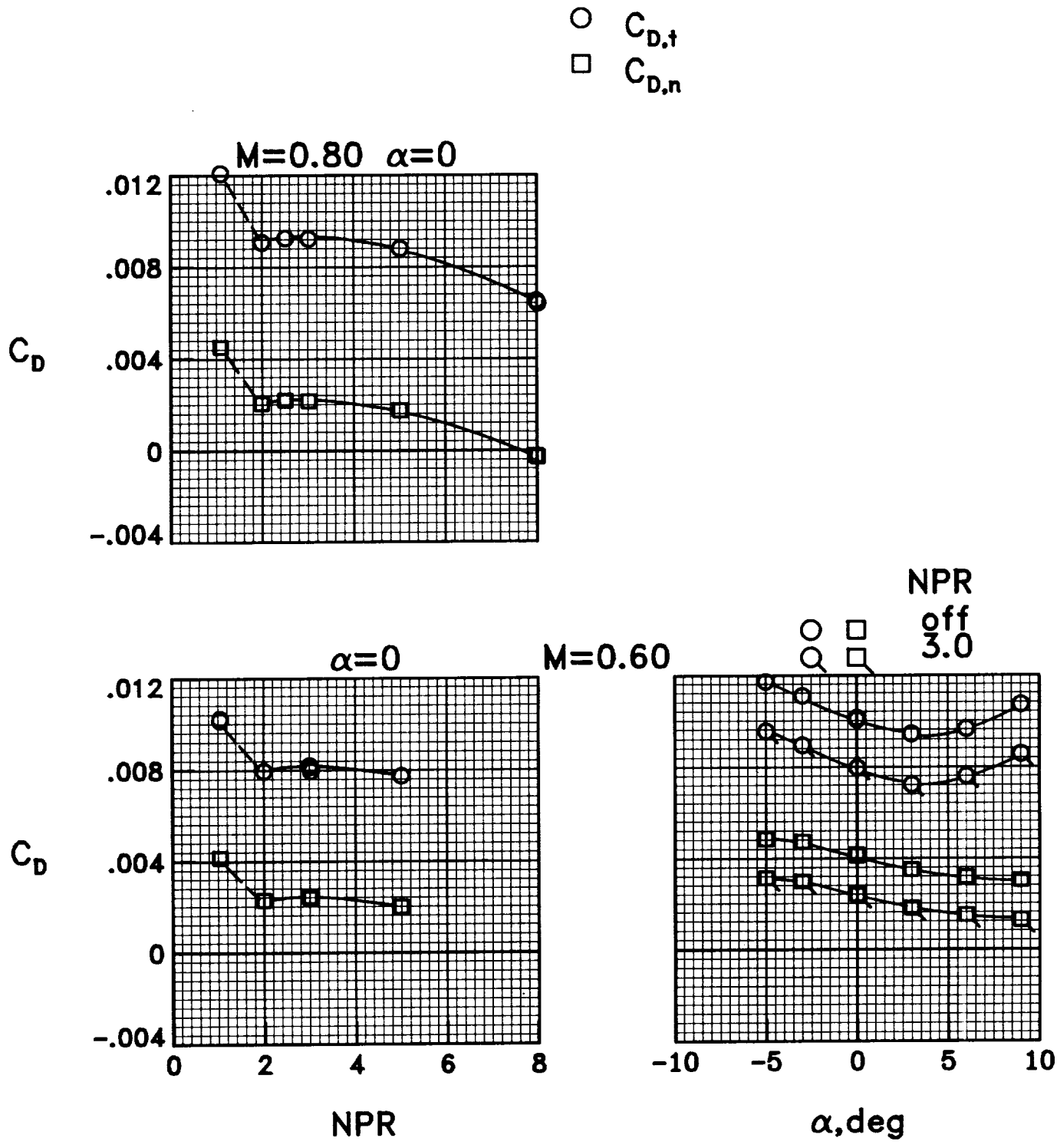

(a) M = 0.60 and 0.80.

Figure 66.- Variation of total drag and nozzle drag coefficients with nozzle pressure ratio and angle of attack for configuration 20.

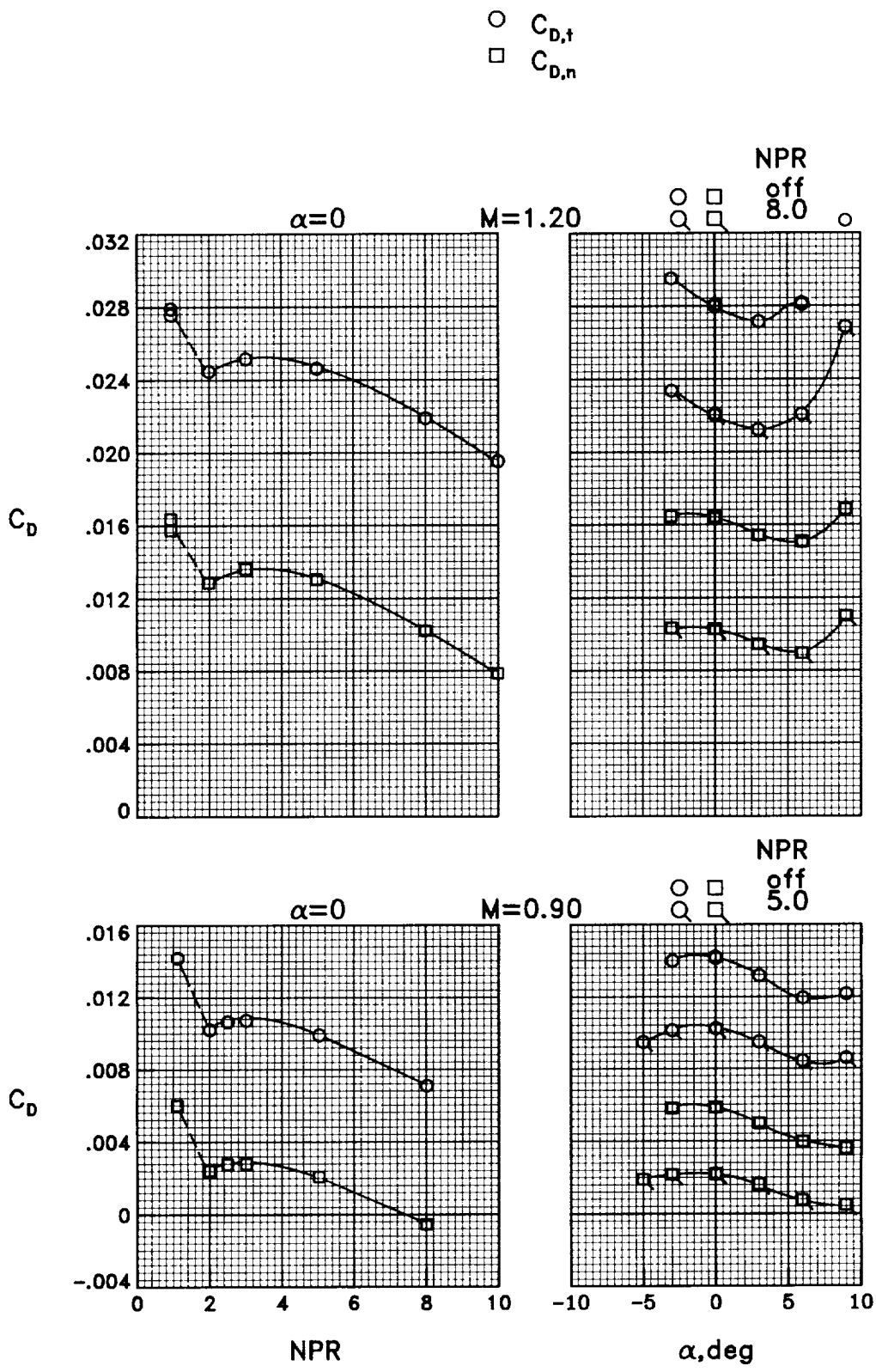

(b) M = 0.90 and 1.20.

Figure 66.- Concluded.

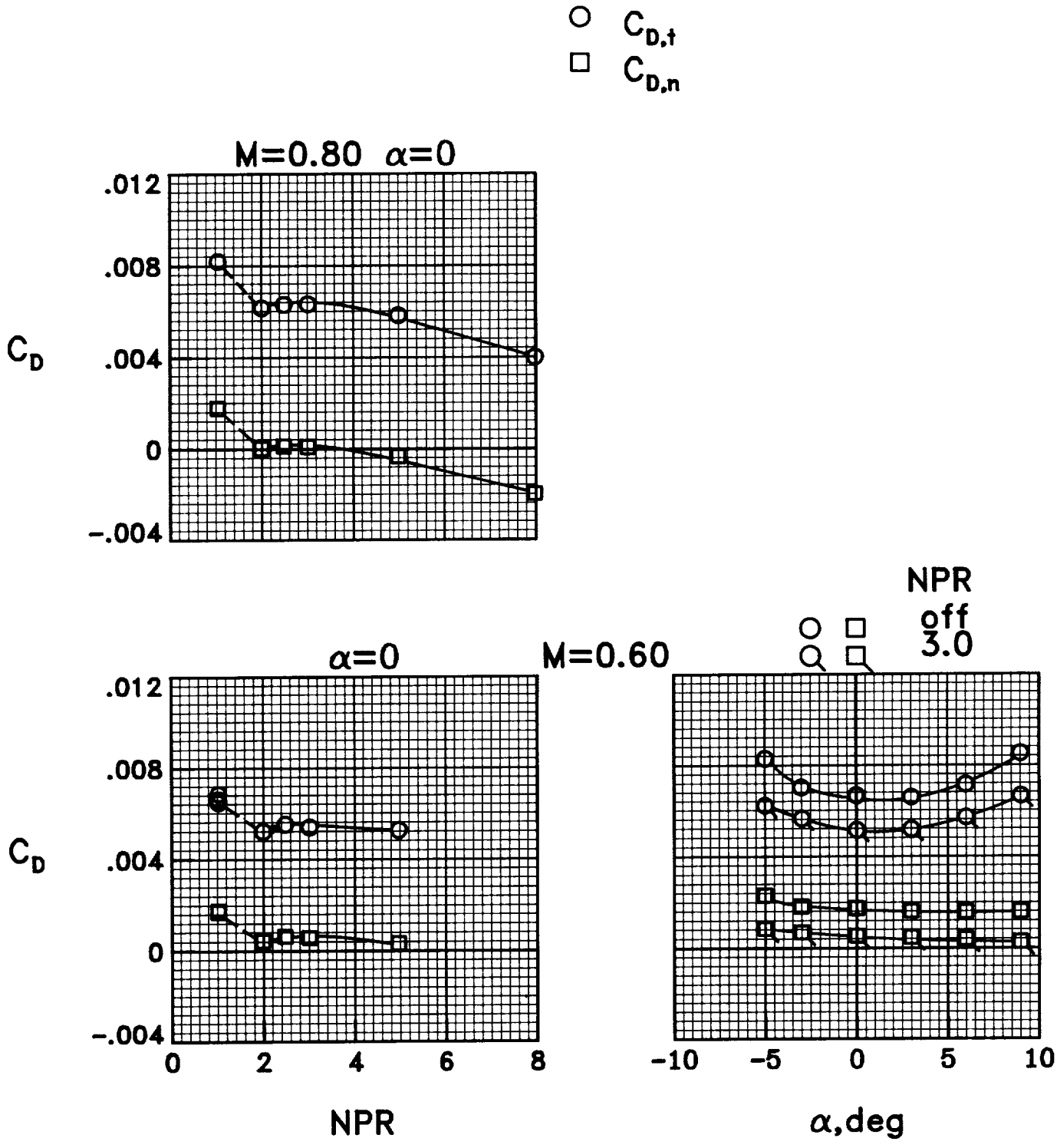

(a) M = 0.60 and 0.80.

Figure 67.- Variation of total drag and nozzle drag coefficients with nozzle pressure ratio and angle of attack for configuration 21.

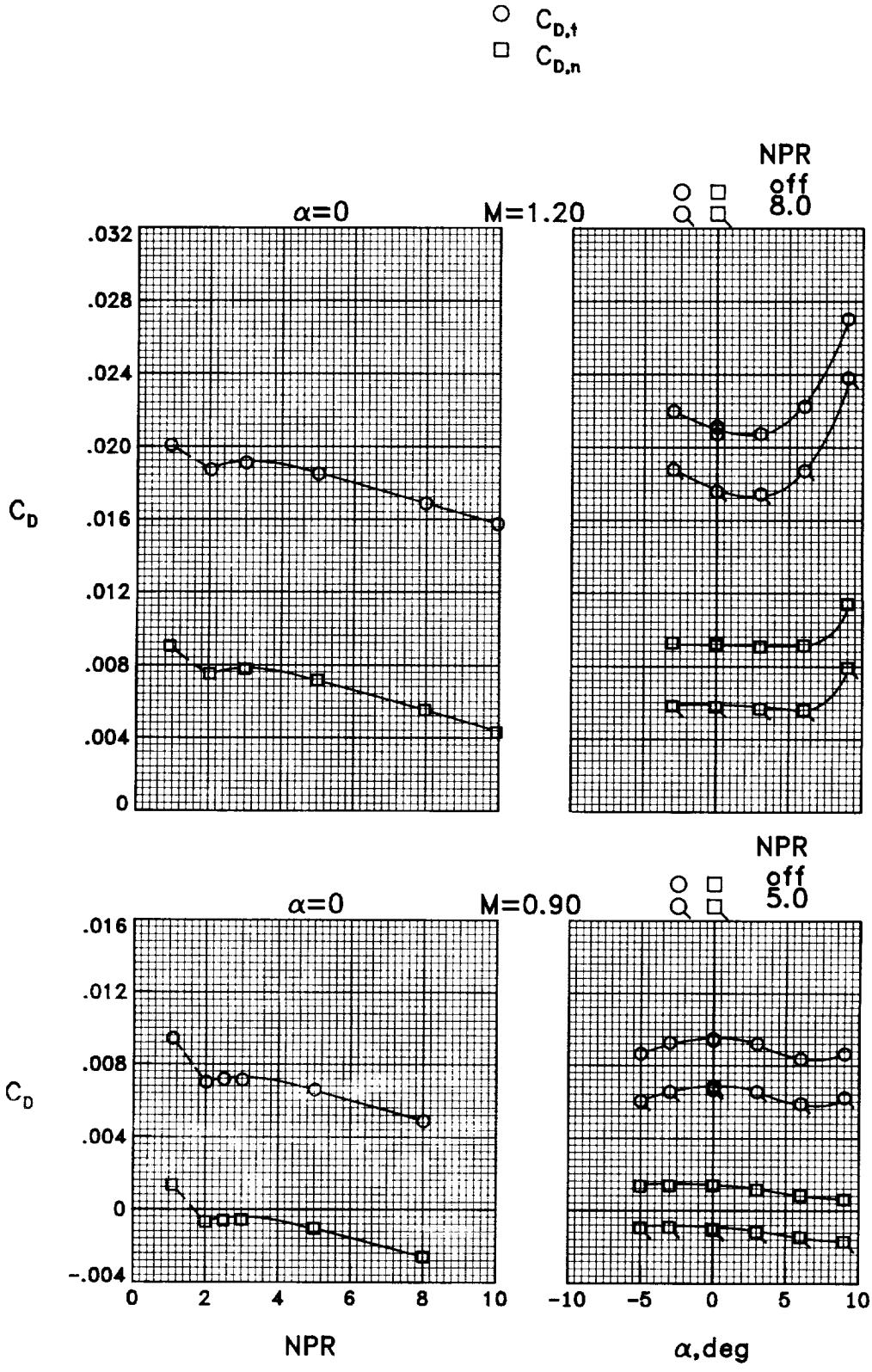

(b) M = 0.90 and 1.20.

Figure 67.- Concluded.

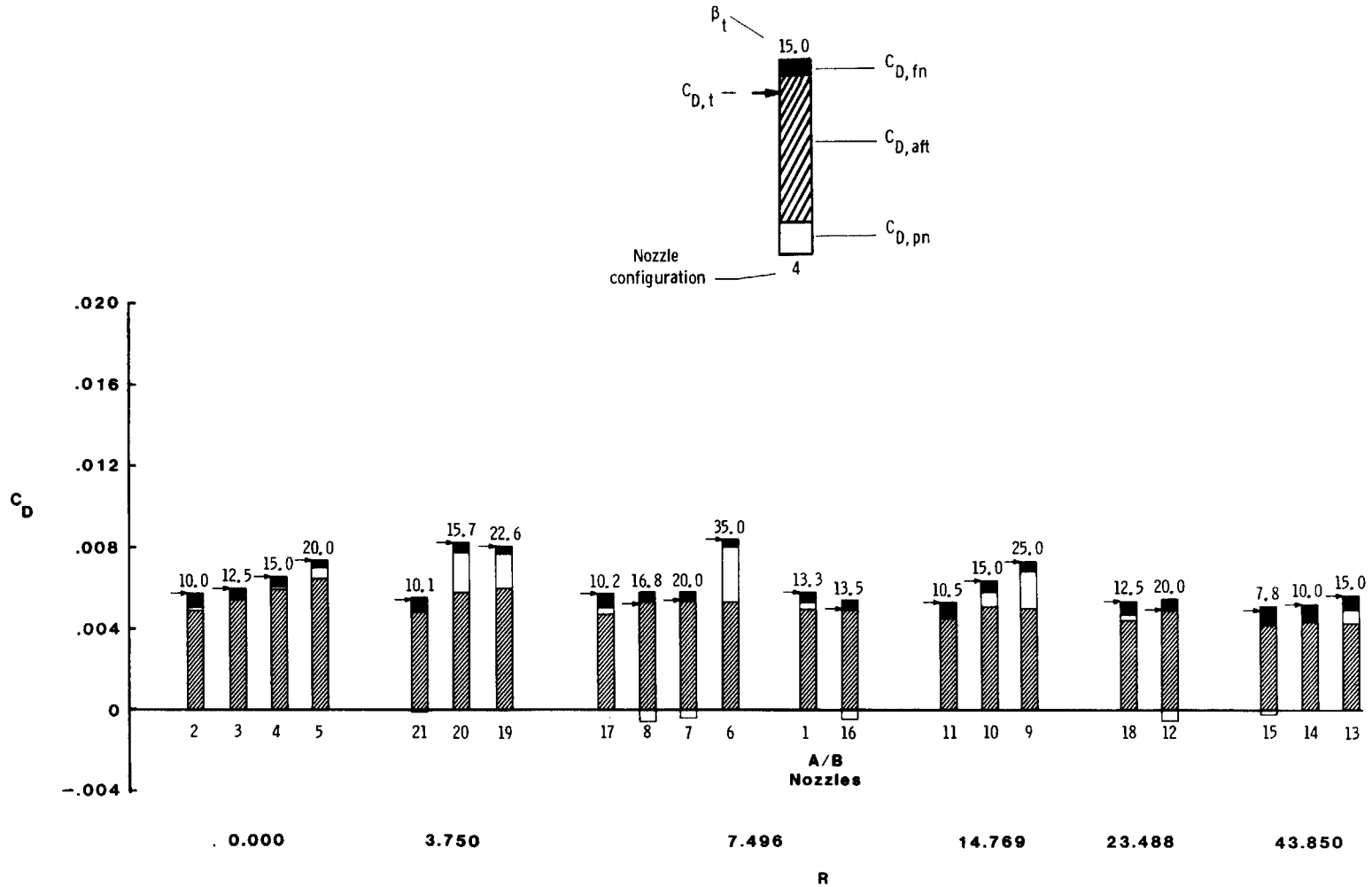

(a) M = 0.60; NPR = 3.0.

Figure 68.- Summary of afterbody/nozzle drag coefficient data grouped by nozzle boattail circular arc radius.

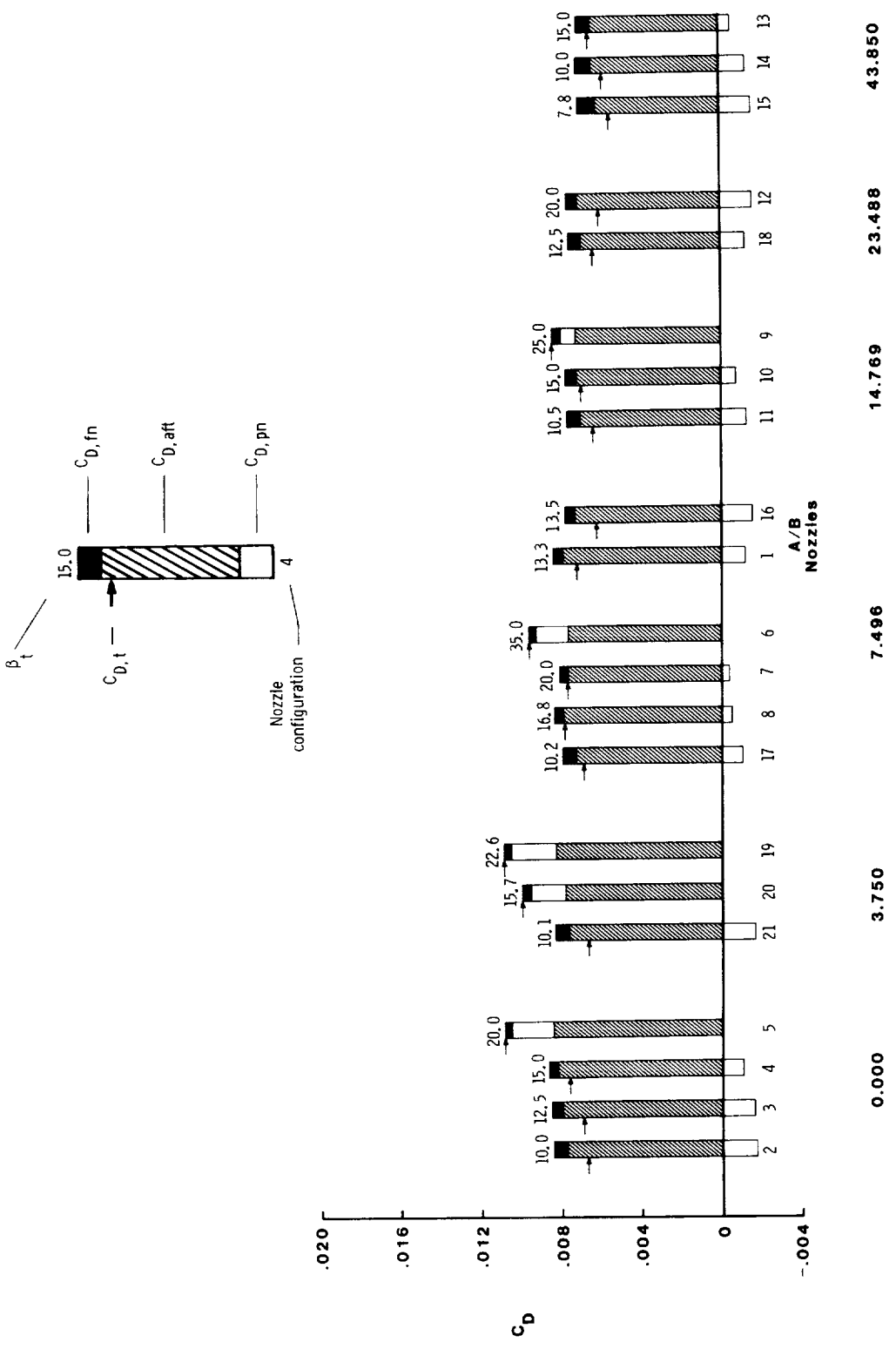

(b) M = 0.90; NPR = 5.0.

Figure 68.- Continued.

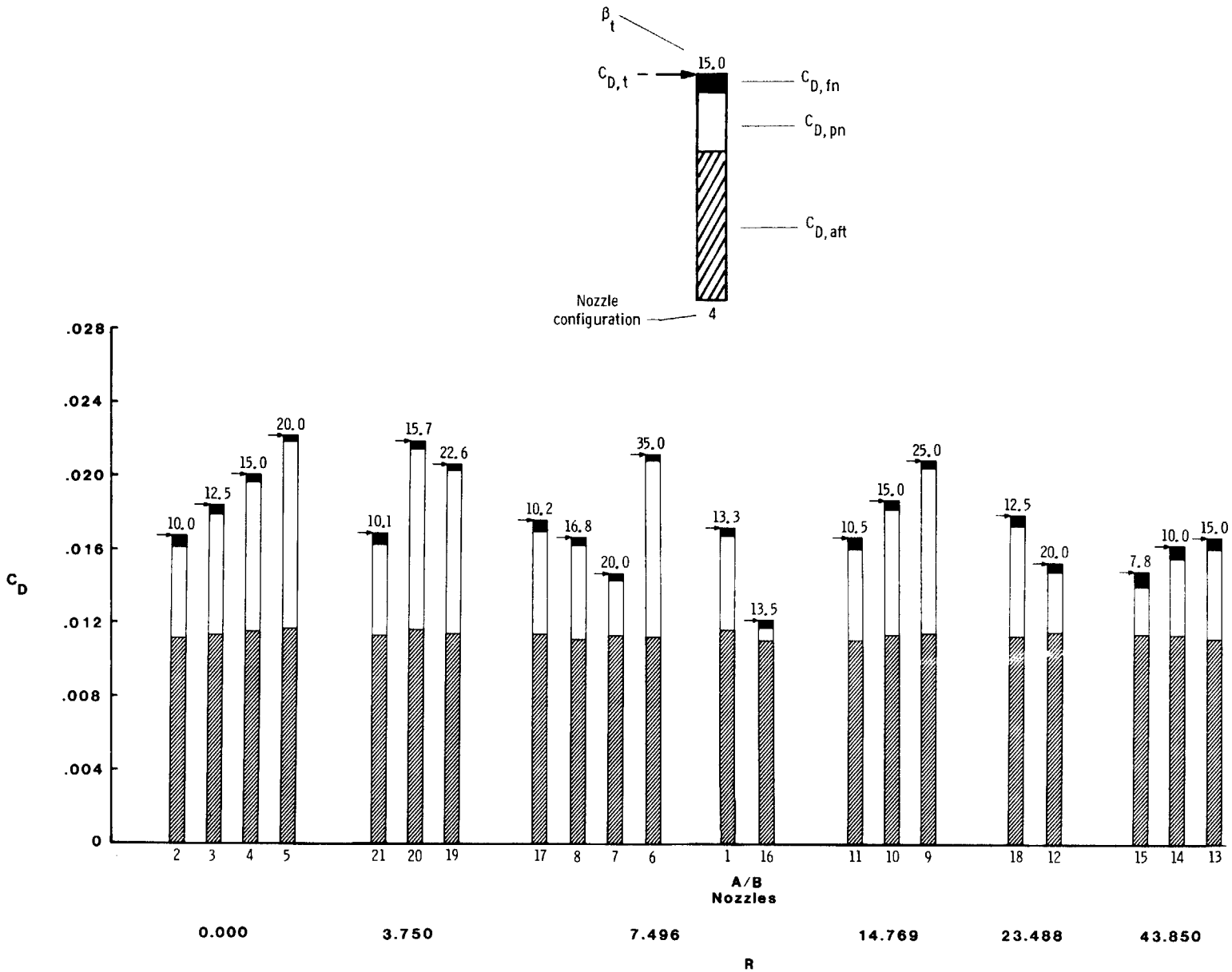

(c) M = 1.20; NPR = 8.0.

Figure 68.- Concluded.

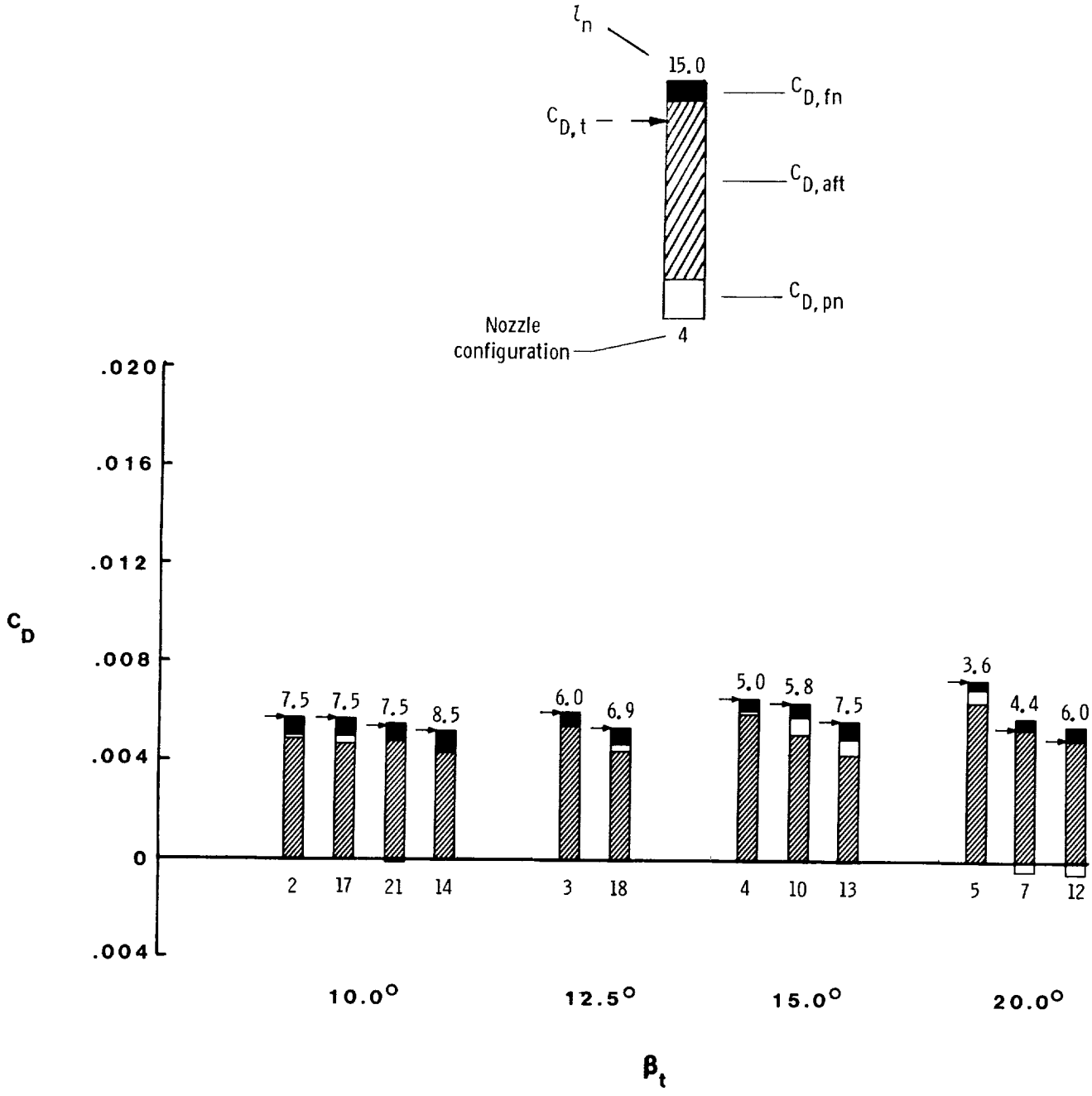

(a) M = 0.60; NPR = 3.0.

Figure 69.- Summary of afterbody/nozzle drag coefficient data grouped by nozzle boattail terminal angle.

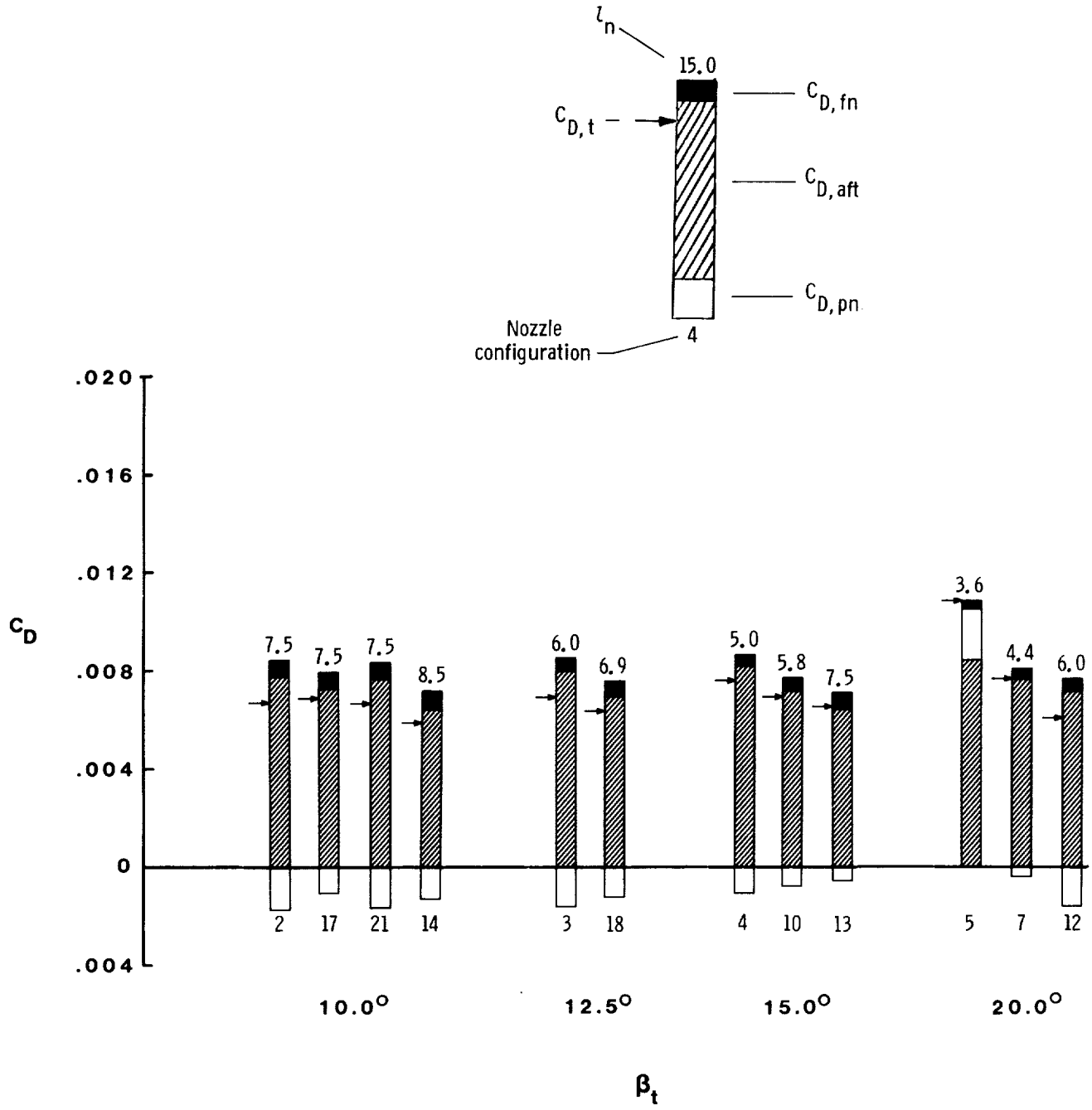

(b) M = 0.90; NPR = 5.0.

Figure 69.- Continued.

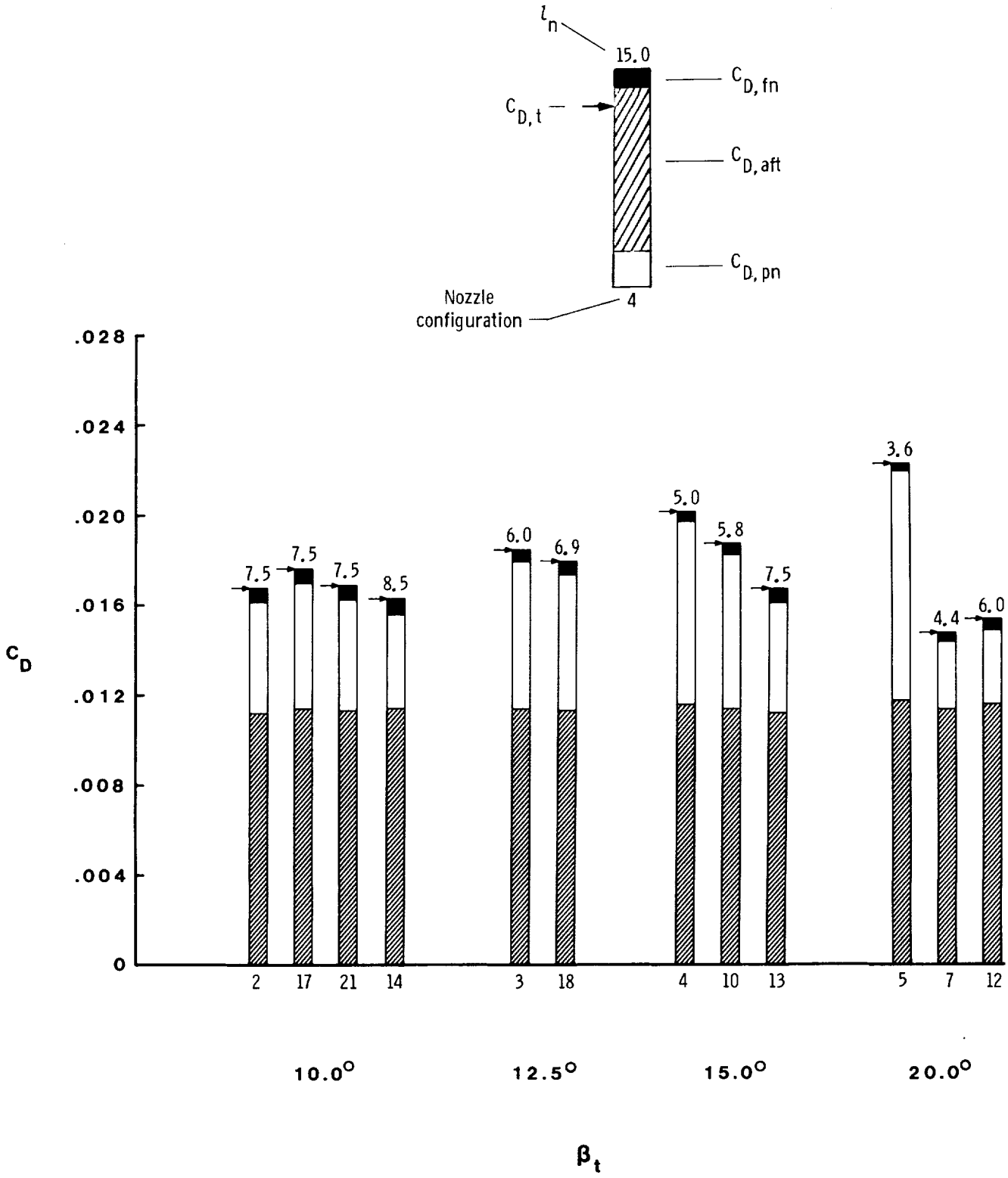

(c) M = 1.20; NPR = 8.0.

Figure 69.- Concluded.

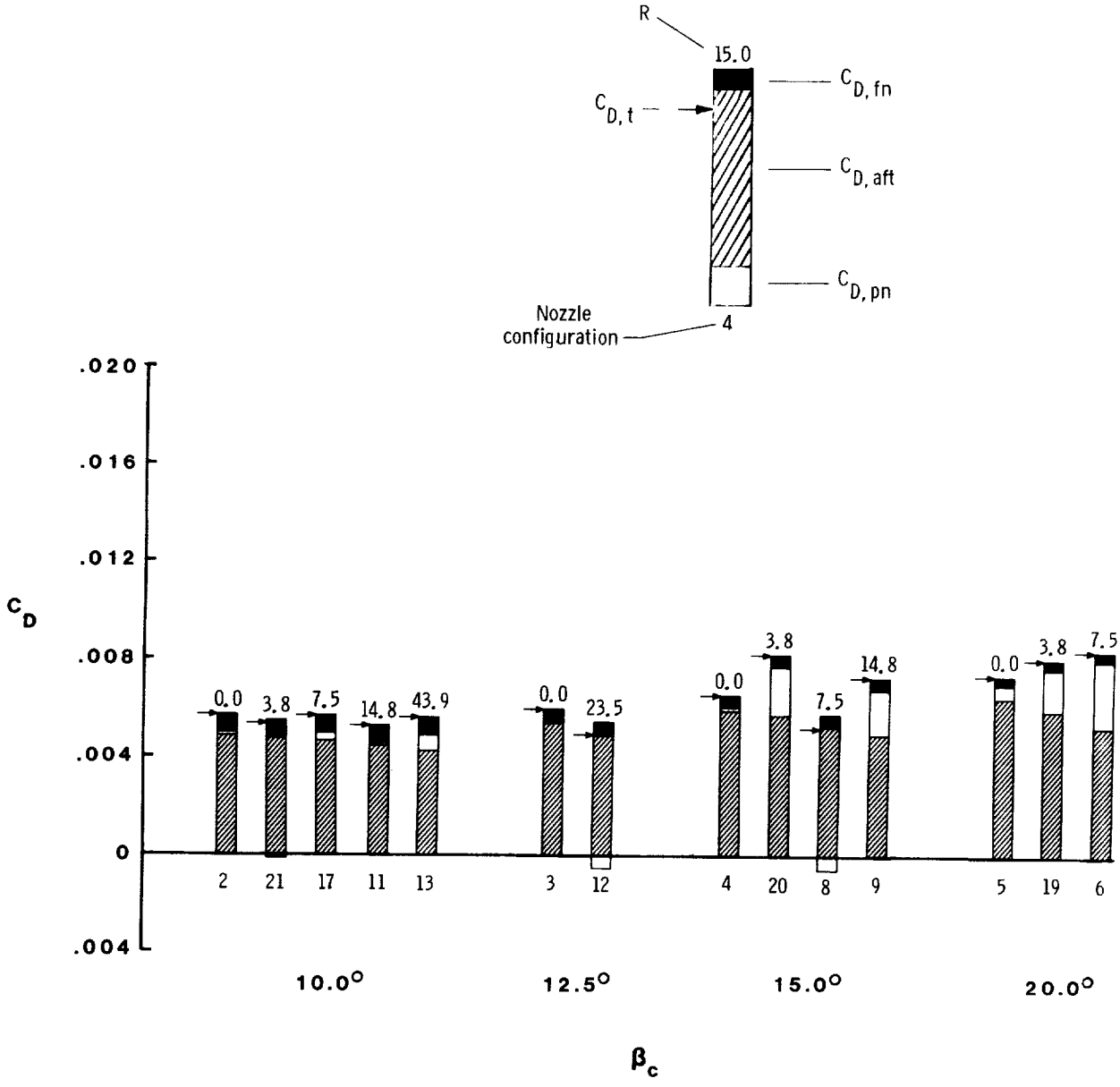

(a) M = 0.60; NPR = 3.0.

Figure 70.- Summary of afterbody/nozzle drag coefficient data grouped by nozzle boattail chord angle.

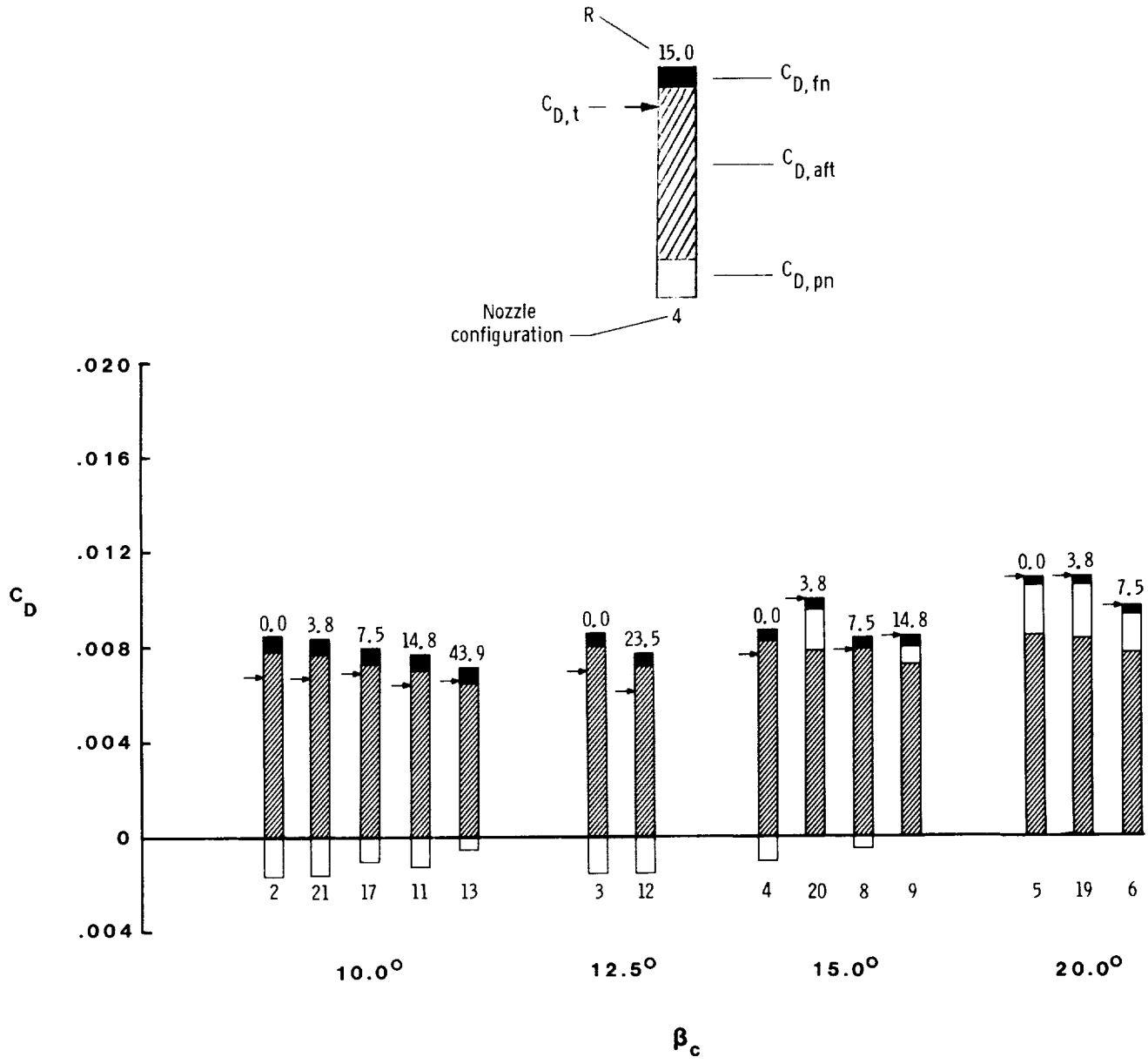

(b) M = 0.90; NPR = 5.0.

Figure 70.- Continued.

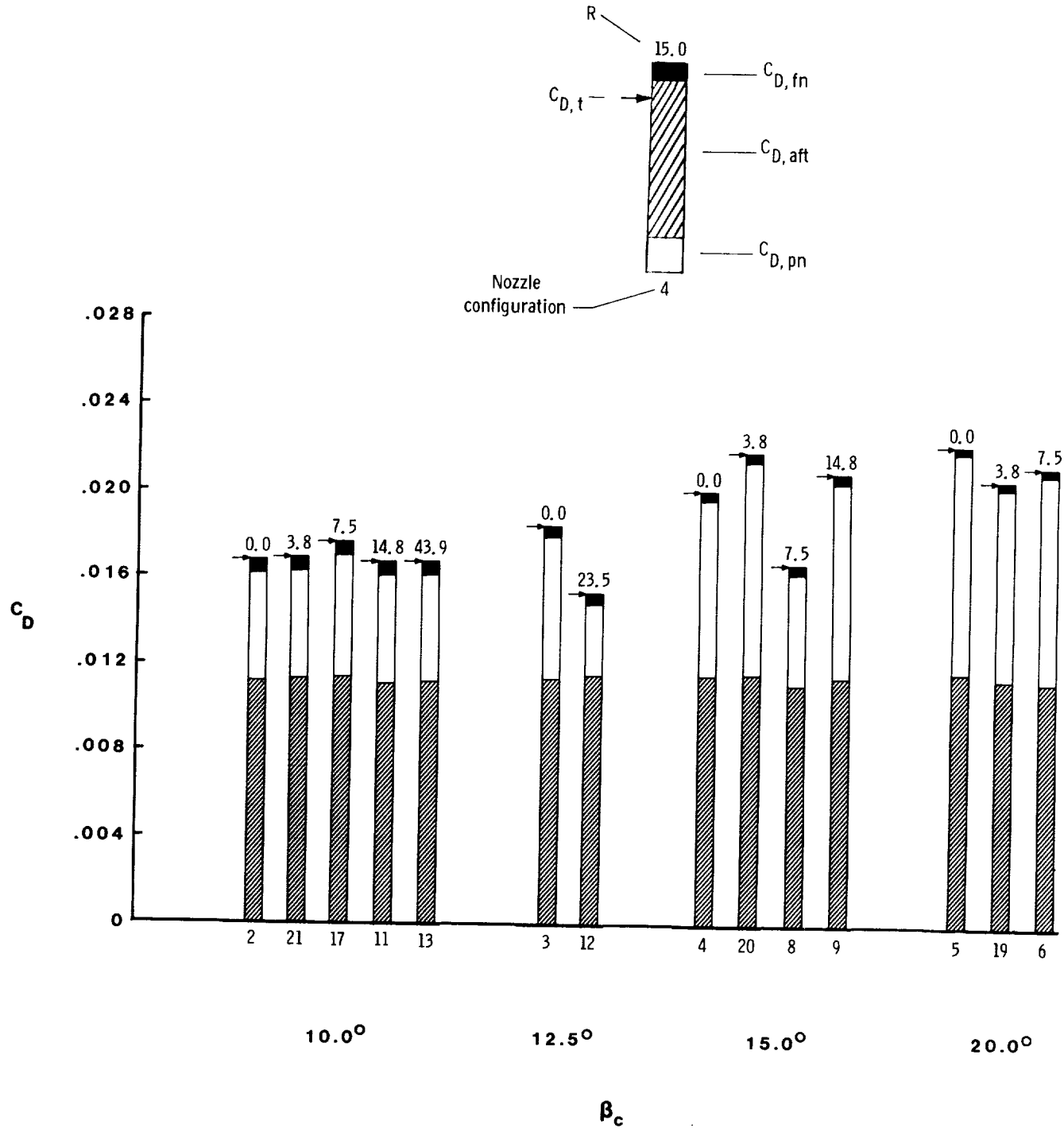

(c) M = 1.20; NPR = 8.0.

Figure 70.- Concluded.

Standard Bibliographic Page

1. Report No.	2. Government Accession No.	3. Recipient's Catalog No.
NASA TP-2640		

4. Title and Subtitle	5. Report Date
Parametric Study of Afterbody/Nozzle Drag on Twin Two-Dimensional Convergent-Divergent Nozzles at Mach Numbers From 0.60 to 1.20	October 1986
	6. Performing Organization Code: 505-62-91-01
7. Author(s): Odis C. Pendergraft, Jr., James R. Burley II, and E. Ann Bare	8. Performing Organization Report No.: L-16158
9. Performing Organization Name and Address: NASA Langley Research Center, Hampton, VA 23665-5225	10. Work Unit No.
	11. Contract or Grant No.
12. Sponsoring Agency Name and Address: National Aeronautics and Space Administration, Washington, DC 20546-0001	13. Type of Report and Period Covered: Technical Paper
	14. Sponsoring Agency Code

15. Supplementary Notes

16. Abstract

An investigation has been conducted in the Langley 16-Foot Transonic Tunnel to determine the effects of upper and lower external nozzle flap geometry on the external afterbody/nozzle drag of nonaxisymmetric two-dimensional convergent-divergent exhaust nozzles having parallel external sidewalls installed on a generic twin-engine, fighter-aircraft model. Tests were conducted over a Mach number range from 0.60 to 1.20 and over an angle-of-attack range from -5° to 9°. Nozzle pressure ratio was varied from jet off (1.0) to approximately 10.0, depending on Mach number.

17. Key Words (Suggested by Authors(s))	18. Distribution Statement
Pressure distributions Afterbody/nozzles Two-dimensional convergent-divergent nozzles Circular arc nozzle flaps Straight nozzle flaps Combination nozzle flaps	[redacted] Until October 1988 Subject Category 02

19. Security Classif.(of this report)	20. Security Classif.(of this page)	21. No. of Pages	22. Price
Unclassified	Unclassified	265	A12

[redacted]

NASA-Langley, 1986